JOURNAL OF THE MYANMAR ACADEMY OF ARTS AND SCIENCE

Physics

Vol. XVIII, No.2A, July, 2020

Myanmar Academy of Arts and Science

Journal of the Myanmar Academy of Arts and Science

Vol. XVIII, No.2A

Contents

Physics

Edition

2020, July, 1000 Copies

Published by

Dr Aung Min (00322) Chairman, Journal Publication Committee,
Myanmar Academy of Arts and Science

ISSN 2520-0186
LCCN 2003-323143

Printed by

U Win Aung (00171), Manager,
Universities Press, Yangon, Myanmar

J. Myanmar Acad. Arts Sci. 2020 **Vol. XVIII.No.2A**

EFFECT OF SINTERING TEMPERATURE ON STRUCTURAL PROPERTIES OF BETA-TRICALCIUM PHOSPHATE*

Cho Cho Khin[1], Nay Win Tun[2], Aye Aye Thant[3] and Khin Khin Win[4]

Abstract

Beta-tricalcium phosphate material (β-TCP) has excellent biocompatibility for medical science applications as bone substitutes. In this research,β-tricalcium phosphate powders, β-TCP, were prepared by the wet chemical precipitation method with calcium nitratetetrahydrate, $Ca(NO_3)_2.4H_2O$, and diammonium hydrogen phosphate, $(NH_4)_2HPO_4$. The pH of the system was controlled by adding sodium hydroxide solution. The dry precipitate was calcined at 700°C and the pellets were sintered at 800°C, 900°C, 1000°C and 1100°C for 6h each. The phase formations of these samples were characterized by using X-ray Diffraction (XRD) analysis. The crystallite sizes and lattice parameters were estimated from the XRD data. The rhombohedral structure of β-TCP phase has been stable after sintering upto 1100°C.The crystallite size is in nano-range and increased with increasing temperatures. The morphological feature of theβ-TCP samples were studied by Scanning Electron Microscope (SEM). Importantly, the dense microstructure without pores could be obtained at sintering temperature of 1100°C.Fourier Transform Infrared Spectroscopy (FTIR) was applied to study the molecular vibrations of functional groups in β-TCP. The presence of β-TCP with the same vibrational modes in all samples has been proved consistently.

Keywords: β-tricalcium phosphate, wet chemical precipitation, XRD, SEM, FTIR

Introduction

Tricalcium phosphate is one of the most important biomaterials and currently recognized as ceramic material that significantly simulates the mineralogical structure of bone.β-tricalcium phosphate powders are widely applied in the biomedical fields because of their biocompatibility and osteoconductivity [Behzad, M., et al., 2012].β-TCP is found to be resorbable in vivo with new bone growth replacing the implanted β-TCP. Theoretically, resorbable β-TCP is an ideal implant material. After implantation, β-TCP will degrade with time and be replaced with natural tissues. It leads to the regeneration of tissues instead of their replacement and so the problem of interfacial stability has been solved[Behzad M., et al, 2014]. β-TCP is known to have significant biological affinity, activity and hence responds well to physiological environments. Because of these positive characteristics, β-TCP is regarded as an ideal bone substitute. In the physiological environment, they are able to gradually degrade, absorb and promote bone growth. They are capable of replacing damaged bone with new tissue [Asmae, M., et al., 2014]. In the present research, a wet chemical precipitation method was carried out to prepare β-TCP and the effect of sintering temperature on its structural properties was investigated.

---

[1] Lecturer, Department of Physics, Mawlamyine University

[2] Dr, Assistant Lecturer, Department of Physics, Dagon University

[3] Dr, Professor, Department of Physics, University of Yangon

[4] Dr, Professor and Head of Department, Department of Physics, University of Yangon

[*] Best Paper Award Winning Paper in Physics (2019)

Materials and Method

Experimental Procedure

β-TCP powders have been synthesizedby the reaction of calcium nitrate tetrahydrate$Ca(NO_3)_2.4H_2O$ with diammonium hydrogenphosphate $(NH_4)_2HPO_4$. The chemical equation that describes the reaction is as shown below.

$$2(NH_4)_2HPO_4+3Ca(NO_3)_2.4H_2O+2NaOH \rightarrow Ca_3(PO_4)_2+4NH_4NO_3+14H_2O+2NaNO_3$$

The Ca:P ratio for stoichiometric β-TCP is 1.5. Keeping that ratio constant, the amount of $(NH_4)_2HPO_4$ required was calculated and the solution was prepared by dissolving $(NH_4)_2HPO_4$ in distilled water. The prepared solution of $(NH_4)_2HPO_4$was added slowly in drop-wise into the $Ca(NO_3)_2.4H_2O$ solution. Throughout the mixing process, the pH of the mixed solution was maintained at pH value of 8 by adding sodium hydroxide (NaOH) solution. The obtained white suspension was stirred for 12 h. The synthesized precipitate was washed with distilled water for four times and then washed with ethanol for three times to improve the dispersion characteristics. After filtrating the compact, the filtered cake was dried at 80°C for 24 h. The dried powders were then crushed with A-gate mortar and pestle and calcined at 700°C for2 h. The synthesizedβ-TCP powders have been pressed into pellet by uniaxial hydraulic press. The pellets were sintered at 800°C, 900°C, 1000°C and 1100°C for 6h each. The phase formations of these samples were characterized by using X-ray Diffraction (XRD) analysis. The crystallite sizes and lattice parameters were estimated from the XRD data. The morphological feature of β-TCP samples was studied by Scanning Electron Microscope (SEM). Fourier Transform Infrared Spectroscopy (FTIR) was applied to study the molecular vibrations of functional groups in β-TCP. Figure 1 shows the flowchart of wet chemical precipitation process used for preparation of β-TCP sample.

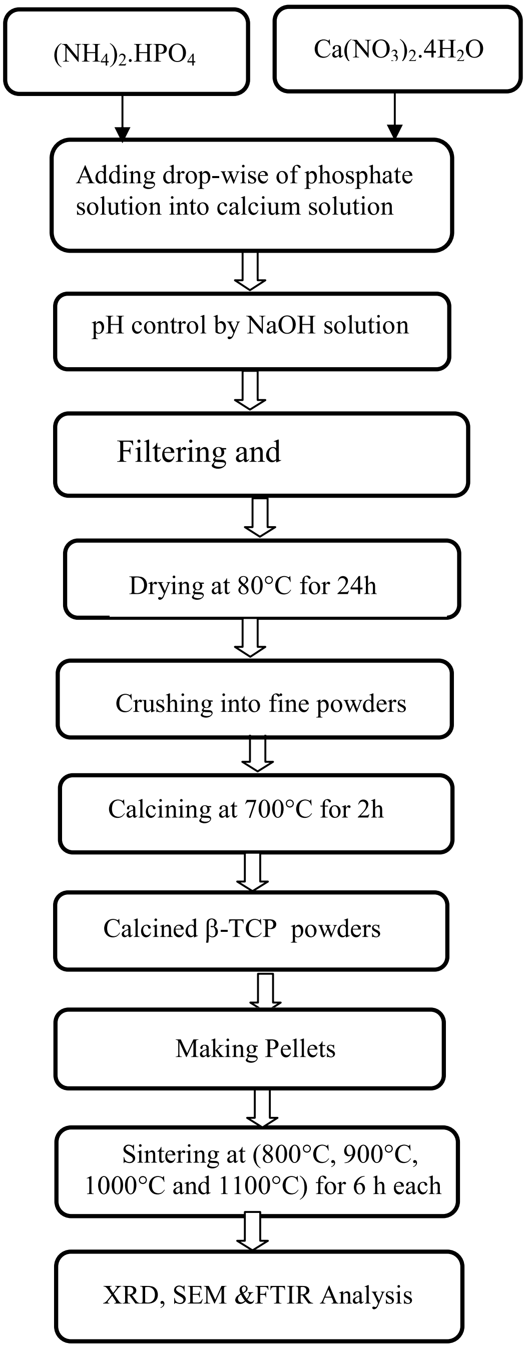

Figure 1 Flowchart of wet chemical precipitation process used for preparation of β-TCP sample

Results and Discussion

Phase Formation by XRD Analysis

Prior to the preparation of β-TCP, the phase of the raw materials was characterized by using XRD analysis. The XRD pattern of $(NH_4)_2HPO_4$ is shown in Figure 2. The pattern has confirmed that the powder can be considered as single phase, $(NH_4)_2HPO_4$. All diffractions could be indexed as $(NH_4)_2HPO_4$ according to ICDD card (76-0414). It is confirmed that there is no impurity and only the phase of $(NH_4)_2HPO_4$ presents in the sample. The XRD pattern of $Ca(NO_3)_2.4H_2O$ is shown in Figure 3. All diffractions could be indexed as $Ca(NO_3)_2.4H_2O$

according to ICDD card (73-0988). It is confirmed the presence of the phase $Ca(NO_3)_2.4H_2O$in the sample.

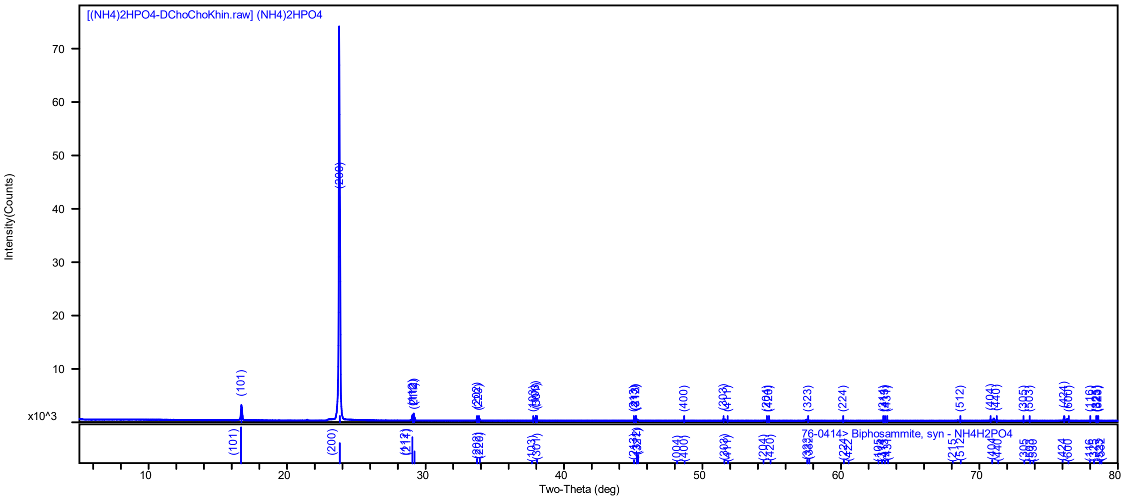

Figure 2 XRD pattern of raw $(NH_4)_2HPO_4$ powder

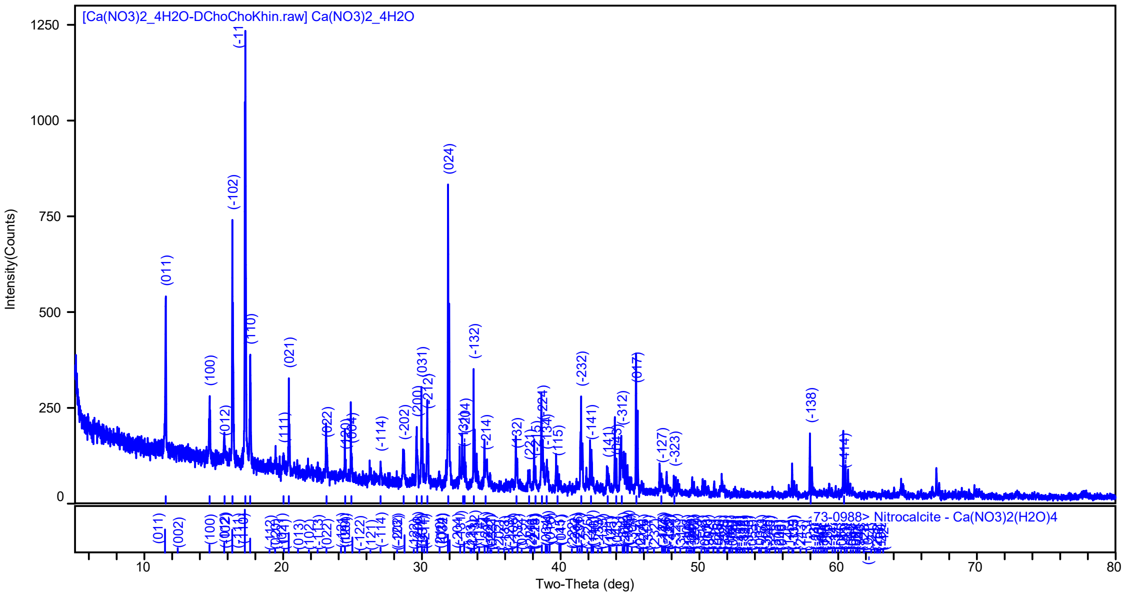

Figure 3 XRD pattern of raw $Ca(NO_3)_2.4H_2O$ powder

β-tricalcium phosphate powders were prepared by the wet chemical precipitation method with calcium nitrate tetrahydrate, $Ca(NO_3)_2.4H_2O$, and diammonium hydrogen phosphate, $(NH_4)_2HPO_4$.After drying at 80°C for 24 h, the dried powders were characterized by using X-ray diffraction to identify the phase formed after the processing. The pattern has revealed that the phase precipitated out in the samples is rhombohedral structure ofβ-TCP. The dried powders were calcined at 700°C for 2 h after crushing with A-gate mortar and pestle. XRD analysis was also conducted to check the phase of the calcined powders. The XRD patterns of dried and calcined β-TCP powder are shown in Figure 4. After calcination, the crystallinity becomes increased and the diffractions peaks are more distinct. The samples revealed the formation of single phase β-TCP structure.

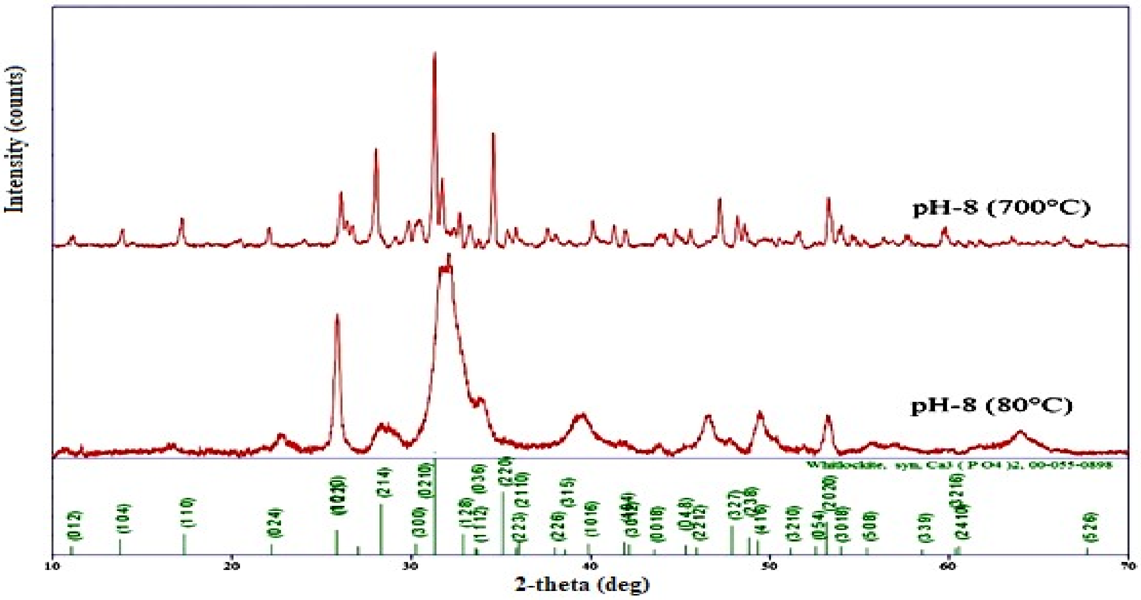

Figure 4 XRD patterns of β-TCP powder dried at 80°C and calcined at 700°C

The synthesized β-TCP powders were pressed into pellet by uniaxial hydraulic press. The β-TCP pellets were sintered at 800°C, 900°C, 1000°C and 1100°C for6 h each. The phase formations of these samples have been characterized by using X-ray Diffraction (XRD) analysis. The XRD patterns of sintered β-TCP pellets are shown in Figure 5.The XRD patterns exhibit that the phase in each sintered pellet is rhombohedral structure of β-TCP. The peaks were sharper as the sintering temperature was increased. The results show that the calcined powders and sintered pellets contain only a single phase β-TCP structure. Therefore, it has been confirmed that rhombohedral structure of β-TCP phase has been stable after sintering upto 1100°C.

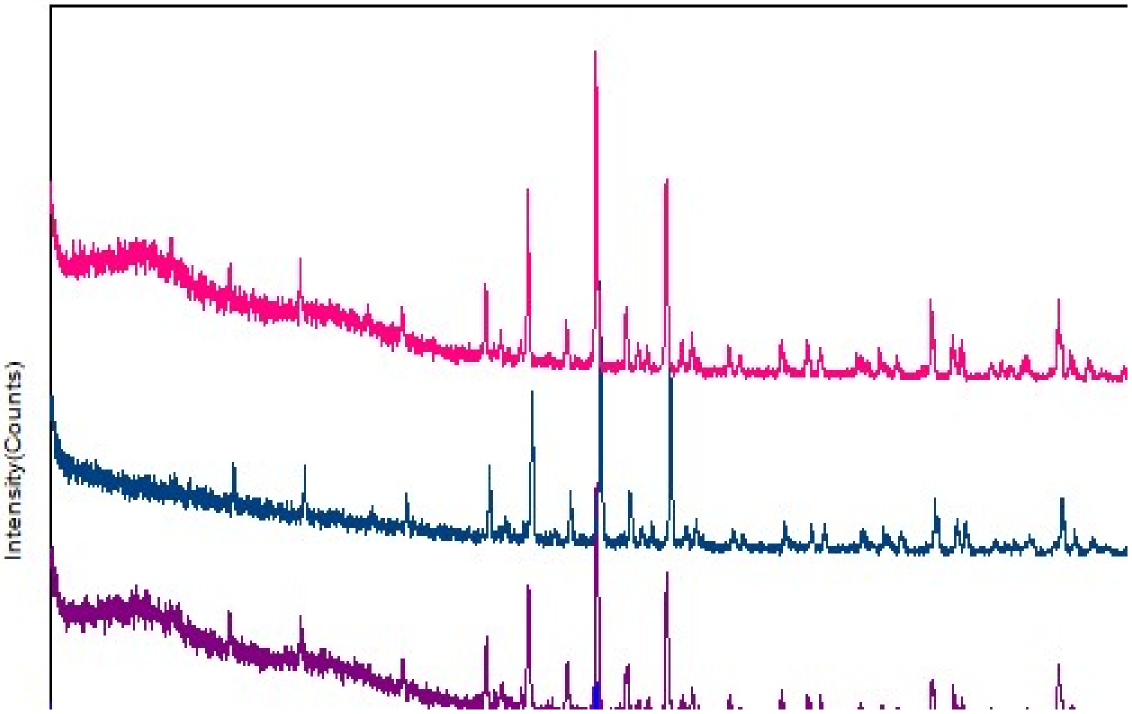

Figure 5 XRD patterns of β-TCP pellets sintered at 800°C, 900°C, 1000°C and 1100°C

Determination of Lattice Parameters and Crystallite Size

The lattice parameters ‘a’ and ‘c’ have been calculated by using ‘d’ value of the intense peak. The crystallite sizes have been estimated by the Scherrer equation. The values of crystallite size and lattice parameters of dried powders after drying at 80°C for 24 h, calcination at 700°C for 2 h and sintered pellets at 800°C, 900°C, 1000°C, 1100°C for 6 h are summarized in Table1. It has been investigated that the lattice parameters of the samples well agree with the typical values for β-TCP structure as discussed in other research of β-TCP [Yashima, M., et al., 2003].It is worth to note that the crystallite size is in nano-range and increased with increasing temperatures.

Table 1 The value of crystallite size and lattice parameter of β-TCP samples

Type of Heat Treatment	Crystallite Size D (nm)	Lattice Parameter	
		‘a’ (Å)	‘c’ (Å)
Dried at 80°C	18.58	10.36	36.77
Calcined at 700 °C	44.83	10.37	37.10
Sintered at 800°C	52.54	10.47	37.50
Sintered at 900°C	59.91	10.48	37.57
Sintered at 1000°C	61.93	10.42	37.29
Sintered at 1100°C	63.99	10.47	37.57

Morphological Analysis by SEM Technique

The surface morphology of β-TCP powders after heat-treatment at 80°C and 700°C have been investigated by using Scanning Electron Microscope. Figure 6(a) shows the SEM micrograph of the β-TCP powders for 80°C. It is seen that the as-prepared powders consists of aggregated particles with broad size distribution. Figure 6(b) shows the SEM micrograph of the β-TCP powders calcined at 700°C. The β-TCP powders are highly agglomerated with almost spherical particles having average size of approximately 0.57 μm. SEM micrographs of β-TCP pellets obtained by sintering at 800°C, 900°C, 1000°C and 1100°C for 6 h are shown in Figure 7. The value of average grain size for the pellets sintered at 800°C, 900°C, 1000°C and 1100°C have been estimated and presented in Table2. The SEM micrographs of pellets which were sintered at different temperatures exhibit that the average grain size is increased with increasing sintering temperature. The pores become smaller with increase in sintering temperature and finally the dense microstructure without pores could be obtained at sintering temperature of 1100°C.

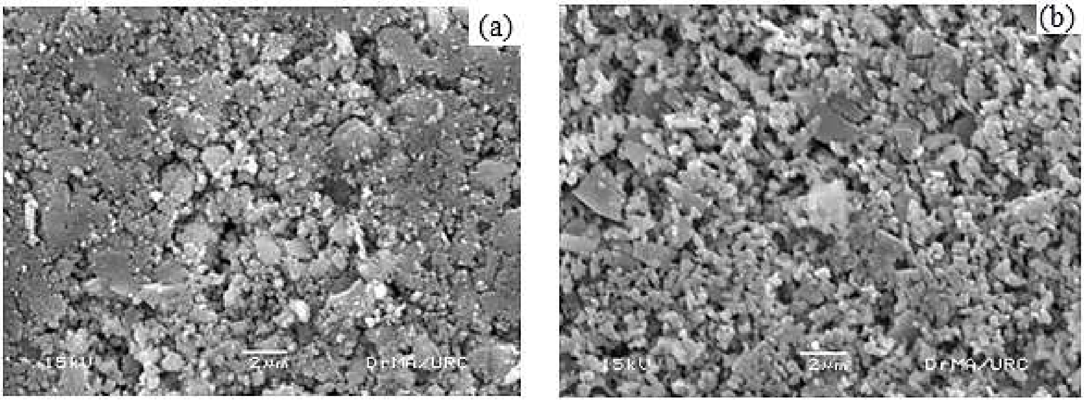

Figure 6 SEM micrographs of β-TCP powders at (a) 80°C and (b) 700°C

Table 2 The value of grain size of β-TCP pellets at different temperatures

Sintered Temperature (°C)	Grain Size (μm)
800	0.68
900	1.16
1000	2.05
1100	3.79

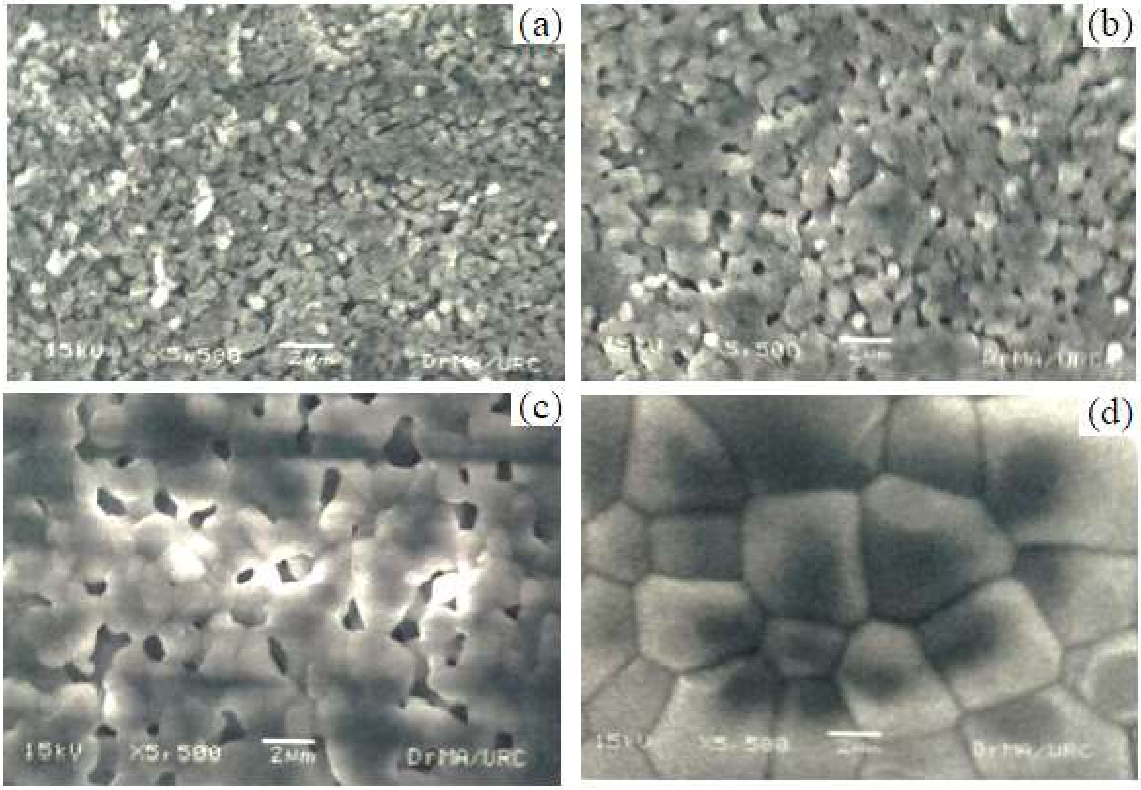

Figure 7 SEM micrographs of β-TCP pellets at (a) 800°C, (b) 900°C, (c) 1000°C and (d)1100°C

FTIR Analysis of Calcined and Sintered β-TCP samples

The functional groups present in calcined and sintered β-TCP were ascertained by Fourier transform infrared spectroscopy (FTIR). The transmission spectra have been recorded in the wavenumber region of 400-4000 cm^{-1}. The FTIR spectra of calcined and sintered β-TCP with different temperatures at700 °C, 800 °C, 900 °C, 1000 °C and 1100 °C are shown in Figure8. Transmission bands of chemical bonds in the calcined and sintered β-TCP are summarized in Table 3. The most characteristic chemical groups in the FTIR spectra of β-TCP are found to be PO_4^{3-}, $P_2O_7^{4-}$, hydroxyl and CO_3^{2-} groups. After sintering, the hydroxyl groups were disappeared.

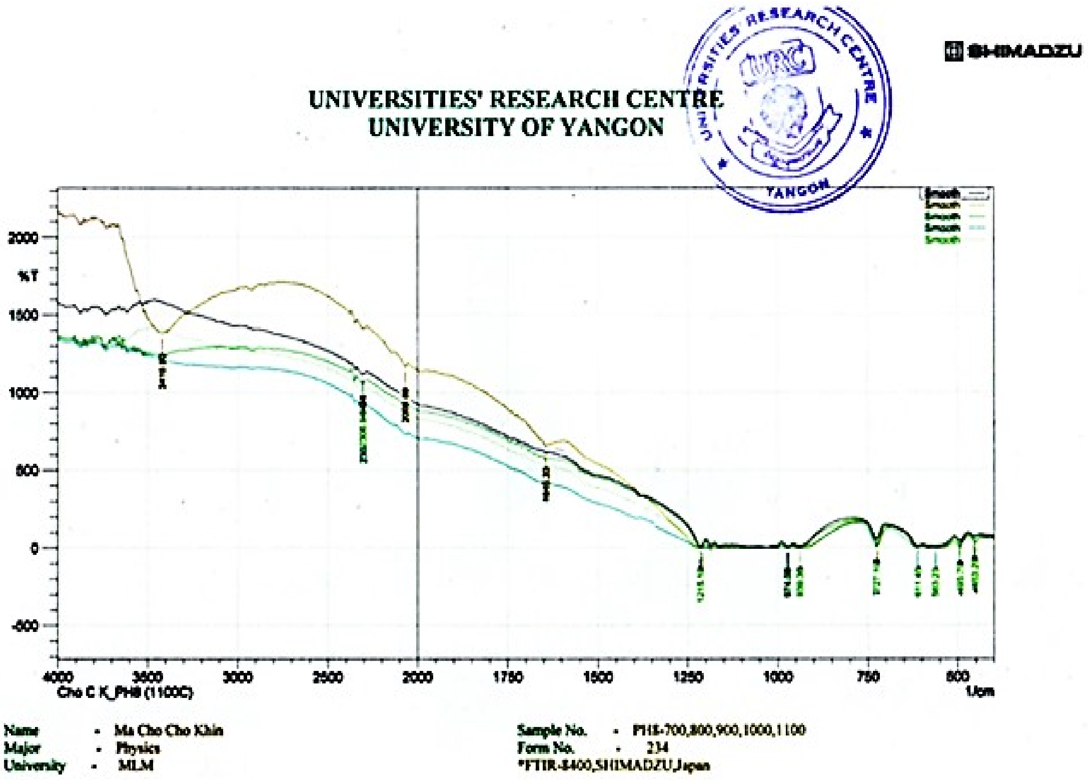

Figure 8 FTIR spectra of β-TCP samples at different temperatures

Table 3 The FTIR transmission bands of β-TCP samples at different temperatures

Chemical Group	**Vibrational Mode**	**Wavenumber(cm^{-1})**				
		Calcined temperature	**Sintered temperature**			
		700°C	**800°C**	**900°C**	**1000°C**	**1100°C**
PO_4^{3-}	ν_1 Symmetric P-O Stretching	939.36	974.08	939.36	939.36	939.36 974.08
	ν_2 O-P-O bending	453.29 493.79	453.29 493.79	453.29 493.79	453.29 493.79	453.29 493.79
	ν_4 O-P-O bending	611.45	611.45	563.23 611.45	563.23 611.45	563.23 611.45
$P_2O_7^{4-}$	Pyrophosphate	727.19 1215.19	727.19 1215.19	727.19 1215.19	727.19 1215.19	727.19 1215.19
CO_3^{2-}	Carbonate	2069.69	2306.94	2306.94	2306.94	2306.94
OH^-	Hydroxyl	1645.33 3419.9	-	-	-	-

Conclusion

β-TCP powders were prepared by wet chemical precipitation method. The XRD analysis has revealed that the phase precipitated out in the samples are rhombohedral. The lattice parameters of β-TCP well agree with the typical values for β-TCP structure. Moreover, the crystallite size of the particles in β-TCP powders estimated from diffraction intense peak (0 2 10) is obtained in nano-range and found to be increased with increasing temperatures. The XRD results proved that the single phase β-TCP was successfully obtained at different sintering temperatures with increased crystallite size. The SEM observation has confirmed the formation of homogeneous powders via wet chemical precipitation method. The surface morphology of β-TCP powders after heat-treatment at 80°C consists of aggregated particles with broad size distribution. After calcination and sintering at different temperatures, the average grain size has increased with increasing temperature. This increase in grain size with temperature well agrees with the increase in crystallite size. This finding pointed out that the synthesis route is consistent with different sintering temperatures. Most importantly, the dense microstructure without pores could be obtained at sintering temperature of 1100°C.The various vibrational modes in the FTIR transmission bands have clearly revealed the presence of respective chemical groups in β-TCP. Based on the results obtained, it is concluded that the sintering temperature could effect on structural properties of beta-tricalcium phosphate and it can tune the applications for bone replacement.

Acknowledgements

The authors are grateful to the Department of Physics and Universities' Research Centre, University of Yangon, for the supports with research facilities and also. The authors are also grateful to the colleagues from the Department of Physics, Mawlamyine University for their encouragement to this work.

References

Asmae, M., et al., (2014), "Synthesis and characterization of nano-sized β-Tricalcium phosphate: Effects of the aging time", Journal of Applied Chemistry, vol.7, pp.57-61.

Bahman, M., et al., (2011), "Synthesis of nano-sized β-tricalcium phosphate via wet precipitation", Processing and Application of ceramics, vol.4, pp. 193-198.

Behzad, M., et al., (2012), "Sintering effects on the hardness of β-TCP", Standard Research Instite, Journal of Ceramic Processing Research, vol. 13, pp. 486-490.

Behzad, M., et al, (2014), "Densification and mechanical behavior of β-tricalcium phosphate bioceramics", International letters of chemistry, Physics and Astronomy, vol. 36, pp37-49.

Tarek Elkhooly, A., (2007), "Preparation and characterization of calcium phosphate ceramics containing some rare earth oxides for using as biomaterials", Faculty of Science, Mansoura university.

Yashima, M., et al, (2003), "Crystal structure analysis of β-tricalcium phosphate $Ca_3(PO_4)_2$ by neutron powder diffraction" Journal of Solid State Chemistry, vol. 175, pp. 272-277.

J. Myanmar Acad. Arts Sci. 2020 **Vol. XVIII.No.2A**

INFLUENCE OF SOME PARAMETERS ON STABILITY OF COLLOIDAL SILVER NANOPARTICLES

Myo Myint Aung[1], San Yu Swe[2], Myo Lay[3]

Abstract

Colloidal silver nanoparticles (AgNPs) were prepared using silver nitrate ($AgNo_3$) as a precursor, sodium borohydride ($NaBH_4$) as a reducing agent and Poly Vinyl Alcohol(PVA) a surfactant stabilizing material. By using molar ratios of reducing agents (4mM, 6mM and 8mM) and stabilizing agent in the formation of AgNPs, the influence of parameters such as reducing agent concentration, stirring period on the sample stability and the degree of dispersion of AgNPs were investigated. The quality of the synthesized samples was characterized by UV-Vis and Cyclic Voltammetry measurements.

Keywords: Colloidal silver nanoparticles, reducing agents, stirring period, UV-Vis, Cyclic Voltammetry

Introduction

The application of nanoscale materials and structures is an emerging area of nanoscience and nanotechnology. Silver nanoparticles (AgNPs) are increasingly used in various fields, including medical, food, health care, consumer, and industrial purposes, due to their unique physical and chemical properties. These include optical, electrical, and thermal, high electrical conductivity, and biological properties. Nanotechnology is the design, characterization, production and application of materials, devices and systems by controlling the shape and size of the nanometre scale. Nanoparticles are particles that have a size of 1 to 100 nm in at least one dimension and possess unique physical and chemical properties due to their large surface area to volume ratio and smaller size.

There are two basic approaches used in nanoparticle synthesis: the top-down (communication and dispersion) approach and the bottom-up (nucleation and growth)approach. The decision on which method to adopt depends on the approach that can deliver the specified properties and on cost. The three main methods of nanoparticle synthesis are physical, chemical and biological. Each method has advantages and disadvantages with common problems being costs, stability, particle sizes and size distribution and so on. Physical and photochemical methods to prepare nanoparticles are usually need the very high temperature and vacuum conditions, and expensive equipment. Among the existing methods, the chemical methods have been mostly used for production of AgNPs.

It is well known that chemical method can successfully produce pure, well-defined nanoparticles and is also the most common method because of its convenience and simple equipment. Chemical methods provide an easy way to synthesize AgNPs in solution, because they can be implemented under simple and mild conditions. In chemical approach, the preparation of AgNPs with colloidal dispersions in water or organic solvents is performed by chemical reduction.

---

[1] Dr, Associate Professor, Physics Department, Yangon University of Distance Education, Myanmar
[2] Associate Professor, Physics Department, University of Mandalay, Myanmar
[3] Student, Physics Department, University of Yangon, Myanmar

The reduction of silver ions in solvents yields colloidal silver nanoparticles with different particle diameters. An increasingly common application of AgNPs can be found use in electronics industry. For example, inks, pastes and filler utilize AgNPs for their high electrical conductivity; molecular diagnostics and photonic devices take advantage of the novel optical properties of AgNPs. Extracts from bio-organisms may act both as reducing and capping agents in silver nanoparticles synthesis. The reduction of Ag+ ions by combinations of biomolecules found in these extracts such as enzymes/proteins, amino acids, polysaccharides, and vitamins.

Characterization of AgNPs is important to understand and control nanoparticles synthesis and applications. Various techniques are used for determination of different parameters. The morphology of AgNPs is obtained using transmission and scanning electron microscopy (TEM, SEM). The size distribution of AgNPs can be measured with a Zetasizer Nano Series analyzer. Energy dispersive X-ray spectroscopy(EDS) measurements are used with an emission scanning electron microscope equipped with an EDS instrument. X-ray photoelectron spectroscopy (XPS), X-ray diffractometry(XRD), Fourier transform infrared spectroscopy (FTIR), and UV-Vis spectroscopy are also used to characterize AgNPs. UV-Vis spectroscopy is used to confirm AgNPs formation by showing the Plasmon resonance. Cyclic Voltammetry Characterization is the electrochemical activity of the synthesized nanoparticles.

In this review, we describe the chemical reduction methods based on our studies, which are successful in the synthesis of AgNPs. The parameters are such as concentration of reducing agent, stirring time, stabilization with a stabilizing agent used during AgNPs synthesis. During this research the above-mentioned parameters will be controlled to find a reliable way for manufacturing AgNPs with certain characteristics. We also describe there action mechanism of AgNPs and parameters affecting particle size. The characterization of synthesis of pure colloidal silver nanoparticles was investigated by UV-Vis spectroscopy and Cyclic Voltammetry measurement.

Materials and Methods

Chemical reduction of silver nanoparticles involves the reduction of a silver salt such as silver nitrate$AgNO_3$with a reducing agent like sodium borohydride and Poly Vinyl Alcohol (PVA), used as stabilizing agents. The syntheses were performed at room temperature.

Preparation of Silver Nitrate Solution: The analytical grade silver nitrate (99.5% purity) was purchased from market in Yangon. About 0.0085grams of analytical grade $AgNO_3$(99.5% Purity) was weighed using an analytical weighing balance and then transferred into a250 mL volumetric flask that contained 100 mL of distilled water. This was followed by stirring for 15 min to ensure that all the solid $AgNO_3$ dissolved. The concentration of silver nitrate was determined to be 0.001 M.

Preparation of Sodium borohydride ($NaBH_4$ ***) Solution***: One of the most popular methods to synthesize silver nanoparticles is by the use of ice-cold sodiumborohydride$NaBH_4$ to reduce silver nitrate. The solution sodium borohydride$NaBH_4$ in different concentration (4mM, 6mM, 8mM) were prepare by dissolving in distilled water 100ml, add a magnetic stir bar and place the flask in an ice bath stirring constantly on a magnetic stirrer plate. Ice bath is used to slow down the reaction and give better control over final particle size/ shape. Stir and cool the liquid for about 20 minutes.

Preparation of stabilizing agent Poly Vinyl Alcohol(PVA) Solution: The stabilizer solution of PVA in concentrations (0.004M) was prepared by dissolving in 100ml distilled water. The stabilizing agent will prevent aggregation of the nanoparticles by lowering the surface tension between the solid particles and the solvent. This is achieved through adsorption of stabilizer-ions onto the nanoparticles in solution. The stabilizing agent ensures formation of metal-surfactant complexes in the reaction solution.

Synthesis of Silver Nanoparticles (AgNPs):Silver nanoparticles (AgNPs) were prepared by reacting silver nitrate solution (0.001 M) with the solution of sodium borohydride$NaBH_4$ (0.004M,0.006, 0.008M) as the reducing agent. The 10 ml of each of $NaBH_4$ solution and 2ml of $AgNo_3$ solution was added and allowed to dissolve stirring constantly on a magnetic stirrer plate for 15 min. From the first series of experiments, the best result AgNPs mixture solution was controlled by using the PVA solution in different concentrations, which were stirring on a magnetic stirrer plate for 5 min. The effect of reducing agent concentration on the formation of silver colloids was also studied by monitoring the UV-Vis absorption spectrum. The stability of AgNPs were also investigated.

The second series of experiments were carried out of the variation of stirring times(10min, 20min, 30min). For this work, the reducing agent concentration ratio at room temperature that gave the best results (most distinct and most narrow UV-Vis peak) from the first series were performed again.

Results and Discussion

The nanosized silver colloids were prepared by a chemical reduction process in aqueous solution in the presence of PVA as a stabilizing agent. During the experiments, colour changes in the solutions were noticeable. In this study, the UV-Vis spectrophotometer and cyclic voltammetry were used to characterize the AgNPs of various formulations and process parameters of AgNPs in laboratory scale.

Firstly this work investigated the effect of the concentration of sodium borohydride$NaBH_4$as a reducing agent in the aqueous solution of silver nitrate on the optical properties of colloidal silver nanoparticles AgNps. The UV-Vis spectraFig-1A illustrate strong peak round about 400nm in all samples, which proved AgNPs formation. The UV-Vis Characterization showed that the highest and narrow absorbance peak and shifted somewhat to shorter wavelengths of NaBH4:AgNO3 (4:1) AgNPs colloid. The AgNPs (4:1) SPR became more distinctive and sample colour also change to bright yellow colour. Fig-1Bshow colloidal AgNPs sample with different concentration (4mM, 6mM, 8mM) of sodium borohydride$NaBH_4$. After that the stability of the synthesized AgNPs were investigated for time taken 4-days, 8-days and 16-days.Fig-2show the stability test for UV-Vis spectra of colloidal AgNPs with different concentration of sodium borohydride$NaBH_4$in different times. From the figure, the best result of stability AgNPs was obtained at the (4:1) ratio and the AgNPs sample (6:1 and 8:1) ratios have wider SPR peak after 8- days and 16-days. Also, another SPR peak shows at 550 nm indicating that some of the particles have aggregated for sample (6:1 and 8:1) ratios. It was seen that peak intensity and stability of AgNPs colloidal depend on concentration of $NaBH_4$ reducing agent.

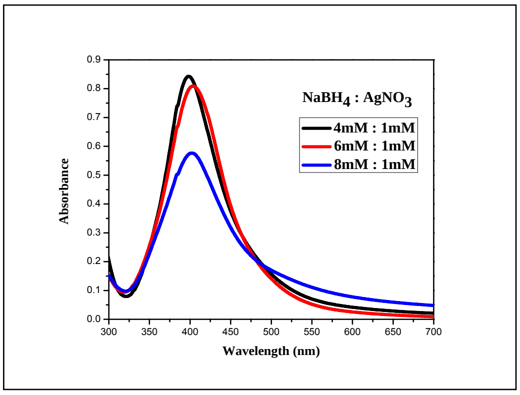

Figure 1A UV-Vis Optical absorption spectra of colloidal AgNPs with different concentration of $NaBH_4$.

Figure1B colloidal AgNPs with different $NaBH_4$ concentration.

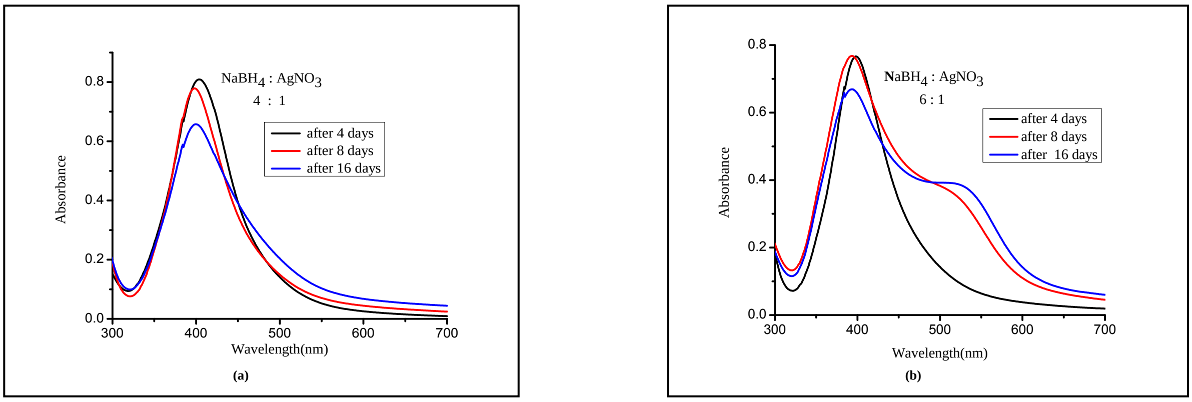

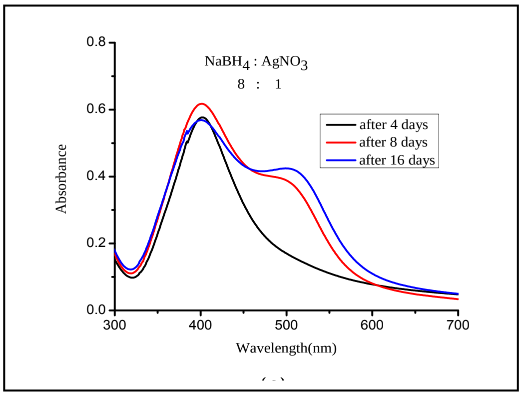

Figure 2 UV-Vis spectrum of Stability test of AgNPs with different concentration ($NaBH_4$:$AgNO_3$) (a) (4:1 ratio) (b) (6:1 ratio), (c) (8:1 ratio)

The best result absorbance and stability of (NaBH4:AgNO3 (0.004M:0.001M)) of AgNPs colloid was used for investigate the effect of sterring time in AgNPs. The reaction time for 10 min, the colour of AgNPs was clear yellow. When the stirring was extended for 20min and 30 minutes, the solution started to turn darker yellow, then dark brown as the nanoparticles aggregate. This is presented in Fig- 3. The reaction trends show that the reaction time for 10 min resulted in a very high NPs nucleation process. However, increase in the reaction time for 20 and 30 min favored the agglomerations and coalescence of the nanoparticles by forming large particle size. UV-Vis graphs in Fig-4show that the SPR peak became started wider and shift towards longer wavelengths when stirring was extended. Therefore prolonged stirring increases the probability of collision between particles, leading to aggregation.

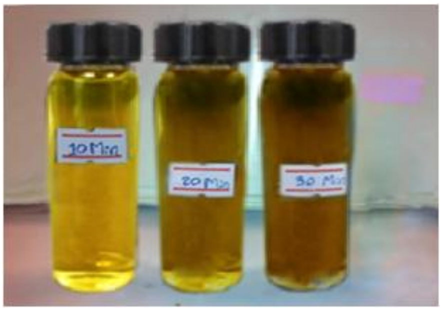

Figure 3 stirring time of Colloidal AgNPs sample (a)for 10- min, (b) for 20-min, (c) 30 min

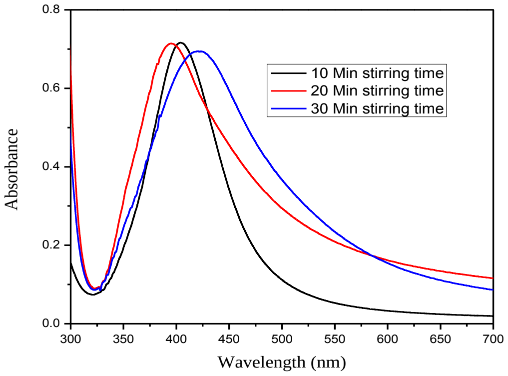

Figure 4 UV-Vis spectrum of effect of stirring time of Colloidal AgNPs (a)for 10 min, (b) for 20-min, (c) 30 min

Electrochemical behavior of Ag+/0 was studied by carrying out cyclic voltammetry in the potential range +0.5 V to -0.5V vs Ag/ AgCl in a repetitive scanning mode at a scan rate of $10mVs^{-1}$, consuming almost 200s for one cycle of forward cathodic and reverse anodic scan. Fig- 5 shows the record of cyclic voltammograms of 1mM silver salt solution in aqueous 0.1M KNO_3 medium. In AgNPs (4:1) cyclic voltammograms a well defined redox signal with anodic peak at +0.55V (E_{pa}) vs Ag/AgCl electrode correspond to the electrochemical re-oxidation Ag^0 to Ag^+ during first anodic scan. CV scanning was continued for 5 more cycles, as revealed in Fig- 5. The anodic current (I_{pa}) is 0.002μA produced by chemical reduction of Ag^+ giving rise to cathodic current along with electrochemical diffusion current (EC mechanism). Further, shift of anodic peak shifted towards more positive potential and marked decrease in peak current observed in subsequent cycles is also an indication of stabilized Ag^0 undergoing oxidation.

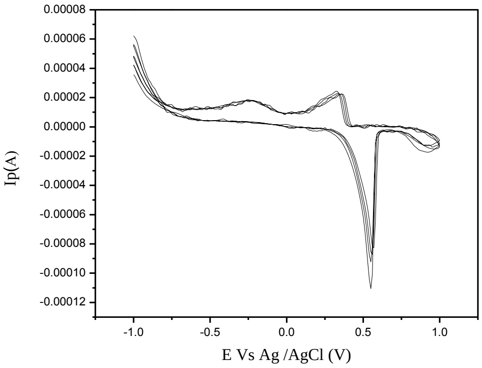

Figure 5 Cyclic voltammograms of AgNPs (4:1) colloids.

Conclusion

Silver nanoparticles were prepared by chemical reduction method. The UV-vis spectra were observed strong peak over 400nm in all samples, which proved AgNPs formation for the effect of concentration of sodium borohydride$NaBH_4$ as a reducing agent in the aqueous solution of silver nitrate ($AgNO_3$). The optimum conditions for this process were reactant ratio $NaBH_4$:$AgNO_3$ (4:1) and 10 min stirring time. This process yields stable, spherical silver nanoparticles of AgNPs colloids. The electrochemical characterization performed by using cyclic voltammetry show significant response for change in reduction potential of Ag^+ ion from higher oxidation state to Ag^0 oxidation state. The formation of silver nanoparticles can be observed by using other parameters such as effect of temperature, and of pH value.

Acknowledgement

I acknowledge to Professor Dr Tin Mg Hla, Rector, Professor Dr Khin That Zin, Pro Rector, Yangon University of distance education , for their kind permission to contribute this paper.

I am greatly indebted to Professor Dr Moh Moh, Professor and Head, Department of Physics, Yangon University of distance education, for her warmly support, understanding and guidance to do this work.

I am deeply grateful to Professor Dr Mar Lar Myint, Department of Physics, Yangon University of distance education, for her fruitful discussions throughout this work.

References

A. lennon, *et a*l., (2007), in: Proceedings of the NIP 23 and Digital Fabrication Conference.

H. Kato, (2011) "In vitro assays: tracking nanoparticles inside cells."*Nature Nanotechnology*,vol.6,no.3,pp.139–140.

Iravani, *et a*l., (2014) "Synthesis of silver nanoparticles: chemical, physical and biological methods", *Research in Pharmaceutical Sciences*, vol.9, pp.385-406.

J. Natsuki *et al*., (2015) "A Review of Silver Nanoparticles: Synthesis Methods, Properties and Applications", *International Journal of Materials Science and Applications*,vol.5,No.5, pp.325-332.

K. M. M. El-Nour, *et a*l., (2010)"Synthesis and applications of silver nanoparticles", *Arabian J.Chem.* vol.3, pp.135-140.

K. Toisawa, *et a*l., (2010) "Synthesis of highly concentrated Ag nanoparticles in a heterogeneous solid-liquidsystem under ultrasonic irradiation", *Materials Transactions*, vol.51, pp.1764-1768.

P.Mukherjee, et al.,(2001) "Fungus-mediated synthesis of silver nanoparticles and their immobilizationin the mycelial matrix: A novel biological approach to nanoparticle synthesis.", *Nano Lett.*,vol. 1, pp. 515–519.

R. Jeremy,(2009)*Essentials of Nanotechnology*, Ventus Publishing, ebook, Frederiksberg, Denmark.

S.Gurunathan, *et al*., (2015) "Comparative assessment of the apoptotic potential of silver nanoparticles synthesized by Bacillus tequilensis and Calocybe indica in MDA-MB-231 human breast cancer cells: Targeting p53 for anticancer therapy" *Int. J. Nanomed*, vol.10, pp. 4203–4222.

S.M.Landage, *et a*l.,(2014) " Synthesis of Nanosilver using Chemical Reduction Methods" *D.K.T.E. Society's, Textile & Engineering Institute, Ichalkaranji*, India, vol.3, No.5, pp.13-22.

S. Tsuruga, and T. Abe, (2008) "Preparation of electro-conductive inkjet inks through silver halide photographic emulsion", *Proceedings of the Pan-Pacific Imaging Conference*, pp.56-59.

Z. Anna, *et a*l., (2009) "Preparation of silver nanoparticles with controlled particle size*", Procedia Chem.* vol.1, pp.1560-1566.

J. Myanmar Acad. Arts Sci. 2020 **Vol. XVIII.No.2A**

SYNTHESIS AND CHARACTERIZATION OF NICKEL DOPED BISMUTH FERRITE MATERIALS

Lei Lei Aung[1], Aye Aye Khine[2], Khin Nyo Win[3]and Min Maung Maung[4]

Abstract

Nickel substituted bismuth ferrites($BiFe_{1-x}Ni_xO_3$; x = 0.1, 0.2, 0.3, 0.4 and 0.5) materials was synthesized using combustion technique. The synthesized material powders were sintered at 900°C for 4 hours. X-ray diffraction technique (XRD)was used to confirm the nano-crystallite structure and phase formation. The particle size was estimated by the full width half maximum (FWHM) of the strongest X-ray diffraction (XRD) peak. The characterization of these materials was analyzed by Fourier Transform Infrared spectroscopy (FTIR). The optical band gap of these materials was also investigated from the transmittance spectrum. The energy band gap $E_g$is in the range of 4.7 eV to 5.1 eV for prepared samples.

Keywords: bismuth ferrites; Auto-combustion technique; XRD; crystallite size; FTIR; FWHM.

Introduction

Transition metal oxides constitute one of the most interesting classes of solids, exhibiting a variety of structures and properties. The rich and novel behavior of transition metal oxides arises from the complex interactions between their charges, orbital, spin and lattice degrees of freedom. The interactions in these materials can be modified through the effect of local symmetry breaking, charge transfer, electrostatic coupling and frustrations leading to fascinating new phenomena. The magnetic and ferroelectric orders also couple with each other such that the magnetic degree of freedom can be manipulated by an electric field and ferroelectric degree of freedom by magnetic field. The magneto-electric coupling (ME) in multiferroics promises important technological applications in several multifunctional devices like data storage, spinotronics, sensor and actuator devices etc. Perovskite structure possesses high structural flexibility; a vast number of different but closely related structures can be prepared with the general chemistry ABX_3. Doping leads to further ways to chemically tune structural and physical properties.

Bismuth ferrite is one of multiferroic systems showing a large magneto-electric coupling in single phase at room temperature. It is one of the most promising lead- free piezoelectric materials exhibiting multiferroic properties at room temperature. $BiFeO_3$ crystallizes in a distorted rhombohedral perovskite with space group $R3c$. This crystal structure transforms to pseudocubic structure by adding adoping such as Pb, Ba, Ca and Sr. The transformation of crystal symmetry affects multiferroic properties in $BiFeO_3$. Ferroelectricity in $BiFeO_3$ comes from existence of Bi^{3+}lon pairs on 6s orbital creating dipolar moment, while anti-ferromagnetism comes from the Fe^{3+} site through anti-ferromagnetic coupling of two adjacent crystal planes. Both Bi^{3+} and Fe^{3+}play the major role in the origin of multiferroicity in$BiFeO_3$, then substitution on A and/or B siteenhance its multiferroic properties.

---

[1] Dr, Associate Professor, Department of Physics, Yangon University of Distance Education.

[2] Dr, Associate Professor, Department of Physics, Yangon University of Distance Education.

[3] Dr, Associate Professor, Department of Physics, Dagon University.

[4] Dr, Associate Professor, Department of Physics, University of Yangon.

In $BiFeO_3$structure FeO_6 octahedron form a basic module which play a major role in determining the properties. The substitutions at Bi-sites are indirect to environment of FeO_6 octahedron structure whereas Fe-site substitutions directly affect the octahedron structure. The substitution at both A site and B site simultaneously is supposed to compensate the distortions/strain produced in the structure formation of pure phase materials. Therefore multiferroics are rare and it exhibits weak magnetism at room temperature. As for $BiFeO_3$ bulk ceramic is concerned, synthesis of single phase material is difficult because of the volatility of bismuth oxide at high temperature. The kinetics of phase formation most frequently leads to impurity phases such as $Bi_2Fe_4O_9$, Bi_2O_3, and $Bi_{25}FeO_{39}$ etc. The presence of undesired secondary phases and formation of cationic/anionic vacancies, it is difficult to observe ferroelectric loop due to low resistivity of the material resulting in large leakage current, low dielectric constant and high loss. Generally this problem can be resolve by doping of cations at the Bi/Fe sites, or/and both Bi and Fe sites of BFO, single phase synthesis or forming solid solution with other perovskite structure.

The objective of the present work was to be studied the effect of nickel substitution on Bismuth ferrite. The structural characterization of these materials was also identified by XRD, SEM and FTIR spectroscopy. The optical energy band gap was also estimated by the aid of UV-Vis spectroscopy.

Experimental Procedure

Preparation of the powders

$BiFe_{1-x}Ni_xO_3$;(x = 0.1, 0.2, 0.3, 0.4 and 0.5) powders were prepared bya sol-gel method. Starting materials were bismuth nitrate, ferric nitrate and nickel nitrate. Each of the above chemicals was weighed according to the stoichiometric ratio and dissolved in the deionized water by constant stirring at the temperature 40-50°C. After ensuring no sediments/precipitate, some citric acid was added and the solution was well mixed for 1-2 hrs. The chelated/complexed acqueous solutions were mixed together and kept at about 70°C for 3–4 days with vigorous stirring to form a viscous gel solution. The gel was dried at about 120°C, which was then collected and pulverized in an agate mortar by grinding. The resultant powders were decomposed at 400°C in an oven to remove the organic solvents. The obtained aqueous powder was sintered at 900°C for 4 hrs.

Results and Discussion

X-Ray Diffraction Study

X-ray powder diffraction (XRD) was done to check the phase using the CuK_α radiation. Figure 1 shows the XRD pattern of the sintered Ni doped Bi ferrites powders. The strongest reflection of (311) plane represent cubic spinel structure. The BFO powders contained secondary phases such as $Bi_{25}FeO_{40}$ and $Bi_2Fe_4O_9$. Some minor phases were also present. Well defined peaks are (200), (111), (311) and (400) of spinel structure can be observed in the XRD patterns. Moreover, peaks related with$NiFe_2O_4$ were still observed in the XRD patterns of BNFO ceramics. The XRD patterns reveal that $BiFeO_3$ substituted at A site and simultaneously substituted $BiFeO_3$, the XRD patterns are more cleaner in comparison to B site substituted samples. This may be due to compensation of strains produced to substitutions at A and B both sites simultaneously. $NiFe_2O_4$ consumed some Fe, resulting in the excess of Bi in the samples and therefore increase the formation of the Bi-rich phase, $Bi_{25}FeO_{40}$.The formation of $BiFeO_3$ decrease with increasing of Ni substitution. The XRD patterns of 1 mol% Ni-doped BFO samples (x = 0.1), a pure phase was found. For the 3 mol% Ni-doped BFO (x = 0.3), the above two impurity phases appeared. In the 5 mol% Ni-doped BFO samples (x = 0.5) always contained the Bi-enriched intermediate phase, suggesting that the Ni doping was certainly over the solubility limit.

Using the broadening reflections of 311 and Scherrer's relation X-ray line, the nano-sized nature of the attained ferrite leads to broadening of the powder XRD peaks. The crystallite size of Ni doped Bi ferrite samples was calculated. $D = k\lambda/\beta\cos\theta$ where $\lambda$is the wavelength of the X-ray radiation (1.5406Å), k is a constant taken as 0.89, θ is the diffraction angle and β is the full width at half maximum (FWHM), the crystallite size was found to be varied from47.7 nm to62.9 nm.

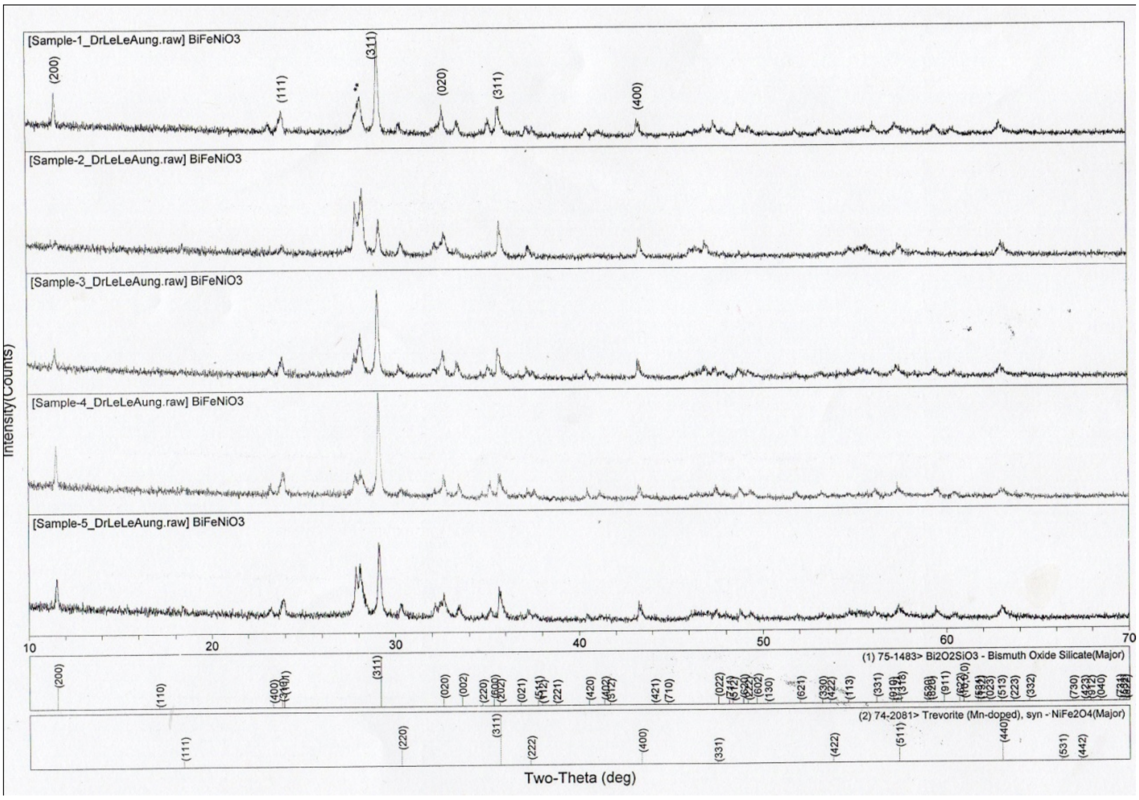

Figure 1 The XRD pattern of the sintered Ni doped Bi ferrites powders

Table 1 Lattice parameters, FWHM and crystallite size of $BiFe_{1-x}Ni_xO_3$

Prepared samples	a = b = c (Å)	FWHM	Crystallite size (nm)
$BiFe_{0.9}Ni_{0.1}O_3$	9.2846	0.163	49.7
$BiFe_{0.8}Ni_{0.2}O_3$	8.2496	0.129	62.9
$BiFe_{0.7}Ni_{0.3}O_3$	7.7995	0.170	47.7
$BiFe_{0.6}Ni_{0.4}O_3$	9.3026	0.164	49.5
$BiFe_{0.5}Ni_{0.5}O_3$	10.0177	0.170	47.7

TGA-DTA Analysis

Figure2shows the thermo gravimetric analysis (TGA) trace of Ni doped $BiFeO_3$ samples. The decomposition process consists of three regions. They are 50–150°C, 150–480°C and 480–600°C. Owing to the initial breakdown of the complex and spontaneous combustion, the first weight loss region from 50–150°C indicates the evaporation of absorbed water. With the liberation of H_2O, CO_2 andNO_3 and the nitrate ions providing an oxidizing environment for the combustion of the organic components, the spontaneous combustion is caused from the interactions of ethylene glycol, citrate and nitrate ions in the gel. The second weight loss region observed between 150°C and 480°C is ascribed to dehydration of OH group in the spinel structure of some constituents such as NO_3, that lead to two degradation systems involving both inter and intra-molecular transfer reaction, the oxidation of complexes and formation of semi-organic carbon metal/metal oxide. The third weight loss region in the temperature range of 480–600°C is believed to be due to the formation of corresponding metal oxide and the spinel phase. From this study, it is seen that the TGA curve is steady, demonstrating the absolute volatility of water, organic compound, nitrates in the composites, the completion of crystallization route and the immediate formation of pure nickel ferrite.

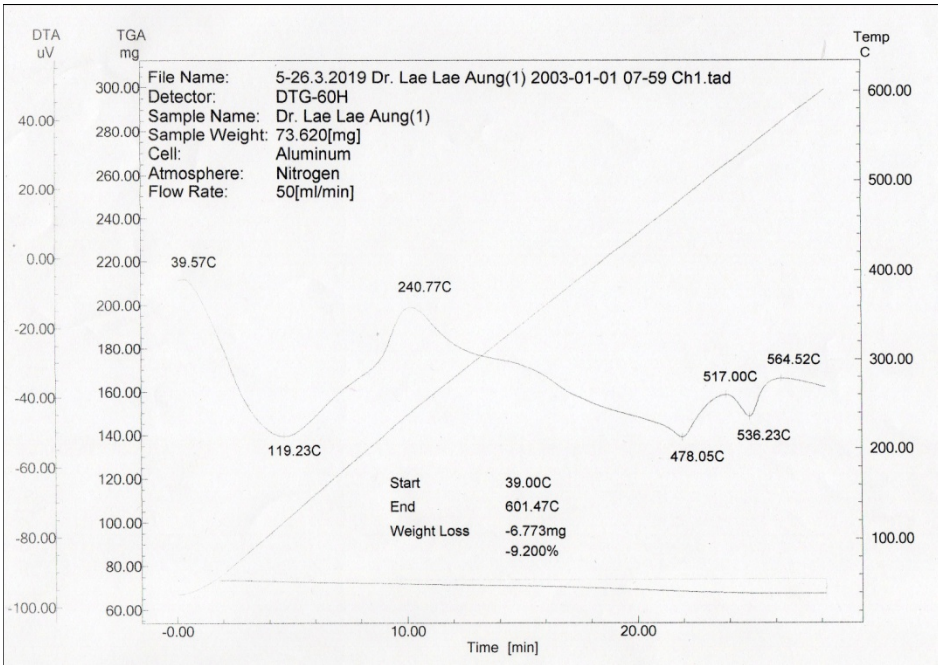

Figure 2 The thermogravimetric analysis (TGA) and Differential Thermal Analysis (DTA) of Ni doped $BiFeO_3$ samples

SEM analysis

The morphologies of the samples were observed by the scanning electron microscopy (SEM). Figure 3 shows the SEM images of nickel substitution in the bismuth ferrite samples. It was observed that surface of the images was appeared roughly not a smooth surface. The compact sample revealed that the heterogeneous grain size distribution. The surface morphology showed that the shape of the synthesized material approximately uniform in micron size determined by line intercepts method. Moreover, it was observed that the grain size decreases with the increase of nickel substitution in the bismuth ferrite.

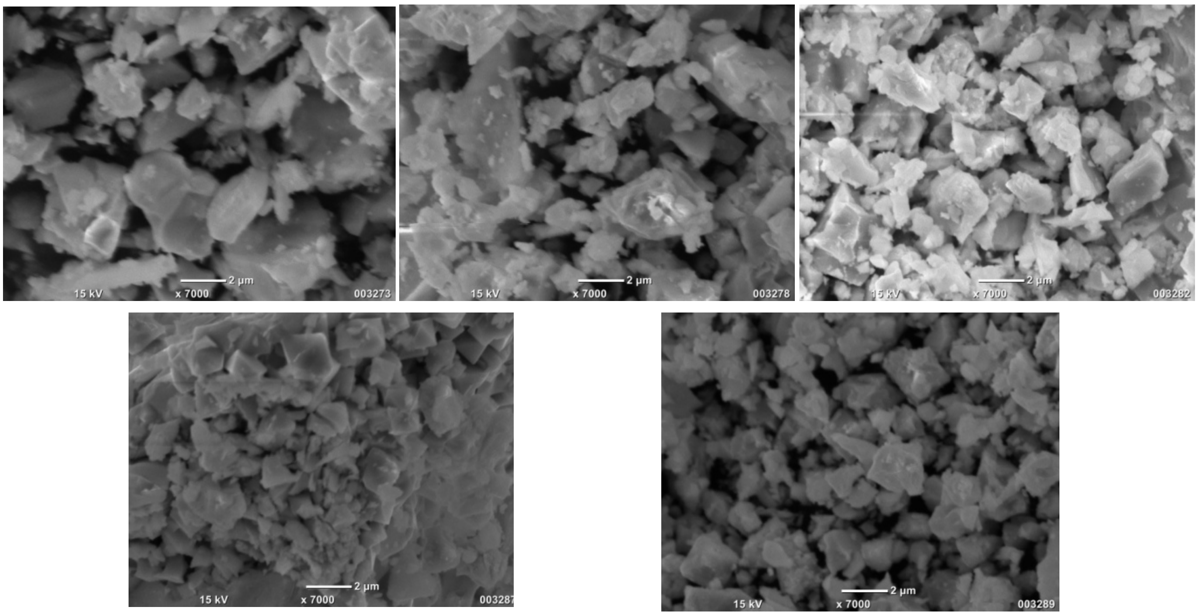

Figure 3 The SEM image of Ni doped $BiFeO_3$ samples

FTIR Analysis

Figure 4 shows the FTIR spectra of prepared samples. The plot shows some distinct peaks. The strong absorption peaks around 400-600 cm^{-1} are attributed to the Fe–O stretching and bending vibrations which are fundamental absorptions characteristics of FeO_6octahedral group in the perovskite structure. The formation of perovskite structure can be confirmed by the metal oxygen band. The band at 1387.52 cm^{-1} is due to the presence of trapped nitrate. Typical band characteristics of oxygen metal bonds were observed in the 450-640 cm^{-1} region. A distinct change is noticed that the both side nickel substituted $BiFeO_3$ sample shows two positive peaks near 3000 cm^{-1} compared to the other two compositions. The bands between 3400 and 3784 cm^{-1} could be attributed to the O–H stretching vibration of H_2O absorbed by the sample and the surface O–H or EG. The bands with the peaks at488, 670 and 809 cm^{-1} are assigned to the deformation vibration of Fe–OH groups. The two main metal–oxygen bands at 670 cm^{-1} and 488 cm^{-1} are observed in the FT-IR spectrum of the synthesized Ni doped $BiFeO_3$ samples. These two bands are usually assigned to vibration of ions in the crystal lattices. This indicates the presence of uniformly distributed ferrite particles. The band at 1050 cm^{-1} shows the presence of C–O group vibration modes. At1360 cm^{-1} there is a significant change in the irrelevant peak of –CH bending band. The 1316 cm^{-1} peak is attributed to the characteristic $–CH_3$ bending.

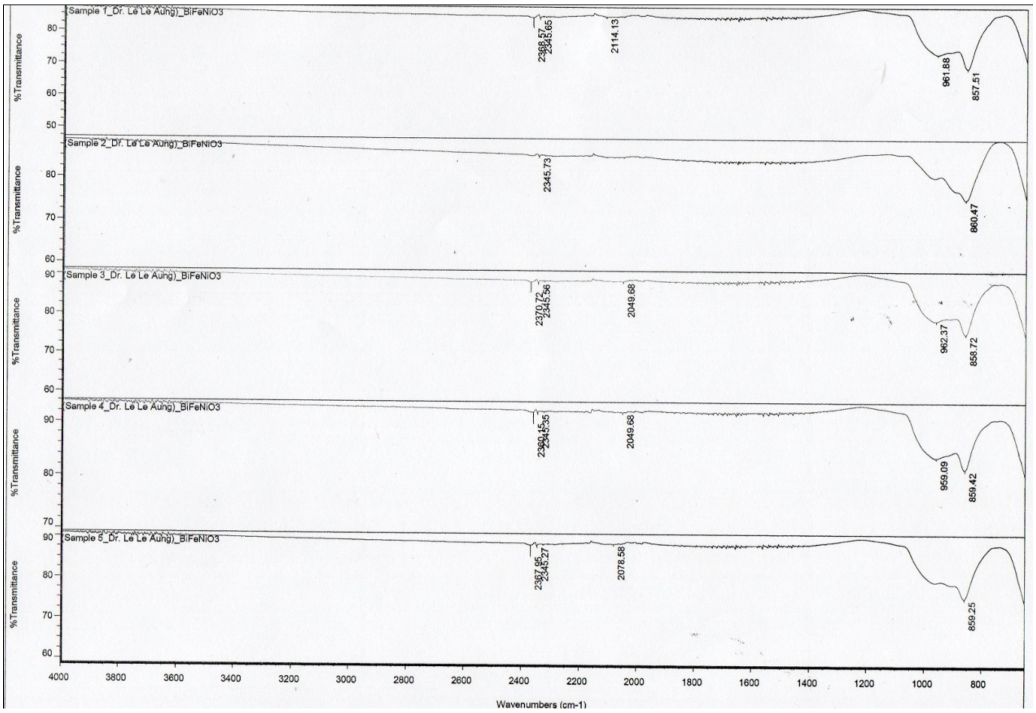

Figure 4 The FTIR spectrum of Ni dopes $BiFeO_3$ samples

Optical Band gap Analysis

The energy band gap of the material is determined by using UV-visible spectra according to Tauc relation $\alpha h\nu = A(h\nu - Eg)^n$, where Egis the energy gap, constant A is different for different transitions, ($h\nu$) is the energy of the photon and n is an index which assumes the value 1/2, 3/2, 2 and 3 depending on the nature of the electronic transition responsible for the reflection. The value of n is 1/2 for allowed and 2 for forbidden direct energy gap for ferrites. Further, the value of α has been calculated by the following relation, $\alpha = 4\pi k/\lambda$, where λ is wavelength in nm and k is absorption index. Figure 5 illustrated the UV-visible absorbance spectra of the Ni substituted Bi ferrites, the absorbance decreases as the doping of Ni. The value of optical energy band gap E_g has been calculated for the all samples by$(\alpha h\nu)^2$vshνplots. The values of E_g for different samples were found by extrapolating the linear portion to the *hv* determine the energy band gap $E_g$to be from 4.7 to 5.1 eV. It was observed that by increasing the concentration of the Ni, the band gap of these materials increased.

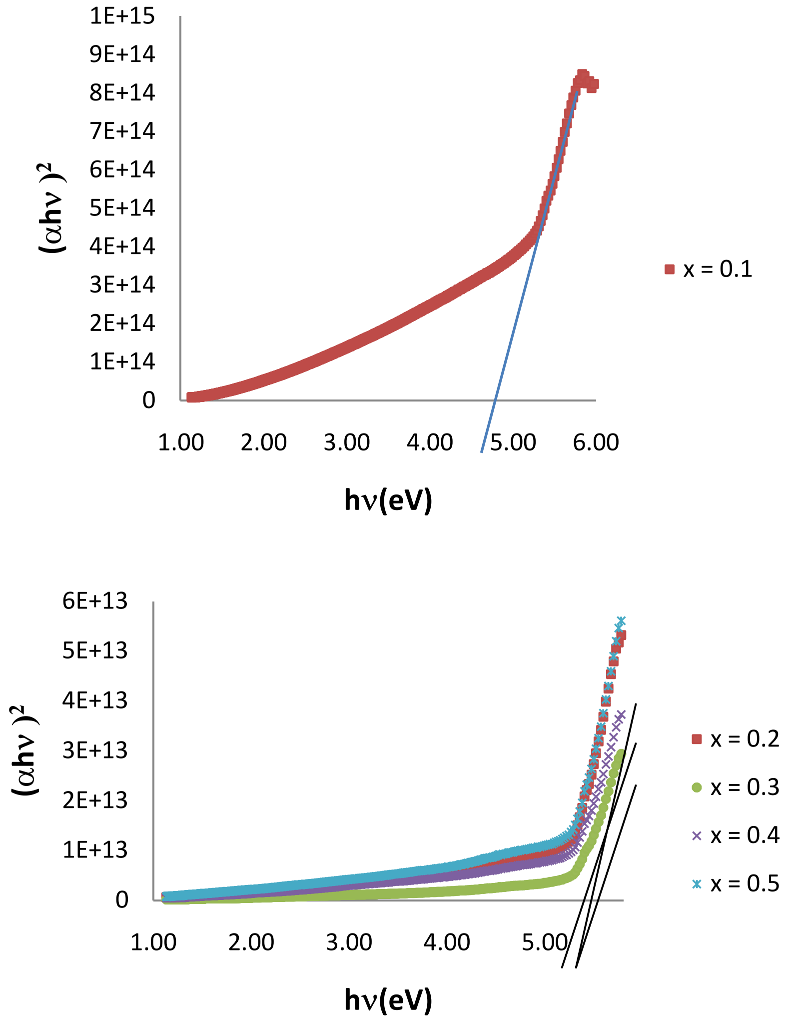

Figure 5 The energy band gap of Ni dopes BiFeO$_3$ samples

Conclusion

BiFe$_{1-x}$Ni$_x$O$_3$; (x = 0.1, 0.2, 0.3, 0.4 and 0.5) nano-particles were successfully synthesized by auto combustion method using citric acid as fuel. XRD patterns indicate presence of undesired phases in all samples which get suppressed with simultaneous substitutions on both sites in comparison to substitutions at A-site or B-site in BiFeO$_3$. Ni substitution decreases the formation of BiFeO$_3$, while increase the formation of secondary phases. The Ni substitution has strengthened the magnetic properties of the bismuth ferrite system. The observation of absorption peaks around 400-600 cm^{-1} in FTIR spectra are attribute to Fe-O stretching and bending vibrations and are fundamental absorption peaks of FeO$_6$ octahedron in perovskites. SEM revealed that the synthesized samples have heterogeneous grain size distribution. The energy band gap $E_g$is in the range of 4.7 eV to 5.1 eV for prepared samples.

Acknowledgement

We are deeply grateful to Rector Dr Tin Maung Hla, Yangon University of Distance Education, for his kind permission to carry out our research work. We would like to thank Professor Dr Moh Moh, Head of Department of Physics and Professor Dr Mar lar Myint, Department of Physics, Yangon University of Distance Education, for their kind permission to carry out this research work. We would like to thank Dr Min Maung Maung, Associate Professor, Department of Physics University of Yangon and for his valuable suggestion and support.

References

Ahmad S et al, (2004), “Ferroelectric Ceramics Processing Properties and Applications”, Department of Ceramic Science and Engineering, Rutgers University: USA

“Instruction Manual LCR meter GW 820”, USA

Moulson A J & Herbert J M, (1997), “Electroceramic Materials Properties Applications”, New Delhi: Thomson Press

Suryanarayana C. and Norton M. G. (1998), X-ray Diffraction A Practical Approach, (New York: Plenum)

Tyagi M S, 1991, “Introduction to Semiconductor Materials and Devices”, New York: Wiley

Xu Y, 1991, “Ferroelectric Materials and their Applications”, New York: Elsevier Science Publishing Co. Inc.

J. Myanmar Acad. Arts Sci. 2020 **Vol. XVIII.No.2A**

SYNTHESIS AND MAGNETIC PROPERTIES OF COBALT FERRITE MATERIALS

Min Maung Maung[1], Thein Tun Linn[2], and Aung Min[3]

Abstract

Cobalt ferrite powders with general formula $CoFe_2O_4$ was synthesized by sol-gel auto combustion method starting from metal nitrates and citric acid ($C_6H_8O_7$) as a fuel. X-ray diffraction technique (XRD) was used to confirm the crystallite structure and phase formation. The particle size was estimated by the full width half maximum (FWHM) of the strongest X-ray diffraction (XRD) peak (311). The average particle size was observed in the range of 42 to 54 nm. The scanning electron microscopy (SEM) was used to study the grain size, grain distribution of these samples. The dielectric property measurements were carried out by the help of a LCR meter. The dielectric constant and the loss tangent decreases rapidly with increasing frequency, and then reaches a constant value.The room temperature magnetization and demagnetization measurement was done by PERMAGRAPH L apparatus.

Keywords: Hysteresis; magnetic properties; remanence; coercivity; Permagraph L; XRD; Grain size.

Introduction

Magnetic materials form an important class of materials used practically in all electric machines such as motors, generators, transformers, relays and electromagnets. With respect to their magnetic behavior, magnetic materials may be classified into diamagnetic, paramagnetic, ferromagnetic, antiferromagnetic and ferrimagnetics. Magnetic ceramics may be divided into one of three different classes; spinel ferrites, hexagonal ferrites and the rare earth ferrites (garnet materials). Ferrites have dc resistivity of many orders of magnitude higher than that of iron and are used for frequencies up to microwave range in transformer cores. They are of greatest interest from the electrical engineering point of view because they have as ferromagnetic materials in as much as they show spontaneous magnetization below a certain temperature [Rajagopal K. (2009)].

Ferrite materials are insulating/semiconductor metal oxides that exhibit moderate saturation magnetization, high coercivity, high electrical resistance, low eddy current and dielectric loss with moderate permittivity. No other material has such a wide range of properties and therefore these materials are exploited for vast applications in various fields like transducers, activators, recording media, permanent magnets, phase shifters, electrode material for Lithium ion batteries, solid oxygen fuel cells and computer technology. In addition with, the ferrite nanoparticles are used in magnetic fluids, humidity and gas sensors, drug delivery etc [Ranjit Kumar Panda, (2015)].

The ferrites exhibit dielectric properties and do not conduct electricity easily therefore ferrites became an alternative for the metal magnets like iron, nickel which conduct electricity readily. Therefore, the processing of these materials is important to modify its properties as per the desired applications. Ferrites are classified into three types depending on the structure namely spinel, garnets and hexagonal ferrites. Garnets have the general formula $M_{3+}Fe_5O_{12}$ where M = Y,

---

[1] Dr, Associate Professor, Department of Physics, University of Yangon.

[2] Lecturer, Department of Physics, Hpaan University.

[3] Lecturer, Department of Physics, Mawlamyine University.

Sm, Eu, Gd,Tb etc. and have applications in microwave systems. The hexagonal ferrites represented by the formula $Me_{2+}Fe_{12}O_{19}$where M = Ba, Sr, Ca are important in permanent applications. The spinel ferrites are represented by the general formula $MFe_2O_4$where Mis the divalent cation M = Co, Mn, Zn, Ni, Cd [Ranjit Kumar Panda, (2015)].

Among all the ferrites, cobalt ferrite is one of the potential candidates which exhibit moderate saturation magnetization, high coercivity, electrical insulation with low eddy current loss, and chemical stability etc. Therefore it has been extensively used in high density storage, transformer core, high quality filters, phase shifters etc. Cobalt ferrite is selected as representative for the spinel ferrites to study the electric and magnetic properties and relate its structural modifications. Bulk cobalt ferrite has inverse spinel structure that shifts to partial inversion for nano ferrites [Ranjit Kumar Panda, (2015)].

In this research work, cobalt ferrite was prepared by sol-gel auto combustion method. The structural property, the surface morphology and the bond structural properties were also analyzed by X-ray diffraction (XRD), scanning electron microscope (SEM) and Fourier transforms Infrared(FTIR) spectroscopy. The optical band gap of this material was also investigated by the aid of UV-Vis spectroscopy. The frequency dependence dielectric properties and magnetization behavior were also determined by LCR meter and PERMAGRAPH L technique.

2. Experimental procedure

Cobalt nitrate $Co(NO_3)_2 \cdot 6H_2O$, ferric nitrate $Fe(NO_3)_3 \cdot 9H_2O$, citric acid and liquor ammonia have been used as starting materials for preparation of cobalt ferrites by the sol-gel auto-combustion method. Stoichiometry amounts metal nitrates were dissolved in minimum amount of mixture solution of deionised water and poly ethylene glycol(5:1) separately to make clear solution and citric acid was dissolved in a separate beaker, finally three solutions are mixed in another beaker. The opaque solution was then vigorously stirred for a few minutes in order to have a lucid and homogeneous solution. A small amount of liquor NH_3 was added to the solution to adjust the pH value at 7.Thefinal solution was simultaneously heated and mixed using magnetic stirrer. The solution was heated gradually up to 100°C, to evolve reddish brown color gases and finally the dried gel was burnt-out completely to form loose powders. The obtained powder was sintered at 900°C, 1000°C and 1100°C for 4 hr. The flow chart of sample preparation was shown in figure 1.

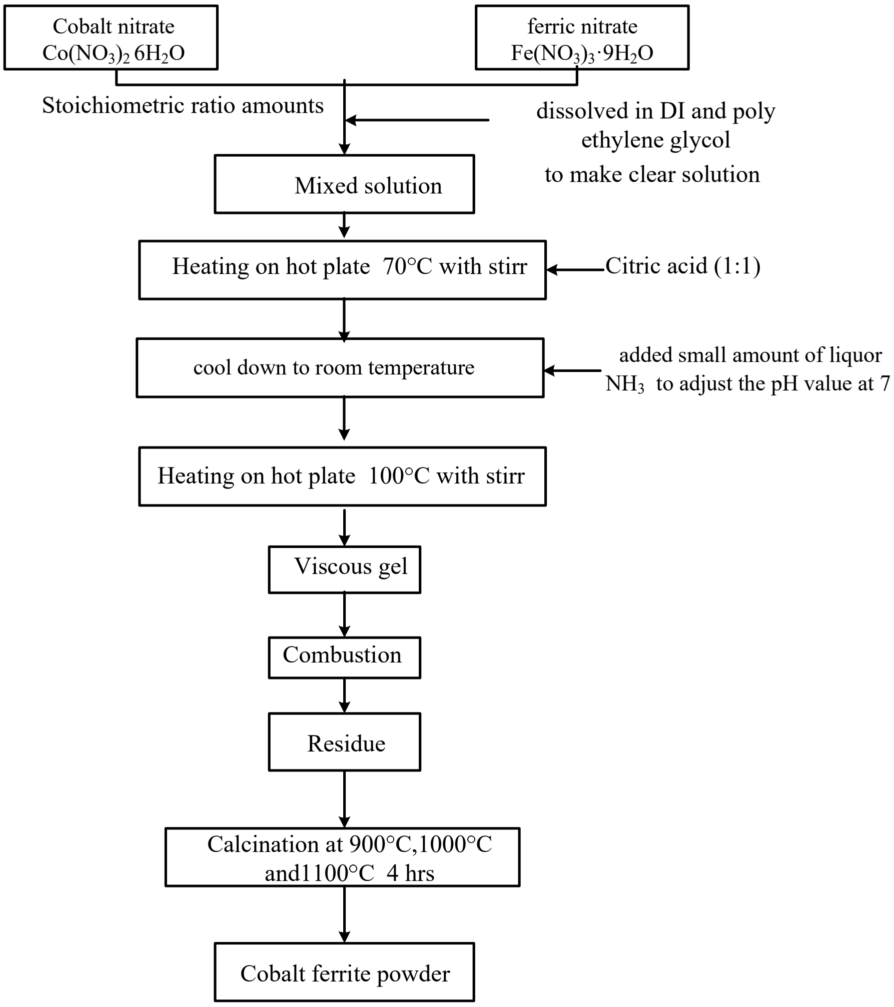

Figure 1 The flow chart of preparation of cobalt ferrite

Results and Discussion

3.1 XRD analysis

X-rays powder diffraction of the samples was carried out at room temperature using Schimadzu model: XRD 6100 using CuK$_\alpha$ (λ = 0.154 nm) radiation, with a diffraction angle between 20° and 70°to check the formation of the required product and structural related properties. The model unit cell of $CoFe_2O_4$ was shown in figure 2. The XRD patterns of the bulk cobalt ferrite nanoparticles annealed at 900°C, 1000°C and 1100°C were shown in Figure 3(a), (b) and (c). The strongest reflection comes from the [311] plane, which denoted the spinel phase. The peaks indexed to [111], [220], [311], [222], [400],[422], [511] and [440] planes of a cubic unit cell, all planes were the allowed planes which indicated the formation of cubic spinel in single phase and no other impurity phases. The average crystallite size of these samples could be calculated using Scherrer's formula(FWHM = 0.299 broading peak (311), angle 35.5°). The average crystallite size and their porosity were listed in table 1.

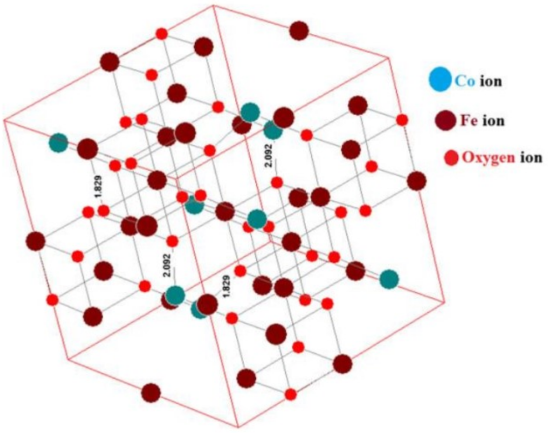

Figure 2 The unit cell of cobalt ferrite[Ranjit Kumar Panda, (2015)].

Table 1 The average crystallite size of cobalt ferrite

Annealing temperature	Lattice parameter a = b = c (Å)	Crystallite size (nm)	X-ray Density (g cm^{-3})	Measured Density (g cm^{-3})	Porosity (P)
900°C	8.36	42.36	5.33	4.05	0.23
1000°C	8.33	45.53	5.33	3.83	0.28
1100°C	8.37	53.05	5.33	3.87	0.27

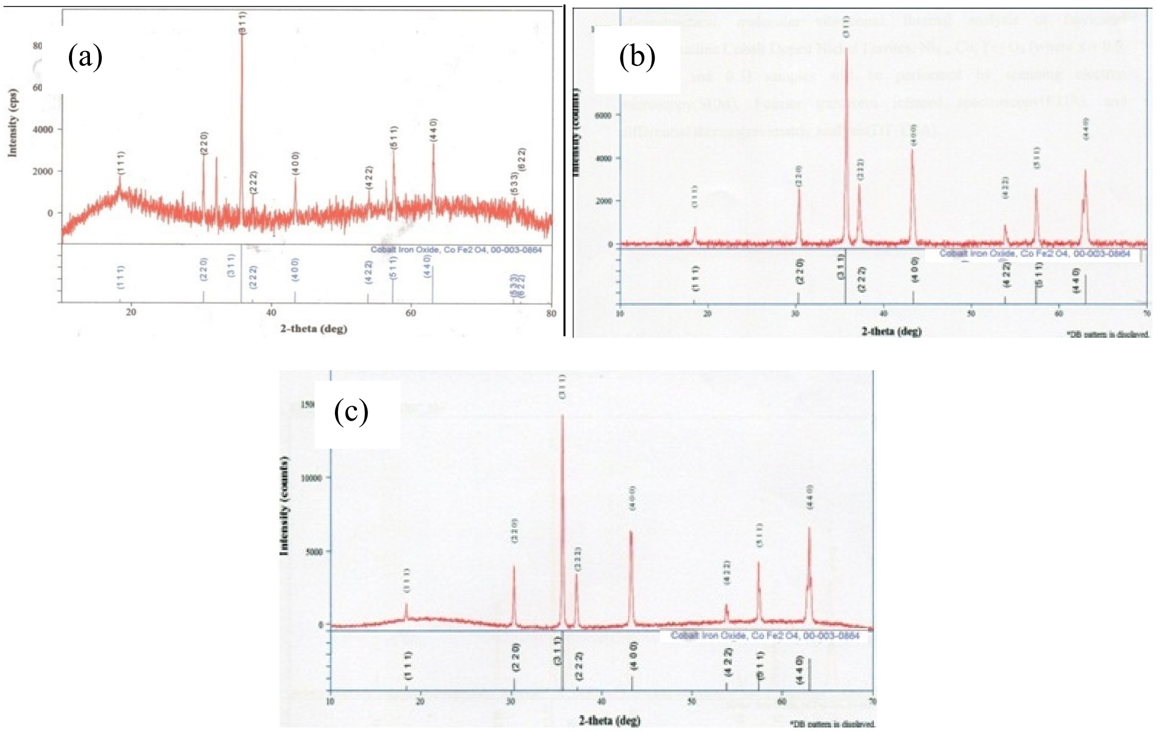

Figure 3 The XRD pattern of cobalt ferrite annealed at (a) 900°C (b) 1000°C (c) 1100°C

3.2 SEM analysis

The morphology and the distribution of $CoFe_2O_4$ nanoparticles were determined using SEMJEOL (JSM-67001). Typical SEM images of $CoFe_2O_4$ synthesized particles were shown in Figure 4. SEM micrograph depicted that the samples contain micrometrical aggregation of tiny particles. The existence of high dense agglomeration indicated that pore free crystallites are present on the surface. Two types of grain growth were observed. The first type was around 10 µm and second type was 2 µm.

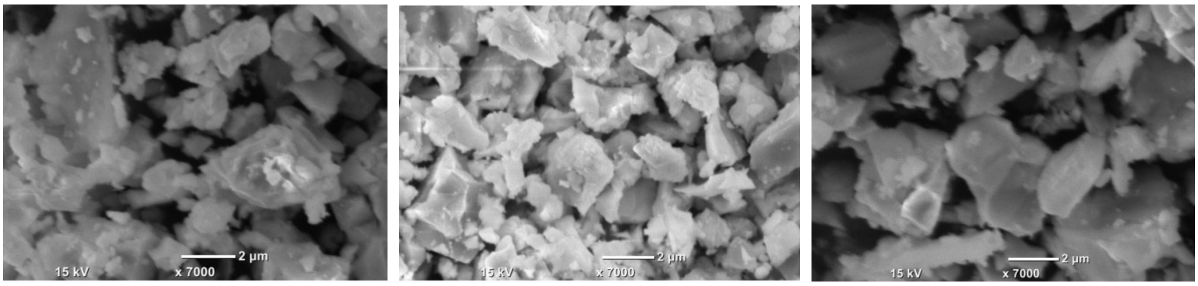

Figure 4 The SEM image of cobalt ferrite annealed at (a) 900°C (b) 1000°C (c) 1100°C

3.3 FTIR Analysis

In order to determine the chemical structure of the sample, the FTIR spectrum was observed cobalt ferrite in the frequency range of 4000-800 cm^{-1} as shown in Figure 5. The decomposition of hydroxide to oxide phase for the formation of spinel ferrites was well reflected in the FTIR spectrum. It had been reported that the IR bands of solids were usually attributed to the vibration of ions in the crystal lattice. The bands around 601 cm^{-1} and 461 cm^{-1} represented tetrahedral and octahedral modes of $CoFe_2O_4$, respectively. The band located around 3336 cm^{-1} could be attributed to the symmetric vibration of –OH groups. The peak at 1616.4 was related to the O-H vibrations related to the adsorbed water.

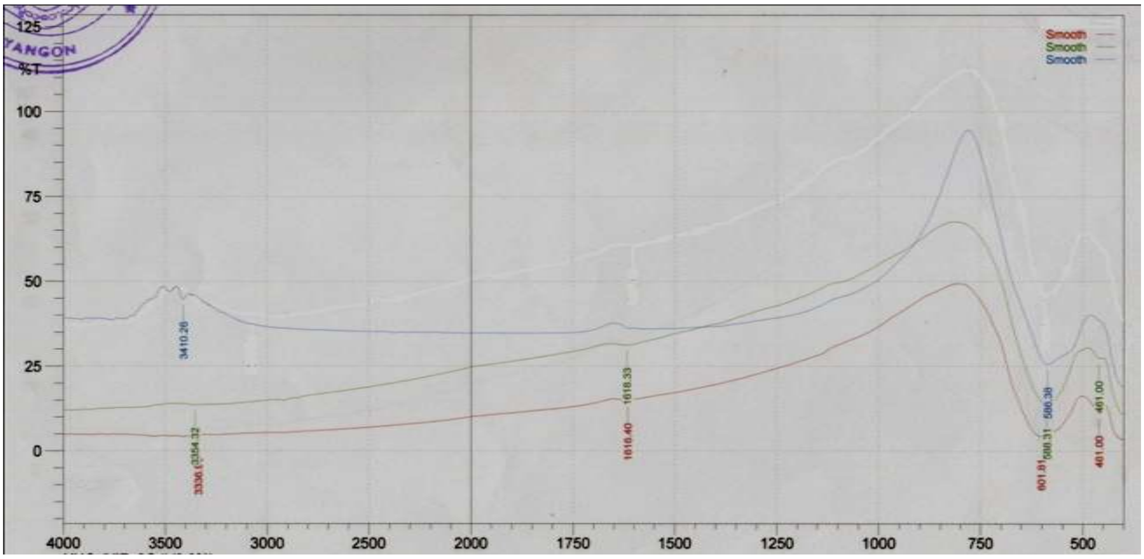

Figure 5 The FTIR spectrum of cobalt ferrite samples annealed at 900°C, 1000°C and 1100°C

3.4 UV-Vis measurement

The plot of $(\alpha h\nu)^2$ versus photon energy (hν) was shown in figure 6. In the direct transition, the absorption coefficient (α) related with the optical band gap (E_g) is given by, $\alpha h\nu = A(h\nu - Eg)^{1/2}$, where hν is the photon energy and A is a constant for a direct transition. The energy gap E_g could be estimated from the intercept of $(\alpha h\nu)^2$vshν for direct transitions. By extrapolating the linear portion of the energy axis at zero absorption gives the direct band gap of these materials. The energy gap of this sample was observed to be 3.24 eV.

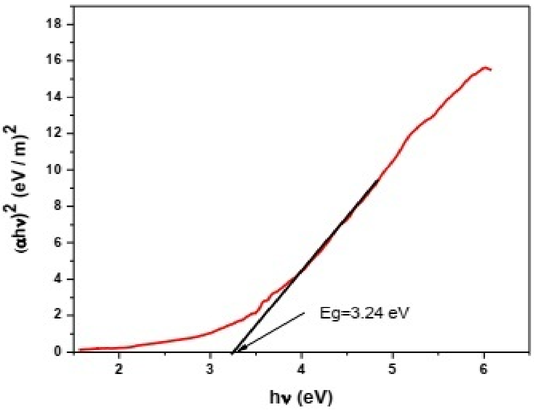

Figure 6 The estimated energy band gap value of $CoFe_2O_4$sample (1000°C)

3.5 Dielectric Properties

The dielectric properties of the ceramic$CoFe_2O_4$ were analyzed using GW Instek 8110 LCR meter over the frequency range 100Hz- 2MHz. The dielectric constant of $CoFe_2O_4$was studied at different temperatures. For measurements, the samples were obtained with the diameter of ~13 mm and thickness ~2 mm pellets; it was placed between the silver electrodes having a conventional two terminal sample holder with applied temperature. The capacitance of these samples was measured with temperature range 303 to 353 K with 10 K step and frequency ranging from 100 Hz to 2MHz. The variation of dielectric permittivity with temperature at different frequencies was shown in Figure 7. The low frequency regime observes high permittivity value whereas the high frequency regime observes comparatively low value. The relative permittivity value increased with elevation of temperature. The high dielectric permittivity was found at low frequencies and high temperatures. In present study, the maximum temperature of measurement is only 353K and hence no decrease in dielectric permittivity was observed. The low value of the dielectric constant with increasing frequency could be ascribed to the loose or weak bond of ions at the lower frequency range.

The decrease in dielectric constant with frequency was obvious because of the fact that any effect contributing to polarization was found to show lagging behind the applied field at higher and higher frequencies. By increasing the frequency beyond a certain frequency limit, the electron hopping could not follow the electric field fluctuations causing a decrease in the dielectric constant. Koop argued that the dielectric constant at low frequency comes from the grain boundaries which have a high dielectric constant due high resistivity at the grain boundary region. The dielectric constant at high frequency comes from the grains which have a small value of dielectric constant due to low resistivity. At high temperature, space charges near grain boundaries and electrode contacts were activated and had their displacement along the field direction. This caused space charge polarization which was highly temperature dependent.

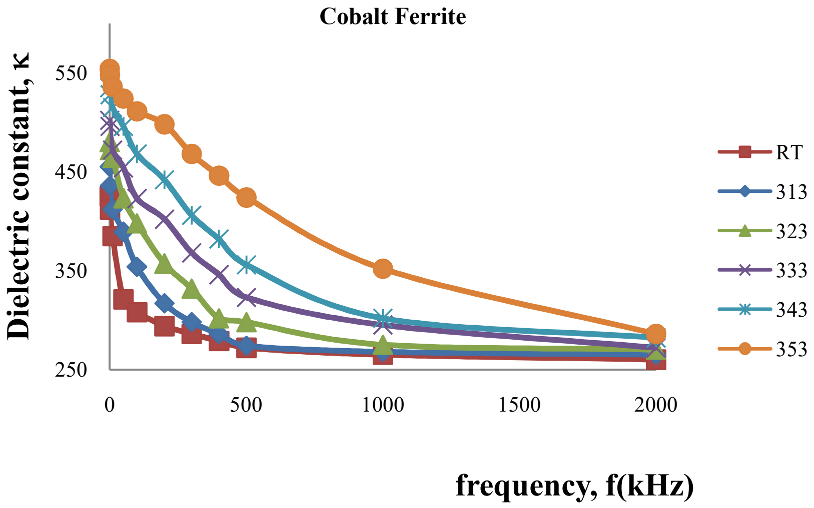

Figure 7 Dielectric Constant (κ) behaviour of the $CoFe_2O_4$samples(1000°C) in the Frequency Range 100Hz to 2MHz

3.6 AC Conductivity analysis

Figure 8 represented the ac conductivity behavior of polycrystalline cobalt ferrite. The low temperature region showed a slow transition from a weak frequency dependent conductivity to strong frequency variant part. The fast frequency dependent region appeared at high frequency regime as the conduction process, was due to the localized relaxation hopping mechanism of ions or electrons. According to jumping relaxation model the conductivity in ferrites was due to the hoping mechanism of charge carriers**.** As frequency approaches relaxation point, charge carriers hop through short distance before the cycle changes. Beyond relaxation frequency, thermal energy could not drive the ions to a long range in order to follow the changing ac cycle rather a localized movement was possible which gave the fast frequency variant region.

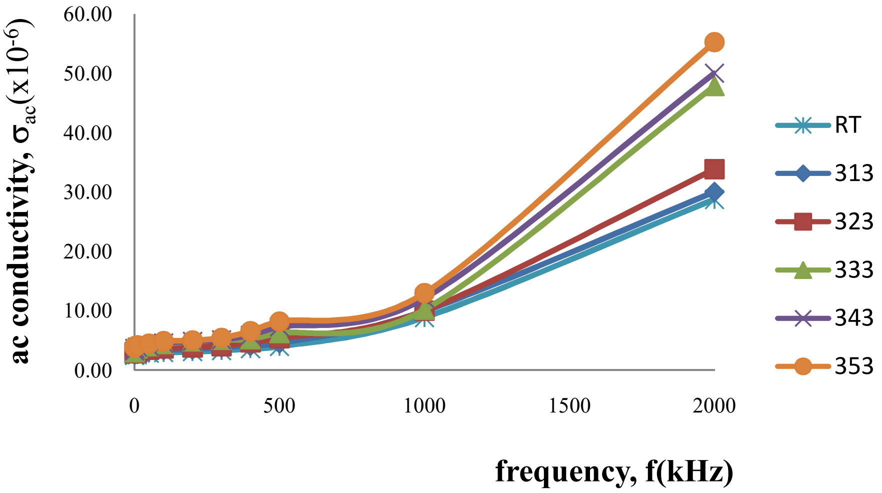

Figure 8 Variation of AC conductivity of $CoFe_2O_4$samples(1000°C)with frequency

3.7 Magnetic measurements

The magnetic behavior of $CoFe_2O_4$ nanoparticles was investigated using PERMAGRAPH L. Room temperature field dependent magnetic properties of the cobalt ferrite was shown in the figure 9. It exhibited B-H loop at room temperature which represents the ordered state of sample at room temperature. The magnetic property of the cobalt ferrite strongly depends on the cation distribution between the tetrahedral and octahedral sites and grain/particle size of the ferrites. In ferrimagnetic materials net magnetization was equal to difference between the individual magnetic moments of antiferromagnetically interacted octahedral (A) and tetrahedral (B) sites. The estimation of magnetostrictive constant (λ_S) for the ceramic $CoFe_2O_4$samplewas to be $13.44x10^{-5}$. In bulk form cobalt ferrite exhibits inverse spinel structure where cobalt occupies only octahedral site and iron equally distributed in octahedral and tetrahedral sites. The remanent and coercivity value for the $CoFe_2O_4$nanoparticle was observed about 8.7338×10^{-3}emu/g and 427.03 G respectively.

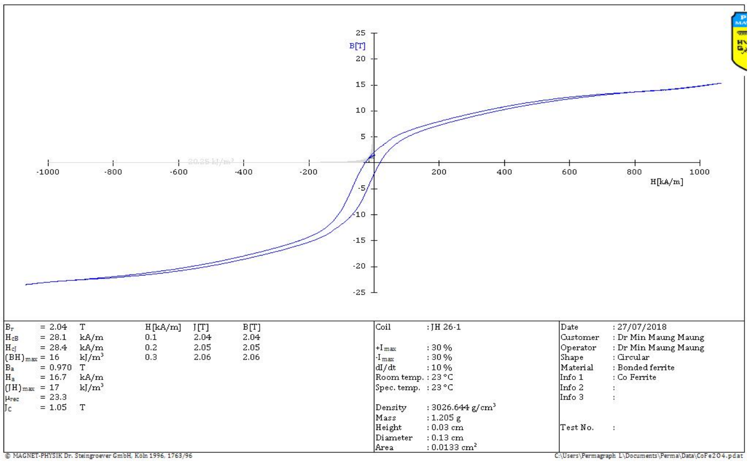

B_r = 2.04 T
H_{cB} = 28.1 kA/m
H_{cJ} = 28.4 kA/m
$(BH)_{max}$ = 16 kJ/m³
B_a = 0.970 T
H_a = 16.7 kA/m
$(JH)_{max}$ = 17 kJ/m³
μ_{rec} = 23.3
J_C = 1.05 T

H[kA/m]	J[T]	B[T]
0.1	2.04	2.04
0.2	2.05	2.05
0.3	2.06	2.06

Coil : JH 26-1

$+I_{max}$: 30 %
$-I_{max}$: 30 %
dI/dt : 10 %
Room temp. : 23 °C
Spec. temp. : 23 °C

Density : 3026.644 g/cm³
Mass : 1.205 g
Height : 0.03 cm
Diameter : 0.13 cm
Area : 0.0133 cm²

Date : 27/07/2018
Customer : Dr Min Maung Maung
Operator : Dr Min Maung Maung
Shape : Circular
Material : Bonded ferrite
Info 1 : Co Ferrite
Info 2 :
Info 3 :

Test No. :

© MAGNET-PHYSIK Dr. Steingroever GmbH, Köln 1996, 1763/96

C:\Users\Permagraph L\Documents\Perma\Data\CoFe2O4.pdat

Figure 9 Room temperature B-H behavior of $CoFe_2O_4$samples(1000°C)

Conclusion

The cobalt ferrite ($CoFe_2O_4$) samples of different particle size were successfully prepared by nitrate route. The X- Ray diffraction (XRD) patterns of all the samples showed the single phase spinel structure of nanoparticles. FTIR spectrum also supported the formation of $CoFe_2O_4$ attributed to the vibration of ions in the crystal lattice. The surface morphology was observed to be densely packed with irregular grains. From the dielectric studies it became evident that the dielectric constant and the loss decreases rapidly with increasing frequency, and then reaches a constant value. Room temperature B-H loop indicates the orderedness of the ferrimagnetic cobalt ferrite. Low dielectric constants materials were required for high frequency application in electrical circuits, to reduce dielectric losses and skin effect. The high value of electrical resistivity in ferrite was suitable for the high frequency application where eddy current losses are appreciable. The resistivity was decreased with increase in temperature and the material behaved like a semiconductor. Bulk ferrites remained a key group of magnetic materials, while nanostructured ferrites showed a dramatic promise for applications in even significantly wider fields.

Acknowledgements

I would like to express my profound thanks to Professor Dr Khin Khin Win, Head of Department of Physics, and Professor Dr Myo Lwin, Professor Dr Aye Aye Thant, Professor Dr Yin Maung Maung, Department of Physics, University of Yangon, for their kind permission to carry out this work, their encouragement and help during this work.

References

Moulson A J & Herbert J M (1997) Electroceramic Materials Properties Applications (New Delhi: Thomson Press)

Rajagopal K. (2009) Textbook of engineering physics part II. New Delhi-110001.

Ranjit Kumar Panda, (2015) Studies on Electric and Magnetic Propertiesof Cobalt Ferrite and its Modified Systems,National Institute of Technology, India

Steingroever GmbH. Dr, (2010), Computer controlled permagraph® L” Cologne-Germany.

Suryanarayana C. and Norton M. G. (1998), X-ray Diffraction A Practical Approach, (New York: Plenum)

Xu Y, (1991) Ferroelectric Materials and their Applications, New York: Elsevier Science Publishing Co. Inc.

J. Myanmar Acad. Arts Sci. 2020 **Vol. XVIII.No.2A**

STRUCTURAL CHARACTERIZATION OF COBALTDOPED BISMUTH FERRITE MATERIALS

Aye Aye Khaine[1], Lei Lei Aung[2], Myo Myint Aung[3]and Min Maung Maung[4]

Abstract

Bismuth ferrite ($BiFeO_3$)and cobalt doped $BiFeO_3$($BiFe_{1-x}Co_xO_3$) materials was prepared by combustion method. The X-ray diffraction (XRD) method confirmed crystalline phase and crystalline size of these materials. The average crystallite size was obtained 30.26 nm. The shifting of peaks to higher angles was observed in cobalt doped $BiFeO_3$. The formation of bonding structure was also identified by Fourier Transform infrared Spectroscopy (FTIR), it confirms the existence of Fe-O and Bi-O bands. The energy band gap was also evaluated from the measurement of UV spectrophotometer. It was observed that the increase in optical band gap with increasing in cobalt doping concentration in the $BiFeO_3$ structure.

Keywords: bismuth ferrite; Auto-combustion technique; XRD; crystallite size; FTIR; FWHM.

Introduction

Multiferroicoxides have the unique properties of both ferromagnetism and ferroelectricity in a single crystal. This opens broader applications in transducers, magnetic field sensors and information storage industry. These include $BiFeO_3$, $BiMnO_3$, $TbMnO_3$, $TbMn_2O_5$, $YMnO_3$, $LuFeO_4$ and $Ni_3B_7O_{13}I$. Among these oxides $BiFeO_3$ (BFO) is the only material which gives ferroelectricity and antiferromagnetism at room temperature. Due to coexistence of both ferromagnetism and ferroelectricity in the same material, it is expected to exhibit ferromagnetic & ferroelectric properties or a coupling of these two properties in a single material. This increases the current range of application and moreover interesting physics may be observed.

A single phase multiferroic material is one that possesses two of the three ferroic ‟ properties i.e ferroelectricity, ferromagnetism and ferroelasticity. Generally current trend is to exclude the requirement for ferroelastic property. Magnetoelectric coupling describes the coupling between magnetic and electric order parameters. $BiFeO_3$ is the only prototype among all other multiferroic oxides which shows both ferromagnetism and ferroelectricity in a single crystal above room temperature. It has ferroelectric Curie temperature T_c = 1143K and antiferromagnetic Neel temperature T_N= 643K. The ions responsible for the production of ferroelectricity and magnetism are Bi^{3+} and Fe^{+3} ions. Ferroelectricity is produced due to Bi^{3+} and antiferromagnetism is due to Fe^{+3} ions. It is having rhombohedrally distorted perovskite structure with R3c space group at room temperature. Bi^{3+} ion occupy the corner position, Fe^{3+} in the body centred position, and O_2- in allface centred position. The lattice parameters are a = 5.587 Å, b = 5.587 Å and c = 13.867 Å with $\alpha = \beta = 90°$ and $\gamma =120°$. The Orthorhombic unit cell contains 6 formulas.

In the present work, cobalt doped bismuth ferrite was prepared by sol-gel combustion method. The XRD, SEM and FTIR analyses indicate the formation of single phase materials with particle size in the nanometer range. The energy band gap measurement was also done by using UV spectrophotometer.

---

[1] Dr, Associate Professor, Department of Physics, Yangon University of Distance Education.

[2] Dr, Associate Professor, Department of Physics, Yangon University of Distance Education.

[3] Dr, Associate Professor, Department of Physics, Yangon University of Distance Education.

[4] Dr, Associate Professor, Department of Physics, University of Yangon.

Experimental Procedure

The samples were prepared by sol – gel combustion route. The fuel chosen for the synthesis was ethylene glycol. The stoichiometric amount of $Bi(NO_3)_3.5\ H_2O$salt was dissolved in the mixture of ethylene glycol and deionized water by constant stirring at the temperature 40-50°C. Then $Fe(NO_3)_3.9H_2O$salt was added to the mixture. Now the colour of the solution changes from colour less to brick red then red and finally blackish red. After 1 hour of continuous stirring the solution is heated with stirring at a temperature of 70°C. After 3hours of heating and stirring the solution became transparent gel. Then after few minutes and in some elevated temperature yellow colour precipitation occurred. This precipitate was found to be hygroscopic when left for 10 hours. So the sample was then again heated at a temperature100°C, to vaporize all the water content from the sample. After some time the powder in the bottom of beaker turned black, gradually the whole powder become blackish. The black powder was also found to be hygroscopic. The powder collected was then calcined for 4 hours at a temperature of 900°C. The furnace heating rate is maintained as 4° / minute. After cooling, the sample is collected from the furnace and is grinded by agate-mortar. The grinded powder is now ready for necessary characterization. To obtain the Co doped BFO, $Co(NO_3)_3.6H_2O$ is added after $Bi(NO_3)_3\ .5\ H_2O$ then followed by $Fe(NO_3)_3.9H_2O$.

Result and Discussions

XRD Analysis:

Phase analysis was studied using the room temperature powder X-ray diffraction with filtered 0.154 nm Cu Kα radiation. Samples were scanned in a continuous mode from 20°–80° with a scanning rate of30/minute. XRD patterns of Co doped $BiFeO_3$ (BCFO) ceramic calcined at 900°C were shown in the figure 1.The prominent peaks in XRD plot were indexed to various hkl planes of BCFO, indicating formation of BCFO. Besides these prominent peaks, some other peaks of low intensity are also observed, which do not belong to BFO. The literature survey of BFO synthesis relates these impurity peaks to be that of $Bi_2Fe_4O_9$ and $Bi_{25}FeO_{39}$. The appearance of these extra phases at 900°C could be due to large bismuth loss at higher temperature. These results indicates that on cobalt doping up to 5 mol % at Fe site, the Orthorhombic structure of BFO does not change appreciably, except increase in $Bi_{25}FeO_{39}$ and $Bi_2Fe_4O_9$ impurity phases at 330 and 280. The intensity of impurity peaks increases with increase in doping concentration, indicating increasing concentration of impurity phases. The crystallite parameter and the average crystallite size were listed in the table 1.

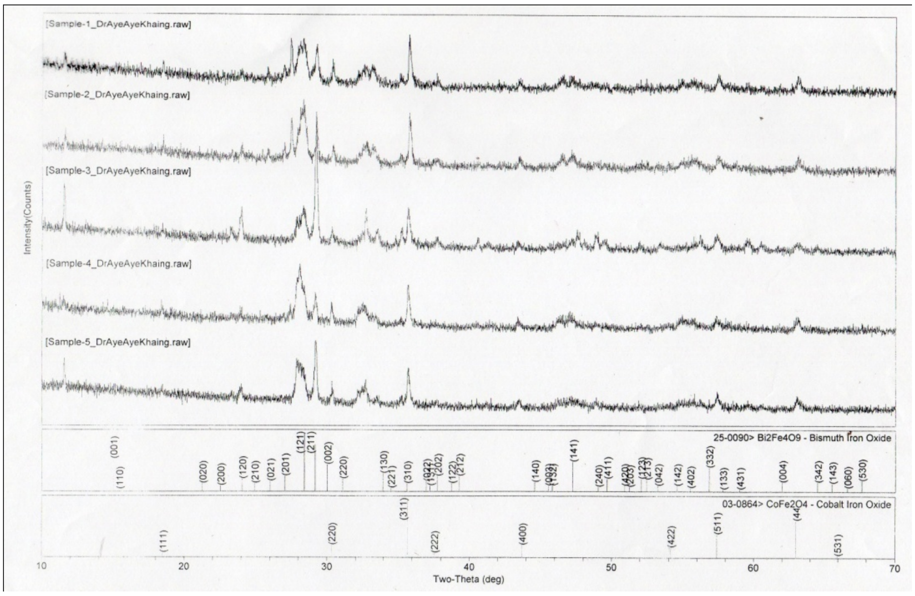

Figure 1 The XRD pattern of Co doped $BiFeO_3$ materials Lattice parameters, FWHM and crystallite size of $BiFe_{1-x}Co_xO_3$

Prepared samples	a (Å)	b (Å)	c (Å)	FWHM	Crystallite size (nm)
$CoFe_{0.9}Ni_{0.1}O_3$	6.4500	9.6271	5.8773	0.299	27.6485
$CoFe_{0.8}Ni_{0.2}O_3$	7.8436	8.8917	5.9115	0.303	27.282
$CoFe_{0.7}Ni_{0.3}O_3$	6.6096	9.6105	5.3578	0.274	30.133
$CoFe_{0.6}Ni_{0.4}O_3$	7.5978	8.8636	5.9532	0.242	29.240
$CoFe_{0.5}Ni_{0.5}O_3$	7.7436	9.0019	5.8609	0.223	37.031

TGA-DTA analysis:

The TGA-DTA analysis of all the three samples was carried out using thermo gravimetric analysis and differential scanning calorimetric (DSC-TG) by heating the sample at 10 °C/min. The plot was shown in the figure 2. Figure showed the TGA-DTA analysis of unleached & calcined BFO, by taking heat flow and mass loss in Y – axis and temperature in X – axis. The TGA plot of BFO reveals a broader decrease in mass near 100°C due to evaporation of water molecules. As gradually increase the temperature there was a considerable loss of mass around 300 - 400°C, which is a broader one. It may be due to bismuth loss around this temperature, as bismuth is having boiling point of275°C. The mass was gradually decreasing and around 350°C there wais an increase in mass which may be due to formation of some new compounds by reaction of the sample with the atmosphere. The broader depression around 430°C may be due to melting of the compound and presence of some liquid phase. The broader endothermic peak around 280°C showed there was a consider able amount of liquids are formed at this temperature. The mass loss plot showed there is a continuous decrease of mass as increase the temperature and around 500°C the mass loss rate was decreased and again it was saturated.

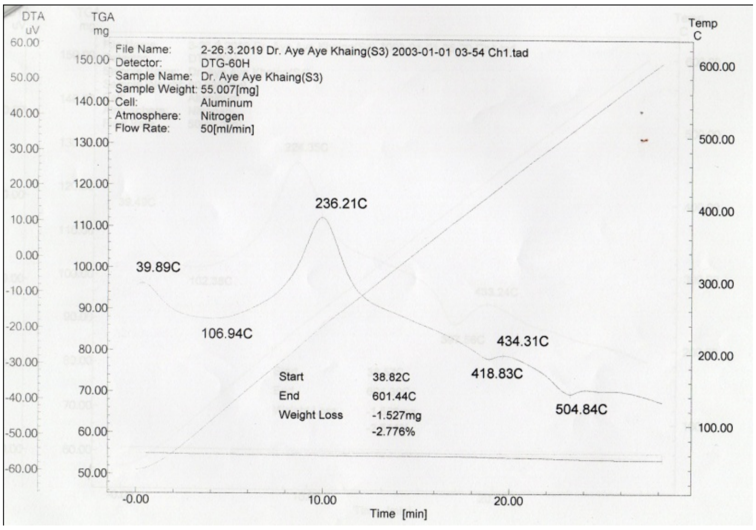

Figure 2 The TGA-DTA plot of Co doped $BiFeO_3$ materials

SEM Analysis:

Microstructural features were studied using Scanning Electron Microscope. The SEM microstructure of all samples is given in figure 3. All the samples are leached and sintered. The samples were in agglomerated form and it had no definite shape and size. The microstructure of the samples sintered showed appearance of sharp features and blocks of various shapes and sizes (100 nm to 1μm). Another important thin gone may observe while comparing the micrographs of the sintered samples that the grain size goes on increasing as increase the doping concentration of Cobalt. This result is well agreement with the x-ray diffraction data, which showed decrease in lattice volume with cobalt concentration.

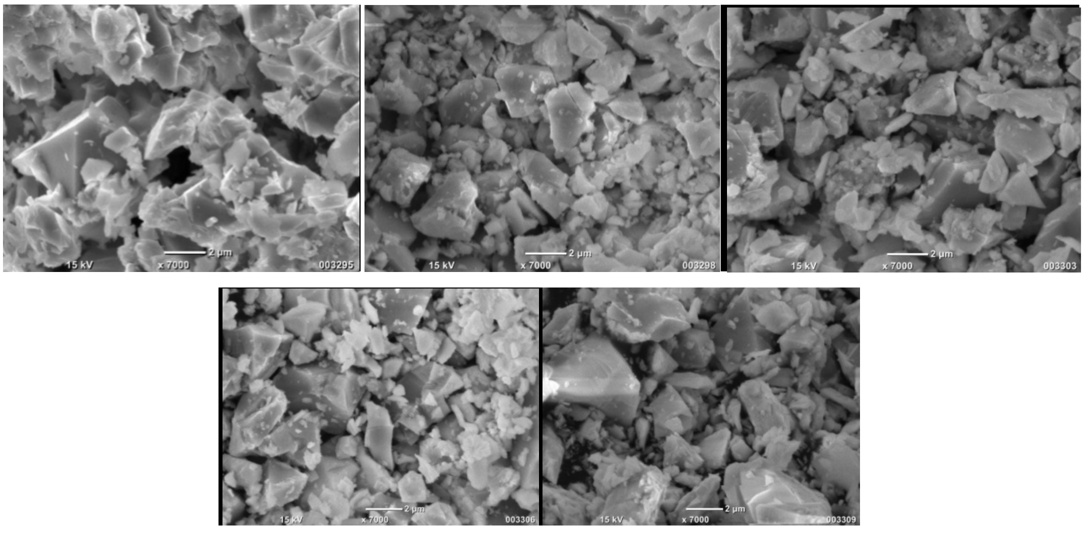

Figure 3 The SEM images of Co doped $BiFeO_3$ materials

FTIR Analysis

The FT-IR spectra of $CoBi_xFe_{2-x}O_4$, (where x = 0.1, 0.2,0.3, 0.4, 0.5) nano ferrite particles, synthesised at room temperature was represented in the figure 4. As shown, four characteristic IR peaks together with some weak peaks appeared for BCFO precursor using citric acid as chelating. The above broad frequency range corresponds to O-H stretching, H-O-H bending vibration of water molecules and spinal structure with sub-lattices respectively Samples had two sharp and one wide IR peaks, which correspond to the stretching vibrations of C=O and –OH. The IR wide peaks located at 2370 cm^{-1} were assigned to the stretching vibrations of structural hydroxyl (OH) groups, and the intense peaks at 1368.52 cm^{-1} were assigned to the stretching vibrations of C=O. The IR peaks located at 1368.52 cm^{-1} were attributed to the symmetry bending vibration of C–H. The IR peaks below 1000 cm^{-1} (such as 617, 591, 683,898, and 990 cm^{-1}) were corresponding to the vibrations bonds of Bi–O or Fe–O, respectively. The presence of frequency bands in this specific range explained the normal mode of vibration of tetrahedral cluster was higher than that of octahedral cluster in the spinel ferrites. The highest one corresponds to the intrinsic stretching vibrations of the metal at the tetrahedral site, whereas the lowest band was assigned to octahedral-metal stretching. This difference between the tetrahedral and octahedral clusters of spinel ferrite was because of the variation in distance between Fe^{3+}-O^{2-}ions in tetrahedral and octahedral sites. The wave band v_1 showed an increase in the values with increase in Bi concentration which may be due to dissimilarity in the cations-oxygen bond length.

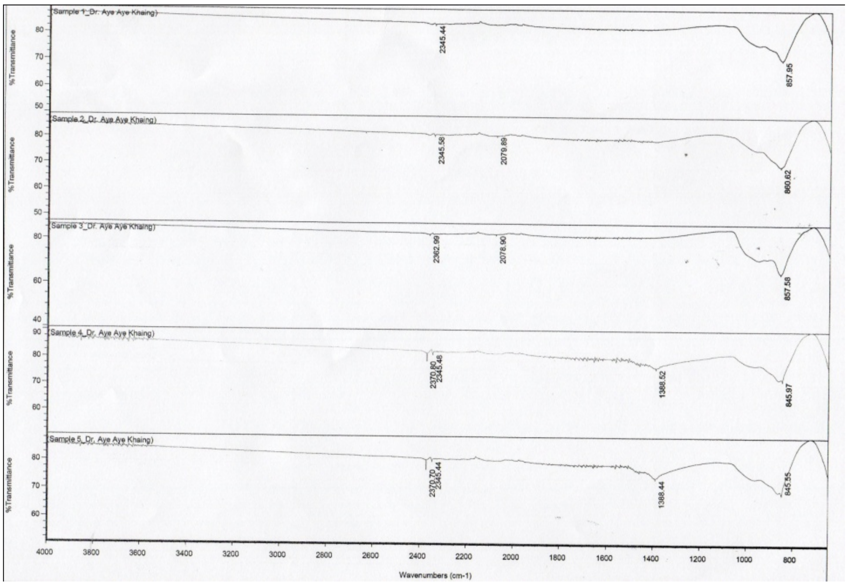

Figure 4 The FTIR spectrums of Co doped $BiFeO_3$ materials

Energy Gap measurement

The energy band gap of the material was measured using Tauc relation $(\alpha h\nu) = A (h\nu - E_g)^n$ where αwas the absorption coefficient, A was an energy independent constant of the absorption frequency, h was Planck's constant, E_g was band gap, m was frequency of incident photon and n is the index which depends on electronic transitions responsible for optical absorption. The value of optical energy band gap E_g has been calculated for the all samples by $(\alpha h\nu)^2$vs*hν*plots The values of E_g for different samples were found by extrapolating the linear portion to the *hν* determine the energy band gap E_g to be from 4.5 to 5.2 eV.

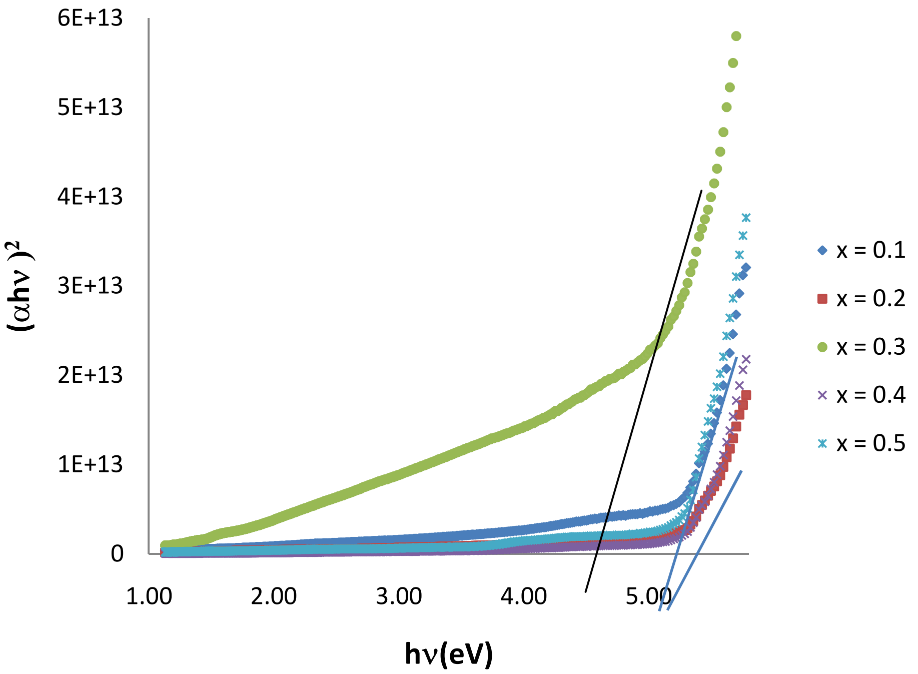

Figure 5 The energy band gap of Co doped $BiFeO_3$ materials

Conclusion

The samples were successfully prepared by sol-gel combustion synthesis method. Small amount of impurity phases are observed by x-ray diffraction results. The lattice parameters are a = 7.8436Ȧ, b = 8.8917Ȧ, c = 5.9115Ȧ and the crystral structure is Orthorhombic. The impurity phase growed with temperature from the literature survey, the impurity phases could be indexed to$Bi_2Fe_4O_9$ and $Bi_{25}FeO_{39}$. The cobalt doped BFO also found to be having impurity phases and it increases with increase in concentration of cobalt. Upon co-doping, the lattice volume of BFO decreases with cobalt concentration. This may be due to smaller ionic radius of cobalt (74 pm) than that of iron (78pm).From the SEM images of the BFO unsintered powder it is observed the powder is agglomerated and when this powder is sintered at 900°C and the SEM image revealed grains of tiny block with grain size varying from 100nm to 1µm. With increase in cobalt concentration there was shrinkage in grain size. The IR peaks below 1000 cm^{-1} were corresponding to the vibrations bonds of Bi–O or Fe–O, respectively. This difference between the tetrahedral and octahedral clusters of spinel ferrite was because of the variation in distance between Fe^{3+}-O^{2-}ions in tetrahedral and octahedral sites. The wave band ν_1 showed an increase in the values with increase in Bi concentration which may be due to dissimilarity in the cations-oxygen bond length. The energy bond gap Eg is the range of 4.7eV to 5.2eV for prepared samples.

Acknowledgement

We are deeply grateful to Pro-Rector Dr Tin Mg Hla, Yangon University of Distance Education, for her kind permission to carry out our research work. We would like to thank Professor Dr Moh Moh, Head of Department of Physics and Professor Dr Mar-lar Myint, Department of Physics, Yangon University of Distance Education, for their kind permission to carry out this research work. We wish to express our sincere thanks to everyone who gave suggestion and help to make this research reality.

References

Ahmad S et al, 2004, “Ferroelectric Ceramics Processing Properties and Applications”, Department of Ceramic Science and Engineering, Rutgers University: USA

“Instruction Manual LCR meter GW 820”, USA

Moulson A J & Herbert J M, 1997, “Electroceramic Materials Properties Applications”, New Delhi: Thomson Press

Suryanarayana C. and Norton M. G. (1998), X-ray Diffraction A Practical Approach, (New York: Plenum)

Tyagi M S, 1991, “Introduction to Semiconductor Materials and Devices”, New York: Wiley

Xu Y, 1991, “Ferroelectric Materials and their Applications”, New York: Elsevier Science Publishing Co. Inc.

J. Myanmar Acad. Arts Sci. 2020 Vol. XVIII.No.2A

COMPARATIVE STUDY ON PHOTOVOLTAIC BEHAVIOR IN ORGANIC- INORGANIC HYBRID PHOTOVOLTAIC CELLS OF SI AND FTO SUBSTRATES

May Thu Aung[1], Myo Min Thein [2], Cho Cho Khing[3], Ei Ei Phyu Htwe[4]

Abstract

Organic Inorganic hybrid Photovoltaic cells were fabricated by using Polyaniline (PANI) nanofibers and semiconducting oxide (BSO). PANI-BSO hybrid polymeric blend were coated on two different substrates Si and FTO by using spin coating method. The structure and surface morphology of PANI-BSO/Si film and PANI-BSO/FTO film were characterized by using XRD, SEM, and AFM respectively. UV-vis spectroscopy was carried out to study light absorption behavior of fabricated films. Especially, comparison between photovoltaic properties of fabricated hybrid photovoltaic cells was studied.

Keywords: Hybrid Photovoltaic cell, Spin coating, XRD, SEM

Introduction

Organic-inorganic photovoltaic (PV) solar energy conversion is an attractive method for clean and green energy generation. Organic –inorganic hybrid have attracted considerable attention as possible next-generation thin-film solar cells because of advantages such as low-cost, environmentally safe, flexible, light weight and inexpensive[D.G. Michael et al 2009].A typical OPV device consists of one or several photoactive materials sandwiched between two electrodes. An organic photovoltaic cell (OPV) composed of a film of organic photovoltaic active layer (electron transport layer, hole transport layer) is sandwiched between transport electrode (anode and cathode). There are two fundamental functions: photogeneration of charge carriers (electron and hole) in a light absorbing material and separation of the charge carriers to a conductive interaction to transmit electricity. The active region of an organic device consists of two materials, one which acts as, an electron donor and the other as an electron acceptor[H. Jin, H. Sang & K.Nazeeruddin 2013]. Organic photovoltaics were extensively investigated because of their potentially low-cost nature and simplicity in fabrication. The interest in organic/inorganic heterojunctions (HJs) has grown simultaneously with most studies on BSO based photovoltaics. The active participation of polymer in photocurrent generation was also confirmed [D.J. Hermant et al 2011].

In recent decades, several studies have been carried out to enhance polyaniline-metal oxide hybrid nanocomposites materials. The electrical property of polyaniline is an important factor which could be modified by the addition of inorganic fillers such as metal oxide nanostructures with dimensions in the nanoscale. In this study, hybrid photovoltaic devices use a blend of aniline polymers and n-type semiconductive oxide, BSO to convert sunlight into charges. There are several types of interlayer materials including the conductive polymeric materials, self- assembled molecules and metal oxides. One of the key components in the inverted OPV is the electron transport layer (ETL) materials on conducting oxide electrodes such as titanium oxide (TiO_2), zinc oxide (ZnO), Lead Sulphide (PbS), Barium Stannate ($BaSnO_3$) and

---

[1] Dr, Demonstrator, Department of Physics, Maubin University.

[2] Assistant lecturer, Department of Physics, Maubin University.

[3] Professor and head, Department of Physics, Maubin University.

[4] Lecturer, Department of Physics, West Yangon University.

Cadmium Suiphide (CdS), cesium carbonate (Cs_2CO_3). Perovskite structure$BaSnO_3$has gained increasing attention recently as a candidate material for next generation oxide electronic devices. This material has shown notably high electron mobility at room temperature, reported to be up to 320 $cm^2V^{-1}s^{-1}$in bulk single crystal ,with good optical transparency in the visible region. These properties are desirable in transparent conducting materials for solar cells, displays, high-mobility channels for transistors, and other applications[J. Cerda, et al 2002].Hole transport layer (HTL), polyaniline which is more effective charge transport properties in hybrid photovoltaic cell. Herein, we demonstrate that we have successfully synthesized highly crystalline and discrete $BaSnO_3$ nanoparticles, which enable the fabrication of mesoporous films with improved photovoltaic properties. We demonstrate the photovoltaic performance of hybrid photovoltaic cells based on two different electrodes. [N. Go spodinova, & Terlemezyan1998].

In this research, PANI-BSO/Si and PANI-BSO/FTO nanocomposite film were fabricated and comparative Study on Photovoltaic Behavior of fabricated hybrid photovoltaic cells was carried out.

Experimental

Synthesis of polyaniline (PANI) polymer

Polyaniline has been synthesized by chemically in emeralidine salt from using redox polymerization of aniline in presence of ammonium peroxyd isulfate (APS) as an oxidant and HCl as a dopant. Aniline 43 ml in 10ml of 1M HCl solution at room temperature was stirrered for 1hr,then 20g of APS solution was added at a rate of 5 drop/min. After adding complete solution of APS the mixture was stirring for 2hr. The precipitate was washed with ethanol, acetone and DI water and then filter with filter paper. To get fine and dry PANI polymer, the specimen was annealed at 100ºC for 5hr.The structure and particle size of the PANI nanoparticles were characterized by XRD.

$BaSnO_3$ (BSO) Nanoparticle fabrication

Perovskite $BaSnO_3$ was successfully synthesized by solid state reaction method. $BaCO_3$ and SnO_2 were used as precursors. (1:1) weight ratio of $BaCO_3$ and SnO_2 were grinded by mortar and pestle. 2methoxythanol was used as solvent. To obtain homogeneous mixture, the mixture was grinded for 3hr. Then, the specimen was preheated at 900°C for 4hr.This ceramic is high melting point. So the sample was calcined at 1100°C for 4hr in order to disappear coformation of Ba_2SnO_4 phases along with $BaSnO_3$. To obtain fine powder of BSO nanoparticles the specimen were crushed with mortar and pestle and then sieved with mesh for three times.

Preparation of Nanocomposite Films

Nanocomposite films of inorganic materials (BSO) and PANI were prepared by mixing (1:2) weight ratio of PANI and inorganic nanoparticles. 2-methoxythanol was used as solvent. At first, the desired composition of inorganic materials, organic material and solvent were mixed and the mixture was stirred with magnetic stirrer for 1hr. To get homogeneous mixture, this solution was refluxed with water bath at 100ºC for 1hr. For the substrate, FTO coated glass was used. Before the deposition of thin film, the substrate was also cleaned with ethanol, acetone and deionized water respectively. After that nanocomposite mixture was deposited on FTO substrate using spin coating machine. The deposition parameters were 3000 rpm deposition speed and 1 min deposition time at room temperature. After heated at 400 ºC for 1hr and dried at room temperature, a good nanocomposite films were obtained. To determine their microstructure, optical absorption and photovoltaic cell properties, SEM, AFM, UV-visible spectroscopy and current density-voltage characteristics measurement analyses were carried out.

Results and Discussion

Structural Characterization of PANI and BSO

XRD technique was used to examine toward studying phase analysis, powder structure, crystallographic investigation and lattice parameters for fabricated samples. The structural properties were determined by using a Diffractometer (Rigaku RINT 2000). XRD was performed using monochromatic CuK$_\alpha$ radiation (λ= 1.54056Å) operate at 40 kV(tube voltage) and 40 mA (tube current). Sample was scanned from 10° to 70° in diffraction angle.

The XRD spectrum of BSO and PANI samples were indicated as shown in Figure 1(a&b). Upper side of XRD profile was represented the observed profile while the lower side indicated the standard/ reference profile was JCPDS (Joint Committee on Powder Diffraction Standards) library file.

The XRD spectrum of polyaniline (PANI) samples was indicated as shown in Figure 1(a). In these spectrums, six diffraction patterns were observed and all of these patterns were consistent with standard polyaniline. Study of standard data JCPDS 00-0531890 confirmed that the synthesized materials were orthorhombic structure. In these spectrum, (110) diffraction plane was the most intense. The two extra peaks of (100) and (110) was observed and it was due to formation of poly(aminobenzene).

In XRD spectrums of BSO sample was shown in Figure1(b). these spectrums, five diffraction patterns were observed and all of these patterns were consistent with standard BSO. Study of standard data JCPDS 15-0780 confirmed that the synthesized materials were cubic BSO phase (perovskite structure). In these spectrum, (110) diffraction plane was the most intense. The calculation of lattice constant and crystallite size for PANI and BSO samples were listed in Table1 and 2.

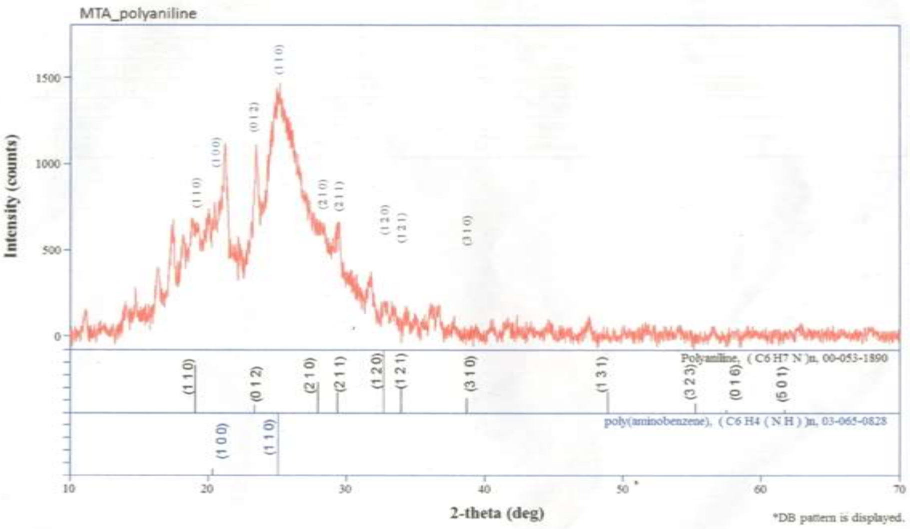

Figure 1 (a) XRD Profile of PANI

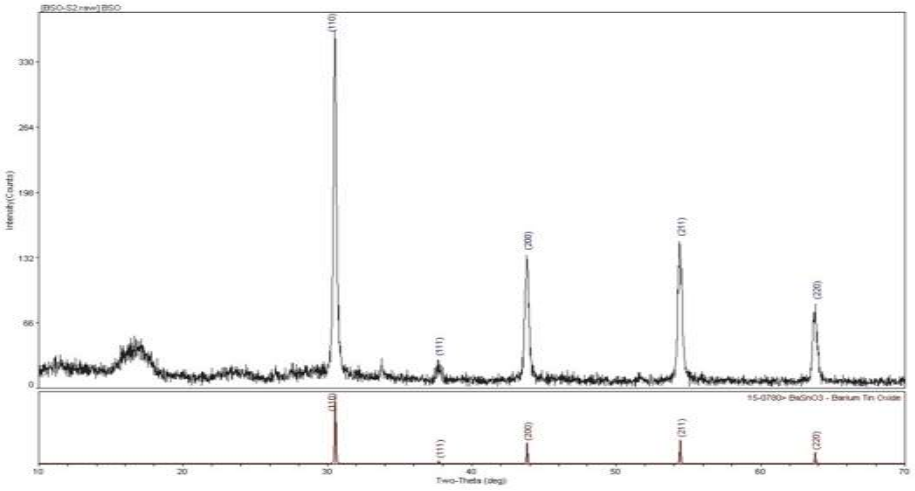

Figure 1 (b) XRD Profile of BSO

Table 1 The value of lattice constant and crystal structure of fabricated PANI, PbS and BSO samples.

Sample	Lattice constant a (Å)	Lattice constant c (Å)	Lattice Strain c/a	Phase
PANI	7.7148	5.7956	0.7512	Orthorhombic
BSO	4.1301	4.1301	1	Cubic

Table 2 The variation of crystallite size of fabricated PANIandBSOsamples

Sample	G(nm)
PANI	34.52
BSO	30.72

Microstructural Properties of Polyaniline and BSO Samples

The microstructural properties of fabricated samples were studied by Scanning Electron Microscopy (SEM). Figure 2(a) showed the SEM images of polyaniline. In this figures, polyaniline nanofibers was clearly observed. The connectivity between grain were observed and they were agglomerated to each other. Figure 2(b) showed the SEM images of BSO. In this figures microstructural particles were observed. The surface morphology was rough and dense. All grains have circular feature. The connectivity between grains were pronounced. It was consistent with XRD results. The average grain size of these samples were found to vary from 0.2 to 0.3 µm. It was consistent with XRD results.

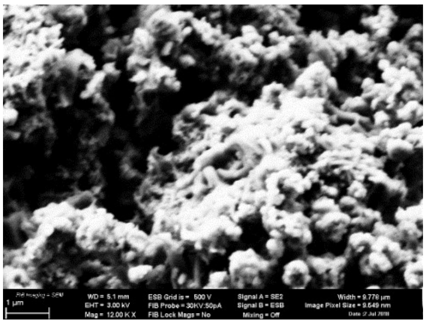

Figure 2 (a) Scanning Electron Image of PANI

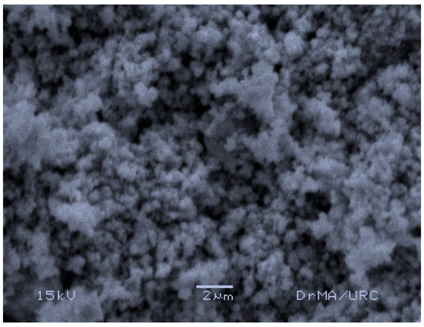

Figure 2(b) Scanning Electron Image of BSO

AFM studied of PANI-BSO/Si and PANI-BSO/FTO Nano Hybrid

The properties of a broad range of materials and performance of different devices depend strongly on their surface characteristics. The morphological and surface roughness of the functionalized nanocomposite films were characterized by atomic force microscopy(AFM).In order to understand the morphological and roughness changes with different high work function electrode layer, Si and FTO. The AFM image of PANI-BSO/Si and PANI-BSO/FTO films were shown in Figure 3(a&b). In these figures, the films were accompanied by picometric roughness. Compact distributions of micro size well defined particles were observed in AFM image. The picorange (10^{-12}) of root mean square roughness of the active layer showed that the improvement of exciton dissociation and has a significant effect on the performance of OPV. It was found that the smoother the interlayer of the active layer (with a larger donor /acceptor interfacial area in the active layer that facilitates exciton dissociation. The bright area in figure is interpreted as BSO rigid nanomaterials and the darker areas as polymer of soft material. The surface roughness for PANI-BSO/Si film was 190.5 pm^2 and the surface roughness for PANI-BSO/FTO film was 297 pm^2. They are suitable for hybrid solar cell because it is a simple way to fabricate the low cost and high efficiency hybrid solar cells at one time**.**

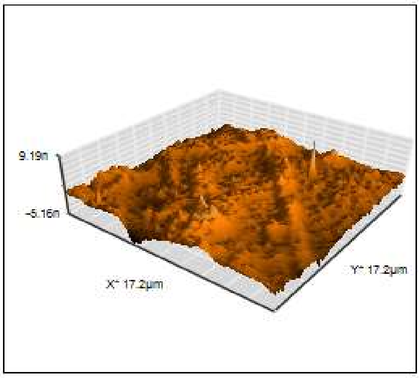

Figure 3 (a) AFM Image of PANI-BSO/Si Film

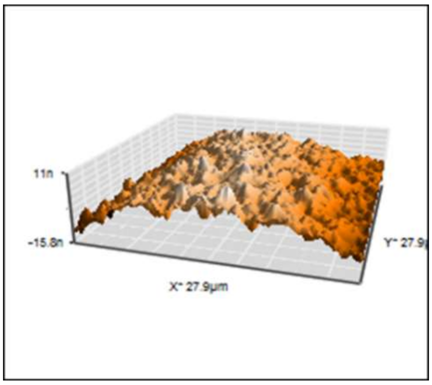

Figure 3 (b) AFM Image of PANI-BSO/FTO Film

UV-vis Absorption Spectrum of PANI-BSO Nanocomposite

The optical properties and energy band gap value of the functionalized nanocomposite films were characterized by UV-vis microscopy. The absorption spectrum of PANI-BSO was shown in Figure4. From the spectrum an excitonic absorption peak was noted at wavelength of about454nm and 302nm. So, it indicate that the absorbing nature of material were high and the band gap of PANI-BSO has 3.24eV. It is clearly observed that the optical band gap of this material was situated between (1~4)eV and it is good for construction of hybrid photovoltaic cells.

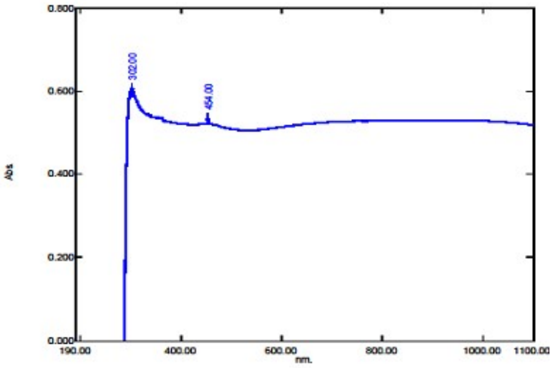

Figure 4 UV-Vis Absorption Spectrum of PANI-BSO Nanocomposite

Photovoltaic Cell Performance of PANI-BSO/Si and PANI-BSO/FTO

Current-voltage measurements were performed, under illumination in order to determine the performance and electrical characteristics of the photovoltaic devices. A typical current voltage characteristic of PANI-BSO/Si and PANI-BSO/FTOPV cells under illumination were shown in Figure 5(a & b). The current density under illumination at zero applied voltage V_{oc} is called the short-circuit current density J_{sc}. The conditions include the light intensity (10000 lux). In these figures, the current density–voltage characteristic showed photovoltaic cell nature. The increased voltages and the current density were probably caused by the effect of the different high work function electrodes such as Si and FTO layers. The PCE of PANI-BSO/Si was higher than that of PANI-BSO/FTO with the influence of increased Jsc and this increase was probably a consequence of a better junction at the high work function electrodes caused by the PANI-BSO layer. The calculated solar cell parameters such as open circuit voltage(V_{oc}), short circuit current density(J_{sc}), maximum current density (J_m), maximum voltage(V_m), fill factor(FF) and energy conversion efficiency(η) were listed in Table 4.

Table 4 Photovoltaic cell parameters of PANI-BSO/Siand PANI-BSO/FTOCells

Parameter	PANI-BSO/Si	PANI-BSO/FTO
V_m(mV)	189	275
J_m(μAcm^{-2})	101	60
V_{oc}(mV)	320	350
J_{sc}(μAcm^{-2})	140	120
FF(%)	43	39
η (%)	1.31	1.12

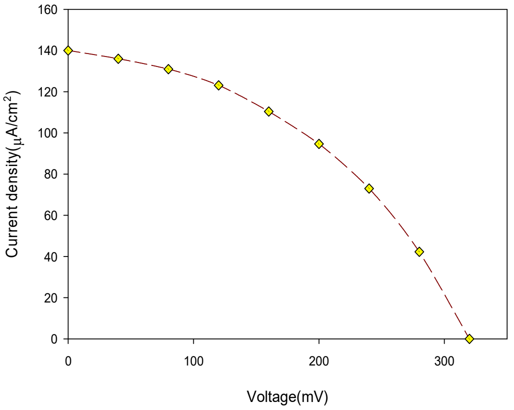

Figure 5(a) J-V characteristic curve of PANI-BSO/Si

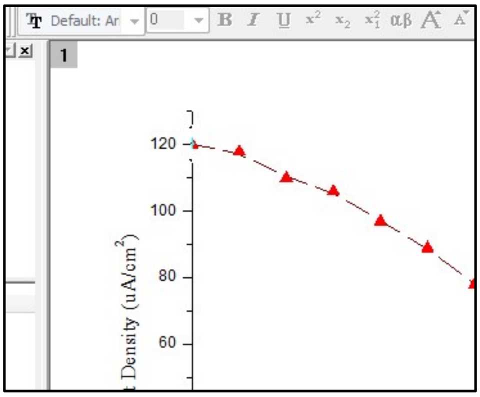

Figure 5(b) J-V characteristic curve of PANI-BSO/FTO

Conclusion

PANI-BSO/Si and PANI-BSO/FTO nano hybrids films have been fabricated by spin coating method. Compact distribution of micro size well defined particles were observed in AFM image. The surface roughness for PANI-BSO/Si film was 190.5 pm^2 and The surface roughness for PANI-BSO/FTO film was 297 pm^2. The pico range (10^{-12}) of root mean square roughness of the active layer show that the improvement of exciton dissociation and has a significant effect on the performance of OPV. According to AFM and SEM results, it was clear that of the nanocomposite materials has good crystallinity. The calculated band gap energy values for PANI-BSO film was 3.24eV and it can be shown as good light absorption nature. The energy efficiency of fabricated PANI-BSO/Si and PANI-BSO/FTO were 1.31%.and 1.12% respectively. The different cell efficiency occurred is due to the nature of different substrates. In summary, it was observed that the nanostructure PANI-BSO/Si and PANI-BSO/FTO hybrid photovoltaic cells were fabricated by simple method and these materials were quite promising specimens for photovoltaic cells application.

Acknowledgements

This result was totally implemented at Department of Physics, University of Yangon, Myanmar(2018-2019). We would like to thank Professor Dr Khin Khin Win, Head of Department of Physics, University of Yangon for her kind permission to carry out this work. We are delighted to thank, Dr Cho Cho Khine, Professor and Head of Department of Physics, Maubin University for her kind permission and help. We would like to express our gratitude to several of my supervisor for making useful suggestion.

References

A.J. Heeger, (2014). "Bulk Heterojunction Solar Cells: Understanding the Mechanism of Operation", Advanced Materials Journal, 26, 10–28.

D.J. Hermant, E.G. Joshua, C. Stephen, & T.M. Daniel, (2011). "Orienting Periodic Organic – Inorganic Nanoscale Domains Through One-Step Electro deposition", American Chemical Society Nano Journal, 5(1), 565-573.

D.G. Michael, (2009). "Nanostructured Organic–Inorganic Hybrid Solar Cells", Material Research Society Bulletin journal, 34, 96-100.

G. Serap, &Gunes, (2007). "Conjugated Polymer-Based Organic Solar Cells", Chem. Review, 107, 1324-1338.

H. Jin, H. Sang, & K.Nazeeruddin, (2013). "Efficient inorganic–organic hybrid heterojunction solar cells containing perovskite compound and polymeric hole conductors", Nature Photonics Journal, 7, 486-49.

J. Cerda, J. Arbiol, R. Diaz, G. Deanneau, & J.R. Morante, (2002). "Synthesis of Perovskite-type $BaSnO_3$ Particles Obtained by a New Simple Wet Chemical Route Based on a Sol-gel process", Material letters, 56, 131-136.

N. Gospodinova, &Terlemezyan, (1998). "Conducting polymers prepared by Oxidative polymerization: polyaniline", Science Journal, 23, 1443–1484.

J. Myanmar Acad. Arts Sci. 2020 **Vol. XVIII.No.2A**

DEVELOPMENT OF P(Py-2FPy)/ ZnO COMPOSITE FILMS AND INVESTIGATION OF THEIR ELECTRICAL PROPERTIES

Nyunt Win[1], Cho Cho Thet[2], Lwin Ko Oo[3] and Ye Chan[4]

Abstract

Poly (pyrrole-2formyl pyrrole) /zinc oxide, P(Py-2FPy)/ZnO composite film has been developed in this work. The inorganic ZnO nanoparticles were synthesized by room temperature solution method. While the pure copolymer P(Py-2FPy) film was prepared by spin coating through copolymerization, the copolymer composited with ZnO, (P(Py-2FPy)/ZnO) films, were prepared by novel *ex-situ* copolymerization method. The volumes of ZnO in the copolymer matrices were varied from 0.1, 0.2, 0.3, 0.4 and 0.5 mL. ZnO nanoparticles and the composite film formation were characterized by Ultraviolet visible spectroscopy (UV-Vis), Fourier transform infrared spectroscopy (FT-IR) and X-ray diffraction (XRD) analysis. The important parameters of films including dissipation factor and capacitance depending on AC (alternating current) frequencies in the range from 1MHz to10 MHz were measured by LCR meter. The electrical conductivities of pure copolymer film and organic-inorganic composite films were investigated based on their measurements of electrical parameters. It was found out that the composite films were conductive and AC conductivities of composite films increase with increasing the volume of ZnO nanoparticles.

Keywords: copolymer, ZnO, composite film, conductivity, polymerization, *ex-situ*, spin coating.

Introduction

Polymeric nanocomposites are materials by combining of one or more inorganic nanoparticles with a polymer to obtain unique properties of such composite materials. They possess novel characteristics such as tunable conductivity, structural flexibility, enhanced thermal, mechanical and chemical stabilities. Organic polymers are considered to be good hosting matrices for composite materials since they can easily be tailored to yield a variety of bulk physical properties. Conductive polymer films can be used in many applications in light emitting diode, transistor, electrochromic device, actuator, electrochemical capacitor, photovoltaic cell and sensor.

The enhanced conductivities of these composite films depended on density and mobility of charge carries along the polymer chains. The concentration of charge carriers can be greatly increased by doping of inorganic nanoparticles in organic polymer matrix. Doping mechanism became oxidation/reduction process which in turn created the polarons and bipolarons in the polymer. They serve as the charge carriers in both degenerate and non- degenerate systems of polypyrrole (PPy). While the p-type doping in polymer create the oxidation process, n type doping became reduction one.

Inorganic nanoparticles possess outstanding optical, catalytic, electronic and magnetic properties which are significantly different their bulk states. As the result, by combining the attractive functionalities of both components, nanocomposites derived from organic polymers

---

[1] Lecturer, Department of Physics, West Yangon University
[2] Associate Professor, Department of Physics, Myeik University
[3] Assistant Lecturer, Universities' Research Centre, University of Yangon
[4] Professor and Head, Universities' Research Centre, University of Yangon

and inorganic nanoparticles, are expected to display synergistically improved the electrical properties of composite films. Therefore, polymer-based inorganic nanoparticle composites films will be interesting in several applications as new conductive polymeric materials.

ZnO is a n-type, direct band gap, II–VI semiconductor material with a wide band gap (3.37 eV) and a large exciton binding energy (~60 MeV at room temperature).Compared with other synthetic techniques, room-temperature solution process has been generally applied due to its simplicity and ease of fabrication with polymer. While polymers have flexibility, low-dielectric constant and processability, the properties of inorganic component have rigidity, durability and thermal stability. The mixing of organic polymers and inorganic nanoparticles is opening pathways for engineering flexible composites materials that show a better magnetic, electrical, optical, or mechanical property.

In this work, inorganic ZnO nanoparticles in organic Py-2FPy copolymer were composited. The composite P(Py-2FPy)/ZnO film was prepared in order to study the electrical properties of films. The conductivities of composite films depending on various volumes of inorganic ZnO are investigated by using LCR meter. The physical properties are characterized by UV-Vis and FT-IR. This work focuses on investigation the enhancement of electrical conductivity from the development of organic-inorganic composite films.

Experimental Details

Preparation of P(Py-2FPy)/ZnO composite film

Pure copolymer films was prepared by two monomers (Py and FPy), chloroform and trifluoroacetic acid (TFA). 207 µL of Py and 286 mg of FPy were dissolved in 2 mL of chloroform ($CHCl_3$). The monomer solution was stirred at room temperature for 30 min. Then, 1 mL of TFA acid in 2 mL of $CHCl_3$ was added to the monomer solution. Then, the mixed solution was spin-coated onto the 9 cm diameter Petri dish at 20 rpm by using a homemade spin coater. The polymerization was carried out for 40 min at room temperature, and finally the metallic greenish black copolymer film was formed in a Petri dish.

ZnO nanoparticles were synthesized by room temperature solution method. Zinc acetate dihydrate ($Zn(CH_3COO)_2.2H_2O$) and ethanolamine ($NH_2CH_2CH_2OH$) and 2-methoxyethanol were used as a starting precursor, a solution stabilizer and a solvent. 1g of $Zn(CH_3COO)_2.2H_2O$ and 0.28 mL of ethanolamine in 10 mL of 2-methoxyethanol were vigorously stirring for 12 h for the hydrolysis reaction in air.

The composite films were prepared by ex-situ copolymerization method through spin coating. The different volumes 0.1, 0.2, 0.3, 0.4 and 0.5 mL of as-synthesized ZnO nanoparticles was added to a fixed weight 486 mg of monomer solution. The composite solution was continuously stirred until ZnO were well dissolved in polymer solution. Then, the solution containing 1 mL of trifluoroacetic acid (TFA) and 2 mL of $CHCl_3$ was additionally put to composite solution at room temperature. After that, the mixed solution was spin-coated onto the Petri dish at 20 rpm using a spin coater until the complete formation of copolymerization was formed. After that, the film was successively washed by excess distilled water and acetone and they were kept in a desiccator for 24 h. Before measuring the electrical conductivity, chemical doping was performed on the films. For the doping process, a small amount of iodine (I_2) 215 mg was put in a closed vessel containing composite films and the vessels were kept for 24 h. The electrical conductivity of the I_2 doped film was measured by LCR meter. The schematic diagram of *ex-situ* synthesis of composite film is illustrated in Fig. 1 and spin coating process and photo of composite film are shown in Fig. 2 and Fig. 3 respectively.

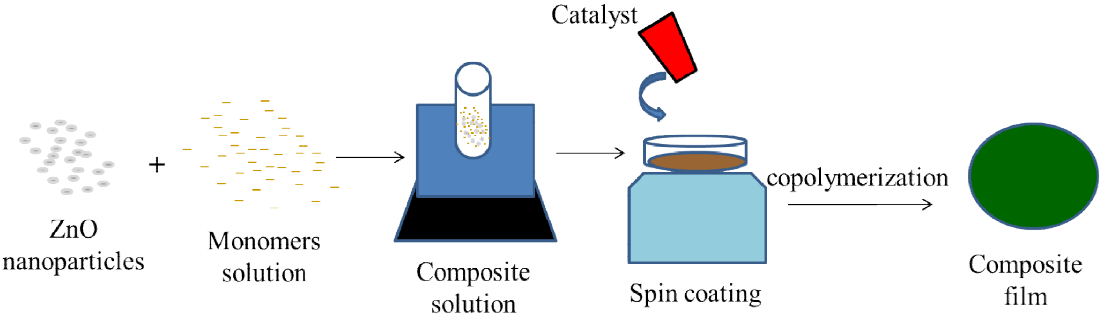

Figure 1 Schematic diagram of development of composite film by ex-situ chemical copolymerization

Figure 2 Spin coating process

Figure 3 Photo of P(Py-2FPy)/ZnO composite film casted in the Petri dish

Characterization Tools

The UV-Vis spectroscopy was performed in order to examine the absorbance values of all synthesized samples. The UV-Vis spectra were obtained by using Shimadzu UV-1800 UV-Vis spectrophotometer. The identification of functional group was investigated by FT-IR. The absorption spectra formations of ZnO, pure copolymer film and composite film were obtained by FTIR 8400 Shimadzu spectrophotometer using a KBr pallet in the mid IR radiation (4000 cm^{-1} - 400 cm^{-1}) range with a resolution of 4 cm^{-1}. The electrical properties were measured by (GW Instek LCR-8110G) LCR meter.

Results and Discussion

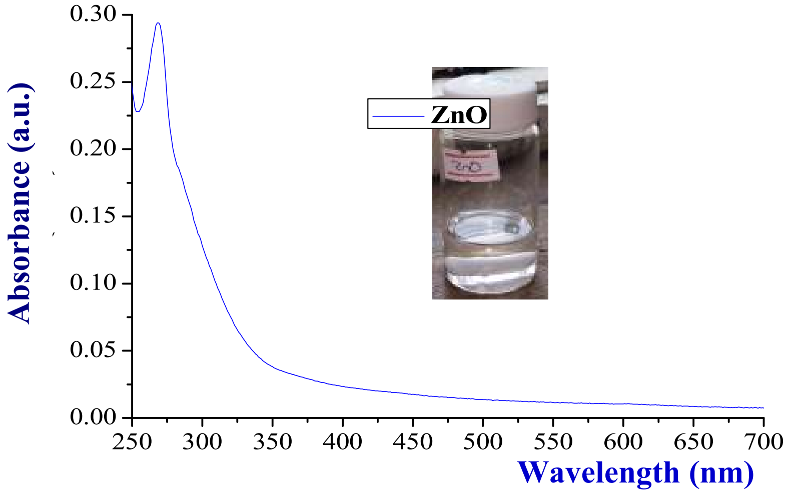

Figure 4 UV-Vis spectrum of as-synthesized ZnO nanoparticles. Inset shows ZnO nanoparticles

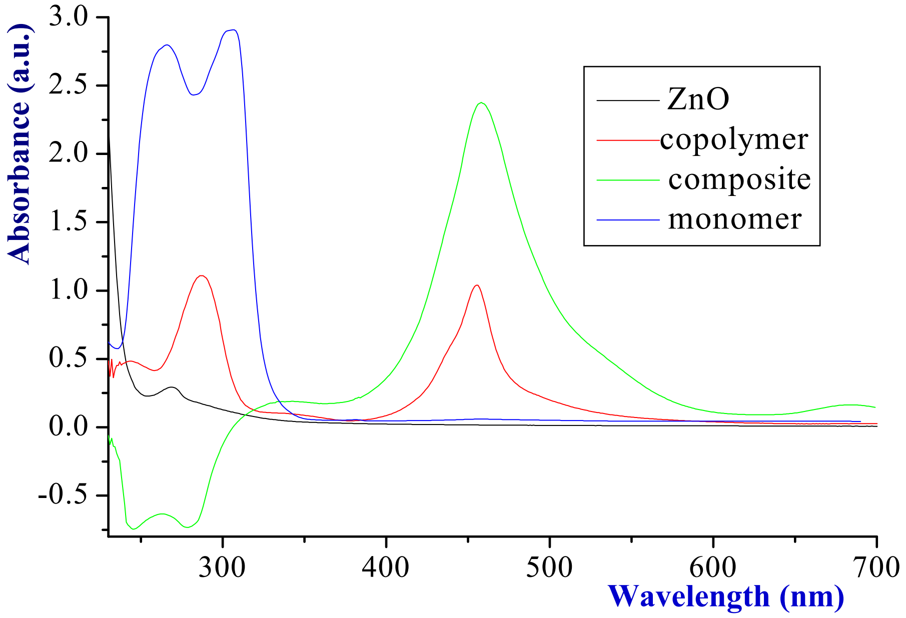

Figure 5 UV-Vis spectra of as- synthesized ZnO, copolymer and composite solutions with TFA catalyst

The UV-Vis absorption spectrum of as-synthesized ZnO nanoparticles was shown in Fig. 4. The maximum absorption wavelength was appeared at 268 nm. This shorter wavelength of ZnO nanoparticles tended to decrease in their size. Thus, room temperature solution method can be successfully obtained smaller size of ZnO particles which are very well dispersed in the solution as shown in the inset of figure 4. The optical band gap (E_g) of ZnO nanoparticles was estimated from its UV-Vis spectrum. Since the band edge wavelength was found out to be 359.78 nm, the optical band gap was about 3.4465 eV. Blue shift occurs since the wavelength of ZnO nanoparticles was decreased than the bulk ZnO due to smaller size of ZnO which is well dispersed in the solution. Thus, room temperature solution method was an excellent synthesis for

ZnO nanoparticles since the smaller size of inorganic part can combine very well in the copolymer matrix, P(Py-2FPy) to integrate the composite film.

Figure 5 shows the comparative UV-Vis spectra of ZnO, copolymer film and P(Py-2FPy/ZnO) composite films respectively. The optical absorption wavelengths of monomers, FPy and PPy, are found at 266 and 305 nm. However, the new copolymerization peak was formed at the wavelength 454 nm after TFA catalyst was added. This peak indicated that the FPy group was incorporated into the chemical structure of the conjugated polymer chains . When ZnO was present in the copolymer matrix of composite film, the absorption intensity of polymer chains was greatly increased. Besides, the weaker band was additionally appeared around 680 nm. This was due to strong interaction of ZnO with pyrrole segments to form bipolaron state which can enhance the electrical conductivity of composite films than pure copolymer film. The movement of polarons and bipolarons along the polymer backbone up lifts to enhanced conductivity of polymer film.

Figure 6 represents the FT-IR spectra of as-dried ZnO nanoparticles (a), copolymer films (b) and composite films (c). The OH band was observed in 3300-3400 cm^{-1} in ZnO. However, this peak disappeared in the copolymer and composite films. These results meant that O-H band of TFA catalyst has been removed and the C=O group was interacted with the Py-FPy film. The peak around 3124 cm^{-1} was due to aromatic C-H stretching band. The strong peak around 1672 cm^{-1} was due to C=O stretching band. The peaks of C=N stretching at 1487 cm^{-1} were attributed to the formation of the conjugated structure in the film. The peak observed at 1258 cm^{-1} was assigned to -C=CH- stretching from methine group of the copolymer. C-H out-of-plane deformation vibration from methine group occurred at 1003 cm^{-1}and that peak of the aromatic C-H out-of-plane deformation vibration are appeared 829 cm^{-1}. Peaks around 563, 515 and 420 cm^{-1} are related to the C-O stretching of PPy and FPy which have been overlapped with ZnO. Thus, it clearly mentioned that ZnO nanoparticles were well incorporated in the polymer matrix through *ex-situ* polymerization method.

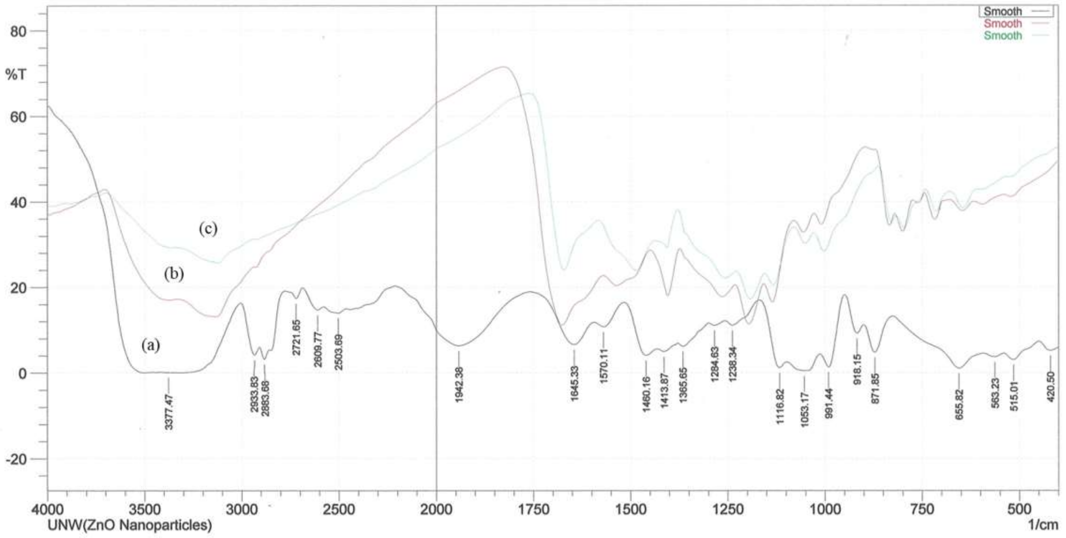

Figure 6 FTIR spectra of (a) ZnO nanoparticles (b) pure copolymer P(Py-2FPy) films without ZnO nanoparticles and (c) P(Py-2FPy) /ZnO composite films

The electrical properties of conductive films were studied by using the LCR meter. The diameter of the sample size is 9.578 mm in a circular shape for each film. The parameters including capacitance and dielectric loss in the frequency range 1 MHz to 10 MHz are measured. Dielectric constant (κ) was calculated by using the formula:

$$\kappa = \frac{Cd}{\varepsilon_0 A} \tag{1}$$

where, κ *is* dielectric constant or relative permittivity of the medium, C is capacitance, d is the thickness of the sample, A is the cross sectional area of the sample and ε_0 is the relative permittivity of vacuum (8.854 x 10^{-14} F/cm).Then dielectric loss ($\tan\delta$) is determined by the formula:

$$\tan\delta = \frac{D}{\kappa} \tag{2}$$

where, D is the dissipation factor obtained from LCR measurement. Finally, the AC conductivity (σ_{ac}) was determined by using the relationship:

$$\sigma_{ac} = 2\pi f \tan\delta \ \varepsilon_0 \kappa \tag{3}$$

where, f is the frequency of applied field. Iodine (I_2) doping was carried out for all investigated films since it can generate the new charge carriers (electrons and holes) which can transport through the polymer chain. I_2 doping takes the form of vapor-phase. In this doping, polymers are exposed to the vapors of iodine dopant compounds. The level of doping is determined by the vapor pressure and reaction time.

In Fig. 7, the AC conductivity of the pure copolymer film, that is there is no ZnO nanoparticles in the composite film, showed the lowest conductivity values while the conductivity of composite films improved with the increasing volume of ZnO. It was found out that the highest conductivity was obtained for the film composited with 0.5 mL of ZnO nanoparticles among the investigated volume limits of ZnO nanoparticles. The electrical conductivity measurement shows that the enhanced conductivity of the conducting P(Py-2FPy/ZnO) polymer films due to the presence of ZnO nanoparticles in the composite films. Figure 8 shows the summarized graph for the average AC conductivity of the films versus different volumes of ZnO nanoparticles. The conductivities are increased with an increasing volume of ZnO.

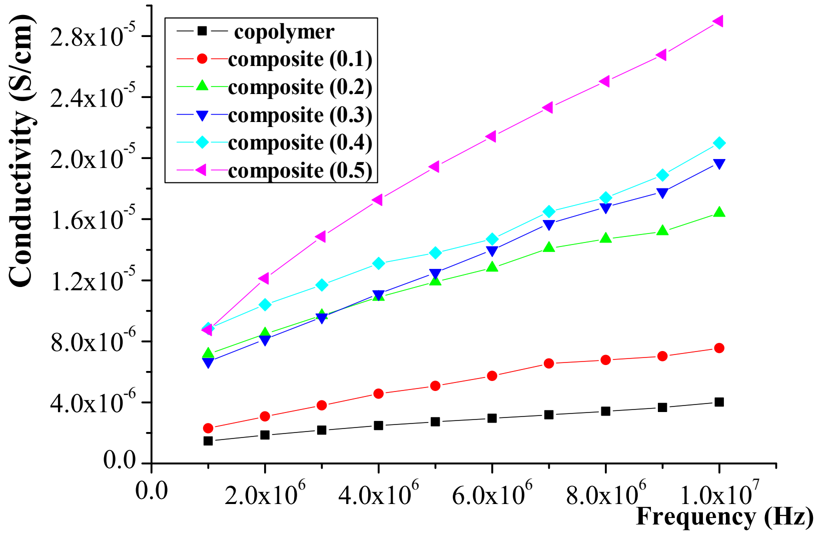

Figure 7 Electrical conductivities of composite films at different ac frequencies

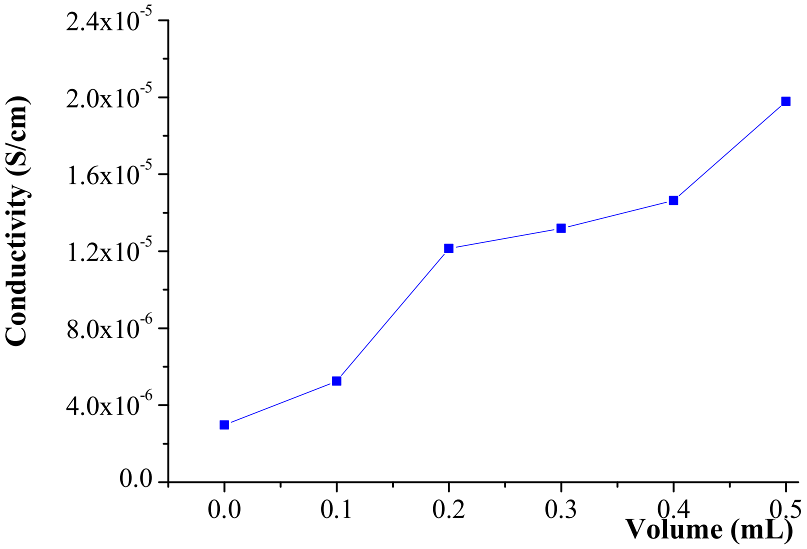

Figure 8 Average electrical conductivities of composite films depending on different volumes of ZnO nanoparticles

Conclusions

To sum up, the enhancement of conductivity of P(Py-2FPy)/ZnO composite film has been studied. The electrical conduction properties of copolymer-ZnO composite films with different volumes of ZnO are investigated for frequencies range from 1MHz to 10 MHz.

The conductivities of composite films are better than pure copolymer film. The composite film for highest volume of ZnO shows the greatest electrical conductivity. It can be explained that ZnO nanoparticles are strongly interacted with pyrrole segments which are intended to form bipolaron state. The movement of such bipolarons by excitation of AC frequencies along the polymer backbone up lifts to enhanced conductivity of composite films. The novel formation of composite film was identified and characterized by UV- Vis and FT-IR. The resulted films show that the inorganic ZnO nanoparticles can be successfully incorporated into the organic copolymer matrix and also scalable. The composite polymer films can be applied in the electrochemical devices technology.

Acknowledgements

We would like to acknowledge to Professor Dr Khin Khin Win, Head of Department of Physics, University of Yangon, for giving me the chance to participate in this event. Moreover we specially thank to the Professor Dr Moe Ohmar, Head of Department of Physics, West Yangon University who gives us valuable suggestions to this work.

References

Ajahar Khan, Ravi Kant Jain, Priyabrata Banerjee, Bhaskar Ghosh, Inamuddin, Abdullah M. Asiri, "Development, Characterization and Electromechanical Actuation Behavior of Ionic Polymer Metal Composite Actuator based on Sulfonated Poly(1,4-phenylene ether-ether-sulfone)/Carbon Nanotubes," 2018.

Aimee M. Bryan, Luciano M. Santino, Yang Lu, Shinjita Acharya, Julio M. D'Arcy, " Conducting Polymers for Pseudo capacitive Energy Storage," *Chem. Mater.,* 28,17,5989-5998, 2016.

Bredas, J.L, G.B. Street, "Polarons, Bipolarons, and Solitons in Conducting Polymers," *Acc. Chem. Res*., 18,309-315, 1985.

Clarice Steffens, Alexandra Nava Brezolin, and Juliana Steffens, "Conducting Polymer-Based Cantilever Sensors for Detection Humidity," *Hindawi Scanning*, Article ID 4782685, 1-6, 2018.

Kun Seok Lee , Youngbin Lee , Jun Young Lee , Jong-Hyun Ahn , Jong Hyeok Park, "Flexible and platinum-free dye-sensitized solar cells with conducting-polymer-coated graphene counter electrodes," *Special Issue: Flow Chemist*ry 5,2, 2012.

Mohamad Saleh AlSalhi , Javed Alam , Lawrence Arockiasamy Dass and Mohan Raja, " Recent Advances in Conjugated Polymers for Light Emitting Devices," *Int. J. Mol. Sci. 12*, 2036-2054, 2011.

Pengfei Zhao, Qingxin Tang, Xiaoli Zhao, Yanhong Tong, Yichun Liu, "Highly Stable and Flexible Transparent Conductive Polymer Electrode Patterns for Large-Scale Organic Transistors," *Journal of Colloid and Interface Science*, 520, 15, 58-63, 2018.

Robert Brooke, Jesper Edberg, Donata Iandolo, Magnus Berggren, Xavier Crispin and Isak Engquist , "Controlling the electrochromic properties of conductive polymers using UV-light," *Journal of Materials Chemistry C*., 17, 2018.

Y. Hoshina and T. Kobayashi "Electrically Conductive Films Made of Pyrrole-Formyl Pyrrole by Straightforward Chemical Copolymerization,"*Ind. Eng. Chem. Res*., 51, 5961-5966, 2012.

Y. Sun, J. H. Seo, C. J. Takacs, J. Seifter and A. J. Heeger, "Inverted Polymer Solar Cells Integrated with a Low-Temperature-Annealed Sol-Gel-Derived ZnO Film as an Electron Transport Layer," *Adv. Mater.*, 2011, 23, 1679-1683.

Yusuke Hoshina, Takaomi Kobayashi, "Effect of Acidic Catalyst on Properties of Novel Conductive Copolymer Films Made of Pyrrole and Formyl Pyrrole" *Engineering*, 4, 139-145, 2012.

Thanh-Hai Le, Yukyung Kim and Hyeonseok Yoon, "Electrical and Electrochemical Properties of Conducting Polymers," *Polymers*, 9, 150, 1-32, 2017.

STRUCTURAL PROPERTIES AND NON-LINEAR BEHAVIOR OF Mn DOPED ZnO VARISTORS

Pwint Yi Thein[1], Pwint Hlaing Ni[2], Win Win Yee[3], Zin Oo Hlaing[4] and May Aye Khing[5]

Abstract

Mn doped ZnO ceramics are prepared in solid state reaction method and conventional funance annealing process. Mn (2 mol, 4 mol, 6 mol, 8mol & 10mol) are doped into ZnO, and heat treated at 500°C (melting point of Mn is 535°C) for 3 hrs. After pre heat treated at 500°C, samples are heat treated again at 1100°C for 2 hrs. XRD investigations are carried out to determine the structural properties, such as lattice parameters, crystalline size and micro strain of the samples. Mn doped ZnO ceramics are prepared as varistors and non-linear coefficients of varistors are studied. Optical band gaps of the ceramic samples are also determined.

Keywords : XRD, varistor& ceramics.

Introduction

Varistors are voltage dependent, nonlinear devices which have an electrical behavior similar to back - to - back zener diodes. The symmetrical sharp breakdown characteristics enable to the varistor to provide excellent transient suppression performance. When exposed to high voltage transients, the varistor impedance changes may orders of magnitudes from a near open circuit to a highly conductive level, thus clamping the transient voltage to a safe level. The potentially destructive energy of incoming transient pulse is absorbed by the varistor, there by protecting vulnerable circuit component.

Research activity in the area of ZnO based ceramics has been traditionally fuelled by the need for ideal candidate as intrinsic voltage regulator in the context of circuit protection. Consequently, a wide range of doped ZnO based systems have studied. Among the dopant materials, Mn is widely investigated as nonlinearity enhancer in ZnO varistor system.

In this research work, Mn doped ZnO ceramics with desired stoichiometric compositions are prepared by solid state reaction method and conventional annealing process. Structural properties of the prepared ceramics samples are investigated by using XRD. Band gaps of the ceramics samples are studied by using UV-V is spectrometer, (SHIMADZU UV-1800). Important parameters of the prepared ceramic varistors, such as, nonlinearity coefficient, threshold voltage and leakage current are also examined.

Experimental Procedure

Mn doped ZnO ceramics were prepared, using the solid state sintering method. Starting materialanalar grade ZnO and MnO_2 powders were mixed with (1 - x) ZnO + (x)MnO_2, where x = 0, 2 mol % , 4 mol % , 6 mol % , 8 mol % and 10 mol %respectively.The mixtures were mixed in agate mortarfor 2 hrs. After mixing the powders, the mixture was pre heated at 500°C (the melting point of MnO_2 is 535°C) for 3 hrs. After that, the mixture was grinded with ball

---

[1] Dr, Professor, Department of Physics, Nationalities Youth Resource Development Degree College, Yangon.

[2] Department of Physics, University of Information Technology, Yangon.

[3] Department of Physics, University of Computer Science, Yangon.

[4] Department of Physics, University of Maubin.

[5] Department of Physics, University of Kyaing Tong.

milling for 6 hrs. Then, the mixture was heated at 500°C for 3 hrs. After heat treatment, the mixture was grounded again with ball milling for 6 hrs. Finally, the mixture was heated again at 1100°C for 3 hrs.

Structural characteristics of the ceramics were investigated from the XRD spectra, using Rigaku Multiflux. The diffraction patterns were recorded at room temperature from 10°to 70° of 2θ using Cu/K_α(λ = 1.5408Å) radiation at 0.01 degree/sec scanning speed. Structural properties of the ceramics were investigated from the XRD spectra. Optical characteristics of the ceramics samples were examined in the wavelength range from 190 nm to 700 nm, using UV Vis spectrometer, (SHIMADZU UV-1800). From the optical absorption spectra, band gaps of the ceramics were determined.

The mixture powder was uniaxially pressed into discs of 20 mm in diameter and 3.5 mm in thickness at a pressure of 19.5tons. Silver paste was coated on the both faces of the samples and the electrodes were formed by heating at 600°C for 10 min. The lnV - lnI characteristics of the ceramics were measured using, high voltage DC power supply. The threshold voltage (V_{1mA}) was measured at current 1mA and the leakage current was measured at 0.8 V_{1mA}.From the lnVvs lnI curve, nonlinear coefficient of the ceramics was studied.

Result & Discussion

Figure (1) shows the XRD spectra of Mn doped ZnO ceramics with different Mn contents. Peaks search algorithm, known as Jade software is used to identify the peaks in this study. Only the diffraction peaks corresponding to reference hexagonal wurtize ZnO(75 - 0576 > JCPDS library file) are observed. Mn has a solid solubility limit of about 13% in ZnO matrix . In this research, the Mn concentration of the samples are smaller than the solid solubility limit and Mn ions are possibly diluted in the ZnO host matrix. In addition, a shift of (101) peak maximum position is observed. This is probably due to substitution of the relatively large ionic radius Mn^{2+}(0.08 nm) at the smaller ionic radius Zn^{2+}(0.074 nm) sites.

No considerable changes in the lattice parameters are found for different Mn doping concentrations, as seen in figure (2).Figure (3) depicts the variation of lattice distortion with Mn concentration. These results can interpret as a unchanged of wuritize structure of ZnO, and the doping process is successful. Crystallite size and micro strain of ceramic samples, applying Debye-Sherrer formula is listed in table (1).

Table 1 Crystallite size and micro strain of Mn Doped ZnO Ceramics.

Mn concentration	crystallize size (nm)	micro strain
Pure ZnO	98.37	2.638×10^{-3}
Mn 2mol%	91.87	1.212×10^{-3}
Mn 4mol%	97.19	1.146×10^{-3}
Mn 6mol%	85.32	1.305×10^{-3}
Mn 8mol%	58.47	1.905×10^{-3}
Mn 10mol%	42.22	1.132×10^{-3}

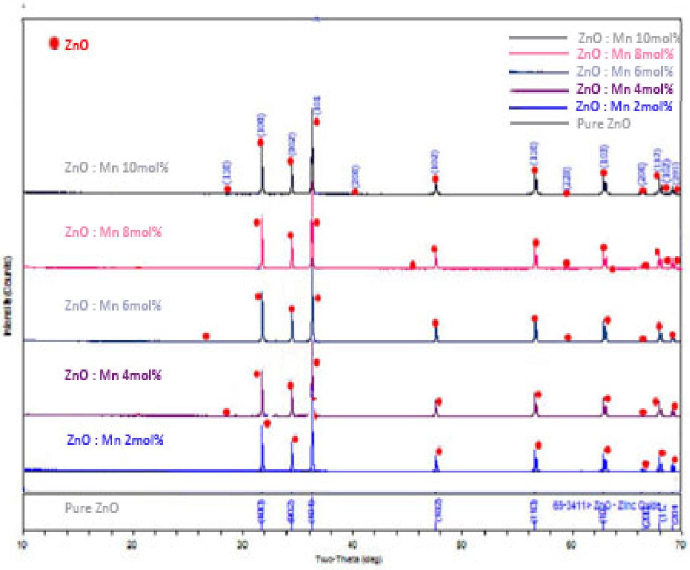

Figure 1 XRD spectra of Mn doped ZnO ceramics with different Mncontents.

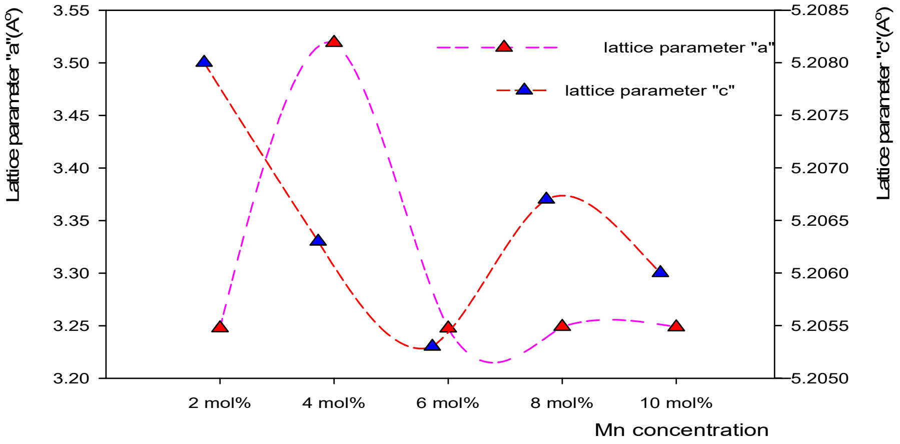

Figure 2 The variation of lattice parameters" a " and " c " with dopant Mnconcentration.

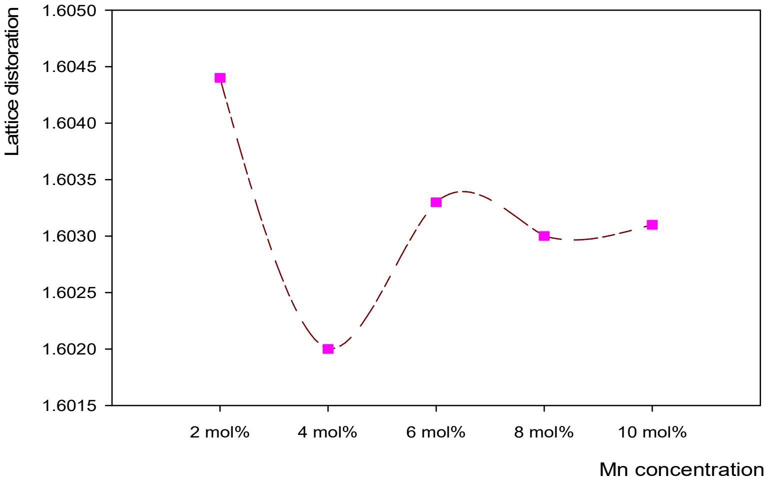

Figure 3 The variation of lattice distortion with dopant Mn concentration.

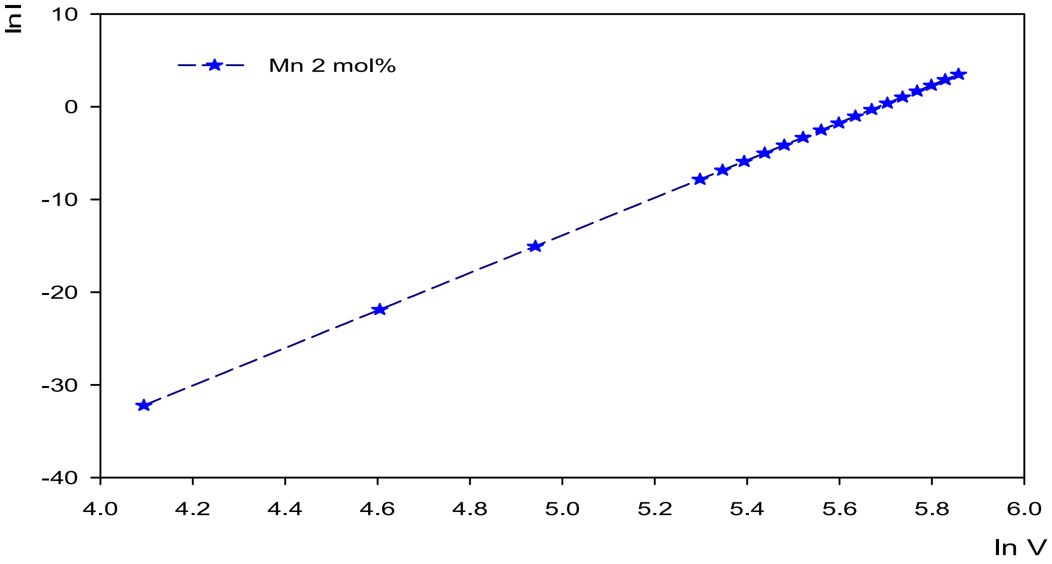

Figure 4 (a) Non- linear behavior of Mn 2mol% doped ZnO ceramics.

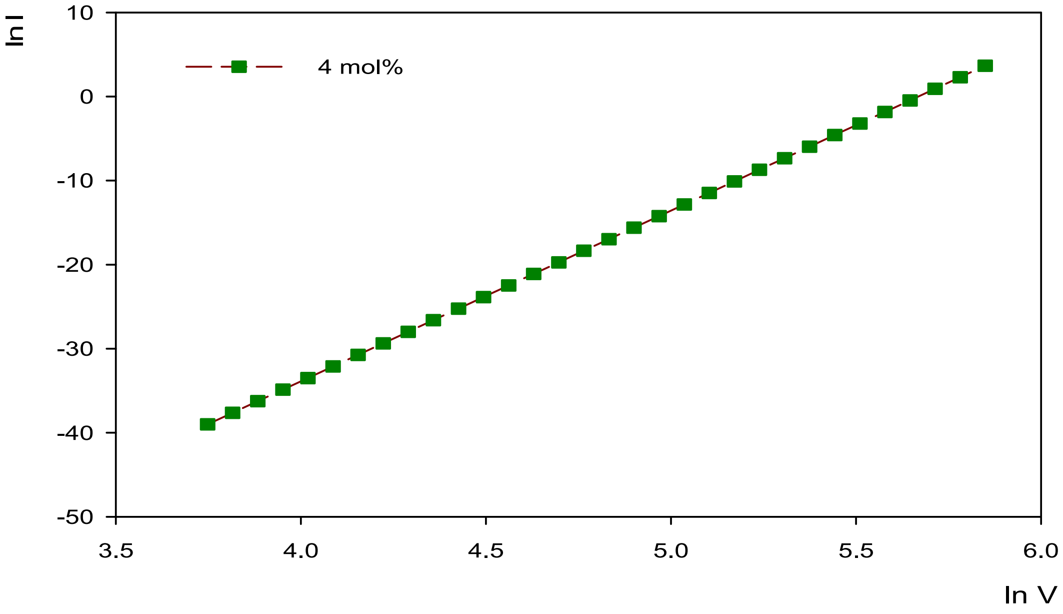

Figure 4 (b) Non- linear behavior of Mn4 mol% doped ZnO ceramics.

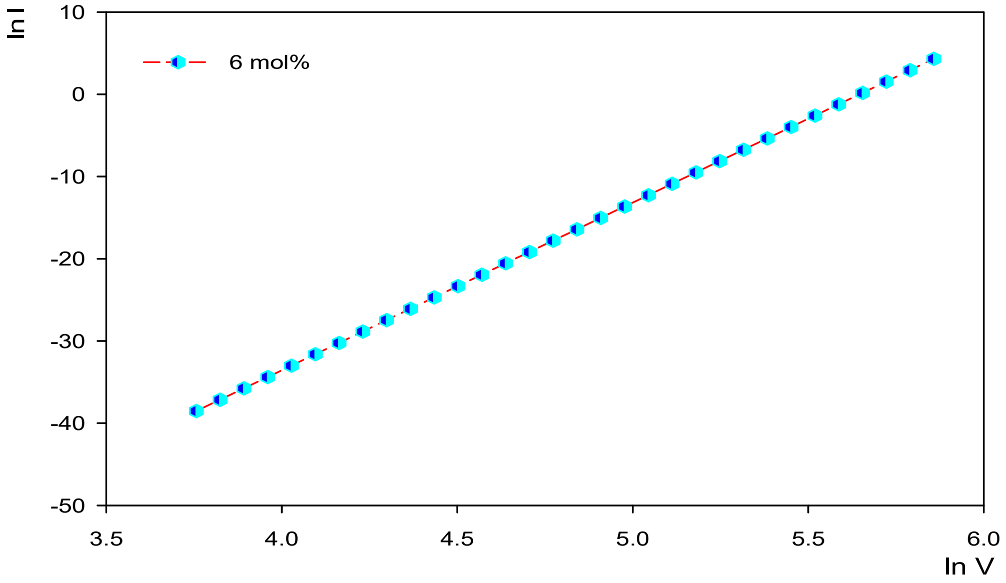

Figure 4 (c)Non- linear behavior of Mn 6 mol% doped ZnO ceramics.

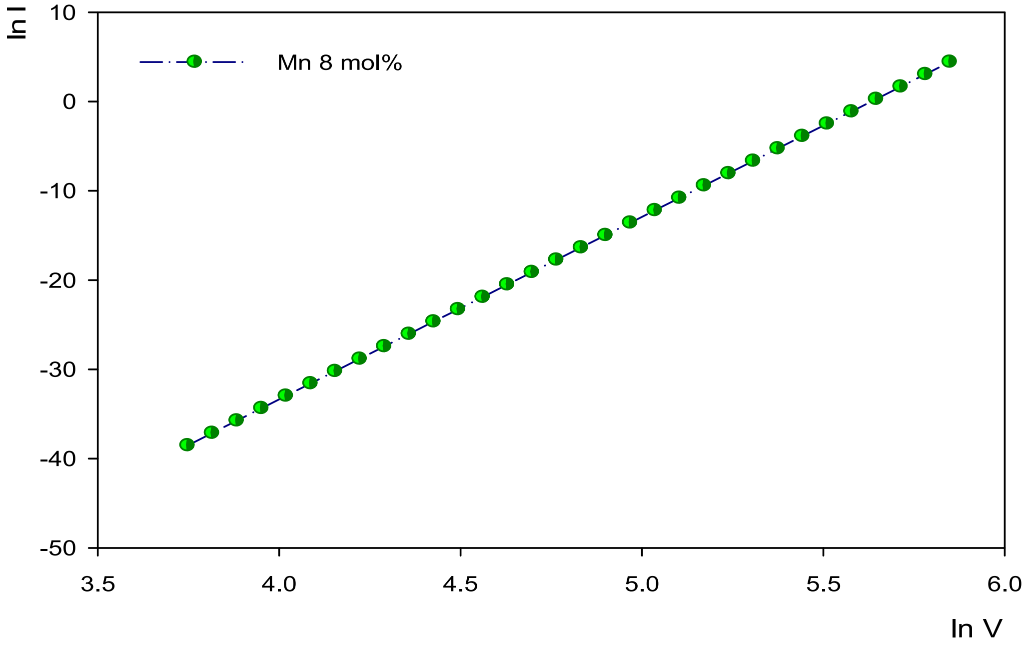

Figure 4 (d)Non- linear behavior of Mn 8mol% doped ZnO ceramics.

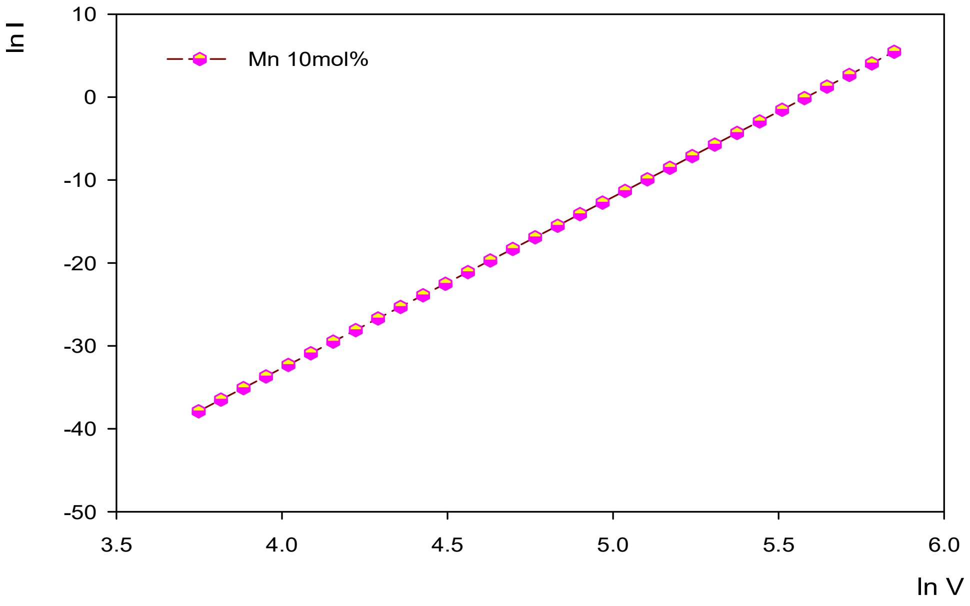

Figure 4 (e) Non- linear behavior of Mn10mol%doped ZnO ceramics.

Varistor behavior of the ceramic samples are investigated from the current - voltage characteristics of the samples (lnV vs lnI curves), as depicted in figure (4).From the

lnV vs lnI curves, nonlinear coefficients of the samples are obtained by the following relation.

$$\propto = \frac{\log\left({}^{I_2}/_{I_1}\right)}{\log\left({}^{V_2}/_{V_1}\right)}$$

where, I_1= 1 mA and I_2 = 10 mA and, V_1 and V_2 are the voltages corresponding to I_1 and I_2.Threshold voltages ($V_{1\ mA}$), which are measured at current 1 mA and leakage currents are studied at 0.8 $V_{1\ mA}$. Data are collected and listed in table (2).

Table 2 Threshold voltage, leakage current and non-linear coefficient of Mn Doped ZnO Ceramics.

Mn concentration	Threshold Voltage V_{th}(V)	Leakage Current I_L(mA)	Non-linear coefficient
Mn 2mol%	167.20	0.01675	19.57
Mn 4mol%	163.60	0.01636	20.18
Mn 6mol%	160.24	0.0160220.28	
Mn 8mol%	158.24	0.01582	21.17
Mn 10mol%	151.04	0.01510	21.23

An attractive properties of the metal oxide varistor, fabricates from ZnO, is that the electrical characteristics are related to the bulk of the device. Each ZnO grain of the ceramics acts as if it has a semiconductor junction at the grain boundary. Since the non electrical behavior occurs at the boundary of each semiconducting ZnO grain, the varistor can be considered as multi - junction device composed of many series and parallel connections of grain boundaries.

The nonlinear coefficient is enhanced when Mn content increases from 2 mol % up to 10mol %,as listed in table (2)This suggests that the segregation of Mn in grain boundary has promoted the development of essential potential barrier at interface. It is also believed that the transition metal oxides, like Mn, are involved in the formation of interfacial states and deep bulk traps, both of which contribute to highly nonohmic behavior. Threshold voltage and leakage current decrease with increasing Mn content, as listed in table (2).In general, the threshold voltage is affected by the number of grain boundaries across a series between the electrodes, which is inversely proportional to the average grain size. It is probably due to the increase of grain size which leads to lower threshold voltage in this study. The nonlinearity is required for the suppression of leakage current during the clamping of transient voltage. The higher the value of alpha, the lower the leakage current, the better the varistor ceramics.

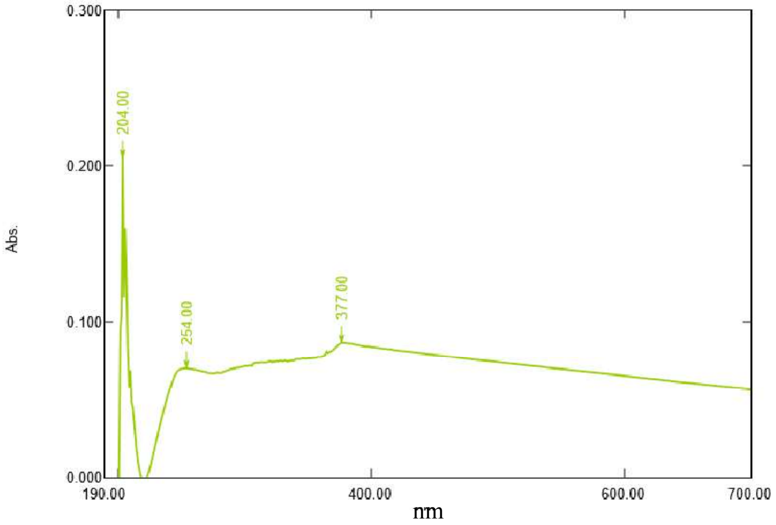

Figure 5 (a) Absorbance spectrum of pure ZnO ceramics

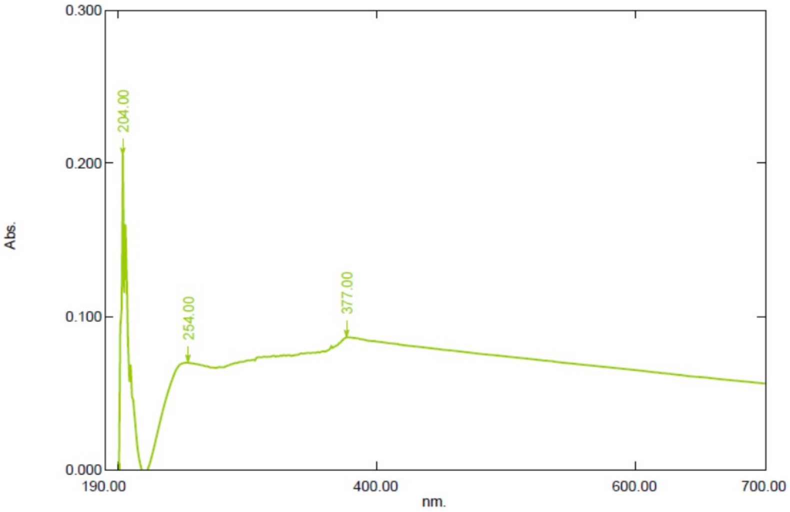

Figure 5 (b) Absorbance spectrum of Mn-2 mol % doped ZnO ceramics

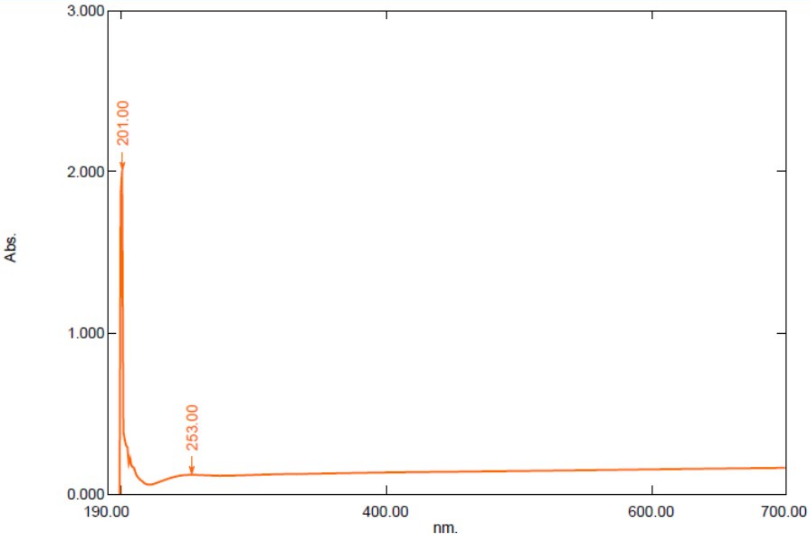

Figure 5 (c) Absorbance rum n-4 mol % doped ZnO ceramics.

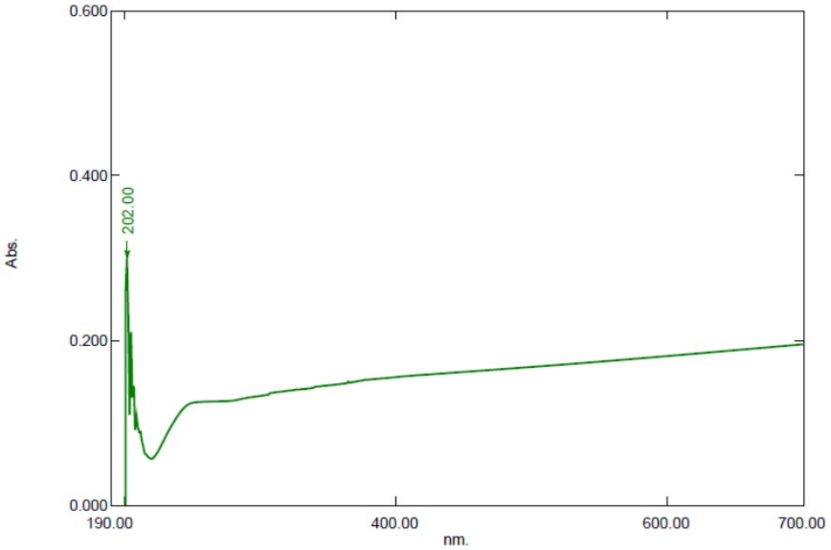

Figure 5 (d) Absorbance spectrum of Mn-6mol % doped ZnO ceramics.

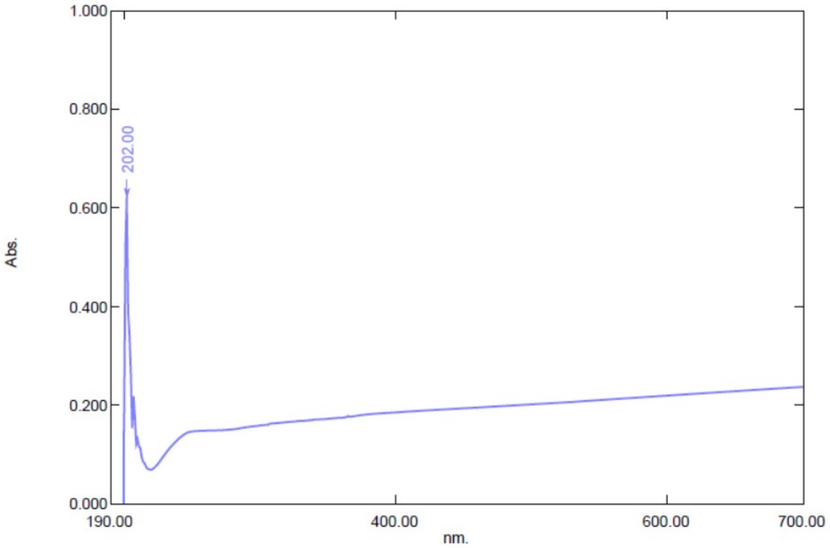

Figure 5 (e) Absorbance spectrum of Mn-8 mol % ZnO doped ceramics.

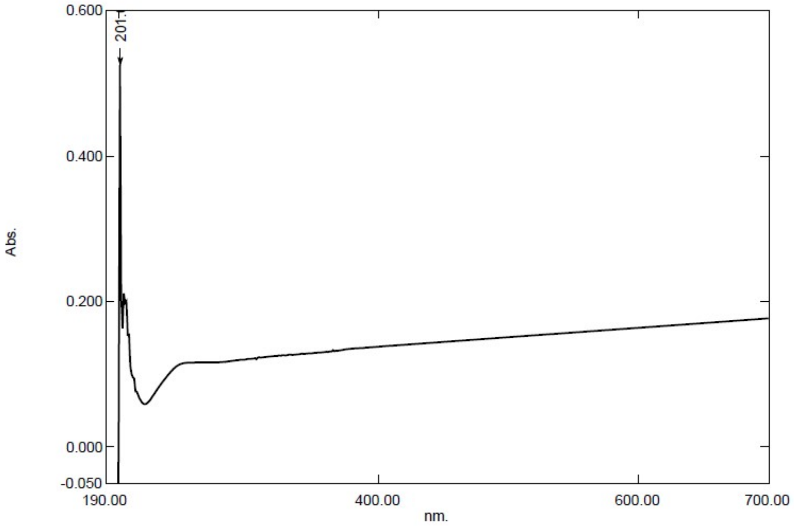

Figure 5 (f) Absorbance spectrum of Mn-10 mol % doped ZnO ceramics.

Figure (5) shows the optical absorption spectra of ZnO:Mn ceramic samples in the wavelength range 190 nm to 700 nm. It is observed that absorbance increases with Mn doping concentration. The optical bandgaps of the samples were determined by applying Tauc - Mott relation. Optical bandgaps of the samples at different Mn contents are listed in table(3). It is noted that, optical bandgap varies with Mn content. It is possible due to the quantum confinement effect. In semiconducting materials, when particle/crystallite size (in nano scale) decreases,the increases or widen up the band gap and ultimately band gap energy also increases, known as quantum confinement effect.

Table 3 Energy gaps of ZnO cermanics at different Mn Contents

Mn concentration	**Energy gap (eV)**
Pure ZnO	3.274
Mn 2mol%	3.315
Mn 4mol%	3.377
Mn 6mol%	3.417
Mn 8mol%	3.446
Mn 10mol%	3.523

Conclusion

Transition metal oxide, Mn ions were successfully doped into ZnO host matrix via solid state sintering method in this study. XRD technique was used to analyze the structural properties of ceramic samples. Influence of dopant materials Mn on lattice parameters, latttice distortion, crystallite size and micro strain were examined. Ceramic samples were prepared with standard varistor preparation process and non- ohmic properties of the samples were determined. Variation of dopant materials Mn with varistor parameter, such as, threshold voltage, leakage current and nonlinearity factor were determined. Furthermore, optical bandgaps of the samples were evaluated.

Acknowledgments

The authors would like to acknowledge the Universities Research Centre (URC), University of Yangon, for XRD measurements.

References

Buneo P R, Varela J A and Longo E (2008) : " *SnO2, ZnO and related Polycrystalline Compound Semiconductors : An Overview and Review on Voltage Dependent Resistance(Non-Ohmic). Fearure*" , J.Eur.Cer.Soc., 28(3), 505 - 529.

Clarke D R (1999): " *Varistor Ceramics* " , J.Am.Cer.Soci. , 82(3), 485 - 492.

Duan L, Liu J, Geng E. Xie H and Chen S (2011): "*Structural, Thermal and Magnetic Investigations of Heavily Mn Doped ZnO Nanoparticles*" , J.Mag.Mag.Mater., 323, 2374 - 2379.

Gupta T K (1990) : *" Application of ZnO Varistors* " , J.Am.Cer.Soci., 71(3), 1817 - 1840.

Han J, Mantas P G and Senos A M R (2000): "*Grain Growth in Mn Doped ZnO* ", J.Eur.Cer.Soci. , 20, 2753 - 2758.

Han J, Senos A M R and Mantas P G (2002):" *Varistor Behavior of Mn Doped ZnO Ceramics*", J.Eur.Cer.Soci., 22 , 1653 - 1660.

Jing C, Jing Y, Bai W, Chu J and Liu A (2010) : *" Synthesis of Mn Doped ZnO Diluted Magnetic Semiconductors in the Presence of Ethyl Acetoacetate under Solvothermal Conditions* " , J.Mag.Mag.Mater., 322, 2395 - 2400.

Leite E R , Varela J A and Longo E (1992) : " *A New Interpretation for the Degradation Phenomenon in ZnOVaristor* " , J.Mat.Sci., 27, 5527 - 5529.

Levine J D (1975) : " *Theory of Varistor Electronic Properties* " , Critical Review of Solid State Science, Vol 5 , 597 - 608.

Levison L M and Philipp H R (1975): *" Physics of Metal Oxide Varistors*", J.Appl. Phys., 46(3), 1332 - 1341.

Li Q, Wang Y, Kong W and Ye B (2014): "*Structural and Magnetic Properties in Mn Doped ZnO Films Prepared by Pulse Laser Deposition* " , Appl. Surf. Sci., 289, 42 - 46.

Martzloff F D and Levinson L M (1998): " *Surge Protective Devices : Electronic Ceramic Properties, Devices and Applications ",* Marcel Dekker Inc., New York.

PoonsukPoosimma (2014)" *Stability of Zinc Oxide Varistors* ", PhD dissertation, School of Materials, Faculty of Engineering and Physical Sciences, University of Manchester, U K(Unpublished)

Ravichandran K, Karthika K, Sakthivel B, Tabena Begum N, Snega S, Swaminathan K and Senthamilselvi V (2014) : " *Tuning the Combined Magnetic and Antibacterial Properties of ZnONanopowders through Mn Doping for Biomedical Applications* ",J.Mag.Mag.Mater., 358 - 359,50 - 55.

Riyadi S, Muaffif A A, Rusydi A and Tjia M O (2007) : "*Mn Dopant Induced Effects in Zn(1-x) Mn (x) O Compounds* " , J.Phys. Cond, Matt., 12, 1 - 8.

Ruan H B, Fang L, Li D C, Saleen M, Qin G P and Kong C Y (2011): "*Effect of Dopant Concentration on Structural, Electrical and Optical Properties of Mn Doped ZnO Films* " , Thin Solid Films, 519, 5078 - 5081.

Sinha A and Sharma B P (1997) :" *Novel Route for Preparation of High Voltage Varistor Powder*", Mat.Res.Bull., 32, 1571 - 1579.

Wang Y G, Lau S P, Lee H W, Yu S F, Tay B K, Zhang X H and Hng H H (2003) : "*Photoluminescence Study of ZnO Films Perpared by Thermal Oxidation of Zn Metallic in Air* ", J.Appl.Phys.,94, 354 - 359.

J. Myanmar Acad. Arts Sci. 2020 **Vol. XVIII.No.2A**

MICROCONTROLLER BASED SECURITY LOCKSYSTEM WITH PASSWORD

Khin Mar Lar Lwin[*]

Abstract

Microcontroller based security lock system is an access control system that allows only authorized persons. The electronic controlled assembly allows the system to unlock the device with password. This system has a keypad which the password can be entered through it. If the entered password is correct then the word “CORRECT” will display on LCD and the lock opens. If the incorrect password is entered three times then the word “THIEF” will display on LCD and the alarm will ring by producing sound from buzzer. This circuit can be used in bank for security, steel safe and security door lock to secure them against thief. The microcontroller based security lock system is designed and constructed by using major components programmed microcontroller PIC18F452, 4×4 keypad, LCD (Liquid Crystal Display) and abuzzer.

Keywords: microcontroller, keypad, LCD, security lock

Introduction

Security is a prime concern in day-to-day life. Everyone wants to be as much secure as possible. An access control for doors forms a vital link in a security chain. The microcontroller based digital lock for door is an access control system that allows only authorized persons to access a restricted area. An electronic lock or digital lock is a device which has an electronic control assembly attached to it. They are provided with an access control system. This system allows the user to unlock the device with a password. The password is entered with the use of a keypad. The user can also set the password to ensure better protection. The password is stored in the EEPROM so that the user can change it at any time. The system has a keypad by which the password can be entered through it. When the entered password equals with the password stored in the memory then the system opens the door by rotating door motor and a message is displayed on LCD. If the password entered in keypad is incorrect, then the security alarm is rung and a message is also displayed on LCD. Keypad and LCD are very commonly used input and output devices. It is very interested to design and construct a security lock system. So, in this research, the security lock system based on PIC 18F452 microcontroller was designed and constructed with a password control. This system consisted of a programmed microcontroller PIC18F452, 4×4 keypad to enter password and LCD to display the message.[microcontroller projects]

Materials and Methods

Block Diagram of the Constructed System

The security lock system was designed and constructed by using major components programmed PIC18F452, 2 lines 16 character LCD module, 8 MHz crystal oscillator, 4×4 keypad and a buzzer. The whole system consisted of power supply section, main processing section, motor driving section, display section and alarm section. The block diagram of the whole system was presented in figure 1.

---

[*] Dr, Associate Professor, Department of Physics, Pathein University

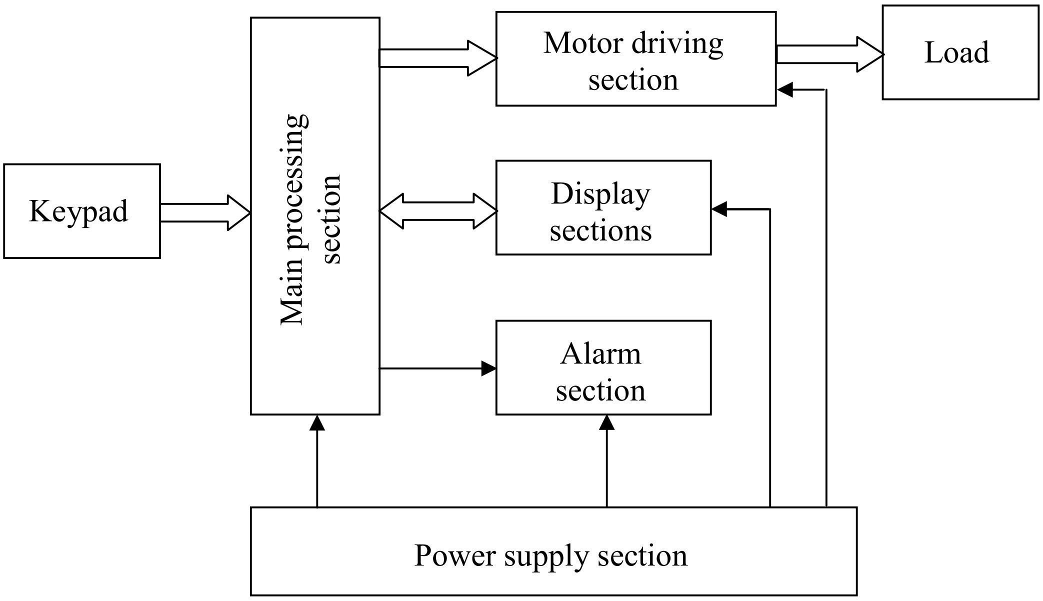

Figure 1 Block diagram of security lock system

PIC Microcontroller

The microcontroller is an exciting new device in the field of electronics control. It is a complete computer control system on a single chip. Microcontrollers are constructed with the Harvard Architecture and used mostly in RISC (Reduced Instruction Set Computer) method, which has separate address bus and data bus, so can have different bit widths. Microcontroller includes EPROM (Erasable Programmable Read Only Memory) program memory, user RAM (Random Access Memory) for storing program data, timer circuits, an instruction set, special function registers, power on reset, interrupt, low power consumption and a security bit for software protection. The Microchip's PIC is a special type of microprocessor called microcontroller. PICs use data memory (RAM) of a small number of 8 bit registers and program memories (EEPROM) are 12 bits, 14 bits or 16 bits wide. The number of instructions of the microcontroller of midrange is usually less than 50.

Primarily, the microcontroller is capable of storing and running a program (its most important feature). The microcontroller contains a CPU (Central Processing Unit), RAM , ROM , I/O (Input/Output) lines, serial and parallel ports, timers and sometimes other built-in peripheral such as analog-to-digital converter and digital-to-analog converter.

The PIC18F452 contains 32K bytes of flash program memory type, 16384 single word instructions on chip program memory, 1536 bytes on chip RAM and 256 bytes of data EEPROM[Datasheetspdf.com]. The pin diagram and photograph of PIC18F452 is shown in figure 2 and figure 3.

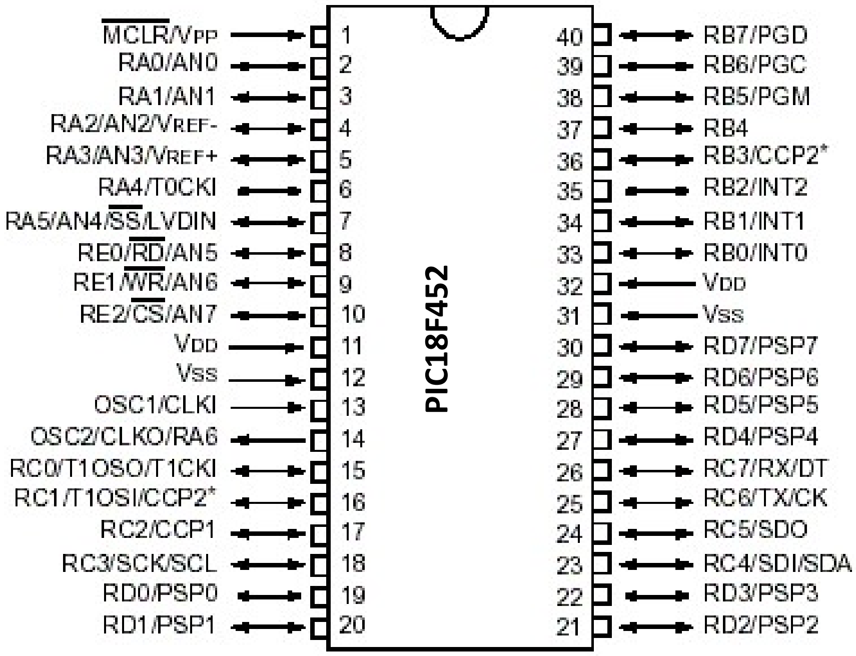

Figure 2 Pin diagram of PIC18F452

Figure 3 Photograph of PIC18F452

Design and Construction of the System

Power Supply Section

In this section, + 5V regulated power supply circuit was constructed by using step-down transformer, full-wave rectifier, filter capacitors and 7805 regulator IC. Firstly, AC 220V was reduced to AC 12V by using step-down transformer and it was converted into corresponding DC voltage with the help of full-wave rectifier. This DC voltage was filtered with 470 μF capacitor. The filtered DC voltage was applied to the input terminal of 7805 voltage regulator. The common terminal of L7805 was grounded and the output terminal produced +5V. In order to filter the fluctuation, the regulated + 5V line was also filtered with 10 μF capacitor. Schematic diagram of power supply section was shown in figure 4.

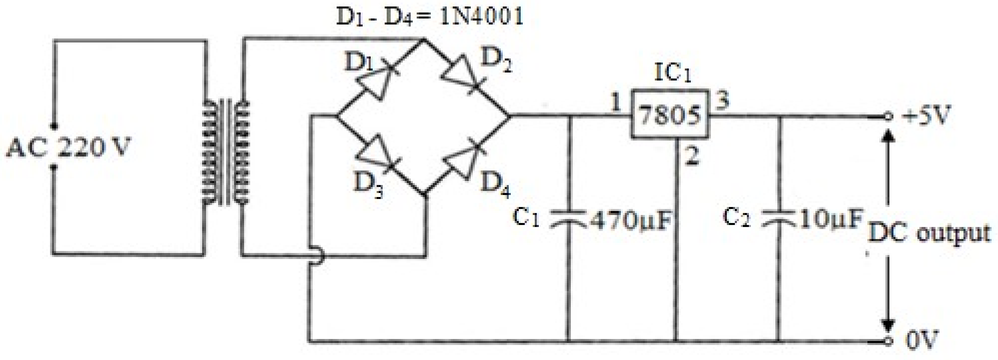

Figure 4 Schematic diagram of power supply section

Main Processing Section

The main processing device of the whole system was PIC18F452 microcontroller. An 8MHz crystal was fitted between OSC 1 and OSC 2 pins of microcontroller and these pins were also filtered with 22 pF capacitors. PORTD of PIC18F452 microcontroller was configured as input. This PORT accepted the data from keypad. In this circuit, the alphanumeric data were sent to LCD by using 4-bit mode. PORTB of microcontroller was used as the digital output to send the data and also to control the LCD. RA0 and RA1 of microcontroller were used to display LED. When the password from keypad was correct, the correct LED was on and the password was incorrect, the incorrect LED was on. RC2 of microcontroller was used as to produce alarm sound from buzzer. RC4 to RC7 of microcontroller were used as the digital output to control the stepper motor. Pin 12 and pin 31 of microcontroller were connected to ground and pin 11 and pin 32 are connected to + 5V dc supply voltage. Schematic diagram of main processing section was shown in figure 5.

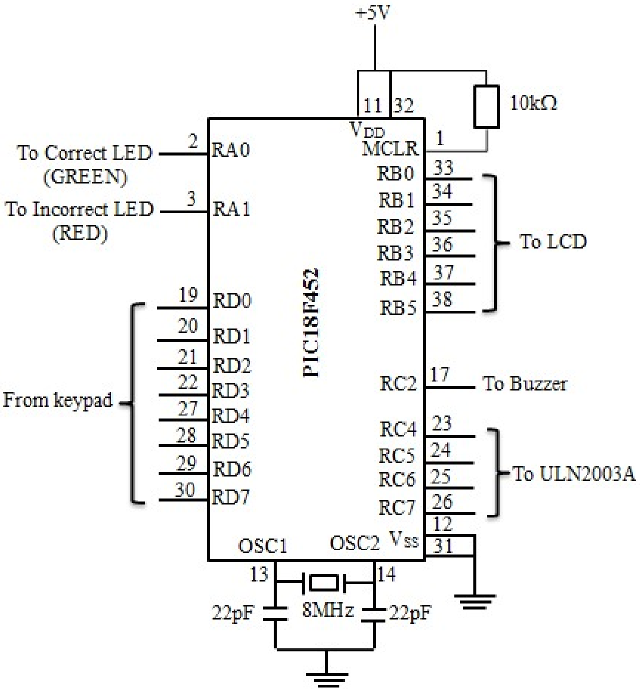

Figure 5 Schematic diagram of main processing section

Motor Driving Section

The motor driving circuit was constructed by using ULN2003A IC. In this circuit, pin 8 of motor driving IC was connected to ground and pin 9 was connected to +5V. Pin 1 to pin 4 of motor driver IC was controlled by RC4 to RC7 of microcontroller IC. Schematic diagram of motor driving section was shown in figure 6.

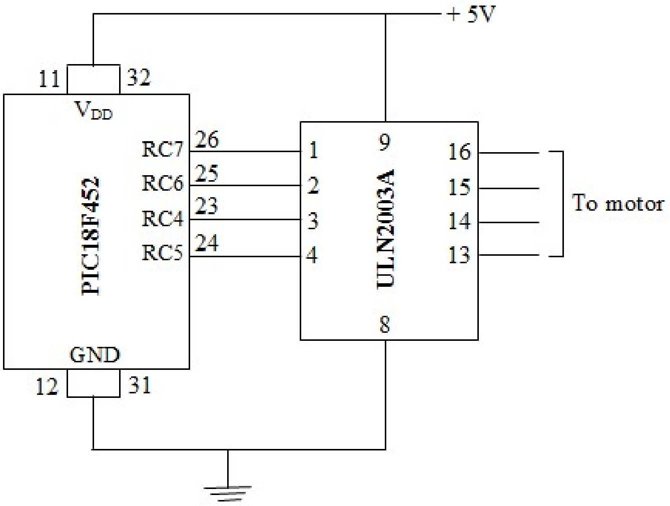

Figure 6 Schematic diagram of motor driving section

Display and Alarm Section

The security lock system consisted of two display sections, LCD and LED. A2-line 16-character LCD was used to display the data from microcontroller. Pin 1 of LCD was connected to ground. Pin 2 of LCD was connected to + 5V and pin 3 was connected to the ground via 10 kΩ variable resistor to adjust the contrast of LCD character. Pin 4 (RS) of LCD was controlled by RB4. Pin 5 of LCD was connected to ground. Pin 6 (E) of LCD was controlled by RB5. Data bits of LCD were connected to RB0 to RB3 respectively. LCD back light pins were directly applied +5V and ground. RA0 and RA1 were connected to “Correct LED” and “Incorrect LED”. Schematic diagram of display section was shown in figure 7.

The alarm section consisted of a transistor and a buzzer. The power supply pin of buzzer was connected to + 5V and ground pin of buzzer was connected to collector of transistor. Schematic diagram of alarm section was shown in figure 8.

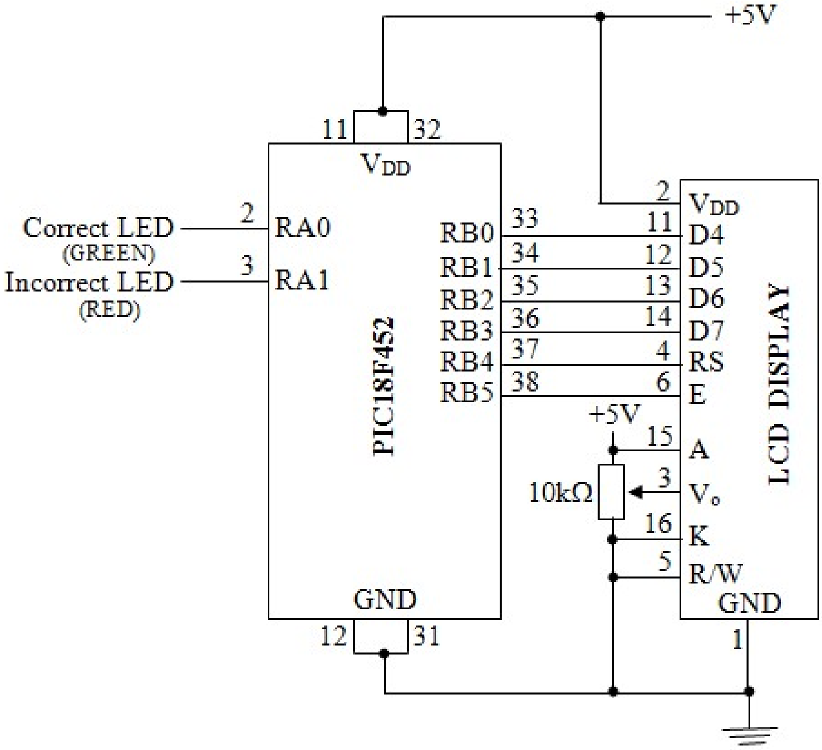

Figure 7 Schematic diagram of display section

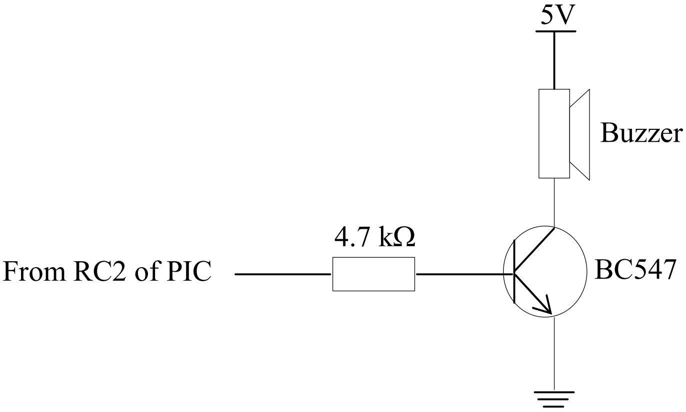

Figure 8 Schematic diagram of alarm section

Complete Circuit of the Whole System

The keypad, main processing section, display section, alarm section, motor driving section and power supply section altogether formed the complete circuit of the whole system. The columns of keypad are connected to RD0 to RD3 and rows are connected to RD4 to RD7. The LCD is connected to PORTB. The password is entered with the use of keypad. When the entered password is correct, the security door lock system will open. When incorrect password is entered, the security alarm will ring. Complete circuit diagram and flow chart of security lock system is shown in figure 9 and figure 10.

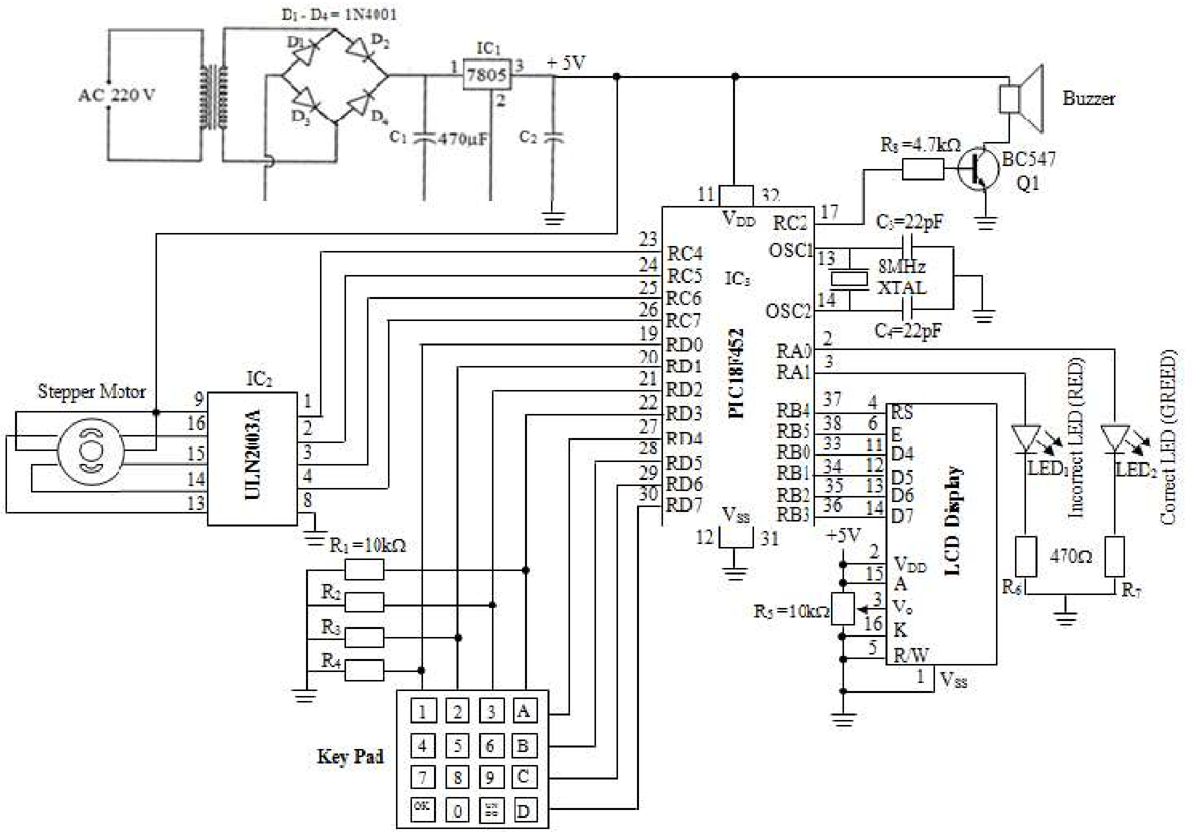

Figure 9 Complete circuit diagram of security lock system

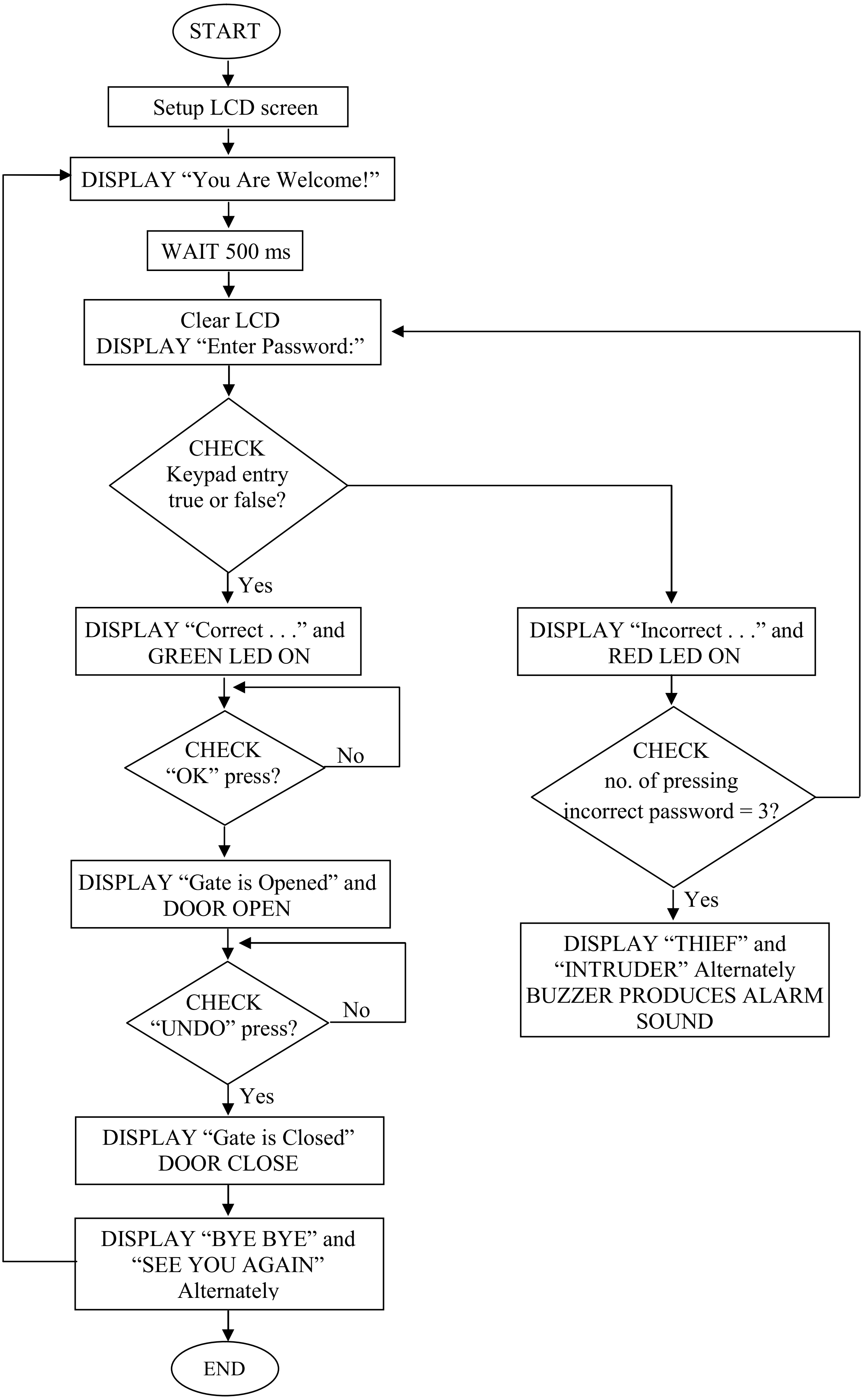

Figure 10 Flow chart of security lock system

The Printed Circuit Board (PCB)

The circuit is constructed on a single sided PCB (printed circuit board) which is manually drawn by the use of Trax Maker PCB software. The bottom layer (solder side) is printed on the single sided copper clad. The unwanted portion of the copper is etched by ferrous chloride. After being etched, the holes are drilled. And then the top layer (component side) is printed. After that, the components are fitted to proper locations subsequently soldered the leads. Bottom layer and top layer PCB layout of security lock system are shown in figure 11 and figure 12. Multilayer PCB layout of security lock system is shown in figure 13. The blue colour represents the bottom layer and the red colour and yellow colour represent top layer.

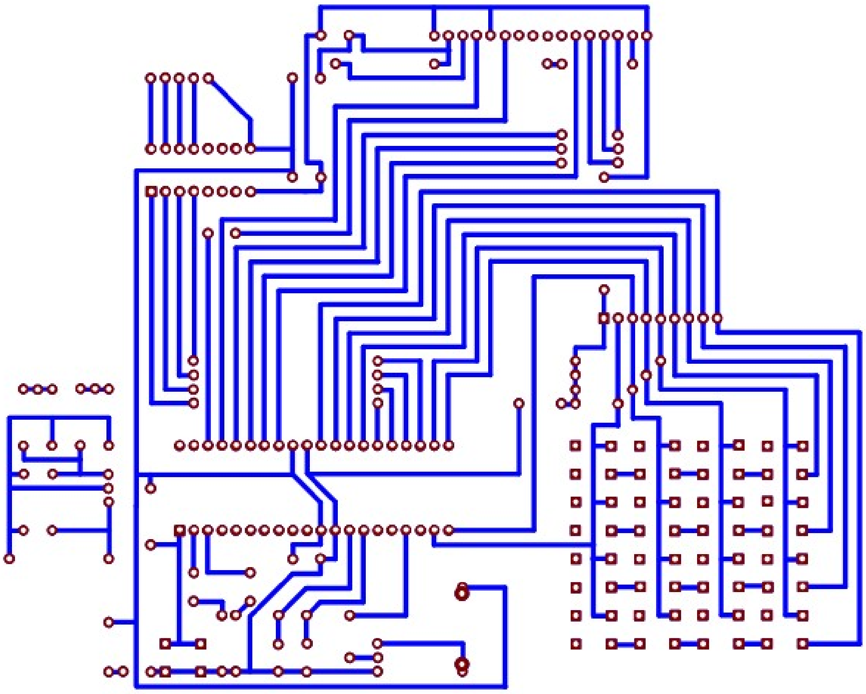

Figure 11 Bottom layer PCB layout of security lock system

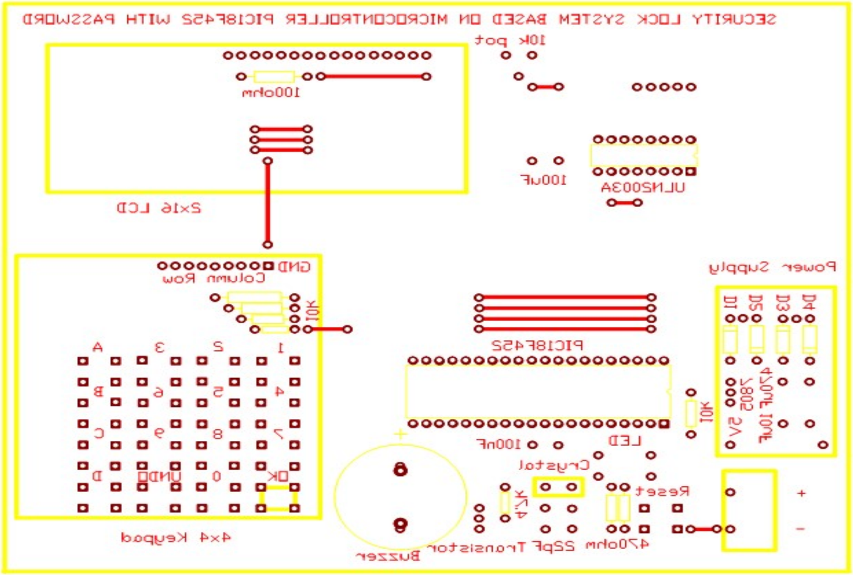

Figure 12 Top layer (Mirror View) PCB layout of security lock system

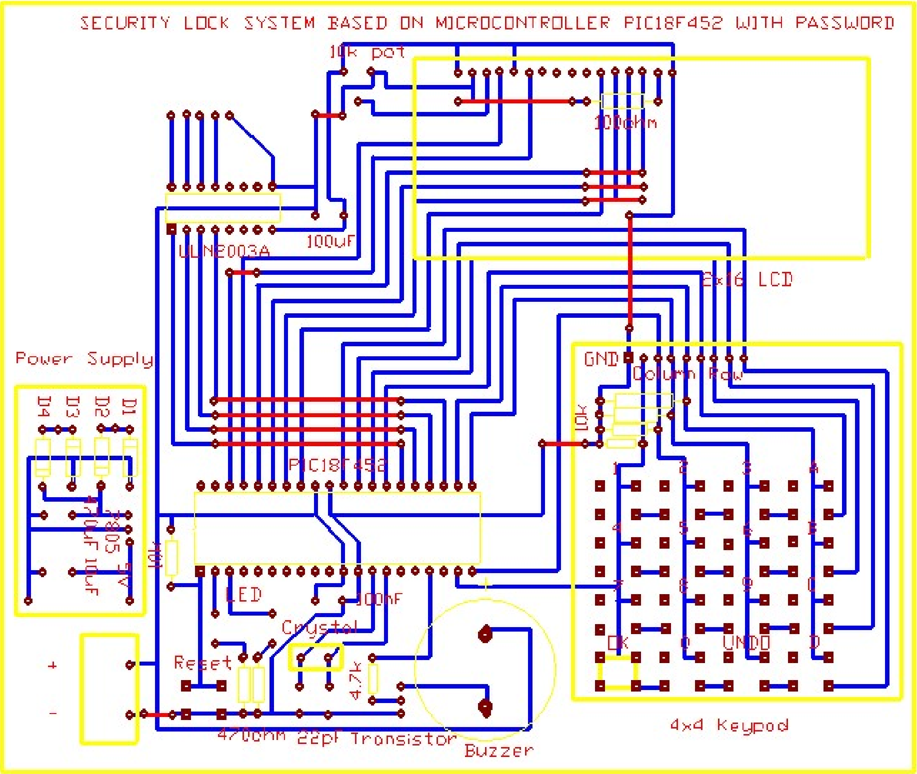

Figure 13 Multilayer PCB layout of security lock system

Results and Conclusion

Results

In the constructed system, 4×4 keypad was used to enter the password, LCD was used to display the message, the buzzer was used to produce the alarm sound and the motor was used to open and close the door. The heart of the whole system was low power, high performance PIC18F452. The program required for security lock system was written in MikroC language and the hexadecimal code was downloaded to microcontroller with the aid ofPIC-KIT2 programmer. Figure 14 showed photo of security lock system.

As soon as the power supply was connected to the circuit, the system initialized with “You Are Welcome!” on the LCD display for 500 ms. This initializing stage was shown in figure 15. Then the display of cursor jumped to the second row first column of LCD and flashing the cursor. The password combination was composed with eight digit characters “2016ABCD”. After pressing input combination, it was required to press OK button to check the password. If the entry password was correct, the LCD displayed the word “Correct…” and the green LED illuminated. Figure 16 showed entering correct password stage. But the door opening stepper was not opening. In this case, the “OK” button was required to press again. If the “OK” button was pressed, the LCD displayed “Gate is Opened” and the door started slide opening. This gate open stage was shown in Figure 17. After the door was fully opened, the motor stopped and the door entrance was opened. Then the door can be closed by pressing “UNDO” button. When the “UNDO” button was pressed, the LCD displayed the word “Gate is Closed” and the door slided closing until the door was fully closed. Gate close stage was shown in figure 18. Then the system greeted with “BYE BYE” and “SEE YOU AGAIN” alternately on the LCD.

When the enter password was incorrect, LCD displayed the words “Incorrect” and “Try Again” and the red LED was illuminated. Figure 19 showed entering incorrect password stage. After that, the word “Enter Password” displayed on LCD. If incorrect password was pressed over three times, the buzzer produced the alarm sound and the words “THIEF” and “INTRUDER” displayed alternately on LCD. This stage was shown in figure 20. In this way, unauthorized entry can be easily alert the residence and neighbors to protect from burglars and thief.

Figure 14 Photo of security lock system

Figure 15 Initializing stage of security lock system

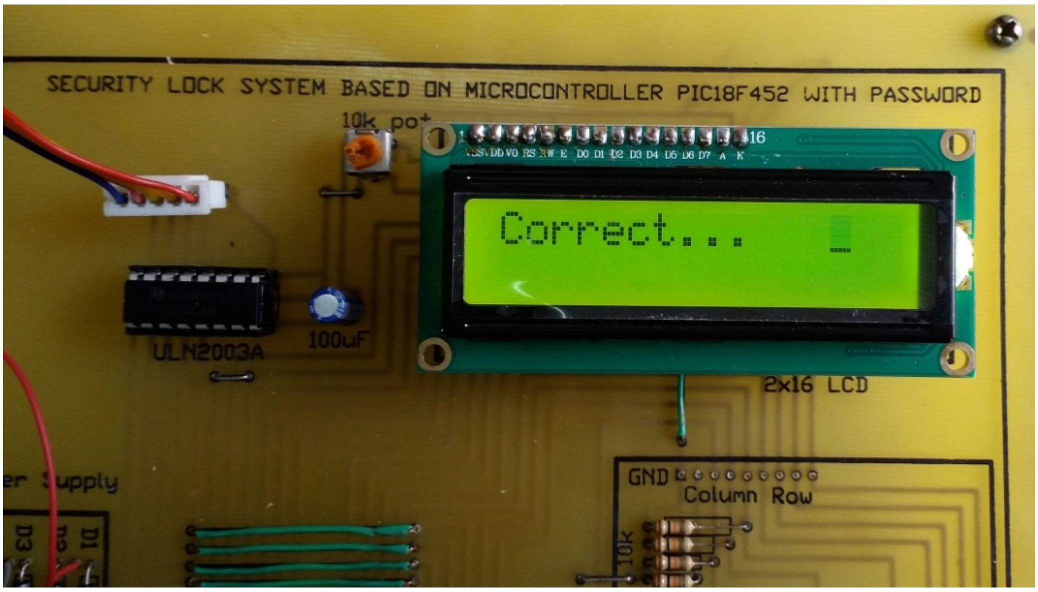

Figure 16 Entering correct password stage

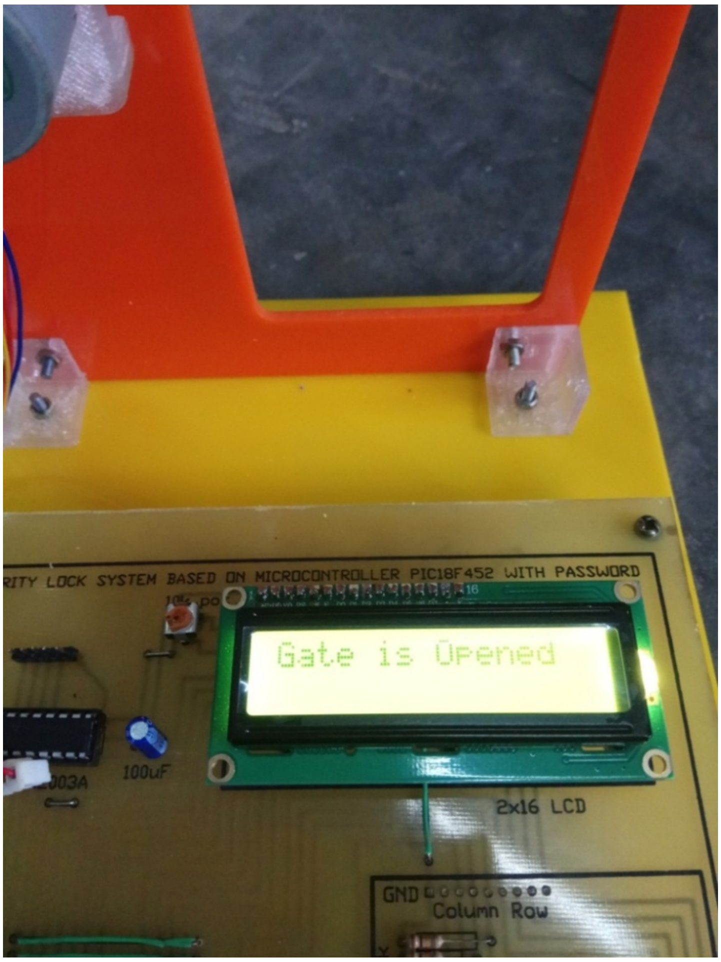

Figure 17 Gate open stage of security lock system

Figure 18 Gate close stage of security lock system

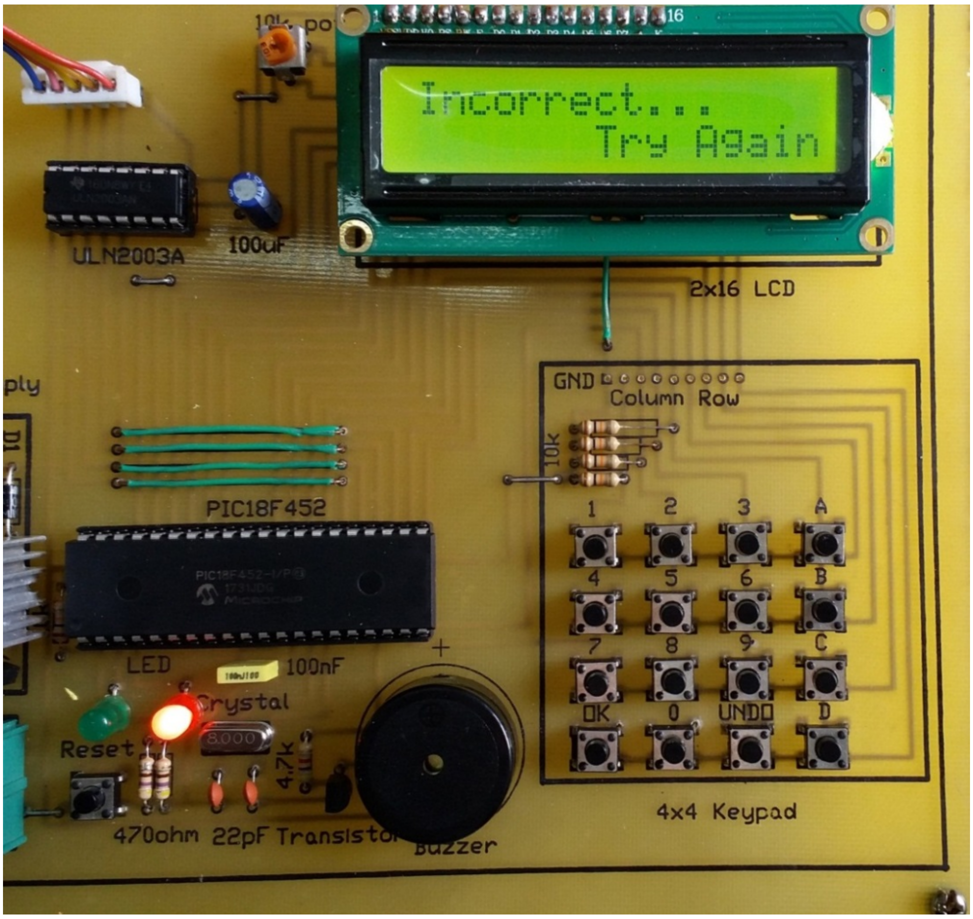

Figure 19 Entering incorrect password stage

Figure 20 Entering incorrect password three times

Conclusion

In day-to-day life, security of any object or place plays a major role. Automatic systems have less manual operations, so that the flexibility, reliabilities are high and accurate. The various innovations in security access system include code based lock, keycard lock and thumb print scan. Code based locking system is best suited in most applications because of its simplicity and reliability. Since the code based locking system is always resident in the area to be protected, there are fewer chances of security branches unlike the keycard lock system in which the access card can fall into unauthorized hands. The microcontroller based electronic combination door lock system with the alarm has successfully presented a functional and an easy way to combat crime and theft using a low cost device and can be applied everywhere security is needed. The advantages of using a security lock system are increased safety, no undetected strangers, reduce theft and no more lost keys. This circuit can be used in bank for security, steel safe and security door lock to secure them against thief.

Acknowledgements

I would like to thank Professor Dr Khin Khin Win, Head of Department of Physics, University of Yangon, for her kindly permission to submit this research paper.

References

Bates M, (2006) “Interfacing PIC Microcontroller” (London: Elsevier)
R A. Penfold, (1997) “An Introduction to PIC Microcontroller” (England : Bernard Babani)
http://microcontrollerprojects00.blogspot.com/
http://www.datasheetspdf.com/pdf/Microchip/PIC18F452
https://embedjournal.com/interface- 4×4 matrix keypad with Microcontroller
https://en.wikipedia.org/wiki/Stepper_motor
https://electrosome.com/uln2003-high-voltage-current-driver/

J. Myanmar Acad. Arts Sci. 2020 **Vol. XVIII.No.2A**

STUDY ON PROPERTIES OF TiO_2-GO BY TERAHERTZ SPECTROSCOPY

Kyauk Khe Sein[1], Ye Chan[2]

Abstract

The terahertz time-domain spectroscopy (THz-TDS) is a noncontact tool to measure the optical and electrical parameters of the nanometrics semiconductors/semimetals. Terahertz electromagnetic waves from 0.1 to 10 THz, bounded between the infrared and microwave regions of the spectrum, has been intensively attracted to explore scientific and engineering phenomena for the materials. Terahertz time domain spectroscopy (THz TDS) is a powerful tool for both, to characterize the free carrier response of graphene and probe the inter and intraband response of excited carriers with sub-ps (pico second) time resolution. This work presents application of noncontact THz-TDS techniques and analysis for the terahertz properties of TiO_2-GO in the new generation of optoelectronic devices.

Keywords: Terahertz time domain spectroscopy

Introduction

The far-infrared, or terahertz (THz) region of the electromagnetic spectrum hosts a wealth of intriguing and highly complex interactions between radiation and matter in physical, chemical and biological systems. With photon energies in the millielectronvolt (meV) range, electromagnetic radiation at THz frequencies interacts strongly with systems that have characteristic lifetimes in the picoseconds range and energetic transitions in the meV range. Examples of such systems include bound electrical charges, free charge plasmas, strongly confined charge plasma, excitons, transient molecular dipoles, phonons in crystalline solids, weakly bonded molecular crystals, relaxational dynamics in aqueous liquids, and hydrated biological matter.

Terahertz Spectroscopy is a spectroscopic technique in which the properties of a material are probed with short pulses of terahertz radiation, which consists of electromagnetic waves at frequencies from 0.3 to 3 terahertz (THz). It is proved as a reliable technique for characterization and identification of chemical substances due to characteristic lowest vibrational energy modes of organic molecules. On the other hand, THz radiation can penetrated through most of opaque to visible light materials, for example plastic, paper or cloths. Therefore, pure chemical substances such as explosives and illicit drugs can be detected via THz imaging techniques through the packaging. Moreover, the THz imaging techniques have potential to be used for biomedical microscopy applications and cancer diagnosis (Peter Uhd Jepsen, et.al., (2011)). THz spectroscopy is also found to be an excellent tool for material characterization to investigate optical and mechanical properties. THz spectroscopy was used for qualitative investigation of nanomaterials, polymers, glasses and paper. Oils, both lubricating and edible ones, are also the subject for qualitative and quantitative THz spectroscopy analysis (Ehsan Dadrasnia, (2015)).

For a molecular system, the frequency region for the normal modes spans approximately from tens of to 4000 cm^{-1}. The high frequency normal modes arise from covalent bonds; the upper limit is determined by the stretching modes of O-H and/or N-H bonds, which possess small

---

[1] Dr, Assistant Lecturer, Department of Physics, Sagaing University

[2] Dr, Professor, Head of Universities' Research Centre, University of Yangon

reduced masses. The low frequency normal modes are due to non-covalent interactions, normally featuring intermolecular vibrations and the intra molecular collective vibrations of backbones. The advances in the terahertz (THz) technique in the past two decades have made it possible to generate and detect electromagnetic radiation in the low frequency region, particularly below 100 cm^{-1}, under ordinary laboratory conditions. THz vibrational spectroscopy is therefore a promising tool for molecular characterization.

In this work, we investigate the properties of TiO_2-GO by using terahertz technology.

Terahertz spectroscopy

Recently, it has been demonstrated that THz radiation can be generated using air. Air does not show a second-order nonlinear coefficient, but it has a third order nonlinear coefficient instead. By generating plasma with a pulsed laser, it is possible to mix a fundamental wave and its second harmonic through the third order nonlinearity leading to efficient THz generation. This process opens up the possibility of using THz techniques for remote sensing by propagating a laser beam far from the source, generating THz locally, and transforming the reflected THz radiation into an optical beam again and returning it to the point of origin.

The traditional detection techniques in pulsed THz technology are EO sampling and the use of PC antennas. PC antennas, which are widely used for pulsed THz generation, can also be used to detect THz pulses. Rather than applying a bias voltage to the electrodes of the antenna, a current amplifier and ammeter are used to measure the transient current generated by an optical pulse and biased by the instantaneous THz field. The biased current is proportional to the applied THz field. It is possible to use a PC antenna for broadband THz wave detection by properly selecting the substrate materials. Ultrahigh bandwidth detection has been demonstrated using photoconductive antenna detectors made of LTG-GaAs with detectable frequencies in excess of 60 THz. The apertures of the PC antennas are usually in the micron range, and the optical alignment is more difficult compared to free-space EO sampling.

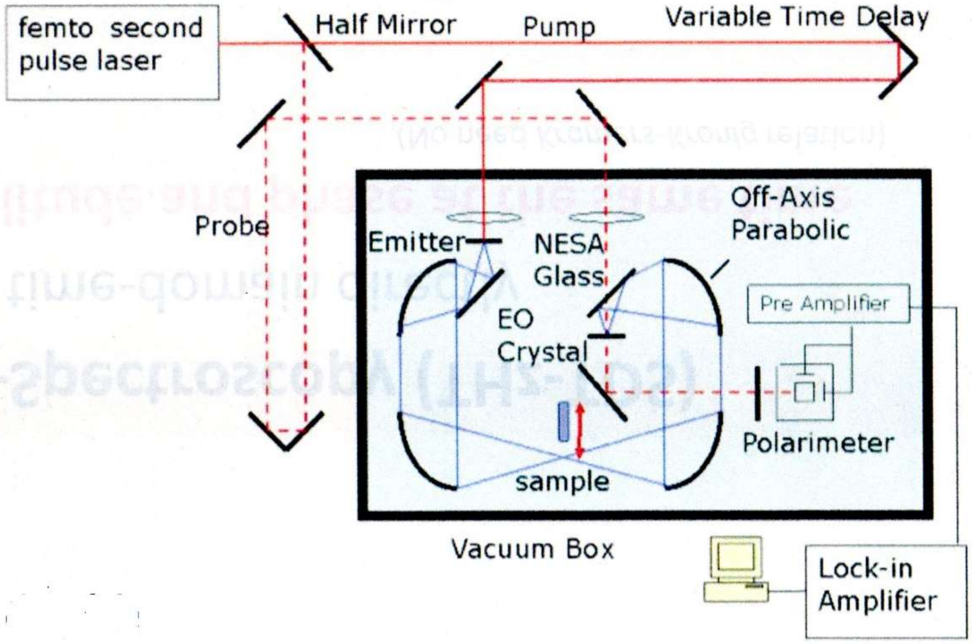

Figure 1 Principle of Terahertz Spectroscopy

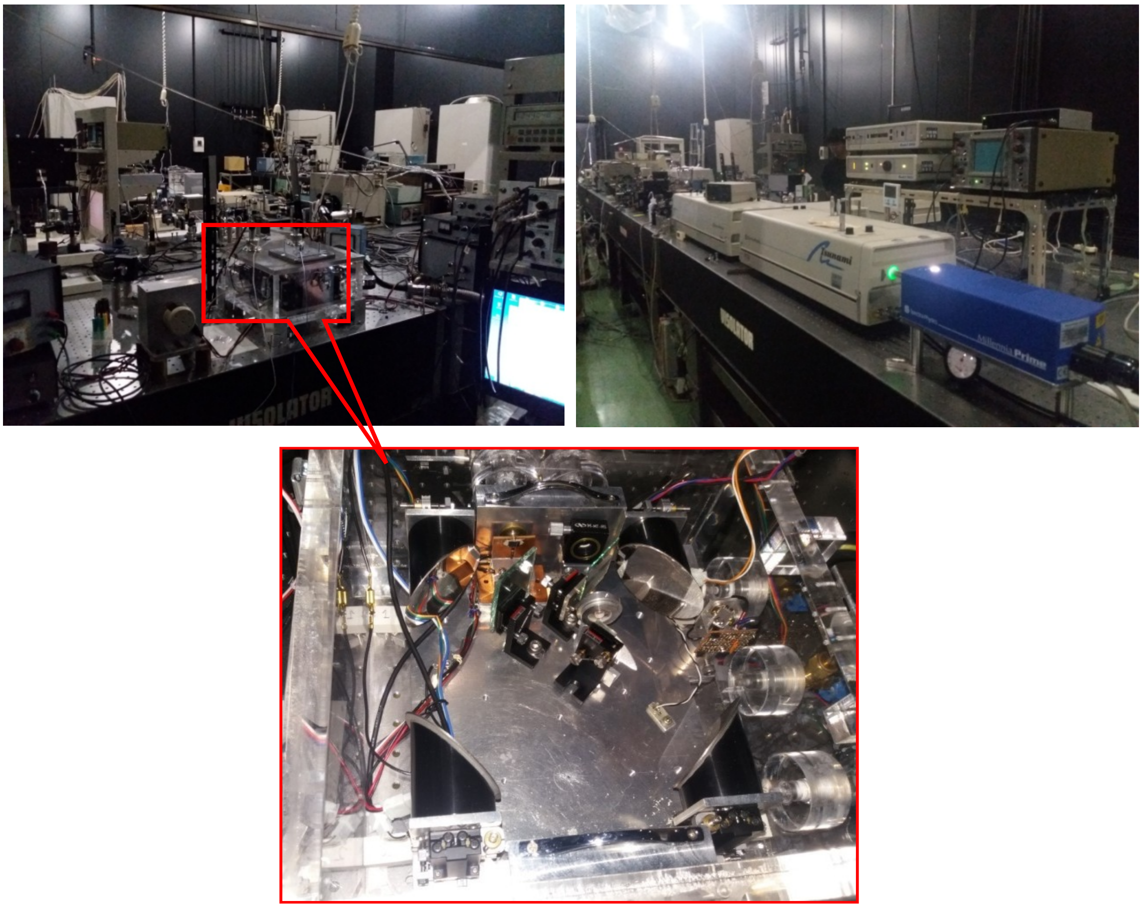

Figure 2 Terahertz Spectroscopy

Material and Method

The anatase TiO_2 powder are collected from commercial and wet milling to form nano crystaline powder. Graphite oxide (GO) make by Hammer's method. 1g of graphite and 0.5g of $NaNO_3$ are mixed with 23ml of H_2SO_4 in ice bath for 30 min. 3g of $KMNO_4$ was added gradually with stirring and cooling the mixture was stirred at 35˚C for 30 min. 46ml of distilled water was slowly added to cause in temperature to 98˚C for 15min. Then, adding 140ml of distilled water followed by 10ml of 30% H_2O_2 solution.

The solid product was separated by centrifugation, washed repeatedly with 5% HCl solution and then washed 3-4 times with distilled water until it turns to ph 6. Finally, graphite oxide gel are obtained by centrifugation.

3.55 ratio of TiO_2/GO are dispersed in DI water with ultra-sonicater and stirring for 3 hours to obtain a homogeneous TiO_2/GO solution. Hydroiodic acid (HI) are added into TiO_2/GO to reduce oxide for 30 mins and then washed 3-4 times with distilled water until it turns to pH 6 and TiO_2/graphene are obtained by centrifugation.

TiO_2/GO solution and TiO_2/graphene are dried in vacuum furnace with different temperature. Then sample and Teflon powder are together made pellet to analysis Terahertz spectroscopy.

Result and Discussion

The absorbance (a.u)Vs frequency (THz) graph of TiO_2 GO/graphene with different annealing temperature sample is shown in Figure 3. It is found that terahertz absorbance of samples are nearly the same under 2 THz frequency for different annealing temperature. But above the frequency 2 THz, it is found that the absorbance is different. It is also found that the absorbance of TiO_2/graphene before dry (black line) is a little shift. It is due to moisture in sample. The between 2 THz and 3 THz band, the transmittance is occur, it is due to intermolecular vibrations does not take place in these regions.

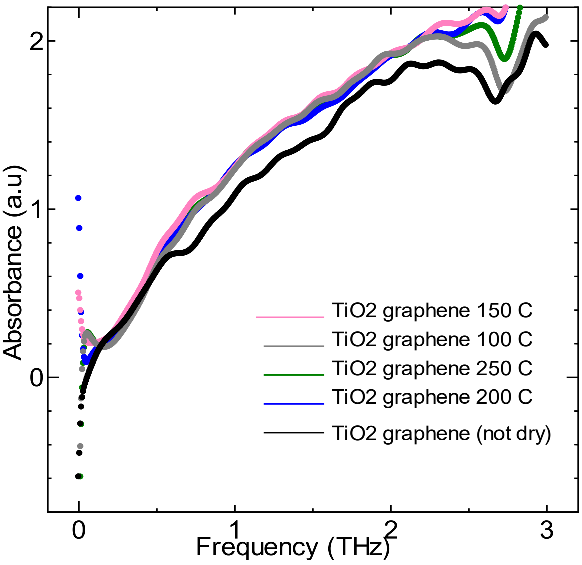

Figure 3 Terahertz absorbance of TiO_2 /graphene at different annealing temperature

Terahertz absorbance comparison of TiO_2-GO and TiO_2-rGO is shown in Figure 4. The absorbance is nearly the same. But the absorbance peak of TiO_2-rGO is occurred in high frequency (2.9 THz). It is due to intermolecular vibrations of graphene. And Figure 5 shows the SEM image of TiO_2-rGO.

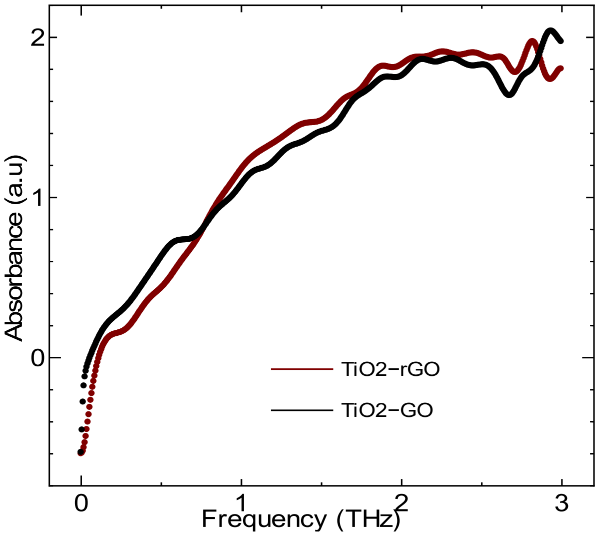

Figure 4 Terahertz absorbance of TiO_2-GO and TiO_2-rGO

Characteristic FT-IR spectra of natural graphite, GO and TiO_2-GO composites (Hui Zhang, Xiaoyan Wang, et. al., (2018)) were shown in Figure 5. All spectra present a broad peak around 3384 cm^{-1} belongs to the bending and stretching modes of O-H groups, and the peak at 1616 cm^{-1} is assigned to the C=O stretching vibration on the GO surface. Also, the peak at 1053 cm^{-1} band is due to the C-O stretching vibrations. These surface oxygen-containing functional groups render the possibility of covalent linkage of TiO_2 onto the GO surface. As for TiO_2-GO composites, the broad absorptions at low frequencies below 1000 cm^{-1} were ascribed to the vibration of Ti-O-Ti and Ti-O-C. This demonstrates that the TiO_2 particle were strong chemically bonded on the GO.

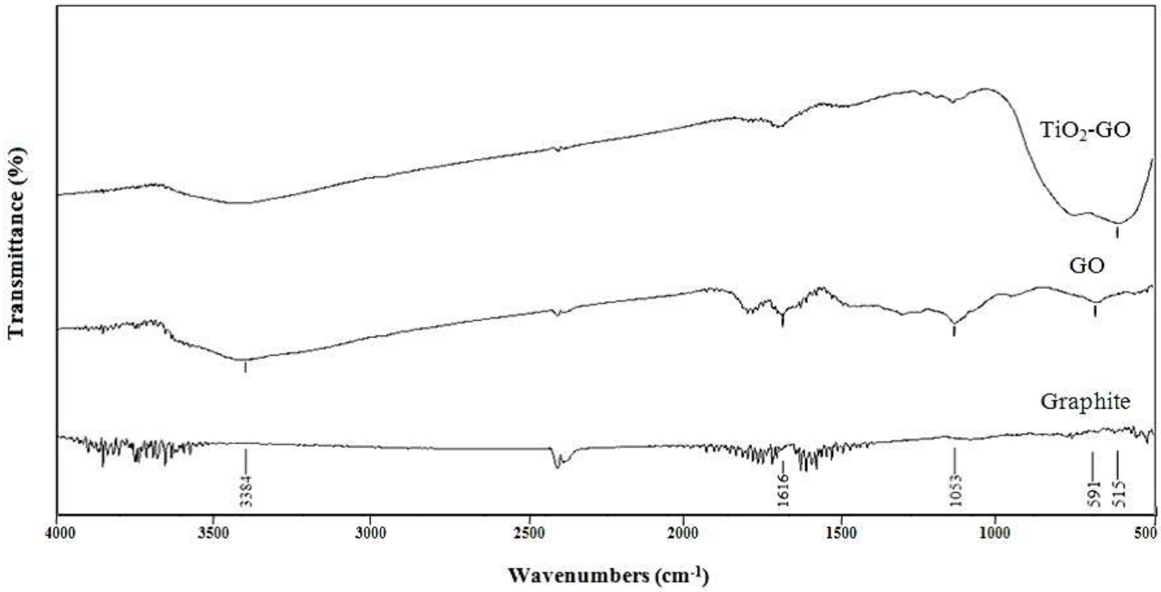

Figure 5 FT-IR spectra of graphite, GO and TiO_2-GO composites.

Figure 6 shows the SEM image of TiO_2/graphene sample. It is found that the graphene layers and TiO_2 are mixed but the sample is not homogeneous.

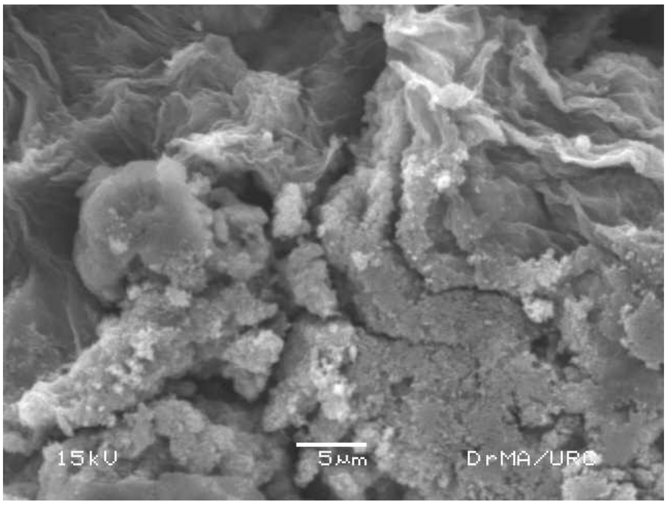

Figure 6 SEM image of TiO_2/graphene sample

Conclusions

This work presents application of noncontact THz-TDS techniques. TiO_2-GO and rGO was studied with different annealing temperature by THz spectroscopic methods. It is not occurred the free carrier response of TiO_2-GO in the THz regions.

References

Callum J. Docherty · Michael B. Johnston., (2012), "*Terahertz Properties of Graphene",* Springer Science + Business Media, LLC.

Ehsan Dadrasnia, (2015), "*Terahertz Time-Domain Spectroscopy to Characterize Graphene Nanostructures for New Optoelectronic Applications*", University of Carlos III, Madrid.

Feng Zhang, et. al., (2016) "*Application of THz vibrational spectroscopy to molecular characterization and the theoretical fundamentals: an illustration using saccharide molecules"*, Chemistry - An Asian Journal.

Hui Zhang, Xiaoyan Wang, et. al., (2018), "Synthesis and characterization of TiO_2/graphene oxide nanocomposites for photoreduction of heavy metal ions in reverse osmosis concentrate", Royal Society of Chemistry Journal.

Peter Uhd Jepsen, et.al., (2011), "*Terahertz spectroscopy and imaging – Modern techniques and applications*", Laser Photonics Rev. **5**, No. 1, 124–166

Søren A. Jensen, et.al., (2013), *"Terahertz Depolarization Effects in Colloidal TiO_2 Films Reveal Particle Morphology",* Journal of Physical Chemistry.

DETERMINATION THEEFFICIENCY OF SOLAR CELL DERIVED FROM POINSETTIA DYE EXTRACTION

Sandar Kyaw[1], Than Than Win[2], Yin Maung Maung[3]

Abstract

In this research, the natural dyes, Poinsettia leaves were used as photosensitizer. These dyes were measured with ethanol solvent at different temperatures (25℃,45℃,65℃). The absorbance and energy levels of the dye solution were characterized using UV-Vis Spectroscopy measurement. XRD measurement was used to know the purification and structural properties of TiO_2 powder. The sandwich structure of DSSC consisted of TiO_2as photo electrode, carbon layer as counter electrode, poinsettia as photosensitizer and electrolyte as electron transfer media. The efficiencies of DSSC were calculated by using I-V measurement.

Keywords – Natural Dye, TiO_2, UV-Vis, XRD

Introduction

Dye Sensitized Solar Cells (DSSCs) are device that convert solar to electric energy by light sensitization established on wide energy band semiconductor. A DSSC is the third generation photovoltaic device for low cost conversion of solar energy into electrical energy. DSSCs have received an increasing interest due to the simple fabrication process and relatively high conversion efficiency. Moreover, DSSCs is gaining traction due to their unique advantages such as flexibility and low manufacturing cots. The principle operation of DSSCs is based on sensitization of a wide band gap metal oxide semiconductor to the visible region by an absorbed molecular dye. TiO_2 is a potential material for Dye Sensitized Solar Cells (DSSCs. The DSSC consists of a dye sensitizer, a metal oxide semiconductor, an electrolyte and transparent conductors which are responsible for determining the efficiency.

Experimental Procedure

Preparation of Natural Dye

In this research, Poinsettia Leaves were used as sensitizer. Firstly, Poinsettia leaves were washed with distilled water and cut into small pieces. After that, 10 g of sample was mixed with 200 ml of ethanol and the samples were stirred using magnetic stirrer at 25℃, 45℃ and 65℃ for 1 hr respectively. The procedure continued with the filtration of the samples to remove large residue. Subsequently, the extracts were centrifuged at 4000 rpm using a Denley BS 4000 (UK) centrifuge machine for 10 minutes to separate any remaining residues. The band gap energy of these dyes was determined by UV-Vis spectroscopy measurement.

Preparation of Glass Substrate

Indium doped Tin Oxide (ITO) glass sheets with resistance of 10 Ω were cut into 25 cm square pieces. Each of the sheets was cleaned with ethanol and rinsed with deionized water.

---

[1] Demonstrator, Department of Physics, Kyaukse University

[2] Dr, Professor, Department of Physics, PangLong University

[3] Dr, Professor, Department of Physics, University of Yangon

Preparation of photo electrode

Titanium Dioxide (TiO_2) powder was used as photo electrode material. TiO_2powder was checked by X-Ray Diffraction (XRD) method.TiO_2 paste was prepared by adding 1 g of TiO_2 powder and 3 ml of ethanol solvent and then grinding the mixture for an hour at 180℃. TiO_2 paste was deposited on the ITO glass substrate by rolling method. And then, the electrodes were immersed in the dye solution and kept overnight at room temperature to absorb the dye on theTiO_2 surface. They were kept in the dye until being used in a cell.

Preparation of counter electrode

Carbon powder was used as carbon catalyst counter electrode. Firstly, 1 g of carbon was put in a mortar and pestle. And then, 3 ml of ethanol was poured drop by drop into a mortar and pestle. After grinding for 1hr, the carbon solution was obtained. The glass sheet was coated by using spray method.

Preparation of Electrolyte

1 g of iodine and 2 ml of ethanol were mixed in a beaker. The mixture was dissolved for 30 min and brown solution was obtained.

DSSC Assembly

DSSC is composed of five elements: two transparent conductive substrates, TiO_2 layer Carbon layer, dye molecules and electrolyte. Firstly, TiO_2 photo electrode and carbon counter electrode were assembled to form a solar cell. And then, a drop of iodine electrolyte solution was sandwiched between the positively and negatively charged electrodes and clipped together to form a complete cell. The photo electric conversion efficiency measurement was carried out using I-V measurement.

Results and Discussion

UV-Vis Analysis

The energy band gaps were examined from UV-Vis Spectroscopy measurement. By using Tauch Mehod, $(\alpha h\nu)^2 = A(h\nu - E_g)^n$,the energy band gaps of the dyes andTiO_2 photo electrode were obtained as shown in Fig 1 (a-d) and the results were listed in Table (1) Table (2).

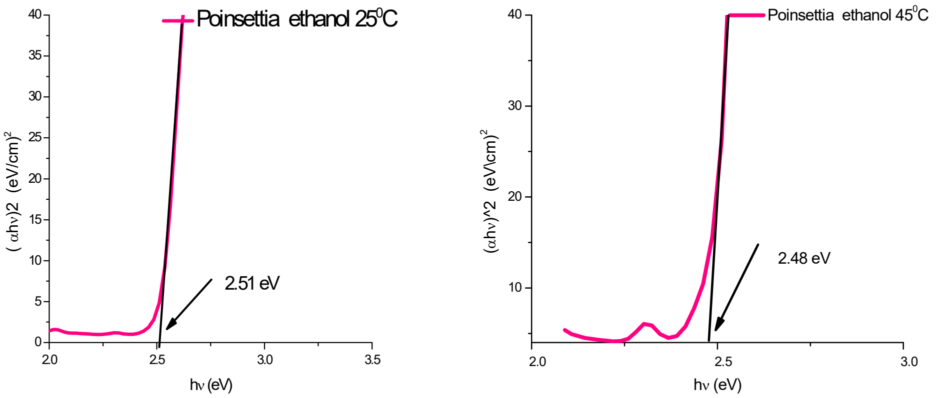

(a) Poinsettia Dye at 25℃ (b) Poinsettia Dye at 45℃

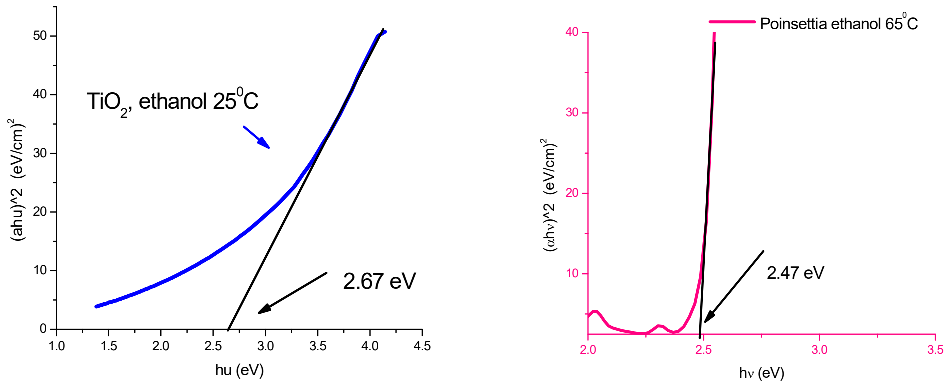

(c) Poinsettia Dye at 65℃ (d) TiO_2 photo electrode

Figure 1(a-d) The relation between energy (hν) and $(\alpha h\nu)^2$

Table 1 Energy band gap for Poinsettia Dye with Ethanol at 25℃, 45℃, 65℃

Temperature (˚C)	Wavelength (nm)	Energy Band gap (E_g)(eV)
25	492	2.51
45	498	2.48
65	499	2.47

Table 2 Energy band gap for TiO_2 photo electrode at 25 ˚ C

Temperature(˚C)	Wavelength (nm)	Energy Band gap (E_g)(eV)
25	462	2.67

XRD Analysis of TiO_2 photo electrode

XRD analysis was carried out to study the phase assignment and crystallographic properties of TiO_2 powder. According to XRD result, eight distinct peaks as shown in Fig (2) were observed such as (101), (103), (004), (112), (200), (105), (211) and (204). All peaks were well matched with the standard profile of TiO_2. Thus, the sample of TiO_2 was indicated the pure phase. The crystallite size was calculated by Debye Scherer equation using FWHM and Bragg angle obtained from the XRD data. From calculated result, the crystallite size of TiO_2 was 39.949 nm.

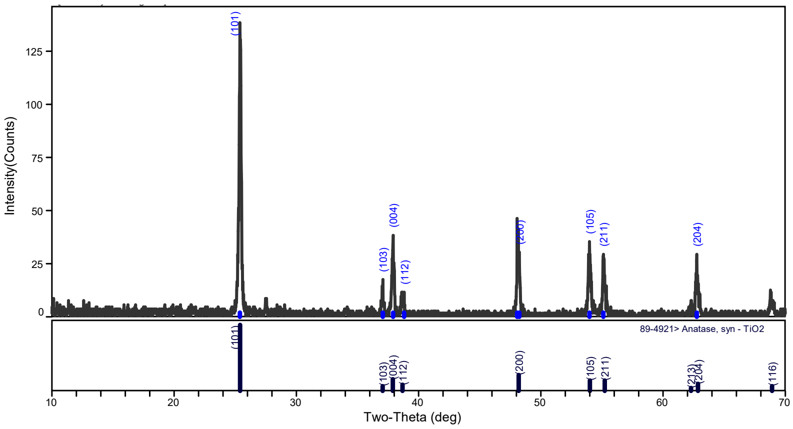

Figure 2 XRD Spectrum of TiO_2

Photovoltaic analysis of DSSC

The current-voltage characteristic of the solar cell was studied by I-V measurement. The I-V characteristic of the dye at 25℃ was shown in Figure (3). The photovoltaic parameters ofDSSC were obtained from I-V data and the results were shown in Table (3). The Fill Factor and total energy conversion efficiencies were calculated using equations(1) and (2)

$$FF = [(I_{max} \times V_{max}) / (I_{sc} \times V_{oc})] \qquad (1)$$

$$\eta = [((I_{max} \times V_{max}) / P_{in}) \times 100] \qquad (2)$$

Where, I_{max} and V_{max} denote the maximum output value of current and voltage respectively. I_{sc} and V_{oc} denote theshort circuit current and open circuit voltage respectively. And, P_{in} is the energy of incident photon.

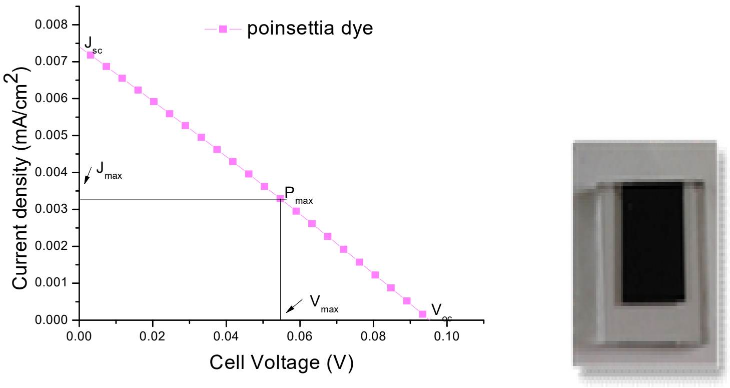

Figure 3 I-V characteristics of poinsettia dye sensitized TiO_2 based DSSC

Table 3 The photovoltaic parameters of the DSSC sensitized for three dyes

Dye	I_{max} (mA/cm^2)	V_{max} (V)	J_{sc} (mA/cm^2)	Voc (V)	Efficiency (%)	FF
Poinsettia	3.96×10^{-3}	0.0461	7.40×10^{-3}	0.096	0.75	0.2582

Conclusion

Poinsettia dyes were studied for photovoltaic applications. From UV-Vis measurement, the band gap energies of the dyes were similarly equal. The band gap energy of the dye (2.51 eV) at 25 ° C wasalmost matched well with that of TiO_2 photo electrode (2.67eV). According to XRD result, the powder of TiO_2 was pure and crystallite size was 35.349 nm. From I-V measurement, photovoltaic parameters of DSSC were obtained. Fill Factor and efficiency of the dye were 0.2582 and 0.75 %. Therefore, solar energy to electrical conversion efficiency was very low. Advanced fabrication procedure followed many result in obtaining good efficiency measurement. The photo electrode presents nanowire, nanotube, nanorod and nanofiber can also be performed to extend present research work.

Acknowledgements

Firstly, I would like to acknowledge to Professor Dr Cheery Than, Head of Department of Physics, Kyaukse University, for her constructive criticism and permission for doing this research. I also would like to thank to DrNwetNwet Aye, Professor, Department of Physics, Kyaukse University, for her valuable guidance and helping about my research. I also thank to Materials Laboratory members from Mandalay University for their helpful discussion.

References

O. Adedokun*et al.,* (2016) "Review on Natural Dye -Sensitized Solar Cells (DSSCs)."*International Journal of Engineering Technologies*, vol.2, pp. 34-41

S.A.Taya*et al.,*(2013) "Dye -Sensitized Solar Cells using fresh and dried natural dyes." *International Journal of Materials Science and Application*, vol.2, pp. 37-42

D.Wook Chang *et al.,*(2014)" Graphene in photovoltaic applications: organic photovoltaic cells (OPVs) and dye - Sensitized Solar Cells (DSSCs)." *Journal of Materials Chemistry*, vol.2, pp. 2

R.Oommen *et al.,*(2012) " Optical Characteristic of TiO_2 thin films sensitized with the natural dye of ClitoriaTernatea." *International Journal of Applied Physics and Mathematics,*vol.2, pp. 439

P.Murugakoothan*et al.,* (2014) "Natural Dye Extracts of Areca Catechu Nut as dye Sensitizer for Titanium dioxide Based Dye Sensitized Solar Cells. "*Journal of Nanotechnology and Electronic physics*, vol.6, pp.1

J. Myanmar Acad. Arts Sci. 2020 Vol. XVIII.No.2A

MICROCONTROLLER BASED AUTOMATIC DOOR OPENING AND LIQUID PETROLEUM GAS DETECTING SYSTEM

Sabal Phyu Thein[1], Wah Wah Myint[2] and Khin Mar Win[3]

Abstract

The purpose of the current research is to construct “Automatic Door Opening and Liquid Petroleum Gas Detecting System”. The design is based on an Arduino Uno board, PIR (passive infrared) motion sensor, L298N motor driver, CD tray with 5V DC motor, Gas sensor MQ3, 0.96 I2C LCD driver and jumper wires. The PIR sensor is used to open and close the door automatically. The MQ3 sensor is used as liquid petroleum gas detecting system because it is suitable for detecting alcohol, benzine, CH4, hexane, LPG and CO. The Arduino UNO board is used to control all sensors’ operation and gives an output. The controlled program is written in C programming language. The system can also be expanded with an inductive detector for metal detection purpose of security.

Keywords: Arduino UNO, PIR motion sensor, L298N motor driver, CD tray with 5V DC motor, Gas sensor MQ3, 0.96 I2C LCD driver, LCD, inductive detector

Introduction

The opening and closing of doors is always a tedious job, especially in places like shopping malls, hotels and theaters where a person is always required to open the door for visitors. In this research work, an Arduino Uno board connected with a PIR sensor is used to open and close the door automatically. Here, we used HC SR 501 passive infrared (PIR) sensor to detect the presence of humans near the surroundings of a door and then used the Atemega 328 microprocessor to control L298N motor drivers. If the PIR sensor detects a human, it gives a pulse or signal to a microcontroller and the gate will open by turning on the motor driver. The proposed design can be applied in many places such as industry, offices, Universities, shopping centers, airport and hospital etc. The liquid petroleum gas detection system is also constructed by using an Arduino Uno microcontroller interfacing with a gas sensor and an LCD module associate with a buzzer. The system can be expanded with an inductive detector for metal detection purpose of airport security. The block diagram of the proposed system is shown in Figure (1). It consists of power supply section, PIR sensor, MQ-3 gas sensor, inductive detector, gate entrance, LCD and alarm. The various units were designed and tested separately.

---

[1] Dr, Lecturer, Department of physics, Meiktila University

[2] Lecturer, Department of physics, Meiktila University

[3] Associate Professor, Department of Engineering Physics, Mandalay Technologiccal University

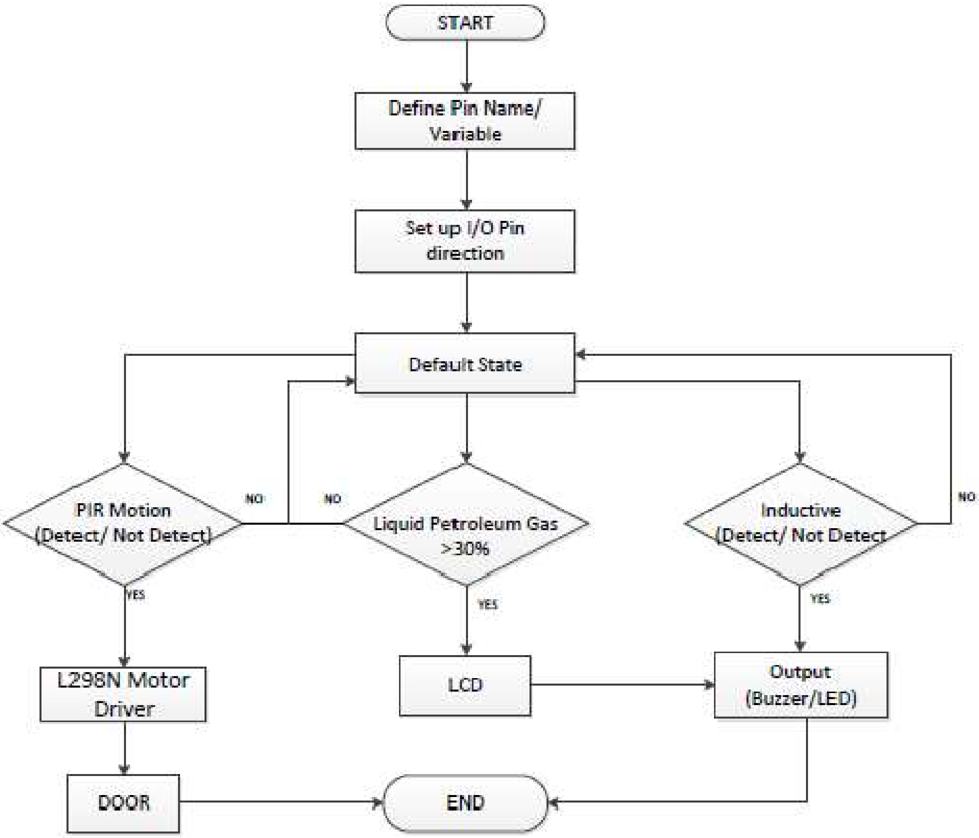

Methodology of the System

Design and Construction of the System

This circuit is based on Arduino Uno board with atmega328 microcontroller which is quite compact and it is connected with the PIR sensor, MQ3 gas sensor and inductive detector. There are automatic door opening and closing system using PIR sensor, liquid petroleum gas detecting system using MQ3gas sensor and metal detection system using inductive sensor performed in this constructed system. Each part of the system is controlled by the firmware program and it is written in C programming language. The photograph of the Arduino Uno, PIR sensor, MQ-3 gas sensor and inductive sensor are shown in Figure (2-5). The complete circuit diagram is shown in Figure (6).

Circuit Design and Connection between Arduino and Sensor Units

In this circuit diagram the output pin of PIR is connected with digital pin4 of arduino. A 5V pin of it is connected with VCC pin of sensors and GND pin is connected to GND pin of sensor. The digital output pin2 and pin3 of arduino are connected to input 1 and input 2 of L298N motor driver. Output 1 and 2 of motor driver are connected to 5V motor CD tray. For gas detection system, analog output pin Ao of MQ3 gas sensor is connected to analog pin A0 of arduino and digital pin D0 is connected to digital pin 8 of arduino. A 5V and GND pins of arduino are connected to VCC and GND pins of gas sensor. Analog output pin (A4, A5) of arduino are connected to SDA and SCL pins of I2C LCD driver. A LCD is used to indicate the detected gas percentage and a LED and a buzzer are used as the over gas percentage indicator. 5V and GND pins of arduino are connected to VCC and GND pins of LCD driver. Digital output pins (9, 10) of arduino are connected to buzzer and LED. For inductor detection system, analog input pin A1 of arduino is connected to signal pin of inductive detector. A 5V and GND of arduino are connected to VCC and GND pins of inductive detector. The alarm unit used is buzzer which indicates when metals are detected. The flow diagram of microcontroller based automatic door opening and liquid petroleum gas detecting system is shown in figure (7).

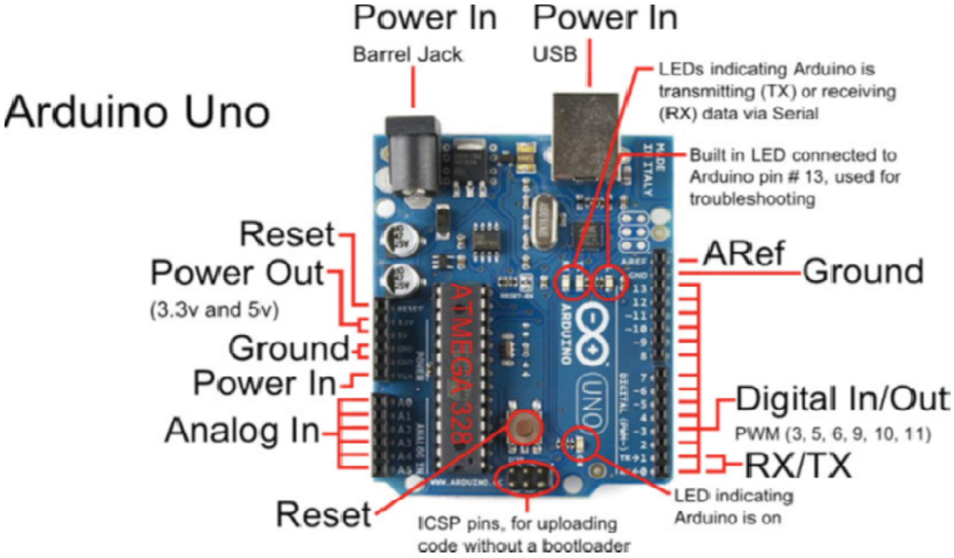

Figure 2 The pin configurations of arduino uno board

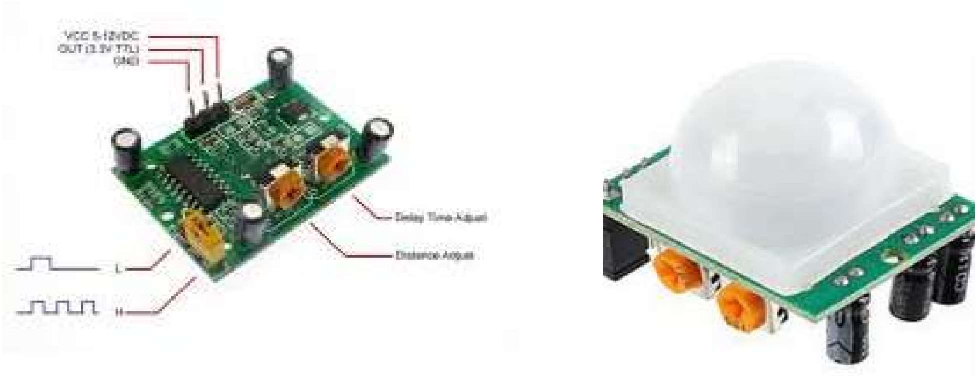

Figure 3 The photograph of PIR sensor

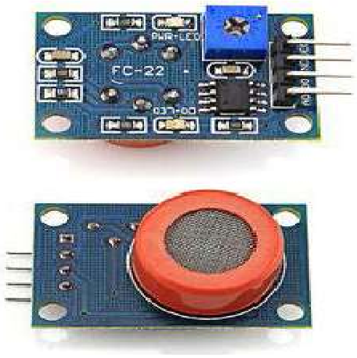

Figure 4 The photograph of MQ3 gas sensor

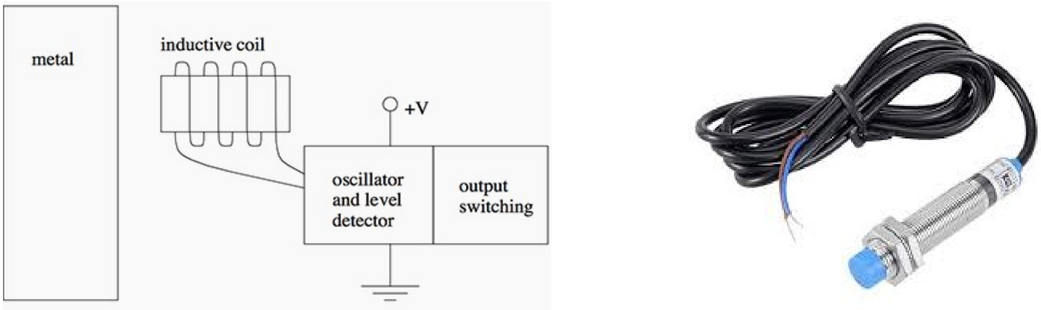

Figure 5 The photograph of inductive detector

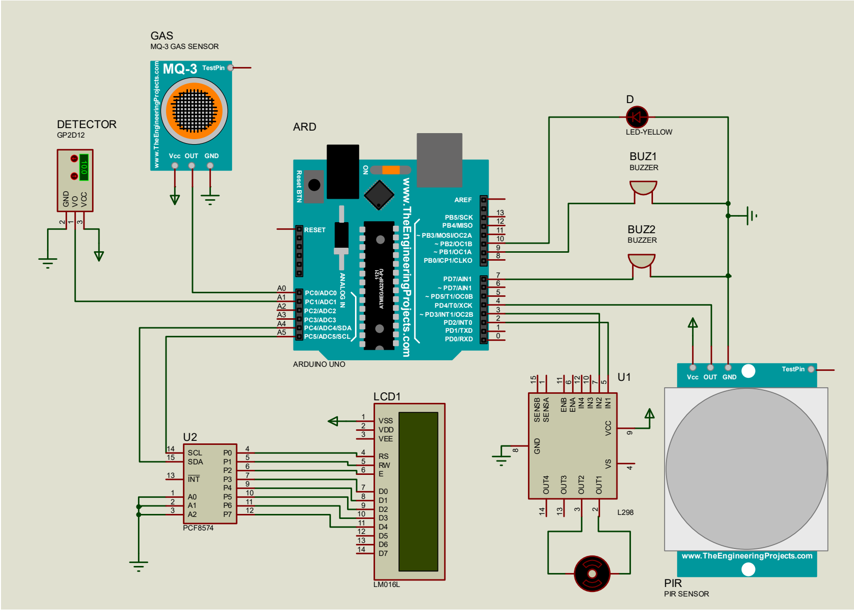

Figure 6 The circuit diagram of Microcontroller Based Automatic Door Opening and Liquid Petroleum Gas detecting system

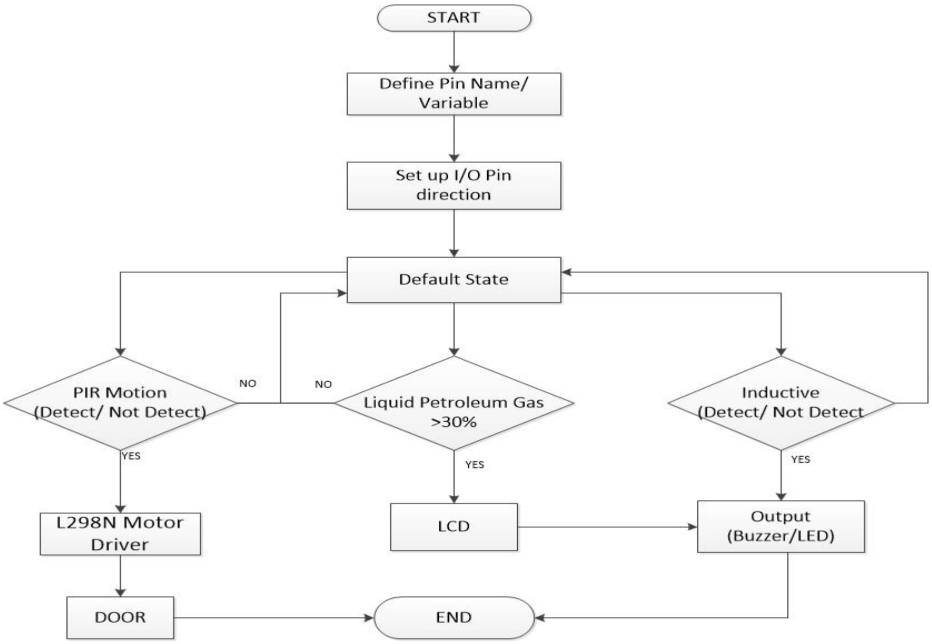

Figure 7 The flow diagram of microcontroller based automatic door opening and liquid petroleum gas detecting system

Discussion

This research proposes a system of automatic opening and closing of door by sensing anybody movement near the door. This is achieved with help of a PIR (Passive Infrared) sensor. Alive body generally emits infrared energy which is sensed by the PIR sensor from a considerable distance. This sensing signal is fed to a microcontroller to operate a door motor through motor driver IC. When a body approaches within the operating range of the sensor, it sends a logical command to open the door. The door automatically closes with a fixed time delay. The hardware demonstration of automatic door opening is shown in Figure (8). The detected analog voltage values of MQ3 gas sensor are read by the microcontroller. The Arduino Uno board is 10-bit device that changes an analog voltage on a pin to a digital number. The system will link input voltages from 0 to 5 V with decimal values from zero to 1023 to generate 5Vs for every 1024 units. The system will process the analog signal and convert it to digital value of 0 or 1. Also, the analog values from the gas sensor will be scaled to percentage. If the percentage is greater than 30, the alarm and the orange LED indicator will be ON. The sensor value only reflects the approximated trend of gas concentration in a permissible error range it does not represent the exact gas concentration .The detection of certain components in the air usually requires a more precise and costly instruments, which cannot be done with a single gas sensor. The gas sensor module is useful for gas leakage detection in home and industry. The hardware demonstration of liquid petroleum gas detecting system is shown in Figure (9).The inductive sensor can determine when a metal have been brought nearby. The hardware demonstration of inductor detecting is shown in Figure (10). The compiled sketch program is shown in Figure (11).

Conclusion

Also this research will aim to develop automatic door opening and liquid petroleum gas detecting system. The system proposes a system of automatic opening and closing of door by sensing anybody arriving near the door. This is achieved with help of a PIR motion sensor. The proposed design can be applied in many places such as industry, offices, Universities, shopping centers, airport and hospital etc. For the detecting system MQ3 gas sensor and inductive sensor are used. These sensors will detect fuel gas any metals and so these detection systems can be used in airport, classrooms and meeting rooms' security.

Figure 8 Hardware demonstration of automatic door opening

Figure 9 Hardware demonstration of liquid petroleum gas detecting system

Figure 10 Hardware demonstration of inductor detecting metal

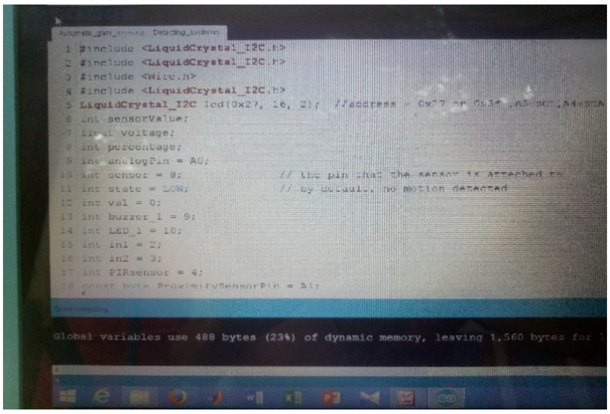

```
#include <LiquidCrystal_I2C.h>
#include <LiquidCrystal_I2C.h>
#include <Wire.h>
#include <LiquidCrystal_I2C.h>
LiquidCrystal_I2C lcd(0x27, 16, 2);   //address = 0x27 or 0x3F ,A5=SCL,A4=SDA
int sensorValue;
float voltage;
int percentage;
int analogPin = A0;
int sensor = 8;                    // the pin that the sensor is attached to
int state = LOW;                   // by default, no motion detected
int val = 0;
int buzzer_1 = 9;
int LED_1 = 10;
int in1 = 2;
int in2 = 3;
int PIRsensor = 4;
const byte ProximitySensorPin = A1;
```

```
Global variables use 488 bytes (23%) of dynamic memory, leaving 1,560 bytes for
```

Figure 11 The photograph of compiled sketch program

Appendix

```
#include <LiquidCrystal_I2C.h>
LiquidCrystal_I2C lcd(0x27, 16, 2);  //address = 0x27 or 0x3f ,A5=SCL,A4=SDA
int sensorValue;
float voltage;
int percentage;
int analogPin = A0;
int sensor = 8;              // the pin that the sensor is attached to
int state = LOW;             // by default, no motion detected
int val = 0;
int buzzer_1 = 9;
int LED_1 = 10;
int in1 = 2;
int in2 = 3;
int PIRsensor = 4;
const byte ProximitySensorPin = A1;
const byte Buzzer_2 = 6;
const byte LED_2 = 7;
long duration;
int distance;
void setup() {
  // put your setup code here, to run once:
  Serial.begin(9600);
  Serial.println("LPG Tester");
  // initialize the LCD
  Wire.begin();
  lcd.begin();
  lcd.setCursor(0, 0);
  lcd.print("LPG Tester");
  pinMode(sensor, INPUT);    // initialize sensor as an input
  pinMode(buzzer_1, OUTPUT);
  pinMode(LED_1, OUTPUT);
  delay(100);
  pinMode(in1, OUTPUT);
    pinMode(in2, OUTPUT);
    pinMode(PIRsensor, INPUT);
   Serial.begin(9600);
  pinMode(ProximitySensorPin, INPUT_PULLUP);
  pinMode(Buzzer_2, OUTPUT);
 pinMode(LED_2, OUTPUT);
}
void loop() {
```

```
  {
  //---------------------------------------------
   sensorValue = analogRead(A0);  // read the input on analog pin 0:
  percentage = map(sensorValue, 200, 1023, 0, 100); //
  if (percentage <0) percentage =0;
  lcd.clear();
  lcd.print(percentage);
  lcd.print("% LPG  ");
  digitalWrite(buzzer_1,LOW);
  digitalWrite(LED_1,LOW);
  lcd.setCursor(0, 1);
  lcd.print(sensorValue);
  lcd.print(" adc");
  Serial.print(sensorValue);
  Serial.print("Adc ");
  Serial.print(percentage, 1);
  Serial.println("%");
if (percentage >30)
 {
  digitalWrite(buzzer_1,HIGH);
  digitalWrite(LED_1,HIGH);
  delay(1000);
}
else
{
 digitalWrite(buzzer_1,LOW);
digitalWrite(LED_1,LOW);
}
delay(100);
  }
{
if(digitalRead(PIRsensor)==HIGH)
  {
       digitalWrite(in1,HIGH);
       digitalWrite(in2,LOW);
       delay(2000);
       digitalWrite(in1,LOW);
       digitalWrite(in2,LOW);
       delay(2000);
       digitalWrite(in1,LOW);
       digitalWrite(in2,HIGH);
       delay(5000);
}
```

```
   else
{
  digitalWrite(in1,LOW);
  digitalWrite(in2,LOW);
}
delay(100);
if(digitalRead(ProximitySensorPin))
  {
   Serial.print("Object detected!");
  digitalWrite(Buzzer_2, HIGH);
  digitalWrite(LED_2,HIGH);
  delay(1000);
  }
else{
  digitalWrite(Buzzer_2, LOW);
  digitalWrite(LED_2,LOW);
}
delay(100);
}
}
}
```

Acknowledgement

The authors would like to acknowledge Professor Dr Khin Khin Win, Head of Department of Physics, University of Yangon, for her kind permission to carry out this work. The authors also thank to Professor Dr Hla Hla Than, Head of Department of Physics, Meiktila University and Professor Dr Daw Hla Win, Department of Physics, Meiktila University , for their kind permission to carry out this work.

References

Arduino-Arduino Board BT. (n.d.). Retrieved January 14, 2018, from http://www.arduino.cc

Muhammad, W.(2017) "Human Sensed Automatic Door Opening and Closing System using PIR Sensor in Green PAK™."PDF-(487KB).

Altaf, S.V., S. Abhinay, E. Ansari, M.D. Kaunain, & R. Anwer (2017) "Alcohol Detection and Mortor Locking System." International Journal of Advanced Research in Electrical, Electronics and Instrumentation Engineering.*"* 6(2): pp.989-993.

Winncy Y. Du. (2014) "Resisitive, Capacitive, Inductive and Magnetic Sensor Technologies." CRC Press, ISBN 1439812446, Chapter 4 Inductive Sensors.

Kousikan M, Sundaraj M. (2014) "Automatic Drunken Drive Prevention System". International Journal of Students Research in Technology and Management. 2(2): 75-77.

*J. Myanmar Acad. Arts Sci. 2020*Vol. XVIII.No.2A

DESIGN AND IMPLEMENTATION OF MICROCONTROLLER BASED MUSIC REACTIVELED CUBE

Wah Wah Myint[1], Sabal Phyu Thein[2]& Khin Mar Win[3]

Abstract

A music reactive LED cube is constructed by Arduino Microcontroller ATmega328P. The components used in this system are Arduino Uno Board, 512 LEDs, npn-transistors (2N2222), 74HC595 ICs, speaker, some resistors. The LEDs are designed into 8×8×8 cube which contains eight rows and eight columns. The output of the system shows various pattern designs of LEDs and also produces melody sound. The controlled program source code is written in C programming language. The error free source code is uploaded to the A Tmega 328P microcontroller and it controls the operation of the whole system. This system can be used for altar decoration, house and advertisement decoration.

Keywords: Arduino UNO, LEDs, Transistors (2N2222), 74HC595 ICs, Speaker

Introduction

Nowadays, LED cube is the next generation display piece of art and are adored among the electronic enthusiasts around the globe. LED cube is a set of components that can produce display of animation on the LED assembled part. The suitable software and hardware that will be involved are important aspects to take account about it. In this work, the design and construction of a music reactive 8×8×8 LED cube by Arduino microcontroller is constructed. The constructed music reactive LED cube contains eight layers. Each layer has sixty four LEDs and total eight layers have altogether five hundred and twelve LEDs. So the LED cube contains eight rows and eight columns[Chria. (2012)].The display panel of this circuit is 512 LEDs. This circuit is designed to display various pattern designs together with melody sound. Lighting and sound will be operated simultaneously. To control the functions of the cube circuit, Arduino Uno board is used in this work. The ICs used in this circuit are 74HC595 for the purpose as the layer selector and column selector. The block diagram of music reactive LED cube control system is as shown in Figure (1). The patterns are displayed on a 3D structure which is made up of copper rods. The message can be changed as per user need by rewriting the Arduino in built memory. The complete display system circuit is power supply run on 5V and 2A current which is provided externally. This unique way of displaying messages is very fantastic and eye catching therefore it is widely used in the field of advertising and toys, etc.

Construction and Operation of the System

Circuit Construction and Operation

In this circuit, Arduino microcontroller LEDs, npn transistors (2N2222), nine 74HC595 ICs, some resistors, speaker and +5V power supply are used for the circuit operation. The total combination of LED in the LED cube is 512 pieces. The arrangement of the LEDs must be carefully arranged so that the LED cube will firmly and steadier. Measuring the cathode wire of the LEDs, it’s about 17 cm. The cathode wire will be connecting to the cube horizontally.

---

[1] Dr, Lecturer, Department of Physics, Meiktila University

[2] Lecturer, Department of Physics, Meiktila University

[3] Associate Professor, Department of Engineering Physics, Mandalay Technological University

The Anode wire is about 16 cm. The Anode wire will make all of the vertical connections. The multiplexing circuit controls all the data input from the microcontroller to the LED cube. Nine 74HC595 ICs are used in this work. There are 16 pins in 74HC595 ICs, pin 8 and 16 are connected to ground and power supply. Pin 11, 12, 14 are connected to Arduino. Pin 1, 2, 3, 4, 5, 6, 7, 15 are connected 220Ω resistors to join the Anode layer cube. Eight of ICs are connected in above way. Pin 1, 2, 3, 4, 5, 6, 7 and 15 of the last 74HC595 ICs are connected with npn (2N2222) transistors to join the cathode layer cube. The pin 10 and pin 13 of 74HC595 ICs must be held high and low for this operation.

Transistors have been used to be the switch for the LED connected to the ground. The transistors will be turned on if the data was transmitted to the transistors. The LEDs cathode leg will be attached to the ground and it also will be the controller for each level of the LED cube. The wires were made connections to each of the 8 horizontal layers and the wire down routed through the holes alongside the LED. These wires will be used with the cathode/layer control. Each row is labeled 0 to 7. This corresponds to one of each of the 74HC595 ICs. The Layer 1 wire connects to pin 1 of the cathode control header, all the way up to pin 8 connecting to layer 8's wire. The leads of the cable wire and get some solder on the bottom of the LEDs and one-by-one connect each of the 8 rows of LEDs to a connector. There are all together nine connectors, eight for LED anode connections and one for each horizontal layer's cathode of the LEDs. Since the cabling done connected all the cables to the drive board and give the system a test run. The output digital pin 1 is connected to speaker for melody sound. The circuit connection of audio system is shown in Figure (2) and the circuit diagram of 8-column connection in 8×8×8 LED cube is shown in Figure (3). After finishing verifying, the hex code of the sketch is appeared at the bottom window as shown in Figure (5). The photograph of the music reactive LED cube by Arduino Microcontroller is shown in Figure (6).

Power Supply Circuit

The power supply uses the locally available 3-terminal voltage regulator IC LM 7805. The booster transistor MJ 2955 can handle a maximum current of about 15 A but limited to about 2.0 A. During normal operation a current of about 25 mA flows through the IC, the rest current will flow through the booster transistor. The circuit diagram of power supply is shown in Figure (4).

Conclusion

The music reactive LED cube is successfully constructed. The constructed system contains 512 LEDs and each LED current limits is 25 mA. To operate this music reactive LED cube, 2 A current limit power supply is required. This power supply system is also constructed by the use of the regulator LM7805 IC and pnp power transistor MJ 2955. The LED cube is constructed by 8-row (layers) and 8-column. Various patterns of displays are produced by controlling the column and layer selection. To do this work, 74HC595 ICs are used as layer and column selectors. The various pattern designs together with melody sound are also produced by C programming source codes and this source codes are uploaded and then the system start to run. The display pattern can be 3-D graphics LED display, various fantastic pattern of blinking LEDs, light decoration and sound based on the Arduino source codes. This circuit of this work is very useful for altar decoration, home decoration, advertising and toys, etc.

Acknowledgement

The authors would like to acknowledge Professor DrKhinKhin Win, Head of Department of Physics, University of Yangon for her kind permission to carry out this work. The authors also would like to thank Professor DrHlaHlaThan (HOD) and Professor DrHla Win, Department of Physics, Meiktila University, for their kind permission to carry out this work.

References

Brain, M., Evans. (2007). “Arduino Programming Notebook”. California: USA. Retrived December 16, 2016, from https://www.apress.com/us/book

Chria. (2012). “Building the 8×8×8 LED Cube Template”. Retrived October 12,2016, fromhttps://www.pyroelectro.com/projects/8×8×8_led_cuve/parts.html

Githyp.com/ Anopmm/LED-CUBE. 8×8×8https://electronics.stackexchange.com/questions/20697/code-for-ripple-effect-of-an-8×8×8-led cube arduino

Jolli, C. (November 16, 2010). “Led Cube 8×8×8”._Retrived December 17, 2016, from https://www.instructables.com / id/LED Cube_8×8×8

Muhammad Faris, B. A. (January, 2015). “Hardware Design and Construction:Controlling the LED Cube Patterns with Arduino Input Signal”.University TEKNOLOGI Malaysia.Retrived October 18,2016, from www.led-cube pattern/parts.html

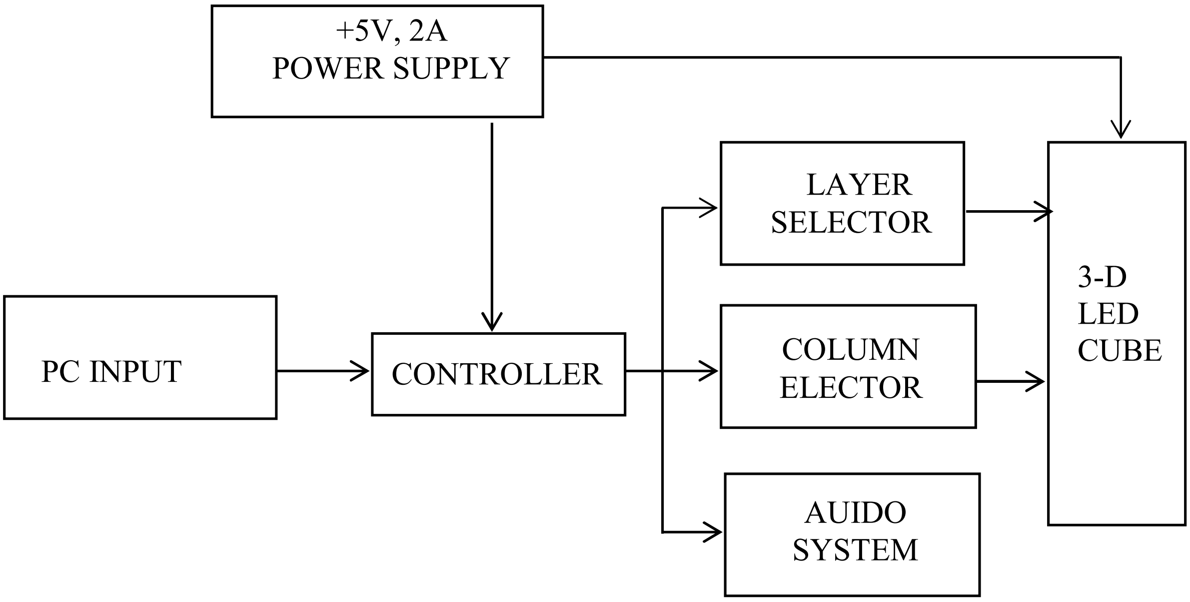

Figure 1 Block Diagram of Music Reactive LED Cube Control System

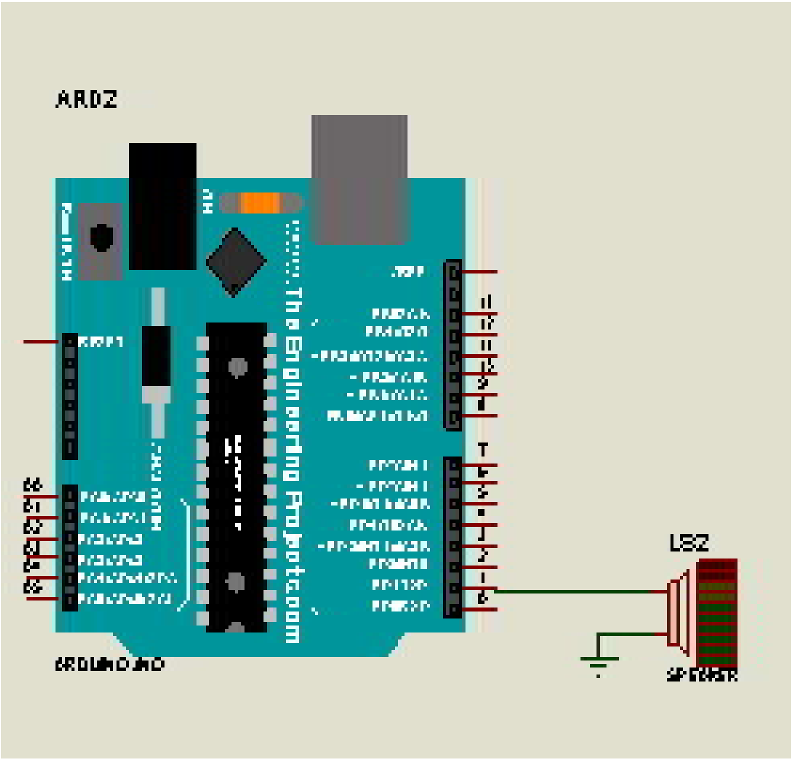

Figure 2 Circuit Diagram of Audio System

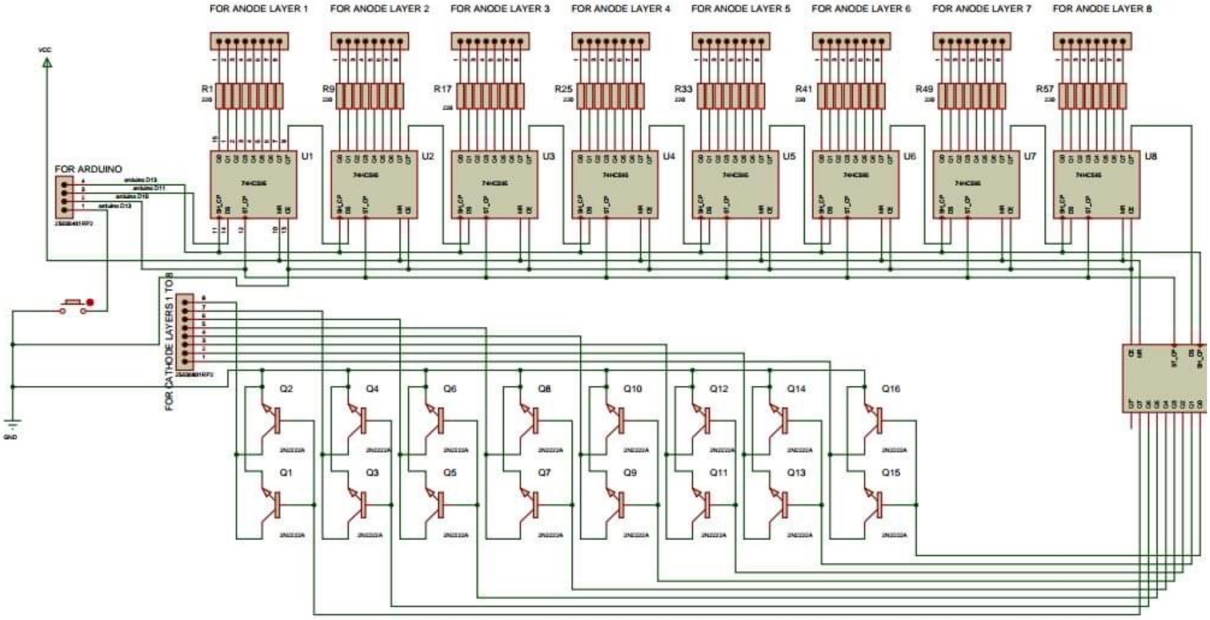

Figure 3 The circuit diagram of 8-column connection in 8×8×8 LED cube

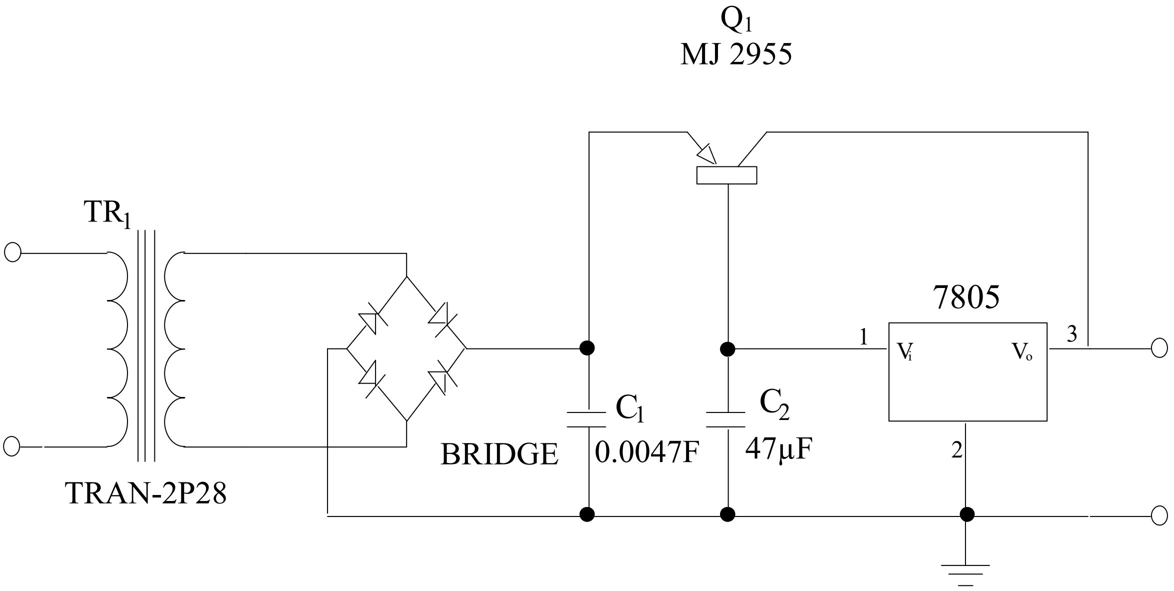

Figure 4 The circuit diagram of power supply

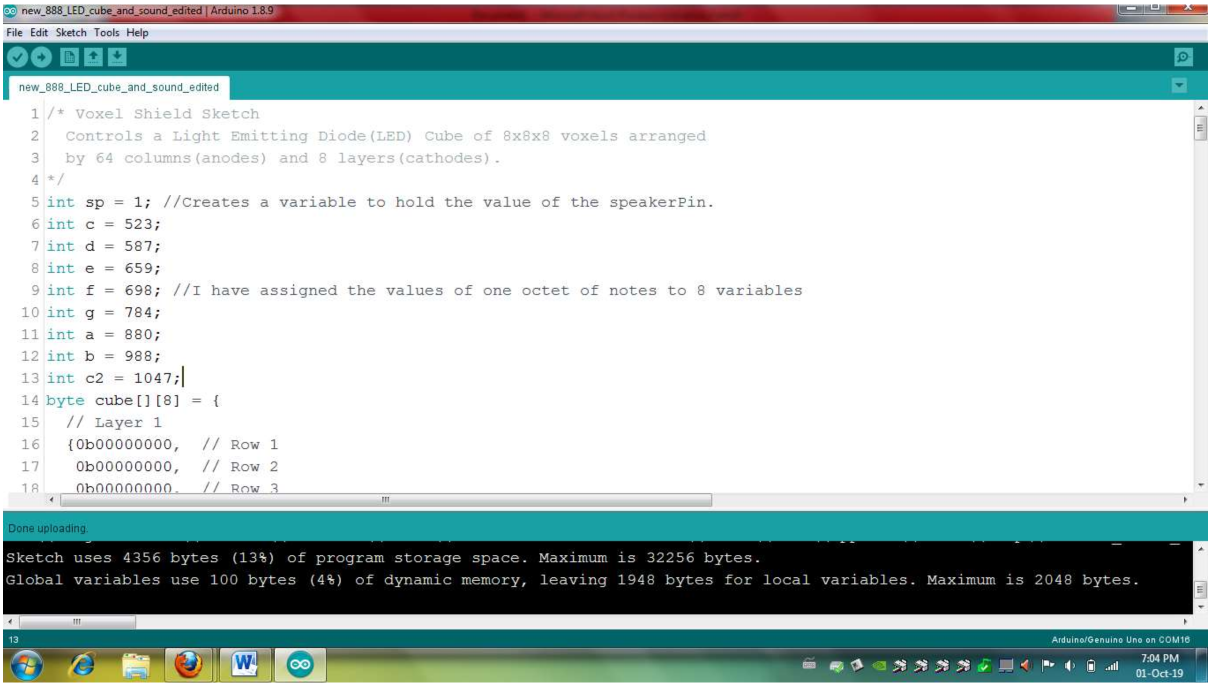

```
/* Voxel Shield Sketch
  Controls a Light Emitting Diode(LED) Cube of 8x8x8 voxels arranged
  by 64 columns(anodes) and 8 layers(cathodes).
*/
int sp = 1; //Creates a variable to hold the value of the speakerPin.
int c = 523;
int d = 587;
int e = 659;
int f = 698; //I have assigned the values of one octet of notes to 8 variables
int g = 784;
int a = 880;
int b = 988;
int c2 = 1047;
byte cube[][8] = {
  // Layer 1
  {0b00000000,  // Row 1
   0b00000000,  // Row 2
   0b00000000,  // Row 3
```

Done uploading.

```
Sketch uses 4356 bytes (13%) of program storage space. Maximum is 32256 bytes.
Global variables use 100 bytes (4%) of dynamic memory, leaving 1948 bytes for local variables. Maximum is 2048 bytes.
```

Figure 5 The photograph of the error free Arduino sketch showing .hex file after successfully verifying case

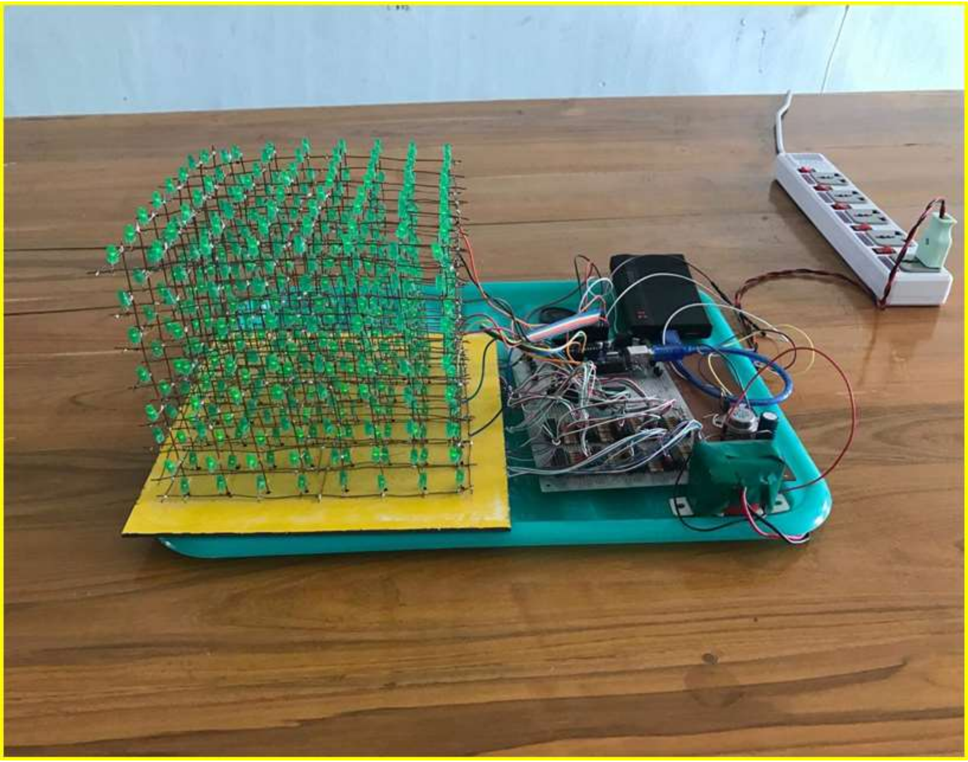

Figure 6 The photograph of the music reactive LED cube by Arduino Microcontroller

APPENDIX

Program Listing

```
/* Design and construction and music reactive LED cube*/
/* Voxel Shield Sketch
  Controls a Light Emitting Diode(LED) Cube of 8x8x8 voxels arranged
by 64 columns(anodes) and 8 layers(cathodes).
*/
intsp = 1; //Creates a variable to hold the value of the speakerPin.
int c = 523;
int d = 587;
int e = 659;
int f = 698; //I have assigned the values of one octet of notes to 8 variables
int g = 784;
int a = 880;
int b = 988;
int c2 = 1047;
byte cube[][8] = {
  // Layer 1
  {0b00000000,  // Row 1
   0b00000000,  // Row 2
   0b00000000,  // Row 3
   0b00000000,  // Row 4
   0b00000000,  // Row 5
   0b00000000,  // Row 6
   0b00000000,  // Row 7
   0b00000000}, // Row 8
  // Layer 2
  {0b00000000,  // Row 1
   0b00000000,  // Etc ...
   0b00000000,
   0b00000000,
   0b00000000,
   0b00000000,
   0b00000000,
   0b00000000},
  // Layer 3
  {0b00000000,
   0b00000000,
   0b00000000,
   0b00000000,
   0b00000000,
   0b00000000,
   0b00000000,
   0b00000000},
  // Layer 4
  {0b00000000,
   0b00000000,
   0b00000000,
   0b00000000,
   0b00000000,
   0b00000000,
   0b00000000,
   0b00000000},
  // Layer 5
  {0b00000000,
   0b00000000,
   0b00000000,
   0b00000000,
   0b00000000,
```

```
   0b00000000,
   0b00000000,
   0b00000000},
  // Layer 6
  {0b00000000,
   0b00000000,
   0b00000000,
   0b00000000,
   0b00000000,
   0b00000000,
   0b00000000,
   0b00000000},
  // Layer 7
  {0b00000000,
   0b00000000,
   0b00000000,
   0b00000000,
   0b00000000,
   0b00000000,
   0b00000000,
   0b00000000},
  // Layer 8
  {0b00000000,
   0b00000000,
   0b00000000,
   0b00000000,
   0b00000000,
   0b00000000,
   0b00000000,
   0b00000000}
};
// Shift Register pin assignments
intdataPin    = 11;
intclockPin   = 13;
intlatchPin   = 10;
intmasterClear = 4;
// Cube indicies
introwIndex   = 0;        // used for shifting out the data
intlayerIndex = 0;
void all(){
  cube[0][0] = 255; cube[1][0] = 255; cube[2][0] = 255; cube[3][0] = 255; cube[4][0] = 255; cube[5][0] = 255;
cube[6][0] = 255; cube[7][0] = 255;
  cube[0][1] = 255; cube[1][1] = 255; cube[2][1] = 255; cube[3][1] = 255; cube[4][1] = 255; cube[5][1] = 255;
cube[6][1] = 255; cube[7][1] = 255;
  cube[0][2] = 255; cube[1][2] = 255; cube[2][2] = 255; cube[3][2] = 255; cube[4][2] = 255; cube[5][2] = 255;
cube[6][2] = 255; cube[7][2] = 255;
  cube[0][3] = 255; cube[1][3] = 255; cube[2][3] = 255; cube[3][3] = 255; cube[4][3] = 255; cube[5][3] = 255;
cube[6][3] = 255; cube[7][3] = 255;
  cube[0][4] = 255; cube[1][4] = 255; cube[2][4] = 255; cube[3][4] = 255; cube[4][4] = 255; cube[5][4] = 255;
cube[6][4] = 255; cube[7][4] = 255;
  cube[0][5] = 255; cube[1][5] = 255; cube[2][5] = 255; cube[3][5] = 255; cube[4][5] = 255; cube[5][5] = 255;
cube[6][5] = 255; cube[7][5] = 255;
  cube[0][6] = 255; cube[1][6] = 255; cube[2][6] = 255; cube[3][6] = 255; cube[4][6] = 255; cube[5][6] = 255;
cube[6][6] = 255; cube[7][6] = 255;
  cube[0][7] = 255; cube[1][7] = 255; cube[2][7] = 255; cube[3][7] = 255; cube[4][7] = 255; cube[5][7] = 255;
cube[6][7] = 255; cube[7][7] = 255;
}
void none(){
  cube[0][0] = 0; cube[1][0] = 0; cube[2][0] = 0; cube[3][0] = 0; cube[4][0] = 0; cube[5][0] = 0; cube[6][0] = 0;
cube[7][0] = 0;
```

```
  cube[0][1] = 0; cube[1][1] = 0; cube[2][1] = 0; cube[3][1] = 0; cube[4][1] = 0; cube[5][1] = 0; cube[6][1] = 0;
cube[7][1] = 0;
  cube[0][2] = 0; cube[1][2] = 0; cube[2][2] = 0; cube[3][2] = 0; cube[4][2] = 0; cube[5][2] = 0; cube[6][2] = 0;
cube[7][2] = 0;
  cube[0][3] = 0; cube[1][3] = 0; cube[2][3] = 0; cube[3][3] = 0; cube[4][3] = 0; cube[5][3] = 0; cube[6][3] = 0;
cube[7][3] = 0;
  cube[0][4] = 0; cube[1][4] = 0; cube[2][4] = 0; cube[3][4] = 0; cube[4][4] = 0; cube[5][4] = 0; cube[6][4] = 0;
cube[7][4] = 0;
  cube[0][5] = 0; cube[1][5] = 0; cube[2][5] = 0; cube[3][5] = 0; cube[4][5] = 0; cube[5][5] = 0; cube[6][5] = 0;
cube[7][5] = 0;
  cube[0][6] = 0; cube[1][6] = 0; cube[2][6] = 0; cube[3][6] = 0; cube[4][6] = 0; cube[5][6] = 0; cube[6][6] = 0;
cube[7][6] = 0;
  cube[0][7] = 0; cube[1][7] = 0; cube[2][7] = 0; cube[3][7] = 0; cube[4][7] = 0; cube[5][7] = 0; cube[6][7] = 0;
cube[7][7] = 0;
}
void box(){
  cube[0][0] = 0b11111111; cube[1][0] = 0b10000001; cube[2][0] = 0b10000001; cube[3][0] = 0b10000001;
cube[4][0] = 0b10000001; cube[5][0] = 0b10000001; cube[6][0] = 0b10000001; cube[7][0] = 0b11111111;
  cube[0][1] = 0b10000001; cube[1][1] = 0b00000000; cube[2][1] = 0b00000000; cube[3][1] = 0b00000000;
cube[4][1] = 0b00000000; cube[5][1] = 0b00000000; cube[6][1] = 0b00000000; cube[7][1] = 0b10000001;
  cube[0][2] = 0b10000001; cube[1][2] = 0b00000000; cube[2][2] = 0b00000000; cube[3][2] = 0b00000000;
cube[4][2] = 0b00000000; cube[5][2] = 0b00000000; cube[6][2] = 0b00000000; cube[7][2] = 0b10000001;
  cube[0][3] = 0b10000001; cube[1][3] = 0b00000000; cube[2][3] = 0b00000000; cube[3][3] = 0b00000000;
cube[4][3] = 0b00000000; cube[5][3] = 0b00000000; cube[6][3] = 0b00000000; cube[7][3] = 0b10000001;
  cube[0][4] = 0b10000001; cube[1][4] = 0b00000000; cube[2][4] = 0b00000000; cube[3][4] = 0b00000000;
cube[4][4] = 0b00000000; cube[5][4] = 0b00000000; cube[6][4] = 0b00000000; cube[7][4] = 0b10000001;
  cube[0][5] = 0b10000001; cube[1][5] = 0b00000000; cube[2][5] = 0b00000000; cube[3][5] = 0b00000000;
cube[4][5] = 0b00000000; cube[5][5] = 0b00000000; cube[6][5] = 0b00000000; cube[7][5] = 0b10000001;
  cube[0][6] = 0b10000001; cube[1][6] = 0b00000000; cube[2][6] = 0b00000000; cube[3][6] = 0b00000000;
cube[4][6] = 0b00000000; cube[5][6] = 0b00000000; cube[6][6] = 0b00000000; cube[7][6] = 0b10000001;
  cube[0][7] = 0b11111111; cube[1][7] = 0b10000001; cube[2][7] = 0b10000001; cube[3][7] = 0b10000001;
cube[4][7] = 0b10000001; cube[5][7] = 0b10000001; cube[6][7] = 0b10000001; cube[7][7] = 0b11111111;
}
void box2(){
  cube[0][0] = 0b00000000; cube[1][0] = 0b00000000; cube[2][0] = 0b00000000; cube[3][0] = 0b00000000;
cube[4][0] = 0b00000000; cube[5][0] = 0b00000000; cube[6][0] = 0b00000000; cube[7][0] = 0b00000000;
  cube[0][1] = 0b00000000; cube[1][1] = 0b01111110; cube[2][1] = 0b01000010; cube[3][1] = 0b01000010;
cube[4][1] = 0b01000010; cube[5][1] = 0b01000010; cube[6][1] = 0b01111110; cube[7][1] = 0b00000000;
  cube[0][2] = 0b00000000; cube[1][2] = 0b01000010; cube[2][2] = 0b00000000; cube[3][2] = 0b00000000;
cube[4][2] = 0b00000000; cube[5][2] = 0b00000000; cube[6][2] = 0b01000010; cube[7][2] = 0b00000000;
  cube[0][3] = 0b00000000; cube[1][3] = 0b01000010; cube[2][3] = 0b00000000; cube[3][3] = 0b00000000;
cube[4][3] = 0b00000000; cube[5][3] = 0b00000000; cube[6][3] = 0b01000010; cube[7][3] = 0b00000000;
  cube[0][4] = 0b00000000; cube[1][4] = 0b01000010; cube[2][4] = 0b00000000; cube[3][4] = 0b00000000;
cube[4][4] = 0b00000000; cube[5][4] = 0b00000000; cube[6][4] = 0b01000010; cube[7][4] = 0b00000000;
  cube[0][5] = 0b00000000; cube[1][5] = 0b01000010; cube[2][5] = 0b00000000; cube[3][5] = 0b00000000;
cube[4][5] = 0b00000000; cube[5][5] = 0b00000000; cube[6][5] = 0b01000010; cube[7][5] = 0b00000000;
  cube[0][6] = 0b00000000; cube[1][6] = 0b01111110; cube[2][6] = 0b01000010; cube[3][6] = 0b01000010;
cube[4][6] = 0b01000010; cube[5][6] = 0b01000010; cube[6][6] = 0b01111110; cube[7][6] = 0b00000000;
  cube[0][7] = 0b00000000; cube[1][7] = 0b00000000; cube[2][7] = 0b00000000; cube[3][7] = 0b00000000;
cube[4][7] = 0b00000000; cube[5][7] = 0b00000000; cube[6][7] = 0b00000000; cube[7][7] = 0b00000000;
}
void box3(){
  cube[0][0] = 0b00000000; cube[1][0] = 0b00000000; cube[2][0] = 0b00000000; cube[3][0] = 0b00000000;
cube[4][0] = 0b00000000; cube[5][0] = 0b00000000; cube[6][0] = 0b00000000; cube[7][0] = 0b00000000;
  cube[0][1] = 0b00000000; cube[1][1] = 0b00000000; cube[2][1] = 0b00000000; cube[3][1] = 0b00000000;
cube[4][1] = 0b00000000; cube[5][1] = 0b00000000; cube[6][1] = 0b00000000; cube[7][1] = 0b00000000;
  cube[0][2] = 0b00000000; cube[1][2] = 0b00000000; cube[2][2] = 0b00111100; cube[3][2] = 0b00100100;
cube[4][2] = 0b00100100; cube[5][2] = 0b00111100; cube[6][2] = 0b00000000; cube[7][2] = 0b00000000;
  cube[0][3] = 0b00000000; cube[1][3] = 0b00000000; cube[2][3] = 0b00100100; cube[3][3] = 0b00000000;
cube[4][3] = 0b00000000; cube[5][3] = 0b00100100; cube[6][3] = 0b00000000; cube[7][3] = 0b00000000;
```

```
  cube[0][4] = 0b00000000; cube[1][4] = 0b00000000; cube[2][4] = 0b00100100; cube[3][4] = 0b00000000;
cube[4][4] = 0b00000000; cube[5][4] = 0b00100100; cube[6][4] = 0b00000000; cube[7][4] = 0b00000000;
  cube[0][5] = 0b00000000; cube[1][5] = 0b00000000; cube[2][5] = 0b00111100; cube[3][5] = 0b00100100;
cube[4][5] = 0b00100100; cube[5][5] = 0b00111100; cube[6][5] = 0b00000000; cube[7][5] = 0b00000000;
  cube[0][6] = 0b00000000; cube[1][6] = 0b00000000; cube[2][6] = 0b00000000; cube[3][6] = 0b00000000;
cube[4][6] = 0b00000000; cube[5][6] = 0b00000000; cube[6][6] = 0b00000000; cube[7][6] = 0b00000000;
  cube[0][7] = 0b00000000; cube[1][7] = 0b00000000; cube[2][7] = 0b00000000; cube[3][7] = 0b00000000;
cube[4][7] = 0b00000000; cube[5][7] = 0b00000000; cube[6][7] = 0b00000000; cube[7][7] = 0b00000000;
}
void box4(){
  cube[0][0] = 0b00000000; cube[1][0] = 0b00000000; cube[2][0] = 0b00000000; cube[3][0] = 0b00000000;
cube[4][0] = 0b00000000; cube[5][0] = 0b00000000; cube[6][0] = 0b00000000; cube[7][0] = 0b00000000;
  cube[0][1] = 0b00000000; cube[1][1] = 0b00000000; cube[2][1] = 0b00000000; cube[3][1] = 0b00000000;
cube[4][1] = 0b00000000; cube[5][1] = 0b00000000; cube[6][1] = 0b00000000; cube[7][1] = 0b00000000;
  cube[0][2] = 0b00000000; cube[1][2] = 0b00000000; cube[2][2] = 0b00000000; cube[3][2] = 0b00000000;
cube[4][2] = 0b00000000; cube[5][2] = 0b00000000; cube[6][2] = 0b00000000; cube[7][2] = 0b00000000;
  cube[0][3] = 0b00000000; cube[1][3] = 0b00000000; cube[2][3] = 0b00000000; cube[3][3] = 0b00011000;
cube[4][3] = 0b00011000; cube[5][3] = 0b00000000; cube[6][3] = 0b00000000; cube[7][3] = 0b00000000;
  cube[0][4] = 0b00000000; cube[1][4] = 0b00000000; cube[2][4] = 0b00000000; cube[3][4] = 0b00011000;
cube[4][4] = 0b00011000; cube[5][4] = 0b00000000; cube[6][4] = 0b00000000; cube[7][4] = 0b00000000;
  cube[0][5] = 0b00000000; cube[1][5] = 0b00000000; cube[2][5] = 0b00000000; cube[3][5] = 0b00000000;
cube[4][5] = 0b00000000; cube[5][5] = 0b00000000; cube[6][5] = 0b00000000; cube[7][5] = 0b00000000;
  cube[0][6] = 0b00000000; cube[1][6] = 0b00000000; cube[2][6] = 0b00000000; cube[3][6] = 0b00000000;
cube[4][6] = 0b00000000; cube[5][6] = 0b00000000; cube[6][6] = 0b00000000; cube[7][6] = 0b00000000;
  cube[0][7] = 0b00000000; cube[1][7] = 0b00000000; cube[2][7] = 0b00000000; cube[3][7] = 0b00000000;
cube[4][7] = 0b00000000; cube[5][7] = 0b00000000; cube[6][7] = 0b00000000; cube[7][7] = 0b00000000;
}
void draw(){
  // Repeat p many times before moving on to next frame
  // change what p is less than; more for slower annimation, less for faster
for(int p = 0; p < 10; p++){
   // Reset to first layer
layerIndex = 0;
for(int q = 0; q < 8; q++){
     // Reset to row 1
rowIndex = 0;
     // Make shift registers accept new data
digitalWrite(latchPin, LOW);
     // Shift out the layer data first
shiftOut(dataPin,clockPin,MSBFIRST,0b00000001<<layerIndex);
for(int t = 0; t < 8; t++){
       // Shift out the rows of data
shiftOut(dataPin,clockPin,MSBFIRST,cube[layerIndex][rowIndex]);
       // Move onto the next row then repeat
sound();
rowIndex++;
     }
     // Move onto the next layer and repeat
layerIndex++;
digitalWrite(latchPin, HIGH);
   }
  }
}
void setup()
{
pinMode(sp,OUTPUT); // This code runs only once. It assigns pin 1as output, and this is where we'll connect out
speaker.
randomSeed(analogRead(A0)); //This creates a random 'seed'. An initial point for the randomization to start.
//The value of this seed is from Analog input 0, which is empty. Hence it generates a random noise value.
  // Setup the pin modes
```

```
pinMode(dataPin,     OUTPUT);
pinMode(clockPin,    OUTPUT);
pinMode(latchPin,    OUTPUT);
pinMode(masterClear, OUTPUT);
  // Clear the shift registers
digitalWrite(masterClear, LOW);
delay(10);
digitalWrite(masterClear, HIGH);
}
void sound()
{
int notes[] = {c,d,e,g,a,c2,random(33,102),random(200,4978)}; //Creates an array of all notes used; A sort of dictionary which is indexed by numbers 0 to 7
  //I added 2 random notes here to add some spice to the tonality. The notes I chose belong to a pentatonic scale.
inti = random(0,8); //Generates a random value between 0 & 8, the maximum and minimum indexes of the notes
delay(70); //Creates a delay of 150 ms between each note, so it can be heard distinctly.
tone (sp,notes[i],80); //And finally, the tone function generates a tone sent to pin 'sp',of a random frequency from index i.
//The length of each note chosen is 80.
}
void loop()
{ //This is the main code, and it runs repeatedly.
  //Expanding Box Animation
  // Repeat 10 times
for(int k = 0;k < 10;k++){
box();
draw();
box2();
draw();
box3();
draw();
box4();
draw();
box3();
draw();
box2();
draw();
  }
}
```

J. Myanmar Acad. Arts Sci. 2020 **Vol. XVIII.No.2A**

STUDY ON TEMPERATURE DEPENDENCE SUPERIONIC CONDUCTIVITY OF SOLID ELECTROLYTE LITHIUM-COBALT-NICKEL OXIDES

Nyo Nyo Myint[1], Aye Aye Lwin[2], Win Kyaw[3] and Soe Myint[4]

Abstract

Superionic conductors or solid electrolyte materials are mainly useful in batteries and various sensors. In the present work, Lithium-Cobalt-Nickel Oxide, $LiCo_{1-x}Ni_xO_2$, (where $x = 0.00 – 1.00$ with the step of 0.25) were prepared by solid state reaction method. Lithium Hydroxide Monohydrate ($LiOH.H_2O$), Cobalt Oxide (CoO) and Nickel Oxide (NiO) with desired stoichiometric compositions were used as the starting materials. X-ray diffraction (XRD) patterns indicated that the samples belong to hexagonal structure from the observed diffractograms were compared with the JCPDS data. To confirm the phase formation of the samples, Fourier Transform Infrared (FTIR) spectroscopic method was used to analyze the vibrational characteristics. Temperature dependence electrical conductivities of the samples were investigated in the temperature range of 303 K – 773 K. It was found that the samples exhibited as the superionic conductors in the high temperature.

Keywords: $LiCo_{1-x}Ni_xO_2$, XRD, hexagonal, FTIR, superionic conductors.

Introduction

Solid-State Ionics, thrust area of research in the branch of Materials Science, deals mainly with the solid materials which exhibit rapid/fast ion transport through the bulk [Arico, (2005)]. The ionic conductivity of these solids is exceptionally high and comparable to that of liquid/aqueous electrolytes [Azurdia, (2006)]. Hence, they can be potentially used as excellent alternates of liquid/aqueous electrolytes to fabricate solid-state electrochemical devices viz. batteries [Julian, (2003)]. Research in the field of fine grain mixed oxide systems has gained immense importance because of their potential applications in many areas of technology [Kumar, (2009)].

In materials science, fast ion conductors are solids in which ions are highly mobile. These materials are important in the area of solid-state ionics, and are also known as solid electrolytes and superionic conductors. These materials are mainly useful in batteries and various sensors [Fey, (2002)]. Fast ion conductors are used primarily in solid oxide fuel cells. As solid electrolytes they allow the movement of ions without the need for a liquid or soft membrane separating the electrodes. The phenomenon relies on the hopping of ions through an otherwise rigid structure [Fey, (2003)].

Lithium transition-metal oxides are functional intercalation compounds for their applications in rechargeable lithium-ion batteries [Wang, (2010)]. They have been widely studied in search of structural stability and improved electrochemical performance [Tao, (2011)]. This work deals with the Lithium-Cobalt-Nickel Oxides, $LiCo_{1-x}Ni_xO_2$ prepared by solid state reaction method and their structural, vibrational and temperature dependence superionic conductivity are reported.

---

[1] Dr, Associate Professor, Department of Physics, Yenanchaung Degree College

[2] Dr, Associate Professor, Department of Physics, Loikaw University

[3] Dr, Associate Professor, Department of Physics, Pyay University

[4] Dr, Professor and Head, Department of Physics, Yenanchaung Degree College

Materials and Method

Preparation of the Sample

Lithium-Cobalt-Nickel Oxide, $LiCo_{1-x}Ni_xO_2$, (where x = 0.00, 0.25, 0.50, 0.75 and 1.00) were prepared by using the starting materials of Analytical Reagent (AR) grade $LiOH.H_2O$, Co_3O_4 and NiO. Flow diagram of the sample preparation procedure is shown in Figure 1.

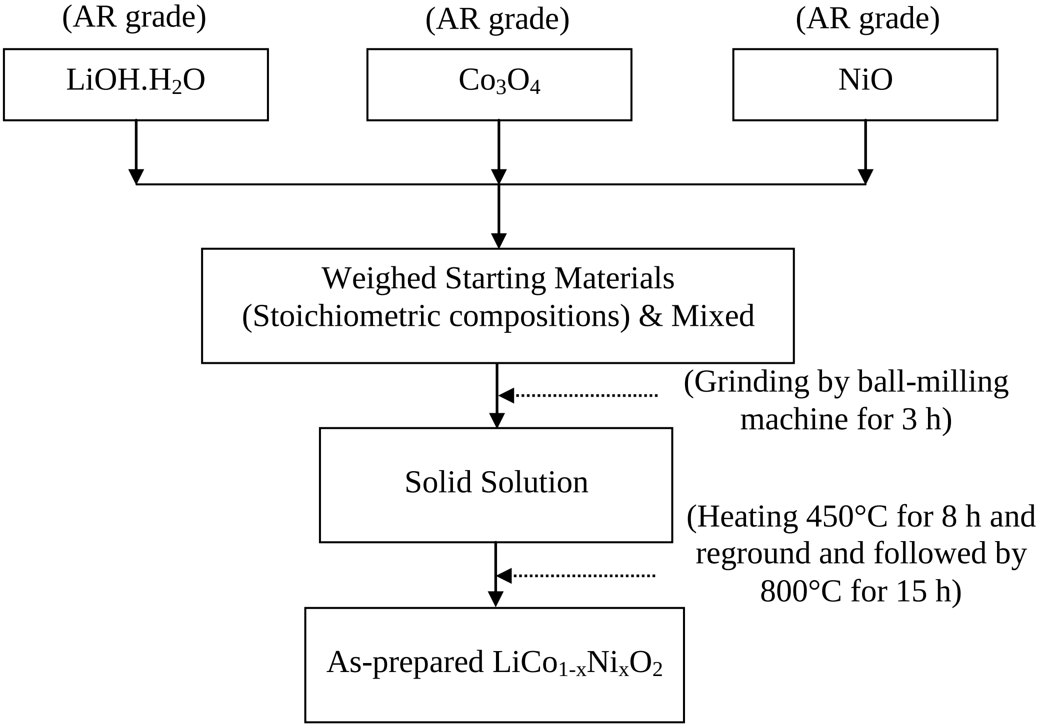

Figure 1 Flow diagram of the sample preparation procedure of $LiCo_{1-x}Ni_xO_2$

XRD, FTIR and Temperature Dependent Electrical Resistance Measurements

X-ray diffraction (XRD) analysis of the powder samples was performed to investigate the crystal structure, lattice parameters and crystallite sizes. The XRD patterns were observed by RIGAKU MULTIFLEX X-ray Diffractometer using CuK_α (λ = 1.54056 Å) radiation in the diffraction angle range of 10º - 70º [Universities′ Research Centre (URC), University of Yangon].

Vibrational frequencies of a molecule can be probed by using infrared and Raman spectroscopy. Infrared (IR) spectroscopy is an important relatively inexpensive and efficient analytical method for characterizing materials. FTIR transmission spectra of the samples were observed by PC-controlled SHIMADZU FTIR-8400 Spectrophotometer using Potassium Bromide, KBr pellet at room temperature.

For the temperature dependent electrical resistance measurement, the samples were made into pellets by SPECAC hydraulic press using 5 ton (~70 MPa). The area and thickness of the pellets were 1.14×10^{-4} m^2 and 4.77 mm respectively. The electrical resistances of the samples were observed by using FLUKE 189 digital multi-meter in the temperature range of 303 K – 773 K by the use of Autonics TCN4L – 24R Temperature Controller.

Results and Discussion

Structure Analysis

XRD patterns of the samples are shown in Figure 2. The observed XRD lines were identified by using standard JCPDS data library files of (i) Cat. No. 50-0653>$LiCoO_2$ – Lithium Cobalt Oxide for x = 0.00 sample, (ii) Cat. No. 50-0653>$LiCoO_2$ – Lithium Cobalt Oxide and Cat. No. 89-3601 > Lithium Nickel Oxide for x = 0.25, 0.50 and 0.75 samples and (iii) Cat. No. 88-1605>$Li_{068}Ni_{1.32}O_2$ – Lithium Nickel Oxide and Cat. No. 89-3601 > Lithium Nickel Oxide for x = 1.00 sample. XRD patterns show the formation of single phase hexagonal structure with dominant peak corresponding to (003) reflection in x = 0.00 – 0.75 samples and (104) reflection in x = 1.00 sample indicating that the crystallites are preferentially oriented along these planes. The lattice parameters are evaluated by using the equation, $\frac{1}{d^2} = \frac{4}{3}\left(\frac{h^2 + hk + k^2}{a^2}\right) + \frac{l^2}{c^2}$, where d is interplanar spacing (Å), a, c are the lattice parameters and (hkl) is the Miller indices. The lattice parameters ($a = b$ and c) of the $LiCoO_2$ sample were found to be increased with increase in Ni concentration due to the lattice substitution of Ni on Co. Tao, et. al. (2011) has reported that the lattice parameters of the $LiCo_{0.25}Ni_{0.75}O_2$ sample are $a = b = 2.90$ Å and $c = 14.29$ Å respectively. Thus, the obtained lattice parameters in the present study are found to be agreed with the results of Tao, et. al. (2011). The crystallite sizes of the samples are estimated by using the Scherrer formula, $D = \frac{0.9\lambda}{B\cos\theta}$, where D is the crystallite size (nm), λ is the wavelength of incident X-ray (Å), θ is the diffraction angle of the peak under consideration at FWHM (°) and B is the observed FWHM (radians). To examine the nanosized $LiCo_{1-x}Ni_xO_2$ materials, the FWHM of the observed peaks of the XRD patterns were used to calculate the average crystallite sizes. The lattice parameters and the crystallite sizes are also presented in Table 1. The obtained crystallite sizes decreased with increase in Ni concentration and as shown in Figure 3.

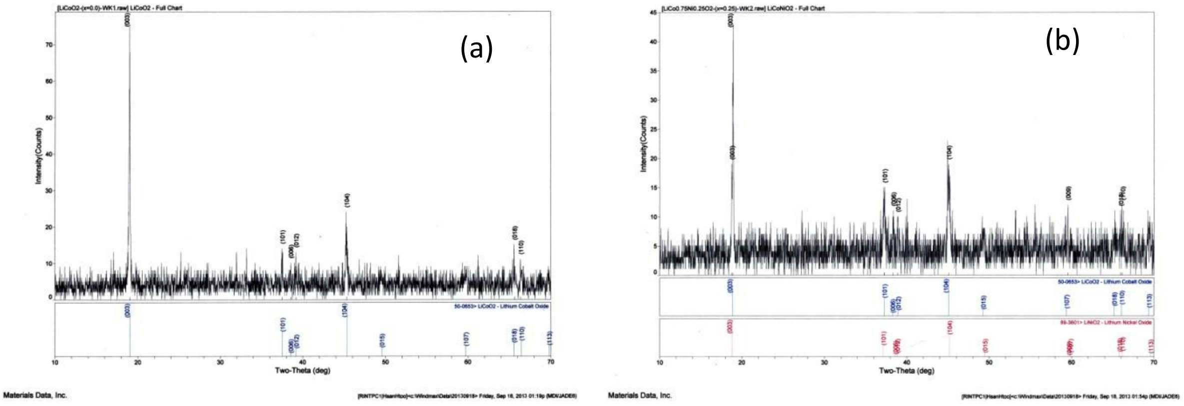

Figure 2 XRD patterns of $LiCo_{1-x}Ni_xO_2$ where (a) x = 0.00, (b) x = 0.25

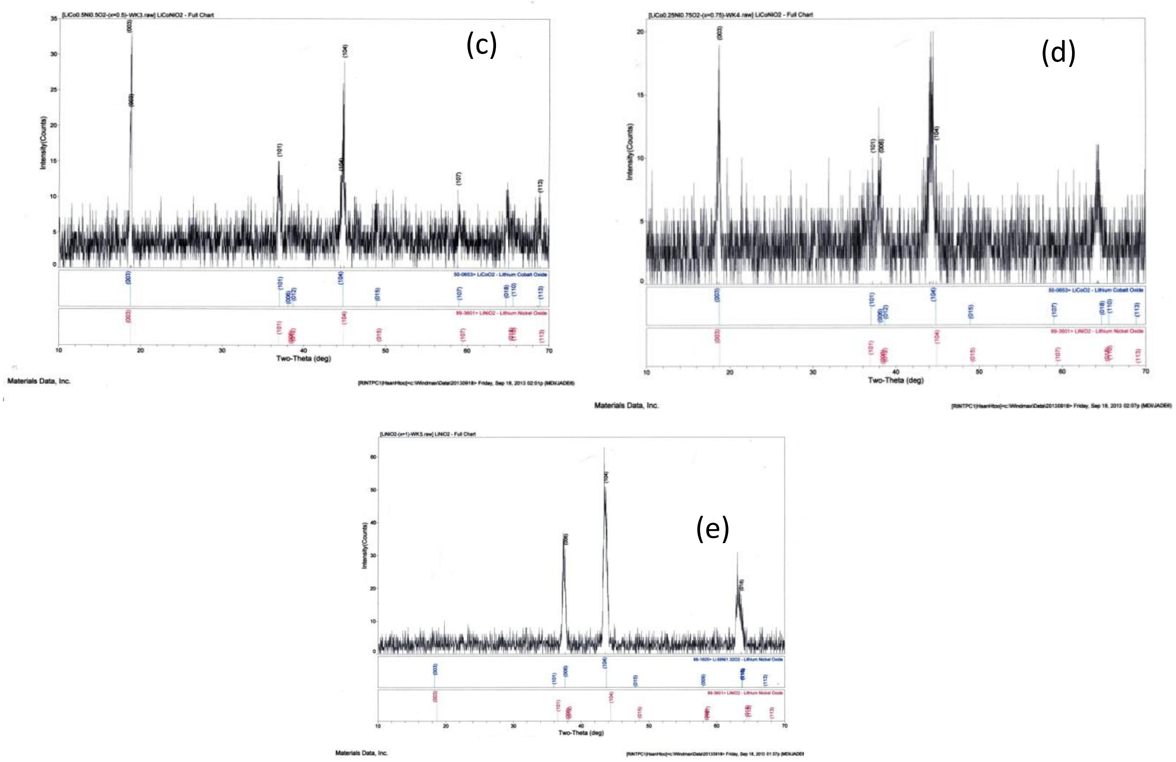

Figure 2 XRD patterns of $LiCo_{1-x}Ni_xO_2$ where (c) x = 0.50, (d) x = 0.75 and (e) x = 1.00

Table 1 The lattice parameters and crystallite sizes of $LiCo_{1-x}Ni_xO_2$

Sample (Contents x of Ni)	Obs. *a*=*b*, *c* (Å)	Cal. *a*=*b*, *c* (Å)	*D* (nm)
0.00	$a=b=2.82$ $c=13.96$	$a=b=2.62$ $c=14.09$	82.72
0.25	$a=b=2.82$ $c=14.07$	$a=b=2.77$ $c=14.17$	65.86
0.50	$a=b=2.85$ $c=14.19$	$a=b=2.72$ $c=14.21$	45.81
0.75	$a=b=2.87$ $c=14.30$	$a=b=2.87$ $c=14.30$	32.85
1.00	$a=b=2.94$ $c=14.41$	$a=b=2.94$ $c=14.43$	21.26

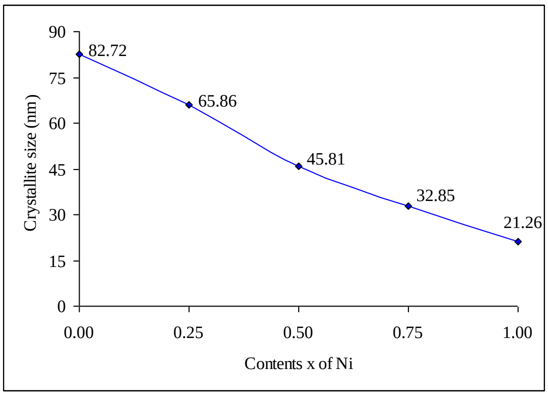

Figure 3 Variation of crystallite size with increase in Ni concentration of $LiCo_{1-x}Ni_xO_2$

Vibrational Analysis

According to the molecular vibrational theory, a diatomic molecule has two types of normal vibrations: (1) transverse-optical and (2) longitudinal-optical vibrations and also a non-linear tri-atomic molecule, has three types of vibrations: (1) ν_1-mode (symmetric-stretching), (2) ν_2-mode (bending) and (3) ν_3-mode (asymmetric-stretching) respectively [Ross, (1972)]. FTIR transmission spectra of the samples are shown in Figure 4. Vibrational characteristics and mode assignments of constituent molecules of the samples are tabulated in Table 2.

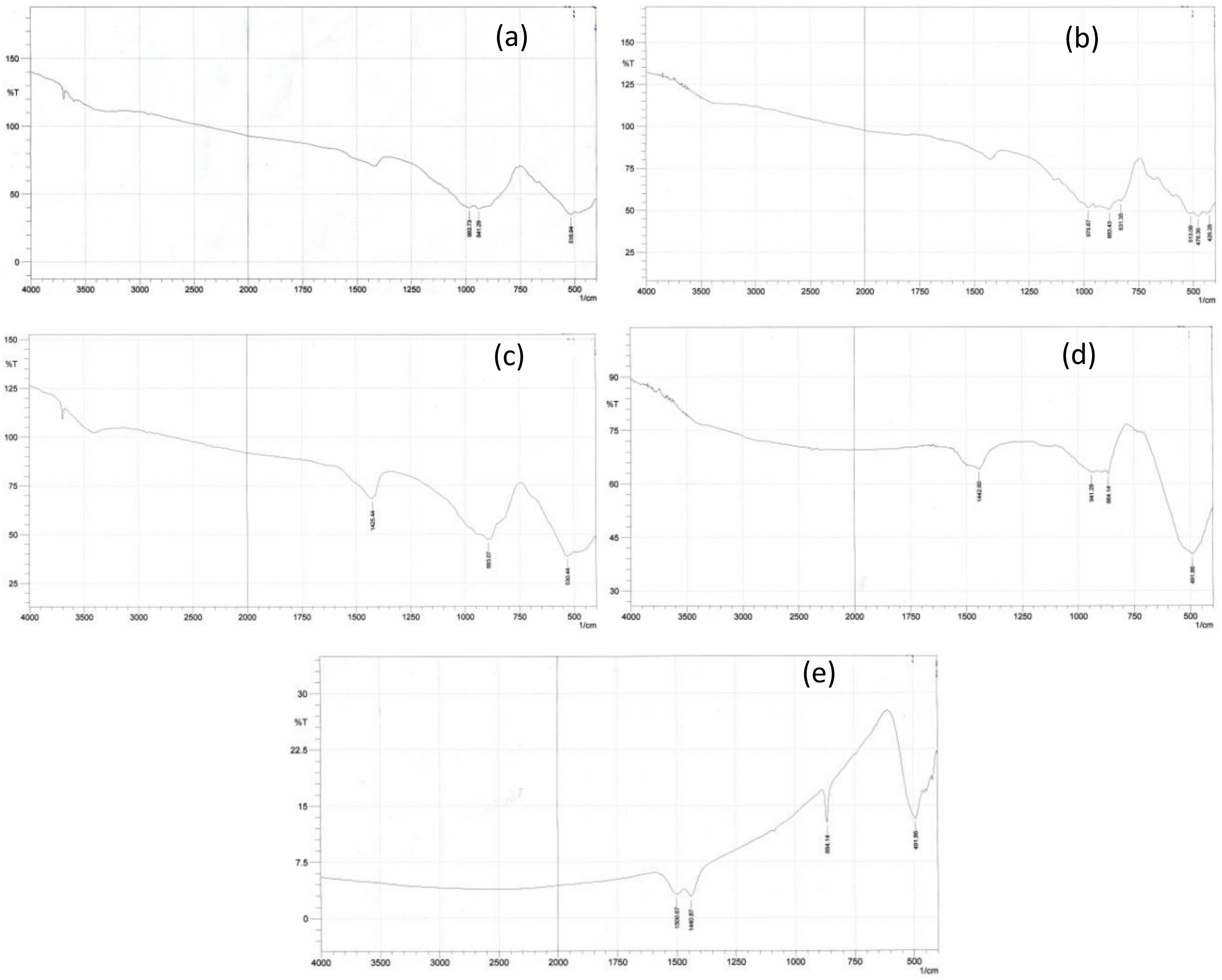

Figure 4 FTIR transmission spectra of $LiCo_{1-x}Ni_xO_2$ where (a) x = 0.00, (b) x = 0.25, (c) x = 0.50, (d) x = 0.75 and (e) x = 1.00

The obtained data (observed wavenumbers) are found experimentally that the $LiCo_{1-x}Ni_xO_2$ molecular networks emitted frequencies with $\bar{\lambda} = \bar{\nu}$ = wavenumbers. The collected wavenumbers and their corresponding vibrational characteristics of molecules (wavelength, frequency, oscillation time and energy) of the crystal are tabulated in Table 3. According to experimental results, the samples are high frequency oscillators due to their frequencies are found to be $\nu > 10^{12}$ Hz.

Table 2 (a) Wavenumbers and corresponding vibrational characteristics and mode assignments of $LiCo_{1-x}Ni_xO_2$ where x = 0.00

Wavenumbers (cm^{-1})	**Characteristics and Mode Assignment**	**Molecules**
517	ν_{TO}-stretching	$LiCoO_2$
941	ν_{TO}-stretching	$LiCoO_2$
984	ν_{LO}-stretching	$LiCoO_2$

Table 2(b) Wavenumbers and corresponding vibrational characteristics and mode assignments of $LiCo_{1-x}Ni_xO_2$ where x = 0.25

Wavenumbers (cm^{-1})	**Characteristics and Mode Assignment**	**Molecules**
426	ν_{TO}-stretching	$LiNiO_2$
478	ν_{TO}-stretching	$LiNiO_2$
513	ν_{TO}-stretching	$LiCoO_2$
831	ν_{LO}-stretching	$LiNiO_2$
980	ν_{LO}-stretching	$LiCoO_2$

Table 2(c) Wavenumbers and corresponding vibrational characteristics and mode assignments of $LiCo_{1-x}Ni_xO_2$ where x = 0.50

Wavenumbers (cm^{-1})	**Characteristics and Mode Assignment**	**Molecules**
530	ν_{TO}-stretching	$LiCoO_2$
983	ν_{LO}-stretching	$LiCoO_2$
1425	ν_1-symmetric stretching	$LiNiO_2$

Table 2(d) Wavenumbers and corresponding vibrational characteristics and mode assignments of $LiCo_{1-x}Ni_xO_2$ where x = 0.75

Wavenumbers (cm^{-1})	**Characteristics and Mode Assignment**	**Molecules**
492	ν_{TO}-stretching	$LiNiO_2$
864	ν_{LO}-stretching	$LiNiO_2$
941	ν_{LO}-stretching	$LiCoO_2$
1443	ν_1-symmetric stretching	$LiNiO_2$

Table 2(e) Wavenumbers and corresponding vibrational characteristics and mode assignments of $LiCo_{1-x}Ni_xO_2$ where x = 1.00

Wavenumbers (cm^{-1})	Characteristics and Mode Assignment	Molecules
492	ν_{TO}-stretching	$LiNiO_2$
864	ν_{LO}-stretching	$LiNiO_2$
1441	ν_1-symmetric stretching	$LiNiO_2$
1501	ν_3-asymmetric stretching	$LiNiO_2$

LO = Longitudinal optical & TO = Transverse optical

Table 3(a) Wavenumber and calculated wavelength, natural frequency, oscillation time and energy of $LiCo_{1-x}Ni_xO_2$ where x = 0.00

$\bar{\nu}$ (cm^{-1})	**λ (nm)**	**ν (Hz)**	**τ (s)**	**E (eV)**
517	19342	1.550E+13	6.452E-14	0.0642
941	10627	2.821E+13	3.545E-14	0.1168
984	10163	2.950E+13	3.390E-14	0.1221

Table 3 (b) Wavenumber and calculated wavelength, natural frequency, oscillation time and energy of $LiCo_{1-x}Ni_xO_2$ where x = 0.25

$\bar{\nu}$ (cm^{-1})	**λ (nm)**	**ν (Hz)**	**τ (s)**	**E (eV)**
426	23474	1.277E+13	7.830E-14	0.0529
478	20921	1.433E+13	6.978E-14	0.0593
513	19493	1.538E+13	6.502E-14	0.0637
831	12034	2.491E+13	4.014E-14	0.1032
980	10204	2.938E+13	3.404E-14	0.1216

Table 3 (c) Wavenumber and calculated wavelength, natural frequency, oscillation time and energy of $LiCo_{1-x}Ni_xO_2$ where x = 0.50

$\bar{\nu}$ (cm^{-1})	**λ (nm)**	**ν (Hz)**	**τ (s)**	**E (eV)**
530	18868	1.589E+13	6.294E-14	0.0658
983	10173	2.947E+13	3.393E-14	0.1220
1425	7018	4.272E+13	2.341E-14	0.1769

Table 3 (d) Wavenumber and calculated wavelength, natural frequency, oscillation time and energy of $LiCo_{1-x}Ni_xO_2$ where x = 0.75

$\bar{\nu}$ (cm^{-1})	λ (nm)	ν (Hz)	τ (s)	E (eV)
492	20325	1.475E+13	6.780E-14	0.0611
864	11574	2.590E+13	3.861E-14	0.1072
941	10627	2.821E+13	3.545E-14	0.1168
1443	6930	4.326E+13	2.312E-14	0.1791

Table 3(e) Wavenumber and calculated wavelength, natural frequency, oscillation time and energy of $LiCo_{1-x}Ni_xO_2$ where x = 1.00

$\bar{\nu}$ (cm^{-1})	**λ (nm)**	**ν (Hz)**	**τ (s)**	**E (eV)**
492	20325	1.475E+13	6.780E-14	0.0611
864	11574	2.590E+13	3.861E-14	0.1072
1441	6940	4.320E+13	2.315E-14	0.1789
1501	6662	4.500E+13	2.222E-14	0.1863

Electrical Conductivity Study

The electrical nature of a material is characterized by its conductivity (or, inversely, its resistivity) and its dielectric constant and coefficients that indicate the rates of change of these with temperature, frequency at which measurement is made, and so on. For crystalline materials with a range of chemical composition as well as variable physical properties of porosity and fluid content, the values of electrical properties can vary widely. Electrical conductivity σ of the ceramic obeys an Arrhenius expression, $\sigma = \sigma_0 \exp(\frac{-E_a}{kT})$, where, σ_0 is the pre-exponential factor, E_a is activation energy, k is Boltzmann's constant and T is absolute temperature. Arrhenius plots of the variation of dc electrical conductivity of the samples are shown in Figure 5.

According to the theory of ionic conductivity, the slope of the electrical conductivity in each of the figure, e.g., in Figure 5(a) for $LiCo_{1-x}Ni_xO_2$ (x = 0.00) sample, corresponding to the activation energy for creating of defect states due to the ionic motions of the sample. From Figure 5(a), the activation energy E_a can be obtained by using the slope of the ln(σ) versus 10^3/T graph.

$E_a/k = 5.8981 \times 1000$

$E_a = 5.8981 \times 1000 \times k$

$E_a = 5.8981 \times 1000 \times 1.38E\text{-}23$

$E_a = 8.14 \times 10^{-20}$ J

$E_a = 0.5087$ eV

As shown in Figure 5, electrical conductivities of the samples increased with increase in temperature. The obtained activation energies of the samples are listed in Table 4. From the experimental results, the samples exhibited as superionic conductors at high temperature because their electrical conductivities are found as $\sigma \geq 10^{-3}$ S m^{-1}. In the ln σ – 1000/T graphs, the starting point of superionic phase indicates with the circle and the superionic phase temperatures T_{SI} presented in Table 4. As shown in tables, the $LiCo_{1-x}Ni_xO_2$ (x = 0.75) sample is the lowest (superionic phase) temperature 403 K among the investigated samples.

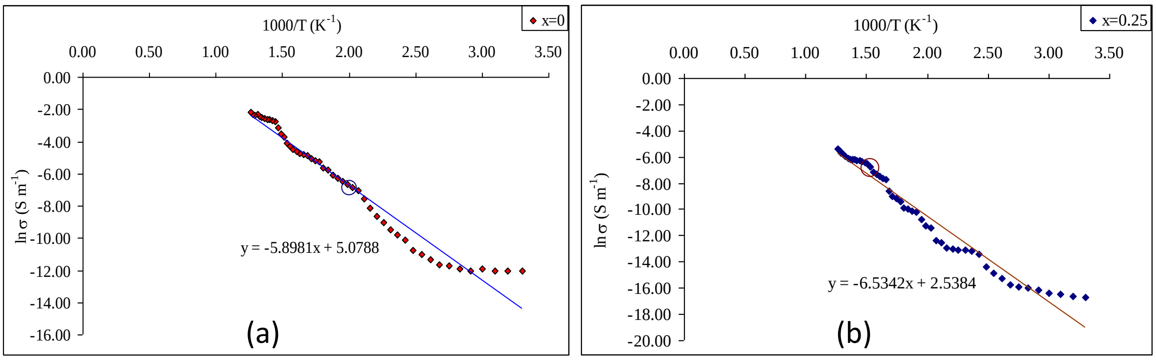

Figure 5 Arrhenius plots of the ln σ versus 1000/T graphs of $LiCo_{1-x}Ni_xO_2$ where (a) x = 0.00, (b) x = 0.25

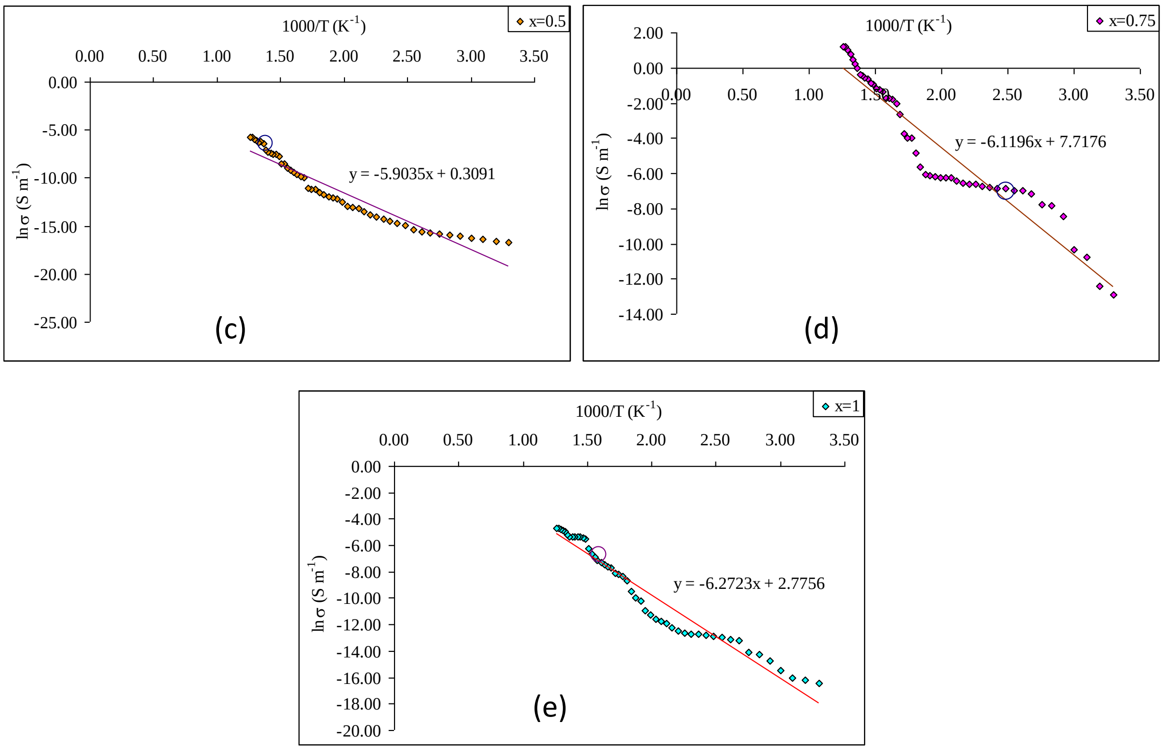

Figure 5 Arrhenius plots of the ln σ versus 1000/T graphs of $LiCo_{1-x}Ni_xO_2$ where (c) x = 0.50, (d) x = 0.75 and (e) x = 1.00

Table 4 The activation energies of the $LiCo_{1-x}Ni_xO_2$ samples

Sample (Contents x of Ni)	**Superionic Phase Temperature T_{SI} (K)**	**E_a (eV)**
0.00	503	0.5087
0.25	653	0.5636
0.50	733	0.5092
0.75	403	0.5278
1.00	643	0.5410

Conclusion

Lithium-Cobalt-Nickel Oxide, $LiCo_{1-x}Ni_xO_2$, (where x = 0.00, 0.25, 0.50, 0.75 and 1.00) were successfully prepared by solid state reaction method. XRD patterns reveal that the samples analogous to hexagonal structure. The lattice parameters of the $LiCo_{1-x}Ni_xO_2$ samples increased with increase in Ni concentration. The crystallite sizes of the samples decreased with increase in Ni concentration. FTIR spectra showed that the vibrational characteristics and mode assignments of constituent molecules of the samples. It can be assumed that the phase confirmation of the samples. The samples exhibited as the superionic conductors in the high temperature with the activation energies as in the range of 0.5087 eV – 0.5636 eV (i.e., $E_a < 1$ eV) and it indicated that the samples were advanced superionic conductors. According to experimental results, the samples can be used as the solid electrolyte materials.

Acknowledgement

The authors would like to acknowledge Professor Dr Khin Khin Win, Head of Department of Physics, University of Yangon, for her valuable suggestion and comments for this work.

References

Arico, A.S., Bruce, P., Scrosati, B., Tarascon, J.M. & Shalkwijk, W. (2005). Nanostructured materials for advanced energy conversion and storage devices. *Nature*, 4, 366-377.

Azurdia, J., Marchal, J. & Laine, R.M. (2006). Synthesis and Characterization of Mixed-Metal Oxide Nanopowders along the CoO_x-Al_2O_3 Tie Lie Using Liquid Feed Flame Spray-Pyrolysis. *Journal of American Ceramic Society*, 89(9), 2749-2756.

Fey, G.T.K., Subramanian, V. & Chen, J.G. (2002). Electrochemical performance of Sr^{2+} doped $LiNi_{0.8}Co_{0.2}O_2$ as a cathode material for lithium batteries synthesized via a wet chemical route using oxalic acid. *Materials Letters*, 52, 197-202.

Fey, G.T.K., Chen, J.G. & Subramanian, V. (2003). Electroanalytical and thermal stability of multi doped lithium nickel cobalt oxides. *Journal Power Sources*, 119-121, 658-663.

Julian, C. (2003). Local structure and electrochemistry of lithium cobalt oxides and their doped compounds. *Solid State Ionic*, 157, 57-71.

Kumar, A., Thomas, R. & Katiyar, R.S. (2009). Structural and Electrochemical Characterization of Pure $LiFePO_4$ and Nanocomposite C-$LiFePO_4$ Cathodes for Lithium Ion Rechargeable Batteries. *Journal of Nanotechnology*, 1, 1-10.

Tao, H., Feng, Z., Liu, H., Kan, X. & Chen, P. (2011). Reality and Future of Rechargeable Lithium Batteries. *The Open Materials Science Journal*, 5(2), 204-214.

Wang, G., Liu, H., Liu, J., Qiao, S., Lu, G.M., Munroe, P. & Ahn, H. (2010). Mesoporous $LiFePO_4$/C Nanocomposite Cathode Materials for High Power Lithium Ion Batteries with Superior Performance. *Advanced Materials*, 22, 4944-4948.

J. Myanmar Acad. Arts Sci. 2020 Vol. XVIII.No.2A

EXPERIMENTAL INVESTIGATION ON THE IMPROVEMENT OF MECHANICAL PROPERTIES OF CLAY BRICK USING CORYPHA FIBRES

Tin Tin Myint[1],Yin Yin Thein[2], Naw Htoo Lar Phaw[3]

Abstract

The currently used local bricks from Hmawzar Acient City, Pyay distinct, Bago division, were determined their compressive strengths. EDXRF,XRD techniques were used for the quality of earthling. In order to obtain the desired bricks, layers of coryphe fibres were inserted inside the bricks with distinct positions. Then the newly created bricks were used to investigate their mechanical properties such as compressive strength and density by using universal testing machine. This research work is intended to be able to use the qualitative bricks for the benefit of construction sites.

Keywords: EDXRF, XRD, compressive strength, density

Introduction

In Myanmar, clay bricks have been used as major construction materials. In Hmawzar village, Pyay district, the local currently used bricks are made by the mixture of clay and paddy shell and then baked for the construction of buildings. Bricks from that region are widely used due to their fair compressive strength. In this work, clay was used as raw material to make brick samples and they were examined by EDXRF method at Universities Research Centre (URC), Yangon.

In the present research work, layers of coryphe fibres were introduced by inserting them in bricks. And then the mechanical properties of those bricks such as the compressive strength and density were determined by universal testing machine from the structural laboratory at department of civil engineering in Yangon Technology University. Bricks with these properties can be expected to develop and to give more compressing resiliency from the effects caused by weather as well as the earthquake.

Corypha Palm

Corypha umbraculifera, the talipot palm, is a species of palm native to eastern and southern India and Sri Lanka. It is also cultivated in Southeast Asian countries of Myanmar, Thailand and the Andaman Islands. It is also grown sparsely in China. This palm tree is known as Paypin in Myanmar. It is a flowering plant with the largest inflorescence in the world. It is one of the largest palms with individual specimens having reached heights of up to 25 m (82 ft) with stems up to 1.3 m (4.3 ft) in diameter. It is a fan palm, with large, palmate leaves up to 5 m (16 ft) in diameter, with a petiole up to 4 m (13 ft), and up to 130 leaflets. The corypha palm is monocarpic, flowering only once, when it is 30 to 80 years old. It takes about a year for the fruit to mature, producing thousands of round, yellow-green fruit 3–4 cm (1–1.5 in) in diameter, each containing a single seed. The plant dies after fruiting. Historically, the leaves were written upon in various Southeast Asian cultures using an ironto create palm leaf manuscripts. In Philippines,

---

[1] Dr, Lecturer, Department of Physics, Pyay University

[2] Dr, Associate Professor, Department of Physics, University of Computer Studies, Banmaw

[3] Dr, Professor, Department of Physics, Pyay University

it is locally known as *buri* or *buli*. The leaves are also used for thatching, and the sap is tapped to make palm wine. In South India, the palm leaves are used to make umbrellas for agricultural workers. [https:// en.m.wikipedia.org]

Experimental Procedure

A ditch of clay having volume with dimensions is 5′× 5′× 1′ from Hmawzar village, Pyay district was thoroughly mixed with a bushel of paddy shell and suitable amount of water. That mixture was kept for 24 hours. Then it was mixed again with a bushel of paddy shell to prepare the soil for moulding as in Figure1(a). That soil was tested by EDXRF and XRD.

The stem of corypha palm was cut into strips and dried to make coryphe fibres. Thickness of coryphe fibres applied for the research was about$0.0394''$as shown in Figure 1(b) and (c).To obtain the proper bricks for measuring the compressive strength and density, mould with dimensions of$9.14'' \times 4.4'' \times 2.57''$ in Figure 2(a)was used.

For the second stage, to investigate the compressive strength, the soil was transformed into$9.14'' \times 4.4'' \times 2.57''$bricks.Five bricks were taken as a non-layer sample bricks. Next, corypha-fibres which want to be used to make layered bricks were sandwiched between soil in the mould so as to from alternate layers of coryphe fibres and soil. In this way, bricks containing one layer of coryphe fibres, two layers of coryphe fibres and three layers of coryphe fibres each for five bricks were made as shown in Figure 2(b)and (c). [Chee Ming, 2011]

To measure the density, five bricks with none -layer, five bricks with one layer and five bricks with two layers and five bricks with three layers were made as well. And then the modified sample bricks, both the non-layered bricks and layered bricks were heated under the sunlight for 15 days, and baked in the wood fire for 3 to 5 days. Then the sample bricks as shown in Figure 2(d)were then ready to be tested. [https://civilseek.com, 2019]

(a) (b) (c)

Figure 1 (a)Mixture of soil and paddy shell(b) Strips of Corypha palm's stem (c)Dried coryphe fibres

(a) (b)

Figure 2 (a) Mould for sample preparation (b) Making bricks

(c) (d)

Figure 2 (c) Brick before baking (d) Bricks for testing

Experimental Results

In this work, clay and paddy shell were used as raw materials to make brick samples and they were examined by EDXRF and XRD methods at Universities Research Centre (URC), Yangon.

Fine Powder of clay was obtained from dried nature clay under the sunshine. Then the dried powder was made pellet at URC and named M1 for Hmawza clay. Furthermore, the natural clay and paddy shell was mixed thoroughly and then has dried the mixture. The well dried mixture was made pellet at URC and also named M2.

EDXRF Result

The two pellet samples M1, M2 were investigated by Energy Dispersive X-Ray Fluorescence Spectroscopy (EDXRF) in Figure 3(a) and (b) to study the contents in the samples. According to the results in table 1, iron (Fe) is mainly contained in Hmawza clay.

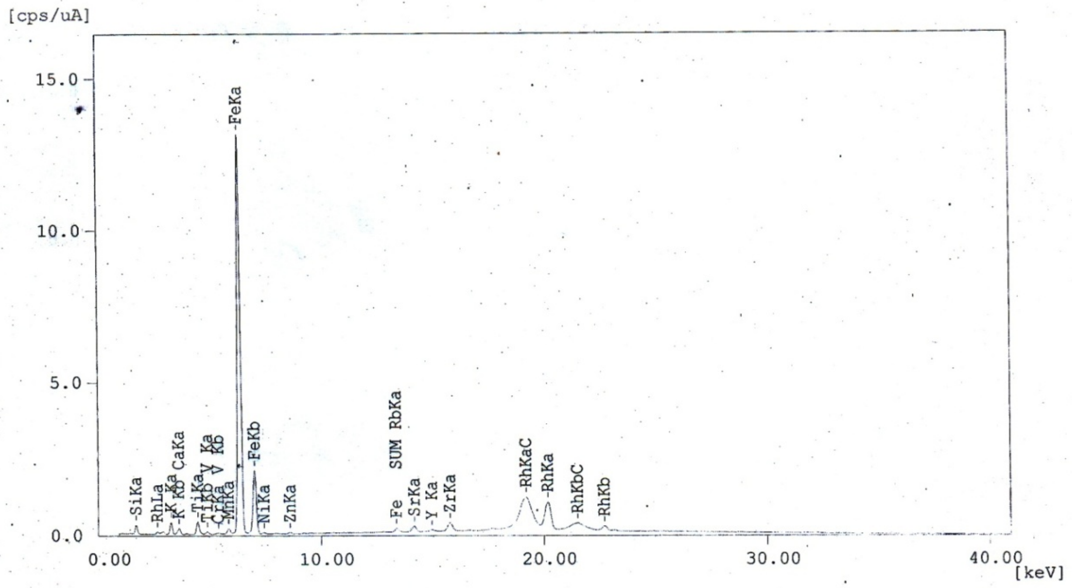

Figure 3(a) EDXRF pattern for sample M1

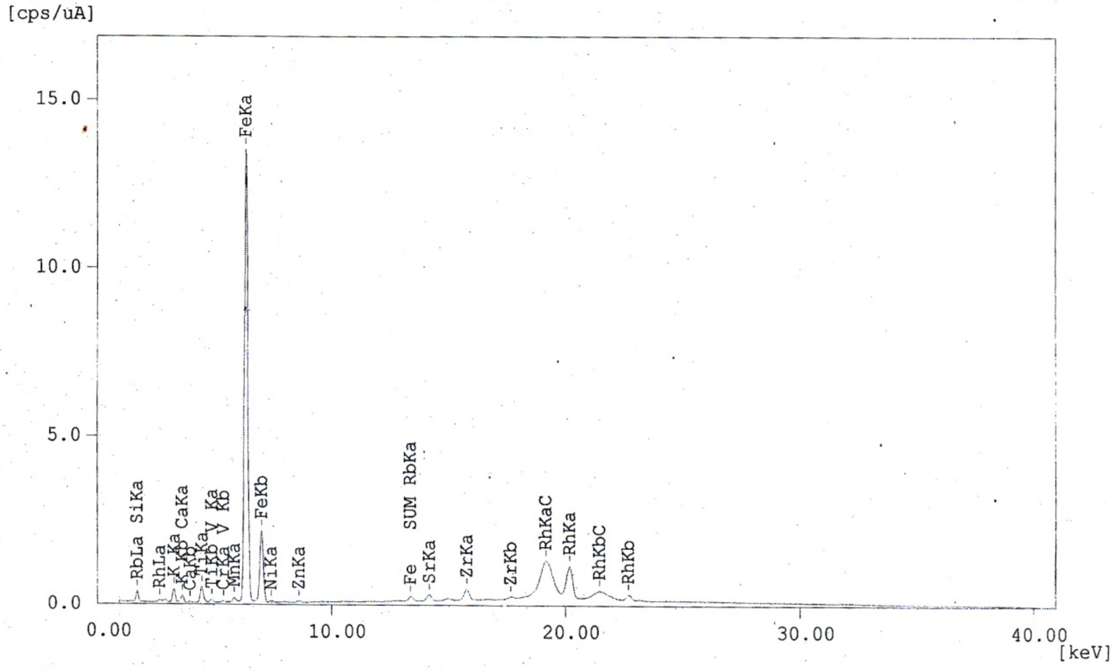

Figure 3(b) EDXRF pattern for sample M2

Table 1 Elements concentration for samples M1 and M2

Element	Sample M1(cps)	Sample M2(cps)
Si	1.7160	1.7286
Fe	107.3177	106.3175
K	2.7758	2.1158
Ti	3.1558	3.5481
Ca	1.2756	1.5121
Mn	1.3955	1.5853
Zr	3.5353	4.1870
Cr	0.2691	0.0691
Sr	1.9485	2.0211
Zn	0.4279	0.5125
Y	0.6680	0.2651
Rb	0.0318	0.0784

XRD Result

Pelleted samples M1and M2 are analyzed by XRD technique and the results were examined with Joint committee on Powder Standard (JCPDS) data library file:Cat.No 85-0795 for XRD to study the content of silicon dioxide SiO_2 and 23-1009 for aluminium oxide Al_2O_3, that were properties of cement. All samples show sharp peaks of $SiO_2$and Al_2O_3 peaks were studied. The results were shown in Figure 4(a), (b) and table 2 respectively.[Callister,1997]

According to XRD results, the clay and the clay with chaff from Hmawzar village have the properties of cement. The XRD results show that in sample S1, the planes (011), (112), (100), (110), (121), (200), (111), (301) and (022) identify with the planes of sample S2. But the plane (122) can be seen in the simple S2 only. All the planes can be attributed to silicate (SiO_2) plane which is matched well with the standard library file.The planes in sample S1 and S2 which (403),(710), (113), (-603), (-601), (-112), (111), (-111), (-210),(001) and (200) identify with the planes in AL_2O_3 from the library file in XRD. [Guy,1992]

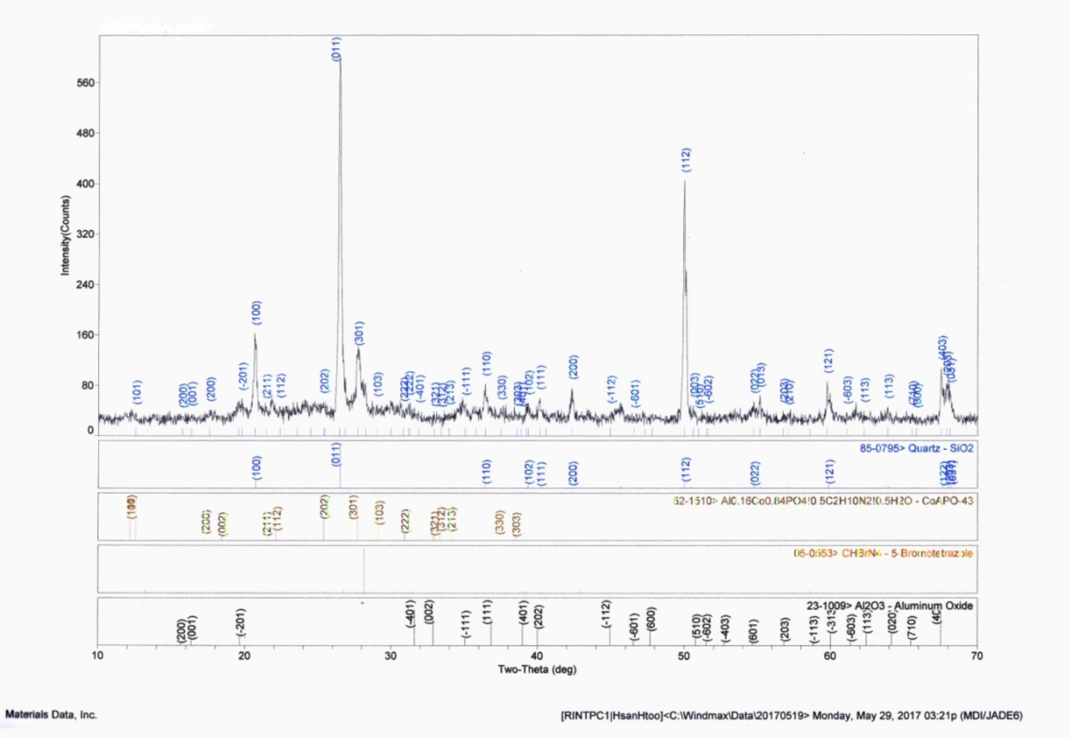

Figure 4(a) XRD pattern for sample M1

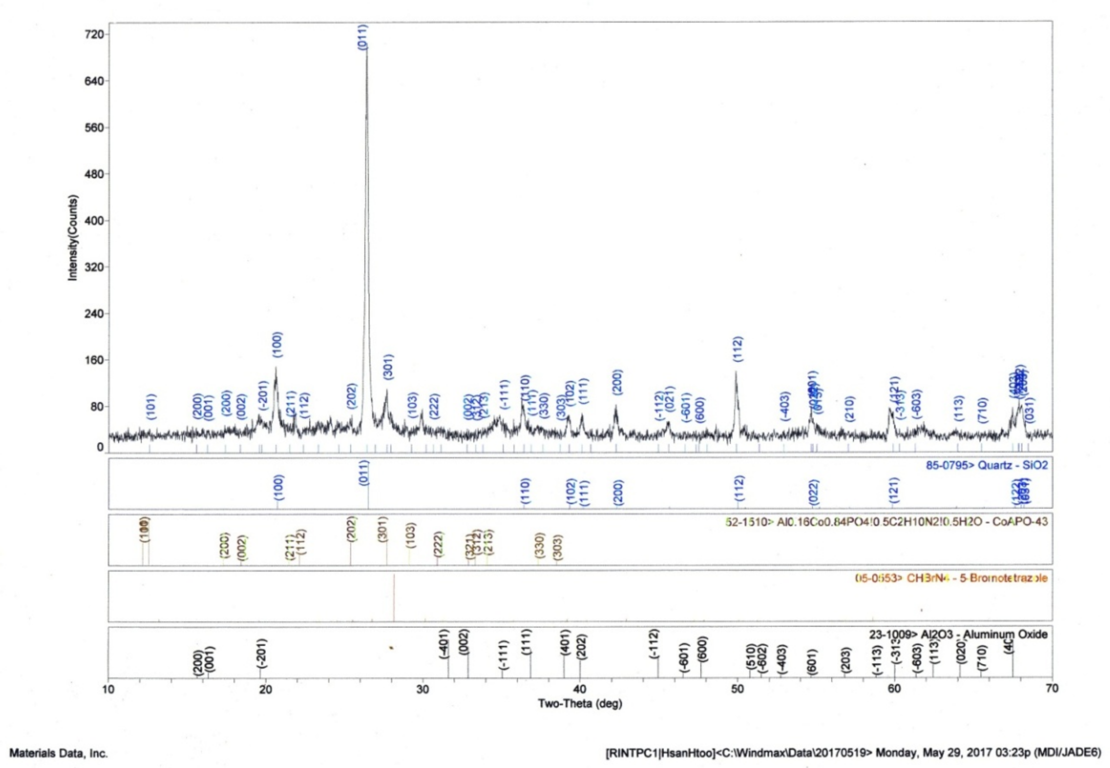

Figure 4(b) XRD pattern for sample M2

Table 2 XRD results for samples M1 and M2

	Plane	
	M1	**M2**
SiO_2	(011),(112),(100),(110),(121),(200), (111), (031), (022)	(011), (112), (100), (110),(121),(200), (111), (031), (022), (122)
Al_2O_3	(403), (710), (113), (-603), (-601), (-112), (111), (-111),(-210), (001), (200),(202), (-602)	(403), (710), (113), (-603), (-601),(-112), (111), (-111), (-210), (001), (200), (601), (-403), (600)

Compressive Strength and Density Results

The compressive of brick sample were determined by compressive strength testing machine (RBU-250), shown in Figure 5,from the structural laboratory at department of civil engineering in Yangon Technology University.

The density of bricks or weight per unit volume depends mostly on the type of clay used and the method of brick molding. The results of compressive strength and density are shown in Table 3.

Table 3 Results of Compressing Strength and Density

Test Name	None (without fibres)	One layer	Two layers	Three layers
Average value of compressiveStrength (psi)	947.1	2543.5	2880	2288.5
Average value of density (gcm^{-3})	2.074	1.605	1.5529	1.4615

Figure 5 Compressive strength testing machine

Conclusion

According to EDXRF results, iron (Fe) contains the highest concentration of 107.3177cps in M_1 and 106.3175cps in M_2. The elements Si, K, Ti, Ca, Mn, Zr, Sr, V, Cr, Zn, Ni and Y are contained in sample M_1 and M_2 but different in little values. Rb element contains in M_1 as the value of 0.0318cps and contains in M_2 as the value of 0.0784 cps. Very small amount of some metal elements are also contained in clay powder samples from Hmawza village. From the results of XRD, silicon dioxide and aluminium oxide are contained in clay powder samples. Silicon dioxide peaks are more dominant than aluminium oxide peaks. Both silicon and aluminium are contents of cement elements and so the property of cement can be seen in those clay samples. [Chris,1992]

The average value of compressive strength of brick samples were made by the mixture of natural clay and paddy shell without inserting coryphe fibres is 947.1 psi (lb in^{-2}). This value is very agree with the BIS (Bureau of Indian Standard, BIS 1077-1992) standard values of ordinary class clay brick.So that conventional bricks currently used in Hmawza village is safe in construction. When the coryphe fibres of one and two layers were inserted in bricks, the compressive strength are increasing to 2543.5 psi and 2880 psi respectively. For the three layers of coryphe fibres, the value is decreasing to 2288.5 psi. According to the measurement results, the graph shows that the compressive strength of the bricks with two fibred layers is optimum. The observation is shown in Figure 6. [https://civilseek.com ,2019]

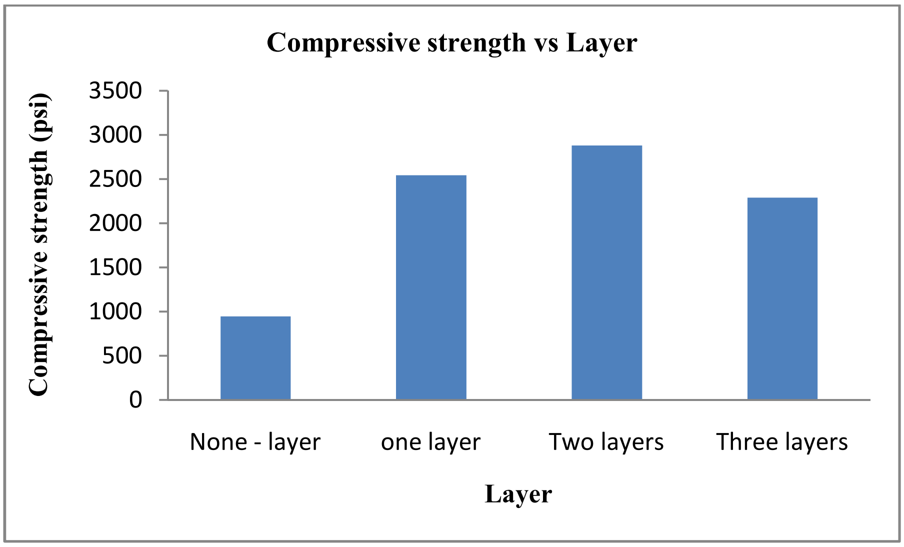

Figure 6 Compressive strength vs layer graph

The heat and sound conductivity of bricks vary greatly with their density. Very dense and heavy bricks conduct heat and sound at a greater rate. They have, therefore, poor thermal and acoustic (sound) insulation quality. For this reason, bricks should be so designed that they are light, strong and give adequate insulation. In this event, it shows that density of brick is decreasing continuously with increasing fibre contains. The sample bricks made from coryphe fibres are comparatively lighter than non-fibred layered bricks. The density of all layered bricks decreased with increased in volume fraction of coryphe fibres. Result of density test is shown in Figure 7. [https://civilseek.com, 2019]

Therefore it can also be concluded that, the present work has primarily been focused upon the compressive strength and density that will be supported for further studies concerning with the environmental safety and protecting the buildings from damaging by the natural disasters such as earthquakes, storm, land-slide, etc.

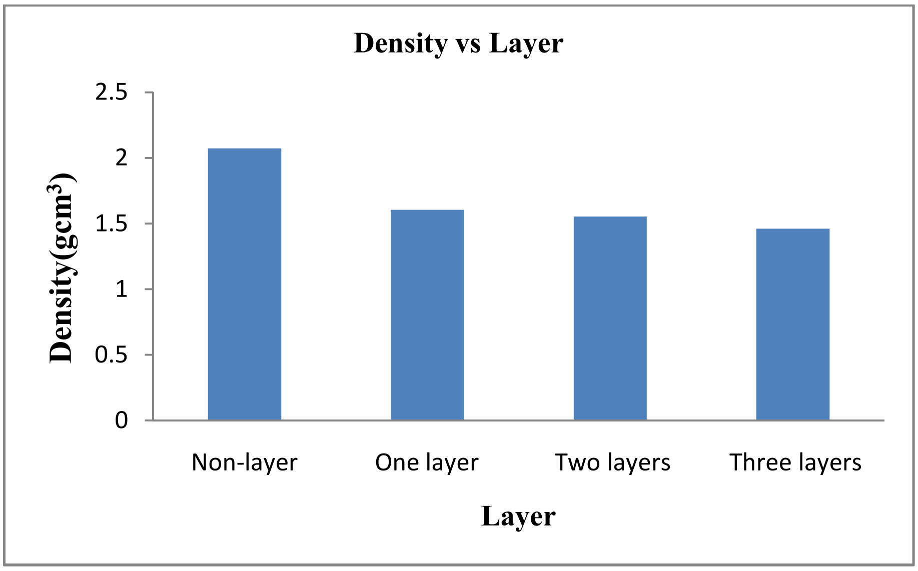

Figure 7 Density vs layer graph

Acknowledgements

I wish to express my sincere thanks to Dr Aung Aung Min, Acting Rector of Pyay University, Dr Thwe Linn Ko, Pro-Rector of Pyay University. I would like to thank Professor Dr Soe Soe Nwe, Head of Department of Physics, Pyay University, Professor Dr Naw Htoo Lar Phaw, Department of Physics, Pyay for their kind permission to do this work.

I also would like to thank Rector(YU) Dr Pho Kaung, Professor Dr Khin Khin Win (Head of Department of Physics, YU) for their permission to present this research report.

Finally, I would like to express my gratitude to all teachers for their kind advices and help in completing this research work.

References

Callister.W.D., (1997), *Materials Science and Engineering* (Toranto: Wiley)

Chris Pellant, (1992), *Rocks and Minerals* (Dorling Kindersley limited, London)

CM Chan,World Academy of Science, Engineering and Technology International Journal of Civil and Environmental EngineeringVol:5, No:1(2011) scholar.waset.org/1307-6892/4241

Guy.A.G., (1992), *Introduction to Materials Science* (London: Mc Graw-Hill)

https://civilseek.com>Properties of Brick| A Complete Guide (15-3-2019)

https:// en.m.wikipedia.org

*J. Myanmar Acad. Arts Sci. 2020*Vol. XVIII.No.2A

IMPROVINGTHEMECHANICAL PROPERTIES OF CONSTRUCTION MATERIALS FROM HMAWZAR VILLAGE APPLYING SAWDUST (WOOD FIBRES)

Mar Lar Aye[1], Tun Lin Htet[2] and Naw Htoo Lar Phaw[3]

Abstract

The elementary concentrations of local clay from Hmawzar village, Pyay District, Bago Division were investigated by using EDXR Fand XRDtechniques. The mechanical properties of currently used local bricks from Hmawzar village were investigated by using compressive testing machine and bending strength testing machine. Sawdust (wood fibres) with different weight ratios were thoroughly mixed to the local natural clayin homogenously and then this mixture is made into bricks. Then the properties of newly created bricks were measured. From the results of this research, sawdust (wood fibres) is the appropriate additive to prepare bricks with higher mechanical propertiesbut not more than 1wt% fibres content. It is intended to be able to improve the quality construction materials for the benefit of the nation by using the acquired out-coming knowledge and data investigated from this research.

Keywords : EDXRF, XRD, compressive strength, bending strength modulus

Introduction

Clay bricks are the most popular construction materials. It has been used as a major construction material because it can tolerate with severe weathering action and flexible properties.Traditional bricks which are made by the clay and chaff with paddy shell and then fired in kiln.

The mechanical properties of fibres include strength, elongation, elasticity and modulus of elasticity. In this research,wood fibers such as sawdust from sawmill are used as coupling agent in brick making process. Wood is a porous and fibrous structural tissue found in the stems and roots of trees and other woody plants. Sawdust is a waste from the wood and timber industry. The mechanical properties of wood are its fitness and ability to resist applied forces (Nicoleet. al,2003).

The various weight ratio of sawdust is mixed with clay to make the clay brick and to determine the effect of different fiber content.From this research, the mechanical properties of those bricks such as the compressive strength and the flexible bending strength can be expected to improve and so to give more effect in environment benefit.

Experimental Procedure

Fine powder of clay was obtained from dried natural clay at Hmawzar Village under sunshine. Then the dried powder was made pellets S1at Universities Research Center (URC). Furthermore, the natural clay and chaff of paddy shell were thoroughly mixed and had dried them. The well dried mixture was made pellet S2 at URC. Pellet samples S1 and S2were analyzed by Energy Dispersive X-ray Fluorescence Spectroscopy(EDXRF) and X ray Diffraction (XRD) techniques at URC, Yangon.

---

[1] Dr, Lecturer, Department of Physics, Pyay University
[2] Assistant Lecturer, Department of Physics, Pyay University
[3] Dr, Professor, Department of Physics, Pyay University

A ditch of clay which is $(5' \times 5' \times 1')$ from Hmawzarvillage was thoroughly mixed with a bushel of paddy shell and suitable amount of water. This mixture is kept for 24 hours. Then it is mixed with a bushel of paddy shell again.

The brick samples were made in three different molds (214mm × 97mm × 57mm) rectangular shape, (25.4 mm × 25.4 mm) dumb-bell shaped and(345.7mm×106mm ×58.4mm) rectangular shape in Figure 2. Firstly, five brick samples for one kind were made clay and chaff only had been collected. And then, the sawdust (wood fiber)content of 0.5wt%, 1wt% and 1.5wt%were homogeneously mixed with clay to prepare for the molding bricks in Figure 1.Five bricks for one kind were dried under sunlight for 3 days. The dried brick samples were baked in kiln about 5 days for measuring compressive strength and bending strength. And then, the burnt brick samples had been investigated.

The compressive strength and bending strength of the prepared brick samples were examined by universal testing machine (GUNT HAMBURG)from structural laboratory at department of mechanical engineeringin Pyay Technology University and UPM-4 testing machine fromstructural laboratory department of civil engineeringin Yangon Technology University.

Figure 1 Sawdust (Wood-fibres) with clay mixture

Figure 2 Twomouldswith required measurements

Figure 3 Bricks for measuring the compressive and bending strength

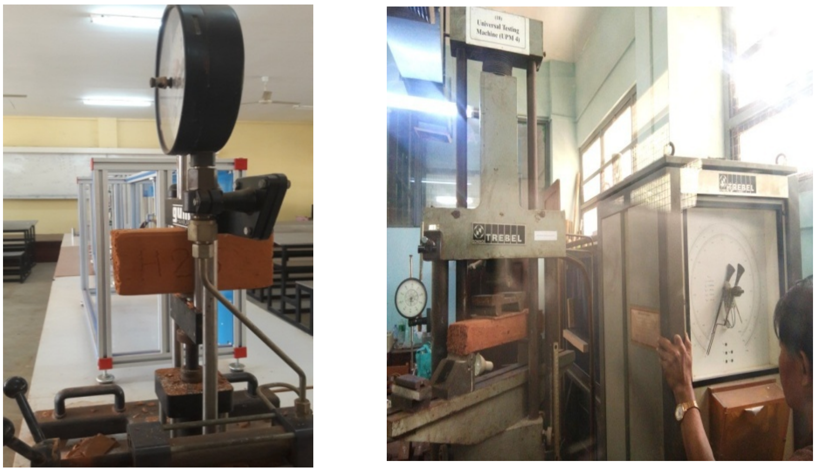

Figure 4 Compressive and bending strength testing machines

Experimental Results

EDXRF Analysis

The two pellet samples S1, S2 were investigated by EDXRF tostudy the contents of elements in these samples. Figure 5 and 6 showed the results of the EDXRF as the patterns and the concentrations of elements in sample S1 and S2 were shown in Table 1.

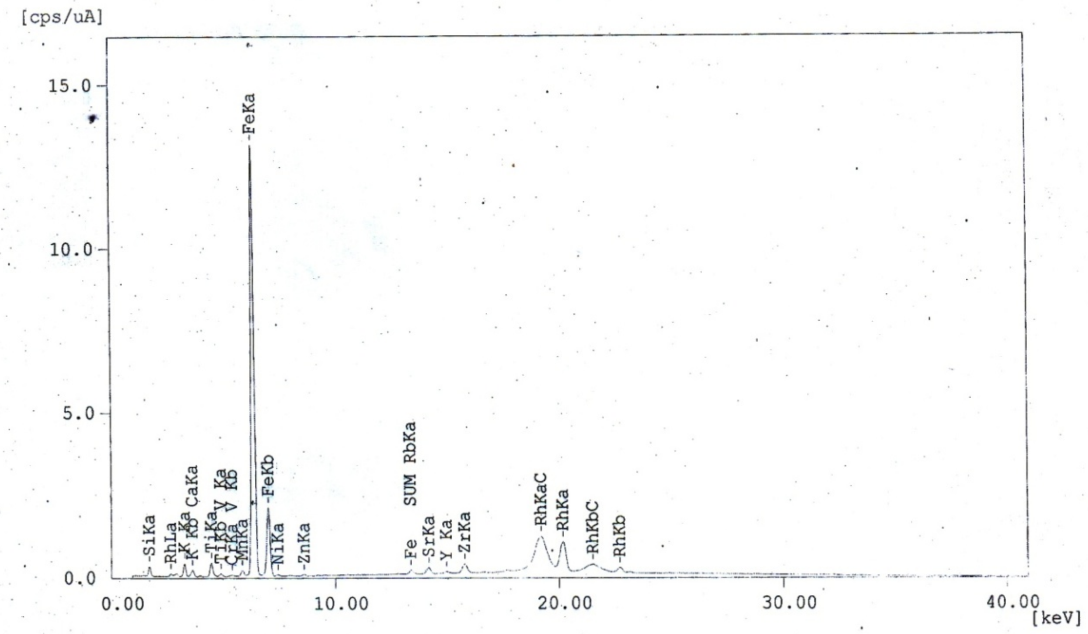

Figure 5 EDXRF pattern for sample S1

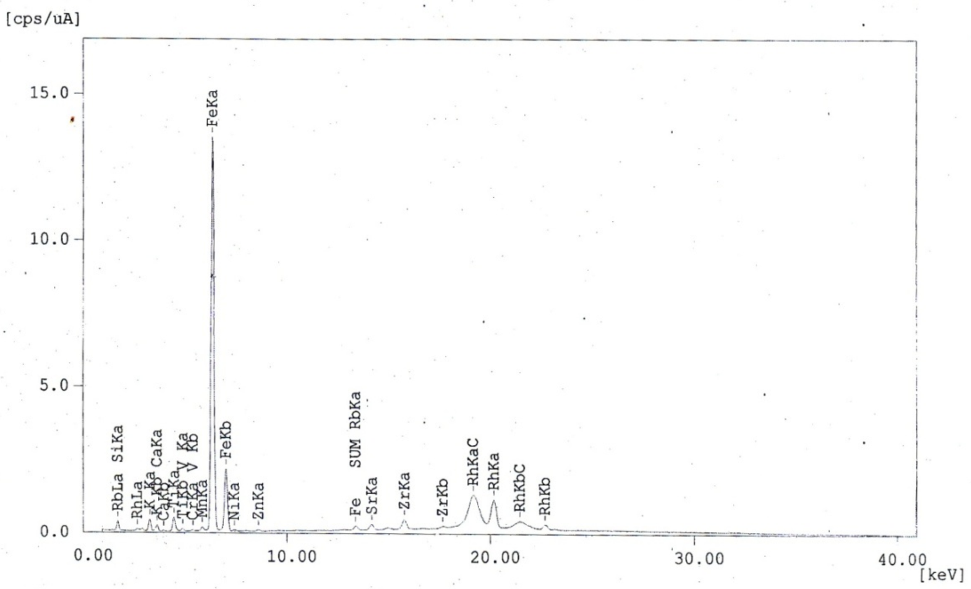

Figure 6 EDXRF pattern for sample S2

Table 1 Elementsconcentration for samples S1 and S2

Element	**Sample S1(cps)**	**Sample S2(cps)**
Si	1.7160	1.7286
Fe	107.3177	106.3175
K	2.7758	2.1158
Ti	3.1558	3.5481
Ca	1.2756	1.5121
Mn	1.3955	1.5853
Zr	3.5353	4.1870
Cr	0.2691	0.0691
Sr	1.9485	2.0211
Zn	0.4279	0.5125
Y	0.6680	0.2651
Rb	0.0318	0.0784

XRD Analysis

Pellet samples S1and S2 were analyzed by XRD technique and the results were examined with Joint Committee on Powder Diffraction Standard (JCPDS) data library file:Cat.No. 85-0795 for SiO_2 and 23-1009 for Al_2O_3, were studied for the content of silicondioxide and aluminum oxide. Theyare properties of cement. The results were shown in Figure 7,8 and their properties were shown in Table 2.

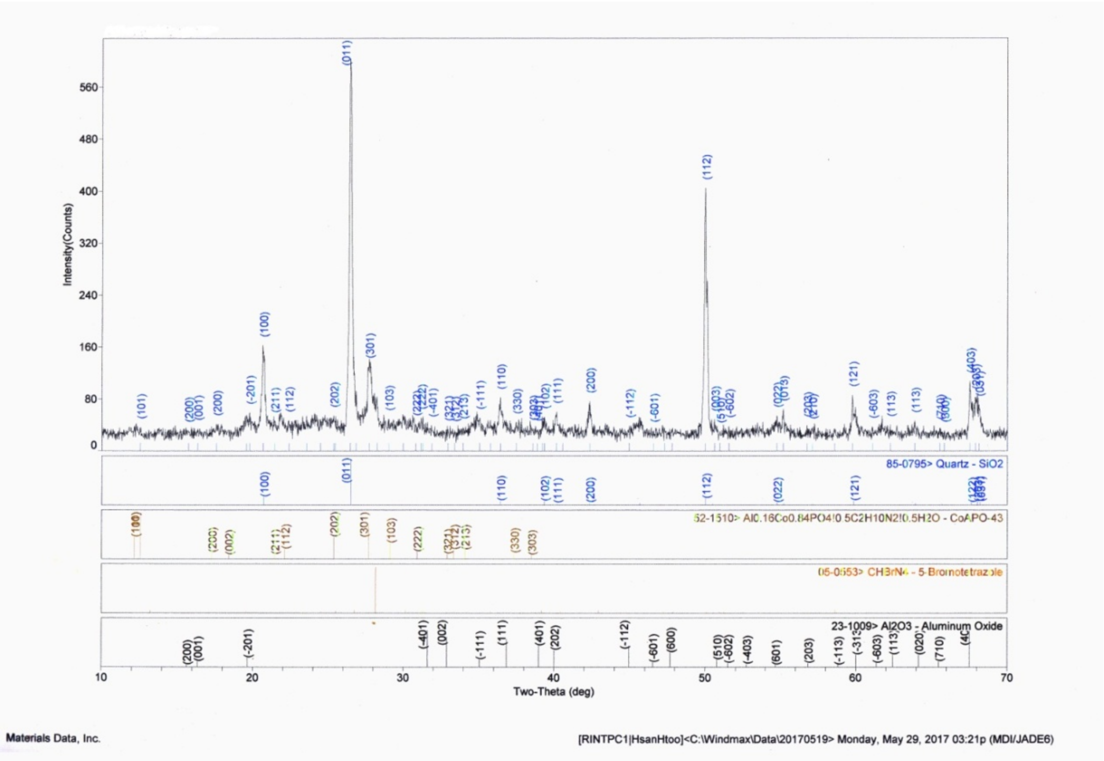

Figure 7 XRD pattern for S1

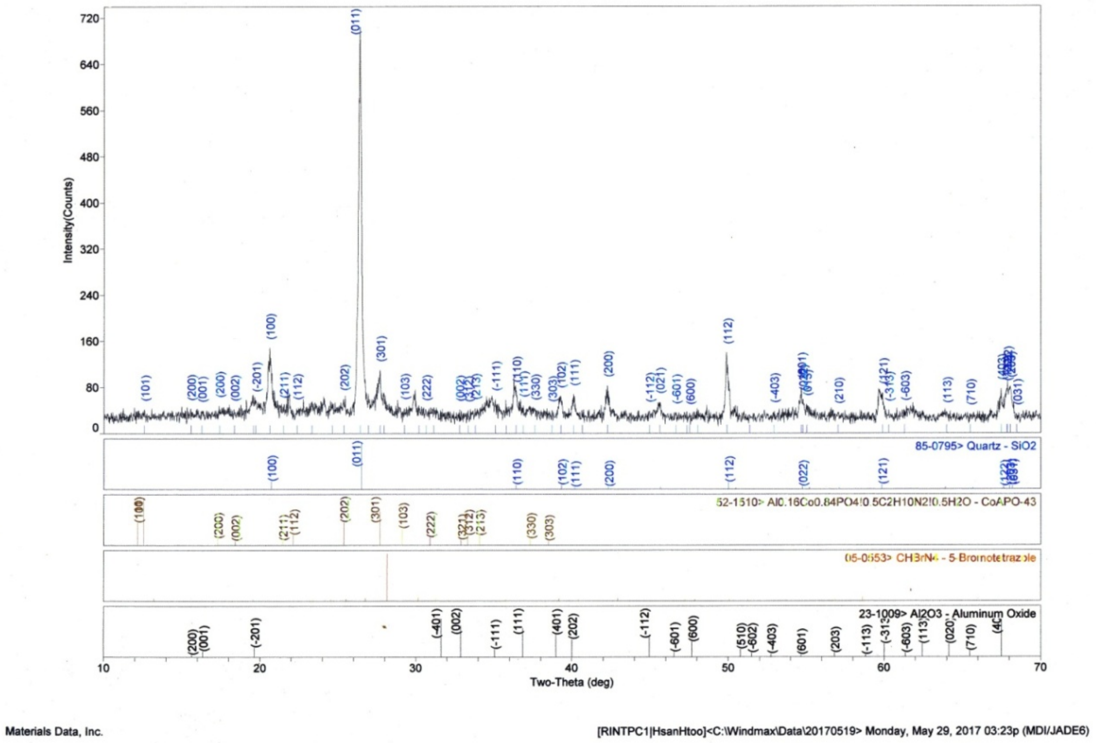

Figure 8 XRD pattern for S2

Table 2 XRD results for samples S1 and S2

	Plane	
	S1	S2
SiO_2	(011),(112),(100),(110),(121),(200), (111), (031), (022)	(011), (112), (100), (110),(121),(200), (111), (031), (022), (122)
Al_2O_3	(403), (710), (113), (-603), (-601), (-112), (111), (-111),(-210), (001), (200),(202), (-602)	(403), (710), (113), (-603), (-601),(-112), (111), (-111), (-210), (001), (200), (601), (-403), (600)

Compressive Strength

Table 3 Results for compressive strength

Sample	Average Compressive strength CS (MPa)
None(without fibres)	6.13
M1 (0.5 wt% of fibres)	6.79
M2 (1 wt% of fibres)	8.66
M3 (1.5 wt% of fibres)	3.76

Bending Strength Modulus

Table 4 Results for bending strength modulus

Load(N)	Average Bending strength modulusE_f (Mpa)			
	None	M1	M2	M3
100	83.9	106.6	117.8	100.6
150	86.6	126.7	139.8	125.1
200	89.2	125.2	161.3	149.1

Discussion

According to EDXRF results,Fe contains the highest concentration of elements in sample S1 and S2. The elements Si, K, Ti, Ca, Mn, Zr, Sr, V, Cr, Zn, Ni, Y and Rb are contained in sample S1 and S2 but different in little values (Chris, 1992).

According to XRD results, the clay and the clay with chaff from Hmawzar village have the properties of cement. The XRD results show that in sample S1, the planes (011), (112),(100), (110), (121), (200), (111), (301) and (022) identify with the planes of sample S2. But the plane(122) can be seen in the simple S2 only. All the planes can be attributed to silicate (SiO_2) plane which is matched well with the standard library file.

The planes in sample S1 and S2which (403),(710), (113), (-603), (-601), (-112), (111), (-111), (-210),(001) and (200)identify with the planes in AL_2O_3 from the library file in XRD. But the planes (202) and (-602) can be seen in sample S1 only. The plane (601), (-403) and (600) can be seen in sample S2 only(Guy, 1992).

According to the five conventional bricks, without wood fibre(None) and currently used in Hmawza of Pyay District, the average compressive strength is 6.13MPa. But The average compressive strength of0.5wt%(M1), 1wt%(M2) and 1.5wt% (M3)wood- fibres content bricks are found to be 6.79MPa, 8.66MPa and 3.761MPa respectivelyin Table 3 and were describedwith bar graph in figure 9.

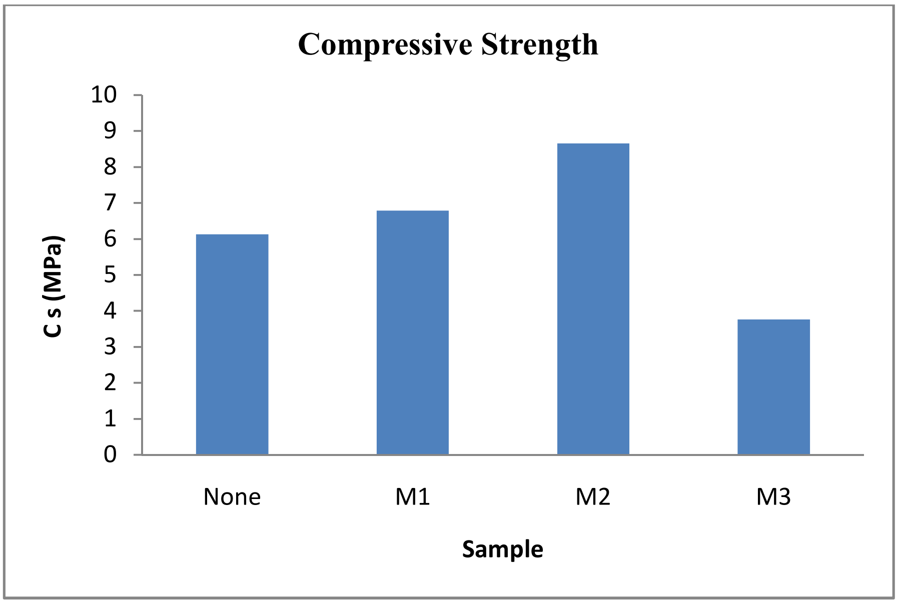

Figure 9 Compressive strength vs different fibres content

The average bending strength modulus of 5 bricks without wood-fibres (None) for each loadsuch as 100, 150 and 200N were 83.9MPa, 86.6MPa, 89.2 MPa. The modulus values of various fibres content bricks M1, M2 and M3 were increasing for every load. It was noted that the average bending strength modulus of M2 which has the highest values were 117.8MPa, 139.84MPa, 161.321MPa respectively. From the results of bending strength modulus were described with bar graph in figure 10.

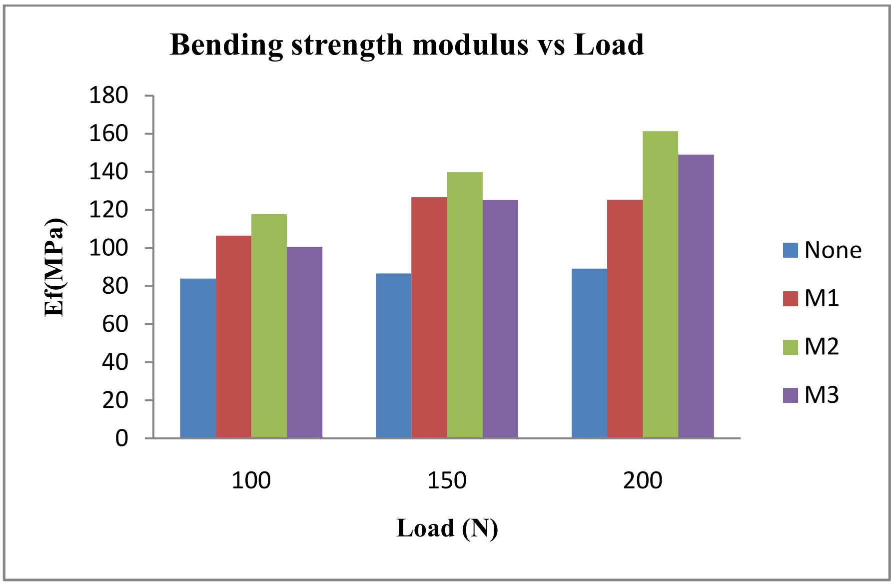

Figure 10 Bending strength modulus vs different fibre contents

Conclusion

According to the EDXRF results,iron (Fe) is the highest concentration in natural clay from Hmawzar village. When the natural clay was mixed with chaff, their consisted values are not changed. But rubidium (Rb) element contains in S2 is greater than S1. Rubidium element has the properties of tracking the trace of oxygen from the materials.

From the XRD results, silicon dioxide and aluminum oxide are found in the natural clayfrom Hmawzarvillage. They have the properties of cement. So, this natural clay has been appropriated for making bricks (Callister, 1997).

The average value of compressive strength of brick samples which were made by the mixture of natural clay and paddy shell without mixing wood fibre is 6.13 MPa. This value is to be agreed with the BIS (Bureau of Indian Standard,BIS 1077-1992) standard values of ordinary class clay brick. So that conventional bricks currently used in Hmawzarvillage is safein construction.

The average bending strength modulus of 5 bricks without wood-fibres (None) for each loadsuch as 100N, 150N and 200N were 83.9 MPa, 86.6 MPa, 89.2 MPa. The modulus values of various fibres content bricks M1, M2 and M3 were increasing for every load.

From the above mentional results, the wood-fibres are the appropriate additive to prepare bricks with higher compressive strength and bending strength modulus but not more than 1wt% fibres content.

And also it can be concluded that, the present work has primarily been focused upon the compressive strength and bending strengrh modulus will be supported for further studies concerning the environmental safety and protecting the building from damaging by the natural disasters such as earthquakes, storm, land-slide, etc.

Acknowledgements

I wish to express my sincere thanks to Dr Aung Aung Min, Acting Rector of Pyay University, Dr Thwe Linn Ko, Pro-Rector of Pyay University.

I would to thank Professor Dr Soe Soe Nwe, Head of Department of Physics, Pyay University for her kind permission to do this work.

I also would like to thank Rector (YU) Dr Pho Kaung, Professor DrKhinKhin Win (Head of Department of Physics,YU) for their permission to present this research report.

Finally, I would to express my gratitude to all teachers for their kind advices and help in completing this research work.

References

Chris Pellant, (1992),*Rocks and Minerals*, Dorling Kindersley limited, London.

Callister.W.D., (1997), *Materials Science and Engineering*, Toranto: Wiley.

Guy.A.G., (1992), *Introduction to Materials Science*, London: Mc Graw-Hill.

Nicole M. Stark & Robert E.Rowlands, (2003), “Effects of Wood Fiber on Mechanical Properties of Wood / Polypropylene Composites”,*Wood and Fiber Science*, Vol 35(2), pp167-174

J. Myanmar Acad. Arts Sci. 2020 **Vol. XVIII.No.2A**

SYNTHESIS AND CHARACTERIZATION OF REDUCED GRAPHENE OXIDE BY CHEMICAL REDUCING METHOD

Saint Zar Hlwar Lwin Aung[1], Hla Toe[2], Cho ChoThet[3]

Abstract

Graphene oxide (GO) and reduced graphene oxide (rGO) were successfully synthesized by modified Hummer's method and chemical reduction method. The essential parameters including oxidation and reduction process were confirmed by both visualization and by using characterization tools. Ultraviolet-visible(UV-vis), Fourier transform infrared (FT-IR) and X-ray diffraction (XRD) were conducted for the formation of targeted product, compound identification and crystal structures of synthesized materials. It was found out that the chemical reduction method could successfully reduce GO to rGO without using high energy consumption. Finally, this method results in high reduction degree of GO and large amount of rGO.

. **Keywords**: graphene oxide, reduced graphene oxide, chemical reduction

Introduction

The conversion of light energy changes directly into electricity by solar cell devices represents one of the most promised for highly remarkable and renewable power. Many different types of solar cells including Si-based, thin film, organic and polymer solar cell and perovskite solar cells have been studied and produced. Among them, perovskite solar cells are the rapidly emerging as the photovoltaic (PV) technology since it has high mobility and fast respond to light, highly efficient and friendly to environment. Perovskites possess properties similar to inorganic semiconductors and the power conversion efficiency of these has improved from 3.8 % to 22.1 % within 7 years (Johan *et al.*, 2017). Recently, graphene-based materials have been used as promising candidates for electron buffer layers for organic electronic applications.

Many believe that perovskites are the future of solar power and researchers are discovering how to combine graphene with perovskites to create even more efficient PV. Recently, planar perovskite solar cells with reduced graphene oxide nanosheets as the hole transport layer was fabricated (Yeo *et al.*, 2014).This perovskite layer is not only highly efficient but also has device stability. Its distinctive structure makes them perfect for enabling low-cost, high efficiency, thin, lightweight and flexible panels. The aim of this research is to synthesize the reduced graphene oxide (rGO) nanoparticles in order to use it as a hole transport layer of perovskite solar cells.

Graphite oxide was firstly produced from pristine graphite by using strong oxidizing agents. However, graphite oxide and GO can be produced by similar in chemical process but different in their structure (Dreyer *et al.*, 2010). Graphite oxide is a bulk solid and itcan be changed into few layer GO by using thermal or mechanical process. Especially, the ultrasonic exfoliation of graphite oxide (sonication method) was an effective way to obtain a single or few layers of GO. GO is the oxide form of graphene, where a large number of oxygen-containing functional groups are bonded with carbon atoms. The presence of oxygen functional groups makes the inter layer spacing of GO larger than graphite. Therefore, GO has high specific surface

---

[1] Assistant Lecturer, Department of Physics, Pyay University

[2] Associate Professor, Department of Physics, University of Yangon

[3] Associate Professor, Department of Physics, Myeik University

area, high mesopore volume, and certain level of electrical conductivity(Hsu *et al.*,2018). In contrast, rGO contains fewer amounts of oxygen functionalized groups as compared to GO which can be synthesized in chemical reagent and thermal reduction and multistep reduction. The reduction of GO is not only for removing the oxygen functional group but also for recovering the conjugated network of the graphitic lattice. These structure changes obtained the more electrical conductivity and other properties of grapheme (Wang *et al.*,2008).

On the other hand, high reduction temperature and strong reducing agents are required for the complete conversion of GO to rGO. High-temperature reduction processes require excessive energy consumption and get wrinkly amount of rGO sheet. Strong reduction agent can be realized GO interacts with chemical reagent and it can produce a large amount of rGO and can exhibit excellent electrical conductivity. There are plenty of reducing agents such as phenyl hydrazine, hydrazine hydrate, sodium borohydride, ascorbic acid, amino acids and strongly alkaline solutions were used in the past and recently work. In this work, the reduced graphene oxide (rGO) was prepared by using strong reducing reagent sodium borohydride ($NaBH_4$) in order to get mass production and more efficient in conductivity. And also, calcium chloride ($CaCl_2$)was used as catalyst to improve the reduction ability of $NaBH_4$.This method is a cheaper and easily available way for the mass production of rGO compared with thermal reduction.

Materials and Methods

Synthesis of Graphite Oxide

In this synthesis, Graphite powder, sulfuric acid(H_2SO_4,98%) and potassium permanganate($KMnO_4$) were used as a graphite oxide source, solvent and oxidizing agent according to the modified Hummers method (Zaaba *et al.*,2017). Typically, graphite powder (1 g) was dissolved in concentrated H_2SO_4 (50 ml) and phosphoric acidH_3PO_4 (5.5 ml) volume ratio (9:1) with stirring and then $KMnO_4$ (3 g) was slowly added to the mixture. The reaction mixture was then heated to 40^0C for 6 h. After that, 100 ml of deionized water (DI) was slowly added to the reaction mixture in order to fully stop the oxidation process. Then, the slurry was quenched inside the ice bath. Hydrogen peroxide (H_2O_2) (30 wt%, 10 ml) was slowly added to remove the excess $KMnO_4$. The resultant suspension of graphite oxide was separated by centrifugation and then the remaining solid was thoroughly washed with 1 Mhydrochloric acid(HCl) followed by DI water and acetone to remove the sulfate and contaminations. The gel-like graphite oxide was dried at only room temperature.

Synthesis of Graphene Oxide (GO)

Subsequently, previous synthesized graphite oxide was filtered and washed with DI water, 1 M HCl and acetone. The filtered paste was dissolved in 100 ml of DI water. And then, the solution was sonicated for 2 h to exfoliate the layers and centrifuged for 20 mins each at 4000 rpm for several times. Finally, GO flake was thus obtained and dried only at room temperature.

Synthesis of Reduced Graphene Oxide (rGO)

For synthesis of rGO, chemical reducing method was used. GO paste, $NaBH_4$, $CaCl_2$and DI water were used as an rGO source and reducing agents and solvent. Firstly, as-prepared GO paste was diluted in DI water to form a suspension of 30 ml, 3 mg/ml. Secondly, $NaBH_4$ (0.342 g) and 50 mM of $CaCl_2$ (0.15 g) then were added to a 30 ml of GO suspension. The mixture was kept stirring at room temperature until complete reduction. The final mixture was centrifuged for 20 minsat 4000 rpm to remove aggregated rGO particles. Finally, the obtained black rGO powder was dried only at room temperature for 24 hours for further characterization.Figure 1 illustrates the experiment procures of reduced graphene oxide (rGO).

Figure 1 Experimental procedures for synthesis of reduced graphene oxide (rGO)

Characterization

Graphite, as- prepared graphite oxide, GO and rGO were analyzed by using several techniques. The absorbance of GO and rGO solutions were detected by EVOLUTION220 UV-Visible Spectrophotometer. FTIR NICOLET iS5 spectrophotometer was used to characterize the presence of functional groups in as-prepared samples. X-ray diffraction (XRD) patterns of graphite, graphite oxide and graphene oxide and reduced graphene oxide were recorded by RIGAKU-RINT 2000 XRD machine to identify the crystal structure of synthesized samples.

Results and Discussion

Figure 2 shows the colloidal graphite oxide, GO, and rGO in water. Graphite oxide synthesized by modified Hummer's method results in a yellow is haqueous suspension when dispersed in water as shown in Figure 2(a). Figure 2(b) is confirmed that the exfoliation of previous graphite oxide by sonication results in a brown color and semitransparency of GO. Hydrophilic properties of GO was due to their negative surface charge induced the electrostatic repulsion among them and making it strongly hydrophilic(Park *et al.*,2009). In contrast, blackprecipitates are formed when the GO was reduced by chemical reduction method, as shown in Figure 2(c). This is a hydrophobic characteristic of rGO orgraphene sheets with less polar functionality on the surface of the sheets, compared to that of GO (Stankovich S *et al.*,2007).

Visualization

Figure 2 (a) Graphite oxide (b) Graphene oxide(GO) (c) Reduced Graphene oxide(rGO)

UV-Vis result

From Figure 3, the strong absorption peak of GO at 230 nm and it is quite similar with the work reported by (Li*et.,al.,* 2008)where the absorption peak was at 231nm.Then, the peak was red-shifted to 297 nm after reduction using $NaBH_4$and $CaCl_2$, respectively. The absorption of rGO peak red shifted to 297nm suggests that the electronic conjugation within graphene sheets was restored (increased electron concentration after the reduction).

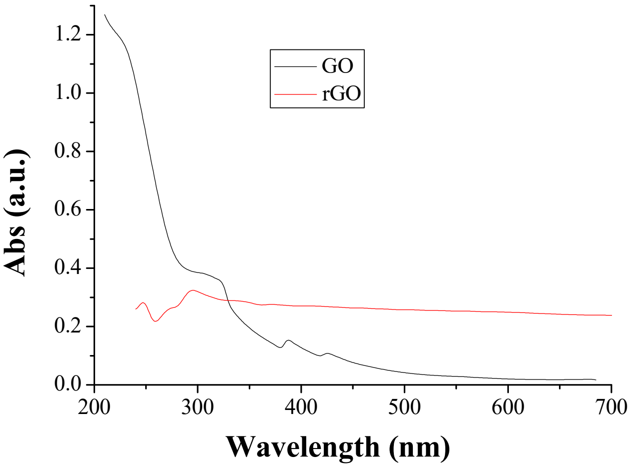

Figure 3 UV-VIS spectrum of graphene oxide and reduced graphene oxide

FT-IR result

The presence of different types of oxygen functional groups in GO and rGO were confirmed by their FT-IR spectra as shown in Figure 4.The broad peaks observed around 3300 cm^{-1}were due to stretching vibration of O-H groups. Besides, the various oxygen functional groups such as alkoxy stretching peak (1030 cm^{-1}), epoxy stretching vibration peak (1152 cm^{-1}) and -C = O stretching vibration peak (1734 cm^{-1}) can be seen in the FT-IR spectra(Zhang *et al.,*2010).The rGO peak at (1617 cm^{-1}) was due to stretching vibration of C=C (Marcano *et al.,*2010).By matching GO and rGO peaks, the rGO peak dramatically reduced after reduction using $NaBH_4$ and $CaCl_2$ where the carbonyl group can be reduced effectively according to Figure 4. The remaining distant peaks for rGO appearing at(1560 cm^{-1}), (1373cm^{-1}), (900 cm^{-1})were assigned to aromatic C=C,O-H in-plane bending and O-H out of plane bendingre spectively(Yang *et al.,* 2015).Thus, some oxygen containing functional group of GO were eliminated by using $NaBH_4$as a reducing agent and $CaCl_2$as a catalysis.

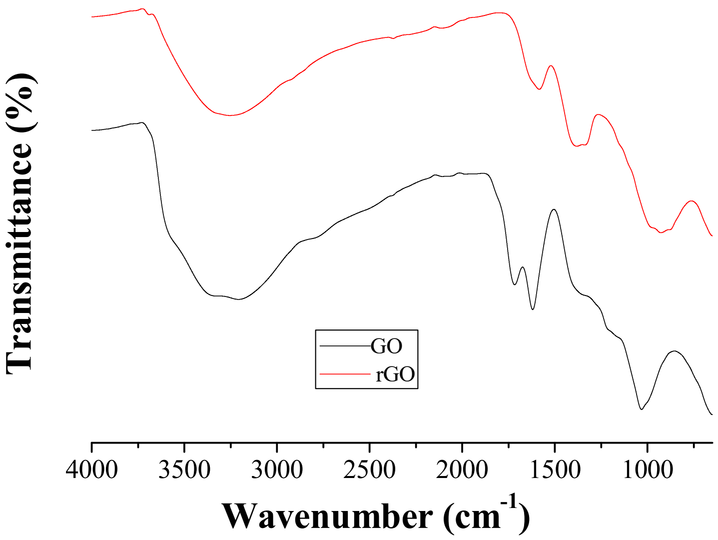

Figure 4 FT-IR spectra of GO and rGO

XRD Result

In this analysis, XRD was used to determine the crystal structure and match the interlayer spacing of graphite, graphite oxide, GO and rGO. The interlayer spacing of obtained samples can be calculated according to the bragg's law (Li *et al.,*2015) .

$$n\lambda = 2d\sin\theta$$

where, n is the diffraction series , λ is the X-ray wavelength($\lambda = 1.54\ A^{\circ}$),d is interlayer spacing and θ is the angle between the wave vector of the incident plane wave.The 2θ peak of graphite powder was at26°, indicating that the interlayer distance of graphite powder was 3.42Å. After chemical oxidation, the 2θ peak shifted to10°, which indicates that the graphite was fully oxidized into graphite oxide with an interlayer distance of 8.83 Å. After sonication, 2θ peak of graphene oxide was also 11°which is similar to graphite oxide's peak and its interlayer distance was 8.03 Å. After reduction, a narrow 2θ peak was found out to be at 25° suggesting that the rGO was almost fully reduced. The interlayer distance of rGO is 3.56 Å which is fairly close to that of graphite powder (3.42 Å). This condition can be obviously seen in Figure 5and Figure 6.

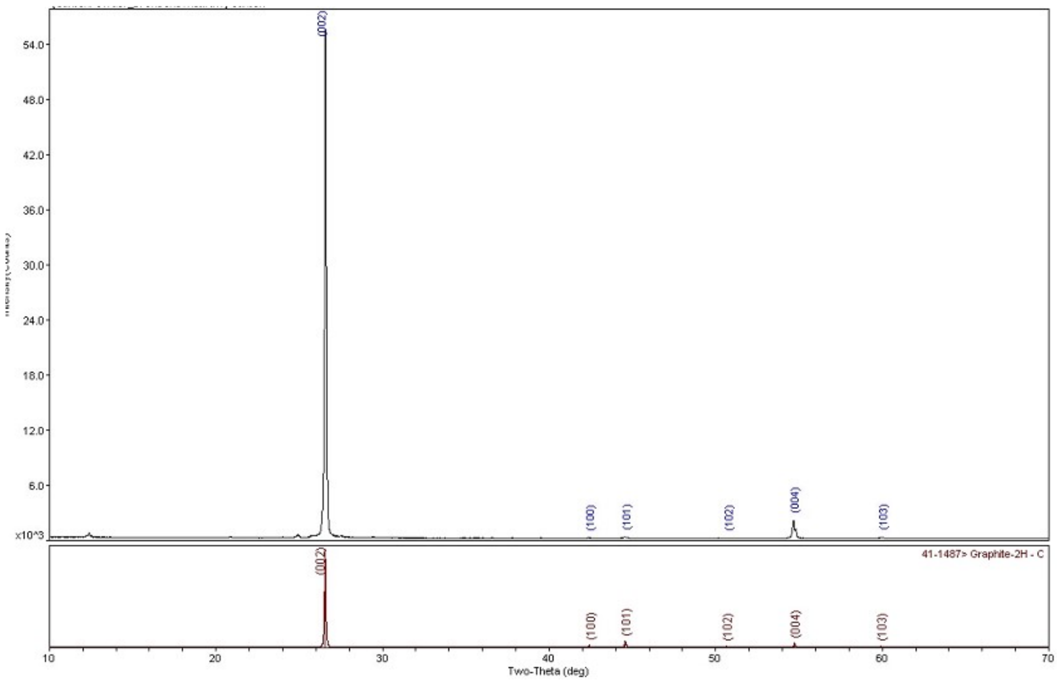

Figure 5 XRD spectrum of Graphite powder

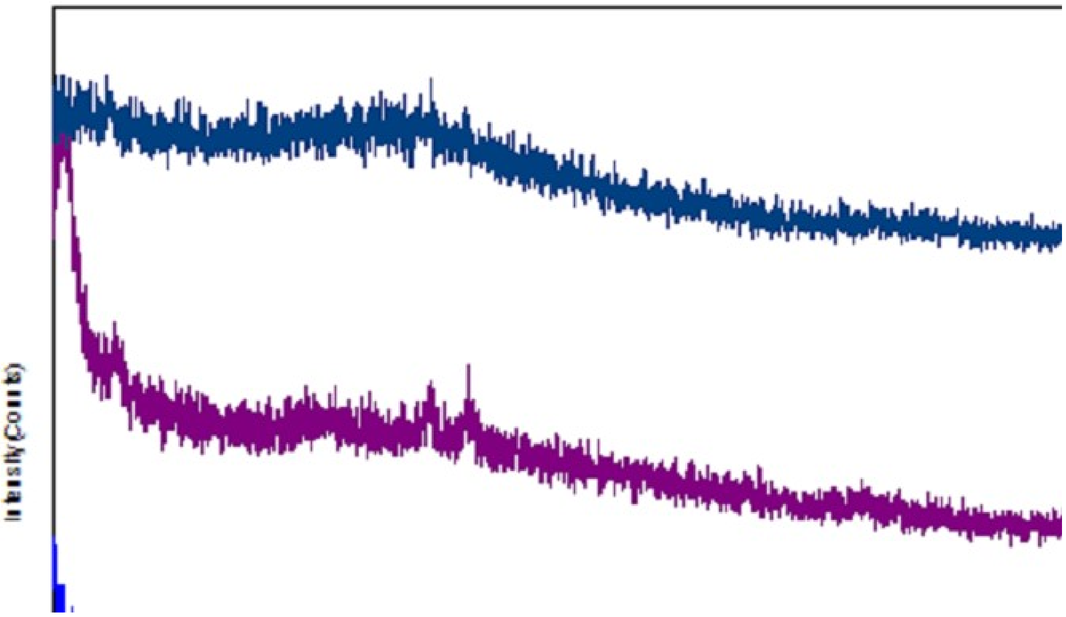

Figure 6 XRD spectra of graphite oxide, graphene oxide and reduced graphene oxide

Conclusion

In this research, graphite to graphite oxide was synthesized by modified Hummer's method by systematically varying the experimental parameters including temperature, reaction time and concentration of $KMnO_4$. Graphene oxide (GO) was successively prepared by sonication process. Reduced graphene oxide (rGO) was effectively synthesized by chemical reduction method using strong chemical reducing agents, $NaBH_4$ together with $CaCl_2$at room temperature. The formation of targeted products including graphite oxide, GO and rGO were completed by observing the color changing throughout the process. Visualized results were additionally confirmed by characterization tools such as UV-vis , FT-IR and XRD.UV-Vis result suggested that maximum absorption wavelength occurred at 230 nm and 297 nm of the synthesized samples were GO and rGO. By FT-IR results, some oxygen containing functional group of GO were successfully eliminated by using strong reducing agent$NaBH_4$ and $CaCl_2$ and this tended to successful formation of rGO. Therefore, it is obviously that $NaBH_4$ and $CaCl_2$are most effective at reducing -C = Ospecies. Finally, the formation of GO and rGO by interlayer distance of XRD results confirmed that the final product was reduced graphene oxide.

Acknowledgements

I would like to acknowledge to Professor Dr Khin Khin Win, Head of Department of Physics, University of Yangon, for her encouragement of this work.I also wish to express my thanks to Professor Dr Aye Aye Thant, Department of Physics, University of Yangon, for her valuable advice for this work. My sincere thanks go to Professor Dr Ye Chan, Head of URC, for allowing me to work at URC.I do specially thank you to my supervisor, Dr Hla Toe, Associate Professor, Department of Physics, University of Yangon, for his valuable advice and suggestions for this work. I also do specially thanks to my co-supervisor, Dr Cho Cho Thet, Associate Professor, Department of Physics, Myeik University, who gives me valuable comments, suggestions, a large number of excellent discussions throughout my work.

References

Dreyer D. R., S. Park, C. W. Bielawski, and R. S. Ruoff, “The chemistry of graphene oxide,” *Chem. Soc. Rev.*, Vol. 39, No. 1, 2010,pp. 228–240.

Hsu H., C. Wang, Y. Chang, J. Hu, B. Yao, and C. Lin, “Journal of Physics and Chemistry of Solids Graphene oxides and carbonnanotubes embedded in poly- acrylonitrile-based carbon nano fi bers used as electrodes for supercapacitor,” *J. Phys. Chem. Solids*, Vol.85, 2015, pp. 62–68.

Johan E. k ., Weis “Graphene Research and Advances Report”,No 1, 2017.

Li D., Muller MB, Gilje S, Kaner RB, Wallace GG, “Processable aqueous dispersions of graphenenanosheets,” Nat Nanotechnol 2008;3(2):101–5.

Li J., X. Zeng, T. Ren, and E. Van Der Heide, “The Preparation of Graphene Oxide and Its Derivatives and Their Application in Bio-Tribological Systems,” Lubricants,2014, Vol. 2, pp. 137–161.

Marcano D. C, Kosynkin DV, Berlin JM, Sinitskii A, Sun Z, Slesarev A, Alemany LB, Lu W,Tour JM,“ Improved synthesis of graphene oxide,” ACS Nano 4(8), 2010, pp. 4806–4814

ParkS.and R. S. Ruoff, “Chemicalmethods for the production of graphenes,” *Nature Nanotechnology*, Vol. 5, No. 4,2009, pp. 217–224.

Stankovich S., D. A. Dikin, R. D. Piner, “Synthesis of graphene-based nanosheets via chemical reduction of exfoliated graphite oxide,” *Carbon* Vol. 45, No. 7, 2007, pp. 1558–1565.

Wang G., J. Yang, J. Park, X. Gou, B. Wang, H. Liu and J. Yao, J. “Phys. Chem,” C, 2008, 112, pp. 8192–8195.

YangZ.Q. Zheng, H. Qiu, J. Li, J.Yang, “A simple method for the reduction of graphene oxide by sodium borohydride with CaCl2 as a catalyst,”Vol. 30,No.1,2015.

Yeo J.S., R. Kang, S. Lee, Y.J.Jeon, N.Myoung, C.L. Lee, D.Y. Kim, J.M. Yun, Y.H. Seo, S.S. Kim, S.I. Na, “Highly efficient andstable planar perovskite solar cells with reduced graphene oxide nanosheets as electrode interlayer,”2014, http://dx.doi.org/10.1016/ j.nanoen.2014.12.022.

ZaabaN.I, K.L.Foo, U.Hasjim, S.J.Tan, W.W. Liu, C.H. Voon, “Synthesis of Graphene Oxide using modified Hummers Method: Solvent Influence,”Procedia Engineering 184, 2017,pp. 469-477

Zhang J., H. Yang , G. Shen , P. Cheng , J. Zhang , S. Guo , “Reduction of graphene oxide via L-ascorbic acid,”*Chem. Commun.* **2010** ,*46* , 1112-4

J. Myanmar Acad. Arts Sci. 2020 **Vol. XVIII.No.2A**

EXPERIMENTAL STUDY OF STRUCTURAL, VIBRATIONAL AND OPTICAL BAND GAP OF NICKEL DOPED TIN OXIDE

Zin Bo Htut[1], Myo Paing Htwe[2], Win Kyaw[3] and Soe Soe Nwe[4]

Abstract

Undoped Tin Oxide (SnO_2) and Nickel doped Tin Oxide, $Sn_{0.5}Ni_{0.5}O_2$ were prepared by chemical co-precipitation method. Analytical Reagent grade Stannous Chloride Double-hydrate ($SnCl_2.2H_2O$) and Nickel Chloride Hexahydrate ($NiCl_2.6H_2O$) were used to prepare the desired materials. De-ionized (DI) water is used as the solvent to prepare saturated solutions. Aqueous Ammonia is used as an agent material. The co-precipitated $SnO_2$and $Sn_{0.5}Ni_{0.5}O_2$were annealed at 350°C for 2 h. The samples were characterized by X-ray Diffraction (XRD), Fourier Transform Infrared (FTIR) and Ultra-Violet Visible-Near Infrared (UV-VIS-NIR) spectroscopy to study the structural, vibrational and optical properties of the samples. XRD patterns showed that the samples analogous to tetragonal structure. The broadening of observed spectral lines indicated the fine particle nature. FTIR spectra confirmed the existence of the sample phase. Optical energy band gaps were determined from $(\alpha h\upsilon)^2$ vs. $h\upsilon$ graphs by using UV-VIS-NIR transmission spectra.

Keywords: SnO_2, $Sn_{0.5}Ni_{0.5}O_2$, co-precipitation method, XRD, FTIR, UV-VIS-NIR.

Introduction

Tin Oxide (SnO_2) is an important material due to its properties such as high degree of transparency in the visible spectrum, strong physical and chemical interaction with adsorbed species, low operating temperature and strong thermal stability in air (up to 500°C) [Azurdia,(2006)].It is an n-type semiconductor with a large band gap(3.6 eV at the room temperature), which can be used in gas sensor, solar cells, glass electrodes and secondary lithium batteries [Julian, (2003)].

A number of attempts have been made by developing effective synthetic techniques in the preparation of metal ions-doped SnO nanoparticles, such as sol-gel, co-precipitation [Khan,(2015)] and chemical vapor deposition [Liu,(2015)]. In this work, undoped SnO_2 and Ni-doped SnO_2 nanoparticles were prepared by chemical co-precipitation method and structural, vibrational and optical characteristics of the as-prepared samples were studied by XRD, FTIR and UV-VIS-NIR spectroscopy.

Experimental Details

Preparation of Samples

Undoped Tin Oxide, SnO_2 and Nickel doped Tin Oxide, $Sn_{0.5}Ni_{0.5}O_2$ were prepared by chemical co-precipitation method. For the preparation of undoped Tin Oxide, SnO_2 sample, the starting materials of Analytical Reagent (AR) grade Tin Chloride Double-hydrate ($SnCl_2.2H_2O$) was used and the Ammonia solution was used as an agent. Also for the preparation of Nickel doped Tin Oxide, $Sn_{0.5}Ni_{0.5}O_2$ sample, Tin Chloride Double-hydrate ($SnCl_2.2H_2O$) and Nickel Chloride Double-hydrate ($NiCl_2.2H_2O$) were used as the starting materials. Flow diagrams of the sample preparation procedure of undoped SnO_2 and $Sn_{0.5}Ni_{0.5}O_2$are shown in Figure 1(a) and (b).

---

[1] Demonstrator, Department of Physics, Pyay University

[2] Lecturer, Department of Physics, Pyay University

[3] Dr, Associate Professor, Department of Physics, Pyay University

[4] Dr, Professor and Head, Department of Physics, Pyay University

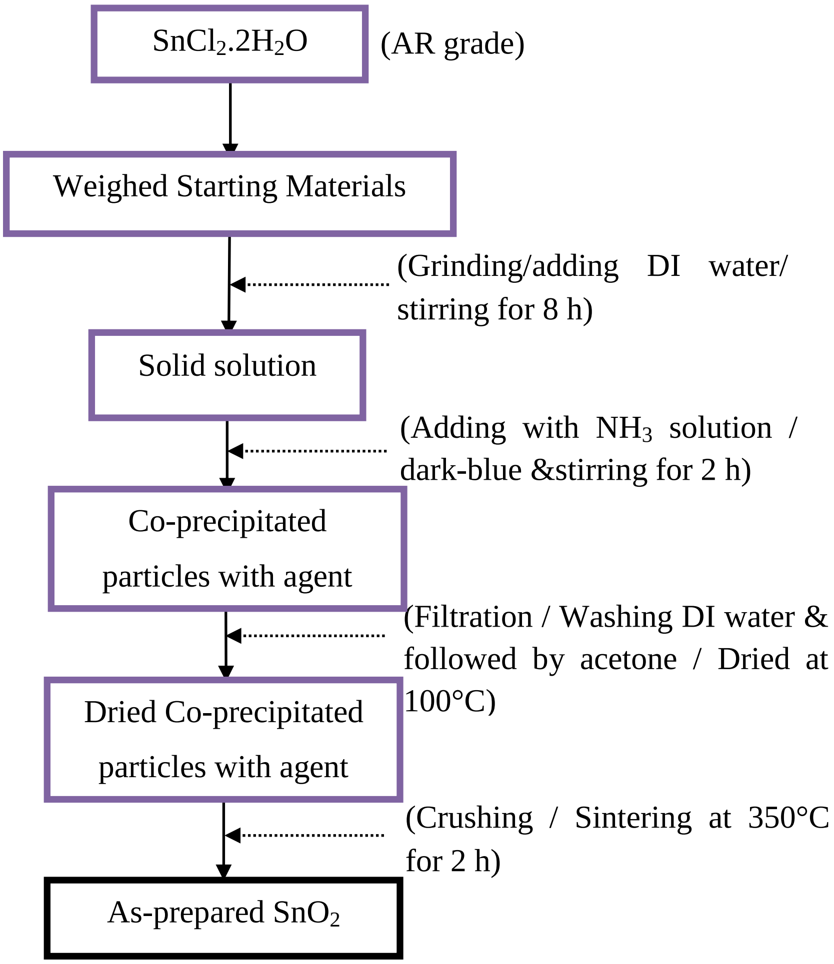

Figure 1 (a) Flow diagram of undoped SnO_2 sample preparation

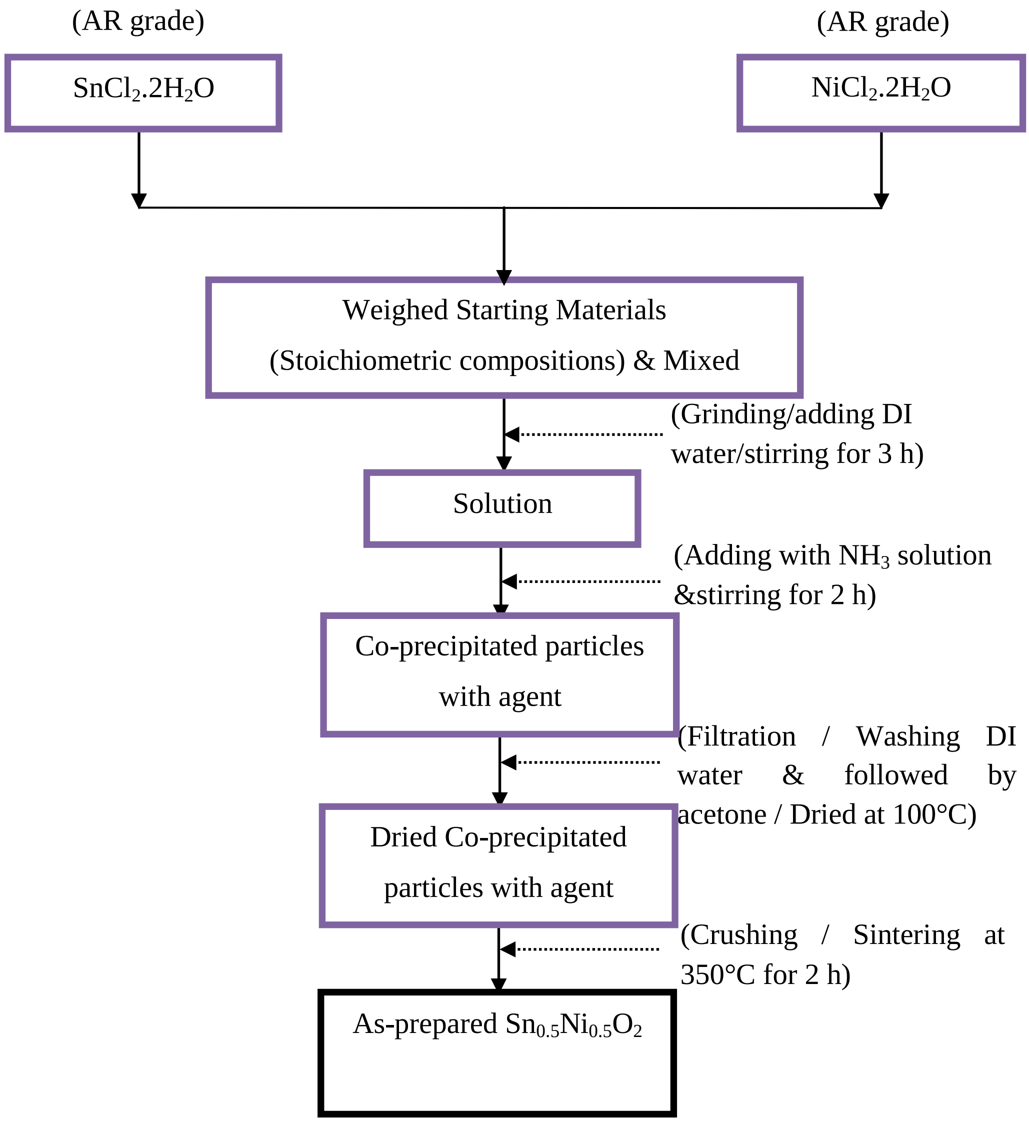

Figure 1(b) Flow diagram of $Sn_{0.5}Ni_{0.5}O_2$ sample preparation

XRD, FTIR and UV-VIS-NIR Measurements

Phase formation, structure analysis, the lattice parameters evaluation and crystallite sizes estimation of Nickel doped Tin Oxide, $Sn_{0.5}Ni_{0.5}O_2$ and undoped Tin Oxide, SnO_2samples were investigated by PC-controlled RIGAKU MULTIFLEX X-ray Diffractometer [Universities' Research Centre (URC), University of Yangon] using Ni-filter with CuK_α radiation, $\lambda = 1.54056$ Å. Vibrational characteristics and mode assignments of the samples were studied by Fourier Transform Infrared (FTIR) spectroscopy. FTIR transmission spectra were observed by PC-controlled SHIMADZU FTIR-8400 Spectrophotometer [Universities' Research Centre (URC), University of Yangon]. Optical transmission and energy band gaps were determined by using Ultraviolet-Visible-Near Infrared (UV-VIS-NIR) spectroscopy. UV-VIS-NIR transmission spectra were collected on PC-controlled UV-1800 Spectrophotometer.

Results and Discussion

Structural Investigation

Powder XRD patterns of Nickel doped Tin Oxide, $Sn_{0.5}Ni_{0.5}O_2$ and undoped Tin Oxide, SnO_2samples are shown in Figure 2(a) and (b). To assign the observed XRD lines, the collected spectral lines were identified by using standard JCPDS data library files of

(i) Cat. No. 77-0447>Cassiterite, syn - SnO_2 and Cat. No. 89-7130>Bunsenite, syn - NiO for theNickel doped Tin Oxide, $Sn_{0.5}Ni_{0.5}O_2$ sample and

(ii) Cat. No. 99-0024>SnO_2 – Cassiterite for undoped Tin Oxide, SnO_2sample.

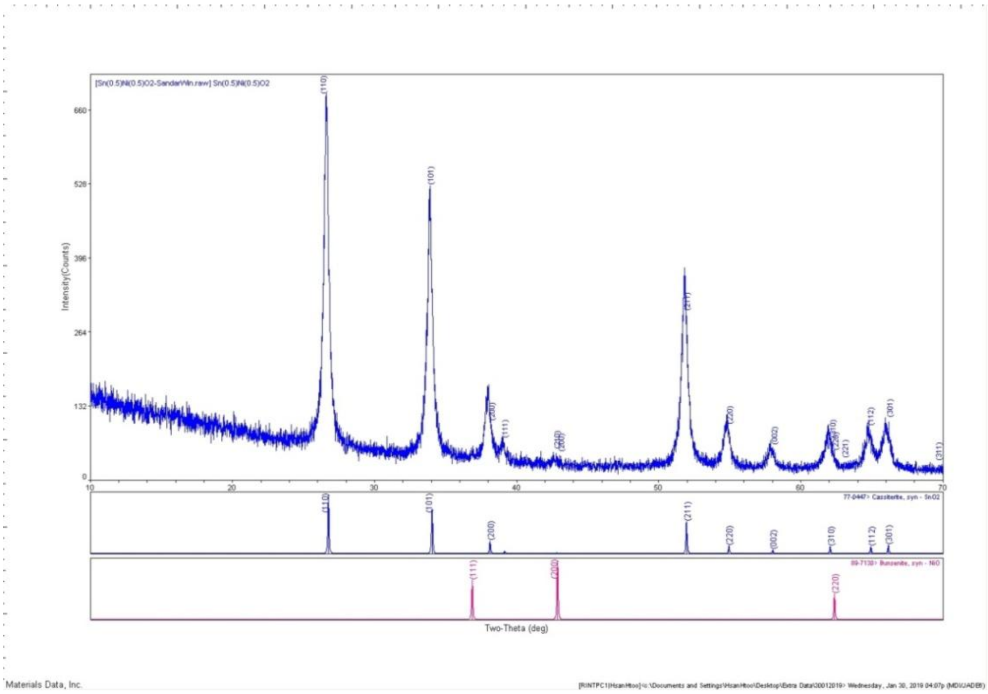

Figure 2 (a) XRD pattern of $Sn_{0.5}Ni_{0.5}O_2$

The observed diffraction lines are found to be mostly agreed with standard JCPDS and it indicates the $Sn_{0.5}Ni_{0.5}O_2$and undoped SnO_2 samples belong to tetragonal structure. The lattice parameters are evaluated by using crystal utility of the equation, $\frac{1}{d^2}=\frac{h^2+k^2}{a^2}+\frac{l^2}{c^2}=\frac{4\sin^2\theta}{\lambda^2}$, where (hkl) is the Miller indices, "d' is the atomic spacing (Å) and "*a* and *c*" are the lattice parameters (Å). The lattice parameters are obtained as a = b = 4.66 Å and c = 3.15 Åfor $Sn_{0.5}Ni_{0.5}O_2$and a = b = 4.74 Å and c = 3.20 Åfor SnO_2.

The crystallite sizes of the samples were estimated by using the Scherrer formula,

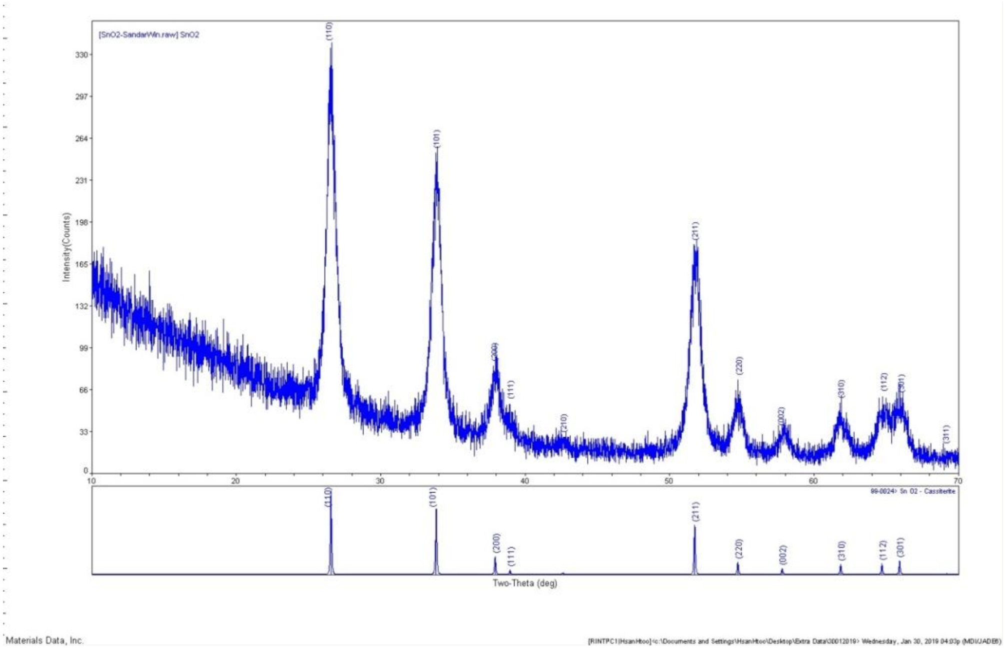

Figure 2 (b) XRD pattern of SnO_2

$D = \frac{0.9\lambda}{B\cos\theta}$,where "*D*" is the crystallite size (nm), "λ' is the wavelength of incident X-ray (Å), "θ" is the diffraction angle of the peak under consideration at FWHM (°) and "B" is the observed FWHM (radians). The crystallite sizes are obtained as 33.82 nm for $Sn_{0.5}Ni_{0.5}O_2$and 27.74 nm for SnO_2. It was found that the crystallite sizes of the samples varied with the dopant effects of Ni on Sn. The obtained crystallite sizes indicate the nanosized nanocrystalline materials and the samples are the very fine particle nature.

Vibrational Analysis

According to the molecular vibrational theory, a diatomic molecule has two types of normal vibrations: (i) transverse-optical and (ii) longitudinal-optical vibrations and also a non-linear tri-atomic molecule such as SnO_2 and $(Sn_{0.5}Ni_{0.5})O_2$ has three types of molecular vibrations: (i) υ_1-mode (symmetric-stretching), (ii) υ_2-mode (bending) and (iii) υ_3-mode (asymmetric-stretching) respectively.

In the present work, FTIR transmission spectra of Nickel doped Tin Oxide, $Sn_{0.5}Ni_{0.5}O_2$ and undoped Tin Oxide, SnO_2samples are shown in Figure 3(a) and (b). The observed wavenumbers corresponding vibrational characteristics of the samples are tabulated in Table 1(a) and (b). The observed wavenumbers of the $Sn_{0.5}Ni_{0.5}O_2$ and $SnO_2$are found to be clearly shifted due to crystalline environments.

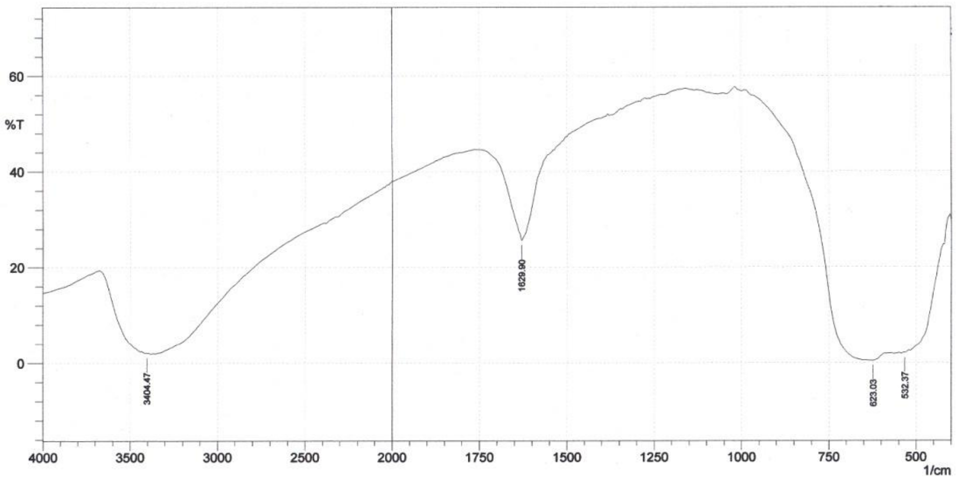

Figure 3 (a) FTIR spectrum of $Sn_{0.5}Ni_{0.5}O_2$

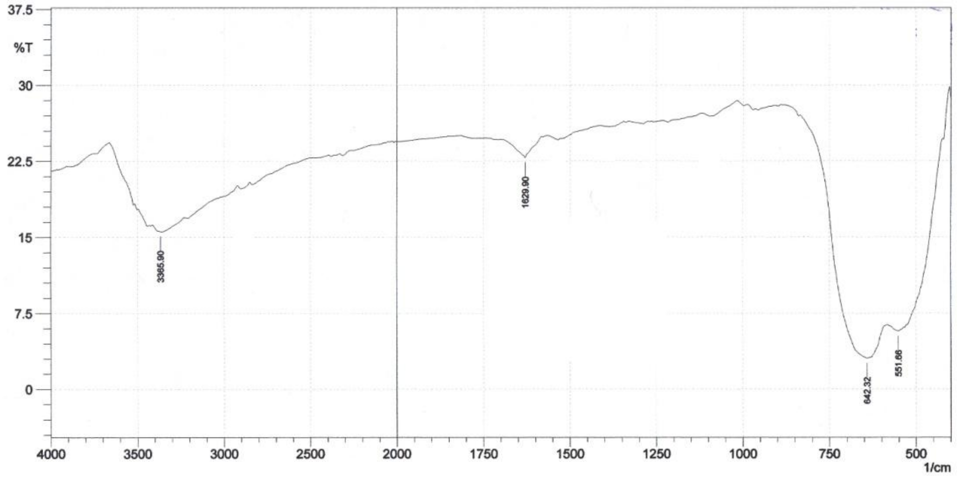

Figure 3 (b) FTIR spectrum of SnO_2

The lines at 1630 cm^{-1} and 3404 cm^{-1}in Figure 3(a) and the lines at 1630 cm^{-1} and 3366 cm^{-1}in Figure 3(b) indicate the (υ_2-mode) bending vibration of H_2O molecules and (υ_3-mode) asymmetric-stretching vibration of H_2O molecules. These lines appear in FTIR spectra of KBr pellet method due to the distribution of moisture in the surrounding of FTIR spectrophotometer.

Table 1 (a) Wavenumbers and corresponding vibrational characteristics of $Sn_{0.5}Ni_{0.5}O_2$

Wavenumbers (cm^{-1})	Vibrational characteristics	Molecules
532	υ_{TO}-stretching	$Sn_{0.5}Ni_{0.5}O_2$
623	υ_{TO}-stretching	$Sn_{0.5}Ni_{0.5}O_2$
1630	υ_2-bending	H_2O
3404	υ_3-asymmetric stretching	H_2O

Table 1 (b) Wavenumbers and corresponding vibrational characteristics of SnO_2

Wavenumbers (cm^{-1})	Vibrational characteristics	Molecules
552	υ_{TO}-stretching	SnO_2
642	υ_{TO}-stretching	SnO_2
1630	υ_2-bending	H_2O
3366	υ_3-asymmetric stretching	H_2O

UV-VIS-NIR Analysis

To determine the optical band energies of the Nickel doped Tin Oxide, $Sn_{0.5}Ni_{0.5}O_2$ and undoped Tin Oxide, SnO_2samples, UV-VIS-NIR transmission spectra were observed. UV-VIS-NIR transmission spectra are shown in Figure 4(a) and (b). The spectra show that the samples demonstrate that less than 100% transmittance of throughout the spectrum. The theory of optical transmission gives the relationship between the absorption coefficient "α" and the photon energy "hν' has a relation; $\alpha = -\ln (1/T)$. Plots of the variation of $(\alpha h\nu)^2$ versus hν graphs are shown in Figure 5(a) and (b). The optical band gap "E_g" can be obtained by using the extrapolating the interception of the highest and linear portion of $(\alpha h\nu)^2$-hν curve on hν (energy) axis. The optical band gaps of the $Sn_{0.5}Ni_{0.5}O_2$ and SnO_2samples are obtained as 3.9 eV and 3.6 eV respectively.

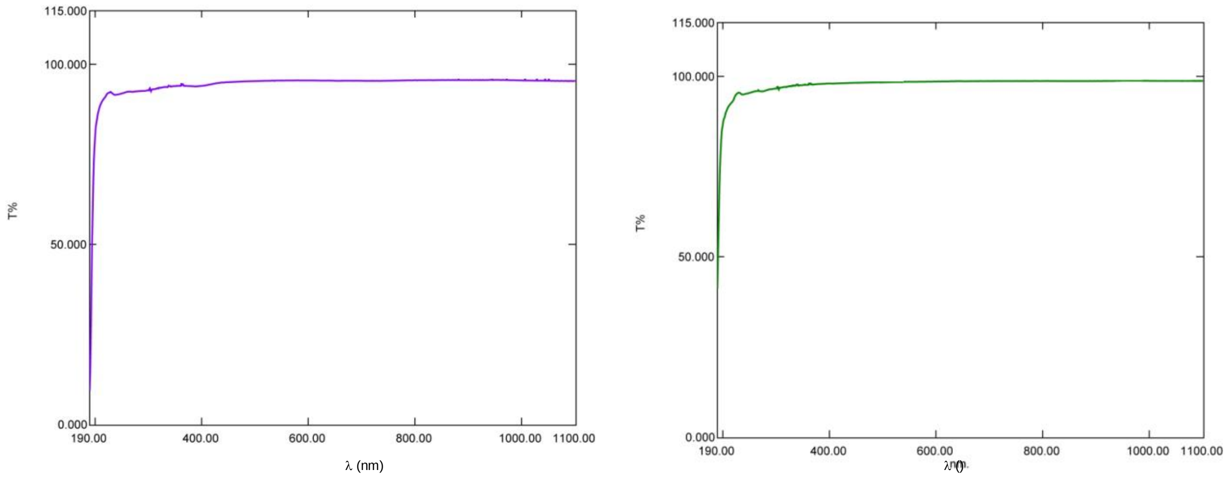

(a) (b)

Figure 4 UV-VIS-NIR transmission spectra of (a) Sn0.5$Ni_{0.5}O_2$ and (b) SnO_2

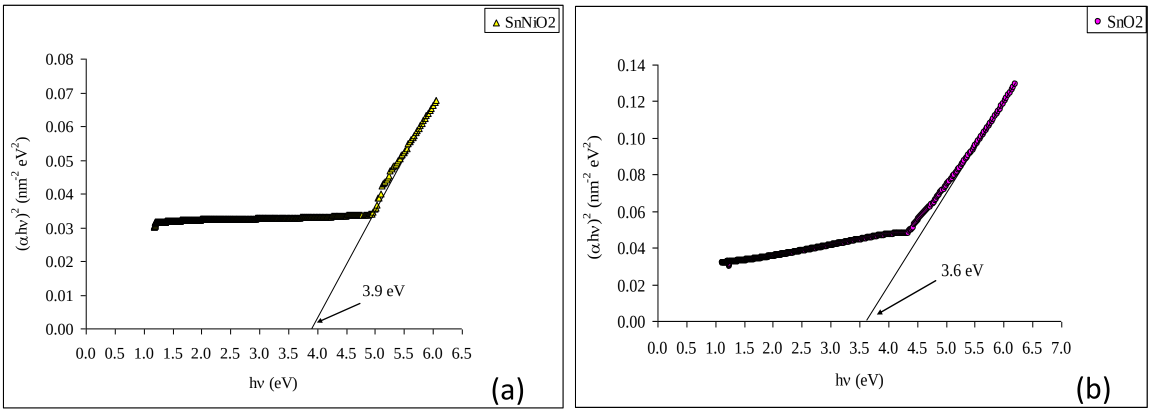

Figure 5 Plots of $(\alpha h\upsilon)^2$ versus hυ graphs of (a) $Sn_{0.5}Ni_{0.5}O_2$ and (b) SnO_2

Conclusion

Undoped Tin Oxide, SnO_2 and Nickel doped Tin Oxide, $Sn_{0.5}Ni_{0.5}O_2$ were prepared by chemical co-precipitation method. Structural, vibrational and optical characteristics were reported in this work. XRD patterns reveal that the samples analogous to tetragonal structure. The lattice parameters are obtained as a = b = 4.66 Å and c = 3.15 Å for $Sn_{0.5}Ni_{0.5}O_2$and a = b = 4.74 Å and c = 3.20 Å for SnO_2. The crystallite sizes are obtained as 33.82 nm for $Sn_{0.5}Ni_{0.5}O_2$and 27.74 nm for SnO_2. It was found that the lattice parameters and the crystallite sizes of the samples varied with the dopant effects of Ni on Sn. FTIR spectra showed the vibrational characteristics of the samples. The observed wavenumbers were found to be shifted due to the dopant effects of Ni on Sn. UV-VIS-NIR transmission spectra showed that the samples demonstrate that less than 100% transmittance of throughout the spectrum. The optical energy band gaps of the $Sn_{0.5}Ni_{0.5}O_2$ and SnO_2samples were obtained as 3.9 eV and 3.6 eV respectively.

Acknowledgement

The authors would like to acknowledge Professor Dr Khin Khin Win, Head of Department of Physics, University of Yangon, for hervaluable suggestionand comments for this work.

References

Azurdia, J., J. Marchal&R. M. Laine (2006). Synthesis and Characterization of Mixed-Metal Oxide Nanopowders along the CoO_x-Al_2O_3 Tie Lie Using Liquid Feed Flame Spray-Pyrolysis. *Journal of American Ceramic Society*, 89(9), 2749 – 2756.

Julian, C. (2003). Local structure and electrochemistry of lithium cobalt oxides and their doped compounds. *Solid State Ionic*, 157, 57-71.

Khan, R. &F. Ming-Hu (2015). Dielectric and magnetic properties of (Zn, Co) co-doped SnO_2 nanoparticles. *China Physical Review B*, 24(12), 127803(1) – 127803(4).

Liu, H. L.,T.Y. Ou-Yang, H.H.Tsai, Lin, P., H.T.Jeng,G. J. Shu, &F. C. Chou, (2015). Electronic structure and lattice dynamics of Li_xCoO_2 single crystals. *New Journal of Physics*, 17(10), 1–8.

J. Myanmar Acad. Arts Sci. 2020 **Vol. XVIII.No.2A**

CALCULATION OF NEUTRON SEPARATION ENERGY OF $^{12}_{6}$C

Cho Cho San[1], Khin Swe Myint[2]

Abstract

Nuclear structure calculations of ^{12}C has been performed by assuming the ^{12}C as a two-body system which is composed of a neutron and a core nucleus ^{11}C. The interaction between the neutron and core nucleus is derived by folding the nucleon-nucleon potential of a Gaussian form with the density distribution of the core nucleus. It is found that the neutron separation energy is in good agreement with the experimental value.

Keywords: neutron separation energy

Introduction

One of most fundamental aspects in nuclear physics is to get knowledge about nucleon-nucleon interactions. Sources which provide information about nucleon-nucleon interactions are scattering data and nuclear binding energies (Willians W.S.C.). In this work, we have determined the last neutron separation energy of ^{12}C by assuming that a nucleon moves in a nuclear potential which is an average effect of the other nucleons.

Since every nucleon is in bound state, the potential is expected to be a potential well. Each nucleon moves in an orbit which is the orbit of a single particle in that potential well. The mean free path of an energetic nucleon moving in nuclear matter is about 2 fm.

The Pauli principle strongly suppressed collisions between nucleons and that provides nearly undisturbed orbits for the nucleons in a nuclear matter. In nuclei the mean field is exclusively produced by the nucleon nucleon interaction. All microscopic models of the nucleus are based on some models of the basic interaction between two nucleons. Firstly, we construct a potential well by using a phenomenological nucleon-nucleon interaction.

Nucleon-Nucleon Interaction

The starting point to study nuclear many-body theory is two-body nucleon-nucleon interactions in the nuclear system. We assume that they give rise to an average single- particle potential. The interaction between two nucleons, nucleon 1 and nucleon 2 is expressed by

$$V_{N-N}(r_1 - r_2) = V_0 f(r_1 - r_2) \tag{1}$$

Where, V_0 = central depth of the potential

r_1 = radial distance of nucleon 1 from the center of mass

r_2 = radial distance of nucleon 2 from the center of mass and

f describes the shape of the potential.

Let $r = r_1 - r_2$

---

[1] Dr, Lecturer, Department of Physics, Mandalay University of Distance Education

[2] Dr, Rector (Rtd), Emeritus Professor, Department of Physics, University of Mandalay

$$V_{N-N}(r) = V_0\, f(r)$$

The function “f” is assumed to be smooth and has short range. In this calculation, we take “f” to be a Gaussian form,

$$f(r) = e^{-\left(\frac{r}{\beta}\right)^2}$$

where, β = range parameter of the interaction.

Then, the equation becomes, $V_{N-N}(r) = -V_0\, e^{-\left(\frac{r}{\beta}\right)^2}$ (2)

According to the nuclear matter calculation (Ring P. and Shuck P.(1980),), V_0 is obtained to be 50 MeV while β varies from 1 fm to 2 fm.We will find out the value of β which reproduces the experimental binding energy of ^{12}C and then, the potential between a nucleon and the core nucleus ^{11}C will be derived.

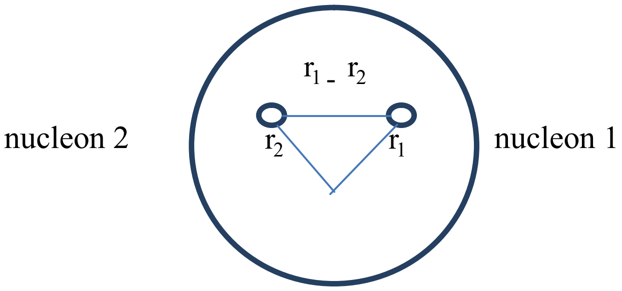

Figure 1.1 Nucleon-Nucleon Interaction

Potential Well of ^{12}C Nucleus

We will derive the nucleon-nucleus potential by folding the nucleon-nucleon interaction with the density distribution of the core nucleus.The average interaction experienced by the nucleon 1 due to the other nucleon is

$$V_{N-Nucleus}(r_1) = \int V_{N-N}(r_1 - r_2)\rho(r_2)d^3r_2$$

$$V_{N-Nucleus}(r_1) = \int V_0 f(r)\rho(r_2)d^3r_2$$

$$r_1 - r_2 = r$$

$$r_2 = r - r_1$$

$$d^3r_2 = d^3r - d^3r_1$$

Therefore, $V_{N-Nucleus}(r_1) = -V_0\ \rho(r)\int e^{-\left(\frac{r}{\beta}\right)^2} d^3r$ (3)

In general, $V_{N-Nucleus}(r) = -V_0\ \rho(r)\int e^{-\left(\frac{r}{\beta}\right)^2} d^3r$

where, $\rho(r)$ = nucleon density distribution.

We will use nucleon density distribution of the nucleus $\rho(r)$ in harmonic oscillator model (Jager C.W., Vires H. & Vires C.(1974)). In the harmonic oscillator model, the density distribution $\rho(r)$ that depends on the radial distance is

$$\rho(r)=\rho_0\left(1+\alpha\left(\frac{r}{a}\right)^2\right)e^{-\left(\frac{r}{a}\right)^2} \tag{4}$$

where, ρ_0 = normalization constant

α = 1.067 fm

a = 1.687 fm.

$\rho(r)$ is normalized as $\int\rho(r)d^3r=z$ where z is the charge number.

$$\int\rho_0\left(1+\alpha\left(\frac{r}{a}\right)^2\right)e^{-\left(\frac{r}{a}\right)^2}d^3r=6$$

Then, we get the normalization constant ρ_0,

$$\rho_0=\frac{6}{\left(\pi a^2\right)^{\frac{3}{2}}\left(1+\frac{3}{2}\alpha\right)}$$

By substituting the values of the parameter α and a, we obtain ρ_0 = 0.086. Finally, we obtain nucleon density distribution of the nucleus as follow:

$$\rho(r)=0.086\left(1+\alpha\left(\frac{r}{a}\right)^2\right)e^{-\left(\frac{r}{a}\right)^2}$$

By substituting the above $\rho(r)$ into equation (1), we obtain

$$V_{N-\mathrm{Nucleus}}=-V_0\,0.086\left(1+\alpha\left(\frac{r}{a}\right)^2\right)e^{-\left(\frac{r}{a}\right)^2}(\pi)^{\frac{3}{2}}\beta^3 \tag{5}$$

Mathematical Formulation

Schrödinger equation for two-body bound system is

$$\left\{-\frac{\hbar^2}{2\mu}\frac{d^2}{dr^2}+\frac{\hbar^2}{2\mu}\frac{\ell(\ell+1)}{r^2}+V(r)\right\}u(r)=E\,u(r) \tag{6}$$

To solve the above equation, we expand the wave function u(r) with Gaussian basis. The Gaussian form for wave function is

$$u(r)= r^{\ell+1}\sum_{j=1}^{N_b} c_j\, e^{-\left(\frac{r}{b_j}\right)^2} \tag{7}$$

wherec_j’s are expansion coefficients, b_j’s are range parameters and N_b is number of basis all of which are to be adjusted in the calculations. b_j’s are chosen to be geometric progression as follow,

$$\frac{b_2}{b_1}=\frac{b_3}{b_2}=\frac{b_4}{b_3}=\cdots=c$$

$$b_{j+1}= cb_j$$

$$b_{N_b}= c^{N_b-1}b_1$$

$$c=\left(\frac{b_{N_b}}{b_1}\right)^{\frac{1}{N_b-1}}$$

The Schrödinger equation for radial part becomes,

$$\left\{-\frac{\hbar^2}{2\mu}\frac{d^2}{dr^2}+\frac{\hbar^2}{2\mu}\frac{\ell(\ell+1)}{r^2}+V(r)\right\}\sum_j c_j\, r^{\ell+1}\, e^{-\left(\frac{r}{b_j}\right)^2} =E\sum_j c_j\, r^{\ell+1}\, e^{-\left(\frac{r}{b_j}\right)^2} \tag{8}$$

Multiplying both sides of the equation by $r^{\ell+1}\, e^{-\left(\frac{r}{b_j}\right)^2}$ from the left and integration through the equation;

$$\int r^{\ell+1}\, e^{-\left(\frac{r}{bi}\right)^2}\left\{-\frac{\hbar^2}{2\mu}\frac{d^2}{dr^2}+\frac{\hbar^2}{2\mu}\frac{\ell(\ell+1)}{r^2}+V(r)\right\}\sum_j c_j\, r^{\ell+1}\, e^{-\left(\frac{r}{b_j}\right)^2} dr$$

$$=E\int r^{\ell+1}\, e^{-\left(\frac{r}{bi}\right)^2}\sum_j c_j\, r^{\ell+1}\, e^{-\left(\frac{r}{b_j}\right)^2} dr \tag{9}$$

$$\sum_j c_j\int r^{\ell+1}\, e^{-\left(\frac{r}{bi}\right)^2}\left\{-\frac{\hbar^2}{2\mu}\frac{d^2}{dr^2}\right\} r^{\ell+1}\, e^{-\left(\frac{r}{b_j}\right)^2} dr+\frac{\hbar^2}{2\mu}\int r^{\ell+1}\, e^{-\left(\frac{r}{bi}\right)^2}\frac{\ell(\ell+1)}{r^2}\, r^{\ell+1}\, e^{-\left(\frac{r}{b_j}\right)^2} dr$$

$$+$$

$$\int r^{\ell+1}\, e^{-\left(\frac{r}{bi}\right)^2} V(r)\, r^{\ell+1}\, e^{-\left(\frac{r}{b_j}\right)^2} dr=E\sum_j c_j\int r^{2(\ell+1)}\, e^{-\left(\frac{r}{bi}\right)^2} e^{-\left(\frac{r}{b_j}\right)^2} dr \tag{10}$$

In this equation, T_{ij}^{ℓ}, N_{ij}^{ℓ}, and F_{ij}^{ℓ} are the kinetic energy, centrifugal potential energy and potential energy matrix elements which are described by as follow:

$$N_{ij}^{\ell}=\frac{(2\ell+1)!!\sqrt{\pi}}{2^{\ell+2}\left(\frac{1}{b_i^2}+\frac{1}{b_j^2}\right)^{\ell+\frac{3}{2}}} \qquad (11)$$

$$F_{ij}^{\ell}=\frac{\hbar^2}{2\mu}\ell(\ell+1)\left(\frac{(2\ell-1)!!\sqrt{\pi}}{2^{\ell+1}\left(\frac{1}{b_i^2}+\frac{1}{b_j^2}\right)^{\ell+\frac{1}{2}}}\right) \qquad (12)$$

$$T_{ij}^{\ell}=-\frac{\hbar^2}{2\mu}\left[\begin{array}{l}\frac{4}{b_j^4}\left(\frac{(2\ell+3)!!\sqrt{\pi}}{2^{\ell+3}\left(\frac{1}{b_i^2}+\frac{1}{b_j^2}\right)^{\ell+\frac{5}{2}}}\right)-\frac{4\ell+6}{b_j^2}\left(\frac{(2\ell+1)!!\sqrt{\pi}}{2^{\ell+2}\left(\frac{1}{b_i^2}+\frac{1}{b_j^2}\right)^{\ell+\frac{3}{2}}}\right)+\\ \ell(\ell+1)\left(\frac{(2\ell-1)!!\sqrt{\pi}}{2^{\ell+1}\left(\frac{1}{b_i^2}+\frac{1}{b_j^2}\right)^{\ell+\frac{1}{2}}}\right)\end{array}\right] \qquad (13)$$

$$T_{ij}^{\ell}+F_{ij}^{\ell}=\frac{\hbar^2}{2\mu}N_{ij}^{\ell}\frac{(4\ell+6)}{b_i^2+b_j^2} \qquad (14)$$

In our calculation we use the folding potential between neutron and core nucleus ^{11}C. Thus the potential energy matrix element with Gaussian basis wave function becomes as follow:

$$V_{ij}^{\ell}=r^{\ell+1}e^{-\left(\frac{r}{b_j}\right)^2}\left[V_{\text{Nucleon-Nucleus}}(r)\right]r^{\ell+1}e^{-\left(\frac{r}{b_j}\right)^2}dr$$

The potential energy matrix element

$$V_{ij}^{\ell}=(-V_0)\rho_0\left(\beta^2\pi\right)^{\frac{3}{2}}\frac{(2\ell+1)!!}{2^{\ell+2}}\frac{\sqrt{\pi}}{\left(\frac{1}{b_i^2}+\frac{1}{b_j^2}+\frac{1}{a^2}\right)^{\ell+\frac{3}{2}}}\times\left[1+\frac{(2\ell+3)}{2}\frac{1}{\left(\frac{1}{b_i^2}+\frac{1}{b_j^2}+\frac{1}{a^2}\right)}\frac{\alpha}{a^2}\right] \qquad (15)$$

The Hamiltonian is expressed by summing of kinetic energy term, centrifugal term and potential term as follows:

$$H_{ij}^{\ell}=T_{ij}^{\ell}+F_{ij}^{\ell}+V_{ij}^{\ell} \qquad (16)$$

$$\sum_j H_{ij}^{\ell} c_j = E \sum_j N_{ij}^{\ell} c_j \tag{17}$$

By writing equation (15) in terms of matrix form as follows:

$$[H][c] = E[N][c] \tag{18}$$

The above equation (16) is solved iteratively by giving an estimate E_0 value and initial set of $c_i^{(1)}$'s. Therefore, the eigen value equation is obtained.

$$E = E_0 + \frac{C^n}{C^{n+1}} \tag{19}$$

where n+1 is the number of iteration. Then we get the neutron separation energy of ^{12}C.

Result and Discussion

We have formulated the kinetic energy matrix elements, the centrifugal potential matrix elements and the potential matrix elements with Gaussian basis. Then, we solved the two-body Schrodinger equation. The parameters b_1, b_N and N_b are adjusted to get the convergent result. We found that the optimum value of the input parameters are b_1= 0.1, b_N = 20.0, N_b= 40. Then we got the neutron separation energy of ^{12}C.

We have calculated the neutron separation energy of ^{12}C by varying the value of β parameter starting from 1.0 fm and increasing it by 0.1 fm. At β = 1.2 fm, the neutron separation energy is -12.04 MeV and at β = 1.3 fm, it is -18.91 MeV. Therefore we found that the experimental neutron separation energy which is -18.72 MeV (Audi G. and Wapstra A.H.,(1993)) should exist between the β value of 1.2 fm and 1.3 fm. The neutron separation energy at various values of β are shown in table (1).

Table 1 The list of neutron separation energy at various β values

β interaction range parameter (fm)	Neutron separation energy (MeV)
1.0	-3.19
1.1	-6.84
1.2	-12.04
1.3	-18.91
1.25	-15.26
1.26	-15.96
1.27	-16.66
1.28	-17.39
1.29	-18.15
1.291	-18.22
1.292	-18.29
1.293	-18.38
1.294	-18.45
1.295	-18.53
1.296	-18.61
1.297	-18.68
1.298	-18.76
1.299	-18.84

At β = 1.29 fm the neutron separation energy is -18.15 MeV which is close to the experimental value. So, the value of β is increased by 0.001 fm between 1.291 fm and 1.299 fm. We found that at β = 1.298 fm, our theoretical neutron separation energy -18.76 MeV is in good agreement with the experimental value (Audi G. and Wapstra A.H.,(1993)).

Conclusion

We have calculated the neutron separation energy of ^{12}C nucleus by solving the two-body Schrodinger equation with Gaussian basis wave function. In our calculation nucleons are assumed to be moving freely in a nuclear potential well. We derived the nucleon-nucleus potential by folding the one range Gaussian nucleon-nucleon interaction with the nucleon density distribution of the ^{12}C nucleus. Then we obtained the neutron separation energy of the last neutron to be -18.76 MeV at V_0 = 50 MeV and β = 1.298 fm in our calculation. We can reproduce the correct neutron separation energy of ^{12}C which is in good agreement with the experimental value -18.72 MeV (Audi G. and Wapstra A.H.,(1993)).

Acknowledgements

I would like to thank Dr Aung Naing Soe, Pro-Rector, Mandalay University of Distance Education for his encouragement. I am grateful to the full support of Professor Dr Kay Thi Nwe, Head of Department of Physics, Mandalay University of Distance Education.

References

Audi G. andWapstraA.H, Nuclear Physics A565(1993), 1.

JagerC.W., Vires H. & Vires C., Atomic Data and Nuclear Data Tables, 14 (1974) 479.

Ring P. and P. Shuck .,(1980) "*The Nuclear-Many Body Problem*", Springer-Verlag, New York,.

Willians W.S.C, (1991) "*Nuclear and Particle Physics*",Oxford University Press, New York.

CONSTRUCTIONOF K^-p SEPARABLE POTENTIALFROM $\Lambda(1405)$ PARAMETERS

Khin Soe Moe[1], Nay Min Oo[2] and Khin Swe Myint[3]

Abstract

K^-p separable potential which is reproduced from the $\Lambda(1405)$ energy and level width, 27MeV and 40MeVhas been constructed. The Schrodinger equation has been solved by using our constructed separable potential. And then, unknown data of potential strength parameter, $\overline{V_0}$, and potential range parameter, b, have been calculated by comparing the binding energy and level width of $\Lambda(1405)$.The constructed separable potential model is $V(\vec{r},\vec{r}') = 1.34\,\frac{1}{r}\frac{1}{r'}\,e^{-\left(\frac{r+r'}{1.26}\right)}$.

Keywords: single K^-p separable potential, potential strength parameter, potential rangeparameter

Introduction

$\overline{K}N$ interaction can be theoretically constructed from the experimental data of $\Lambda(1405)$ quasi bound state and $\overline{K}N$ scattering parameters. It is accepted that $\Lambda(1405)$ is quasi bound state with isospin I = 0 which is composed of K^- and proton. The strange resonance $\Lambda(1405)$ has $J^\pi = \frac{1}{2}^+$ and is found in s-wave $\Sigma\pi$ scattering(Akaishi Y and Yamazaki T.).

It is very important to understand the kaon-nucleon interaction and its modification due to nuclear medium, which leads to the kaon-nucleus optical potential, for the discussion of deeply bound kaonic states. In particular, the understanding of the $\Lambda(1405)$ is essential in order to study the fate of the kaons in the nucleus. We have solved the Schrodinger equation by using our constructed separable potential. And then, unknown data of potential strength parameter, $\overline{V_0}$, and potential range parameter, b, have been calculated by comparing the binding energy and level width of $\Lambda(1405)$.

Theoretical Review on Kaonic Nuclei

The search for deeply bound hadronic states has a long history. The hadron which attracted much attention recently is kaon. The exotic nuclear systems involving a $\overline{K}\left(K^- \text{ or } \overline{K^0}\right)$ as a constituent have been investigated theoretically based on phenomenologically constructed $\overline{K}N$ interaction, which reproduces low-energy $\overline{K}N$ scattering data, kaonic hydrogen atom data and the binding energy and decay width of $\Lambda 1405$.

---

[1] Dr, Lecturer, Department of Physics, Mandalay University of Distance Education
[2] Dr, Lecturer, Department of Physics, Meiktila University
[3] Dr, Emeritus Professor, Department of Physics, Mandalay University

In recent years, there have been important developments in the studies of kaonic nuclear states, which are kaon-nucleus systems bound by the strong interaction inside the nucleus. The very interesting feature of the kaon-nucleus bound systems is based on the fact that the properties of kaons in nuclei are strongly influenced by the change undergone by $\Lambda(1405)$ in nuclear medium, because $\Lambda(1405)$ is a resonance state just below the kaon-nucleon threshold. There are studies of kaonic atoms carried out by modifying the properties of $\Lambda(1405)$ in nuclear medium.

Yamazaki and Akaishi theoretically investigated the possible existence of deeply bound kaonic nuclei. The nuclear ground states of K^- in ^{3}He, ^{4}He and ^{9}Be are theoretically predicted to be discrete states with binding energies of 108 MeV, 86 MeV and 113 MeV and widths of 20 MeV, 34 MeV and 38 MeV respectively. Energy level diagram of the $K^- + {}^3$He system is shown in Fig 1.

For three-body K^-pp system, Akaishi *et al.* have predicted that K^-pp system is bound with a binding energy (E_K = 48 MeV) and a width (Γ_K = 61 MeV). The average distance between two protons in this three-body system is found to be 1.9 fm(Akaishi Y and Yamazaki T.).

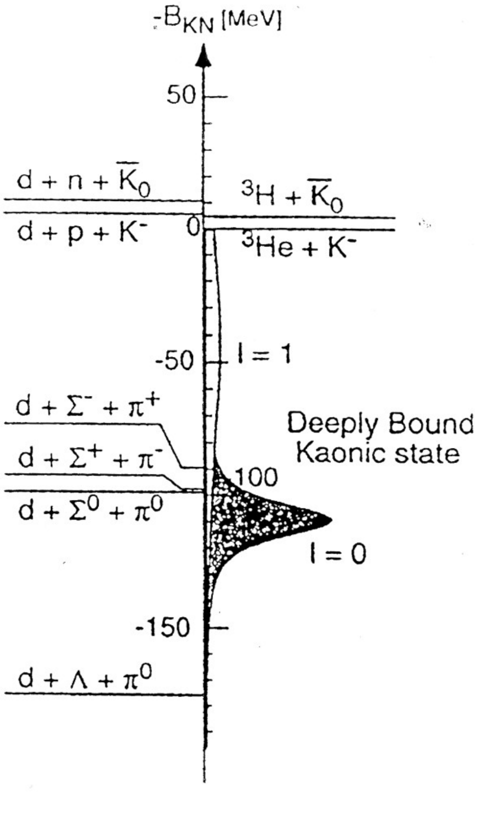

Figure 1 Energy level diagram of the $K^- + {}^3$He system and the energies of relevant decay channels.

$\overline{K}$N **Potential**

Kaonic atoms have been phenomenologically studied, and the large strength of the potential assumed at a time raised hopes that deeply bound states (bound by 50_200 MeV) could exist. However, the imaginary part of the optical potential is large and therefore, the widths of the deeply bound kaonic states come out to be too large to be detected as distinguished states. Hence, one should rely on the microscopic derivation of the kaon optical potential to find a mechanism for small widths of deeply bound kaonic states, if they exist. The microscopic derivation of the optical potential for kaonic atoms is related strongly to the properties of the $\Lambda(1405)$ state, which is located just below the kaon-proton threshold. There have been many studies on the theoretical derivation of kaon nucleus optical potential.

$\overline{K}N$ interaction can be theoretically constructed from the experimental data of $\Lambda(1405)$ quasi bound state and scattering parameters. It is accepted that $\Lambda(1405)$ is a quasi bound state with isospin I = 0 which is composed of K^- and proton.

Akaishi and Yamazaki consider the $\Lambda(1405)$ state as the bound state of the kaon and proton and its width is caused by the coupling to the π - Σ channel.

Mathematical Formulation

A separable potential with a Yukawa type form factor can be expressed as follows.

$$V(\vec{r},\vec{r}') = g(r)\,Y_{lm}\,\frac{\overline{V}_0}{b^3}\,g(r')\,Y_{l'm'}$$

where,

$\overline{V}_0$ = potential strength parameter

b = potential range parameter

g(r) = form factor

We will construct the K^-p optical potential from this separable potential.

Schrodinger equation of two-body system in single channel is expressed as:

$$H|\psi\rangle = E|\psi\rangle \tag{1}$$

$$\langle\psi|T+V|\psi\rangle = E\langle\psi|\psi\rangle \tag{2}$$

$$\iint d\vec{r}\,d\vec{r}'\langle\psi|\vec{r}\rangle\langle\vec{r}|T|\vec{r}'\rangle\langle\vec{r}'|\psi\rangle + \iint d\vec{r}\,d\vec{r}'\langle\psi|\vec{r}\rangle\langle\vec{r}|V|\vec{r}'\rangle\langle\vec{r}'|\psi\rangle = E\int d\vec{r}\langle\psi|\vec{r}\rangle\langle\vec{r}|\psi\rangle \tag{3}$$

$$\begin{gathered}\iint d\vec{r}\,d\vec{r}'\,\psi^*(\vec{r})\left(-\frac{\hbar^2\vec{\nabla}^2}{2\mu}\right)\delta(\vec{r}-\vec{r}')\psi + \iint\iint d\vec{r}\,d\vec{r}'\,\psi^*(\vec{r})g(\vec{r})\,Y_{00}\,\frac{\vec{V}_0}{b^3}\,g(\vec{r}')\,Y_{00}\,\psi(\vec{r}') \\ = E\int d\vec{r}\,\psi^*(\vec{r})\psi(\vec{r})\end{gathered} \tag{4}$$

$$-\frac{\hbar^2}{2\mu}\vec{\nabla}^2\psi(\vec{r}) + g(\vec{r})Y_{00}\frac{\vec{V}_0}{b^3}\int g(\vec{r}')Y_{00}\,\psi(\vec{r}')d\vec{r}' = \frac{\hbar^2}{2\mu}k^2\,\psi(\vec{r}) \tag{5}$$

where

$E=\dfrac{\hbar^2k^2}{2\mu}$; k = wave vector

$$\psi(\vec{r}) = \frac{u(r)}{r}Y_{00} \ ; \quad Y_{00} = \frac{1}{\sqrt{4\pi}}$$

We will rewrite the equation (5) as follows:

$$-\frac{\hbar^2}{2\mu}\frac{\partial^2}{\partial r^2}\frac{u(r)}{r}Y_{00} + g(\vec{r})Y_{00}\frac{\vec{V}_0}{b^3}\int g(\vec{r}')Y_{00}\,d\vec{r}' = \frac{\hbar^2}{2\mu}k^2\frac{u(r)}{r}Y_{00} \tag{6}$$

$$-\frac{d^2}{dr^2}u(r) + G_0\, r\, g(r)\int g(r')\frac{u(r')}{r'}\frac{1}{4\pi}d\overset{r\prime}{r}{}' = k^2u(r) \tag{7}$$

Where, $G_0 = \frac{2\mu}{\hbar^2}\frac{\vec{V}_0}{b^3}$

$$-\frac{d^2}{dr^2}u(r) + G_0\, r\, g(r)\int g(r')u(r')r'\,dr' = k^2u(r) \tag{8}$$

We let $G_0\int_0^\infty g(r')u(r')r'\,dr'$ in equation (8) as G to simplify our calculation.

Then equation (8) is written as:

$$-\frac{d^2}{dr^2}u(r) + r\,g(r)G = k^2u(r) \tag{9}$$

Since wave function u(r) is the total wave function of inhomogeneous wave function $u_0(r)$ and homogeneous wave function $u_1(r)$, the equation (9) can be written as:

$$-\frac{d^2}{dr^2}u_0(r) - \frac{d^2}{dr^2}u_1(r) + r\,g(r)G = k^2u_0(r) + k^2u_1(r) \tag{10}$$

Equation (10) can be separated to inhomogeneous equation and homogeneous equation.

Inhomogeneous equation is

$$-\frac{d^2}{dr^2}u_0(r) + r\,g(r)G = k^2u_0(r) \tag{11}$$

Homogeneous equation is

$$-\frac{d^2}{dr^2}u_1(r) = k^2u_1(r) \tag{12}$$

We will solve equation (11) as follows:

$$\frac{d^2}{dr^2}u_0(r) - r\,g(r)G = -k^2u_0(r) \tag{13}$$

Then

$$u_0(r) = A\,e^{-r/b} \tag{14}$$

where, $A = \dfrac{Gb^3}{1+k^2b^2}$

Then, by solving equation (12), we get

$$u_1(r) = a \sin(kr+\delta) \tag{15}$$

Since $u(r) = u_0(r) + u_1(r)$,

$$u(r) = A\,e^{-r/b} + a\sin(kr+\delta) \tag{16}$$

For boundary condition, u(0) = 0

$$A = -a \sin\delta \tag{17}$$

Therefore, equation (16) can be expressed as follows:

$$u(r) = A\,e^{-r/b} - Ae^{ikr} \tag{18}$$

Since

$$G = G_0 \int_0^\infty g(r)u(r)\,r\,dr,$$

$$\frac{G}{G_0} = \int_0^\infty \frac{b}{r}\,e^{-\frac{r}{b}}\{Ae^{-\frac{r}{b}} - A\,e^{-ikr}\}\,r\,dr \tag{19}$$

Then,

$$\frac{G}{G_0} = -\frac{1}{2}Ab^2\left(\frac{1+ikb}{1-ikb}\right) \tag{20}$$

Since $A = \dfrac{Gb^3}{1+k^2b^2}$

Since $A = -a\sin\delta$, then

$$-a\sin\delta = \frac{Gb^3}{1+k^2b^2} \tag{21}$$

$$G = -a\sin\delta\,\frac{1+k^2b^2}{b^3}$$

When equation (21) is divided by G_0, equation (22) will be as follows.

$$\frac{G}{G_0} = -a\sin\delta\,\frac{1+k^2b^2}{G_0b^3} \tag{22}$$

From equation (20) and equation (22), we get equation (23)

$$-\frac{1}{2}Ab^2\left(\frac{1+ikb}{1-ikb}\right) = A\frac{(1+ikb)(1-ikb)}{G_0b^3} \tag{23}$$

Then. $(1-ikb)^2 = -s$ where $s = \frac{1}{2}G_0 b^5$ (24)

Then, $k = -i\frac{1}{b} \pm \frac{1}{b}\sqrt{s}$ $\quad \frac{\hbar^2}{2\mu}\frac{1}{b^2}$

In calculation, we let as B_0.

Our calculated resonance energy can be written as follows :

$$E_{Res} = B_0(s-1) - i(2B_0\sqrt{s}) \tag{25}$$

Where, $B_0 = \frac{\hbar^2}{2\mu}\frac{1}{b^2}$

Experimental value of resonance energy for $\Lambda(1405)$ is

$$E_{Res} = -27 - i40 \text{ MeV} \tag{26}$$

By comparing our calculated results with the experimental data of $\Lambda(1405)$.

$$-27 - i40 = B_0(s-1) - i(2B_0\sqrt{s}) \tag{27}$$

$$-27 - i\,40 = \frac{\hbar^2}{2\mu}\frac{1}{b^2}\frac{\mu}{\hbar^2}\overline{V}_0\, b^2 - \frac{\hbar^2}{2\mu}\frac{1}{b^2} - i\left(\frac{\hbar^2}{\mu}\frac{1}{b^2}\sqrt{\frac{2\mu\overline{V}_0\, b^2}{2\hbar^2}}\right) \tag{28}$$

By comparing real value and imaginary value of the above equation, we get equation (29) and equation (30).

$$-27 = \frac{\overline{V}_0}{2} - \frac{\hbar^2}{2\mu\, b^2} \tag{29}$$

$$40 = \sqrt{\frac{2\hbar^2\overline{V}_0}{2\mu\, b^2}} \tag{30}$$

Then we get the value of potential strength parameter, $\overline{V}_0$.

$\overline{V}_0 = 21.26$ MeV (or) -75.26 MeV

For $\overline{V}_0 = 21.26$ MeV, $b = 1.26$ fm (or) -1.26 fm

For $\overline{V}_0 = -75.26$ MeV, $b = i2.38$ fm (or) $-i2.38$ fm

For resonance state, it must be $G_0 > 0$ and $s > 0$.

Finally, our suitable results are

$\overline{V}_0 = 21.26$ MeV and $b = 1.26$ fm

Yukawa type non-local potential is

$$V\left(\vec{r}, \vec{r}\right) = g(r)Y_{1m}\frac{\overline{V}_0}{b^3}g(r')Y_{1'm'}$$

Then, we get our constructed separable potential by using calculated results of potential strength parameter, $\overline{V}_0$, and potential range parameter, b.

$$V(\vec{r},\vec{r}') = 1.34\frac{1}{r}\frac{1}{r'}e^{-\left(\frac{r+r'}{1.26}\right)}. \tag{31}$$

Results and Discussion

To analyze the existence of the kaonic nucleus, we must have a reliable kaon nucleon interaction in the nuclear medium. For this requirement, we construct the $\overline{K}N$ separable potential. It is Yukawa type separable potential and is constructed analytically and numerically. In our constructed separable potential model, unknown data of potential strength parameter, $\overline{V}_0$, and potential range parameter, b, have been computed.

By comparing our calculated resonance energy with the energy of $\Lambda(1405)$, we calculate the unknown data of $\overline{V}_0$ and b. In our calculation, the value of potential strength parameter, $\overline{V}_0$, is 21.26 MeV. That of potential range parameter, b, is 1.26 fm. Then, the $\overline{K}N$ Yukawa type separable potential, which reproduces the experimental values of $\Lambda(1405)$, is constructed as

$$V(\vec{r},\vec{r}) = 1.34\frac{1}{r}\frac{1}{r}e^{\left(\frac{r+r}{1.26}\right)}.$$

This potential is non-local potential that can separate the local form. So, it is also called separable potential.

Computation difficulty will be encountered in solving the kaon nucleus system with the separable potential in coordinate space. This difficulty can be overcome by constructing a local potential which is equivalent to the non- local separable potential.

Conclusion

By using our constructed separable potential, we can calculate the binding energy of kaonic nuclei and can do the structure analysis of this system.

Scattering parameters such as cross section, phase shift, scattering length, effective range, etc. can be computed by using our constructed potential. If the calculated results will be confirmed experimentally, we can say that our constructed separable potential is good and our present work is a timely research in this frontier of physics.

If anyone interest in research, he can continue to calculate the scattering parameters by using our constructed separable potential and compare the experimental results.

Acknowledgements

I would like to thank Dr Aung Naing Soe, Pro-Rector, Mandalay University of Distance Education for his encouragement. I am grateful to the full support of Professor Dr Kay Thi Nwe, Head of Department of Physics, Mandalay University of Distance Education. I am deeply indebted to Professor Dr Khin Swe Myint, Rector (Rtd), Emeritus Professor, Department of Physics, University of Mandalay for all her enthusiastic discussion, collaboration and encouragement.

References

Akaishi Y, Dote A and Yamazaki T., Prog. Theor .Phys. Suppl., 146 (2003) 508.

Akaishi Y and Yamazaki T., Phys. Rev .C 65 (2002) 044005.

Kamimura M., Phys . Rev A 38 (1987) 621.

Martin A.D ., Nucl . Phys .B 179 (1981) 33.

Muller-GroelingA ,Holinde K and Speth J., Nucl .Phys. A 513 (1990) 557.

Suzuki T et al., Phys. Lett .B 597 (2004) 263.

J. Myanmar Acad. Arts Sci. 2020 **Vol. XVIII.No.2A**

COMPARISON BETWEEN SINGLE PARTICLE ENERGY STATES OF Λ-HYPERNUCLEUS AND Σ^--HYPERNUCLEUS WITH WOODS-SAXON POTENTIAL

Thida Wint[1], Win Win Maw[2], Maung Maung Chit[3] and Khin Swe Myint[4]

Abstract

In this research, Λ and Σ^- single particle energy states are compared to study the role of Λand Σ hyperons in nuclear medium. Energy states are calculated by solving one body Schrödinger equation with Woods-Saxon central potential including central part and spin-orbit coupling. Coulomb potential is taken into account for the calculation of Σ^- particle energy states. Wave function expanded into Gaussian basis is used in our calculation. Root-mean-square distance for various orbital angular momentum states are also calculated. The characteristic of Λ and Σ^- single particle energy states in light and heavy nuclei are discussed.

Keywords: Λ single particle energy states, Σ single particle energy states, Woods-Saxon potential, Coulomb potential

Introduction

For the study of nuclear physics, the baryon-baryon interaction is fundamental and important. To complete the knowledge of baryon-baryon interaction, it is essential to understand Nucleon (N)-Nucleon (N) interaction, Hyperon (Y)-Nucleon (N) interaction, Y-Y interaction which can be obtained from normal nuclei, strangeness -1 (S = -1) hypernucei and strangeness -2 (S = -2) hypernuclei respectively. N-N interaction has been continuously studied for more than 60 years. Regarding the Y-N interaction and Y-Y interaction, where Y is a Σ or Λ hyperon, its research is steadily progressing. For strangeness (S = -1) system, about 40 Λ-hypernuclei and one Σ-hypernucleus were found experimentally [Bando H, Motoba T and Zofka J, 1990]. Hyperons do not suffer from Pauli blocking by the other nucleons, it can penetrate into the nuclear interior and form deeply bound hypernuclear states. However, it is predicted that the average Σ potential in nuclear matter must be shallow due to the Σ→Λ strong conversion channel. There are many open questions about Σ - hypernuclei such as production reaction, widths and related Coulomb field assistance, quasi-free spectrum competition and decay channels. It is difficult to get the information about the Σ-hypernuclear states from experimental data with low statics. Due to lack of the information on a phenomenological side, the theoretical calculation plays an important role in understanding the behavior of a Σ-hyperon in nuclei.

In this research, single particle energy states of Λ-hyperon and Σ^--hyperon in light hypernuclei ${}^{16}_{\Lambda}O$ and ${}^{16}_{\Sigma^-}C$ and heavy hypernuclei ${}^{208}_{\Lambda}Pb$ and ${}^{208}_{\Sigma^-}Hg$ are investigated to study the role of Λ and Σ hyperons in nuclear medium. In this calculation, we considered that a Λ or Σ^- -hyperon moves freely in an average potential well generated by the other nucleons. Energy states are calculated by solving one body Schrödinger equation with Woods-Saxon central potential including spin-orbit coupling. Coulomb potential is taken into account for the calculation of Σ^- particle states to investigate the Coulomb effect in Σ^--hypernuclei. Gaussian basis wave is used as a trial wave function in our calculation. Root-mean-square (RMS) distance for various orbital angular momentum states are also calculated. ΛandΣ^- single particle energy states in light and heavy nuclei are calculated and discussed about the characteristic of those two hyperons in different nuclear medium.

Solving the Schrödinger Equation with the Gaussian Basis Wave Function

Single particle energy levels of a hyperon in a potential well are numerically determined by solving the Schrödinger radial equation using the power inverse iteration method.

The Schrödinger Radial Equation (SRE) is

$$\frac{d^2u(r)}{dr^2}+\frac{2m}{\hbar^2}\left[E-V(r)-\frac{\hbar^2}{2m}\frac{l(l+1)}{r^2}\right]u(r)=0 \tag{1}$$

where u(r) = rR_{nl} is the reduced radial wave function.

$$\mathrm{u(r)}=\mathrm{r}^{\ell+1}\sum_{\mathrm{j=1}}^{\mathrm{N}}\mathrm{c_j}\ \mathrm{e}^{-\left(\frac{\mathrm{r}}{\mathrm{b_j}}\right)^2} \tag{2}$$

whereb$_j$'s are the range parameter and are chosen to be geometric progression as follows.

$\frac{b_2}{b_1}=\frac{b_3}{b_2}=\frac{b_4}{b_3}=\ldots=$ constant, $b_{i+1}=\left(\frac{b_N}{b_1}\right)^{1/N-1}$ b_i and N is the number of coefficients and, c_j's are expansion coefficients.

The Schrödinger equation is written as follow.

$$(H_0+V)\,u=E\,u$$

where, E = energy eigen value, u = eigen vector, H_0 = kinetic energy operator and V = potential energy operator.

The Schrödinger equation for radial part is,

$$\left\{-\frac{\hbar^2}{2M}\frac{d^2}{dr^2}+\frac{\hbar^2}{2M}\frac{\ell(\ell+1)}{r^2}+V(r)\right\}u(r)=E\,u(r) \tag{3}$$

$$\left\{-\frac{\hbar^2}{2M}\frac{d^2}{dr^2}+\frac{\hbar^2}{2M}\frac{\ell(\ell+1)}{r^2}+V(r)\right\}r^{\ell+1}\sum_{j=1}^{N}c_j\,e^{-\left(\frac{r}{b_j}\right)^2}=E\,r^{\ell+1}\sum_{j=1}^{N}c_j\,e^{-\left(\frac{r}{b_j}\right)^2} \tag{4}$$

Multiplying both sides of the equation by $\mathrm{r}^{\ell+1}\mathrm{e}^{-\left(\frac{\mathrm{r}}{\mathrm{b_i}}\right)^2}$ from the left and integration through the equation

$$\int r^{\ell+1}e^{-\left(\frac{r}{b_i}\right)^2}\left\{-\frac{\hbar^2}{2M}\frac{d^2}{dr^2}+\frac{\hbar^2}{2M}\frac{\ell(\ell+1)}{r^2}+V(r)\right\}\sum_j c_j\,r^{\ell+1}e^{-\left(\frac{r}{b_j}\right)^2}dr=E\int r^{\ell+1}e^{-\left(\frac{r}{b_i}\right)^2}\sum_j c_j\,r^{\ell+1}e^{-\left(\frac{r}{b_j}\right)^2}dr \tag{5}$$

We can define the above equation as

$$\sum_j \left[T_{ij} + V_{\ell ij} + V_{ij}\right] c_j = E \sum_j N_{ij}\, c_j \tag{6}$$

where T_{ij} is kinetic energy matrix element, N_{ij} is norm matrix element and $V_{\ell ij}$ is the centrifugal potential energy matrix element. H_{ij} is Hamiltonian matrix element. The N_{ij}, T_{ij} and $V_{\ell ij}$ are analytically solved by using standard integral form as follows.

The norm matrix element, $N_{ij} = \int r^{\ell+1} e^{-\left(\frac{r}{b_i}\right)^2} r^{\ell+1} e^{-\left(\frac{r}{b_j}\right)^2} dr$

The kinetic energy matrix element, $T_{ij} = \int r^{\ell+1} e^{-\left(\frac{r}{b_i}\right)^2} \left\{-\frac{\hbar^2}{2\mu}\frac{d^2}{dr^2}\right\} r^{\ell+1} e^{-\left(\frac{r}{b_j}\right)^2} dr$

The centrifugal potential energy matrix element, $V_{\ell ij} = \int r^{\ell+1} e^{-\left(\frac{r}{b_i}\right)^2} \frac{\ell(\ell+1)}{r^2} r^{\ell+1} e^{-\left(\frac{r}{b_j}\right)^2} dr$

The potential energy matrix element, $V_{ij} = \int r^{\ell+1} e^{-\left(\frac{r}{b_i}\right)^2} V\, r^{\ell+1} e^{-\left(\frac{r}{b_j}\right)^2} dr$ The Hamiltonian matrix element, $H_{ij} = \int r^{\ell+1} e^{-\left(\frac{r}{b_i}\right)^2} H\, r^{\ell+1} e^{-\left(\frac{r}{b_j}\right)^2} dr$

where $H_{ij} = T_{ij} + V_{\ell ij} + V_{ij}$.

The Schrödinger equation in matrix form can be written as follows.

$$[H]\,[C] = E\,[N]\,[C] \tag{7}$$

Equation (7) can be expanded as

$$H_{11} C_1 + H_{12} C_2 + \ldots + H_{1N} C_N = E\left(N_{11}C_1 + N_{12}C_2 + \ldots + N_{1N}C_N\right)$$

$$H_{21} C_1 + H_{22} C_2 + \ldots + H_{2N} C_N = E\left(N_{21}C_1 + N_{22}C_2 + \ldots + N_{2N}C_N\right)$$

$$H_{N1} C_1 + H_{N2} C_2 + \ldots + H_{NN} C_N = E\left(N_{N1}C_1 + N_{N2}C_2 + \ldots + N_{NN}C_N\right),$$

which are

$$\sum_{i,j=0}^{N} \left(H_{ij} - E\, N_{ij}\right) C_j = 0$$

In order to determine the energy eigen value E, we solved the following set of linear equations iteratively.

$$\sum_{i,j=0}^{N} \left(H_{ij} - E_0\, N_{ij}\right) C_j^{(k)} = \sum_{i,j=0}^{N} N_{ij}\, C_j^{(k-1)} \quad , k = 1, 2, \ldots, \ell \tag{8}$$

With $$E = E_0 + \frac{C_j^{(k-1)}}{C_j^{(k)}}$$

where E_0 =initial guess value of energy

E = energy eigen value, N = number of coefficients, C = expansion coefficient, and ℓ = number of iterations.

The convergence of iteration is obtained when the ratio of $\frac{C_j^{(k-1)}}{C_j^{(k)}}$ becomes constant. i.e.,

$$\frac{C_j^{(k-2)}}{C_j^{(k-1)}} = \frac{C_j^{(k-1)}}{C_j^{(k)}}.$$

Average Potential Well of a Λ-Hypernucleus

The interaction between lambda and the other nucleons in the core nucleus is derived using phenomenological Woods-Saxon potential which is based upon the sum of a spin-independent central potential and spin-orbit potential. In our calculation, we considered that a Λ-particle moves freely in an average potential well generated by the other nucleons of the core nucleus. The total nuclear interaction between lambda and core nucleus is

$$V(r) = V_l(r) + V_{w\text{-}s}(r) + V_{l\text{-}s}(r) \tag{9}$$

where, $V_l(r)$ = centrifugal potential = $\frac{\hbar^2}{2m_\Lambda}\frac{\ell(\ell+1)}{r^2}$

m_Λ =the mass of lambda and l =orbital angular momentum quantum number.

$V_{l\text{-}s}(r)$ = Woods-Saxon spin-orbit potential = $V_{so}\left(\frac{\hbar}{m_\pi c}\right)^2\left(\vec{\ell}\,.\,\vec{s}\right)\frac{1}{r}\frac{d\rho}{dr}$

If total angular momentum $j = \ell + \frac{1}{2}$, $V_{l-s}(r) = V_{so}\left(\frac{\hbar}{m_\pi c}\right)^2\left(\frac{1}{2}\ell\right)\frac{1}{r}\frac{d\rho}{dr}$

If total angular momentum $j = \ell - \frac{1}{2}$, $V_{l-s}(r) = V_{so}\left(\frac{\hbar}{m_\pi c}\right)^2\left[-\frac{1}{2}(\ell+1)\right]\frac{1}{r}\frac{d\rho}{dr}$

V_{so} = the strength of Woods-Saxon spin-orbit coupling potential term

$\frac{\hbar}{m_\pi c}$ =Compton wavelength of the pion

$V_{w\text{-}s}(r)$ = Woods-Saxon central potential = $-V_0\rho(r)$

V_0 = the strength of the Woods-Saxon potential

$$\rho(r) = \text{the nuclear density} = \frac{1}{1+e^{\frac{r-R}{a}}}$$

In above equation, r =the radial distance from the center,

$$\text{R=the nuclear radius}\left(R = r_0(A-1)^{\frac{1}{3}}\right)$$

a =the diffuseness parameter.

The total interaction between lambda and core nucleus becomes

$$V(r)=\frac{\hbar^2}{2m_\Lambda}\frac{\ell(\ell+1)}{r^2}-\frac{V_0}{1+e^{r-R/a}}-V_{SO}\left(\frac{\hbar}{m_\pi c}\right)^2\left(\frac{\ell}{2}\right)\frac{1}{ra}\frac{e^{r-R/a}}{\left(1+e^{r-R/a}\right)^2} \qquad \text{for } j=\ell+\frac{1}{2} \qquad 10(a)$$

$$V(r)=\frac{\hbar^2}{2m_\Lambda}\frac{\ell(\ell+1)}{r^2}-\frac{V_0}{1+e^{r-R/a}}+V_{SO}\left(\frac{\hbar}{m_\pi c}\right)^2\left(\frac{1}{2}(\ell+1)\right)\frac{1}{ra}\frac{e^{r-R/a}}{\left(1+e^{r-R/a}\right)^2} \qquad \text{for } j=\ell-\frac{1}{2} \qquad (b)$$

Using above potentials as in 10(a) and (b), Λ-single particle energy states in ${}^{16}_{\Lambda}O$ and ${}^{208}_{\Lambda}Pb$ are calculated for different *lj* states.

Average Potential Well of a Σ$^-$-Hypernucleus

In contrast to Λ-hypernuclei where the narrow peak in experimental excitation spectra indicate correctness of the notion of a single particle, such a property for the Σ-hyperon is not so well established. The observation of the ground state of as light species as Σ - hyperhelium ${}^{4}_{\Sigma}\text{He}$ was announced at the 1988 Padova Conference [Hayano R S *et al.*, 1988]. The (K$^-$ stopped, π$^-$) reaction produced ground state at as much as 3.2 ± 0.3 MeV binding with a width of 4.6 ± 0.5 MeV [Harada T and Akaishi Y, 1990][Bressani T *et al.*, 1989]. Such a Σ-hypernucleus state was derived also theoretically with full use of the repulsive core and strong isospin-spin dependence of the Σ-N interaction. In the reference [Hayano R S *et al.*, 1988], the authors claimed that the width may reach as much as a few tens of MeV in nuclear matter due to Σ→Λ strong conversion channel and the average Σ-nucleus potential must be shallow (well depth of $10 \le V_{re} \le 25$ MeV). The spin-orbit splitting seems to be comparable (or larger) than that for a nucleon. For a long time, the strength of the Σ spin-orbit potential (V_{so}) was intensively discussed [Dover C B, 1986]. It was usually believed that its amount may distinguish between quark-gluon and meson-excange pictures of baryon-nucleon interactions. In a simple additive quark model [Pirner H J, 1979] [Pirner H J and Povh B, 1982] a large Σ spin-orbit potential was predicted:

$$V_{SO}^{N}:V_{SO}^{\Lambda}:V_{SO}^{\Sigma}:V_{SO}^{\Xi}=1:0:\frac{4}{3}:-\frac{1}{3},$$

Where as OBE models[Bando H, 1981] predict much smaller values ($V_{SO}^{\Sigma} \sim V_{SO}^{N}/3,\ V_{SO}^{\Sigma} \sim V_{SO}^{\Lambda}$). The experiments [Bertini*et al.*, 1985][Yamazaki T *et al.*, 1986] in the mid-eighties supported the idea of large Σ spin-orbit strength and thus the quark model. Large Σ spin-orbit strength [Dover C B, 1986] would contradict both quark and OBE models. New data are needed to settle this problem.

In this research, Σ spin-orbit strength (V_{so}) is used as 18 MeV according to the reference [Wünsch R and Zofka J, 1988]. Attractive Coulomb interaction is also taken into account for the interaction between Σ^- and core nucleus. The total interaction between Σ^- and core nucleus is

$$V(r) = V_l(r) + V_{w\text{-}s}(r) + V_{ls}(r) + V_c(r)$$

Vc is the Coulomb potential of a homogeneously charged sphere with the radius R_c. The value Rc = 1.25 (A-1) $^{1/3}$fm, is used in this calculation.

The total interaction between Σ^- and the other nucleons in core nucleus for j = *l*+1/2 and for j = *l*-1/2 are as in following equations 11(a) and (b).

$$V(r) = \frac{\hbar^2}{2m_\Sigma}\frac{\ell(\ell+1)}{r^2} - \frac{V_0}{1+e^{\frac{r-R}{a}}} - V_{so}\left(\frac{\hbar}{m_\pi c}\right)^2\left(\frac{1}{2}\ell\right)\frac{1}{ra}\frac{e^{\frac{r-R}{a}}}{\left(1+e^{\frac{r-R}{a}}\right)^2} + V_c(r) \qquad 11(a)$$

$$V(r) = \frac{\hbar^2}{2m_\Sigma}\frac{\ell(\ell+1)}{r^2}\frac{-V_0}{1+e^{\frac{r-R}{a}}} + V_{so}\left(\frac{\hbar}{m_\pi c}\right)^2\left(\frac{1}{2}(\ell+1)\right)\frac{1}{ra}\frac{e^{\frac{r-R}{a}}}{\left(1+e^{\frac{r-R}{a}}\right)^2} + V_c(r) \qquad 11(b)$$

Due to Σ→Λ strong conversion channel, the complex potential is used in which real part of potential gives the bonding energy and imaginary part gives the level width of Σ^- single particle states in Σ-hypernuclei. The parameters which are used in this calculation are summarized in table (1).

Table 1 The potential and range parameters used in our calculation [Bando H *et al.*, 1990]

Types of Parameter	Λhypernuclei	Σ^-hypernuclei
strength of Woods-Saxon central potential	-30 MeV	(-10 - i3) MeV
Diffuseness parameter (a)	0.6 fm	0.6 fm
Radius of single nucleon (r_0)	1.1 fm	1.1 fm
Strength of spin-orbit potential	-4 MeV	-18 MeV

Results and Discussions

In order to know the attractive Coulomb interaction effect in Σ^--hypernuclei, the energy eigen values of Σ^-hypernuclei are calculated within the frame work of Woods-Saxon central potential with and without Coulomb interaction. The results are compared in figure (1).

To investigate the role of Λ and Σ hyperons in hypernuclei, single particle states and root mean square distance of light hypernuclei ${}^{16}_{\Lambda}O$ and ${}^{16}_{\Sigma^-}C$ and heavy hypernuclei ${}^{208}_{\Lambda}Pb$ and ${}^{208}_{\Sigma^-}Hg$ are calculated and the results are compared in table (2) to (5). Energy states are also displayed in figure (2) and (3).

Table 2 Λ and Σ single particle states of light hypernuclei ${}^{16}_{\Lambda}O$ and ${}^{16}_{\Sigma^-}C$ for different *lj* states

Single-particle States	${}^{16}_{\Lambda}O$	${}^{16}_{\Sigma^-}C$		**Single particle states**	${}^{16}_{\Lambda}O$	${}^{16}_{\Sigma^-}C$	
	Single particle energy (MeV)	**Single particle energy (MeV) (without Coulomb Potential)**	**Single particle energy (MeV) (with Coulomb Potential)**		**Single particle energy (MeV)**	**Single particle energy (MeV) (without Coulomb potential)**	**Single particle energy (MeV) (with Coulomb potential)**
1s	-13.04	-1.07-1.27	-4.79-1.60	$1s_{1/2}$	-13.04	-1.07-1.27	-4.79-1.60
1p	-2.34	-	-0.21-0.24	$1p_{3/2}$	-2.76	-	-2.01-0.89
				$1p_{1/2}$	-1.54	-	-

Table 3 Root-mean-square distance of light hypernuclei ${}^{16}_{\Lambda}O$ and ${}^{16}_{\Sigma^-}C$ for different *lj*states

Single-particle States	**RMS distance (fm)**	**RMS distance (fm) (without Coulomb potential)**	**RMS distance (fm) (with Coulomb potential)**	**Single-particle States**	**RMS distance (fm)**	**RMS distance (fm) (without Coulomb potential)**	**RMS distance (fm) (with Coulomb potential)**
1s	2.19	3.87	3.03	$1s_{1/2}$	2.19	3.87	3.03
1p	3.34	-	8.34	$1p_{3/2}$	3.28	-	4.27
				$1p_{1/2}$	3.48	-	-

Table 4 Λ and Σ single particle states of heavyhypernuclei $^{208}_{\Lambda}Pb$ and $^{208}_{\Sigma^-}Hg$ for different *lj*states

Single-particle States	$^{208}_{\Lambda}Pb$	$^{208}_{\Sigma^-}Hg$		Single particle states	$^{208}_{\Lambda}Pb$	$^{208}_{\Sigma^-}Hg$	
	Single particle energy (MeV)	**Single particle energy (MeV) (without Coulomb Potential)**	**Single particle energy (MeV) (with Coulomb Potential)**		**Single particle energy (MeV)**	**Single particle energy (MeV) (without Coulomb potential)**	**Single particle energy (MeV) (with Coulomb potential)**
1s	-25.86	-6.99-2.76	-30.99-2.92	$1s_{1/2}$	-25.86	-6.99-2.76	-30.99-2.92
1p	-21.85	-4.16-2.48	-26.69-2.80	$1p_{3/2}$	-21.91	-5.03-2.39	-27.22-2.75
				$1p_{1/2}$	-21.74	-2.71-2.64	-25.82-2.86
1d	-17.07	-0.93-2.05	-22.10-2.60	$1d_{5/2}$	-17.24	-3.26-1.98	-23.84-2.48
				$1d_{3/2}$	-16.82	-	-19.96-2.79
2s	-15.44	-	-21.60-2.48	$2s_{1/2}$	-15.44	-	-21.60-2.48
1f	-11.64	-	-17.28-2.33	$1f_{7/2}$	-11.98	-	-20.78-2.16
				$1f_{5/2}$	-11.22	-	-13.54-2.57
2p	-9.34	-	-16.60-2.09	$2p_{3/2}$	-9.48	-	-17.59-2.09
				$2p_{1/2}$	-9.18	-	-14.62-2.12
1g	-5.69	-	-12.31-1.98	$1g_{9/2}$	-6.25	-	-17.75-1.89
				$1g_{7/2}$	-5.07	-	-6.58-2.11
2d	-3.16	-	-11.87-1.62	$2d_{5/2}$	-3.63	-	-13.60-1.78
				$2d_{3/2}$	-3.04	-	-9.15-1.33
3s	-2.77	-	-11.86-1.51	$3s_{1/2}$	-2.77	-	-11.86-1.51
1h	-0.30	-	-7.38-1.53	$1h_{11/2}$	-0.21	-	-14.52-1.66
				$1h_{9/2}$	-	-	-1.04-0.71
2f	-	-	-7.59-1.20	$2f_{7/2}$	-	-	-9.50-1.51
				$2f_{5/2}$		-	-5.24-0.73
2g	-	-	-3.60-0.99	$2g_{9/2}$	-	-	-5.50-1.22
				$2g_{7/2}$	-	-	-1.85-0.76
1i	-	-	-2.64-1.06		-	-	

Table 5 Root-mean-square distance of heavy hypernuclei $^{208}_{\Lambda}Pb$ and $^{208}_{\Sigma^-}Hg$ for different *lj* states

Single-particle States	$^{208}_{\Lambda}Pb$	$^{208}_{\Sigma^-}Hg$		**Single particle states**	$^{208}_{\Lambda}Pb$	$^{208}_{\Sigma^-}Hg$	
	RMS distance (fm)	**RMS distance (fm) (without Coulomb potential)**	**RMS distance (fm) (with Coulomb potential)**		**RMS distance (fm)**	**RMS distance (fm) (without Coulomb potential)**	**RMS distance (fm) (with Coulomb potential)**
1s	3.59	4.15	3.37	$1s_{1/2}$	3.59	4.15	3.37
1p	4.25	5.05	4.21	$1p_{3/2}$	4.26	5.25	4.35
				$1p_{1/2}$	4.23	4.66	3.97
1d	4.73	5.99	4.86	$1d_{5/2}$	4.76	6.02	5.14
				$1d_{3/2}$	4.70	-	4.48
2s	4.39	-	4.76	$2s_{1/2}$	4.39	-	4.76
1f	5.13	-	5.44	$1f_{7/2}$	5.17	-	5.72
				$1f_{5/2}$	5.10	-	4.98
2p	4.88	-	5.47	$2p_{3/2}$	4.94	-	5.44
				$2p_{1/2}$	4.93	-	5.47
1g	5.50	-	6.02	$1g_{9/2}$	5.56	-	6.13
				$1g_{7/2}$	5.45	-	5.87
2d	5.45	-	6.31	$2d_{5/2}$	5.74	-	6.01
				$2d_{3/2}$	5.78	-	6.86
3s	6.13	-	6.45	$3s_{1/2}$	6.13	-	6.45
1h	48.53	-	6.67	$1h_{11/2}$	6.03	-	6.43
				$1h_{9/2}$	49.50	-	8.23
2f	-	-	7.14	$2f_{7/2}$	-	-	6.62
				$2f_{5/2}$	-	-	8.00
2g	-	-	7.77	$2g_{9/2}$	-	-	7.29
				$2g_{7/2}$	-	-	8.34
1i	-	-	7.39		-	-	-

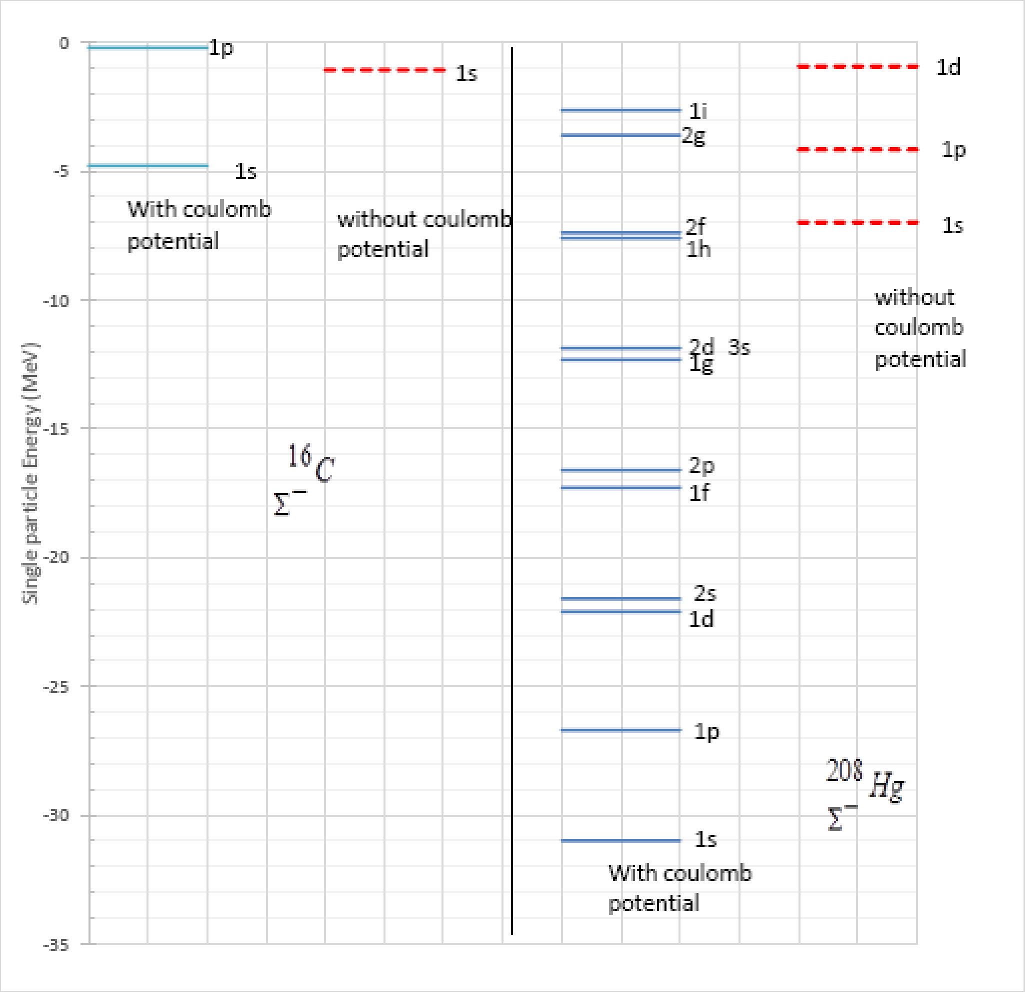

Figure 1 Σ^- single particle states in $^{16}_{\Sigma^-}C$ and $^{208}_{\Sigma^-}Hg$ for different orbital angular momenta states with Coulomb and without Coulomb potential

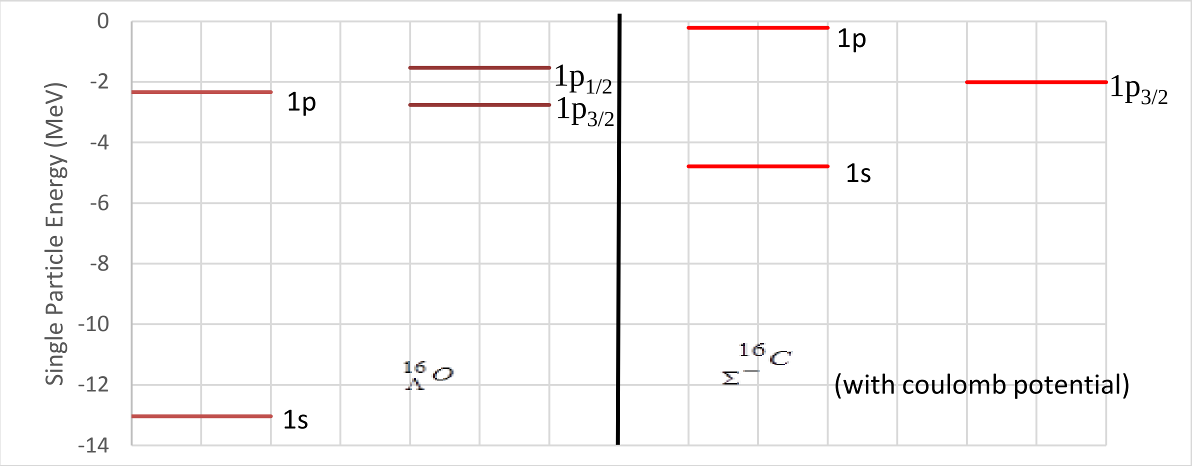

Figure 2 Λ andΣ^- single particle states in light hypernuclei $^{16}_{\Lambda}O$ and $^{16}_{\Sigma^-}C$ for different*lj*states

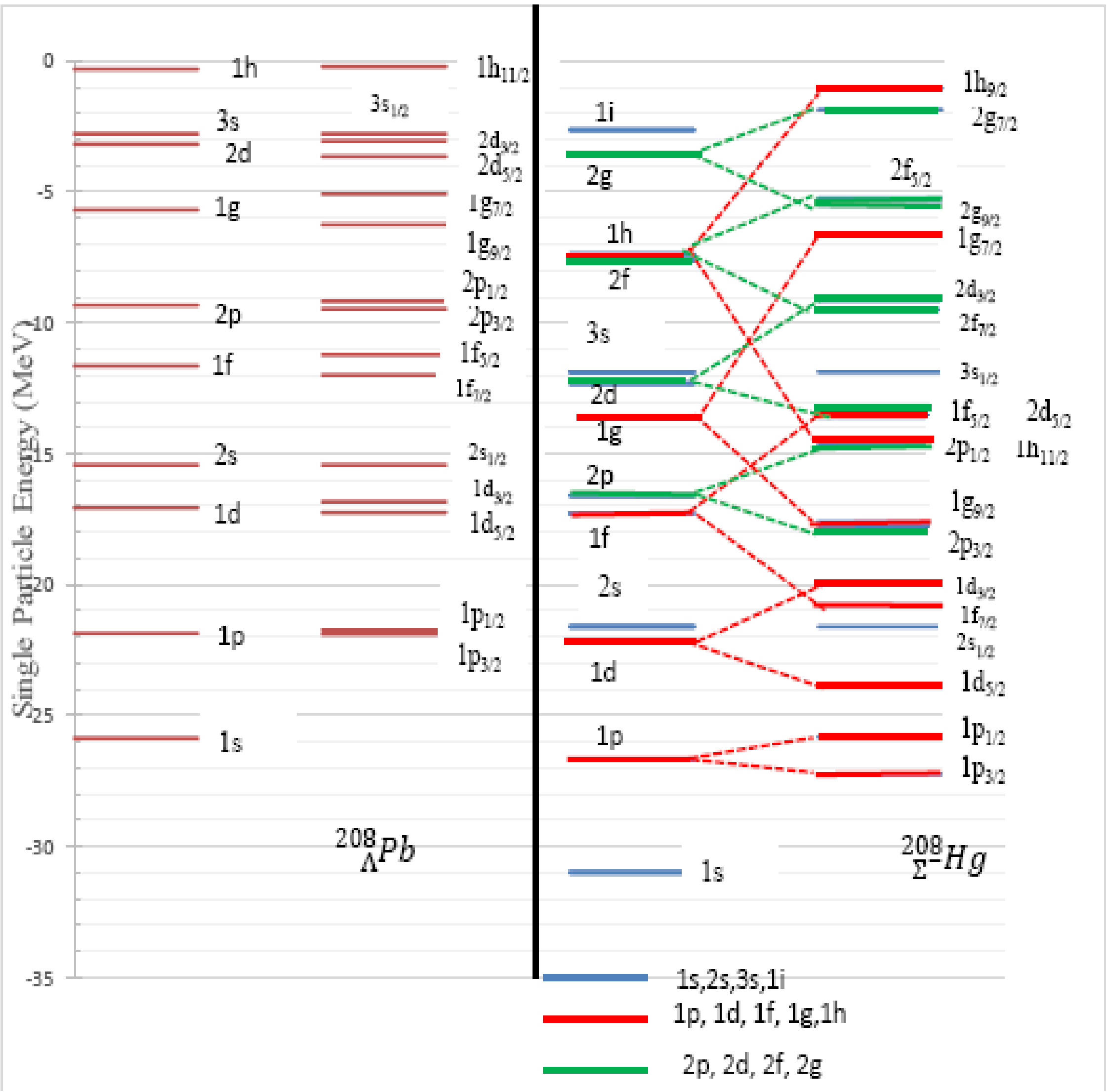

Figure 3Λ andΣ$^-$ single particle states in heavy hypernuclei $^{208}_{\Lambda}Pb$ and $^{208}_{\Sigma^-}Hg$ for different *lj* states

The Coulomb interaction effect can be seen in figure (1). It is found that the energy states without Coulomb potentials are higher than that of with Coulomb potential in both light and heavy Σ$^-$-hypernuclei. Therefore, it can be concluded that it is important to take into account the attractive Coulomb potential between Σ$^-$and core nucleus for the calculation of single particle states in Σ$^-$-hypernuclei.

The energy eigen values and root-mean-square (RMS) distance of light hypernuclei $^{16}_{\Lambda}O$ and $^{16}_{\Sigma^-}C$ are presented table (2) and (3). And, Λ andΣ$^-$single particle states of those two light hypernuclei are displayed in figure (2).According to the calculated results, it is observed that the lowest binding state of $^{16}_{\Lambda}O$ is 1p$_{1/2}$ state while 1p$_{3/2}$ state is lowest binding state in $^{16}_{\Sigma^-}C$. Moreover, it is found that single particle states of $^{16}_{\Lambda}O$ are lower than that of $^{16}_{\Sigma^-}C$ although

Coulomb potential is included in the calculation of energy states of ${}^{16}_{\Sigma^-}C$ hyper nuclei. Therefore, it can be concluded that binding energy of light Λ-hypernucleus ${}^{16}_{\Lambda}O$ is larger than that of light Σ^--hypernucleus ${}^{16}_{\Sigma^-}C$.

Another observation is that the higher the single particle states, the larger the RMS distance with the increase in orbital angular momentum number in those two light hypernuclei.

The energy eigen values and RMS distance of heavy hypernuclei ${}^{208}_{\Lambda}Pb$ and ${}^{208}_{\Sigma^-}Hg$ are presented in table (4) and (5). ΛandΣ^- single particle states in those two heavy hypernuclei for different *lj*states are displayed in figure (3). According to the calculated results, it is found that the lowest binding state of ${}^{208}_{\Lambda}Pb$ is $1h_{11/2}$ state while $1h_{9/2}$ state is lowest binding state in ${}^{208}_{\Sigma^-}Hg$ when the Coulomb potential is included in the calculation of energy levels of ${}^{208}_{\Sigma^-}Hg$ hypernucleus. In the heavy hepernuclei, binding energies of ${}^{208}_{\Sigma^-}Hg$ is larger than that of ${}^{208}_{\Lambda}Pb$ in different orbital angular momentum states.

It is found that RMS distance for Σ hyperon in ${}^{208}_{\Sigma^-}Hg$ gradually increased with the decreasingof energy eigen values within the frame work of the Woods-Saxon central potential including with and without Coulomb potential.

It is also observed that energy splitting of ${}^{208}_{\Sigma^-}Hg$ is larger than that of ${}^{208}_{\Lambda}Pb$ with the increase in orbital angular momentum number. It is due to the larger spin-orbit potential strength of Σ-hypernuclei than that of Λ-hypernuclei.

The interesting result what we found in our calculation is that the RMS distance for Σ-hyperon in ${}^{208}_{\Sigma^-}Hg$ gradually increased with the increasing of energy eigen values when the spin-orbit interaction is switched on.

In order to understand this strange behaviorclearly, the potential and the corresponding wave function have been plotted for various *lj* states of ${}^{208}_{\Sigma^-}Hg$ which are displayed in figure 4 (a) to (d). It is found that the attractive interaction strength of total spin$j = l + s$ state is stronger than that of $j = l - s$ state. The stronger interaction strength gives the greater binding energy. Moreover, the spin-orbit attractive potential works near the nuclear surface. Furthermore, the single-nucleon wave functions for$j = l + s$ are more shifted to the outer region than that having spin state $j = l - s$ and that is why the root-mean-square distance of nuclei for each spin state is larger although the binding energy is large. These effects could explain why both the rms value and binding energy are large.

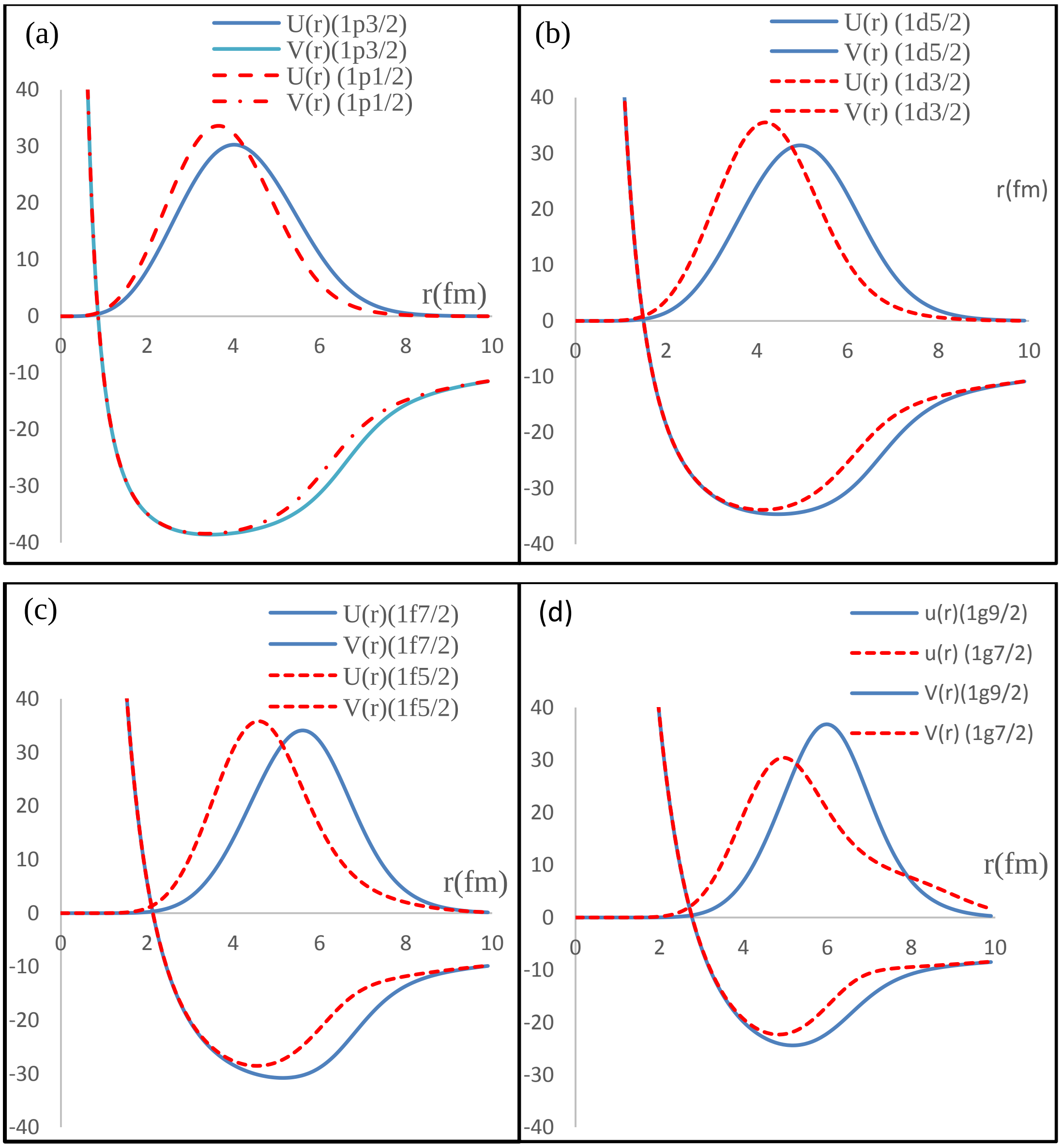

Figure 4 Σ single-particle wave functions and potentials in $^{208}_{\Sigma^-}Hg$ for

(a) 1p state and (b) 1d state(c) 1f state (d) 1g state

Conclusion

We have investigated the characteristic of Λ and Σ hyperons in light hypernuclei $^{16}_{\Lambda}O$ and $^{16}_{\Sigma^-}C$ and heavy hypernuclei $^{208}_{\Lambda}Pb$ and $^{208}_{\Sigma^-}Hg$. Single particle energy states and RMS distance of Λ and Σ hyperons are calculated by solving one body Schrödinger radial equation using power inverse iteration method numerically. For Σ-hypernuclei, Coulomb interaction is included beside Woods-Saxon central potential and Woods-Saxon spin-orbit potential in the calculation of energy eigen values to investigate the effect of Coulomb interaction. It is found that Coulomb interaction is important to take into account in the calculation of energy eigen values for Σ hypernuclei. And, it is observed that the binding energy of light hypernucleus $^{16}_{\Lambda}O$ is larger than that of $^{16}_{\Sigma^-}C$. But, binding energy of heavy hypernucleus $^{208}_{\Lambda}Pb$ is smaller than that of $^{208}_{\Sigma^-}Hg$ due to the Coulomb attractive interaction in heavy hypernucleus $^{208}_{\Sigma^-}Hg$. Therefore, it can be concluded that the Σ-single particle states are coulomb assistant nuclear states. It isfound that the energy splitting of Σ hypernuclei is larger than that of Λ hypernuclei due to the large spin-orbit strength of Σ hypernuclei.

And, it is also find out the interesting observation that the root-mean-square distance of nuclei for each spin state of heavy Σ^--hypernucleus is larger although the binding energy is large.Because, the spin-orbit attractive potential works near the nuclear surface and the single-hyperon wave functions for $j = l + s$ are more shifted to the outer region than that having spin state$j = l - s$.

Acknowledgements

I am deeply grateful to Dr Khin Swe Myint, Emeritus Professor, Rector (Rtd.), University of Mandalay, for her invaluable advices and discussion for this work. And, I thank to the member of Theoretical Nuclear Physics group of Physics department, University of Mandalay for their useful discussions.

References

Bando H, (1981), Prog. Theor. Phys. **66** 1349.

Bando H, Motoba T and Zofka J, (1990), Intl. J. Mod. Phys. **A 5** 4079 and references are therein.

Bertini R *et al.,* (1985), Phys. Lett. **158B** 19.

Bressani T *et al.,* (1989), NuovoCimento**A102** 491.

Dover C B, (1986), Proc. Int. Nucl. Phys. Conf. 99.

Hayano R S *et al*., (1988), INS-Rep. **705**.

Harada T and Akaishi Y, (1990), *phys. Lett*. **B234** 455.

PirnerH J, (1979), Phys. Lett. **85B** 190.

PrinerH J and Povh B, (1982), Phys. Lett. **114B** 308.

Yamazaki T *et al.*, (1986), Nucl. Phys. **450** 1c.

Wünsch R and Zofka J, (1988), J. Phys. **B38** 755.

J. Myanmar Acad. Arts Sci. 2020 **Vol. XVIII.No.2A**

GLUE LIKE ROLEOFTHE Λ-PARTICLEIN α-x-Λ CLUSTER STRUCTURE

Theingi[1], San San Aye[2], Min Min Aye[3],San San Nu[4]and KhinSwe Myint[5]

Abstract

Energy levels of the lambda- hypernuclei$_{\Lambda}^{6}$He, $_{\Lambda}^{7\text{-}8}$Li, $_{\Lambda}^{9}$Be are predicted on the basis of the α-x-Λ three-body model with x = n, d, tand α, respectively. Rearrangement coupled-channels Gaussian basis treatment is used to solve the three-body system. Interactions between the constituent particles are determined so as to reproduce reasonably the observed low-energy properties of the α-x nuclei (^{5}He, $^{6\text{-}7}$Li, ^{8}Be) and the existing data of Λ-binding energies of the x+Λ and α+x+Λ systems ($_{\Lambda}^{3\text{-}4}$H, $_{\Lambda}^{5}$He and $_{\Lambda}^{6}$He,$_{\Lambda}^{7\text{-}8}$Li, $_{\Lambda}^{9}$Be). To solve resonance states with correct boundary condition we have used the proper treatment of the Complex Rotation method. In our calculation, Pauli forbidden states between x and α-clusters were excluded from the solution of Schrödinger equation by implementing the Orthogonality Condition Model (OCM). Structure change of the α+x ordinary nuclei due to the participation of the Λ particle is found to be substantially large.

Keywords: Rearrangement coupled channel method, Complex rotation method, Orthogonality condition model.

Introduction

In nuclear physics, as in almost all branches of physics, the description of resonance is one of the most important tasks. A resonance can be viewed and approached from two different angles; as a delay connected with an enhanced phased shift in a scattering process or as a long-lived but decaying state of a compound system. The main observable characteristics of a resonance are the position and the level width. In the first picture they are to be determined from the phase shift (or cross section) as a function of energy. In the second picture the long-lived state is regarded as an extension of the concept of a bound state in that it is a solution to the Schrödinger equation with purely outgoing asymptotic belonging to complex energy. In our model, it is possible to determine the α-x and Λ-x interactions so as to reproduce all the existing binding of systems in an α-x-Λ three-body system.

Interactions

Interaction between Alpha and x Clusters

We have employed the α-n(t) potentials, parity dependent form with the central and spin-orbit terms, which is introduced by Kanada (Kanada H. et al., (1979)) and Furutani (Furutani H. et al., (1980)). The potential strengths and the range parameters are expressed in the following Gaussian form,

---

[1] Dr, Associate Professor, Physics Department, Mandalay University of Distance Education, Mandalay, Myanmar

[2] Dr, Lecturer, Physics Department, Lashio University, Lashio, Myanmar

[3] Dr, Lecturer, Physics Department, Kyutsee University, Lashio, Myanmar

[4] Dr, Lecturer, Department of Physics, Shwe Bo University, Shwe Bo, Myanmar

[5] Dr, Emeritus Professor, Physics Department, Mandalay University, Mandalay, Myanmar

$$V_{\alpha x}(r)=\sum_{i}^{i_{max}}V_i e^{-\beta_i r^2}+\sum_{i}^{i'_{max}}(-)^{\ell}V_i^{p}e^{-\beta_i^p r^2}+\left[\sum_{i}^{i''_{max}}V_i^{\ell.s}e^{-\gamma_i r^2}+i\sum_{i}^{i'''_{max}}(-)^{\ell}V_i^{\ell s.p}e^{-\gamma_i^p r^2}\right]\vec{\ell}.\vec{s}_x \quad (1)$$

where, $\vec{s}_x$ is the spin of neutron(n) or triton(t).The parameters in Eq.(1) are listed in Table (1) and Table (2). The relative angular momentum between α and neutron (triton) is 1 for ground state. The spin of neutron (triton), $\vec{s}_n$ ($\vec{s}_t$) is 1/2. Therefore, the total angular momenta for ground state and first excited state for ^{5}He(^{7}Li) are $3/2^-$ and $1/2^-$ respectively.

The α-d was also introduced by Furutani (Furutani H. et al., (1980)) as follows;

$$V_{\alpha-d}(r)=-74.42\ e^{-(r/2.236)^2}-8.0\ e^{-(r/1.826)^2}\ \vec{\ell}.\vec{s}_d \text{ for all } \ell. \qquad (2)$$

where ℓ is the relative angular momentum between α andd, and $\vec{s}_d$ is the spin of deuteron. The relative angular momenta between alpha and deuteron (ℓ) are 0 for ground state and 2 for 3^+, 2^+, 1^+ excited states. Since the spin of deuteron ($\vec{s}_d$) is 1, the angular momenta and parity for α-d system are 1^+ for ground state and 3^+, 2^+, 1^+ for three excited states. We have calculated the spin orbit $\vec{\ell}.\vec{s}$ coupling effect as $\vec{\ell}.\vec{s}=\left(j^2-\ell^2-s^2\right)/2$.

The size parameters of interaction are in fm^{-2}and strengths are in MeV.

Table (1) The parameters of α-N interaction. Table(2) The parameters of α-t interaction.

i	**1**	*2*	**3**
β_i	0.36	*0.90*	-
β_i^p	0.20	*0.53*	2.5
γ_i	0.396	*0.52*	2.2
γ_i^p	0.396	*2.2*	-
V_i	-96.3	*77.0*	-
V_i^p	34.0	-85.0	51.0
V_i^{ls}	-20.0	-16.8	20.0
$V_i^{ls,p}$	6.0	-6.0	-

i	**1**	*2*	**3**
β_i	0.0913	*0.1644*	0.2009
β_i^p	0.0913	*0.1644*	0.2009
γ_i	0.28	-	-
γ_i^p	0.28	-	-
V_i	6.9	*-43.35*	-51.7
V_i^p	6.9	43.35	-51.7
V_i^{ls}	-1.2	-	-
$V_i^{ls,p}$	1.2	-	-

The α-α potential is also given in Gaussian form as follows;

$$V_{\alpha-\alpha}(r)=-1.742\ e^{-(r/3.0)^2}-395.9\ e^{-(r/1.898)^2}+299.4\ e^{-(r/1.738)^2}. \qquad (3)$$

These potentials reproduce reasonably well the low-lying states and low-energy scattering phase shifts of the α-x systems.We have also employed the OCM-based cluster model study of light nuclei (Hasegawa A. et al., (1971)).

Lambda- x Potential

In our calculations, we use the effective lambda-neutron Nijmegen model potential of Akaishi (Akaishi Y. (2007)). It is derived from realistic one-boson-exchange YN potential of Nijmegen model D (Nagels. M.M. et al.,(1977)). The original Nijmegen potential is simulated by

Shinmura so as to reproduce the phase shift parameters as the original Nijmegen potential. Then, the effective Y-N potential is derived by the Brueckner Theory. It is parameterized into five-range Gaussian form and parameters for Λ-n singlet even and triplet even state potentials are given in Table (3).

$$V_{\Lambda-n}^{s,t}(r) = \sum_{k=1}^{5} V_k^{s,t} e^{-(\frac{r}{\mu_k})^2} \qquad (4)$$

where s, t stand for singlet and triplet state, respectively.

Table 3 Strength parameters for Λ-n interaction

μ_k (fm)	V_k^s (MeV)	V_k^t(MeV)
0.1800000	47.99645	-46.25826
0.3286335	-272.7777	-43.8389
0.6000000	679.7185	493.1045
1.095445	-160.1574	-136.9770
2.000000	-2.74696	-0.5687829

The phenomenological Λ-d potential was also constructed by adjusting the parameters to fit the value B_Λ=(0.13±0.05) MeV (Bertini R. et al., (1979)).For the Λ-t interaction in $_\Lambda{}^4$H system, we have applied isle type potential which is derived from Dalitz hard core ΛN interaction (Dalitz R.H. et al., (1972)).

Among the various Λ-α potentials, we discuss the potential which is introduced by Myint, Shinmura and Akaishi (Akaishi Y. et al., (2003)) which we will call it MSA Λ-α potential. The required Λ-α potential which based on this effective Λ-N potential is constructed by Hartree-Fock method. It is slightly modified so as to reproduce the experimental binding energy of the $_\Lambda{}^5$He hypernucleus. Lambda-x interactions are expressed in the following Gaussian form;

$$V_{\Lambda-x}(r) = \sum_{k=1}^{3} V_k e^{-(\frac{r}{\mu_k})^2}. \qquad (5)$$

The parameters in Eq.(5) are listed in Table (4).

Table 4 The range parameters of Λ-x interactions are in fm and strengths are in MeV. (x=d,t and α)

System	V_1	V_2	V_3	μ_1	μ_2	μ_3
Λ-d	181.70	-103.40	-30.84	1.08	1.32	1.78
Λ-t	359.2	-324.9	-	1.25	1.41	-
Λ-α	91.0	-95.0	-	1.30	1.70	-

Pauli Suppression Effect in Three-Body System

The Pauli principle between nucleons belonging to α and x clusters is taken into account by the Orthogonality Condition Model; OCM (Saito S., (1969)).The OCM projection operator Vpauli is represented by

$$V_{Pauli} = \lim_{\lambda\to\infty} \lambda \sum_{f} \left|\phi_f(\vec{r})\right\rangle\left\langle\phi_f(\vec{r})\right|. \tag{6}$$

which rules out the amplitude of the Pauli forbidden α-x relative states from $\phi_f(r_{\alpha x})$ the two-body total wave function. The forbidden states are f={0S} for n(p), f={0S, 0P}for d, f = {0S, 1S, 0P, 0D} for t (3He) and f = {0S, 1S, 0D} for α. In the calculation, the strength λ forV_{pauli} is taken to be 10^5 MeV, which is large enough to push up away the unphysical forbidden states into the very high energy region while keeping the physical states unchanged. Harmonic oscillator wave functions are applied for forbidden states.

Complex Coordinate Rotation Method

We use the method of complex coordinate rotation (Gyarmati B. and Kruppa A.T., (1985))to investigate the resonance states. According to the complex rotation method,the following coordinate transformation $r \rightarrow r\,e^{i\theta}$ is carried out, whereθ is a real number called rotation angle.Under this transformation, wave function is defined as

$$\Psi(r) \rightarrow \Psi(re^{i\theta}) = \Psi_\theta(r) = \hat{U}(\theta)\Psi(r). \tag{7}$$

Schrödinger Equation under complex rotation is,

$$H_\theta(r)\Psi_\theta(r) = E\ \Psi_\theta(r). \tag{8}$$

Then the asymptotic resonance wave function in Gaussian basis expansion is transformed as

$$\Psi_\theta(r) = \sum_j c_j(\theta)\, e^{-(r/b_j)^2} \tag{9}$$

Schrödinger Equation becomes

$$H(r)\sum_j c_j(\theta)e^{-(r/b_je^{i\theta})^2} = E\sum_j c_j(\theta)e^{-(r/b_je^{i\theta})^2} \tag{10}$$

We have to solve the Schrödinger equation which is the same as bound state system except the range parameter b_j becomes $b_je^{i\theta}$.

Three-Body Schrödinger Equation

Then Schrödinger equation becomes

$$\left[-\frac{\hbar^2}{2\mu_c}\vec{\nabla}^2_{\vec{r}_c} - \frac{\hbar^2}{2M_c}\vec{\nabla}^2_{\vec{R}_c} + \begin{Bmatrix} V_{23}(r_1)+V_{13}(r_2)+V_{12}(r_3) \\ +V_{Paul}+V_{Coul} \end{Bmatrix}\right]\Psi\left(\vec{r},\vec{R}\right) = E\,\Psi\left(\vec{r},\vec{R}\right) \tag{11}$$

where c is the channel, c=1, 2 and 3which are described in Fig.1.

The total wave function with angular momentum J and Z component M,$\Psi_{J,M}$ may be expanded in terms of basis functions spanned over the threeRearrangement coupled-channels Gaussian basis treatment (Kamimura M. (1988)) as follows;

$$\Psi_{JM} = \sum_{c=1}^{3} \sum_{i_cI_cl_cL_c} D^{(c)}_{i_cI_cl_cL_c}\phi^{(c)}_{i_cJ_c}(r_c)\chi^{(c)}_{l_cL_c}(R_c)\times\left[Y_{l_c}(\hat{r}_c)Y_{L_c}\left(\hat{R}_c\right)\right]_{JM} \tag{12}$$

Here l_c (L_c) stands for the angular momentum of the relative motion associated with the coordinate r_c (R_c), and the bracket $\left[Y_{l_c}(\hat{r}_c)Y_{L_c}(\hat{R}_c)\right]_{JM}$ JM represents the vector coupling of the two spherical harmonics.

In Eq. (12), l_c and L_c are restricted as $0 \le \ell_c \le \ell_c^{\max}$, $|J - l_c| \le L_c \le J + l_c$, and $(-1)^{l_c+L_c} = (-1)^J$ .The numbers i_c and I_c specify the radial dependences of $\phi^{(c)}_{i_c l_c}(r_c)$ and $\chi^{(c)}_{I_c L_c}(R_c)$, respectively. The form of the radial functions ϕ and χ is taken as

$$\phi_{il}(r) = r^{\ell} \exp\{-(r/b_i)^2\}\ , \qquad b_i = b_1 a^{(i-1)}, (i = 1 - n),$$

$$\chi_{IL}(R) = R^{L} \exp\{-(R/B_I)^2\} \qquad B_I = B_1 A^{(I-1)}, (I = 1 - N).$$

These basis functions have been verified to be suited for describing both short-range correlations and long-range tail behaviorsof few-body systems. The eigen energy E and the coefficients D in Eq.(12) are to be determined by the variational method.

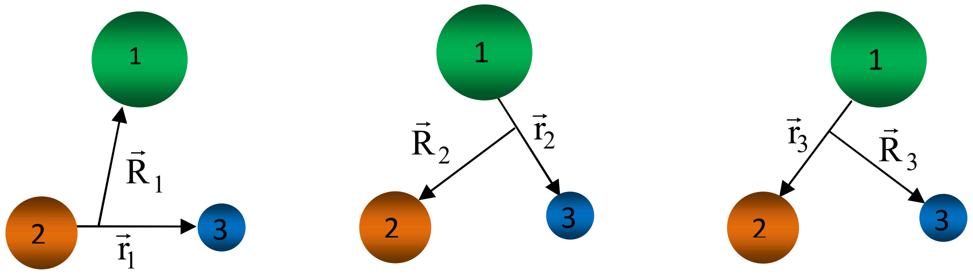

Channel (1) Channel (2) Channel (3)

Figure 1 Three rearrangement channels of the α-x-Λ system and their Jacobian coordinate

Relative Density Distribution and Root Mean Square Distance

The relative density distribution $\rho(r_c)$ is obtained by integrating over the other Jacobian coordinate $\vec{R}_c$ and the angular part of $\vec{r}_c$ as follows;

$$\rho(r_c) = \int |\Psi|^2 \, d\vec{R}_c d\hat{r}_c$$

where Ψ is the total wave functionof three-body.

The root mean square distances corresponding to the above density distributions are defined as

$$\tilde{r}_c = \left[\int r_c^2 \rho(r_c) r_c^2 \, dr_c\right]^{1/2} \tag{13}$$

Results and Discussions

Resonance states of x- α cluster

Studies of resonances are indispensable for understanding the unique properties of drip-line nuclei. We have performed the α+n, α+d, α+t and α+α two- body calculation for ^{5}He, $^{6\text{-}7}$Li, and ^{8}Be. The positions of resonance states in the complex energy plane remains almost unchanged with the variation of rotation angle θ. Pauli operator is applied to push out the forbidden states between α-x clusters. The results and discussion are summarized as follows;

1) The ^{5}He system has been investigated as the typical example of the α-n model. The energies and level widths of these systems we obtained are in good agreement with the experimental values (Tilley D.R. et al., (2002))

2) The excited states of $^{6\text{-}7}$Li have been calculated as resonance states of the α-d and α-t system. All our calculated results are in good agreement with the experimental values except for the excited 2^+ resonance state of ^{6}Li, which lies about 0.735 MeV above the experimental one (2.836±0.022 MeV). Since there are two 2^+ resonance states with different isospin (I=0 and I=1). Our interaction is independent of isospin and it is not suitable to treat isospin dependent resonance states.

3) The energies and level widths of ^{8}Be have been investigated with α-α model. The obtained binding energies agree with the experimental values within the experimental error (Tilley D.R. et al., (2004)).Therefore to summarize our results, almost all the bound states and excited resonance states we examined are well reproduced by this α-x cluster model with complex rotation method.

Table 5 The energy eigen values of ^{5}He, ^{6}Li, ^{7}Li and ^{8}Be systems

States	**Energy Level, E (MeV)**		**Level Width, Γ(MeV)**	
	Our Results	**Exp: Results (Tilley D.R. et al., (2002))**	**Our Results**	**Exp: Results (Tilley D.R. et al., (2002))**
^{5}He(3/2$^-$)	0.89	0.886±0.008	0.596	0.648±0.006
^{5}He(1/2$^-$)	2.15	2.068±0.021	5.009	5.570±0.056
^{6}Li(1$^+$) g.s	-1.470	-1.474	0	stable
^{6}Li(3$^+$)	0.703	0.712±0.002	0.024	0.024±0.002
^{6}Li(2$^+$)	3.571	2.836±0.022	1.514	1.300±0.100
^{6}Li(1$^+$)	4.266	4.176±0.050	3.792	1.500±0.200
^{7}Li(3/2$^-$)	-2.460	-2.467	0	stable
^{7}Li(1/2$^-$)	-2.065	-1.989±0.003	0.004 eV	0.219±0.006eV
^{7}Li(7/2$^-$)	2.452	2.185±0.011	0.126	0.069±0.003
^{7}Li(5/2$^-$)	3.357	4.137±0.207	0.400	0.918±0.046
^{8}Be(0$^+$)	0.085	0.091	0.040	0.005±0.25eV
^{8}Be(2$^+$)	3.148	3.121±0.010	1.686	1.513±0.002

Total Binding Energies and Lambda Binding Energy ofα-x-Λ cluster

The binding energies of single lambda hypernuclei with α-x-Λ cluster structures have been studied within the coupled-rearrangement channel Gaussian basis treatment. In order to understand the role of Λ particle attached to the ordinary nuclei, it is useful to compare the obtained energy level structures of the α-x-Λ hypernuclei with those of α-x nuclei. The calculated binding energies in two-body and three-body are described in Table (5). Then we can see clearly how the ground and excited states of α-x nuclei are changed due to the participation of Λ-particle. One sees clearly that injection of Λ-particle leads to stronger binding of the whole system.

Table 6 The total binding energies in two-body and three-body and lambda binding energies; B_Λ

System	B.E (MeV) (α-x)Two-body	B.E (MeV) Three-body	B_Λ(Cal.) (MeV)	B_Λ(Exp.) (MeV)
$_\Lambda^6$He(α-n-Λ)	-0.89	3.29	4.18	4.18±0.10
$_\Lambda^7$Li(α-d-Λ)	1.47	7.31	5.84	5.58±0.03
$_\Lambda^8$Li(α-t-Λ)	2.50	9.32	6.82	6.80±0.03
$_\Lambda^9$Be(α- α -Λ)	-0.09	6.64	6.73	6.71±0.03

Structural change of the α-x nucleus

It is interesting to look at the structural change of the (α-x) ordinary nucleus which occurs due to the participation of Λ-particle. In order to see shrinkage effect in (α-x-Λ) system, we have calculated the two physical properties; the density distribution $\rho(r_{\alpha-x})$ and r.m.s distance between α and x, $\tilde{r}_{\alpha-x}$.Calculated r.m.s distances betweenα and x, $\tilde{r}_{\alpha-x}$ in ordinary nuclei and single Λ-hypernuclei are listed in Table (6). The r.m.s distances of ^{5}He and ^{8}Be ($\tilde{r}_{\alpha-n}$ and $\tilde{r}_{\alpha-\alpha}$) are not calculated since they are resonant states. For ^{6}Li→$_\Lambda^7$Li case, r.m.s distance $\tilde{r}_{\alpha-d}$ changes as 4.10 fm to 3.44 fm. Participation of the Λ-particle gives rise to about 19% reduction of $\tilde{r}_{\alpha-d}$ in three-body system.The r.m.s distance between alpha and triton $\tilde{r}_{\alpha-t}$ reduces from 3.7fm (^{7}Li) to 3.3fm ($_\Lambda^8$Li). It isdue to the glue like role of the attached Λ–particle.

Table 7 Calculated r.m.s distances between α and x(x= n, d, t, α); $\tilde{r}_{\alpha-x}$ (fm) in ordinary nuclei (two-body) and single Λ-hypernuclei (three-body).

System	$\tilde{r}_{\alpha-x}$ (fm) (two-body)	$\tilde{r}_{\alpha-x}$ (fm) (three-body)	Shrinkage (%)
$_\Lambda^6$He(α-n-Λ)	-	5.79	-
$_\Lambda^7$Li(α-d-Λ)	4.10	3.44	19
$_\Lambda^8$Li(α-t-Λ)	3.70	3.30	12
$_\Lambda^9$Be(α- α -Λ)	-	3.78	-

Summary

In this paper, we have investigated the structural change of the α-xordinary nucleus by the participation of the Λ-particle. We have carried out structure calculations of $_\Lambda^6$He, $_\Lambda^{7\text{-}8}$Li, $_\Lambda^9$Be within the frame work of α-x-Λ cluster model (x= n, d, t, α). The three-body calculations of the system were performed by using the Jacobian-coordinate Gaussian basis coupled-rearrangement-channel method. The Pauli forbidden states between α and x particles have been excluded from the solution of Schrödinger equation with OCM model. In our calculation, the optimum set of parameters are b_1= B_1=0.1 fm and a=A=1.996. Calculated lambda binding energies of $_\Lambda^6$He, $_\Lambda^{7\text{-}8}$Li, $_\Lambda^9$Be are in good agreement with the experimental values and injection of Λ-particle leads to stronger binding of the whole system. Dynamical change of the α-x ordinary nucleus by the participation of the Λ-particle is seen in Λ-hypernucleus; there occurs 19% shrinkage of the α-d and 12% shrinkage of the α-t distance compared with the distance in ordinary nucleus. Therefore we conclude that glue like role of the Λ-particle is important to study the Λ-Hypernuclei.

Acknowledgement

The authors greatly acknowledge Professor Y. Akaishi, RIKEN Nishina Center, Saitama, Japan for his valuable discussion and advice.

References

Akaishi Y.,Private communication.

Bertini R. et al.,(1979). Phys. Lett. **B83** 306.

Dalitz R. H. et al.,(1972).Nucl. Phys. **B47** 109.

Furutani H. et al.,(1980).Prog. Theor. Phys. Suppl. **68** 193.

Gyarmati B. and KruppaA.T., (1985).Phys. Rev. **C34** 1.

Hasegawa A. and NagataS., (1971).Prog. Theor. Phys. **45** 1786.

KanadaH. et al.,(1979).Prog. Theor. Phys. **61** 1327.

Kamimura M.,(1988). Phys. Rev. **A 38**621.

Myint K.S., Shinmura S. and Akaishi Y., (2003).Eur. Phys. J. **A 16** 21.

NagelsM.M., RijkenT.A. and de SwartJ.J.,(1977). Phys. Rev. **D 15** 2547.

SaitoS., (1969).Prog. Theor. Phys. **41**705.

Tilley D.R. et al.,(2002).Nucl. Phys. **A708** 3.

Tilley D.R. et al., (2004).Nucl. Phys. **A745** 155.

J. Myanmar Acad. Arts Sci. 2020 **Vol. XVIII.No.2A**

PHYSICOCHEMICAL ANALYSIS OF WATER FROM INLE LAKE

Ohnmar Oo[1], Min Min Myat Swe[2]

Abstract

Present study involves the analysis of water from Inle Lake using some physicochemical parameters such as pH, electrical conductivity, total dissolved solids, salinity, and elemental concentrations. Water samples were collected from three sites located in Inle Lake for the period of one year i.e. August 2013 to August 2014. As a result, some physiochemical parameters such as temperature, pH, Total dissolved solids, salinity and elemental concentrations at three sites are in normal range and within the permissible limits.

Keywords: Inle Lake, physicochemical parameters, electrical conductivity

Introduction

Water pollution is defined as any contamination of water that lessens its value to humans and nature. Pollution represents imbalance of one or more elemental cycles. Water pollutants for the lakes are sediments nutrients, oxygen demanding organic wastes, thermal pollution, disease organism, and toxic organic wastes by United Nation Environmental Programme International Environmental Technology Centre/International Lake Environment Committee Foundation (UNEP-IETC/ILEC, 2001). Water quality and water resources play a vital role for both natural ecosystem and human development (Zaw Lwin and Sharma, 2012; Akaishi *et al*., 2006).

The Inle Lake, the second largest lake in Myanmar, is located in Shan state in the Northeastern side of the country. It is an important water resource for more than 170000 people inhabiting the lake surrounding. The main business in Inle Lake is agriculture on the floating gardens and tourism. Nowadays the lake is impacted by many factors including pesticides from agriculture, chemical dyes from textile processing, excess siltation from watershed erosion, and the dumping of wastes and garbage.

It was reported that the water quality had declined at an increasing rate and the government initiated the Inle Lake preservation project (Butkus and Myint, 2001; Su, M. and Jassby, 2000).

According to the assessment of its water quality in 2012, the tropic state index of the Inle Lake is found to be in the range of eutrophication**.**

The aim of this paper is to assess the some physicochemical properties of water from Inle Lake in order to monitor the surface water quality of Inle Lake.

Materials and Methods

Sampling Area

Inlay Lake is located at latitude 20° 46'N and longitude: 97° 01'E. The temperature is between12°C-28°C. The populations of the Intars are about 80,000. Inle Lake is a huge lake (22 km long and 10 km across) located in Shan State, over 900 meters above sea-level, and it is outrageously beautiful.

---

[1] Dr, Associate Professor, Department of Physics, Mandalay University of Distance Education

[2] Lecturer, Department of Physics, Mandalay University of Distance Education

Inlay Lake is a freshwater lake located in the Nyaungshwe Township of Taunggyi District of Shan State, part of Shan Hills in Myanmar. It is the second largest lake in Myanmar with an estimated surface area of 44.9 square miles (116 km^2), and one of the highest at an elevation of 2900 feet (880 m). During the dry season, the average water depth is 7 feet (2.1 m), with the deepest point being 12 feet (3.7 m), but during the rainy season this can increase by 5 feet (1.5 m). Water samples were collected from three different places of Inle lake such as Thalay village (sample name P), Heya Ywama Village (Silver smith) (sample name S), Inn paw khon (Weaveing) (sample name W) starting August 13, 2013 finishing August 14, 2014 for measuring metals residues. Map of Inle Lake is shown in Figure 1.

Thalay Village

It is situated on the precinct of the Phaung Daw Oo Pagoda and opened daily. Local pilgrims and foreign visitors can buy different products of Inlay region as souvenirs. This region is crowded and very famous for tourist attraction.

Heya Ywama Village

This area is so filled with floating vegetation that it appears more land than lake. There are also many "floating gardens" where farmers plant crops like tomatoes on floating mats of vegetation anchored in place with bamboo poles. Ywama village which Gold Smith & Silver Smith Workshop is located is well known for its gold and silver ware.

Inn paw khon Village

Inn paw khon is also a popular tourist attraction, famous for its weaving workshops.

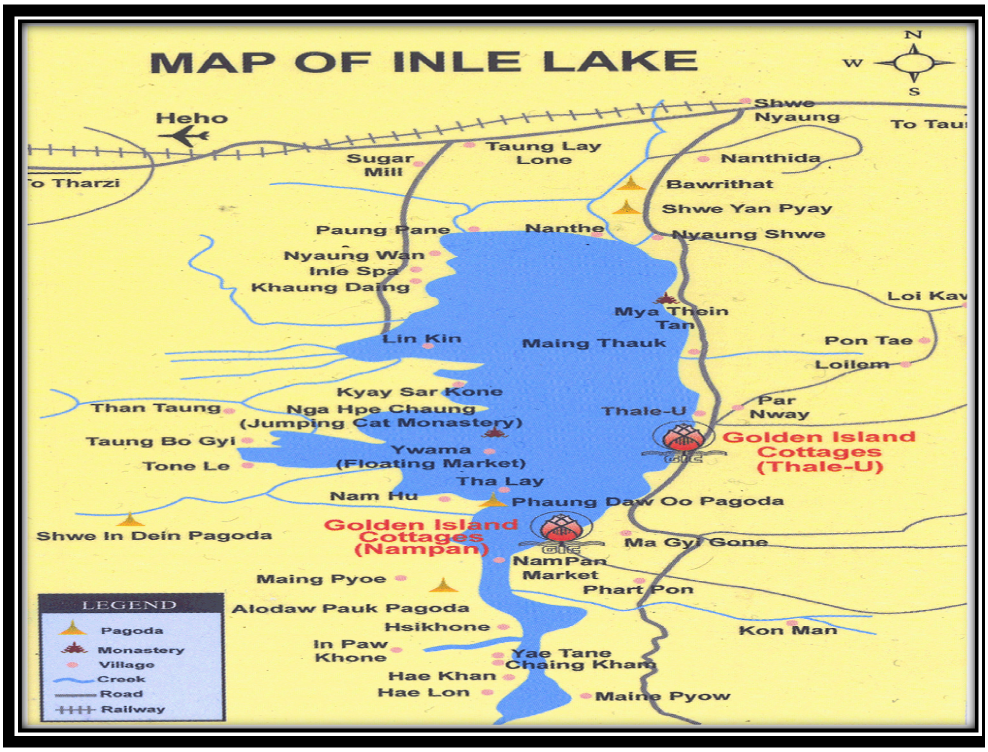

(Source: http://myanmartravelinformation.com/inle-map.html)

Figure 1 Figure 1 Map of Inle Lake

Collection of Water Samples

Water samples were collected from selected study sites to one liter plastic bottles with caps. Collected water samples were sent immediately to the laboratories of URC.

Methods

All water quality parameters were measured by Multiparameter Benchtop Meters (Cyber Scan 6000 Series Meters). Photograph of the Multiparameter Benchtop Meters (Cyber Scan 6000 Series Meters) is shown in Figure 2.

The samples were analyzed by the energy dispersive x-ray fluorescence spectrometry EDXRF (EDX-700), which has an Rh anode tube. This machine can provide the information of elements from silicon to uranium (Si-U). Photograph of the Shimadzu EDX-700 spectrometer is shown in Figure 3.

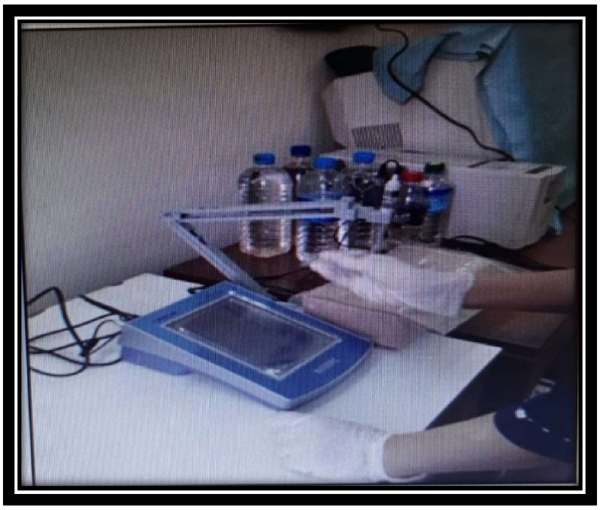

Figure 2 Photograph of the Multiparameter Benchtop Meters (Cyber Scan 6000 Series Meters)

Figure 3 Photograph of the Shimadzu EDX-700 spectrometer Universities' Research Centre (URC), Yangon University

Physicochemical Analysis

The temperatures of the samples were noted at the sampling point itself. Analysis was carried out for various water quality parameters such as pH, electrical conductivity, TDS, salinity, and elemental analysis.

X-ray Fluorescence Analysis (XRF)

The term "X-ray fluorescence analysis" (XRF) refers to the measurement of characteristic fluorescence emission resulting from the de-excitation of inner shell vacancies produced in the sample by means of suitable source of radiation. Numerous variants of the basic process have been studied. They differ both in the type and sources of ionization radiation and in the method employed to measure the fluorescent emission. For routine XRF analysis, two major approaches are distinguishable based on the detector used to measure the characteristic x-ray emission spectra.

The x-ray fluorescent analysis (XRF) is widely accepted as a standard method for elemental analysis since it offers a unique combination of flexibility and accuracy. The XRF analysis is given qualitative and quantitative results. (Tertian R & Claisse F, 1982, Principles of Quantitative X-ray Fluorescence Analysis (London: Heyden))

Results and Discussion

The variation in physicochemical characteristics of the water samples of three locations have been summarized in Figure 4 (a-e).

Water Temperature

The temperature of water samples among the study sites (Thalay village, Heya Ywama village and Inn paw khon village) ranged from a minimum of 23.0 °C to a maximum of 31.2 °C . In case of water samples, temperature of all the three locations was found to be high in April and low in September. (Figure 4 a)

pH

The pH of water at all the study sites showed a range of variation (7.26 - 9.75). Throughout the study period, pH values of all the three locations were found to be high in July and low in first half of August. In all the three locations, pH is always alkaline. (Figure 4 b)

Electrical Conductivity (EC)

Electrical conductivity of water samples at different study sites ranged from a minimum of 185.7 ± 25.368 µS cm^{-1} to a maximum of 463.2 ± 58.313 µS cm^{-1}. EC of all the three locations were found to be high in January and low in second half of August.

There is a sharp increase in conductivity was observed from December to April in all the sites during the study periods. (Figure 4 c)

Total Dissolved Solids (TDS)

The total dissolved solids of water samples ranged from a minimum of 119.3± 16.251 ppm to a maximum of 228.0 ± 27.199 ppm of Thalay village, Heya Ywama village and Inn paw khon village respectively. In case of water samples, TDS of all the three locations were found to be high in January and low in second half of August. In water, total dissolved solids are composed mainly of carbonates, bicarbonates, chlorides, phosphates and nitrates of calcium, magnesium, sodium, potassium and manganese, organic matter, salt and other particles. The minimum values were recorded at three locations in August. (Figure 4 d)

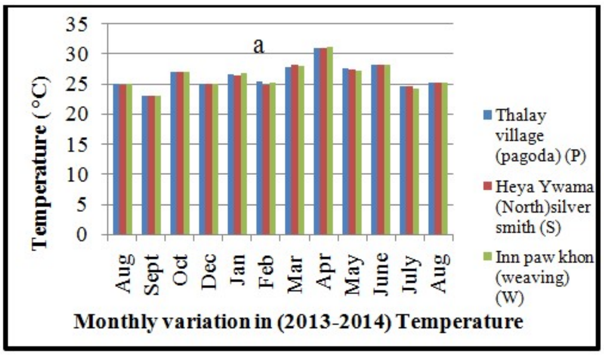

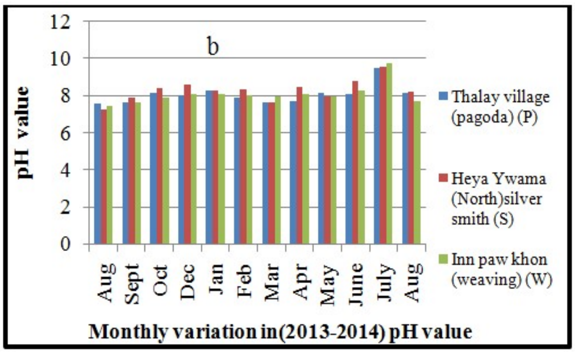

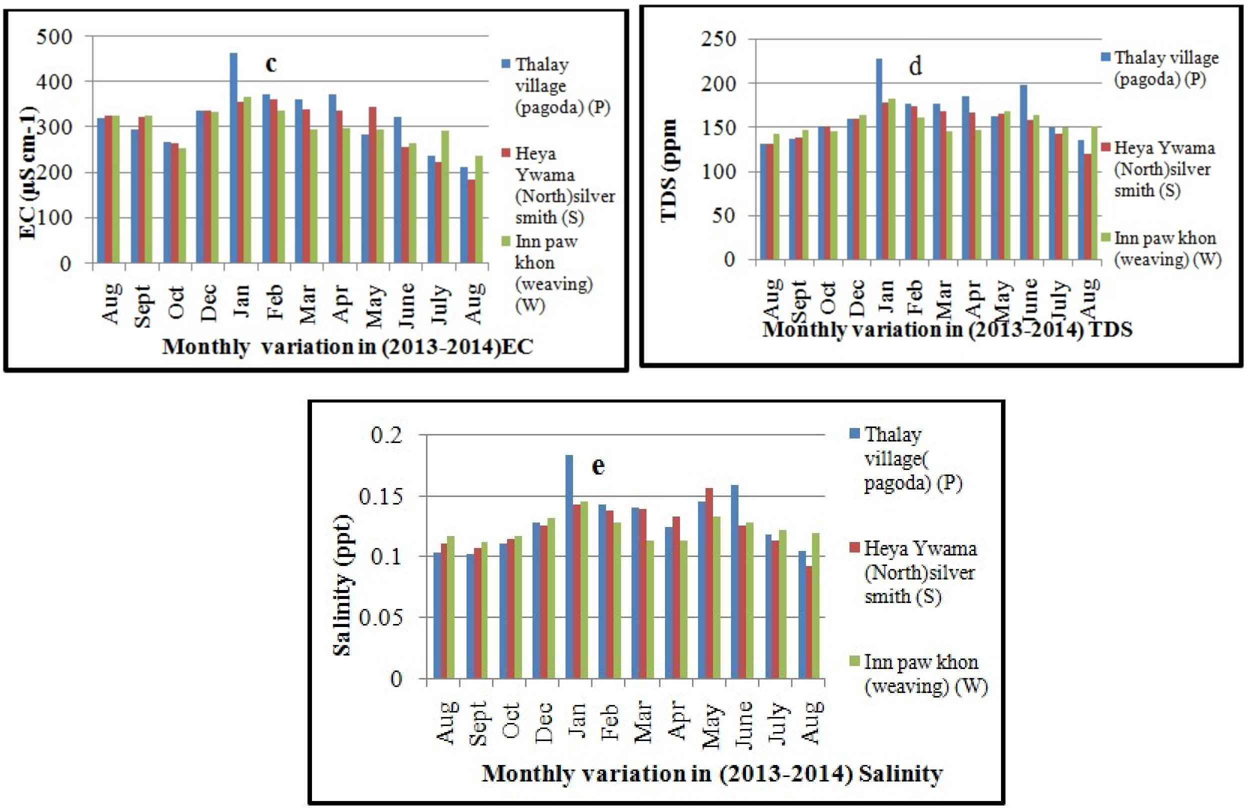

Figure 4 (a-e) Monthly variation of Physicochemical parameter (a = Temperature, b = pH, c = Conductivity, d = Total Dissolved Solid, e = Salinity) of water at three different sites of Inle Lake

Salinity

Salinity of water samples ranged from a minimum of 0.092 ± 0.014 ppt to a maximum of 0.184 ± 0.023 ppt of Thalay village, Heya Ywama village and Inn paw khon village respectively. In case of water samples, Salinity of all the three locations were found to be high in January and low in second half of August. (Figure 4 e)

The values obtained were then compared to available WHO standard. Water-quality standards or recommended limits for selected parameter were listed in Table 1.

Table 1 Water-quality standards or recommended limits for selected parameter

Parameter		Present Study	WHO standard*
pH	Range	7.26 – 9.75	6.5 - 8.5
	Mean	8.16 ± 0.224	
EC (µδ cm^{-1})	Range	185.7 – 463.2	500
	Mean	309.59 ± 25.83	
TDS (mg l^{-1} or ppm)	Range	119.3 – 228.0	500
	Mean	159.78 ± 12.72	
Salinity (ppt)	Range	0.092 – 0.184	Fresh water < 0.5 ppt Brackish 0.5 - 30 ppt Saltwater 30 - 40 ppt Optimum 15 - 25 ppt
	Mean	0.126 ± 0.0159	

The comparison of relative concentrations of elements vs month contained in water samples from Thalay village (Pagoda) P, Heya Ywama (North) (Silver) S, Inn paw khon(Weaving) W by EDXRF in Figure 5 (a-c).

According to these results, all samples have different concentrations of various elements. It was found that calcium (Ca) was contained in all water samples.

In Figure 5 a, the water samples from Thalay village had the same elements (S, K, Ca, Mn, Fe, Cu, Zn) in first half of August, December, February, June. Potassium (K) was not observed in September, March, April and May. Sulfur (S) was not observed in October and January. Zinc (Zn) was not observed in October, March and July. From this figure, the relative concentration of Ca was high in all samples. But the relative concentration of Zn was very few in first half of August, September, January, February, April, May, June and second half of August. And also the relative concentration of Mn was few in October, December and July. Then the relative concentration of Cu was few in March.

In Figure 5 b, the water samples from Heya Ywama had the same elements (S, K, Ca, Mn, Fe, Cu, Zn) in September, October, December, January, July and second half of August. Potassium (K) was not observed in April. Sulfur (S) was not observed in first half of August, February, April, May and June. Zinc (Zn) was not observed in February, April, May and June. Manganese (Mn) was not observed in March and April. From this figure, the relative concentration of Ca was high in all samples. But the relative concentration of Zn was very few in first half of August, September, October, December, January, March, July and second half of August. And also the relative concentration of Mn was few in February and June. Then the relative concentration of Cu was few in April and May.

In Figure 5 c, the water samples from Inn paw khon had the same elements (S, K, Ca, Mn, Fe, Cu, Zn) in first half of August, October, December, January, March, June and July. Potassium (K) was not observed in September, May and second half of August. Zinc (Zn) was not observed in September. Manganese (Mn) was not observed in September, February and April. From this figure, the relative concentration of Ca was high in all samples. But the relative concentration of Zn was very few in first half of August, October, December, January, February, March, April, May, June, July and second half of August. And also the relative concentration of Cu was few in September.

Calcium (Ca) is essential constituent of bone, shell and teeth of the body. The content of Ca in food can provide for nutrition. Aqueous calcium compounds are generally non toxic and represent no known health hazard. Not only is calcium for human life, but it is also an essential nutrient for plant growth.

Potassium (K) is one of the most active metals and it can support the metabolism of the body. It can also support the tonic effect for the body. It did not give toxic effects. It is an essential element and is present in all animal and plant tissues.

Manganese (Mn) is an essential element for medicine use, but excess concentrations in the body can cause toxicity. It is essential to iron and steel production. It can cause both toxicity and deficiency symptoms in plants.

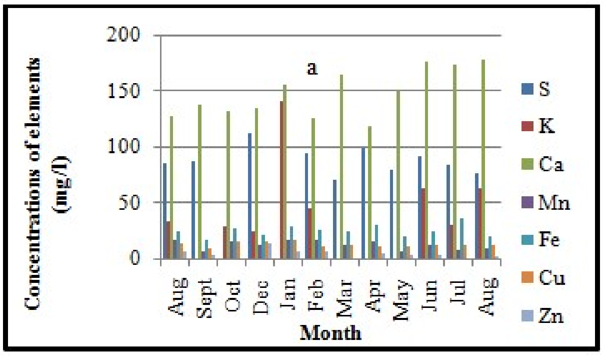

Figure 5 (a) Concentrations of elements vs Month contained in the water samples from Thalay Village (Pagoda) P by EDXRF

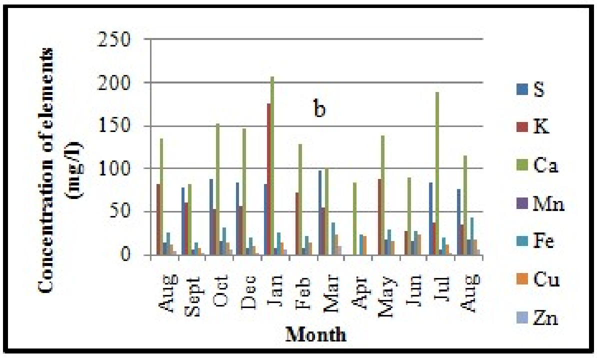

Figure 5 (b) Concentrations of elements vs Month contained in the water samples from Heya Ywama (Silver Smith) S by EDXRF

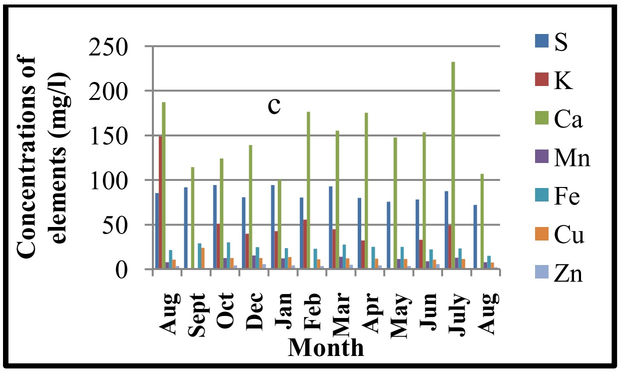

Figure 5 (c) Concentrations of elements vs Month contained in the water samples from Inn paw khon (weaving) W by EDXRF

The amount of copper (Cu) is necessary for normal body metabolism its absence is known to cause nutritional anemia in children. Large oral dosages of copper can cause emesis and may eventually results in liver damage.

Zinc (Zn) is an essential trace element and its necessary roles involve enzymes and enzymatic functions, protein synthesis and carbohydrate metabolism. It is necessary for normal growth and development in mammals. It is an essential trace element for animals and plants.

Sulfur (S) is very useful in medicine use. It is used in pharmaceuticals and it has no critical toxicity from food. It is an essential nutrient for plant.

Iron (Fe) is an essential element in body tissue as the form of hemoglobin in blood. It also has medicinal use. It is toxic when large amounts are taken into the body. When too many iron pills are taken, people (especially children) get sick. It is an essential element for almost all living species.

Conclusion

As a result, some physiochemical parameters such as temperature, pH, electrical conductivity, total dissolved solids, and salinity and elemental concentrations at three sites are in normal range and within the permissible limits.

These experiments are being carried out by using the EDXRF method, we can make conclusion that there are no toxic element which can given trouble for human health.

Acknowledgemnents

I would like to thank Professor to Dr Aung Naing Soe, Pro-Rector, Mandalay University of Distance Education, for his kind permission to carry out this research project. I would also like to express my sincere thanks to Professor Dr Kathi Nwe, Head, Department of Physics, Mandalay University of Distance Education, for her helpful suggestion.

I would like to mention that the research work would not have been possible without the kind permission of Universities' Research Centre. Universities' Research Centre gives the servicing for all measurements. Please let me express my sincere thanks and warmest gratitude to Rector Dr Po Kaung, Retired Professor Dr Aye Aye Myint and colleagues from Universities' Research Centre.

Last, but not the least, I would like to express my sincere thanks to U Win Swe, former Pyithu Hluttaw Representative from Nyaung Shwe Constituency for assisting to get water samples from Inle lake for the whole year round.

References

Akaishi, F., Satake, M., Otaki, M., and Tominaga, N., (2006), 'Surface water quality and information about the environment surrounding Inle Lake in Myanmar', Japanese Society of Limnology, **7**, 57-62

Butkus, S., and Myint Su, (2001), 'Pesticide Use Limits for Protection of Human Health in Inle Lake (Myanmar) Watershed ', Living Earth Institute Olympia, Washington, USA, 2-49

Su,M. and Jassby, A.D., (2000), 'Inle: A large Myanmar lake in transition, Lakes Reservoirs', Research and Management, 5(1), 49-54

Tertain R & Claisse F, (1982), Principles of Quantitative X-ray Fluorescence Analysis (London: Heyden)

Zaw Lwin and Sharma, M. P., (2012), 'Environmental management of the Inle Lake in Myanmar', *Hydro Nepal*, issue no (11) July, 57-60

J. Myanmar Acad. Arts Sci. 2020 **Vol. XVIII.No.2A**

QUANTUM AND CLASSICAL DERIVATIONS OF BLACK HOLE ENTROPY AND PHYSICAL MICROSTATES

Naing Naing Wint Htoon [1], Lei Lei Nyo[2], Nwe Nwe Myint[3], Thant Zin Naing[4]

Abstract

Classical and quantum mechanical derivations of black hole entropy have been studied in detail in the frame work of general relativity ,thermodynamics and quantum mechanics. The black hole entropy and area have been derived from classical thermodynamics. The relationship between the classical and quantum formulas can be shown to be similar to that of black body radiation. Microstates of the black hole entropy and its physical implications have been investigated. Some applications of black hole entropy to astrophysics have also been presented.

Keywords: Black hole entropy.

Introduction

When the core runs out of hydrogen fuel, it will contract under the weight of gravity. However, some hydrogen fusion will occur in the upper layers. As the core contracts, it heats up. This heats the upper layers, causing them to expand. As the outer layers expand, the radius of the star will increase and it will become a red giant. The radius of the red giant sun will be just beyond Earth's orbit. At some point after this, the core will become hot enough to cause the helium to fuse into carbon. When the helium fuel runs out, the core will expand and cool. The upper layers will expand and eject material that will collect around the dying star to form a planetary nebula. Finally, the core will cool into a white dwarf and then eventually into a black dwarf. This entire process will take a few billion years.

When the core runs out of hydrogen, these stars fuse helium into carbon just like the sun. However, after the helium is gone, their mass is enough to fuse carbon into heavier elements such as oxygen, neon, silicon, magnesium, sulfur and iron. Once the core has turned to iron, it can burn no longer. The star collapses by its own gravity and the iron core heats up. The core becomes so tightly packed that protons and electrons merge to form neutrons.

In less than a second, the iron core, which is about the size of Earth, shrinks to a neutron core with a radius of about 6 miles (10 kilometers). The outer layers of the star fall inward on the neutron core, thereby crushing it further. The core heats to billions of degrees and explodes (supernova), thereby releasing large amounts of energy and material into space. The shock wave from the supernova can initiate star formation in other interstellar clouds. The remains of the core can form a neutron star or a black hole depending upon the mass of the original star.

In the ordinary evolution of very massive stars, black holes can be formed. A star is essentially a gigantic nuclear reactor converting hydrogen to helium in a process called nuclear fusion. Think to the star as millions of hydrogen bombs going off at the same time, thereby producing enormous quantities of energy and enormous forces outward from the star. There is an equilibrium between the gravitational forces inward and the forces outward caused by the exploding gases. Eventually, when all the nuclear fuel is used, there is no longer an equilibrium

---

[1] Dr, Lecturer, Department of Physics, University of Yangon.
[2] Dr, Associate Professor, Department of Physics, Technological University of Kalay.
[3] Dr, Lecturer, Department of Physics, Pyay University.
[4] Dr, Retired Pro-Rector (Admin), International Theravāda Buddhist Missionary University, Yangon.

condition. The gravitational force causes the gas to become very compact. If the star is large enough, it is compressed below its Schwarzschild radius and a black hole is formed. For an evolving star to condense into a black hole it must be approximately 25 times the mass of the sun. When the star condenses to a black hole it does not stop at the event horizon but continues to reduce in size until it becomes a singularity, a point mass. That is, the entire mass of the star has condensed to the size of a point.

A star that was initially more massive than about 20reaches the end of its life and collapses, it may create a compact star whose properties differ dramatically from those of white dwarfs or neutron stars. Its greater mass can compress its core so much that pressure is unable to support it, and it totally collapses to form what astronomers call a black hole.(Bekenstein, J.D., 1973)

A black hole is at once the most simple and the most complex object. It is the most simple in that it is completely specified by its mass, spin, and charge. This remarkable fact is a consequence of the so called 'No Hair Theorem'. It is the most complex in that it possesses a huge entropy. The entropy of a solar mass black hole is enormously bigger than the thermal entropy of the star that might have collapsed to form it. Entropy gives an account of the number of microscopic states of a system.

Black holes have very strange properties, and to understand them one needs to review the concept of escape velocity. For a body of mass M and at a radius R from the center of that object , the escape velocityv_{esc} , for an object to travel away from the body is

$$v_{esc}=\sqrt{\frac{2GM}{R}}$$

Where, G = the gravitational constant (6.67×10^{-11}Nm^2/ kg^2)

v_{esc}= the escape velocity (meter per seconds)

R = radius (meters)

M = mass (kilograms)

One can see from the formula that the escape velocity for a body of a given mass will be larger at a smaller radius. When the escape velocity is greater than the speed of light, such an object would become a black hole. (Raine D & Thomas E., 2005)

History of Black Hole Entropy

In 1972, Bekenstein was the first to suggest that black holes should have a well-defined entropy. He wrote that a black hole's entropy was proportional to the area of its (the black hole's) event horizon. Bekenstein also formulated the generalized second law of thermodynamics, black hole thermodynamics, for systems including black holes. Based on his black-hole thermodynamics work, Bekenstein also demonstrated the Bekenstein bound: there is a maximum to the amount of information that can potentially be stored in a given finite region of space which has a finite amount of energy. In 1982, Bekenstein developed a rigorous framework to generalize the laws of electromagnetism to handle inconstant physical constants. His framework replaces the fine-structure constant by a scalar field. However, this framework for changing constants did not incorporate gravity. In 2004, Bekenstein boosted Mordehai Milgrom's theory of Modified Newtonian Dynamics (MOND) by developing a relativistic version.

Meaning of Black Hole Entropy

Black holes are really thermodynamic systems with an actual temperature and entropy. The entropy should be the logarithm of the number of independent states of the black hole.

The Fact that the black hole entropy is even finite is already puzzling. A box of radiation at fixed energy and volume has a finite entropy because the box imposes a long wavelength cut off and the total energy imposes a short wavelength cut off. The Hilbert space describing the radiation field inside the box at fixed energy is thus finite dimensional, and the microcanonical entropy is just the logarithm of its dimension. A black hole in a box at fixed energy would also have a short wavelength cutoff (at the box) but, as emphasized by Hooft, according to standard quantum field theory it has no long wavelength cutoff (at the box). The reason is that the horizon is an infinite redshift surface. The wave vector of any outgoing mode diverges at the horizon, and is red shifted down to a finite value at the box. The entropy of each radiation field around a black hole is therefore infinite due to a divergence in the mode density at the horizon, so it seems the black hole entropy must also diverge. This divergence is equivalent to a divergence in the renormalization of Newton's constant, or rather in $\frac{1}{G}$ .Thus one point of view is that it should be absorbed by "counter terms", and only the total, renormalized entropy is relevant.(Shapiro, S.L , 1983)

Laws of Black Hole Mechanics

1. **Zeroth Law** : The temperature T of body at thermal equilibrium is constant throughout the body. Heat will flow from hot spots to the cold spots. For stationary black hole, one can show that surface gravity k is constant on the event horizon. This is obvious for spherically symmetric horizons but is true also more generally for non-spherical horizons of spinning black holes.
2. **First Law**: Energy is conserved, $dE = T\,dS + \mu\,dQ + \Omega\,dJ$, where E is the energy , Q is the charge with chemical potential μ and J is the spin with chemical potential Ω. For black hole , one has $dM = \frac{\kappa}{8\pi} dA + \mu\,dQ + \Omega\,dJ$ .For a Schwarzschild black hole one has $\mu = \Omega = 0$ because there is no charge or spin.
3. **Second Law**: The total entropy S near decreases, $\Delta S \geq 0$. For black holes one can prove the area theorem that the net area in any process never decreases, $\Delta A \geq 0$. For example, two Schwarzschild black holes with masses M_1 and M_2 can coalesce to form a bigger black hole of mass M. So the area is proportional to the square of the mass and $(M_1 + M_2)^2 \geq M_1{}^2 + M_2{}^2$.

Derivation of Black Hole Entropy

If a black hole has energy E and entropy S, then it must also have temperature T is given by

$$\frac{1}{T} = \frac{\partial S}{\partial E}$$

Where, T = temperature, E = energy, S = entropy

For a Schwarzschild black hole, the area and the entropy scales as $S \sim M^2$.

$$\frac{1}{T} = \frac{\partial S}{\partial M} \approx \frac{\partial M^2}{\partial M} \approx M \tag{1}$$

$$T = \frac{\partial M}{\partial S} = \frac{dM}{dS}$$

$$dM = TdS \tag{2}$$

Where, A_H = the area of event horizon

For Schwarzschild Black Hole's,

$$A_H = 16\pi\, G^2 M^2 \ (\because\ r_H = 2GM\ ) \tag{3}$$

Differentiating equation (3) with respect of M.

$$\frac{dA_H}{dM} = 16 \times 2\pi\, G^2 M$$

$$dA_H = 32\pi\, G^2 M dM$$

$$dM = \frac{dA_H}{32\pi\, G^2 M} \tag{4}$$

For Schwarzschild black hole,

$$\kappa = \frac{1}{4GM}$$

$$\frac{1}{M} = 4G\kappa \tag{5}$$

Substituting equation (5) in equation (6)

$$dM = \frac{dA_H}{32\pi\, G^2} \times 4G\kappa$$

$$= \frac{\kappa\, dA_H}{8\pi\, G}$$

$$= \frac{\kappa\, \hbar}{8\pi\, G\hbar} dA_H \tag{6}$$

Hawking calculation showed that the spectrum emitted by the black hole is precisely thermal with temperature,

$$T = \frac{\hbar\kappa}{2\pi},$$

Since $$\kappa = \frac{1}{4GM},\quad T = \frac{\hbar}{8\pi\, GM} \tag{7}$$

Substituting equation (7) in equation (2), one gets

$$dS = \frac{8\ \pi\ GM}{\hbar} \times \frac{\kappa\ \hbar}{8\pi\ G\ \hbar} dA$$

$$= \frac{\kappa M}{\hbar} dA$$

$$= \frac{1}{4GM} \times \frac{M}{\hbar} dA$$

$$dS = \frac{1}{4G\hbar} dA \tag{8}$$

Taking integration to both sides of equation (8), one gets

$$\int dS = \frac{1}{4G\hbar} \int dA$$

$$S = \frac{A}{4G\hbar}$$

Since, G=$\hbar$ =1(in natural units), on now gets

$$S = \frac{A}{4} \tag{9}$$

Theoretical Validity of S=F(A)

The first law of thermodynamics applied to the system black hole surrounding may be written as

$$dM\ = TdS - dW \tag{10}$$

where, W= work done on the black hole

M= mass of the black hole

T= temperature

S= entropy

The work done due to changes in angular momentum and electric charge is

$$dW = \Phi\ dQ - \Omega\ dJ \tag{11}$$

where, $\Phi =$ the electric potential on the event horizon

$\Omega =$ the angular velocity on the event horizon

J = angular momentum of the black hole

Q= charge of the black hole

Substituting equation (11) in equation (10) gives,

$$TdS = dM - \Phi\ dQ - \Omega\ dJ \tag{12}$$

$$\Phi = \frac{4\pi\ r_+ Q}{A}, \Omega = \frac{4\pi\ a}{A} \tag{13}$$

where $r_+ = M + \sqrt{M^2 - Q^2 - a^2}$ and $A = 4\pi(r_+^2 + a^2), a \equiv \dfrac{J}{M}$

$r_+ =$ radius of the event horizon

$A =$ area of the event horizon

a = specific angular momentum

The first law of black hole mechanics:

$$\frac{1}{8\pi}\kappa\, dA = dM - \Phi\, dQ - \Omega\, dJ \tag{14}$$

where κ is the surface gravity given by

$$\kappa = 8\pi\left(\frac{\partial M}{\partial A}\right)_{J,Q} \tag{15}$$

Kerr-Newman solution is given by,

$$\kappa = \frac{r_+ - r_-}{\left(r_+^2 + a^2\right)} = \frac{\left(M + \sqrt{M^2 - Q^2 - a^2}\right) - \left(M - \sqrt{M^2 - Q^2 - a^2}\right)}{2\left(r_+^2 + a^2\right)}$$

$$\kappa = \frac{M + \sqrt{M^2 - Q^2 - a^2} - M + \sqrt{M^2 - Q^2 - a^2}}{2\left(r_+^2 + a^2\right)}$$

$$\kappa = \frac{2\sqrt{M^2 - Q^2 - a^2}}{2\left(r_+^2 + a^2\right)}$$

$$\kappa = \frac{4\pi\sqrt{M^2 - Q^2 - a^2}}{4\pi\left(r_+^2 + a^2\right)}$$

$$\kappa = \frac{4\pi\sqrt{M^2 - Q^2 - a^2}}{A} \tag{16}$$

According to equation (15) and (16), one has

$$\kappa = 8\pi\left(\frac{\partial M}{\partial A}\right)_{J,Q} = \frac{4\pi\sqrt{M^2 - Q^2 - a^2}}{A} \tag{17}$$

Combining equation (12) and (14) gives

$$\frac{1}{8\pi}\kappa\, dA = T\, dS\,. \tag{18}$$

Integrating both sides of equation (18), one gets

$$\frac{\kappa}{8\pi}\int dA = T\int dS$$

$$\frac{\kappa A}{8\pi} = TS \qquad (19)$$

$$S = \frac{\kappa A}{8\pi T} \qquad (20)$$

The black hole entropy must be a definite function of its horizon area. Therefore, it reads:

$$S = F(A) \qquad (21)$$

Microscopic Derivation of the Black Hole Entropy

The Bekenstein-Hawking black hole entropy is given by

$$S = \frac{Area}{G} = \frac{\pi\sqrt{16GMl^2 + 2r_+^2}}{G} \qquad (22)$$

where, M = mass ,

J =angular momentum

G = gravitational constant

r_+ =radius of the event horizon

$l^2 = -1/\Lambda$(reciprocal of the cosmological constant) ($l >> G$)

It is convenient to choose the additive constants in L_0 and $\overline{L}_0$, so that they vanish for the $M = J = 0$ black hole. One then has

$$M = \frac{1}{l}(L_0 + \overline{L}_0) \qquad (23)$$

while the angular momentum is

$$J = L_0 - \overline{L}_0 . \qquad (24)$$

This is notthe same as AdS$_3$ (three–dimensional anti-de Sitter space)metric which has negative mass $M = -\frac{1}{8G}$.

One wishes to count the number of excitations of the AdS$_3$ (three–dimensional anti-de Sitter space) vacuum with mass M and angular momentum J in the semiclassical regime of large M. The explicit computation of the central charge $c$is

$$c = \frac{3l}{2G} \qquad (25)$$

According to (23) and (25) large M implies

$$n_R + n_L >> c, \qquad (26)$$

where n_R (n_L) is the eigenvalue of L_0 ($\overline{L}_0$). The asymptotic growth of the number states of a conformal field theory with central charge c is then given by (J. A. Cardy, Nucl 1986).

$$S = 2\pi\sqrt{\frac{cn_R}{6}} + 2\pi\sqrt{\frac{cn_L}{6}}\ . \tag{27}$$

Using (25) , (23) and (24) , the expression for blackhole microstates can be written as

$$S = \pi\sqrt{\frac{l(lM + J)}{2G}} + \pi\sqrt{\frac{l(lM - J)}{2G}}, \tag{28}$$

And it is in agreement with the Bekenstein-Hawkingblack hole entropy result (22) for the BTZ (Banados-Teitelboim- Zanelli) black holeentropy.

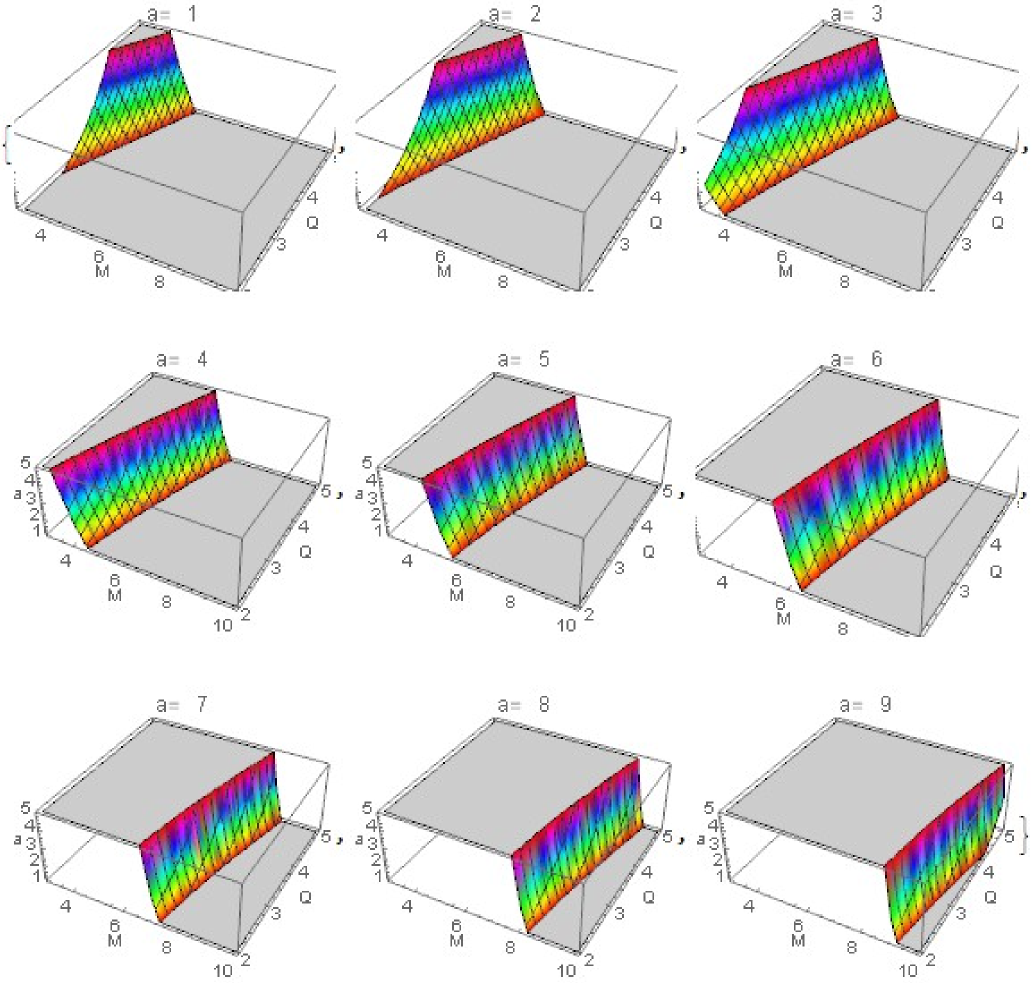

Figure 1 Snapshot Evolution of the surface gravity of the Kerr-Newmann black hole with the constraint $M^2>Q^2>a^2$.

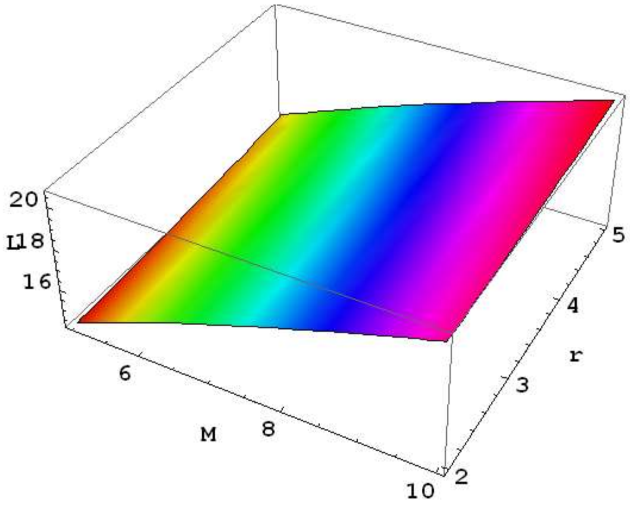

Figure 2 The Profile of Black Hole Entropy in terms of Radius of Event Horizon,M and *l*.

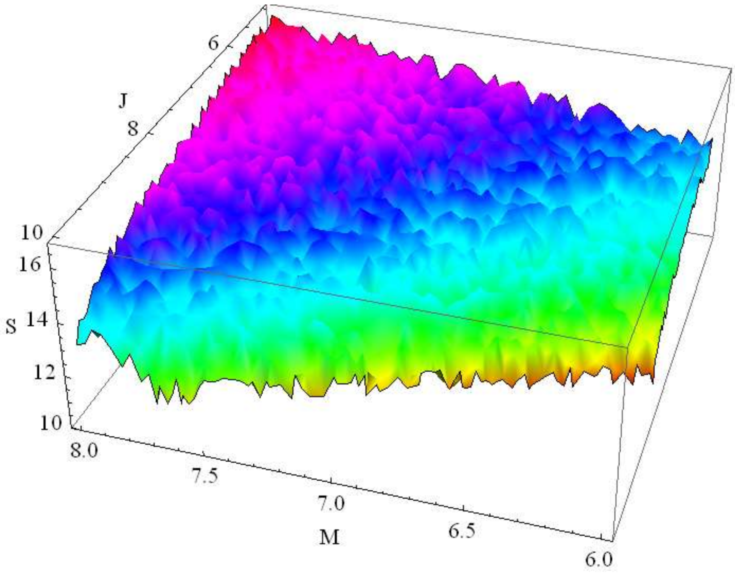

Figure 3 3D Profile of Black hole entropy in terms of M and J.

Concluding Remarks

In this present works, the detailed derivation for black hole entropy in classical aspect has been given and it is found to be the one fourth of the black hole's surface area. Quantum mechanical derivation and some interesting physical interpretations are to be implemented.

Theoretical validity of S=F(A), i.e., the entropy is simply a function of area has been proved using the basic thermodynamic entities like temperature, mass, surface gravity, area of a black hole.. The nature of surface gravity has been visualized in snapshot 3-D evolution of the surface gravity of the Kerr-Newmann black hole with the constraint $M^2 > Q^2 > a^2$ and the discrete nature of the evolution of surface gravity can be observed.The blackhole microstates treatment has been worked out and the result is in well agreement with BTZ blackhole result.

Acknowledgements

Firstly, I would like to express my sincere thanks to Professor Dr Khin Khin Win, Head of Department of Physics, University of Yangon, for her kind permission to carry out this thesis.I am very grateful to all respectable Professors of PhysicsDepartment, University of Yangon, for their useful advice in the preparation of this thesis.Special thanks are due to Professor, Dr Thant Zin Naing, Retired Pro-rector (Admin), International Theravāda Buddhist Missionary University, for his valuable guidance and helpful advice to carry out this work.

References

Banados, M., C.Teitelboim and J.Zanelli, (1992)Phys. Rev. Lett. 69, 1849.

Banados, M., M.Henneaux, C.Teitelboimand J.Zanelli, (1993)Phys.Rev. D48**,** 1506.

Bekenstein, J.D.,(1973) "Black Holes and entropy".

Cardy, J. A., (1986), "Nucl. Phys", B270,186.

Forlov, V.P., D.V.Fursaev and A.L.Zelnikov, (1996), "Black Hole Entropy: Thermodynamics, Statistical Mechanics and Subtraction Prodecure".

Gerard't Hooft, (2009), "Introduction to the Theory of Black Holes", 3508 TD Utrecht, the Netherlands.

Landau L. D &E. M.,Lifshitz, (1965) "Quantum Mechanics", Pergamon Press, Oxford.

Misner, C.W., K.S.Throne, J.A. Wheeler, (1973)"Gravitation", W.H Freeman and Company, San Francisco.

Raine. D &E. Thomas, (2005) "Black holes", Imperial College Press, London.

Shapiro, S.L, S.A., Teukolsky, (1983) "Black Holes, White Dwarfs, and Neutuon Stars".

Schiff L. I., (1985), "Quantum Mechanics", McGraw Hills, Singapore.

J. Myanmar Acad. Arts Sci. 2020 **Vol. XVIII.No.2A**

SOLVING QUANTUM MECHANICAL HARMONIC OSCILLATOR AND CHAOTIC QUANTUM LINEAR MAP

Yu Yu Nge[1], Yee May Thwin[2], Tin Tin Htay[3], Thant Zin Naing[4]

Abstract

Fundamental motion of quantum mechanical harmonic oscillator and chaotic quantum linear map has been investigated using numerical methods and visualization of the results. Periodic chaotic nature is found in visualization of quantum linear map.

Keywords: Harmonic Oscillator and Chaotic Quantum Linear Map

Introduction

Numerical solutions of the time-independent Schrodinger equation have been discussed in various conditions. These solutions utilize numerical techniques for solving a differential time evolution for the time-dependent Schrodinger equation. Many quantum mechanical research problems that are answerable to solution (for example, the behavior of electrons on a small lattice) by using matrix mechanics. In the quantum linear map, although the square of commutator can increase exponentially with time, a simple operator does not scramble but performs chaotic motion in the operator basis space determined by the classical linear map.

The Formalism

The harmonic oscillator is also answerable to analytical solution. Unlike the infinite square well the solutions are unfamiliar and concerned in the initial state.

The infinite square wellis defined as

$$V_{\inf}(x) = \begin{cases} 0 & \text{if } 0 < x < a, \\ \infty & \text{otherwise.} \end{cases} \tag{1}$$

The Hamiltonian is given by

$$H_0 = -\frac{\hbar^2}{2m}\frac{d^2}{dx^2} + V_{\inf}(x), \tag{2}$$

where m is the mass of the particle.

The eigenstates are well known:

$$\psi_n(x) = \begin{cases} \sqrt{\frac{2}{a}}\sin\left(\frac{n\pi x}{a}\right) & \text{if } 0 < x < a, \\ 0 & \text{otherwise,} \end{cases} \tag{3}$$

with eigenvalues,

---

[1] Dr, Lecturer, Department of Physics, University of Yangon.

[2] Dr, Lecturer, Department of Physics, Magway University.

[3] Lecturer, Department of Physics, Kyaukse University.

[4] Dr, Retired Pro-Rector (Admin), International Theravāda Buddhist Missionary University, Yangon.

$$E_n^{(0)} = \frac{n^2\pi^2\hbar^2}{2ma^2} \equiv n^2 E_1^{(0)}. \tag{4}$$

The quantum number $n = 1,2,3,...$ takes on a positive integer value.

The Harmonic Oscillator

For the infinite square well, the harmonic oscillator potential is $V_{HO} = \frac{m\omega^2 x^2}{2}$. In the following all units of distance will be in terms of the square well width a, and all units of energy will be in terms of the (unperturbed) ground state, $E_1^{(0)}$. We will use lower case letters to denote dimensionless energies. The potential V_{HO} can be written in terms of the infinite square well length and energy scales as

$$v_{HO} = \frac{V_{HO}}{E_1^{(0)}} = \frac{\pi^2}{4}\left(\frac{\hbar\omega}{E_1^{(0)}}\right)^2\left(\frac{x}{a} - \frac{1}{2}\right)^2, \tag{5}$$

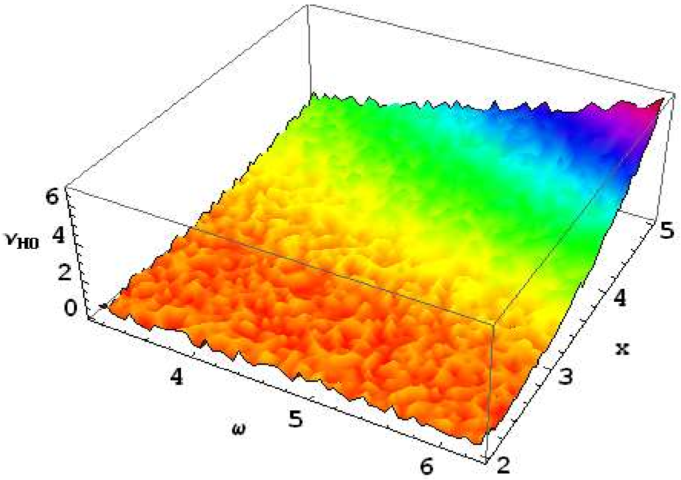

Figure 1 3D Profile of v_{HO} in terms of ω and x.

so that the dimensionless parameter $\frac{\hbar\omega}{E_1^{(0)}}$ determines the stiffness of the harmonic oscillator potential. We expect that for low energy states (the ground state), the solution should be identical to that of the harmonic potential alone, because the wave function will be sufficiently restricted to the central region of the harmonic oscillator potential so that it will not feel the walls of the infinite square well. High energy states will not be well described by the harmonic oscillator results, because they will be primarily governed by the infinite square well. We first use

$$H_{nm} = \delta_{nm}E_n^{(0)} + \frac{2}{a}\int_0^a dx \sin\left(\frac{n\pi x}{a}\right)V(x)\sin\left(\frac{m\pi x}{a}\right) \tag{6}$$

with the potential given by equation (5). The result is

$$= \delta_{nm}\left\{n^2 + \frac{\pi^2}{48}\left(\frac{\hbar\omega}{E_1^{(0)}}\right)^2\left(1 - \frac{6}{(\pi\,\mathrm{n})^2}\right)\right\} + (1-\delta_{nm})\left(\frac{\hbar\omega}{E_1^{(0)}}\right)^2 g_{nm} \tag{7}$$

where. $$g_{mn} = \begin{pmatrix} 1 & 0 \\ 0 & 1 \end{pmatrix}. \tag{8}$$

The g_{nm} remain of order unity close to the diagonal, but for large n the diagonal elements grow as n^2, so the off-diagonal elements become negligible in comparison.

Quantum Linear Map

The operator scrambling in the quantum linear map is an instructive quantum mechanical model with many properties exactly solvable. Before we study this model in detail, we first briefly review the classical linear map.

The classical linear map is the linear automorphism of the unit torus phase space given

by

$$\begin{pmatrix} q \\ p \end{pmatrix} \to \begin{pmatrix} a & \mathrm{b} \\ c & \mathrm{d} \end{pmatrix} \begin{pmatrix} q \\ p \end{pmatrix} \bmod 1 \tag{9}$$

where the matrix $\mathrm{M} = \begin{pmatrix} a & \mathrm{b} \\ c & \mathrm{d} \end{pmatrix} \in SL(2, Z)$. The determinant is equal to one so that this map isarea preserving (canonical). Also it preserves the periodic boundary condition of the torus as M has integer valued entries. The Lyapunov exponents $\lambda_{\pm}$ of the linear map are given by the logarithm of the eigenvalues of M. When TrM > 2, this map is hyperbolic and has $\lambda_{+} > 0 (\lambda_{+} + \lambda_{-} = 0)$. The chaotic linear map is known to be fully ergodic and mixing. If consider a simple case with a = 2; b = 1; c = 3; d = 2 and $\lambda_{\pm} = \log(2 \pm \sqrt{3})$.The linear map can be quantized on the square torus with finite Hilbert space. We define $|q_n\rangle$ and $|p_n\rangle$ to be position and momentum eigenstates with n=0, 1, … ,*K*-1,where K is dimension of the Hilbert space. The position and momentum translation operators are defined through $\hat{\tau}|q_n\rangle = |q_{n+1}\rangle$ and $\hat{\sigma}|p_n\rangle = |p_{n+1}\rangle$. Hence $\hat{\sigma}$ and $\hat{\tau}$ can be represented as Z_K rotor operators,

$$\hat{\sigma} = \begin{pmatrix} 1 & 0 \cdots 0 \\ 0 & \omega \cdots 0 \\ \vdots & \vdots \ddots \vdots \\ 0 & 0 \cdots \omega^{K\text{-}1} \end{pmatrix}, \hat{\tau} = \begin{pmatrix} 0 & \cdots 0 & 1 \\ 1 & \cdots 0 & 0 \\ \vdots & \ddots \vdots & \vdots \\ 0 & \cdots 1 & 0 \end{pmatrix} \tag{10}$$

where $\omega = e^{-2\pi i / K}$. $\hat{\sigma}$ and $\hat{\tau}$ satisfy $\hat{\sigma}^K = \hat{\tau}^K = 1$with the commutation relation given by $\sigma\tau = \omega\tau\sigma$.

In the position representation, the quantum propagator for the quantum linear map with

$$M = \begin{pmatrix} 2 & 1 \\ 3 & 2 \end{pmatrix}$$

is obtained by path integral method and takes this form

$$\hat{U}(q',q)=\left(\frac{i}{K}\right)^{1/2}\exp\left[\frac{i\pi}{K}(2q^2-2qq'+2(q')^2\right] \tag{11}$$

where $q, q' = 0,1,...,K-1$ label the position eigenstates. For any classical observable, one can associate a quantum observable operator $\hat{O}(f)$, which respects

$$\hat{U}^{\dagger}\hat{O}(f)\hat{U}=\hat{O}(f\circ M)$$

This equation usually holds in the limit $N\to\infty$. However due to the map being linear here, it holds even at finite N. Therefore, for $\hat{\sigma}$ and $\hat{\tau}$,

$$\hat{U}^{\dagger}\hat{\sigma}\hat{U}\sim\hat{\sigma}^{2}\hat{\tau}\,\hat{U}^{\dagger}\hat{\tau}\hat{U}\sim\hat{\sigma}^{3}\hat{\tau}^{2}. \tag{12}$$

This result indicates that for any operator of the form $\hat{O}=\hat{\sigma}^{q}\hat{\tau}^{p}$ under unitary time evolution, it performs chaotic motion in the operator basis space spanned by $\hat{\mathrm{B}}_{mn}=\sigma^{m}\tau^{n}$ (with $m,n=0,1,...,K-1$) which satisfies $Tr\hat{B}^{\dagger}{}_{mn}\hat{B}_{m'n'}=K\delta_{m,m'}\delta_{n,n'}$. The evolution of (q,p) is determined by the classical linear map defined in equation (9) and gives rise to the exponential growth of the square of commutator $C(t)=\left\langle\left[\hat{O}(t),\hat{O}\right]\left[\hat{O}(t),\hat{O}^{\dagger}\right]\right\rangle$,i.e., $C(t)\sim e^{2\lambda+t}$ when t is smaller than the Lyapunov time $t_L=\log K/\lambda_+$ .When $t>t_E$, the quantum correction becomes important and $C(t)$ stops to increase exponentially.

The exponential growth of $C(t)$ has a classical origin and is not related withthe operator scrambling. Under unitary time evolution, $\hat{O}(t)$ is always a basis operator anddoes not become more complicated.

To realize operator scrambling, we consider the quantum linear map perturbed by anonlinear shear. The new composite Floquet operator is,

$$\hat{U}=\hat{U}_1\hat{U}_2 \tag{13}$$

where $\hat{U}_2$ is the quantum linear map defined in equation(11) and $\hat{U}_1$ describes a nonlinear shear

$$\langle q'|\hat{U}_1|q\rangle=\exp\left[i\frac{kK}{2\pi}\left(\sin\left(\frac{2\pi q}{K}\right)-\frac{1}{2}\sin\left(\frac{4\pi q}{K}\right)\right)\right]\delta_{q,q'} \tag{14}$$

which will not have much influence on the early time dynamics as long as k is small.

Conclusion

In this paper we describe the Hamiltonian equation, harmonic oscillator and the quantum linear map. In the quantum linear map although the square of the commutator $C(t)$ can grow exponentially with the time and the quantum operator does not scramble at all. The operator scrambling can occur once if one makes some modification in the Floquetoperator. So that the quantum chaos is not always associated with the exponential growth of the square of the commutator $C(t)$. The non-linear shear equation simply shows that only at some selection point of the dynamical variable, it gives chaotic nature. Visualization gives this nature clearly.

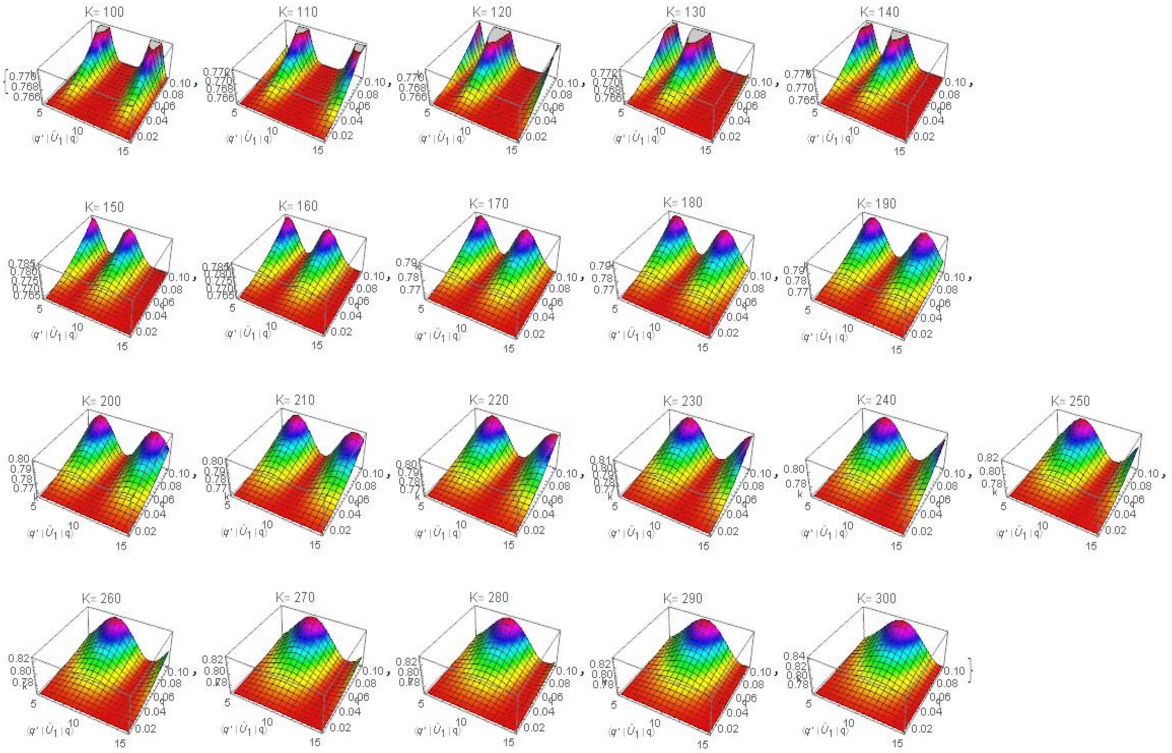

Figure 2 3D Profile of $\langle q'|\hat{U}_1|q\rangle$ in terms of k and q (Real).

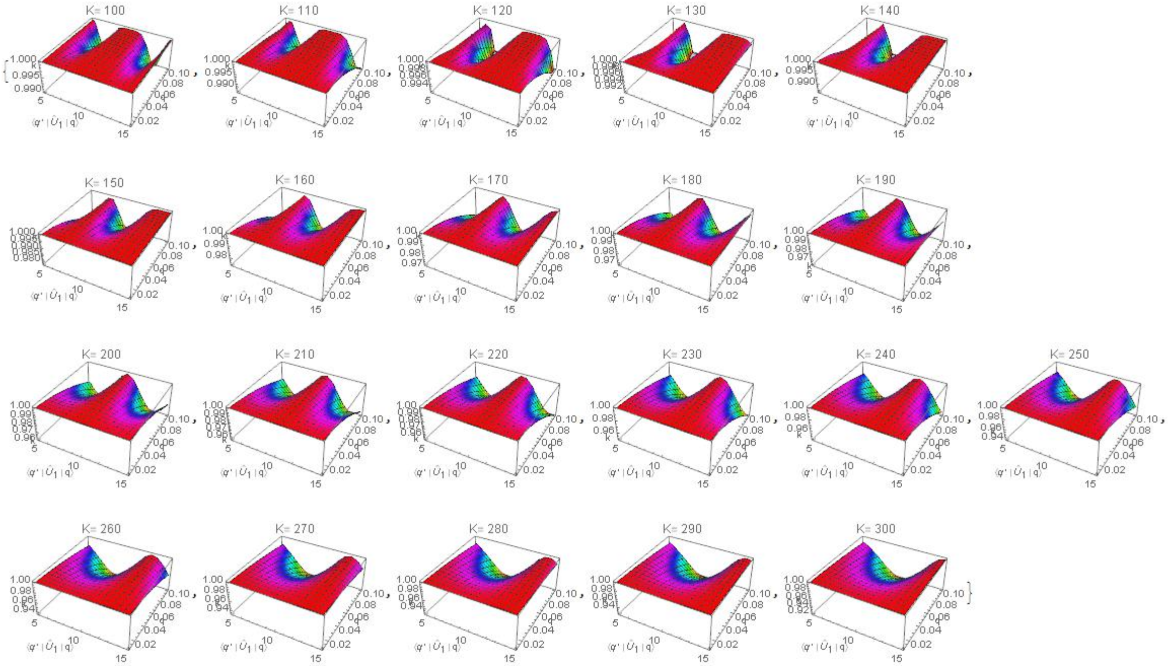

Figure 3 3D Profile of $\langle q'|\hat{U}_1|q\rangle$ in terms of k and q (Imagiary).

Acknowledgements

Firstly, I would like to thank Professor Dr Khin Khin Win, Head of Department of Physics, University of Yangon, for her kind permission and encouragements to carry out this work. I would like to thank all respectable Professors, Department of Physics, University of Yangon, for their kind permission and encouragements to carry out this work. Special thanks are due to Professor, Dr Thant Zin Naing, Retired Pro-rector (Admin), International Theravāda Buddhist Missionary University, for his valuable guidance and helpful advice to carry out this work.

References

Belloni, M. and W. Christian (2008) "Time Development in Quantum Mechanics Using a Reduced Hilbert Space Approach," *Am. J. Phys*. **76**, 385–392

Griffiths, D. J. (2005) *Introduction to Quantum Mechanics*, 2nd ed. Pearson/ Prentice Hall, USA,

Kinderman, J. V. (1990) "*A Computing Laboratory for Introductory Quantum Mechanics*," Am. J. Phys. 58, 568–573

Marsiglo F. (2008) *The Harmonic Oscillator in Quantum Mechanics: A Third Way*. Department of Physics, University of Alberta, Canada

Schmied, R. (2019) *Using Mathematica for Quantum Mechanics*, University Basal, Switzerland

Xiao C., and Z. Tianci (2018) *Operator Scrambling and Quantum Chaos*, University of Illinois, USA

J. Myanmar Acad. Arts Sci. 2020 **Vol. XVIII.No.2A**

EVALUATION OF THE STRUCTURAL AND OPTICAL CHARACTERISTICS OF ZINC OXIDE POWDER PREPARED BY CO-PRECIPITATION METHOD

Amy Aung[1], May Kalayar Kyaing[2], Hnin Yu Wai[3], Moht Moht Than[3]

Abstract

In this research work, nano-sized Zinc Oxide powder (ZnO) were prepared by using Zinc Chloride and Sodium Hydroxide as the precursors and annealed at different temperatures at 400°C, 500°C and 600°C respectively. Structural and optical properties of the observable ZnO powders were characterized by X-ray diffraction (XRD), Scanning Electron Microscopy (SEM) and Ultraviolet visible spectrophotometer (UV-vis).By XRD analysis, Zinc Oxide revealed hexagonal wuritze structure nature. It was found that with increasing the annealing temperature the particle size increased about 38~41 nm by using Debye Scherrer's equation. Lattice strain, c/a ratio and dislocation density parameters were obtained from XRD analysis results. According to the average crystallite size, the size of the particles increases as the annealing temperature is increased. The SEM results have visualized the morphology of ZnO nanoparticles with irregular spherical in shape and highly agglomerated. To investigate the optical results of the grown Zinc oxide, the absorption spectra are evaluated in the ultraviolet-visible (UV-Vis) range. Based on the optical analysis results, the energy band gap of different annealing temperature samples was calculated from the linear extrapolated line of $(\alpha h\gamma)^2$ vs. $h\gamma$ plot.

Keywords: XRD, SEM, UV-vis, Debye Scherrer's equation and spherical in shape.

Introduction

Zinc oxide (ZnO) Nanopowders are multifunctional material which is known as n-type semiconductor with wide energy band gap is used as transparent conductive oxide (TCO) layer in organic and non-organic photovoltaic cell preparation. The families of II-VI nanoscale semiconductors of ZnO material which have a wide band gap and allow devices to operate at higher temperature. In photo electronic fabrication field, Zinc Oxide is recently useful in high research field.

Nanostructures Zinc Oxide is widely used in a number of applications like varistors, UV lasers, gas sensors, photoprinting, electrochemical nanodevices, sunscreen lotion cosmetics, medicated creams, solar energy conversion, optoelectronic devices, catalysis, gas sensors, etc. Zinc Oxide is key element for many industrial processes like paints, ceramics, rubber, soap, textiles and floor coverings.

There are various methods for the preparations of ZnO nanopowders like chemical co-precipitation method, sol-el method, thermal decomposition, hydrothermal method, chemical vapor deposition and electrochemical method. Among the different techniques, the co-precipitation approach to be one of the most promising methods to prepare ZnO nanoparticles due to its interesting properties like wide band gap of 3.39 eV.The as-prepared powders were

---

[1] Dr, Assistant Lecturer, Department of Physics, University of Yangon

[2] Assistant Lecturer, Department of Physics, University of Yangon

[3] Assistant Lecturer, Department of Physics, University of Yangon

[3]Associate Professor, Department of Physics, Mohnyin Degree College

annealed at different temperatures (400˚C, 500˚C and 600˚C) and obtained pure wurtzite hexagonal phase ZnO powder particles.

However, the co-precipitation method became a very attractive preparation method due to simple equipment involved and low cost compared to other techniques. The phase formation behaviour and the microstructures evolution of the samples are investigated by using X-ray diffraction (XRD) and Scanning Electron Microscope (SEM), respectively. The optical characteristics are analyzed by using UV-visible absorption spectrometer.

Experimental Procedure

The synthesized nanoparticles zinc oxide powders are characterized to investigate their microstructures and optical properties. The crystallinity and the phase composition of as-prepared were examined with X-Ray diffractometer, (MD-10) (Rigaku, Japan). The size of the particles and morphology of ZnO were studied by Scanning Electron Microscopy (JEOL-JSM 5610LV). Optical transmission and absorption spectra of ZnO were recorded using Shimadzu UV-Vis spectrophotometer (UV-1800).

Preparation of Zinc Oxide solution

In this process, the starting materials used were zinc chloride ($ZnCl_2$) and sodium hydroxide (NaOH). Aqueous solution was prepared by dissolving 6.8 grams of zinc chloride in 100 ml of distilled water. It was stirred continuously with magnetic stirrer for 30 minutes in ambient atmosphere so that zinc chloride can be dissolved properly. After 30 minutes stirring, the temperature was raised to 80˚C for 2 hours. Sodium hydroxide 5 grams was dissolved in 25 ml distilled water. The prepared aqueous solution of sodium hydroxide was added slowly drop by drop (dropped for 45 minutes) into the stirring solution zinc chloride solution by touching the walls of container/vessel under continuously stirring.

The reaction was allowed to proceed for 1 hour after complete addition of sodium hydroxide and then removed the magnetic stirrer from the container. After that the mixture solution was heated for 1 hour at 60 ~ 80˚C without stirring. A milky white solution was obtained which the reaction was allowed to proceed for 3 hours after complete addition of sodium hydroxide. The precipitate obtained was washed with distilled water many times and filtered using filter paper. The mixture was dried in air at 70˚C for 3 hours. The sample powders were annealed for 1 hour at different temperatures 400°C, 500°C and 600°C respectively. The reaction equations are as follows;

$$ZnCl_2 + 2\,NaOH \rightarrow Zn(OH)_2 + NaCl$$

$$Zn(OH)_2 \rightarrow ZnO + H_2O$$

The flow diagram of sample preparation of ZnO powder was shown in Figure 1. Figure 2 shows the photograph of sample preparation sequence for ZnO powder using the simple co-precipitation method.

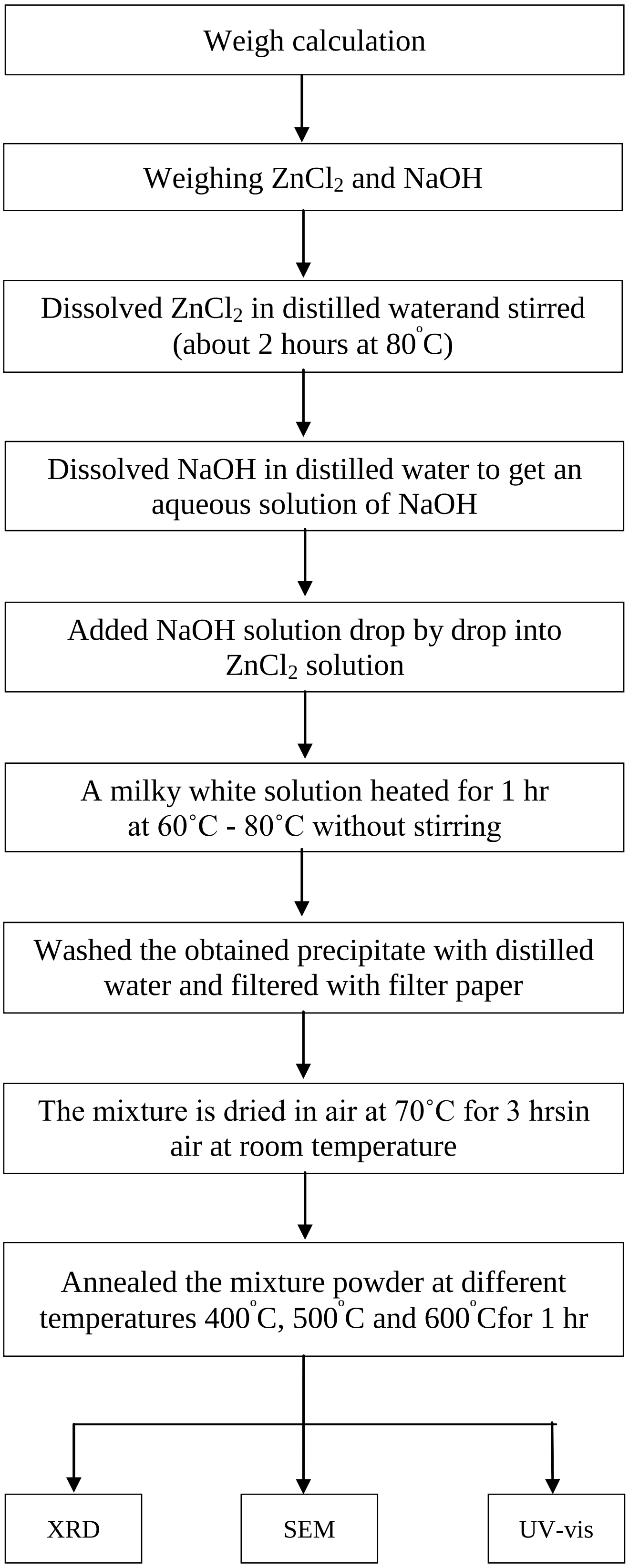

Figure 1 Flow diagram of sample powder preparation

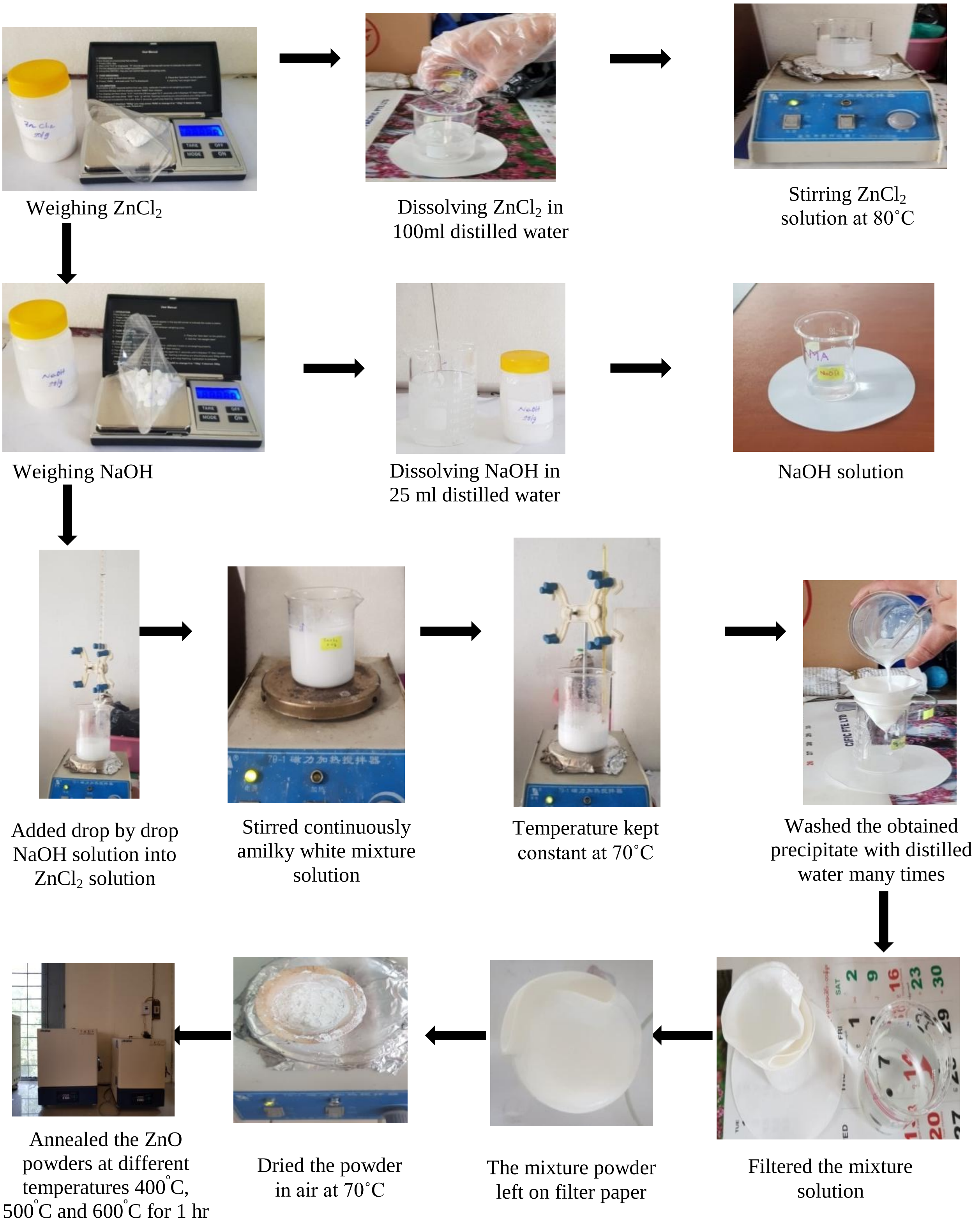

Weighing $ZnCl_2$

Dissolving $ZnCl_2$ in 100ml distilled water

Stirring $ZnCl_2$ solution at 80˚C

Weighing NaOH

Dissolving NaOH in 25 ml distilled water

NaOH solution

Added drop by drop NaOH solution into $ZnCl_2$ solution

Stirred continuously amilky white mixture solution

Temperature kept constant at 70˚C

Washed the obtained precipitate with distilled water many times

Filtered the mixture solution

The mixture powder left on filter paper

Dried the powder in air at 70˚C

Annealed the ZnO powders at different temperatures 400˚C, 500˚C and 600˚C for 1 hr

Figure 2 The photograph of sample preparation sequence for ZnO powders by using simple co-precipitation method

Result and Discussion

XRD Analysis

The XRD patterns of the obtained ZnO powders with different annealing temperatures at400°C, 500°C and 600°C labeled as sample 1, 2 and 3 were shown in Figure 3 (a), (b) and (c). All diffraction peaks can be indexed to the hexagonal wurtzite phase of ZnO crystals a match well with standard data.

The pattern suggests that the ZnO samples with different annealing temperatures are constituted in hexagonal wurtzite structure with a preferred orientation of (101) diffraction plane. No additional peaks correspond to the other impurities were detected in the XRD pattern, such as Zn and O are found in XRD patterns confirming that all the samples exist as main ZnO phase. The phase of ZnO powders can be prepared at different annealing temperaturesat400°C, 500°C and 600°C for 1 hour.

The detected peaks at scattering angles (2θ) values at 31.7°, 34.4°, 36.3°, 47.5°, 56.6°, 62.8°and 66.4° which corresponds to (100), (002), (101), (102), (110), (103) and (200) crystal plane respectively.

To identify the effect of annealing and investigate the reason for the diffraction peak shift the lattice parameters (a and c) were estimated from the relation. The experimental average lattice constant a and c of ZnO powders for lattice planes were determined as at400°C (3.2546, 5.2141), 500°C (3.2484, 5.2035) and 600°C (3.2491, 5.2041) respectively, giving average lattice constant as a =3.2507, c= 5.20723 Å. These values were very close to ZnO ones in the JCPDS card result, i.e, a = 3.264Å and c = 5.219Å.

The mean ratio c/a of ZnO powders were 1.602, 1.601 and 1.601. The values of the lattice parameter 'a' and 'c' decreased with an increase in annealing temperature, attributed the decrease in the values of lattice parameter to the lattice contraction that may have resulted from the presence of dangling bonds on the surface of ZnO. The above structural analysis reveals that an annealing temperature of 500°Cessentially required to obtain ZnO powders with high crystallinity quality and minimum stress.

The sharp diffraction peak of ZnO (101) plane was much stronger than the other peaks. The average crystallite size of the prepared nanopowder ZnO were calculated using the Debye-Scherer formula,

$$D = \frac{0.9\lambda}{\beta \mathrm{Cos}\theta}$$

Where D is the crystallite size, λ is 1.5406Å for $\mathrm{CuK}_{\alpha 2}$, β is the full width at half maximum (FWHM) of the peak in radian and θ is the Bragg angle indicated the calculated particle size of the ZnO diffraction peak. The average crystallite size of the samples 1, 2 and 3 was found to be 38.15nm, 41.38nm and 41.17nm respectively. It was observed that the crystallite size of ZnO nanaopowders increased during annealing point out to the tendency of large grain growth in the nanoparticles that occurs as a result of movement of atoms to the favorable positions to merge into adjacent particles forming larger particles due to annealing.

ZnO powder annealed at 500°C registered the highest intensity, indicative of most enhanced crystallinity and grain growth. Increased in temperature to 600°C, the intensity fell slightly causes to grain boundaries resulting into a little poor crystallinity.

The decreased in the FWHM of the diffraction peaks with the increase of the annealing temperature can be attributed to the coalescences of grains at higher annealing temperatures. The shift to a higher angle of diffraction peak (101) with the increase in annealing temperature is occasioned by a change in stress in the ZnO and may be related to decrease of lattice parameters that come from the oxygen deficiency and strain caused by crystallinity during annealing process.

Additionally, ZnO nanopowders known to have defects such as zinc antisites, oxygen vacancies and lattice disorders, which are reported to disappear with annealing resulting to the contraction of lattice. It was observed that the diffraction peak (101) of the annealed samples were located at a higher diffraction angle, which meant smaller d value. During annealing, oxygen vacancies were generated while the majority of Zn atoms were in the same valence state. It was suggested that oxygen vacancies might reduce the lattice strain and corresponding lattice parameters, at least the c value.

The dislocation density (δ), which represents the number of defects in the sample is defined the length of dislocation lines per unit volume of the crystal and is calculated using the following equation;

$$\delta = \frac{1}{D^2}$$

Where D is the crystallite size. The dislocation density for ZnO films annealed at different temperatures at 400°C, 500°C and 600°C were $6.87 \times 10^{14}\ \mathrm{m}^{-2}$, $5.84 \times 10^{14}\ \mathrm{m}^{-2}$ and $9.82 \times 10^{14}\ \mathrm{m}^{-2}$.In addition, the micro strain (ε) of samples were calculated by the following equation;

$$\varepsilon = \frac{\beta Cos\theta}{4}$$

The macrostrains of the ZnO powders were 9.08×10^{-4}, 8.37×10^{-4} and 10.86×10^{-4} at 400°C, 500°C and 600°C.Table 1 summarized XRD analysis results of ZnO samples at (101) planes.

Table 1 The energy gap, grain size and crystallite size of ZnO powdersat (101) planes

Sample	**Annealing Temp:**	**(hkl)**	**FWHM**	**c/a ratio**	**Grain Size (µm)**	**Crystallite size (nm)**	**Energy Gap (eV)**
1	400°C	(101)	0.219	1.602	0.32	38.15	3.15
2	500°C	(101)	0.202	1.601	0.47	41.38	3.39
3	600°C	(101)	0.203	1.601	0.40	41.17	3.84

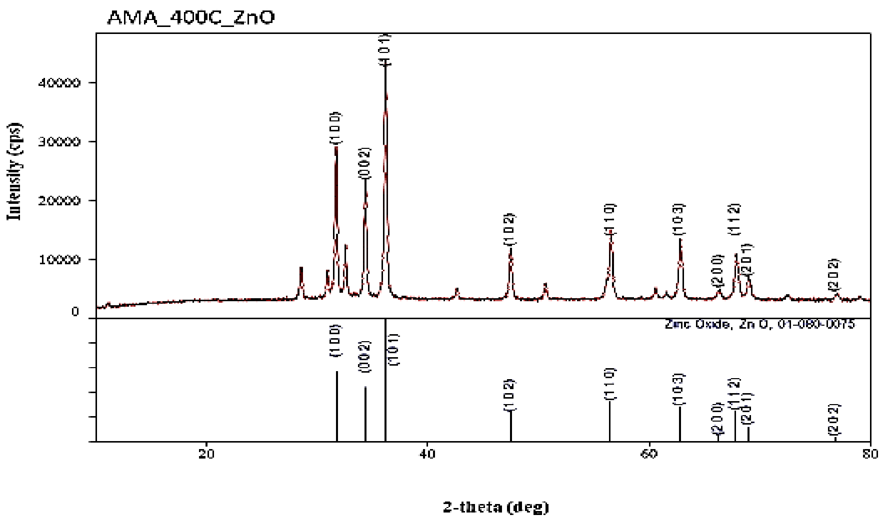

(a) sample 1

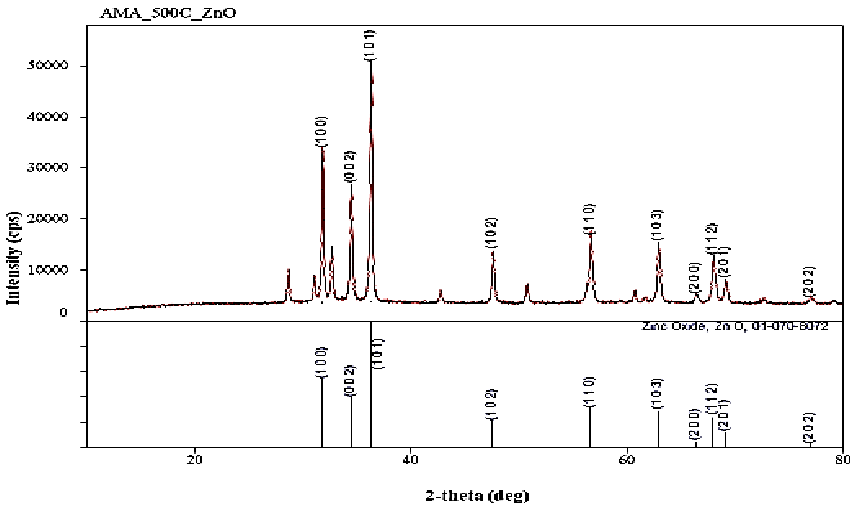

(b) sample 2

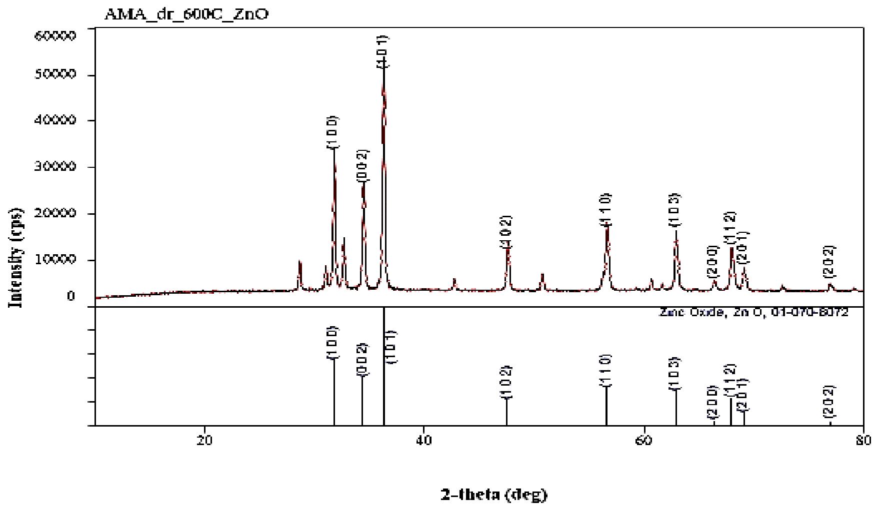

(c) sample 3

Figure 3 XRD patterns of ZnO powders annealed at 400°C, 500°C and 600°C for 1 hour (a) sample 1 (b) sample 2 and (c) sample 3

Scanning Electron Microscopy (SEM)

The investigation of microstructural properties such as grain size, pore and homogeneity are checked by SEM. Figure 4 shows the surface morphology at temperature ranging from 400°C to 600°C. The particle of ZnO powder with the range particle size of 0.32µm, 0.47µm and 0.40 µm for samples 1, 2 and 3. All ZnO powder samples tend to spherical shaped nanoparticles. As the temperature is increased further the shape of the particles is changed and size of the particles also increases. Reaction temperature is an important parameter which influences the structural morphology of the particles as well as the particle size.

As the annealed temperature is increased there is increase in the particle size. In heating process when the particles are formed, they collide and either coalesce with one another to form a larger particle or coagulate. The grain size growths of ZnO powders observed mostly probably based on the shape and distribution of grain for each powder. The average grain sizes of the ZnO particles for the samples are shown in Table 1. As the temperature increased further the shape of the particles is changed and size of the particles also increases. The measurement of Scanning electron microscopy analysis by using the aid of "image J" software.

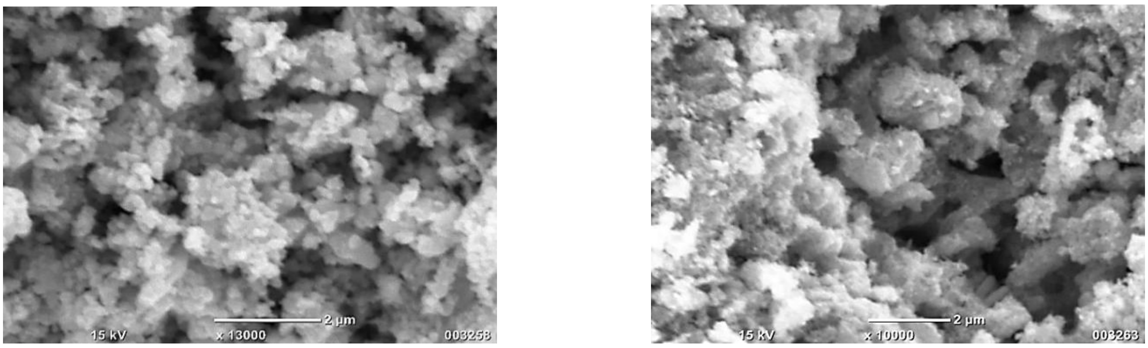

(a) sample 1 (b) sample 2

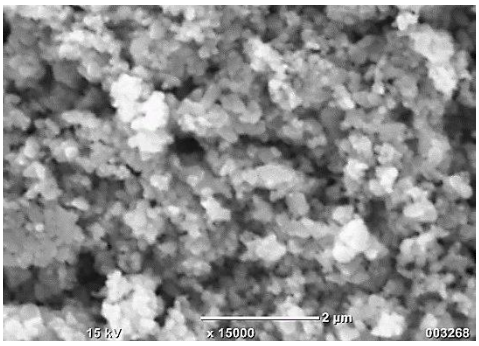

(c) sample 3

Figure 4 SEM images of ZnO powders at different annealing temperatures 400°C, 500°C and 600°C (a) sample 1 (b) sample 2 and (c) sample 3

Optical properties

The optical property of the ZnO powder at different annealing temperature was studied the physical phenomena and optical constant. The preparation of ZnO powder were analysed by UV absorbance spectra. The absorbance of sample may be influenced by grain size, shape and coverage of sample. Absorbance was checked in wavelength range from 200to1100 nm for different annealing temperature 400°C, 500°C and 600°C. All the samples showed absorption edges around 370 nm which corresponded to the optical band gap of ZnO. The UV spectrum of

Zinc Oxide samples are shown in Figure 5 (a), (b) and (c). From the dependence of the absorption band edge on wavelength, the energy band gap of the material can be determined. To determine the optical band gap, absorption coefficient α of the ZnO film was calculated using,

$$\alpha(\gamma) = 2.303\ (A/t)$$

where A is the optical absorbance and tis the thickness of cuvette. The optical band gap of the film was estimated by means of Tauc's equation,

$$(\alpha h\upsilon)^2 = (h\upsilon - E_g)^{1/2}$$

Where hγ is the photon energy and E_g is the optical energy gap. These energy gaps are calculated from the intercept of straight line on the photon energy (hυ) of the $(\alpha h\upsilon)^2$vs (hυ) plot and the value listed in Table 1. The calculated band gap values were 3.15 eV, 3.39 eV and 3.84 eV and treated samples at 400°C, 500°C and 600°C. The UV emission corresponds to near band edge emission due to the fee excitation recombination. The optical band gap of ZnO reduced appreciable with a change in nanoparticle size from 38.15 nm to 41.38 nm as caused by the increase in annealing temperature.

The band gap energy may be attributed to the increase in particle size with increasing annealing temperature as shown by XRD and SEM data. The observed increased in the optical band gap with the increase in annealing temperature could be due to the variation in lattice defects and stress. The annealing process improved the crystallinity, increased the average grain size and band gap energy increased.

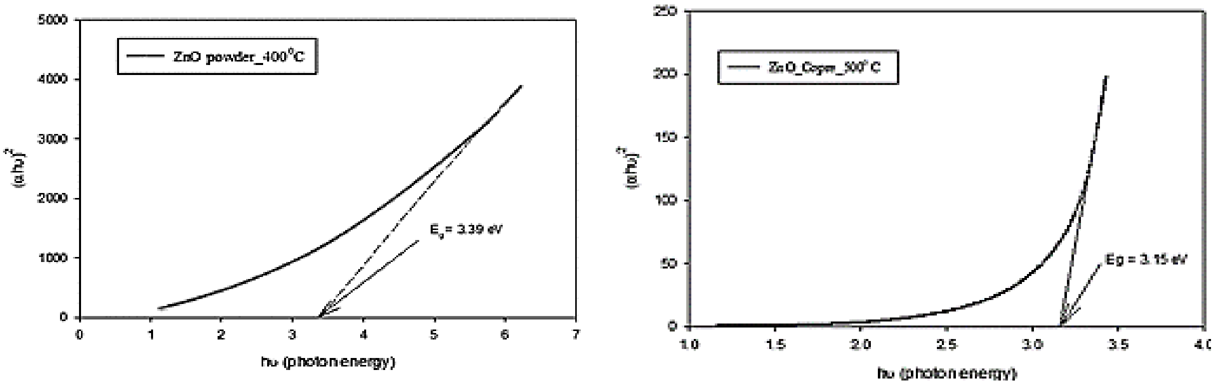

(a)sample 1 (b)sample 2

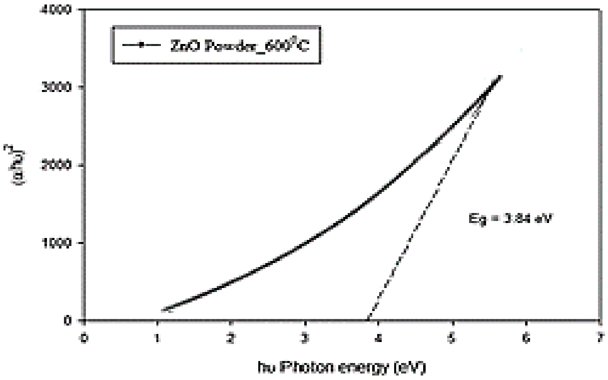

(c) sample 3

Figure 5 Plots of $(\alpha h\upsilon)^2$ vs (hυ) to determine the energy of the optical absorption coefficient for ZnO powder samples with different temperatures
(a) sample 1 (b) sample 2 and (c) sample 3

Conclusion

Zinc Oxide Nano powders by the chemical co-precipitation method and annealed at different temperatures 400°C, 500°C and 600°C. Various properties of ZnO nanostructures have been characterized. The XRD patterns of the samples showed a hexagonal wurtzite crystal structure confirming the synthesis process efficiency. The SEM revealed the formation of agglomerated particles. The research finding, the energy band gap for ZnO was 3.39 eV while the crystallite size 41.38 nm by using UV-vis and XRD. In addition, there was a reaction temperature was important parameter which influences the structural morphology of the particles as well as the particle size. As the reaction temperature was increased there was increased in the particle size. In heating process when the particles are formed, they collide and either coalesce with one another to form a large particle or coagulate. When the temperature was increased, the c/a ratio decreased and the crystallite size increased. The band gap of ZnO powders increased from 3.15to 3.84 eV with an increase in temperature from 400°C to 600°C.The results of this work show that ZnO nanopowders annealed at 500°C is most suitable to make photo electrode which was in a good agreement with the value of optical band gap for ZnO at 3.39 eV and micro strain was the lowest 8.37×10^{-4} because of the dislocation density was found to be 5.84×10^{14} m^{-2}.The results indicate that the ZnO nanopowder prepared by co-precipitation method can be used for solar cell. Then, the samples were characterized by means of XRD, SEM and UV-Vis measurement.

Acknowledgements

I would like to express profound thanks to Professor Dr Khin Khin Win, Head of Department of Physics, University of Yangon for her kind permission and supporting this work.

I also thanks to Dr Myo Lwin, Professor, Department of Physics, Dr Ye Chan, Professor and Head of Universities Research Centre, Dr Aye Aye Thant, Professor, Department of Physics and Dr Than Zaw Oo, Professor, Universities Research Centre, University of Yangon for their helpful advice to carry out this work.

References

Ahamed A.J and Kumar P.V, (2016), "Synthesis and Characterization of ZnO nanaoparticles by Co-precipitation Method at Room Temperature", Journal of Chemical and Pharmaceutical Research, ISSN: 0975-7384, Volume 8(5), pp 624-628.

Baisakh K, Behera s and Pati S, (2017), "Evaluation of the optical characteristics of c-axis oriented zinc oxide film grown by sol gel spin coating technique", IOP Conff. Series: Materials Science and Engineering,

Bhakat C, Singh P.P, (2012), "Zinc Oxide Nanorods: Synthesis and Its Applications in Solar Cell", International Journal of Modern Engineering Research (IJMER), ISSN: 2249-6645, Volume 2(4), pp 2452-2454.

Bhumika G, Nitin K.V, (2015), "Synthesis and Characterization of Pure Zinc Oxide Nanoparticles by Precipitation Method", International Journal of Engineering and Management Research, ISSN: 2250-0758, Volume 8(2), pp 386-389.

Bindu P, Thomas S, (2014), "Estimation of Lattice strain in ZnO nanoparticles: X-ray peak profile analysis", J Theor Appl Phys, Volume 8, pp 123-134.

Davood R, 2013, "Synthesis and microstructural properties of ZnO nanoparticles prepared by precipitation method", Renewable Energy, Volume 50, pp 932-937.

Ebin B, Elif A, Burak O and Sebahattin G, (2012), "Production and characterization of ZnO nanaoparticles and porous particles by ultrasonic spray pyrolysis using a zinc nitrate precursor", International Journal of Minerals, Metallurgy and Materials, Volume 19(7), pp 651-656.

Ezenwa I.A, (2012), “Synthesis and Optical Characterization of Zinc Oxide Thin Film", Research Journal of Chemical Sciences, Volume 2 (3), pp 26-30.

Khalaf A.A, Sahar A, Jean Z and Chafic S, (2017), "Synthesis of ZnO Nanopowders By Using Sol-Gel and Studying Their Structural and Electrical Properties at Different Temperature", International Conference on Technologies and Materials for Renewable Energy, Environment and Sustainability, TMREES17, Volume 119, pp 565-570.

Malevu T.D, Ocaya R.O, (2015), "Effect of Annealing Temperature on Structural, Morphology and Optical Properties of ZnO Nano-Needles Prepared by Zinc Air Cell System Method", International Journal of Electrochemical Science, Volume 10, pp 1752-1761.

Mayekar J, Dhar V, Radha S, (2013), “To Study the Role of Temperature and Sodium Hydroxide Concentration in the Synthesis of Zinc Oxide Nanoparticles”, International Journal of Scientific and Research Publications,ISSN:2250-3153, Volume 3(11).

Mayekar J, Dhar V,Radha S, (2014), “Role of Salt Precursor in Synthesis of Zinc Oxide Nanoparticles”, International Journal of Research in Engineering and Technology, eISSN: 2319-1163, ISSN: 2321-7308,Volume 3, pp 43-45.

Mulmi D.D, Agni D and Buddha R.S, (2014),"Effect of Annealing on Optical Properties of Zince Oxide Thin Films Prepared by Homemade Spin Coater", Nepal Journal of Science and Technology, Volume 15(2), pp 111-116.

Oladiran A.A, Olabisi I. A, (2013), “Synthesis and Characterization of ZnO Nanaoparticles with Zinc Chloride as Zinc Source”, Volume 2(2), pp 141-144.

Okoli N.L, Nkamuo C.J, Elekalachi C.I, (2018), "Effect of Dip Time on Electrodeposited Zinc Oxide Nanofilm", American Journal of Materials Synthesis and Processing, ISSN:2575-2154, Volume 3(2), pp 7-11.

PurwaningsihY, Pratapa S, Triwikantoro and Darminto, (2015), "Nano-sized ZnO Powders Prepared by Co-precipitation Method with Various pH", The 3rh International Conference on Advanced Materials Science and Technology, pp 0200631-1-020063-6.

Pusit P, Issara A, Jiraporn K and Sukon P, (2010), " Effect of pH on Zinc Oxide Powder Prepared by a Chemical Co-precipitation Method", Advanced Materials Research, Volume 93-94 pp 691-694.

Sorna P.R and Kandasamy S, "Synthesis and Characterization of Zinc Oxide and Iron Oxide Nanoparticles Using Sesbania grandiflora leaf Extract as Reducing Agen", Journal of Nanoscience, Volume 2017, pp 1-7

Veemaraj T and Mubeenabanu A, (2017), “Synthesis and Characterization of Nanoparticles Using Co-Precipitation Method: A Comparative Study”, Journal of Chemical and Pharmaceutical Research, ISSN: 0975-7384, Volume 9(6), pp 146-152.

Ungula J, Dejene B.F, Swart H.C, (2017), "Effect of annealing on the structural, morphological and optical properties of Ga-doped ZnO nanoparticles by reflux precipitation method", Volume 7, pp 2022-2027.

J. Myanmar Acad. Arts Sci. 2020 Vol. XVIII.No.2A

STRUCTURAL CHARACTERIZATION OF COBALT DOPED NICKEL FERRITES

Khin New Oo[1] , Moe Moe Aye[2], Min Maung Maung[3] and Khin Khin Win[4]

Abstract

Cobalt Doped Nickel Ferrites with the general formula $Ni_{x-1}\ Co_x\ Fe_2\ O_4$ (x = 0.0, 0.1, 0.2 and 0.3) were prepared by self-combustion method and sol-gel method. Nickel II Nitrate Hexahydrate [$Ni(NO_3)_2\ 6\ H_2O$], Cobalt II Nitrate Hexahydrate [$Co(NO_3)_2\ 6H_2O$] and Iron (III) Nanohydrate [$Fe(NO_3)_3\ 9H_2O$] were used as the starting chemicals. The X-ray diffraction (XRD) analysis was carried out to investigate the crystalline phase formation. Microstructural properties were determined by SEM. Elemental composition characterization of prepared samples were performed by Energy Dispersive Spectroscopy(EDS).

Keyword: Cobalt Doped Nickel Ferrites, XRD,SEM and EDS.

Introduction

Nanoparticles of magnetic ferrites have attracted great research interest because of their applications in permanent magnets, drug delivery, microwave devices and high-density information storage. Cobalt ferrite has been extensively investigated because of its interesting magnetic behavior, chemical stability and mechanical hardness. Cobalt ferrite $CoFe_2O_4$, crystallizes in a partially inverse spinel structure. Nickel-ferrite is an inverse spinel magnetic material. Nickel ferrite is well known hard magnetic material with high coercivity and saturation magnetization while nickel ferrite is soft material with low coercivity and saturation magnetization. Many of these hard and soft magnetic properties make then very promising for candidates for a variety of applications. Nano size ferrites have been prepared by various techniques such as sol-gel, self-combustion, modified oxidation process, forced hydrolysis, hydrothermal process, ball milling and the micro-emulsion method[1,6]. In the present study, Nano-ferrites of the composition $Ni_{1-x}\ Co_x\ Fe_2O_4$ (where x = 0.0, 0.1, 0.2 and 0.3) were synthesized by citrate-gel self- combustion method and sol-gel method. Structural, microstructure properties and atomic and weight concentration of fabricated nano-ferrite were studied by X-ray diffraction (XRD), scanning electron microscopy(SEM) and Energy Dispersive Spectrometer (EDS).

Experimental

In this research spinel like ferrites belonging to the series $Ni_{l-x}Co_xFe_2O_4$, where x varies from 0.0 to 0.3 in steps of 0.1 were prepared by self-combustion method and sol-gel method. $Ni(NO_3)_2.6H_2O$, Nickel nitrate hydrate, $Fe(NO_3)_2.9H_2O$, iron nitrate hydrate and $Co(NO_3)_2.6H_2O$, cobalt nitrate hydrate were used as raw materials for $Ni_{l-x}Co_xFe_20_4$ ferrite. Before preparation of spinel like ferrites the purification of starting materials was checked by X-ray diffraction.

---

[1] Lecturer, Department of Physics, Mawlamyine University.

[2] Dr, Associate Professor, Department of Physics, Mandalay University of Distance Education.

[3] Dr, Associate Professor, Department of Physics, University of Yangon.

[4] Dr, Professor and Head, Department of Physics, University of Yangon.

Experimental Sequence for Nano-ferrites by Self-combustion Method

The self-combustion method was used for preparation because the followings two advantages.

(1) heat generated in the exothermic reaction accelerates the process and

(2) the resulting as prepared powder is fine grained with grain size smaller than that of the starting powers.

Nickel II Nitrate Hexahydrate [Ni $(NO_3)_2 \cdot 6H_2O$], cobalt II Nitrate Hexahydrate [Co $(NO_3)_2$ $6H_2O$] Iron (III) Nanohydrate [$Fe(NO_3)_3$ $9H_2O$] were weighed with desired stoichiometric compositions. The precursor solutions were prepared by dissolving the necessary powders in deionized water by molarity ratio. The mixture solution was stirred by magnetic stirrer at 80°C. Ammonium Hydroxide (NH_4OH) was added to control pH level of mixture solution. After stirring 1h, the mixture solution became viscous gel. Hard gel was obtained by continuous heating at 100°C for 2h. As the temperature increased from 100°C to 190°C, the colour of hard gel changed to black colour. Finally, self-combustion process was done at 280°C and reddish-brown powder was obtained. It was cooled down at room temperature and then ground by agate mortar. After sieved by mesh sieve, $Ni_{1-x}Co_xFe_2O_4$nano ferrite powder was obtained. Experimental sequence of Cobalt doped Nickel Ferrites using self-combustion method was shown in figure 1.

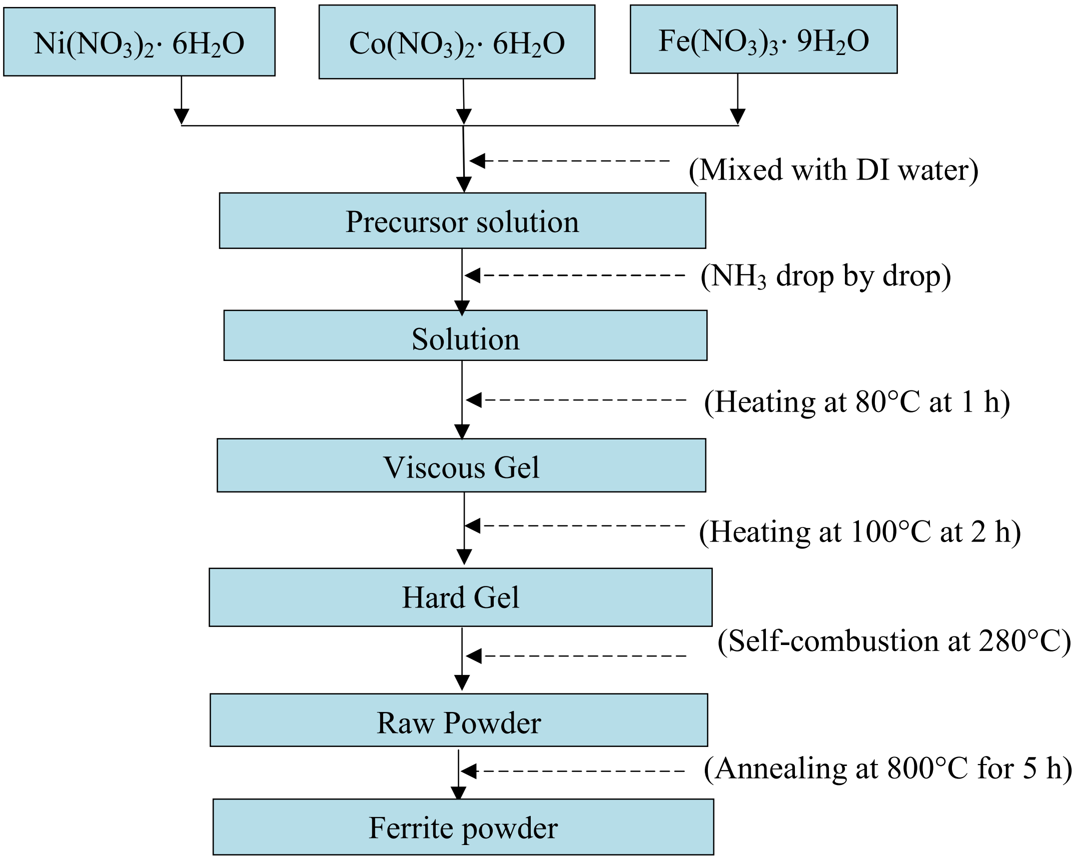

Figure 1 Experimental sequence of Cobalt Doped Nickel ferrites for Self-combustion method

Experimental Sequence for Nano-ferrites by Sol-Gel Method

Sol-gel processing, which is based on chemical engineering methods, is a technique to manufacture ceramic powders, especially oxides. The term *sol* refers to the initial solution of the chemical components for the final powder; whereas the term *gel* describes the final consolidation stage that forms the ceramic product. Sol-gel procedures have been successful in the preparation of bulk metal oxides, e.g., ceramics, glasses, films and fibers and, therefore, they have been applied for nanoparticle synthesis.

The sol-gel process consists of the following five prime steps.

(i) Preparation of a homogeneous solution either by dissolution of metal organic precursors in an organic solvent that is miscible with water, or by dissolution of inorganic salts in water. (ii) Conversion of the homogeneous solution into a sol by treatment with a suitable reagent that is generally water with or without an acid base. (iii) Aging of the solution. (iv) Shaping of the gel. (v) Thermal treatment or sintering of the final product.

Firstly, Metal precursors were prepared by using $Ni(NO_3)_2.6H_2O$, Nickel nitrate hydrate, $Fe(NO_3)2.9H_2O$, ion nitrate hydrate and $Co(NO_3)_2.6H_2O$, cobalt nitrate hydrate and deionized water. The chelating agent was prepared by dissolving the necessary powders in distilled water at 70 °C. The chelating agent solutions were maintained at 70 °C for 2 h, the solution became clear. Metal precursors were dissolved into the chelating agent solution under magnetic stirring. Ammonia (NH_3) was added drop by drop to maintain the pH at 7. The sol-gel reaction was continued for 3 h and the temperature increased to 100 °C for 10 h or until the gel dried into the form of a powder. Finally, all samples were sintered at 800 °C for 5 h and then ground and sieved, nano ferrite powder was obtained. The experimental sequence for nano ferrite powder by sol-gel method was shown in figure 2.

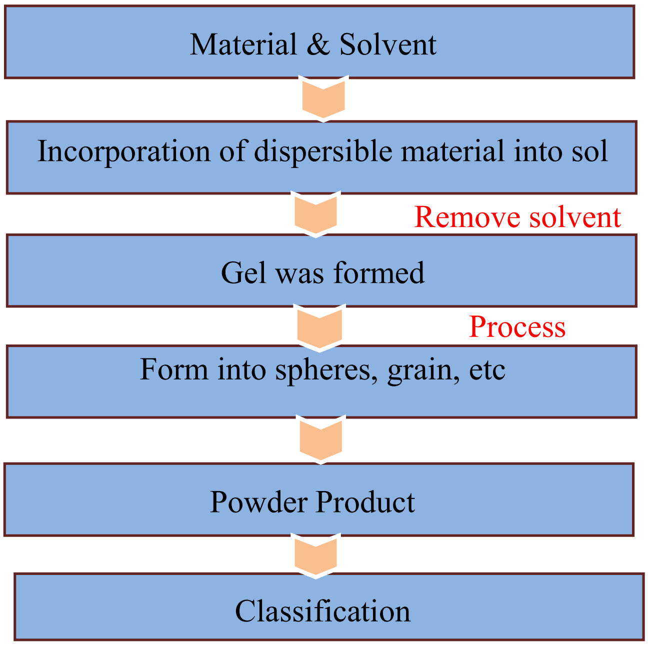

Figure 2 The production steps for sol-gel production route

Results and Discussion

Structural Investigation of Nano-ferrite

The XRD spectra of the cobalt Doped Nickel ferrites, $Ni_{1-x} Co_x Fe_2 O_4$ (x = 0.1, 0.1, 0.2 and 0.3)nano-ferrite were investigate by X-Ray Diffractometer. Figure 3(a-b) showed XRD profile of nano-ferrite fabricated by self-combustion method and sol-gel method with different Co concentration.

In these figures, eight diffraction patterns were clearly observed and all of these patterns were consistent with JCPDS library file No 01-077-9720.It can be seen that all the compounds thus prepared show crystallinity and the diffraction pattern is characteristic of a spinel structure. The interatomic spacing (d) values were in good conformity with that of the reported values. Moreover no other impurity lines corresponding to possible oxides of precursors used for synthesis were noticed. Thus it was ensured that the prepared compounds were single phasic in nature and they exhibit an inverse/ normal spinel structure.

In figure 3(b),all the reflections in the XRD patterns correspond to that of cobalt ferrite and no additional reflections were observed for the samples indicating the phase purity of the samples. The X-ray diffractograms clearly indicate the formation of single phase spinel structure. The XRD patterns were compared and indexed using JCPDS library file no 00-003-0875 for Ni ferrites. The reflections of the samples synthesized by sol-gel methods were shaper than that of the sample prepared by the self-combustion route, indicating the presence of larger crystallites. But their intensities were more intense than nano ferrite by self-combustion method.

The X-ray density of all the $Ni_{1-x}Co_xFe_2O_4$ ($0 \leq x \leq 0.3$) ferrites has been calculated from the molecular weight and the volume of the unit cell using the relation;

$$d_x = \frac{8M}{Na^3} \, .$$

The calculated values were also listed in Table1.

The average particle size of the synthesized ferrite samples was estimated from X-ray peak broadening of diffraction peaks using Scherrer formula. The calculated average crystallite sizes of these starting materials were listed in Table 2.From this results, the average crystallite size was decreased with the increasing of Co content. But at the Co content (0.3%), the average crystallite size increased again due to the material concentration. Average crystallite size of fabricated nano ferrite by sol-gel method was a little larger than that of self-combustion method. Generally the sol-gel technique yields nano size grains in the ferrite systems. But, as the sintering temperature and sintering time (800˚C for 5 h) were very high, this resulted for larger grain size in the prepared ferrite samples. Likelihood, all of fabricated nano ferrite confirmed nano meter range.

Table 1 Variation of X- ray density values for $Ni_{1-x}Co_xFe_2O_4$ nano-ferrite

$Ni_{1-x}Co_xFe_2O_4$ Nano-ferrite	X-ray density (g cm^{-3})	
	Self-combustion Method	Sol-gel Method
x =0.0	5.3530	5.3900
x =0.1	6.7244	6.7070
x = 0.2	7.2942	6.7029
x= 0.3	6.8162	6.7244

Table 2 The crystallite size of starting materials

$Ni_{1-x}Co_xFe_2O_4$ Nano-ferrite	Crystallite Size(nm)	
	Self-combustion Method	Sol-gel Method
x =0.0	45.7951	46.3617
x =0.1	43.1230	45.6355
x = 0.2	41.4354	45.1332
x= 0.3	42.5168	45.7477

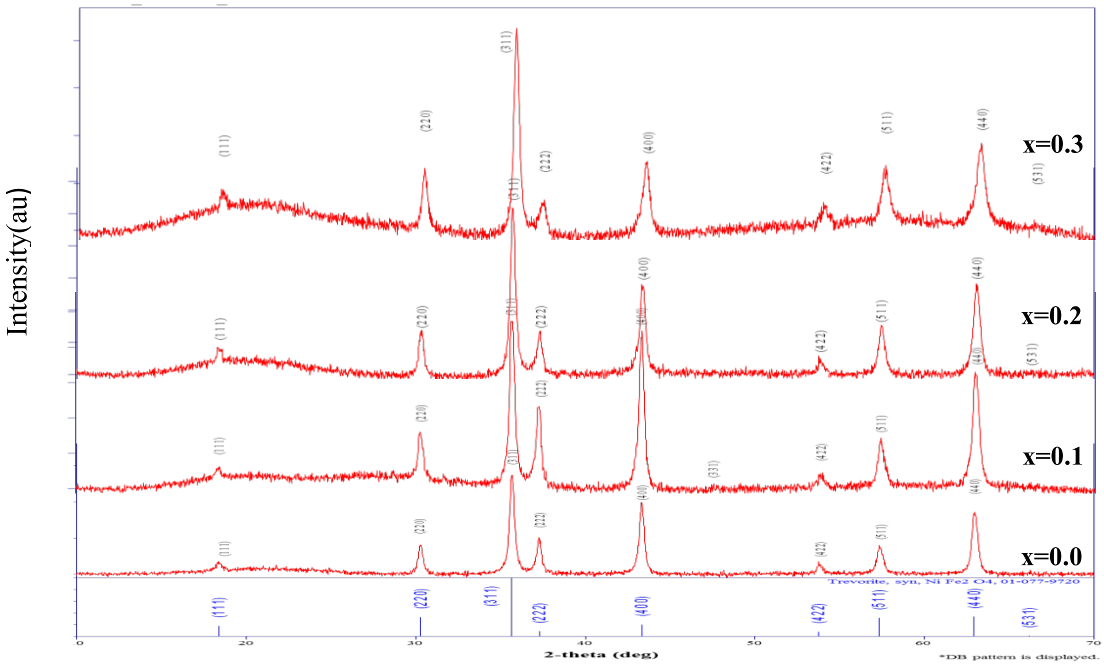

Figure 3 (a) XRD Spectrum of $Ni_{1-x}Co_xFe_2O_4$ferrites with different Co concentration by self-combustion method

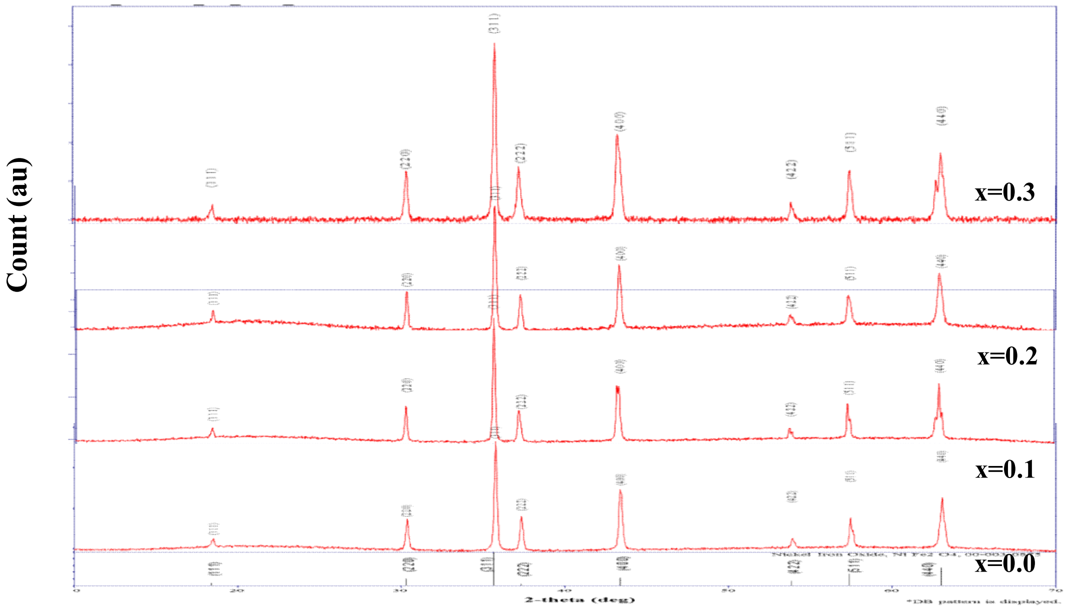

Figure 3 (b) XRD Spectrum of $Ni_{1-x}Co_xFe_2O_4$ ferrites with different Co concentration by sol-gel method

Microstructural Determination

Microstructural properties of Ferrite samples were studied by Scanning Electron Microscopy(SEM). The scanning electron image of ferrite samples by self-combustion method and sol-gel method were shown in figure 4(a&b). In these figures, it can be seen that the morphology of particles for SEM micrographs of various composition is similar. They reveal largely agglomerated, well defined nano particles of the sample powder with inhomogeneous broader grain size distribution. Such broader size distribution is characteristics of mechanically activated nano sized particles.

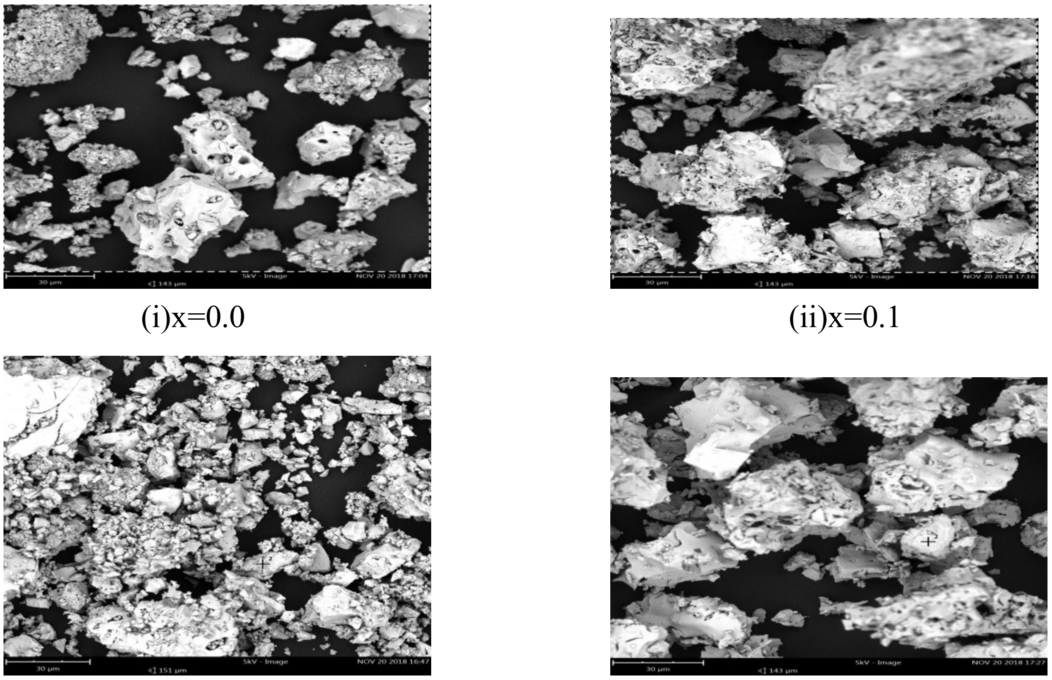

(i)x=0.0 (ii)x=0.1

(iii)x=0.2 (iv)x=0.3

Figure 4 (a) Scanning electron images of $Ni_{1-x}Co_xFe_2O_4$ ferrites nano ferrite with different Co concentration by self-combustion method

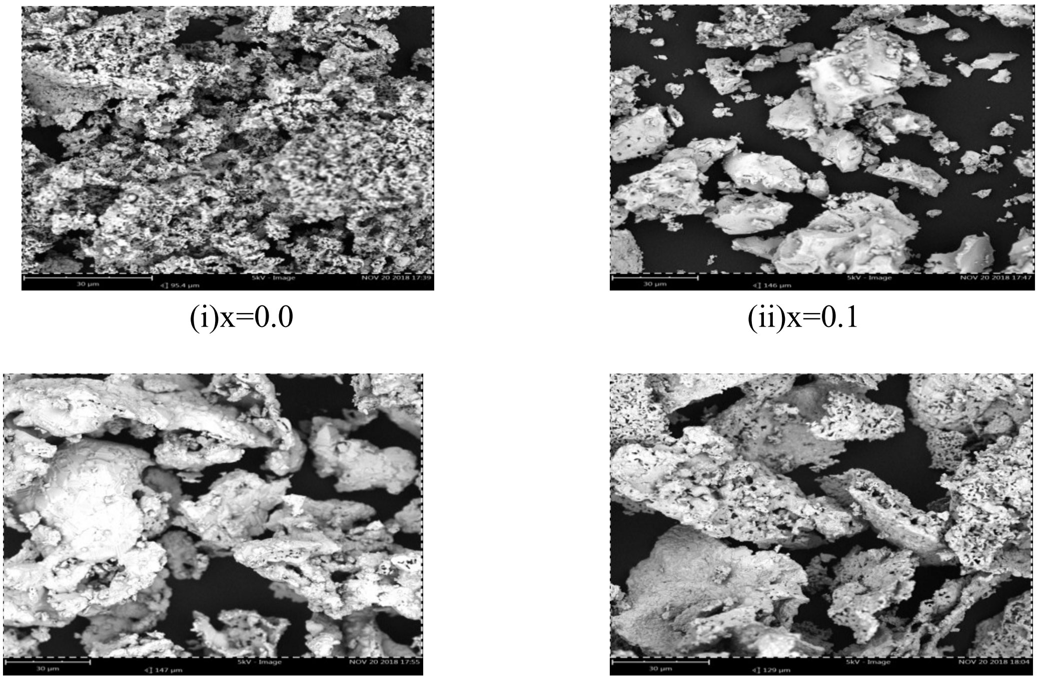

(i)x=0.0 (ii)x=0.1

(iii)x=0.2 (iv)x=0.3

Figure 4 (b) Scanning electron images of $Ni_{1-x}Co_xFe_2O_4$ nano ferrite with different Co concentration by sol-gel method

Elemental Analysis by EDS

The elemental analysis of ferrite samples with different compositions by two different methods were analyzed by Energy Dispersive Spectrometer(EDS).The EDS pattern of nanoferrites samples were shown in figure 5(a & b). In these figure, it was indicated that the elemental and atomic composition. The fabricated nanferrite showed the present of Ni, Co, Fe and O without precipitating cations. The elemental % and atomic % of different elements were shown in Table 3 and 4.

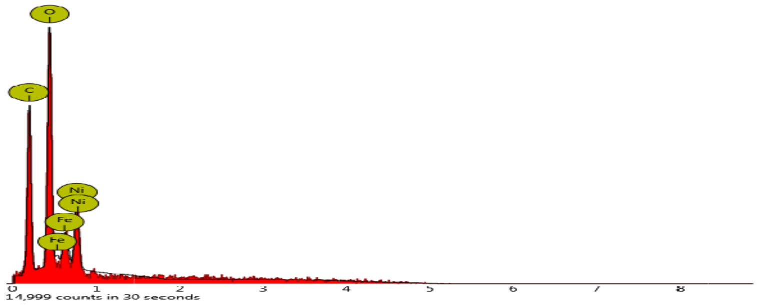

Figure 5(a)(i) EDS pattern of $Ni_{1-x}Co_xFe_2O_4$ nanoferrite with different Co x = 0.0 concentration by self-combustion method

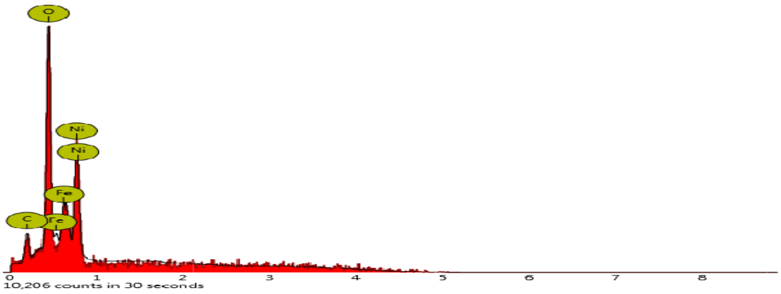

Figure 5(a)(ii) EDS pattern of $Ni_{1-x}Co_xFe_2O_4$ nanoferrite with different Co x = 0.1 concentration by self-combustion method

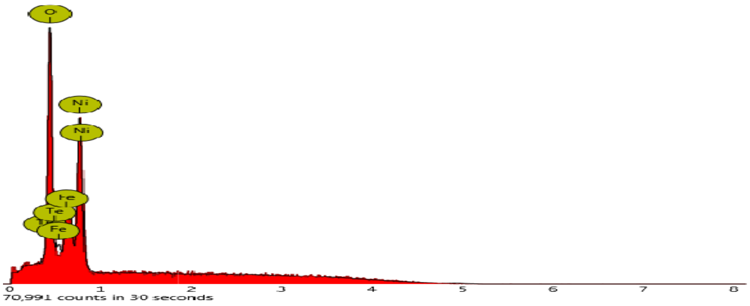

Figure 5(a)(iii) EDS pattern of $Ni_{1-x}Co_xFe_2O_4$ nanoferrite with different Co x = 0.2 concentration by self-combustion method

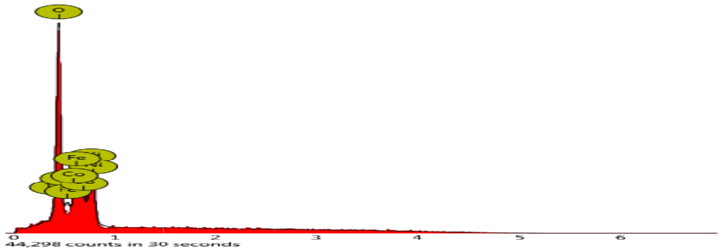

Figure 5 (a)(iv) EDS pattern of $Ni_{1-x}Co_xFe_2O_4$ nanoferrite with different Co x = 0.3 concentration by self-combustion method

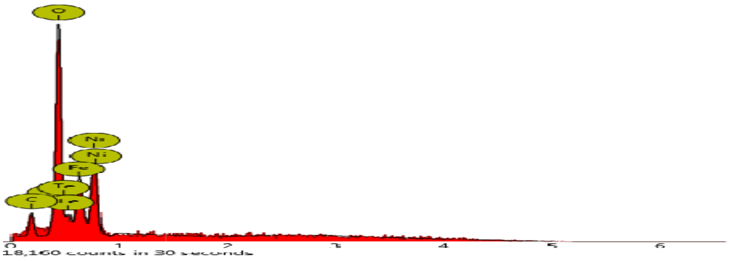

Figure 5(b)(i) EDS pattern of $Ni_{1-x}Co_xFe_2O_4$ nanoferrite with different Co x = 0.0 concentration by sol-gel method

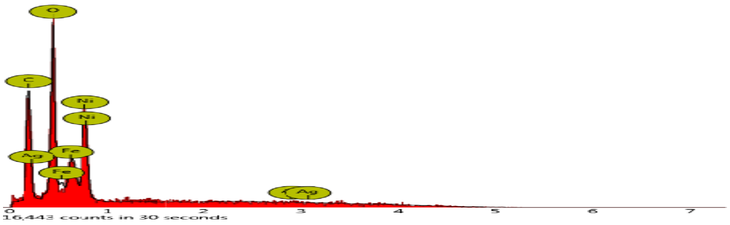

Figure 5(b)(ii) EDS pattern of $Ni_{1-x}Co_xFe_2O_4$ nanoferrite with different Co x = 0.1 concentration by sol-gel method

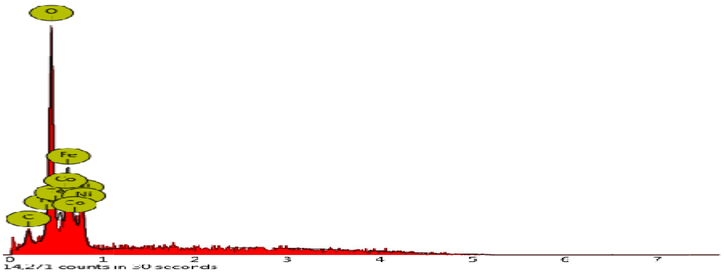

Figure 5 (b)(iii) EDS pattern of $Ni_{1-x}Co_xFe_2O_4$ nanoferrite with different Co x = 0.2 concentration by sol-gel method

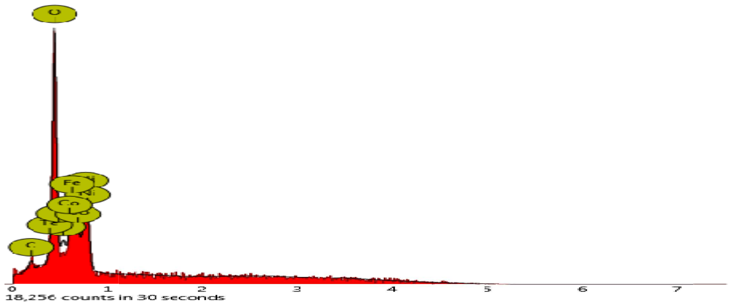

Figure 5 (b)(iv) EDS pattern of $Ni_{1-x}Co_xFe_2O_4$ nanoferrite with different Co x = 0.3 concentration by sol-gel method

Table 3 Atomic and weight concentration of nano-ferrite sample byself-combustion method

Element	Ni		Co		Fe		O	
Ferrite Composition	**Atomic Conc. %**	**Weight Conc.%**	**Atomic Conc. %**	**Weight Conc.%**	**Atomic Conc. %**	**Weight Conc.%**	**Atomic Conc. %**	**Weight Conc.%**
$NiFeO_4$	8.60	25.46			5.16	14.54	38.63	31.17
$Ni_{0.9}Co_{0.1}Fe0_4$	24.13	47.60			10.14	19.04	50.96	27.40
$Ni_{0.8}Co_{0.2}Fe0_4$	33.36	55.64			12.19	19.33	54.36	24.71
$Ni_{0.7}Co_{0.3}Fe0_4$	19.58	34.97	6.65	11.93	13.86	23.57	59.80	29.12

Table 4 Atomic and weight concentration of nano-ferrite sample by sol gel method

Element	Ni		Co		Fe		O	
Ferrite Composition	**Atomic Conc. %**	**Weight Conc.%**	**Atomic Conc. %**	**Weight Conc.%**	**Atomic Conc. %**	**Weight Conc.%**	**Atomic Conc. %**	**Weight Conc.%**
$NiFeO_4$	20.43	39.90			14.38	26.73	50.56	26.92
$Ni_{0.9}Co_{0.1}Fe0_4$	14.50	37.05			6.36	15.46	35.18	24.50
$Ni_{0.8}Co_{0.2}Fe0_4$	13.09	24.01	5.34	9.83	20.87	36.41	52.37	26.18
$Ni_{0.7}Co_{0.3}Fe0_4$	19.25	33.88	6.98	12.33	15.59	26.11	53.46	25.65

Conclusion

Nanocrystalline Cobalt Doped Nickel Ferrites, $Ni_{1-x}Co_xFe_2O_4$ (where x = 0.0, 0.1, 0.2 and 0.3) samples were successfully prepared by self-combustion method and sol-gel method. Their structural analysis was reported by using XRD. The process involved no impurity pick up and material loss. It was a very simple and economical method where no specific heating or cooling rate is required. X-ray diffraction pattern confirms the formation of cubic spinel structure in single phased without any impurity peak. The lattice parameter was not remarkablely changed with the increase of Co substitution in Ni-Co ferrites which indicates that Co content was totally substituted in Ni. Average crystallite size of fabricated nano ferrite observed that in the range between 41 and 46 nm. SEM micrographs of various compositions indicate the morphology of particles is similar and largely agglomerated and inhomogeneous broader grain size distribution. EDS data gives the present of Ni, Co, Fe and O without precipitating cations. From the results, it is concluded that, the two fabrication methods used in this research provided improvement of crystallinity and pronounces of nano particle size.

Acknowledgement

I would like to express my sincere thanks to Professor DrKhinKhin Win, Head of Department of Physics, University of Yangon, for her kind permission to carry out this work and valuable supervisor .

I wish to show my sincere thanks to Professor Dr Aye Aye Thant, Professor Dr Myo Lwin, Professor Dr Yin Maung Maung, Professor Dr Than Zaw Oo, Department of Physics, University of Yangon, for their suggestion and comments for this work.

I am also grateful to my Co-supervisor Dr Moe Moe Aye, Associate Professor, Department of Physics, Mandalay University of Distance Education, for her helpful advice and valuable guidance.

References

C. Venkataraju, G. Sathishkumar and K. Sivakumar, (2010), "Effect of Cation Distribution on the Structural and Magnetic Properties of Nickel Substituted Nanosized Mn-Zn Ferrites Prepared by Co-Precipitation Method," Journal of Magnetism and Magnetic Materials, 322, (2), 230-233.

Gopathi Ravi Kumar& et.al.,(2012), "Synthesis, Structural and Magnetic Properties of Copper Substituted Nickel Ferrites by Sol-Gel Method", Materials Sciences and Applications, 3, 87-91.

Jiang K, Li K, Peng C, Zhu Y., (2012) "Effect of multi-additives on the microstructure and magnetic properties of high permeability MnZn ferrite", Journal of Alloys and Compounds*,* 541, 472-476.

M. Pardavi-Horvath, (2000), "Microwave applications of soft ferrites" Journal of Magnetism and Magnetic Materials, 215, 171–183.

Raul Valenzuela, (2011), "Novel Applications of Ferrites", Physics Research International, 2012, 9.

S. Manjura Hoque, Md. Amanullah Choudhury and Md.Fakhrul Islam, (2002), "Characterization of Ni-Cu Mixed Spinel Ferrite," Journal of Magnetism and Magnetic Materials, 251, (3), 292-303.

J. Myanmar Acad. Arts Sci. 2020 **Vol. XVIII.No.2A**

SYNTHESIS STRATEGY OF F:SnO_2 POWDER FOR TCO-LESS DSSCs FABRICATION

Ohnmar Soe[1],Dr Pho Kaung[2], Dr Aye Aye Thant[3]

Abstract

In order to improve the photo catalytic properties, fluorine doped tin oxide (F: SnO_2) nanopowder was synthesized by sol-gel auto-combustion process. The X-ray diffraction and SEM analysis have confirmed the formation of structure, the grain size and the morphology of nanoporous F:SnO_2 powder. The synthesis strategy reflected from the microstructure has been investigated. In Dye Sensitized Solar Cells (DSSCs) fabrication, SnO_2 is sensitized with chemical dyes to enhance its efficiency. UV-Vis response of pure and doped (F: SnO_2) were investigated by using UV-1800 Shimadzu spectrophotometer. Some of these materials were applied in the fabrication of Dye Sensitized Solar Cells without Transparent Conductive Oxide layer (TCO-less DSSCs). The current-voltage measurements of the fabricated solar cells revealed the enhancement of energy conversion efficiency, long-term stability and cost effectiveness of DSSCs.

Introduction

In the previous century, it is obvious that the consumption of nonrenewable sources of energy has caused more environmental damage than any other human activity. Energy generated from fossil fuels has led to face many problems such as exhaustion of fossil fuels, ozone depletion, global warming, climate change and social and political risks. Therefore, renewable source of energy such as Hydropower, Wind, Solar, Biomass, Geothermal and others have become very important and relevant to today's world.

Solar photovoltaic cells are a promising form of renewable energy. The primary obstacle to the broader uptake of solar photovoltaic technology is the manufacturing cost of current commercial solar cells. Thus, a new type of dye-sensitized solar cells (DSCs) based on nanoporous F:SnO_2 electrode without TCO layer will be fabricated for low-cost solar cell application.

Experimental Details

Preparing Fluorine Doped Tin Oxide (F:SnO_2) Powder

Fluorine doped SnO_2 powder has been prepared by following sol-gel auto-combustion method. Firstly, 5.2 g of $SnCl_4.5H_2O$, 0.4 g of acetylene black and 0.38 g of HF (50%) were weighed by digital balance. Then $SnCl_4$ and HF were dissolved in 20 ml of deionized water. Acetylene black was added to this solution. NH_4OH aqueous solution was added drop wise during constant stirring. After 15 min stirring, the solution turned to gel. This gel was heated at 120 °C for 10 min to get dry gel. The dry gel was further heated at 500 ˚C in air. After 30 min ignition of the dry gel, auto-combustion process took place as shown in Figure 1 and F doped SnO_2 powder was obtained. The colour of as-burnt powder is gray. The sample was further calcined at 550 °C for 30 min. The colour of the sample is light gray. The sample was sintered at 650 °C for 2 hours. The colour of the simple changed to yellow. The sample was sintered at 750 °C for 2 hours. The colour of the simple changed to white. Finally, the nanoporous F doped

---

[1] Dr, Lecturer, Department of Physics, Yangon University of Education

[2] Rector, University of Yangon

[3] Professor, Department of Physics, University of Yangon

SnO_2 powder has been successfully obtained. The Flow chart of F:SnO_2 powder preparation is shown in Figure 2. The structure and morphology was investigated by XRD and scanning electron microscopy (SEM). The crystallite size of the particle can be calculated from the XRD peak broadening of the (110) peak using the Scherrer's formula.

$$g_{crystallite} = \frac{0.9\lambda}{D\cos\theta} \qquad \text{---------- (1)}$$

(a) (b) (c)

Figure 1 The formation of F doped SnO_2 powder via Auto-combustion process

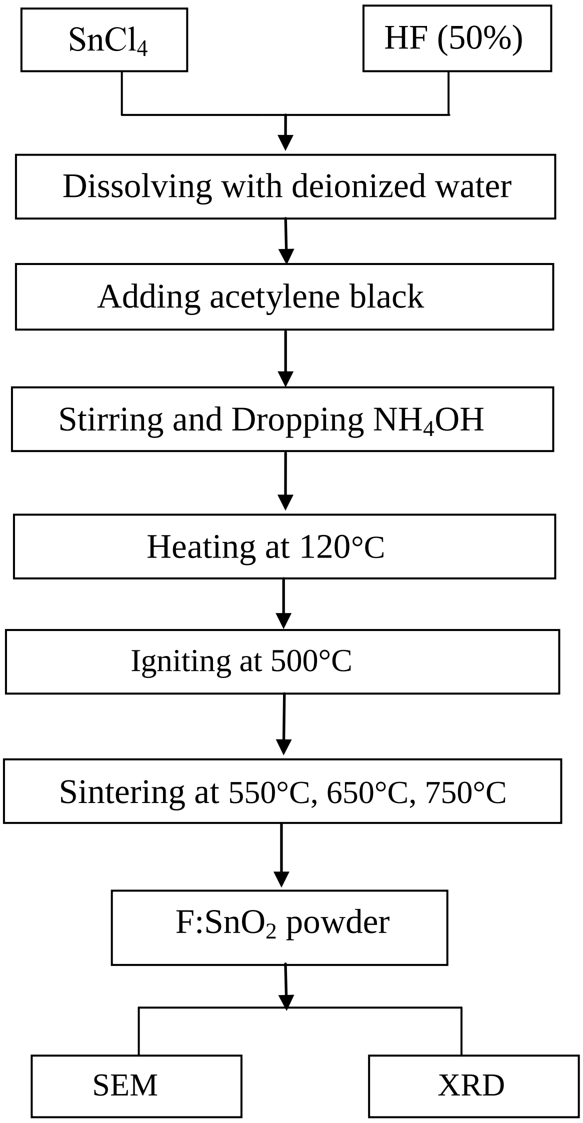

Figure 2 Flow chart of preparation of F:SnO_2 powder

Preparing the Working Electrodes

The well cleaned ordinary glasses have been used as substrates for preparing working electrodes. The scotch tape has been used to cover the three sides of the glass substrates. The nanoporous semiconductor paste was prepared by grinding 2.5 ml of citric acid (pH 2.4) and 1.5 g of fluorine doped tin oxide powder (sintered at 750 ˚C) in the mortar and pestle for about 30 min to break the aggregation of F: SnO_2 powder. One drop of washing powder solution was added to this suspension to reduce surface tension. The resultant paste was put on the masked glass substrates. The flattened paste was distributed by Doctor's Blade Method. These electrodes were put on the hot plate and heated them at approximately 150 ˚C for 30 min and then cooled down slowly.

Preparing Dye Solutions

About 0.2 g of coumarium powder, mercurochrome and methyl blue were dissolved in 100 ml of ethanol in each beaker separately for about 3 hours.

Dipping Working Electrodes in Dye Solutions

The prepared working electrodes were dipped in each dye solution for about (10-30) minutes depending on selected dye solutions and then dried in the dryer. These electrodes were heated mildly at (60-80 ˚C) if coloration is too slow.

Preparing the Counter Electrodes

The cleaned ordinary glasses, silver coated glasses and FTO glasses (which were made in URC lab) were uses as substrates for preparing counter electrodes. The scotch tape was used to cover the three sides of the counter electrodes. The carbon enrich SnO_2 paste was prepared by grinding 2 g of SnO_2 powder, 0.4g of actylene black powder and 0.1 g of graphide powder with 10ml of ethanol and 0.1ml of Triton X-100 in mortar and pestle for about 1 hours. The prepared paste was put and flatten on each glass substrate by doctor's blade method.The counter electrodes were dried on the open hot plate (at about 150 ˚C) and then cooled down slowly.

Preparing the Electrolyte solution

The redox electrolyte solution was prepared by mixing 0.5 M potassium iodide and 0.05 M iodine in unhydrated ethylene glycol. This electrolyte was stored in dark coloured bottle for further use.

Filling Electrolyte solution in the holes and binding two electrodes

The spacers made by cutting plastic film are put on the cooled counter electrodes. Some of the electrolyte solution was dropped into the holes and combine the two electrodes quickly to prevent the solvent from drying out. By fixing them with binder clips the experimental procedure for fabrication of TCO-less and with only TCO glasses involved DSSCs were completed. Figure 3 shows the fabrication processes of DSSCs. Figure 4 shows the prepared working electrodes, counter electrodes and spacers.

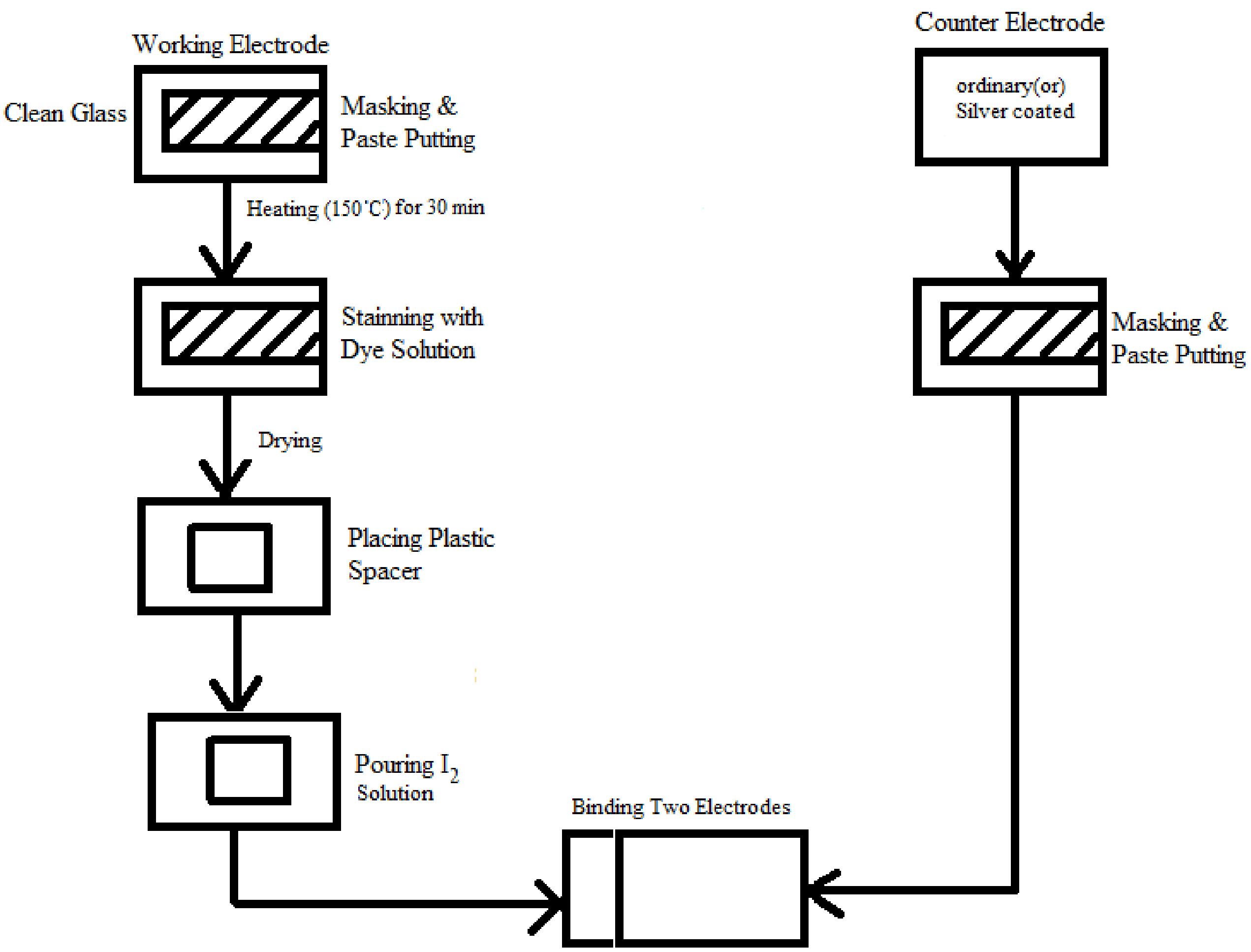

Figure 3 The fabrication processes of DSSCs

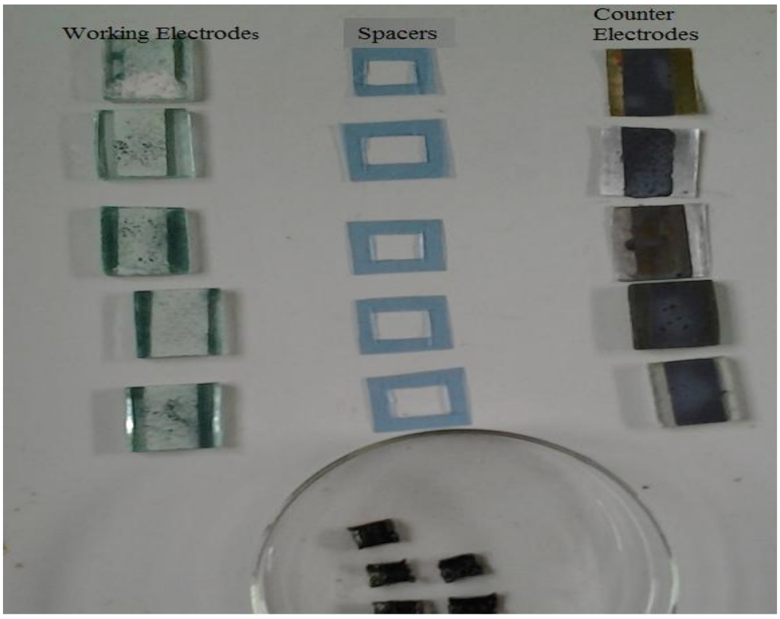

Figure 4 The prepared working electrodes, counter electrodes and spacers

Results and Discussion

Observation on Fluorine Doped Tin Oxide (F:SnO_2) Powder

The phase formation of F: SnO_2 powder is analyzed by X-ray diffraction (XRD) method. XRD patterns of nanoporous F: SnO_2 samples are shown in Figures 5(a), 6(a) and 7(a). Variation of 2θ, d-spacing and FWHM with annealing temperature is listed in Table 1. Crystallite size (g) and lattice parameter (a) is listed in Table 2. According to XRD results, it can be concluded that the annealing temperature can increase crystallization and growing of F: SnO_2 nanocrystallite. The preferred orientation indicates (1 1 0), (1 0 1), (2 1 1) for SnO_2 and (2 0 0) for fluorine, respectively.

The surface morphology of the F:SnO_2 samples has been characterized by Scanning Electron Microscopy (JEOL-JSM 5610LV). The SEM photographs of F doped SnO_2 sample at 550 °C, 650 °C and 750 °C are shown in Figures 5(b), 6(b) and 7(b) respectively. Each photograph exhibits a typical porous structure with many intergrain pores. It is observed that the intergranular pores are linked through the large pores. The pore structure should be regarded as interconnected voids that form a kind of capillary tubes. This structure is preferable for the adsorption of dye solution capable of making photo excitation (pumping out of photo electrons). In the micrograph of F: SnO_2 sintered at 550°C, the grains are spread out and the mean pore size is about 7 nm. After sintering at 750°C, the grains are adhered and the large pores are formed between groups of grains. The mean pore diameter is 7-20 nm. The variation of mean pore size of F: SnO_2 sample with sintered temperature is shown in Table 3.

From UV-Vis Spectroscopy, it was noticed that F:SnO_2 powder has lower absorbance value(<1) and wider band gap value(4.11eV-5.31eV). Therefore it can be used as electron transport mediator semiconductor at working electrode of DSSCs. The VU-Vis spectrum of pure and doped SnO_2 powder is shown in Figure 8. The estimated band gap values and the corresponding wavelengths are listed in Table 4. The band gap values are calculated by

$$E_g = 1240/\lambda.\ \text{eV nm /nm} \qquad \text{----------------}\ (2)$$

Measuring DSSCs' Parameter

To measure open circuit voltage (V_{OC}) and the short circuit current (I_{SC}) for each cell, the cell was connected with external circuits shown in Figure 8(a). Figures 8(b) and 8(c) show the photographs for measuring currents and voltages under sunlight and illuminations. The open circuit voltage (V_{OC}) and the short circuit current (I_{SC}) for each cell were measured under illumination of (1000 W/cm^2) neon bulb and the effective cells' area is 1cm^2.

The measured open circuit voltage (V_{OC}) and short circuit current (I_{SC}), the estimated maximum voltage (V_{MPP}) and maximum current (I_m) and the calculated energy conversion efficiency (η) and fill factor (FF)for each cells were listed in Table 5. The energy conversion efficiency (η) can be calculated by Equation 3.

$$\eta = \frac{MPP}{E \times A_C} \qquad \text{-----------}\ (3)$$

$$MPP = I_m \times V_m \qquad \text{----------} \quad (4)$$

The Fill factor (FF) can calculated by equation 5.

$$FF = \frac{MPP}{I_{sc} \times V_{oC}} \qquad \text{-----------} (5)$$

η = energy conversion efficiency, MPP = maximum power point

E = illumination, A_C = area of cells, I_m = maximum current, V_m = maximum voltage

The working principles of DSSCs can demonstrate as the following Equations 6,7,8,9 and 10.

At Cathode:

$$S + h\upsilon \rightarrow S^* \qquad \text{Absorption} \qquad \text{-----------} (6)$$

$$S^* \rightarrow S^+ + e^- (F:SnO_2) \qquad \text{Electron injection} \qquad \text{-----------} (7)$$

$$2S^+ + 3I^- \rightarrow 2S + I_3^- \qquad \text{Regeneration} \qquad \text{-----------} (8)$$

At Anode:

$$I_3^- + 2e^- (\text{carbon}) \rightarrow 3I^- \qquad \text{-----------} (9)$$

Cell:

$$e^- (\text{carbon}) + h\upsilon \rightarrow e^- (F:SnO_2) \qquad \text{-----------} (10)$$

Table 1 Variation of 2θ, d-spacing and FWHM with annealing temperature

$F:SnO_2$ Powder	**(hkl)**	**2θ (deg)**	**D (Å)**	**FWHM (deg)**
550˚C	(110)	26.676	3.3389	0.326
650 ˚C	(110)	27.139	3.2831	0.546
750 ˚C	(110)	26.498	3.3610	0.641

Table 2 Variation of Crystallite size (g) and lattice parameter (a)

$F:SnO_2$ Powder	Crystallite Size g (nm)	Lattice Parameter a (Å)
550˚C	24.76	4.72
650 ˚C	14.79	4.64
750 ˚C	12.59	4.75

Table 3 Variation of mean pore size with sintering temperature

Sintering temperature (˚C)	Mean pore size (nm)
550	7
650	10
750	12

Table 4 Band gap values calculated from respective wavelength values

sample	First scan (200-400)nm		Second scan (190-1100)nm		Mean value E_g (eV)
	λ	E_g(eV)	λ	E_g(eV)	
Pure SnO_2	230	5.31	237	5.23	5.27
F:SnO_2(550 ˚C)	237	5.23	297	4.175	4.70
F:SnO_2(750 ˚C)	236	5.24	302	4.106	4.67

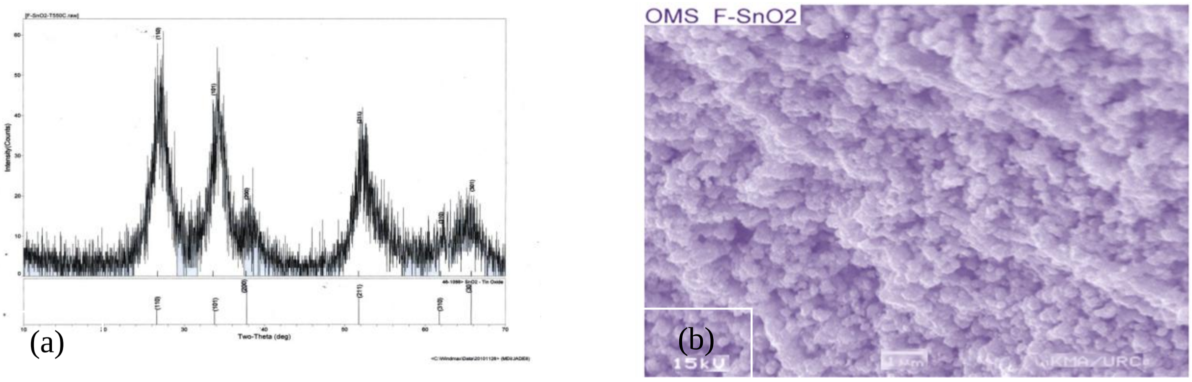

Figure 5 (a) XRD pattern and (b) SEM photograph of nanoporous F:SnO_2 Sample (550°C)

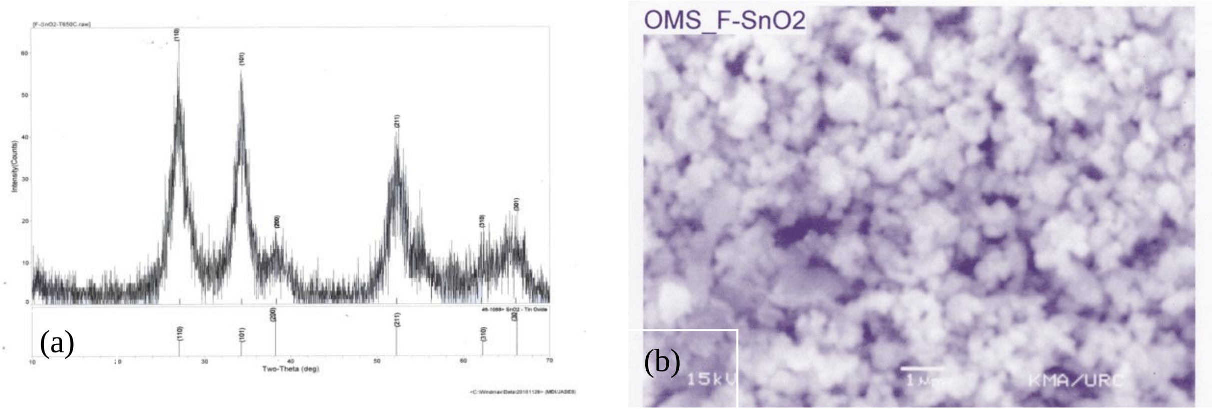

Figure 6 (a) XRD pattern and (b) SEM photograph of nanoporous F:SnO_2 Sample (650°C)

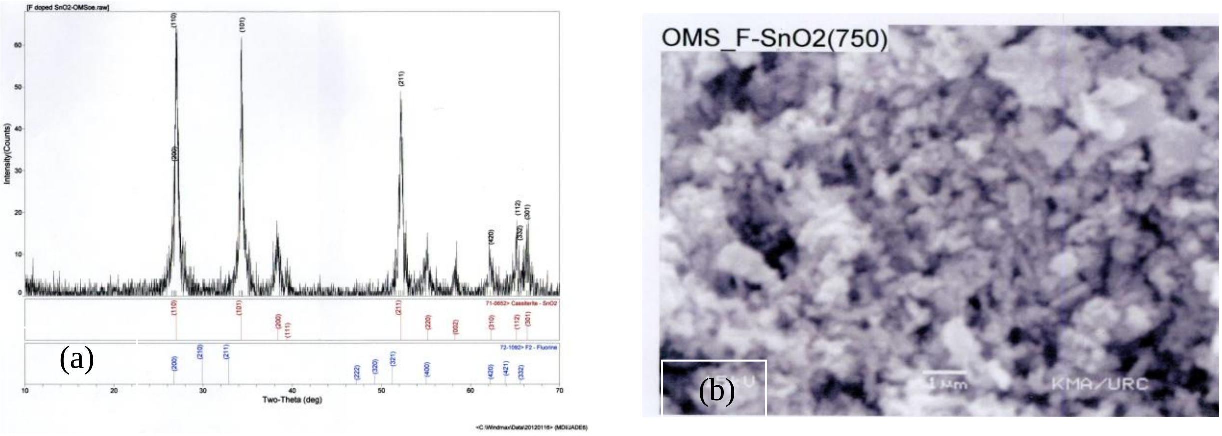

Figure 7 (a) XRD pattern and (b) SEM photograph of nanoporous F:SnO_2 Sample (750°C)

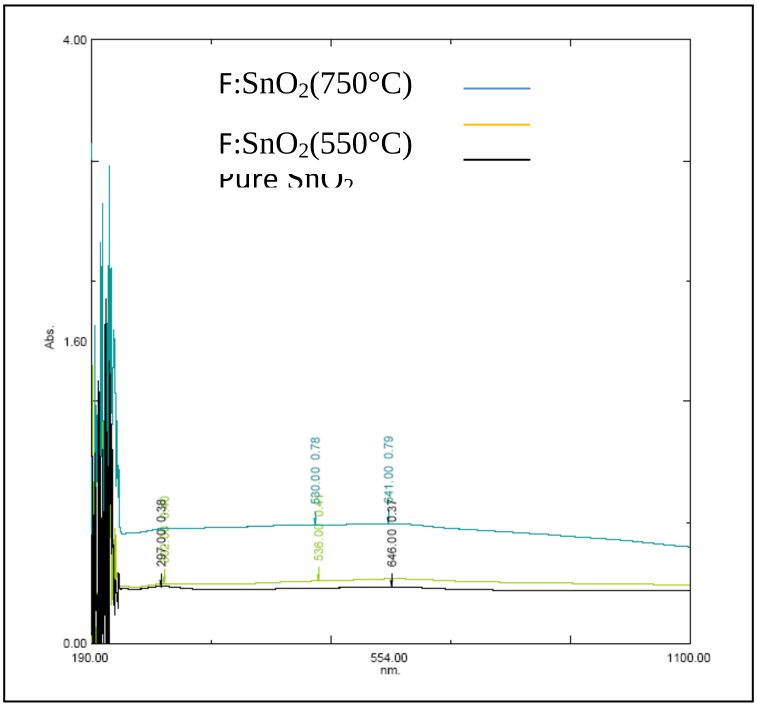

Figure 8 UV-Vis spectrum of pure and F doped SnO_2 Samples

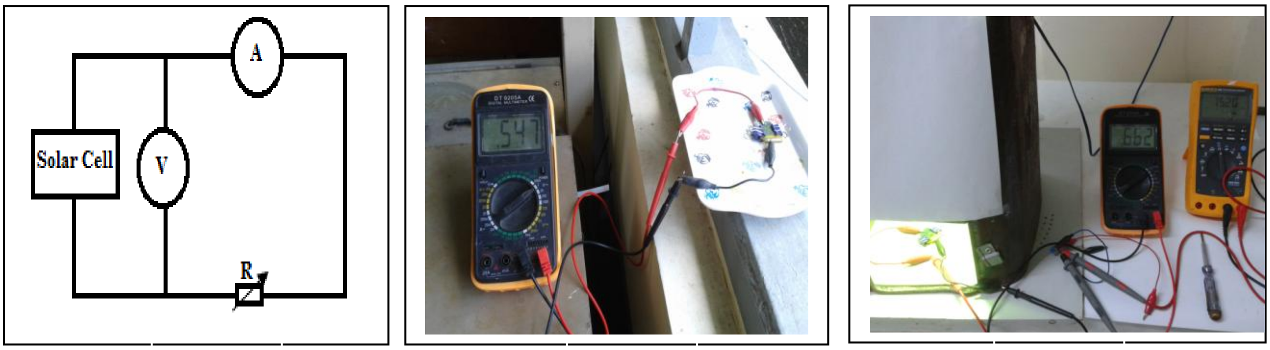

(a) (b) (c)

Figure 9 (a) The experimental setups for measuring the current-voltage characteristics of DSSCs, (b) under Sunlight and (c) under illumination

Table 5 The values of open circuit voltage V_{oc}, short circuit current I_{sc}, estimated maximum voltage V_{MPP}, maximum current I_{MPP}, calculated cells' efficiency (η) and fill factor(FF)

Sample	Type of Counter Electrode	Type of Dye solution	V_{oc} (V)	I_{sc} (mA)	η (%)	V_{MPP} (V)	I_{MPP} (mA)	FF (%)
1	Ordinary	Mecurochome	0.59	0.13	0.0300	0.50	0.060	39.11
2	Ordinary	Methyl blue	0.55	0.11	0.0263	0.47	0.056	43.50
3	Ordinary	Coumarium	0.52	0.09	0.0210	0.42	0.050	44.87
4	Silver	Mecurochome	0.56	0.25	0.060	0.40	0.15	48.00
5	Silver	Methyl blue	0.53	0.22	0.0546	0.42	0.130	46.80
6	Silver	Coumarium	0.46	0.21	0.043	0.33	0.130	44.40

Conclusion

The auto-combustion assisted sol-gel method has been proven as synthesis route for F doped SnO_2 powder. XRD patterns have confirmed that F: SnO_2 powder has been possessing single phase nanocrystalline structure. SEM images (Microstructures) obtained at sintering temperature, 550°C, 650°C and 750°C have proved that a typical porous structure with many intergrain pores has been produced by this method. Since a higher temperature of 750°C can provide larger pore size of around 12 nm, F: SnO_2 powder must be fabricated with this sintering temperature to replace both TCO and TiO_2 layer in Dye Sensitized Solar Cells (DSSCs). It was proved that fluorine doped tin oxide powder can be used in the place of working electrodes of TCO glasses in DSSCs' fabrication. The DSSCs without TCO layer has lower efficiency but higher fill factor. Therefore, it needs further study to increase cells' efficiency.

Acknowledgements

I would like to thank Dr Pyone Pyone Aung, Pro-Rector, Yangon University of Education for her kind permission to carry out this work. I would like to express my deepest gratitude to Professor Dr Khin Swe Oo, Head of Department of Physics, Yangon University of Education for her encouragement and inspiring suggestions.

References

Alex B.F. (2005) "New Architectures for Dye-Sensitized Solar Cells" New York, Willey.

Brinker C J and Scherer G W (1990) "Sol-Gel,Science The Physics and Chemistry of sol-gel Processing" New York, Academic Press.

Gratzel M (2000) "Perspectives for dye-sensitized nanocrystalline solar cells. Prog. Photovolt" : Res Appl.8 171

Richard Rivera Freddy Marcillo Alexander Chamba Patricio Puchaicela and Arvids Stashans (2014) "Quantum Chemical Study of Point Defects in Tin Dioxide" (Springer Science+Business Media Dordrecht)

Robertson J and Falabrett B (2010) "Electronic Structure of Transparent Conducting Oxides" (Springer Science : Business Media Cambridge)

Paul A Lynn (2010) "Electricity from Sunlight: An Introduction to Photovoltaic's" (New York : Willey)

Sandra E Dann (2000) "Reactions and Characterization of Solids", The Royal Society of Chemistry, Cambridge

Suryanarayana C & Grant Norton M (1956) "X-Ray Diffraction, A practical Approach" (New York : Plenum Press)

J. Myanmar Acad. Arts Sci. 2020 **Vol. XVIII.No.2A**

COBALT FERRITE ADSORBENTSFOR THE EFFECTIVE ANDEFFICIENT REMOVALOF ARSENIC

Cho Cho Thet[1], Thu Thu Hlaing[2], Khin Myo Ma Ma Saw[3] and Kobayashi Takaomi[4]

Abstract

The effective and efficient adsorbent for the removal of pentavalent arsenic (As^{5+}) ions was presented in this paper. Cobalt ferrites, $CoFe_2O_4$, adsorbents were prepared by sonochemical synthesis method. The synthesis parameters including pH of the precursor solution and post annealing temperature, based on the formation of spinel cobalt ferrite were discussed. The compound identification, the crystal structure and surface morphology of cobalt ferrite were studied by Fourier transform infrared (FT-IR), X-ray diffraction (XRD) and Scanning electron microscope (SEM) analysis. The adsorption behaviour of As^{5+} ions on the cobalt ferrite has been investigated by batch adsorption method. The amount ofAs concentration adsorbed on cobalt ferrite is measured by atomic absorption spectroscopy coupled with hydride vapour generation (HVG-AAS).The adsorption capacity was fitted with the *Langmuir* isotherm model. The removal efficiency and adsorption amount of As determined from *Langmuir* isotherm model were discussed.

Keywords: arsenic (As), adsorption, $CoFe_2O_{4,}$ ferrite, HVG-AAS, sonochemical, spinel structure.

Introduction

Inorganic arsenic (As^{3+} and As^{5+}) elements are relatively scared to living organisms since they are toxic and carcinogenic elements. Symptoms of arsenic poisoning may include vomiting, abdominal pain, encephalopathy and watery diarrhea. Long-term exposure to arsenic contaminated water could result in thickening of the skin, darker skin, abdominal pain, diarrhea, heart disease, numbness, and cancer [Ratnaike *et al*., 2003]. The permissible limit of total arsenic in drinking water is 0.01 ppm (10 ppb)by world health organization (WHO) [WHO (2011)].Thus, the effective and efficient adsorbents only for selective removal of heavy metal ions (as As) are urgently required. On the other hand, the development of new materials as well as technologies are becoming the challenges to the remediation of waste water treatment since improper separation methods of heavy metals from aqueous solution can be spread to the living organisms and environment.

Heavy metal ions in the waste water are removed by many techniques including reverse osmosis[Mohsen-Nia *et al*., 2007], precipitation [Byambaa *et al*., 2018], solvent extraction [de los Ríos *et al*., 2007], ion exchange [Budak *et al*., 2013]and membrane filtration[Maximous *et al*., 2010].Adsorption [Kang *et al*., 2015]is an alternative method by an adhesion of an adsorbate such as a fluid, liquid, or gas, by creating a thin layer on the surface of an adsorbent.

Most of the common materials using for the removal of heavy metals ions are including biomass-based materials, metal oxides, geopolymers, zeolites, silica and activated carbon, activated alumina and ferrites. Spinel ferrite nanoparticles have been focused on as adsorbents because their unique physicochemical properties are differ from their bulk. The shape and size as well as magnetic properties can be tuned. They also have surface versatility, high surface-to-

---

[1] Dr, Associate Professor, Department of Physics, Myeik University

[2] Assistant Lecturer, Department of Chemistry, Yangon University of Distance Education

[3] Dr, Professor, Department of Physics, Myeik University

[4] Dr, Professor, Department of Materials Science and Technology, Nagaoka University of Technology

volume ratio, long-lasting in water treatment and less aggregation. $CoFe_2O_4$ has a face centered cubic (FCC) structure of normal spinel-type and soft magnetic n-type semiconducting material. Ferrite particles have a wide variety of applications including heterogeneous catalysis, adsorption, sensors and magnetic technology [Sanasi *et al*., 2104; Kirankumar *et al*., 2017; Leroux *et al*., 2014; Ponce *et al*., 2013].

The conventional synthesis methods of cobalt ferrites include ball milling, sol-gel autocombustion, coprecipitation, reverse micelles, hydrothermal, microemulsions, laser ablation, a polyol method, sonochemical approaches and aerosol method. Among these methods, sonochemical synthesis is a relatively new technique for the ferrite, in which they are synthesized using ultrasonic irradiation of the reaction mixture. This route has many advantages over any other methods such as short reaction time, cost efficiency, uncomplicated, compact, on-site treatment and higher purity of the final product. In the present work, the main aim is synthesis of cobalt ferrite by sonication method in order to use them as adsorbents for decontamination of arsenic heavy metal ions. The adsorption behavior of As by cobalt ferrites was investigated by doing batch adsorption process.

Materials and Method

Synthesis of Cobalt Ferrite

Briefly, 6.88 g of $Fe(NO_3)_3{\cdot}9H_2O$ and 2.48 g of $Co(NO_3)_2{\cdot}6H_2O$ were dissolved in 100 mL of distilled water so that the molar ratio of Co:Fe in the solution is 1:2. The solution was constantly stirred at the room temperature. pH 9 of the synthesis solution was adjusted by using 9 MNaOH aqueous solution. The reaction was then continued for 15 min. After that, the solution was transferred to high frequency ultrasonic bath. The sample was exposed at 500 kHzand 50W for 1h at room temperature. The transient motion of cavitation bubbles due to vibrational energy of transducer results in the formation of high-intensity shock waves. The metal oxide particles get drifted in these waves at very high velocities and collide with each other. The energy released during collision can induce reaction between the metal oxide precursors leading to the formation of mixed metal oxide product. The brownish precipitates were separated by centrifugation and washed with excess of distilled water (DW) to remove the impurities followed by washing with acetone. Afterwards, the precipitates were dried at 50 ^{0}C for 24 h. The dry precipitates were grinded by agate motor to get the fine particles. Finally, they were annealed at 600 ^{0}C for 4 h.

Batch Adsorption

The batch adsorption were carried out by adding fixed amount 0.1 g of $CoFe_2O_4$ powders in 50 mL of As^{5+}aqueoussolution having a concentration of 5 ppm. The process was continued by operating at 200 rpm for 1, 5, 10, 15, 20, 25, 30, 45, 60 and 120 min in a shaker at the room temperature (27 ^{0}C). The solution was then filtered by using the Smith filter paper (125 mm) for the separation of the adsorbent particles from the aqueous solution and filtrate was measured by HVG-AAS. The values of initial concentration, C_i, were also varied from 0.1 to 400 ppm and measured equilibrium concentration (C_e) depending on C_i values.

Characterization Tools

UV/VIS/NIR JASCO-V570 spectrophotometer within the wavelength range of 190-1100 nm was utilized to measure the absorbance of the samples. The identification of functional group was investigated by FT-IR (IRPrestige-21 Shimadzu spectrophotometer). The crystal structure of the samples was measured by RIGAKU Smart Lab XRD. Surface morphology of ferrite was revealed by JEOL-JSM 5300 LV scanning microscope. Concentrations of total As in the filtrate were determined by AAS (Shimadzu model AA-6300) coupled with a hydride generation system (HVG-1, Shimadzu). The spectrophotometer was operated at 193.78 nm with a slit width of 1.0 nm. The lamp current was 12 mA. The fuel acetylene (air-acetylene flame) flow rate was 2.0 liters per minute and the burner height of 7 mm. The flow rate of the argon carrier gas was 70 ml per minute at a pressure of 0.35 Mpa.

Results and Discussion

The UV-Visible absorption spectrum of as-synthesized cobalt ferrite is shown in Fig.1. It displays a characteristic band at the wavelength297 nm, which developed particularly according to the dispersion and absorption phenomenon of $CoFe_2O_4$ particles [Mushtaq *et al.*, 2016].

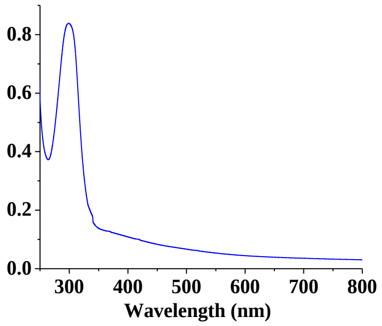

Figure1(a) UV-Vis absorption spectrum of as-synthesized cobalt ferrite.

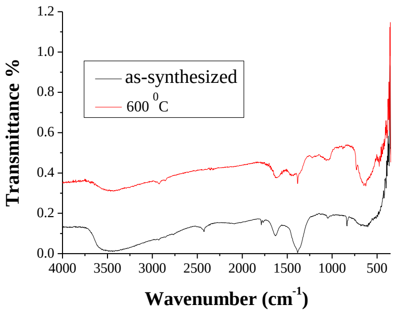

Figure 2 FT-IRspectra of as-synthesized and annealing at 600 °C of cobalt ferrite.

FT-IR spectroscopy is used to identify the functional groups of ferrites. From this in vestigation, it was found out that formation of spinel ferrite strongly depends on post annealing temperature. Only broad band around at 620 cm^{-1}was observed in as-synthesized ferrites. It implies that spinel structure was not obtained without treatment of post annealing. Thus, calcination is treated in order to enhance sufficient activation energy of the formation of ferrites. Complete spinel structures were formed at the band 624 and 476cm^{-1}at the annealing sample as shown in Fig. 2.

The characteristic peaks at 624 cm^{-1}and 476 cm^{-1} correspond to the metal-oxygen (M-O) bond stretching vibration at the tetrahedral sites and octahedral sites[Rumale *et al.*, 2013].The difference between these absorption bands is due to the change in bond length (M-O)at the tetrahedral and octahedral site [Rajasekhar *et al.*, 2017]. The other peaks at 3440 cm^{-1}corresponds to O-H bond stretching vibration revealing the presence of residual hydroxyl groups. The antisymmetric stretching, symmetric stretching, out of plane bending, peaks of the cobalt metals are observed at 1636, 1384, 880 cm^{-1}, respectively [Allaedini *et al.*, 2015].

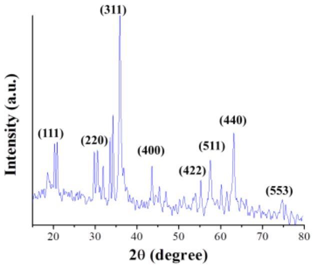

Figure 3 XRD spectrum of spinel cobalt ferrite

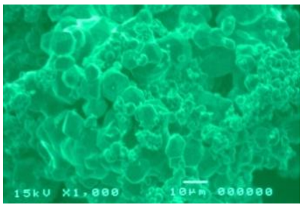

Figure 4 SEM micrograph of spinel cobalt ferrite

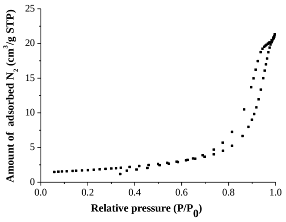

Figure 5 N_2 isotherms of Co-ferrite

XRD measurement was carried out in order to confirm the crystal structure of synthesized material. The diffraction peaks around 2θat 18, 30, 35, 37, 43, 54, 58, 63, and 74 degrees, marked by their corresponding indices (111), (220), (222),(311),(400), (422), (511), (440) and (533), in Fig. 3 are corresponding to the characteristic crystallographic planes of the spinel structure of cobalt ferrites [Allaedini *et al.*, 2015].

The SEM micrograph in Fig.4 shows that the porous structure providing the greater surface area which is an advantage for the adsorption. To evaluate the porosity, nitrogen adsorption was conducted at 25 °C. The surface area of cobalt ferrite measured by Brunauer–Emmett–Teller (BET) method is obtained6.0063 m^2/g. Figure 5shows amounts of adsorbed N_2 in the ferrite at different relative N_2 pressures.

To identify the possible rapidness of removal process As by Co-ferrite, time dependence adsorption test was performed. The removal percent was calculated by the formula equation

$$\text{removal}(\%) = \frac{C_i - C_e}{C_i} \times 100 \qquad (1)$$

The adsorption amount (q_e)of As ion generally is calculated by following formula:

$$q_e = \frac{(C_i - C_e)V}{m} \qquad (2)$$

Where, q_e = equilibrium adsorption amount (mg/g)

C_i = initial concentration (mg/L or ppm)

C_e= equilibrium concentration (mg/L or ppm)

V = volume of the aqueous solution (mL)

m = mass of adsorbent (mg)

The maximum removal percent and equilibrium adsorption amount (q_e) are found out to be 92 %and 1.7402 mg/g at the shaking 30 min until to 2 h as shown in plot 6 (a) and (b).

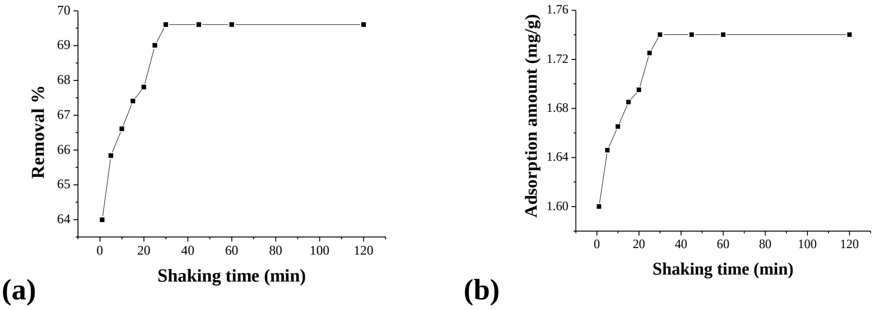

Figure 6 Time course curve of (a) removal % and (b) adsorption amounts of As ions on cobalt ferrite (C_i=5ppm)

Figure 7 (a) illustrates the graphical representation of isotherm which was subjected to sorption isotherm of *Langmuir.* Figure 7(b) represents the adsorption isotherm of As ion on Co-ferrite. The adsorption amount for each equilibrium concentrations can be observed in this plot. The adsorption amount (q_e) is gradually increased until the value of C_e is 44 ppm. Then, the q_e becomes constant beyond this concentration and it implies that adsorption amount of As has been saturated at C_e44 ppm.

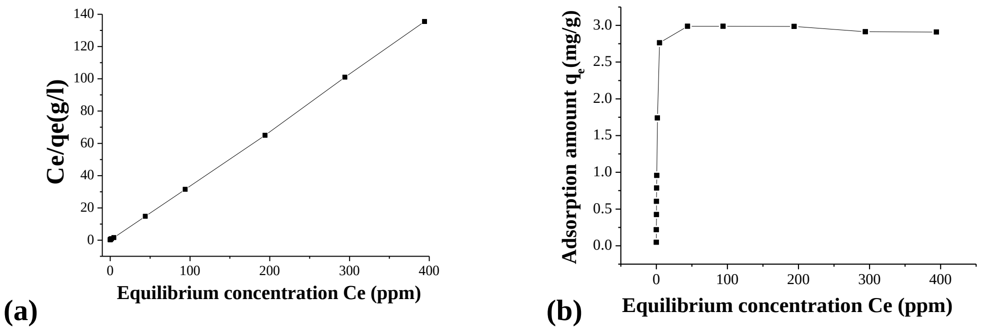

Figure 7 (a) *Langmuir* adsorption isotherm plots of As on cobalt ferrite and (b) adsorption isotherm of As^{5+}ion on Coferrite

The graph shown in Fig. 8illustrates the removal percent of As at different C_i. Ferrite can effectively remove As at the trace level of initial concentrations (0.1 ppm, 100 ppb). In contrast, removal % is gradually decreased with increasing of C_i. Therefore, by using the amount of adsorbent 0.1 g and shaking time 30 min, maximum removal percent is found out 92 %, which is an excellent for the elimination of trace level As concentration. Therefore, cobalt ferrites will be very effective to eliminate the As ions which is usually contained especially in drinking water as a trace level.

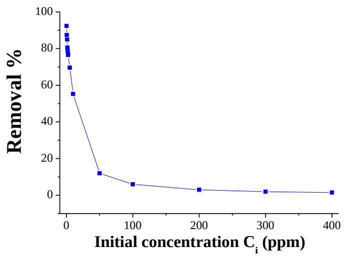

Figure 8 Graph showing the removal % as the function of C_i of As aqueous solution

Conclusions

In this study, $CoFe_2O_4$ spinel ferrites have been synthesized by high frequency (500 kHz, 50 W) ultrasound method. The annealing temperature 600 ^{0}C was systematically investigated to get the novel formation of spinel cobalt ferrite structure and found out that annealing temperature plays the essential parameter in the sonochemical synthesis of cobalt ferrite particles. UV-Vis result informs that the synthesized particle was $CoFe_2O_4$. FT-IR revealed that the cation formation at the tetrahedral and octahedral site in spinel ferrite crystal system. XRD study additionally confirmed that sonochemical synthesis is a good method to form single spinel crystal phase. According to the measurement and calculation results of concentration of arsenic (As) by AAS, the removal efficiency of As was found out to be 92 % from the 100 ppb concentration of As^{5+} aqueous solution. Thus, the cobalt ferrite synthesized at pH 9 and annealing at 600 ^{0}C could be effectively removed to trace level concentration of arsenic from drinking water.

Acknowledgements

We would like to acknowledge to Prof Dr Ni Ni Oo, Rector in charge, Myeik University, for her encouragement and allowing us the chance to participate in this event. We are especially thank you to Prof Dr Win Win Than, Pro-rector, Myeik University, for her permission to contribute of this work. We sincerely thank to Prof Dr Yin Yin Myint, Head of Department of Physics, Myeik University, for her encouragement of this work. Our special thanks go to Dr Ye Chan, Professor and Head of Universities' Research Centre (URC) for the supporting of research facilities and excellent discussion.

References

Allaedini G., S. M.Tasirin, and P. Aminayi.(2015)"Magnetic properties of cobalt ferrite synthesized by hydrothermal method," *Int Nano Lett* 5,183-186.

Budak T. B. (2013) "Removal of heavy metals from wastewater using synthetic ion exchange resin". *Asian Journal of Chemistry*,25 (8) 4207- 4210.

ByambaaM., E. Dolgor,K. Shiomoriand Y. Suzuki. (2018) "Removal and recovery of heavy metals from industrial wastewater by precipitation and foam separation using lime and casein", *Journal of Environmental Science and Technology,*11 (1)1-9.

de los Ríos A. P. , F. J. Hernández-Fernández, L. J. Lozano, S. Sánchez, J. I. Moreno and C. Godínez. (2010) "Removal of metal ions from aqueous solutions by extraction with ionic liquids" *J. Chem. Eng. Data,* 55 (2) 605-608.

Kang D., X. Yu, M. Ge and W. Song. (2015) "One-step fabrication and characterization of hierarchical MgFe2O4 microspheres and their application for lead removal" *Microporous Mesoporous Mater*., 207, 170-178.

Kirankumar V. S., V. Lakshmi Priya, A. Kavi Priya, and S. Sumathi. (2017) "Adsorptionof chromium (VI) on bismuth incorporated cobalt ferrite nanoparticles," *IOP Conf. Series: Materials Science and Engineering*263, 022022.

Leroux C., M. Bendahan, V. Madigou, L. Ajroudi, and N.Mliki. (2014) "Nanoparticles of cobalt ferrite for NH_3 sensing,"*Sensors & Transducers*, 27, Special Issue, 239-243.

Maximous N. N., G. F. Nakhla and W. K. Wan. (2010) "Removal of heavy metals from wastewater by adsorption and membrane processes: a comparative study" *International Journal of Environmental and Ecological Engineering*., 4 (4) 125-130.

Mohsen-Nia M.,P. Montazeri and H. Modarress. (2007) "Removal of Cu^{2+} and Ni^{2+} from wastewater with a chelating agent and reverse osmosis processes" 217, 1-3 (5) 276-281.

Mushtaq M. W., M. Imran, S. Bashir, F. Kanwal, and L. Mitu. (2016) "Synthesis, structural and biological studies of cobalt ferrite nanoparticles,"*Bulgarian Chemical Communications*., 48 (3) 565-570.

Ponce A.S., E. F. Chagas, R. J Prado, C. H. M. Fernandes, A. J Terezo, and E. Baggio-Saitovitch. (2013) "High coercivity induced by mechanical milling in cobalt ferrite powders," *Journal of Magnetism and Magnetic Materials.,* 344**,** 182-187.

Rajasekhar B. K., K. Rama Rao, and B. Rajesh Babu. (2017) "Cu^{2+} modified physical properties of Cobalt-Nickel ferrite," *J. Magn. Magn. Mater.,*434,118-125.

Ratnaike R. N. (2003)."Acute and chronic arsenic toxicity" *Postgraduate Medical Journal.* 79 (933) 391-396.

Rumale N., S. Arbuj, G. Umarji, M. Shinde, U. Mulik, A. Pokle, and D. Amalnerkar. (2013) "Single step solid-solid reaction scheme for the synthesis of cobalt sulphide-oxide nanoparticles in polymer matrix,"*Advances in Nanoparticles*. 2, 28-31.

Sanasi P. D., D. Santhipriya, Y. Ramesh, M. Ravikumar, B. Swathi, and K. Jayarao. (2014) "Nano copper and cobalt ferrites as heterogeneouscatalysts for the one-pot synthesis of 2,4,5-tri substituted imidazoles," *J. Chem. Sci.* 126 (6), 1715-1720.

WHO (2011) Guidelines for drinking water quality, fourth edition.

J. Myanmar Acad. Arts Sci. 2020 **Vol. XVIII.No.2A**

SnO_2 NANOFIBERS PHOTOANODE FOR ENHANCING THE PHOTOVOLTAIC PROPERTIES OF NATURAL DYE SENSITIZED SOLAR CELLS

Zayar Pyae Phyo Aung[1], Su Su Lwin[2], Yin Maung Maung[3], Than Than Win[4]

Abstract

Tin oxide (SnO_2) nanofibers were successfully prepared by electrospinning homoheneous viscous solution of tin acetate in polyvinyl alcohol (PVA). The electrospun nanofibers are calcined at 600 ° C for 2 h. Structural, diameter in size and morphology of heat-treated SnO_2 nanofibers were investigated in detail by X-ray diffraction (XRD), field emission scanning electron microscopy (FESEM) and Atomic Force Microscope (AFM). The optical properties of SnO_2 nanofiber film was also studied by UV-Vis spectroscopy. The nanofiber was sensitized with natural dye and assembled into a DSSC. High performance carbon electrode was prepared onto ITO substrate and used as counter electrode. I-V characteristic was measured and conversion efficiency (η_{con}) and fill factor (FF) were determined.SnO_2 thin film will be deposited onto ITO (Indium doped tin oxide) coated glass substrate by spin coating technique. After that, the solar cell performance of DSSC with nanofibers will be measured and compared to those of DSSC with SnO_2 thin film. According to the I-V measurement, the efficiency of SnO_2 nanofibers based DSSC was greater than that of SnO_2 thin film based DSSC. The SnO_2 nanofiers based DSSC of TCD 12 cm gave the best efficiency and it was 2.71 %. The experimental findings resulted from this research work can be of great help for low-cost and Eco-friendly DSSC application.

Keywords: Tin acetate, polyvinyl alcohol, Nanofibers, TCD, Electrospinning

Introduction

Over billions of years, Mother Nature has been converting light from the sun into energy via photosynthesis. Sunlight is the most abundant and sustainable energy source that is free.[Hong Juan Sun et al (2011), Jie GAO Et Al (2013)]. The Earth receives energy from the sun at the rate of ~12 × 1017 J s−1. This has exceeded the yearly worldwide energy consumption rate of ~1.5 × 1013 J s−1. Therefore, it is a challenge to devise an approach for the effective capture and storage of solar energy for our consumption since fossil fuels such as oil and gas will be depleted in the years to come. In order to imitate the photosynthesis process, Gratzel and coworkers have developed dye-sensitized solar cells (DSSCs) based on the similar working mechanism [HATEM S. EL-GHAMRI et al (2014),T.F. Stoica, T.A. Stoica (2000)]. There are three generation in solar cell and the first and second generations for solar cells are mainly constructed from semiconductors. Among of them, dye sensitized solar cells (DSSCs) have been widely explored as potential alternatives to conventional silicon photovoltaic (PV) devices due to their low cost, abundance of raw material, facile fabrication process and overall good photovoltaic performance [Jiawei Gong, HuiQiao (2015)]. Compared to typical semiconductors used in p-n junction solar cells, the materials employed in a DSSC photoanode may have lower purities, there by leading to lower production costs [Sofyan A. Taya et al (2013)].

---

[1] Dr, Demonstrator, Department of Physics, Myeik University, Myanmar

[2] Demonstrator, Department of Physics, Myeik University, Myanmar

[3] Professor, Department of Physics, University of Yangon, Myanmar

[4] Professor, Department of Physics, Panglong University, Myanmar

The modern version of a dye solar cell, also known as the Grätzel cell, was originally co-invented in 1988 by Brian O'Regan and Michael Grätzel at UC Berkeley and this work was later developed by the aforementioned scientists at the École Polytechnique Fédérale de Lausanne until the publication of the first high efficiency DSSC in 1991. Michael Grätzel has been awarded the 2010 Millennium Technology Prize for this invention [Rajesh Vasita, Dhirendra S Katti (2006), S.S. Dissanayake et al (2016)].

Tin oxide (SnO_2) is one of the most intriguing materials to be investigated today, This is because tin dioxide isa well-known n-type semiconductor with a wide band gap of 3.6-3.8 eV, and for its potential application in transparent conductive electrode for solar cells a gas sensing material for gas sensors devices, transparent conducting electrodes, photochemical and photoconductive devices in liquid crystal display , gas discharge display, lithium-ionbatteries, etc[Ganesh E Patil (2012)]. Many processes have been developed to the synthesis of SnO2 nanostructures, e.g., spray pyrolysis, hydrothermal methods, chemical vapor deposition, thermal evaporation of oxide powders and sol–gel method [Yanika DiahImawanti (2017),M. T. Raposo (2012)]. Its outstanding electrical and optical properties enable applications in solar cells[Sofyan A. Taya et al (2013) , [S.S. Dissanayake et al (2016)].

The DSSCs based on SnO_2 photoanode materials exhibit relatively low open circuit voltages because of their high recombination kinetics with electrolytes. In addition, they reduce the conversion efficiency [Suriati Suhaimi1 et al (2015)]. SnO_2 with various morphologies of nanograin, nanowires, and nanoparticles have been investigated to increase the photoconversion efficiency of SnO_2 based DSSCs. The high recombination rate and poor electron transfer efficiency in SnO_2-based DSSCs are still major challenges for increasing the energy conversion efficiency [Zhengtao Zhu et al (2010)].

Experimental Procedure

Sample Preparation of SnO_2Nanopowder

In this research, Stannous chloride dehydrate ($SnCl_2.2H_2O$) was used as starting materials. Distilled water was used as a solvent. SnO_2nanopowders have been prepared by using precipitation method. SnO_2nanopowders were prepared by means of dissolving of 2 g (0.1 M) stannous chloride dehydrate ($SnCl_2.2H_2O$) in 100 ml distilled water. 10% ammonium hydroxide was slowly added to the solution for complete precipitation of tin hydroxide in the pH range 7.5 - 9.Then the solution was put into thermostat water bath, in which the temperature was kept about 80 ˚C, for 15 minutes until white depositions came out. Then the precipitate was centrifuged and washed several time (pH =7) with distilled water to reduce the amount of ammonium chloride. The resulting gels was filtered and dried at 100 ˚C for 3 h. The obtained powder was collected and grounded in an agate mortar and it is referred "as – prepared". The color of the as-prepared sample is gray. Finally the as-prepared sample was heated in a muffle furnace at 650 ˚C for 6 h in an atmosphere, then the color turned into white. Field emission scanning electron microscopy (FESEM) was employed for morphological study using ZIESS (MERLIN).

Cleaning of the Substrate

In the present study ITO/glass, cut into 1×1 cm square plates have been used as substrates. Prior to deposition the substrates are subjected to the following cleaning process to remove the unwanted impurities normally present on the surfaces of the glass plates exposed to the atmosphere.

1. The glass substrates are washed in soap solution by scrubbing the surfaces with a cotton swab dipped in liquid soap.
2. The glass slides are then rinsed thoroughly in deionized water to remove any trace of the soap solution left on the surface followed by acetone rinsing.
3. Then the slides are soaked in HCl acid and kept in room temperature for about two hours.
4. Finally, the substrates are rinsed thoroughly in deionized water and dried at 100°C for one hour in an oven.

Preparation of SnO_2 Paste and Spin Coating of Tin Oxide Films for Photo Electrodes

The paste has been prepared by 2 g of SnO_2 powder was dissolved into the 100 ml of ethanol. The mixture was stirred by magnetic stirrer for 2 h. The solution was then ultrasonicated for 4 h to reduce particle size. After sonication, the paste was ready to use as spinning paste. After that the film were deposited on ITO/glass substrate. After spin coating at room temperature, and at a speed of 3000 rpm for 30 s, the coated films were dried 15 minutes at 150 ˚C. The formation of ITO films by removing the organic component followed by structural rearrangement was performed by annealing the coated films for one hour at the temperature of 400 ˚C. The structural properties of the films were measured by field emission scanning electron microscope (FESEM).

Low Cost Home-made Electrospinning Set-up for SnO_2 Nanofiber

Electrospinning is a very simple technique that can be used to produce nanofibers under the influence of a high electric field. This home-made electrospinnng set-up consists three components. They are home-made high voltage power supply, syringe (emitter) and collector plate. The positive terminal of the DC source was connected with a needle and the Al-substrate (collector) was connected with the negative terminal to ground it. When the voltage was applied a stream of solution came out through the needle which was subdivided into a number of nano to submicron sized jets and were deposited in the form of nanofibers on the collector pate.

4.4 Design and Construction of Home-made High Voltage Power Supply

The power supply is constructed to obtain large output voltages (dc), at low currents. The output can be adjusted using the potentiometer on the outside of the box. Here are the important specifications.

Output voltage range: 1000 – 20000 V DC

Maximum output current: 20 mA

Input voltage: 210 - 250 V AC

Input current: 0.5-1 Amperes.

Average power of device: 40 – 60 Watts

The power supply is plugged in to the ac-mains to power on. Make sure that before powering up, the potentiometer is tuned to its lowest value, this must be secured in order to minimize the risk of injury, as high voltages can be very dangerous. To use the power supply to get high voltages, connect probes to the positive and negative crocodile clips provided. The potential difference will exist between these two crocodile clips. They can be connected in necessary places in various apparatuses used in high voltage experiments. There is no display to show the output voltages in the power supply itself. This is because common voltmeters available in labs cannot measure voltages more than 1000-1500 volts. So, to measure the output voltages, the user will have to use a variable resistor (EMCOV1G). This device is basically a high voltage step-down resistor, which allows the user to see output voltages across its terminals that are stepped down by a factor of 1000, e.g., if a multlimeter joined to the output of the EMCO device shows 20 V, it means that there is actually a voltage of 20000 V at the output of the high voltage power supply. So, simply connect the resistor to one of the high voltage outputs, and then observe the voltage on a multlimeter. To do so, connect the high voltage input wire of the ECOM device to the high voltage output, and connect the mutlimeter between the ground of the power supply and the positive output of the ECOM device. This home-made HV power supply was composed of five sections and the block diagram are shown in figure 1. The experimental detail for each section are as follow:

Step-down Transformer: This is basically a transformer that connects to the ac –main, steps the voltage down, and gives an output voltage about 40 V. The core is made up of f-type plates. The primary contains about 1000 turns of insulated copper wire. The secondary contains about 200 turns of copper wire. The secondary wire is thicker because more current will flow through the secondary than at the primary, as this is a step-down transformer.

Voltage regulator circuit: This is a simple circuit that as the main source of power for the flyback transformer and its driver. The circuit contains 3 outputs, one 5 V, one 12 V, and a regulated output, between 1-30 V dc. The output voltage of the regulated output can be changed from the variable resistor, and this is the main voltage that is given to the input of the flyback transformer, and hence it controls the output voltage.

Flyback-transformer driver circuit: This is a circuit that basically drives the flyback transformer. The main function of this circuit is to simulate a pulsed (square-wave), high frequency input for the flyback transformer, which then allows it to work. The square wave generated typically has a frequency between 25-100 kHz, in this case it was about 26 kHz, but the exact value can vary from one flyback transformer to another. The circuit consists a 55-timer, which is put in the astable mode, this generates a square wave. The output of the 555-timer is fed into the input of a hex-inverter buffer. The output of this buffer acts as an open-collector, a sink for the 12 V dc from the regulated circuit. Periodic transitions of the output of the buffer from open, to a short sink, allow it to switch the transistor on and off. The transistor being switched on and off is an n-channel mosfet, in our case it is an IRF-540. We chose this particular transistor because of its low drain-source resistance, so it heats up less. The transistor is connected in a heavy-side driver configuration, in which the primary of the flyback transformer is placed between the drain and the regulated input from the voltage regulator circuit.

Flyback-transformer: A flyback transformer is a very interesting transformer. Normal transformers, simply transformer energy from their inputs to their outputs. Flyback transformers, however, not only transfer energy to their secondary, but also they store energy for a considerable amount of time. In fact, flyback transformers act as pure inductors during half a cycle, and then they act as a pure transformer in the other half. This behavior is made possible by an air gap in the ferrite core. This air gap increases the reluctance of the core, which thereby increases its ability to store magnetic energy. Flyback transformers are high frequency transformers, and their low output power and small size make them very useful in generating high output voltages, at relatively low currents. Their main applications are in televisions, monitors, and high voltage power supplies, like this one. The circuit diagram and the photo of homemade high voltage power supply were shown in figure 2 and 3.

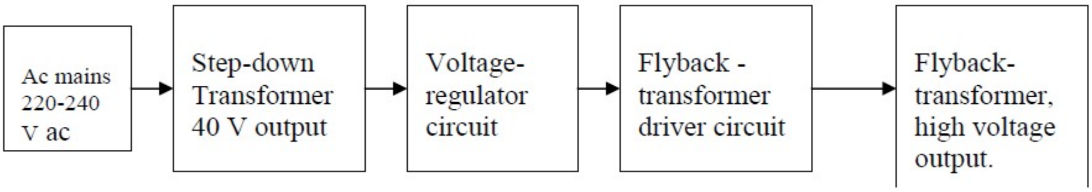

Figure 1 The block diagram for home-made high voltage power supply

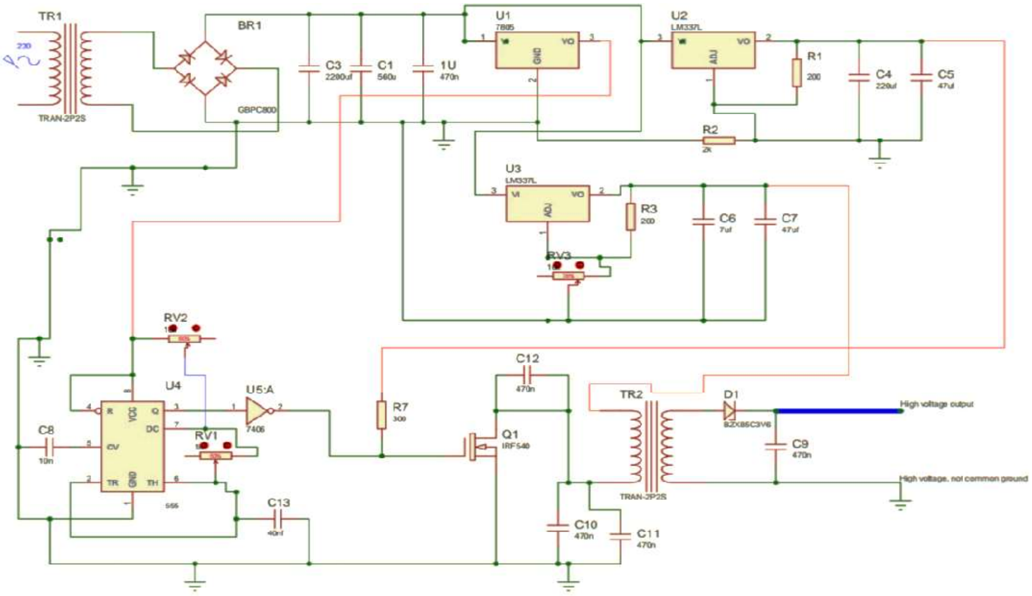

Figure 2 The circuit diagram of HV power supply

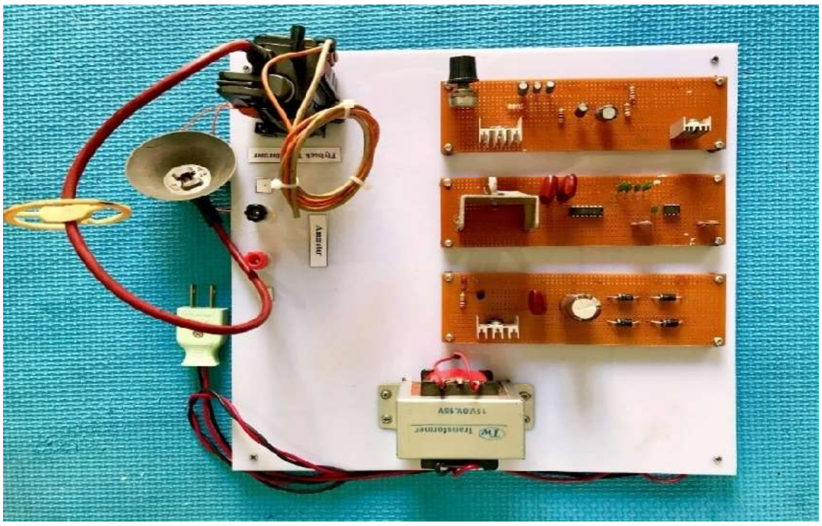

Figure 3 Home-made high voltage power supply

Sample Preparation of SnO_2 Nanofiber

In this study, the flow chart of experimental procedure is shown in figure 4.4. Tin dioxide (SnO_2), Poly Vinyl Alcohol (PVA) and distilled water were chosen as the starting chemicals and solvent. SnO_2 nanofibers were prepared by sol-gel process. 1 g of SnO_2 was dissolved in 2 ml of acetic acid with constant stirring for 10 min to obtain a clear solution of tin acetate in the pH range 1-2. This solution was mixed with 4 ml of 10 % PVA solution. The solution was stirred for 4 h by a magnetic stirrer and a viscous sol-gel was obtained. Nearly 5 ml of the viscous solution was taken in a 20 ml syringe. The distance of 12 cm was maintained between the collector plate and the tip of the needle. Al-substrate was then struck on the collector. When the voltage was applied a stream of solution came out through the needle which was subdivided into a number of nano to submicron sized jets and were deposited in the form of nanofibers on the collector pate. The green nanofibers were calcined at 600 ˚C for 2 h. A sketch and photo electronspinning set up is shown in figure 4 and figure 5. The electrospinning conditions are mentioned in table 1. The obtained sample was characterized by X-ray powder diffraction (XRD) using (Rigaku RINT 2000). The morphology of the fibers was measured by field emission scanning electron microscope (FESEM) and atomic force microscope (AFM).

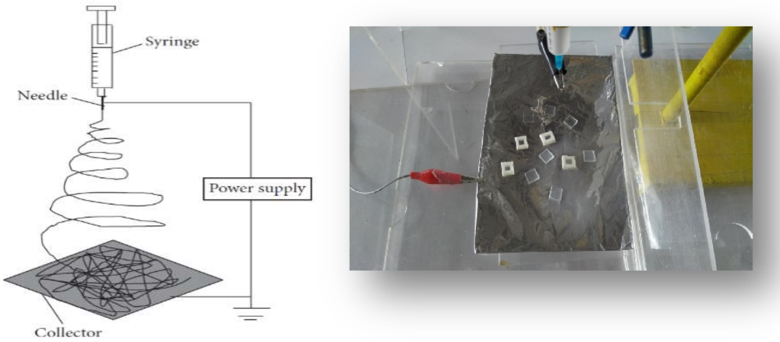

Figure 4 Schematic drawing (a) and photo(b) of the electrospinning process set up

Table 1 The elctrospinning conditions of SnO_2 nanofibers

Syringe capacity	20 ml
Tip to collector distance (TCD)	12 cm
Voltage	20 kV
Annealing temperature	600 ˚C
Annealing time	2 h

Preparation of Natural Dye-Sensitizer

The grass from 16˚ 52’ 59.69” N 97˚ 37’ 51.02” E was used as a dye in this work. Firstly, the grass was washed with deionized water and dried in dark place at room temperature for about 3 months. After drying, the grass was crushed into small pieces using mortar. Then, dried small grass parts were put into thistle of soxhlet extractor and ethanol was used as solvent. Temperature of the instrument was maintained well under boiling point of the ethanol. Several cycles of solvent were run so as to extract all the compounds from plant parts. Next, the ethanol from dye solution was removed by distillation. Finally, the pure natural dye solution (pH=6.67) was obtained and it was ready to be used as a natural dyes sensitizers in DSSCs.

DSSC Assembling

The cathode electrode and the anode electrode were put together, overlapping each other, and a space at the end of each electrode was made. Next, both electrodes were fasten using the double clip. Three drops of iodide solution were added at the end of the electrode and the solutions were spread over the entire electrode. Then, the remaining iodide solution were wiped off using cotton swab soaked with alcohol. After that, a tester with crocodile clip were attached at both ends of the electrode.

Results and Discussion

X-ray Diffraction Methods on Structural Characterization of SnO_2nanofibers

According to the XRD analysis, pure tin oxide nanofibers were matched with standard library of PDF 77-0447 cassiterite tin oxide. The X-ray diffraction (XRD) pattern of SnO_2nanofibers from $SnCl_2.2H_2O$ is shown on figure 5. The peaks at 2θ values of 26.588°, 33.848°, 37.878° and 51.720° can be associated with (110), (101), (200) and (211) respectively. All of the peaks can be indexed to be pure tin oxide structure of tetragonal due to the lattice parameters agreement with the literature. The average crystallite size is 27.49 nm.

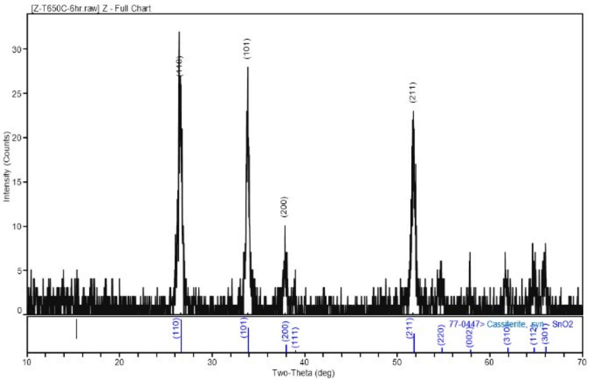

Figure 5 XRDdiffractorgram of tin oxide nanofibers

Table 2 Average crystallite size of pure SnO_2nanofibers from $SnCl_2.2H_2O$ for all identified peaks at 650 °C

No.	Peak	FWHM (deg)	2-Theta(deg)	Crystallite size (nm)
1	(1 1 0)	0.48	26.58	16.90
2	(1 0 1)	0.27	33.84	33.62
3	(2 0 0)	0.27	37.87	34.00
4	(2 1 1)	0.34	51.72	25.44
		Average crystallite size		27.49

Table 3 Lattice parameters (a & c) and lattice distortion c/a for SnO_2nanofibers

	Lattic parameter		c/a
	a(A°)	c(A°)	
$SnCl_2.2H_2O$	4.739	3.193	0.673
Standard	4.737	3.185	0.672

Surface Morphology

The SnO_2 powder was obtained from directed precipitation method. Figure 6 (a) shows the FESEM analysis of the SnO_2 powder. The grain sizes were calculated by using well known bar code system. Bar code size was 1 µm. According to the calculation the grain size is 80 nm – 120 nm. The powders morphology was spherical in shape. The FESEM images of SnO_2 films for 400 ˚C was shown in Figure 6 (b). According to the FESEM images the sizes of the grain are non-uniform. The various sizes of particles spread out on the surface of the film. The average grain sizes of SnO_2 films for all temperature are 75 nm – 300 nm respectively. The SnO_2 fibers on ITO were carried out to examine by FESEM image. According to the FESEM analysis SnO_2 nanofibers reveal the retention of cylindrical shape but with surface roughness. The average diameter of the SnO_2 nanofibers are 80 – 85 nm. The fibers diameter were also confirmed by AFM analysis. Fiber diameter is estimated from fiber height to avoid tip-convolution effects. According to the line profile, the average fibers diameter are 84 nm – 95 nm.

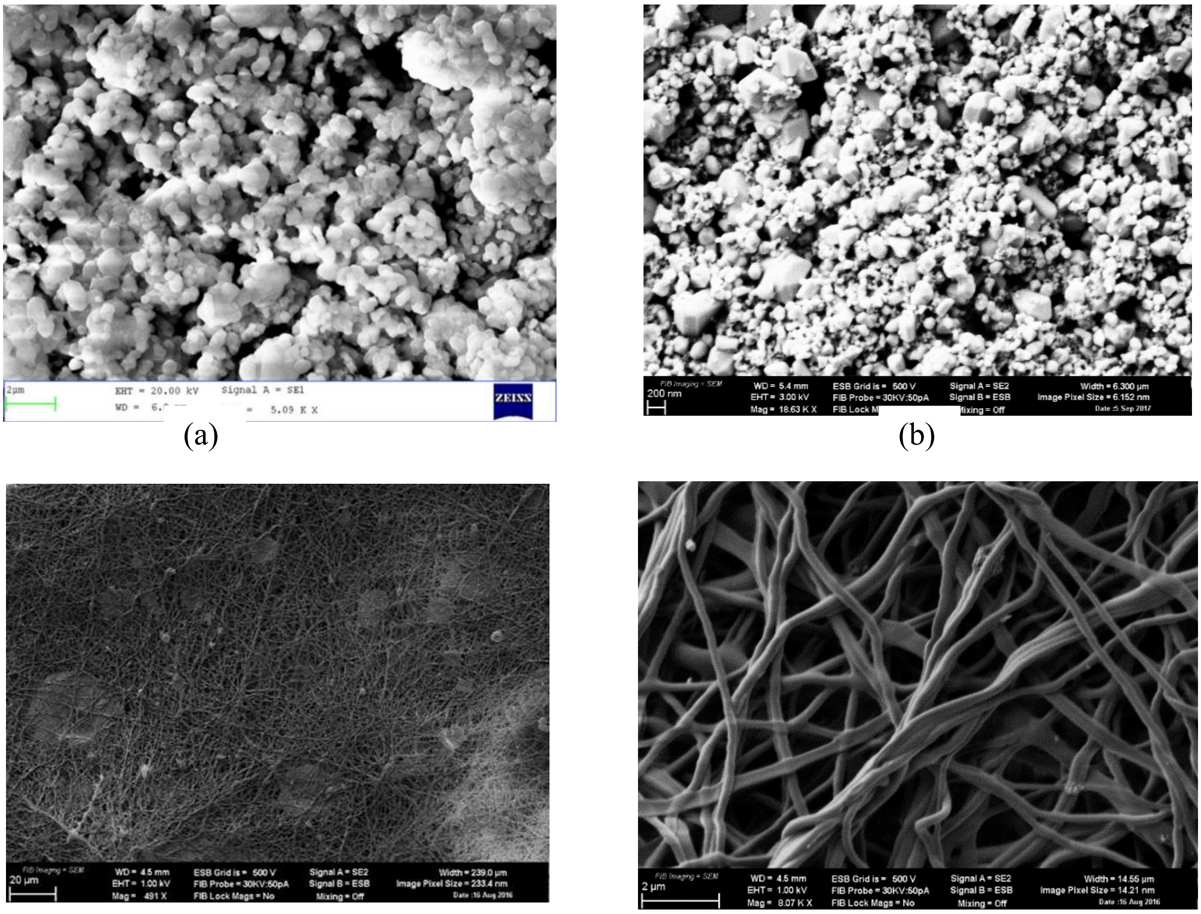

(a) (b)

(c) (d)

Figure 6 The FESEM images of SnO_2 (a) nanoparticle (b) film (c) nanofibers 20µm (d) nanofibers 2 µm.

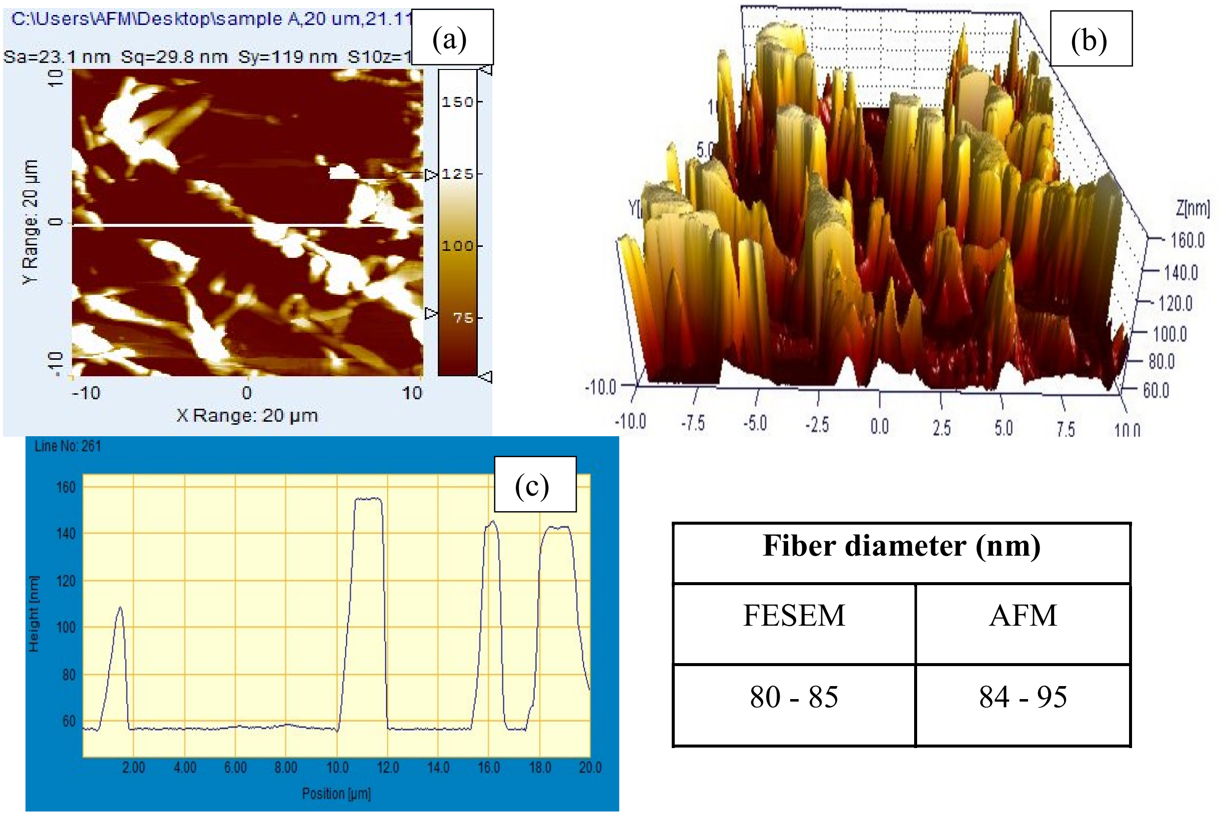

Fiber diameter (nm)	
FESEM	AFM
80 - 85	84 - 95

Figure 7 The amplitude (a), the 3D image (b) and line profile (d) of SnO_2 nanofibers

Optical Characterization of SnO_2 nanofibers and natural dye sensitizer

The UV-Vis spectra of SnO_2nanofibers were recorded with respect to the ITO glass substrate placed in the reference beam using beam spectrometer in the range 190 to 1100 nm. The absorption spectrum of SnO_2 deposited on ITO glass substrate is shown in figure 8 (a). The figure shows high absorption coefficient in the UV region. The resultant values of E_g for SnO_2 is found to be about 3.82 eV. The absorption spectrum of grass dye was obtained from UV-Vis spectroscopy. The wavelength range of spectrum between 400 nm and 800 nm. In this absorption spectrum, it was observed that the wide range absorption peaks and all of absorption peaks were within visible region. The strongest absorption peak was found at the wavelength of 671.50 nm and it was contributed that chlorophyll a. In accordance with the Beer-Lambert law that the absorbance value (A) inversely proportional to the value of transmittance (T) and is proportional to the concentration of the solution (C). The maximum absorbance is obtained in this research for 4.00. It shows the greater the concentration of the extract of grass in the solution, the greater the absorbance values and the smaller the transmittance values. Because the chlorophyll content affects the absorbance value of sample's concentration. The absorbance spectrum of extract grass was described in figure 8 (b). Peak absorbance at a wavelength λ= 469 nm with absorbance at 4.00 and λ= 671 nm and with absorbance of 2.82. So the extract dye from the grass has a greater efficiency when applied to dye-sensitized solar cells (DSSC)

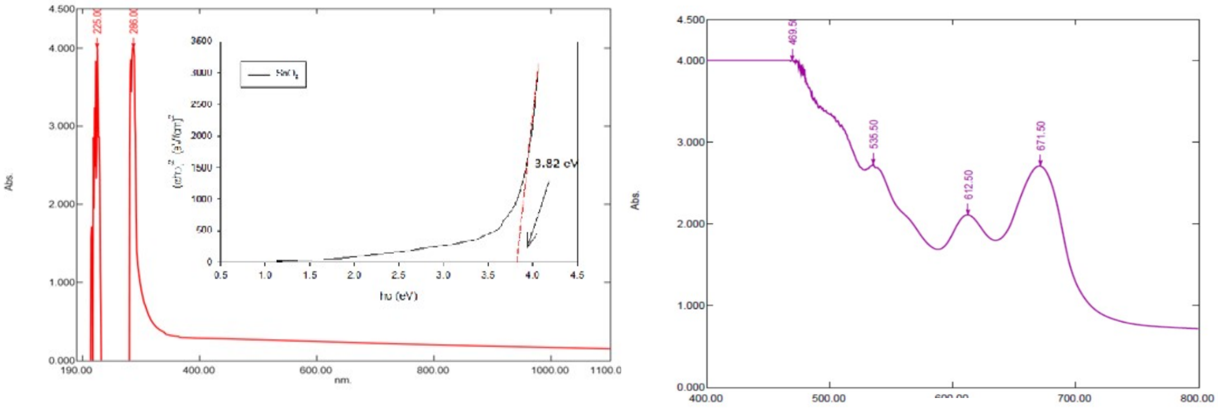

(a) (b)

Figure 8 The absorbance spectrum of SnO_2 nanofibers (a) and dye solution (b).

Photovoltaic Properties

Figure 9 (a) showed the I-V curves of SnO_2naofibersphotoelectrodeDSSC and figure 9 (b) showed I-V curve of SnO_2 film based DSSC under illumination. The summarized photvoltaic parameters were listed in Table 4. From the Figure, it was found that the Photovoltaic behaviors of DSSC were quite acceptable, appropriate and suitable for cost effective DSSC with natural dye extract.

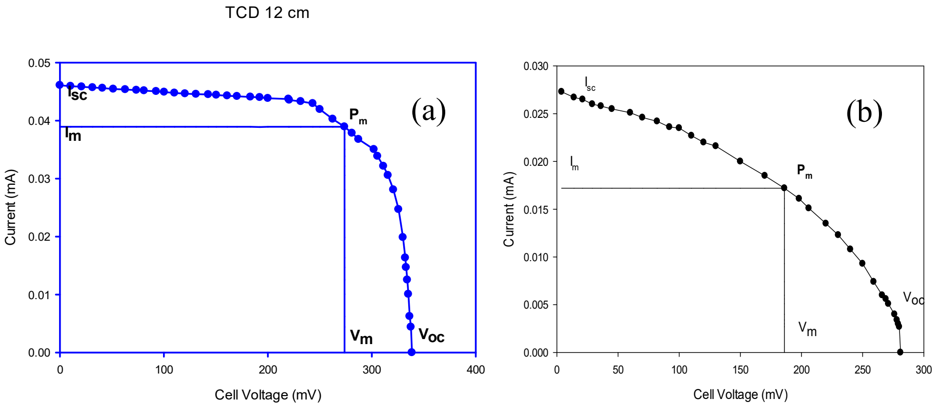

Figure 9 I-V curves of SnO_2 nanofiber photoelectrode (a) and film based photoelectrode (b) DSSC solar cell

Table 4 Photovoltaic parameters of SnO_2 nanofiber and film photoelectrodes with dye sensitizer extract

Sample	Isc(mA)	Jsc(mA/cm2)	Voc(V)	Efficiency (%)	FF	P_m ($mWcm^{-2}$)
Film	2.79E-02	1.40E-02	0.2240	1.147	0.36	3.199E-3
Nanofiber	4.61E-02	4.60E-02	0.2857	2.715	0.68	1.065E-1

Conclusion

Dye-sensitized solar cells based on SnO_2nanofiber and nanopowders were successfully prepared and investigated on their structural, microstructural and light absorption properties. Both SnO_2nanofibers and SnO_2nanopowders were deposited onto indium doped tin oxide (ITO) glass substrates by electrospinning and spin coating method. The experimental data resulted from this research gave that both SnO_2nanofibers and nonopowders were successfully favoured on ITO/glass even though the fabrication technique used in this study was not confused and complicated. . From I-V graphs, the efficiency of nanofibers based DSSC was better than thin films based DSSC. The efficiency of nanofiber based DSSC (TCD 12 cm) 2.715 %. It is expected that both SnO_2 nanofibers based DSSC and SnO_2 thin film based DSSC with grass natural dye are cost effective and Eco friendly DSSC. Moreover, the changing of nanoparticle (0 D) to nanofiber (1 D) is one of the most promising way to enhance the performance of dye sensitized solar cells.

Acknowledgements

I wish to express my profound thanks to Dr Ni NiOo, Rector of Myeik University for her kind permission to carry out this work. The authors also would like to express gratitude to Dr Win Win Than, Pro-Rector of Myeik University. The author also acknowledge the support of Professor Dr Khin Khin Win, Head of Department of Physics and University of Yangon. Moreover, I am greatly indebted to Professor Dr Yin Yin Myint, Head of Department of Physics, Myeik University, for her help with experimental work and discussion.

References

Aris Doyan, Susilawati, and Yanika Diah Imawanti (2017) "Synthesis and characterization of SnO_2 thin layer with a doping aluminum is deposited on quartz substrates" AIP Conference Proceedings Volume 1801, Issue 1 10.1063/1.4973083

D. H. Q. Carvalho, M. A. Schiavon and M. T. Raposo (2012) "Synthesis and characterization of SnO thin films prepared by dip-coating method" Physics Procedia 28 (2012) 22 – 27.

E. Manea et al (2017) "Optical Characterization of SnO2 thin Films, Prepared by Sol Gel Method, for "Honeycomb" Textured Silicon Solar Cells" International semiconductor conference.

Ganesh E Patil, Dnyaneshwar D Kajale, Vishwas B Gaikwad (2012) "Preparation and characterization of SnO_2 nanoparticles by hydrothermal route" International Nano Letters 2012, 2:17.

Hongjuan Sun et al (2011) "Preparation and structural vibration of graphite oxide and graphene oxide"An International Journal, 128:1, 163-170, DOI: 10.1080/10584587.2011.576628

HATEM S. EL-GHAMRI et al (2014) "Dye-sensitized solar cells with natural dyes extracted from plant seeds" Materials Science-Poland, 32(4), 2014, pp. 547-554

J onathan, O. Ajayi David, B. Agunbiaden (2015) "Optical Characterization and Surface Morphology of Sno2 Thin Films Prepared By Spin Coating Technique" IJRASET, Volume 3 Issue VI.

JieGao et al (2013) "Preparation and Characterization of a Graphene Oxide Film Modified by the Covalent Attachment of Polysiloxane" Polymer-Plastics Technology and Engineering, 52: 553–557, 2013.

Jiawei Gong, HuiQiao (2015) "Characteristics of SnO2 nanofiber/TiO2 nanoparticle composite for dye-sensitized solar cells" AIP Advances 5, 067134 (2015); doi: 10.1063/1.4922626

M. Chandraiah, BenudharSahoo and Prasanta Kumar Panda (2014) "Preparation and Characterization of SnO_2 Nanofibers by Electrospinning", Trans. Ind. Ceram. Soc., Vol. 73, 266-269.

Rajesh Vasita, Dhirendra S Katti (2006) "Nanofibers and their applications in tissue Enginerring", International journal of Nanomedicine, Vol. 1, 15-30.

S.S. Dissanayake et al (2016) "Performance of dye sensitized solar cells fabricated with electrospun polymer nanofiber based electrolyte" Materials Today: Proceedings 3S (2016) S104 – S111.

Sofyan A. Taya et al (2013) "Dye-sensitized solar cells using fresh and dried natural dyes" 10.11648/j.ijmsa.20130202.11.

Suriati Suhaimi1 et al (2015) "Materials for Enhanced Dye-sensitized Solar Cell Performance: Electrochemical Application" Int. J. Electrochem. Sci., 10 (2015) 2859 – 2871.

T.F. Stoica, T.A. Stoica (2000) "CHARACTERIZATION OF ITO THIN FILMS PREPARED BY SPINNING DEPOSITION STARTING FROM A SOL-GEL PROCESS" journal of Optoelectronics and Advanced Materials Vol. 2, No. 5, 2000, p. 684-688.

Tarko Fentaw Emiru et al (2016) "Controlled synthesis, characterization and reduction of graphene oxide: A convenient method for large scale production" Egyptian journal of Basic and applied Sciences" Volume 4, Issue 1, March 2017, Pages 74-79.

Zhengtao Zhu et al (2010) "Composite of TiO2 nanofibers and nanoparticles for dye-sensitized solar cells with significantly improved" Research Gate, DOI: 10.1039/c0ee00068j.

J. Myanmar Acad. Arts Sci. 2020 **Vol. XVIII.No.2A**

SYNTHESIS AND ELECTRICAL PROPERTIES OF NANOCRYSTALLINE TITANIUM CARBIDE THIN FILMS

Kyaw Kyaw[1], Hnin Yu Khaing[2], Nyein Wint Lwin[3], Kalayar Thwe[4], Lei Lei Win[5]

Abstract

The main objective of this research work was to synthesize and to characterize structural and electrical properties of nanocrystalline titanium carbide thin films. The spin coating method was used to synthesis titanium carbide thin films, which were obtained from the HCl etching of MAX phase Ti_3AlC_2, The structural and morphological properties of the obtained films were characterized with XRD and SEM. EDXRF confirmed that aluminium (Al) was removed by etching, and the disappearance of Ti_3AlC_2 peaks were revealed from XRD profiles. From the SEM images it was revealed that the fabricated nanocrystalline films composed of several flakes and their sizes up to a few hundred nanometers. The typical microstructure of nanocrystalline titanium carbide thin films consisted of plate like grain and the grain size could be controlled by varying sintering temperature and time. Resistivity measurements were also performed with a four point probe method. The obtained results showed that nanocrystalline titanium carbide thin films could be used for transparent conductive electrodes.

Keywords: MAX Phase, Ti_3AlC_2, HCl, XRD, SEM, Resistivity

Introduction

Two-dimensional (2D) materials, such as graphene, are well known to have unique properties and important applications. In general, 2D materials are produced by exfoliating layered 3D materials with weak Van Der Waals-like coupling between layers. During the last decade, some 2D materials such as hexagonal boron nitride, metal oxides, and chalcogenides have been synthesized by chemical exfoliation or mechanical cleavage of layered 3D precursors. However, there was no report on the synthesis of 2D nanocrystalline materials by exfoliation of layered solids with strong primary bonds until [Naguib et al.] the synthesis of two-dimensional transition metal carbides by HF exfoliating from MAX phases: Ti_3AlC_2, Ti_2AlC, etc.

MAX phases materials are a confirmed class of ternary transition metal carbides or nitrides with a $M_{n+1}AX_n$, chemical formula: M is transition metal, A represents mostly elements from the III A or IV A groups such as Al, Ga, Si, or Ge, X is C and/or N and n = 1, 2, or 3. The etching process removes the A-atoms layer connecting single MX stacks and produces an exfoliated structure where multiple lamellas are piled close to each other but partially separated in an accordion-like structure. The most fascinating feature shown by MXenes is likely their ability to replace A atoms with surface terminating functional groups (typically -OH, -O and -F) which adsorbs on the layers and interact forming weak bonds. Therefore, MXenes have a formula of $M_{n+1}X_nT_x$, where T stands for a generic surface termination group. Thanks to this peculiarity, mechanical action can laminate the exfoliated structure and generate single- or few-layered flakes which can be easily dispersed both in aqueous and non-aqueous suspensions. MXenes possess a unique combination of high electrical conductivities and hydrophilicity. They are thus being

---

[1] Dr, Lecturer, Department of Physics, University of Mandalay

[2] Assistant Lecturer, Department of Physics, Hpa An University

[3] Professor, Department of Physics, University of Mandalay

[4] Professor, Department of Physics, University of Mandalay

[5] Professor(Head), Department of Physics, University of Mandalay

explored for a host of applications, such as electrodes for energy storage, transparent conductive coatings, water purification, and electromagnetic interference shielding, among others.

Experimental Procedure

The MAX phase synthesized in this research work was Ti_3AlC_2. The Ti_3AlC_2 powder was synthesized by mixing of titanium powder (99.5%, China), Al powder and graphite in a 3:1:2 weight ratio and dry ball milling at 500 rpm for 12 hours. The mixed powder was cold pressed to obtain compacted pellet to avoid the presence of air embedded in the mixed powder. The obtained pellets were sintered in homemade tube furnace under the flow of nitrogen at 1000°C for 2 h, at a heating rate of 10 °C/min. The MAX phases powder produced were cooled to room temperature, and the resulting powder compacts were ball milled again to obtain powder. The MAX phase Ti_3AlC_2 powders were sieved through meshes to obtain uniform particles of size less than 10 µm. The 1 g of sieved precursor powders were immersed in 20 ml of HCl acid in a plastic container and stirred at 500 rpm for different etching time. After etching with HCl, the residues were filtered and washed several times using de-ionized (DI) water and centrifuged at 3500 RPM for a few minutes and the liquid was decanted and fresh DI water was added to disperse the sediment. This step was repeated until the decanting liquid had a pH of approximately 5. The obtained Ti_3C_2 powders were dry in vacuum oven at 200 °C for 1 h. The dry powder were mixed with ethanol and deposited onto the chemically cleaned Si substrate using spin coating method. The structural and morphological properties of the obtained films were characterized with XRD and SEM. EDXRF was used to confirm the removing of Al by HCl etching. Electrical resistivities were also analyzed with four points probe method.

Results and Discussion

XRD analysis

X-ray diffraction (XRD) was conducted on RIGAKU multiflex X-ray diffractometer in 10°-70° 2θ range. The XRD pattern of MAX phase Ti_3AlC_2 powders as starting materials was shown in Fig. 1.1. The pattern show peaks corresponding to quite pure Ti_3AlC_2. They could be indexed as hexagonal structure (JCPDS No.52-0875). Fig. 1.2 shows the XRD patterns of samples exfoliated by concentrated HCl at room temperature for 12 h, 24 h and 36 h, respectively. Both 12 h and 24 h etched samples still remain in MAX phase Ti_3AlC_2. In the XRD pattern of 36 h etched sample, the strongest peak of Ti_3AlC_2,(1 0 4) peak at 40°, obviously decreases. It was revealed that the some portions of Ti_3AlC_2 were etched with HCl to form Ti_3C_2. And also (0 0 2) peak at 10° and (0 0 4) peak at 20° were divided into two minor peaks. One minor peak was found in its original position, which belongs to Ti_3AlC_2. The other minor peak moved to low 2θ angle, which belongs to newly formed Ti_3C_2. It could be noted that at least 36 h was required to exfoliate Ti_3C_2 with HCl.

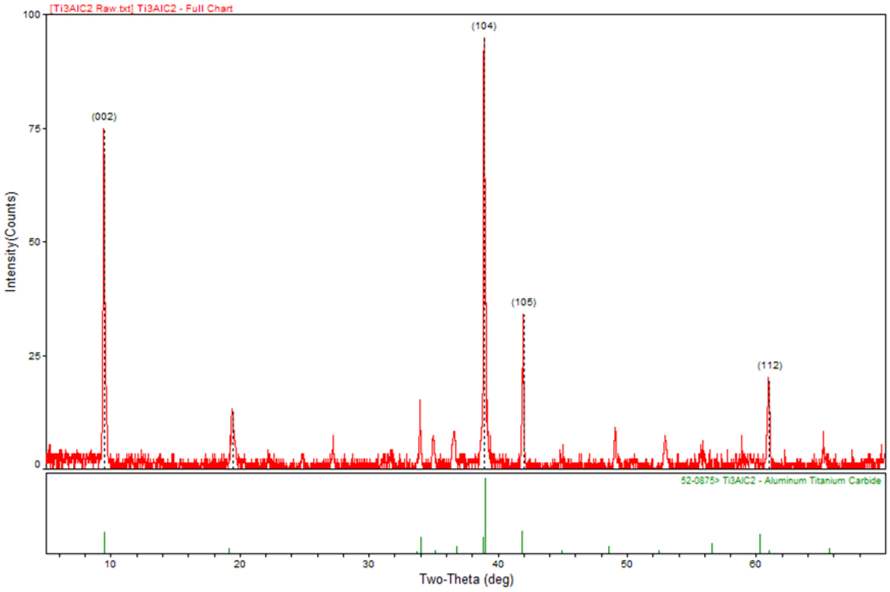

Figure 1 XRD profile of obtained MAX phase Ti_3AlC_2 powder.

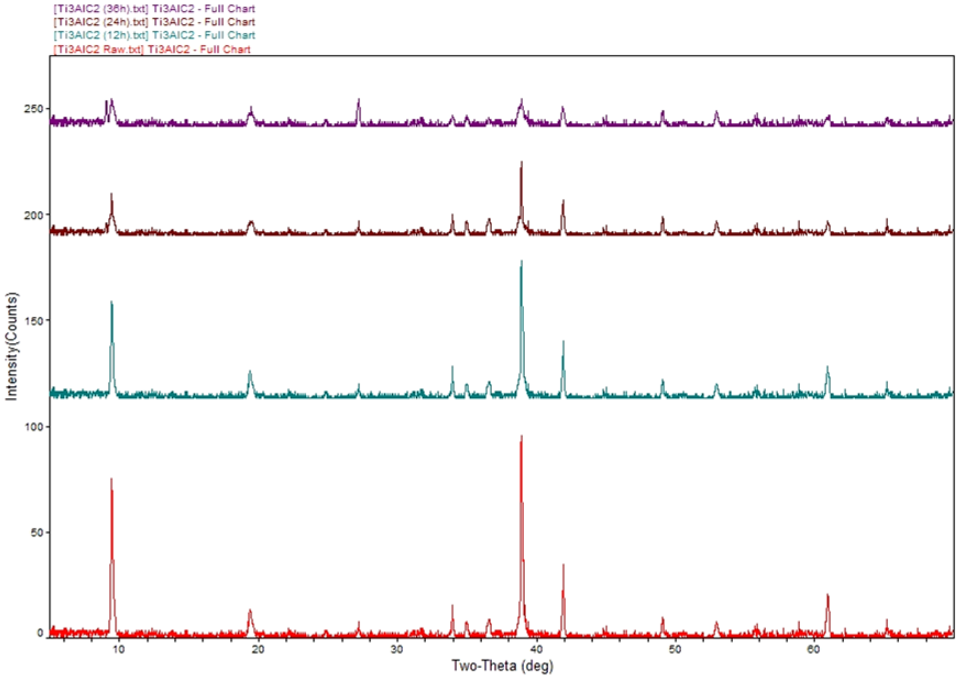

Figure 2 XRD patterns for HCl exfoliated powder for 12 h, 24 h and 36 h.

SEM analysis

The surface morphological properties of the obtained Ti_3AlC_2 powders were characterized through SEM microscopy. The SEM micrograph of obtained Ti_3AlC_2 powders was shown in Fig. 3. It was revealed that the average particle dimensions were smaller than sieve mesh and the agglomerates found in the 5 µm to 10 µm range. And MAX phase particles showed closed packed structures, where adjacent layers stack on each other by A-atoms.

Fig. 4(a),(b) and (c) showed the SEM images of exfoliated Ti_3C_2 particles for different etching time. As shown in Fig. 4(a) and (b), only partial exfoliation appeared in Ti_3AlC_2 grains after 12 h or 24 h etching. When the etching time was extended up to 36 h, more exfoliation was achieved and as shown in Fig. 4(c). The whole grain exfoliated into thin layers with uniform thickness was clearly visible. The average thickness of etched Ti_3C_2 layer was observed to be 60 ± 5 nm, which corresponds to roughly 30 Ti_3C_2 layers. Surface morphological natures of spin coated nanocrystalline Ti_3C_2 thin film was shown in Fig. 5.

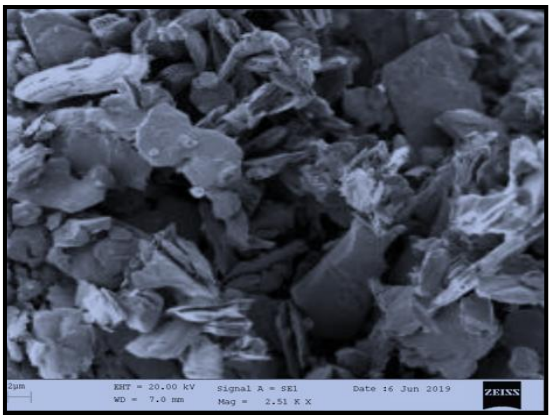

Figure 3 The SEM micrograph of obtained MAX phase Ti_3AlC_2 powders.

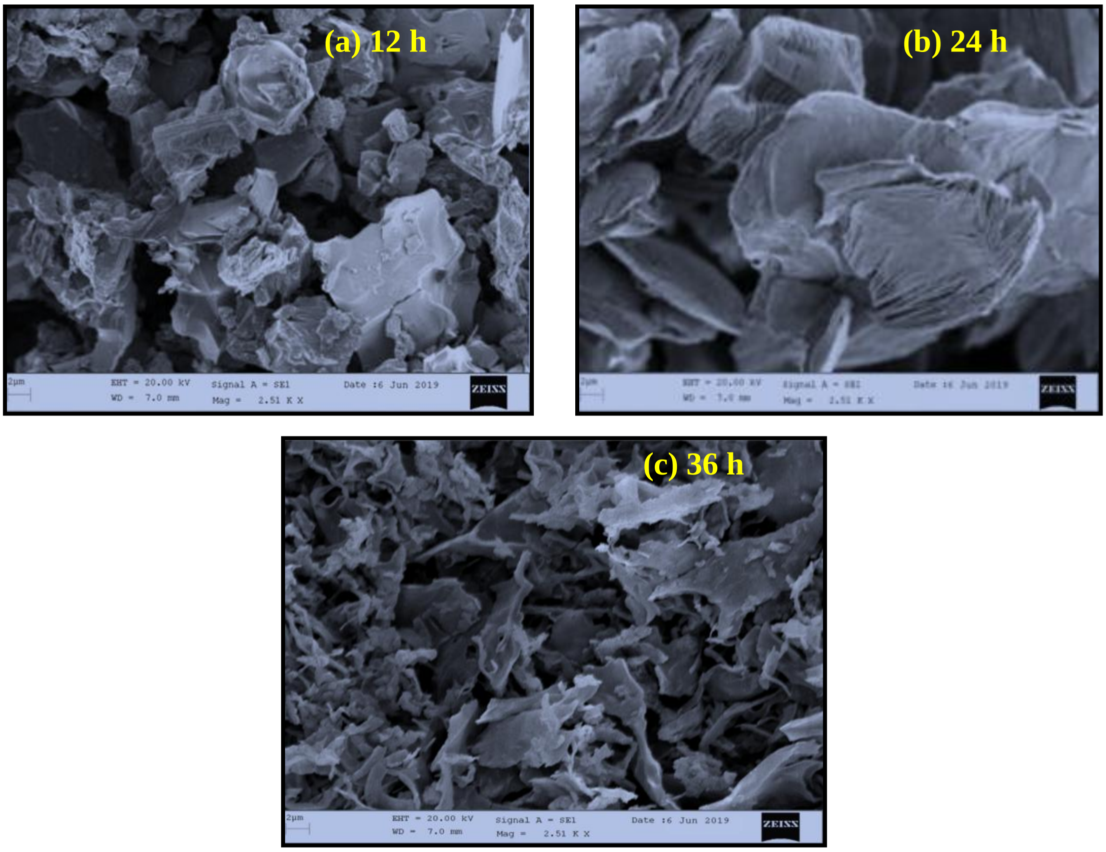

Figure 4 SEM images of exfoliated Ti_3C_2 for different etching time(a) 12 h (b) 24h and (c) 36 h.

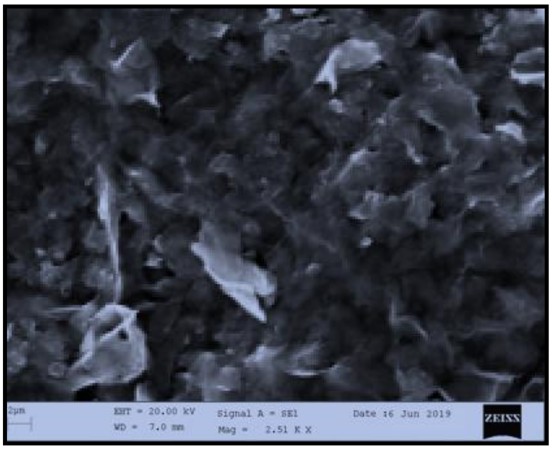

Figure 5 SEM image of spin coated Ti_3C_2 thin film on Si Substrate.

EDXRF analysis was used to confirm the formation of Ti_3C_2. From elemental analysis which showed that the Al content had reduced by HCl etching. The atomic content ratio of Ti: Al: C: O: Cl was observed to be 81% : 0.98% : 16.6% : 1.2% and 0.2%, respectively.

Electrical Properties

The four points probe technique was used for measuring the electrical resistivity of fabricated thin films and it was observed that the resistivities of obtained thin films vary with amount of Al content in the Ti_3C_2 precursors. The electrical resistivities of Ti_3C_2 thin films obtained from MAX phase Ti_3AlC_2 for different etching time were compared. The electrical resistivity of Ti_3C_2 from 12 h etching was observed to be 776 ± 10 μΩcm and that of the electrical resistivities of Ti_3C_2 from 24 h and 36 h etching were also observed to be 432 ± 10 μΩcm and 156 ± 10 μΩcm. Therefore, the Ti_3C_2 films obtained from 36 h etching was more conductive than the other samples from shorter etching time. The electrical resistivities obtained for Ti_3C_2 films in this work compared to the best values reported in literature for this material were tabulated in Table 1.1.

Table 1.1 The electrical resistivities obtained for Ti_3C_2 films in this work compared to the best values reported in literature for this material.

Ti_3C_2 Sample Type	**Electrical Resistivity (μΩ·cm)**	**Reference**
Ti_3C_2 from 12 h etching	776± 10	This research work
Ti_3C_2 from 24 h etching	432± 10	This research work
Ti_3C_2 from 36 h etching	156± 10	This research work
Spin-coated film	154 ± 7	Dillon AD, Ghidiu MJ, et al.
Epitaxial thin film	176 ± 2	Halim J, Lukatskaya M, et al.
Single $Ti_3C_2T_x$ flake	204 ± 44	Lipatov A, Alhabeb M, Boson A, Gogotsi Y. et al
Electrosprayed film	340	Ali A, Belaidi A, Ali S, Helal M.et al
Vacuum Filtered	220 ± 10	Li C, Kota S, Hu C, Barsoum M. et al

Conclusion

Nanocrystalline Ti_3C_2 thin films with hexagonal structure were successfully prepared. The influences of temperature, time and the source of Ti_3AlC_2 on the exfoliating process were studied and researched. Powder compacts partially containing Ti, Al and C were used to synthesize MAX phase Ti_3AlC_2 powder. The best condition to synthesize Ti_3C_2 was achieved in this work, which was etching for at least 36 h at room temperature in HCl. The nanocrystalline Ti_3C_2 powders were readily separated from other phase present, such as Al_2O_3 and TiC, by simply washing and filtrating. The structural and morphological properties of the obtained films were characterized with XRD and SEM. EDXRF confirmed that aluminium (Al) was removed by etching, and the disappearance of Ti_3AlC_2 peaks were revealed from XRD profiles. From the SEM images it was revealed that the fabricated nanocrystalline films composed of several flakes and their sizes up to a few hundred nanometers. The typical microstructure of nanocrystalline titanium carbide thin films consisted of plate like grain and the grain size could be controlled by varying sintering temperature and time. Electrical resistivities measurement was conducted with four probes resistance measurement method. It was revealed that Ti_3C_2 films obtained from 36 h etching was more conductive than the other samples from shorter etching time. Its high conductivity properties could be applied in the transparent conductive oxide applications and DSSC solar cells applications.

Acknowledgments

I would like to thank Professor Dr Lei Lei Win, Head of Department of Physics, University of Mandalay, for her kind permission to carry out this work.

References

Coleman N, Lotya M, O'Neill A, (2011), "Two-Dimensional Nanosheets Produced by Liquid Exfoliation of Layered Materials". Journal of Science, vol 331, pp. 568-571.

Naguib M, Kurtoglu M, Presser V, (2011), "Two-Dimensional Nanocrystals Produced by Exfoliation of Ti_3AlC_2". Journal of Adv Mater, vol. 23, pp. 4248–53.

Naguib M, Mashtalir O, Carle J, (2012), "Two-dimensional transition metal carbides". Journal of ACS Nano, vol. 6(2), pp. 1322-1331.

Naguib M, Mochalin VN, Barsoum MW, Gogotsi Y. (2014), "25th Anniversary Article: MXenes: A New Family of Two-Dimensional Materials." Journal of Adv Materials, vol. 26, pp. 992-1005.

Peng X, Peng L, Wu C, Xiea Y.(2014)," Two dimensional nanomaterials for flexible supercapacitors." Journal of Chem Soc Rev, vol. 43, pp. 3303-3323.

Sun ZM. (2017) Progress in research and development on MAX phases: a family of layered ternary compounds", Journal of Int Mater Rev, vol. 56, pp. 143-166.

J. Myanmar Acad. Arts Sci. 2020 **Vol. XVIII.No.2A**

ANALYSIS OF CONSTITUENTS INAYEYARWADYRIVERWATER SAMPLES FROM MANDALAYAREA BY USING ENERGY DISPERSIVE X-Rays FLUORESCENCE (EDXRF)

Aye Aye Myint[1], May Thwe Oo[2]

Abstract

In this paper, Ayeyarwady River water samples: River water sample 1, River water sample 2 and River water sample 3 were collected from Mandalay environ. The water samples were analyzed to determine the elemental concentration by using Energy Dispersive X-ray Fluorescence (EDXRF) spectrometer. Silicon (0.14% - 0.19%), sulfur (0.31% - 0.33%), potassium (0% - 0.01%), calcium (0% - 0.013%), iron (0 %- 0.001%) and samarium (0% - 0.001%) were detected by using XRF. The physico-chemical properties such as colour, pH, conductivity, alkalinity and total hardness of River water samples were also measured. These results were compared and discussed with WHO standards.

Keywords: EDXRF (Energy Dispersive X-Ray Fluorescence) alkalinity, hardness, conductivity

Introduction

Rivers are vital component of the biosphere that contains less than one percent of the world's fresh water with their higher ecological and social significance which are being polluted by indiscriminate disposal of sewerage, industrial waste, and by excess of human activities affecting their physicochemical characteristics and leads to various deleterious effects on aquatic organisms.The rivers provide water for industries, agriculture, aquaculture, commercial and domestic purpose. Unfortunately the same rivers are being polluted by indiscriminate disposal of sewage and industrial wastes and plethora of human activities. River pollution has already acquired serious dimensions in India. Pollution of rivers first affects its physicochemical quality then systematically destroys the community disrupting the delicate food web.

Quality of river water can be regarded as a network of variables such as PH, oxygen concentration, temperature, etc. and any changes in these physical and chemical variables can affect aquatic biota in a variety of ways. Since the quality river water is directly related to health and is important for determination of water utility, it is very essential and important to test the quality of the water before it is used for drinking, domestic, agricultural or industrial purposes. The utility of river water for various purposes is governed by physicochemical and biological quality of the water.

Materials and Method

Ayeyarwady River water samples: River water sample 1 (RM-1), River water sample 2 (RM-2) and River water sample 3 (RM-3) were collected from Mandalayenviron. River water samples, (RM-1) and (RM-2) were collected at near Yadanarbon bridge and Shanlay Kyune village, River water samples(RM-3) were collected at near the GawweinJetty.

---

[1] Dr, Associate Professor, Department of Physics, Kyaukse University

[2] Dr, Associate Professor, Department of Physics, Technological University(Hmawbi)

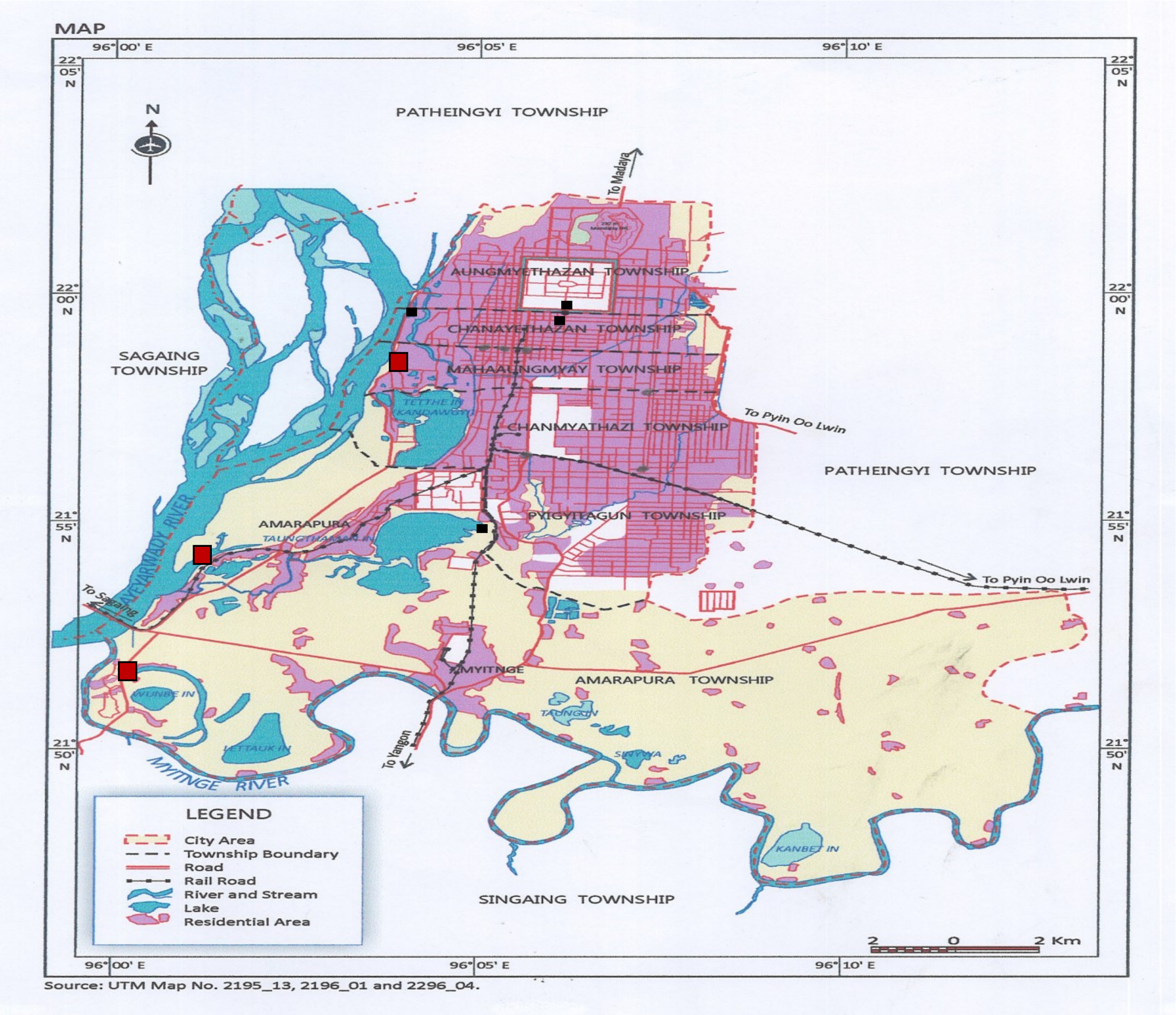

Source: UTM Map No. 2195_13, 2196_01 and 2296_04.

Figure 1 The collection sites of Ayeyawady River from Mandalay Environ

River water samples were collected in good quality polythene bottles of five liter bottles were tightly sealed after collection and labeled. River water samples were taken from each of the collected sites. The elemental content of the water samples were determined by EDXRF technique. Each water samples was prepared for EDXRF analysis. The water sample was put into the sample cup (30 mL) for EDXRF measurements. Each sample was run for about 100 seconds in EDX 7000. The value of pH and Conductivity were determined using pH meter and conductivity meter (Ecoscan Con 5) at Department of Chemistry, University of Mandalay. The colour, alkalinity and total hardness values of the water samples were determined at Public Health Laboratory, Mandalay.

Experimental Results and Discussion

The concentrations of the elements of the three River water samples were determined by EDXRF technique. The results were shown in Table (1-2) and Figure(1-11).The physical properties such as colour, pH and conductivity of three River water samples were determined and the results were presented in Table (3) and Figure(7-9). The chemical properties such as alkalinity and total hardness of three River water samples were determined and the results were presented in Table (4) and Figure (10-11).

Table 1 Concentrations of Elements of River Water Samples Analyzed by EDXRF

No.	Code Name	Concentrations of Elements (%)					
		Silicon (Si)	Sulphur (S)	Potassium (K)	Calcium (Ca)	Iron (Fe)	Samarium (Sm)
1	RM-1	0.16	0.033	0.010	0.013	0.001	ND
2	RM-2	0.197	0.031	0.010	0.013	0.001	0.001
3	RM-3	0.149	0.032	0.010	0.013	0.001	ND

RM-1= River water samples 1
RM-2= River water samples 2
RM-3= Riverwater samples 3

Table 2 WHO Standards of Some Elements for Drinking Water

No	Elements	WHO Standards	
		Highest desirable level	Maximum permissible level
1	Calcium(Ca) (mg/L)	75	200
2	Iron (Fe)(mg/L)	0.3	1.0

Table 3 Analysis of Physical Properties of Water Samples

Parameters	Sample code name			WHO Standards	
	RM-1	RM-2	RM-3	Highest Desirable Level	Maximum Permissible Level
Colour (Platinum, Cobalt Scale)	12	25	18	5	50
pH	7.7	7.6	7.5	6.5	8.5
Conductivity (µS/ cm)	94.1	103.3	89.1	200	800

Table 4 Analysis of Chemical Properties of Water Samples

Parameters	Sample code name			WHO Standards	
	RM-1	RM-2	RM-3	Highest Desirable Level	Maximum Permissible Level
Alkalinity (mg/L)	130	130	260	200	500
Total Hardness(mg/L)	40	40	160	100	500
Calcium(Ca) (mg/l)	8	12	12	75	200
Magnesium(Mg) (mg/l)	5	24	29	50	150
Chlorine(Cl) (mg/l)	20	20	100	250	600

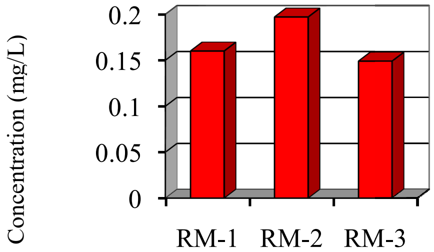

Figure 2 Comparison of silicon Concentration in different water samples

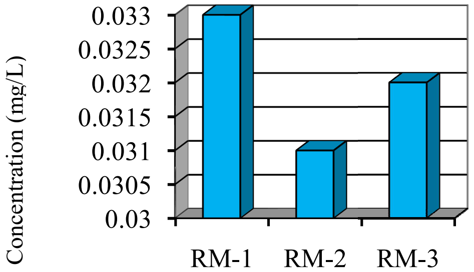

Figure 3 Comparison of sulphur Concentration in different water samples

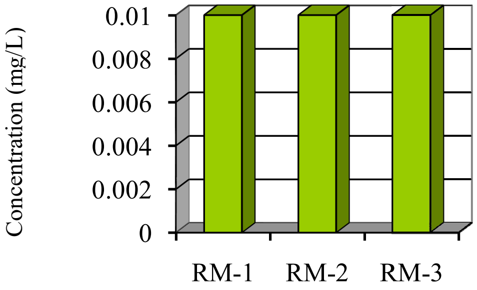

Figure 4 Comparison of potassium Concentration in different water samples

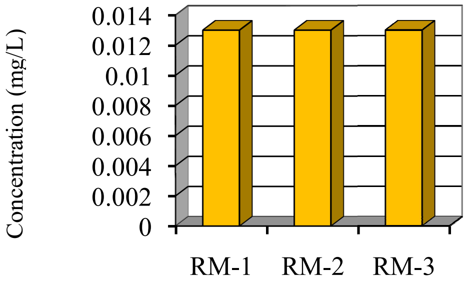

Figure 5 Comparison of calcium Concentration in different water samples

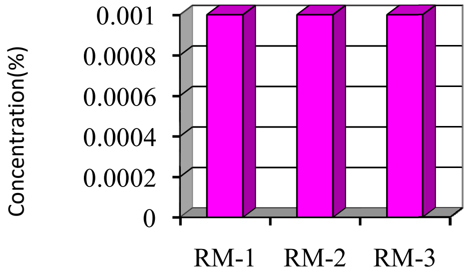

Figure 6 Comparison of Iron Concentration in Different Water Samples

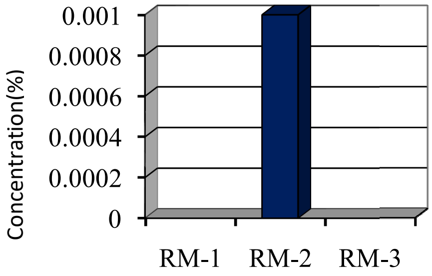

Figure 7 Comparison of Samarium Concentration in Different Water Samples

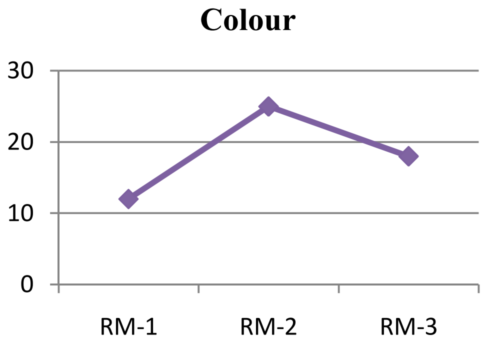

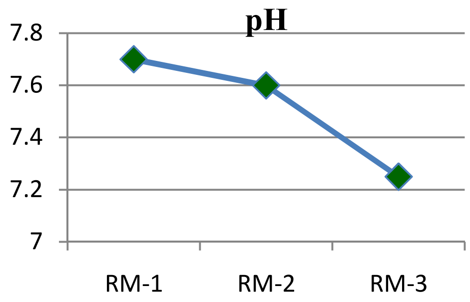

Figure 8 Comparison of Colour in different Water Samples

Figure 9 Comparison of pH in different Water Samples

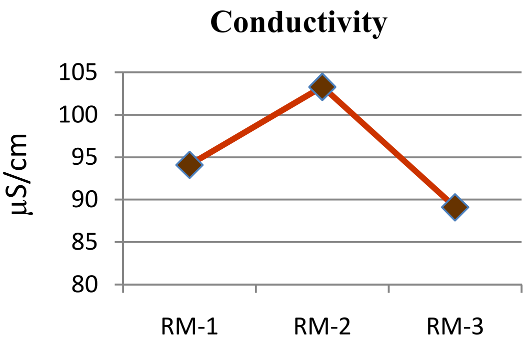

Figure 10 Comparison of Conductivity in different River water samples

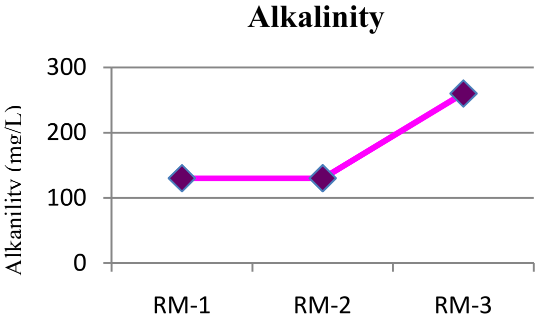

Figure 11 Comparison of Alkalinity in different River waters

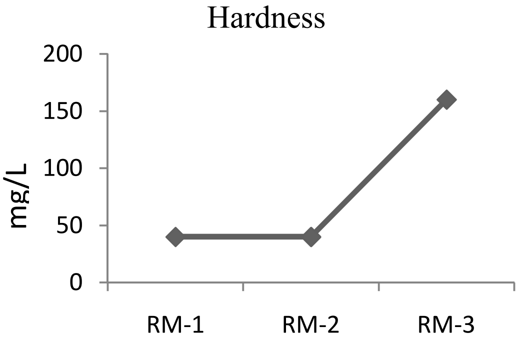

Figure 12 Comparison of total hardness in different River water samples

Comparison of the silicon concentration of River water samples were shown in Table (1) and Figure (2). Silicon concentration of River water samples were found to be varied. River water sample 3(RM-3) contains the lowest silicon concentration. River water sample 2consists of the highest silicon concentration. The amount of siliconin River water sample 2 (RM-2) was larger than other water samples.

Comparison of the Sulphur concentration of Ayeyarwady River water samples are shown in Table (1) and Figure (3). Sulfur concentration of water samples are found to be varied, River water samples 2 (RM-2) has the lowest Sulphur concentration. River water samples 1(RM-1) has the highest Sulfur concentration.

Comparison of the Potassium concentration of Ayeyarwady River water samples are shown in Table (1) Figure (4). Potassium concentration of River water samples are found to be varied. River water samples 1 (RM-1), River water samples 2 (RM-2) and River water samples 3 (RM-3) have the same Potassium concentration.

Comparison of the Calcium concentration of Ayeyarwady River water samples are shown in Table (1)and Figure (5). Calcium concentration of River water samples are found to be varied. River water samples 1 (RM-1), River water samples 2 (RM-2) and River water samples 3 (RM-3) have the same Calcium concentration.

Comparison of the iron concentration of Ayeyarwady River water samples are shown in Table (1)and Figure (6). Iron concentration of water samples, River water samples 1 (RM-1), River water samples 2 (RM-2) and River water samples 3 (RM-3) are found to contain the same value of Iron concentration.

Comparison of the Samarium concentration of Ayeyarwady River water samples are shown in Table (1) and Figure (7). The amount of Samarium in River water samples 1 (RM-1) and River water samples 3 (RM-3) were not be detected by XRF. Samarium was found in River water samples 2 (RM-2)

The Colour of Ayeyarwady River water samples are presented in Table(3) and Figure(8). Colour values range from12-25. Ayeyarwady River water samples 1 (RM-1) has lowest value .The Ayeyarwaddy River water samples 2 (RM-2) has the highest value .

The pH values of Ayeyarwady River water samples are shown in Table (3) and Figure (9). The pH values of River water samples 1 (RM-1), River water samples 2 (RM-2) and River water samples 3 (RM-3) are found to be 7.7, 7.6, and 7.5 respectively. River water samples 3 (RM-3) has the lowest value of pH (7.5). River water samples 1 (RM-1) has the highest value of pH (7.7).

The Conductivity of Ayeyarwady River water samples are presented in Table(3)and Figure (10).Conductivity values range from 89.1-103.3 microsecment/centimeter. Ayeyarwady River water samples 3 (RM-3) has lowest conductivity value (89.1 μS/cm). The Ayeyarwady River water samples 2 (RM-2) has the highest conductivity value (103.3 μS/cm).

Alkalinity of Ayeyarwady River water samples are presented in Table (4)Figure (11). The alkalinity of River water samples 1 (RM-1), River water samples 2 (RM-2) and River water samples 3 (RM-3) are 130 mg/L, 130 mg/L and 260 mg/L respectively. River water samples 1 (RM-1) and River water samples 2 (RM-2) have the same value of lowest alkalinity. River water samples 3 (RM-3) has the highest value of alkalinity.

The total Hardness of Ayeyarwady River water samples are presented in Table(4)and Figure (12). Total Hardness values range from 40-160. Ayeyarwady River water samples 1 (RM-1) and samples 2 (RM-2) contain the same total Hardness value. The Ayeyarwady River water samples 3 (RM-2) has the high value.

Conclusion

In this paper, for drinking water, highest desirable value of pH is 7-8.5 and maximum permissible value is 6.5-9.2. pH values of three Ayeyarwady River water samples were found to be 7.5-7.7. Therefore, pH values of River water samples fall in maximum permissible value.

For drinking water, highest desirable value of conductivity is 200μS/cm and maximum permissible value is 800μS/cm. Conductivity values of Ayeyarwady River water samples are found to be 89-105 μS/cm. Therefore, conductivity values of three water samples fall in maximum permissible value.

For drinking water, highest desirable value of alkalinity is 200 mg/L and maximum permissible value is 500 mg/L. Alkalinity values of three River water samples were found to be 130-260 mg/L. Alkalinity values of River water samples were found to be within the WHO Standards.

For drinking water, highest desirable amount of calcium is 75 mg/L and maximum permissible value is 200 mg/L. The amount of calcium of three Ayeyarwady River water samples are found to be 8-12 mg/L. Therefore, the amount of calcium of three Ayeyarwady River water samples exist lower than the highest desirable value and maximum permissible value.

For drinking water, highest desirable amount of Magnesium is 50 mg/L and maximum permissible value is 150 mg/L. The amount of Magnesium of three Ayeyarwady River water samples are found to be 5-29 mg/L. Therefore, the amount of Magnesium of three Ayeyarwaddy River water samples exist lower than the highest desirable value and maximum permissible value of WHO standard.

For drinking water, highest desirable amount of chlorine is 250 mg/L and maximum permissible value is 600 mg/L. The amount of chlorine of three Ayeyarwady River water samples are found to be 20-100 mg/L. Therefore, the amount of chlorine of three Ayeyarwady River water samples exist lower than the highest desirable value and maximum permissible value.

From the XRF analysis, silicon (0.16% - 0.19%), sulfur (0.31% - 0.33%), potassium (0.10% - 0.12%), calcium (0.007% - 0.013%), iron (0.001% of each) and samarium (0.001% of each) are also present in three Ayeyarwaddy River water samples. Moreover, it is obviously seen that toxic elements are not found in all River water samples.

From the point of view of pH, alkalinity, conductivity, colour, total Hardness and elemental concentration, these three Ayeyarwady River water samples are found to be used for drinking purpose and domestic use.

Among these three Ayeyarwady River water samples, the quality of Ayeyarwaddy River water sample 1(RM-1) is better than others.

Acknowledgement

I would like to express my special thanks to Dr Aung Khin Myint, Rector, Kyaukse University to allow to present this research. My sincere thanks are due to Dr Cherry Than, Professor and Head, Department of Physics, Kyaukse University for her kind encouragements throughout the research.

.

References

Agarwal, B. K., (1979) *X-ray Spectroscopy: An Introduction*. Heidelberg: Springer-Verlag,.

Biddle, M. B. *et al.*,(2012) "Nuclear Instrument and Methods in Physics" *Research, B,* 251,PP 117.

Campbell, I. *et al.*, (2012) *The Use of EDXRF for Pharmaceutical Material Elemental Analysis*, American Pharmaceutical review.

Havrilla, G, J *et al.*, (1996) *X-Ray Fluorescence Is Useful for Actinide Characterization*.

Joshi S. K., B. D Shrivastsva & A. P. Deshpande, (1998) *X-ray Spectroscopyand Allied Area*s , New Youk : Narosa.

Rozmaric, M. and V. Orescanen, (2006) "Nuclear Instrument and Methods in Physics", *Research, B*,251, pp 223.

HOW TO CONTROL SERVOMOTORS WITH POTENTIOMETER BY USING UNOARDUSIM V2.2 SOFTWARE FOR ROBOTIC SYSTEM

Oak Kar Shin[1], KhinThit Sar Shin[2], Cherry Than[3]

Abstract

Servomotor can be controlled by potentiometer with UnoArduSimV2.2 software which consists of a circuit board and can be referred to as a microcontroller and a ready-made software called Arduino IDE which used write and upload the computer code to the physical board and it consists of many I/O devices, we can use inside in it. In this experiment, servo can be connected directly to an Arduino. This arduino can be controlled by four Potentiometer attached to it, each potentiometer is used to control each servo. When we turn the potentiometer, we got the analog value first, after converting this analog value to digital value, we got the degree how to turn the servo with. So we can use these servos by rotating the pots to pick and move the object from one place to another in robotic system. We will connect the power and ground pin directly to the Arduino 5V and GND pins. The PWM input will be connected to one of the Arduino's digital output pins for servos and analog pins for potentiometer. After writing the sketch, compile, upload button and we can run my work inside in this software.

Keywords: Arduino, Arduino IDE, Servomotors.

Introduction

Arduino consists of both a physical programmable circuit board (often referred to as a microcontroller) and a piece of software, or IDE (Integrated Development Environment). The open-source Arduino Software (IDE) makes it easy to write code and upload it to the board. It runs on Windows, Mac OS X, and Linux. Download the Arduino IDE ,ARDUINO 1.8.7 , This software can be used with any Arduino board. And for this project, I just only apply by using UnoArduSimV2.2software and its UnoArduSimV2,2.exe software. Because this software can be used without any external hardware but it can write, read and run easily on it.

Servomotors can be connected directly to an Arduino which is an open source based on an easy - to - use hardware and software. Arduino compiler/IDE accepts C and C++ as-is. In fact many of the libraries are written in C++. We use the Arduino programming language (based on Wiring), and the Arduino Software (IDE), based on Processing.

Arduino Uno

The Arduino UNO is an open-source microcontroller board based on the Microchip ATmega328P microcontroller and developed by Arduino.cc. The board is equipped with sets of digital and analog input/output pins that may be interfaced to various expansion boards and other circuits. Arduino is development platform for developers. It is fairly easy to interface different sensors and actuators with arduino, which makes it quite attractive because it is a small computer on a single chip containing a processor, memory, and input/output. Typically "embedded" inside some device that they control. A microcontroller is often small and low cost.

---

[1] Dr, Demonstrator, Physics Department, Kyaukse University, Myanmar

[2] Dr, Associate Professor, Physics Department, Maubin University, Myanmar

[3] Dr, Professor, Physics Department, Kyaukse University, Myanmar

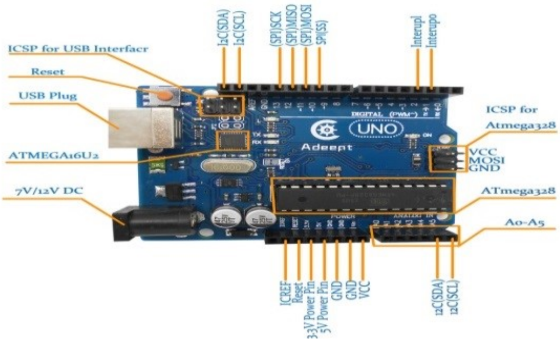

Figure 1 Photographic view of Arduino uno board

Table 1 Arduinouno Technical specifications

Sr No	Specifications	
1	Microcontroller	- ATmega 328
2	Operating voltage	- 5Volts
3	Input voltage	- 7volts to12volts (Recommended)
4	Digital I/O Pins	- 14 (out of which 6 pin provide PWM output)
5	Analog input pins	- 6
6	DC current for I/O Pin	- 40mA
7	DC current for 3.3 volt	- 50mA
8	Pin	- 32 kilo bytes of which 0.5 kB used bybootloader
9	Flash memory	- 2 kilo bytes
10	SRAM	- 1 kilo bytes
11	EEPROM Clock speed	- 16MHz

Servomotor

Servomotor is an electrical device which can push or rotate an object with great precision. If we want to rotate and object at some specific angles or distance, then we can use servomotor. Servomotors are used to control the position of objects, rotate objects. move legs, arms or hands of robots, move sensors etc, with high precision. Servomotor is controlled with the help of servomechanism. Inside a servo there is a small DC Motor, Potentiometer and Control Circuit. The motor is attached gears to the control wheel. A servo system mainly consists of three components namely a controlled device, an output sensor and a feedback system.

Figure 2 The image of a Servomotor

Inside a servomotor there is a small DC motor, potentiometer and a control circuit. The motor is attached by gears to the control wheel.

Figure 3 The internal devices of a servomotor

Methodology

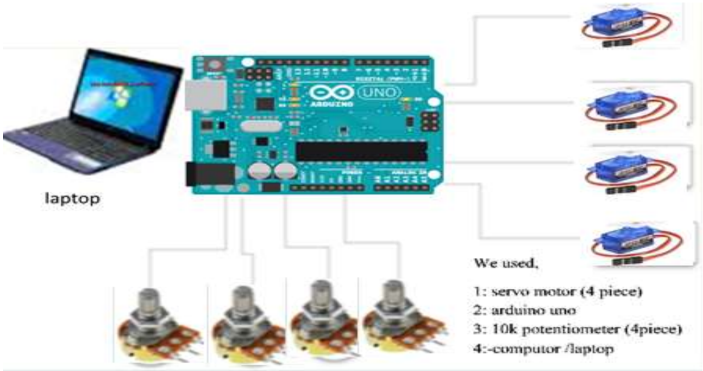

Figure 4 The block diagram of my circuit system

Figure (4) show the block diagram representing for the robotic arm. The components here used arduino uno board, servomotors, potentiometers (pot, variable resistors) and computer. If we want to rotate and object at some specific angle or distance, then servomotor can use to control the position of objects, rotate objects, move legs, arms or hands of robots, move sensors etc, with high precision. Servomotor is controlled with the help of servo mechanism. Inside a servo there is a small DC Motor, Potentiometer and Control Circuit. The motor is attached gears to the control wheel. A servo system mainly consists of three components namely a controlled device, an output sensor and a feedback system. The robotic arm is controlled by four potentiometer that is used to control each servo. We can move these servos by rotating the potentiometer to pick some object and move the object from one place to another. We used small servomotor which has more powerful to pick heavy object.

Components

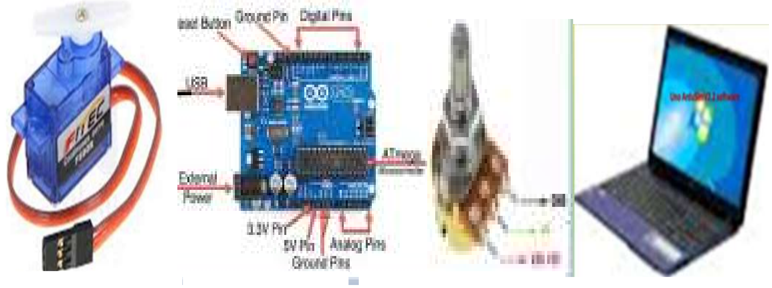

servomotor **Arduino Uno** **Potentiometer** **laptop**

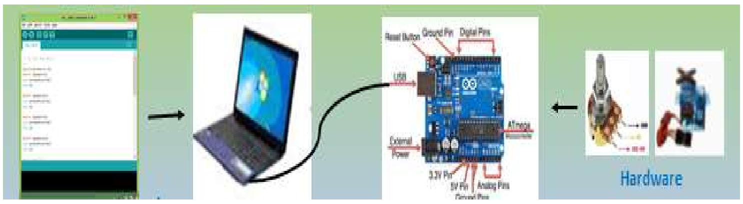

Software **Hardware**

Figure 5 The connecting system of arduino with hardware and software

Controlling system for servomotor

Servomotors can be connected directly to an Arduino. This Arduino can be controlled by four Potentiometer attached to it, each potentiometer is used to control each servo. Servo motors are available at different shapes and sizes. We used small servo motors, here we used four servos. Now we got the voltage provided by these variable resistor (voltage which represents position control) into ADC channels of Arduino. We are going to use four ADC channels of UNO from A0 to A3 for this. After the ADC initialization, we will have digital value of pots representing the position needed by user. We will take this value and match it with servo position.

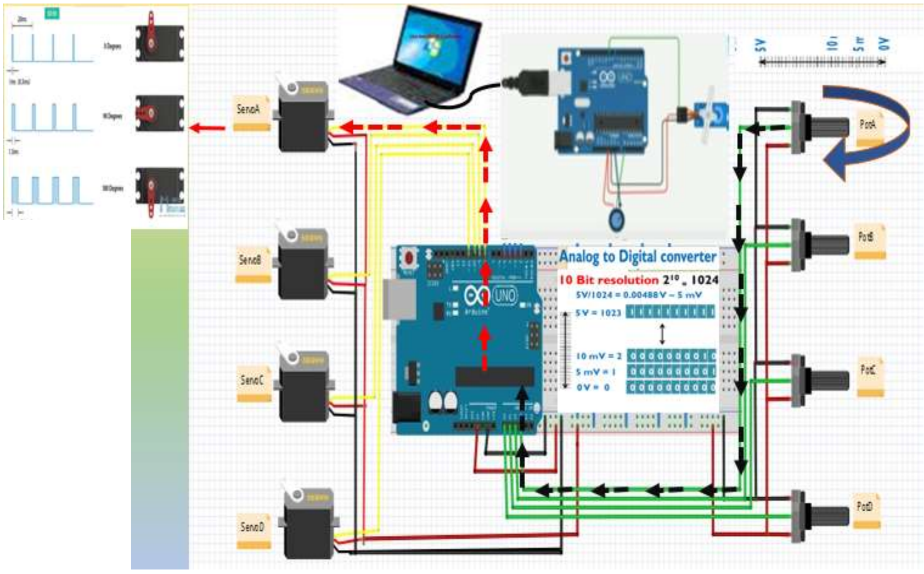

Figure 6 Circuit diagram of the processing system

The library for servomotor

I have created a servo object and declared the initial angle of the servomotor.

- After that I have adjust the rate, the rate at which Arduino communicates with the laptop/computer.
- Then I have defined the pin at which the servo motor is attached to the Arduino UNO's board.
- Inside the main loop, I have applied the condition that in between 0 and 180 degrees, the servomotor's angle will be increased with different steps and each step has 5 degrees of angular movement.
- When maximum limit is reached, the angle will be reduced from 180 to 0 degree with different steps, each step having 5 degrees of angular movement.
- Arduino has six ADC channels. We have used four for our Robotic. The UNO ADC is of 10 bit resolution so the integer values ranging from 0-1023 (2^10=1024 values). This means that it will map input voltages between 0 and 5 volts into integer values between 0 and 1023. So for every (5/1024= 4.9mV) per unit. Learn more about mapping the voltage levels using ADC channels in Arduino here.
- That was the brief description of the Arduino complete source code designed for Servo Motor Control using Arduino.

Source Code Description

- The complete Arduino source code for Servo Motor Control using Arduino is given below.
- By uploading the source code to Arduino board we will be able to control the servo motor using Arduino.
- Once the program is started, rotating the potentiometer should cause the shaft of the servo motor to rotate.

When we write the sketch,

```
/* Servo Motor Control using the Arduino servo library
                    By   Dr Oak Kar Shin
  */

#include<Servo.h>       // Servo Library
Servo myservo1;         // initialize a servo object for the connected servo
int potenPin1=A0;       // initialize the A0 analog pin for potentiometer
int w;                  // let the potentiometer value
Servo myservo2;
int potenPin2=A1;
int x;
Servo myservo3;
int potenPin3=A2;
int y;
```

```
  Servo myservo4;
  int potenPin4=A3;
  int z;
  void setup()
  {
  myservo1.attach(3);// attach the signal pin of servo the pin 3 of arduino
  myservo2.attach(5);
  myservo3.attach(6);
  myservo4.attach(9);
  }
  void loop()
  {
  // put our main code here,to run repeatedly:
  W=analogRead(potenPin1);     // this will read the value from the potentiometer
                               between 0 and 1023 and store it

 W= map(w,0,1023,0,180);        // this will map the value from the    potentiometer
                               to values the servos can use and store it for later se
myservo1.write(w);             // these will make the servos move to the mapped
                               angles
  delay(15);                   //wait for 1 ms
    x=analogRead(potenPin2);
    x= map(x,0,1023,0,180);
    myservo2.write(x);
  delay(15);
    y=analogRead(potenPin3);
    y= map(y,0,1023,0,180);
    myservo3.write(y);
  delay(15);

  z = analogRead(potenPin4);
    z= map(z,0,1023,0,180);
  myservo4.write(z);
  delay(15);

  }
```

Results and Discussion

When I use this software, I can choose I/O devices what I need to control, then they are connected with the circuit and write the sketch and run inside this software. In my project, these all servos are attached with the digital pin 3,5,6 and 9 of the arduino circuit and the 4 potentiometer are connected with the analog pinA0-A3. After connection, I wrote the sketch what I want to control. In this here, we connect with computer and circuit. when I turn the potentiometer, the 0-5V will come out from the arduino circuit. So this voltage flow from the potentiometer to the arduino IC pass through the analog pin. This analog value are converted to digital value which make the servo how will turn as shown in figure 6. So I got the analog value of potentiometer and the digital value. When I used this Uno ArduSimV2.2 software (7.a), I can choose 4 servomotor and 4 analog slider (potentiometer)and tick USB Serial to show connection the computer whit this program from the box of Attaced I/O devices , after choosing I pressed ok key from (7,b). So we get the figure (7.c).

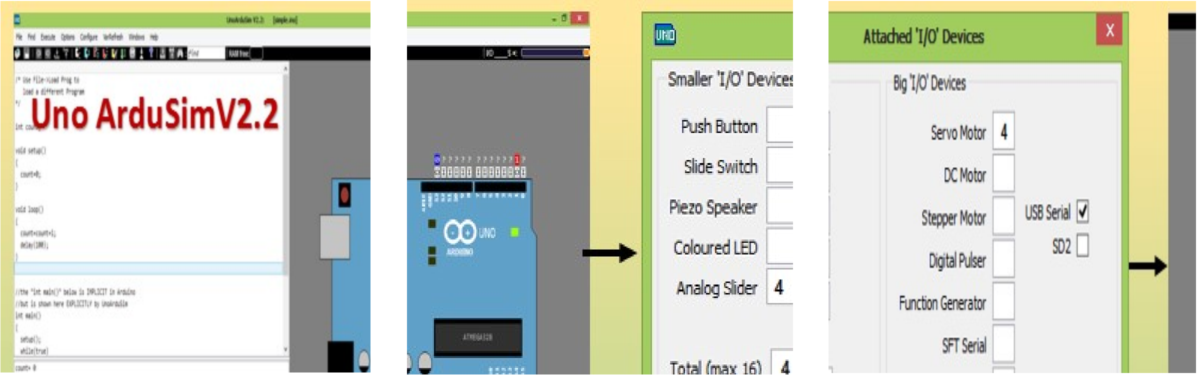

Push Button
Slide Switch
Piezo Speaker
Coloured LED
Analog Slider 4
Total (max 16) 4

Servo Motor 4
DC Motor
Stepper Motor
Digital Pulser
Function Generator
SFT Serial
USB Serial ☑
SD2 ☐

(7. a) (7. b) (7. c)

Figure 7 The usage of the uno ardusim V2.2 software

Connection system and its simulation

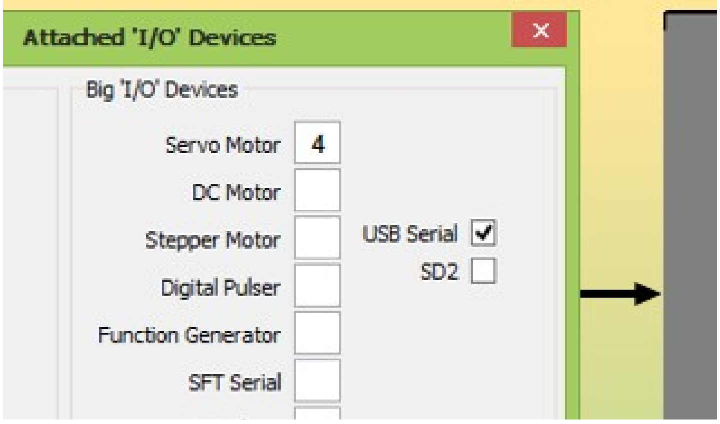

Servo Motor 4
DC Motor
Stepper Motor
Digital Pulser
Function Generator
SFT Serial
USB Serial ☑
SD2 ☐

Figure 8 The connecting system of circuit and devices

This Figure (8)shows the connection of the arduino digital pin 3,5,6,9 and 4 servomotors (1,2,3,4) and then 4 potentiometer are attached with analog pin of arduino (A0 –A3).

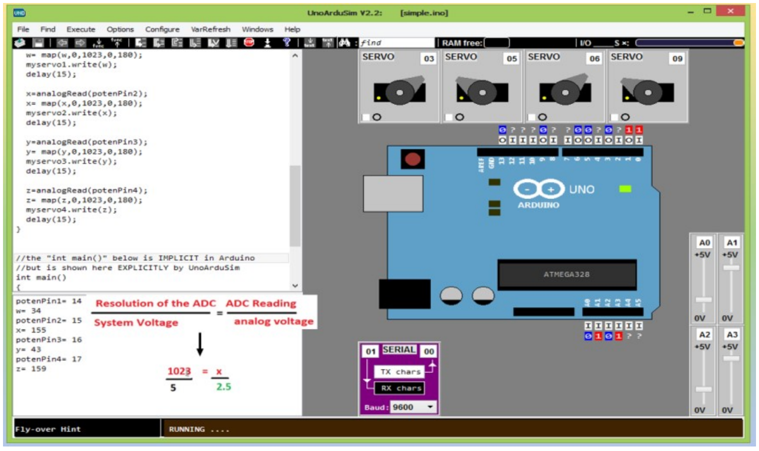

```
  w= map(w,0,1023,0,180);
  myservo1.write(w);
  delay(15);

  x=analogRead(potenPin2);
  x= map(x,0,1023,0,180);
  myservo2.write(x);
  delay(15);

  y=analogRead(potenPin3);
  y= map(y,0,1023,0,180);
  myservo3.write(y);
  delay(15);

  z=analogRead(potenPin4);
  z= map(z,0,1023,0,180);
  myservo4.write(z);
  delay(15);
}

//the "int main()" below is IMPLICIT in Arduino
//but is shown here EXPLICITLY by UnoArduSim
int main()
{
```

```
potenPin1= 14
w= 34
potenPin2= 15
x= 155
potenPin3= 16
y= 43
potenPin4= 17
z= 159
```

$$\frac{\text{Resolution of the ADC}}{\text{System Voltage}} = \frac{\text{ADC Reading}}{\text{analog voltage}}$$

$$\frac{1023}{5} = \frac{x}{2.5}$$

Figure 9 The result of the value and degree for servo

This Figure (9) represents when I turn the slider with different value, firstly we got the analog value which were convered as digital value by ATMEGA328 Arduino IC. So servomotor will rotate any degree according to the digital value.

Analog to Digital converter equation is

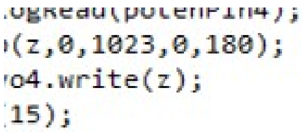

```
.ogRead(potenPin4);
)(z,0,1023,0,180);
'o4.write(z);
'15);
```

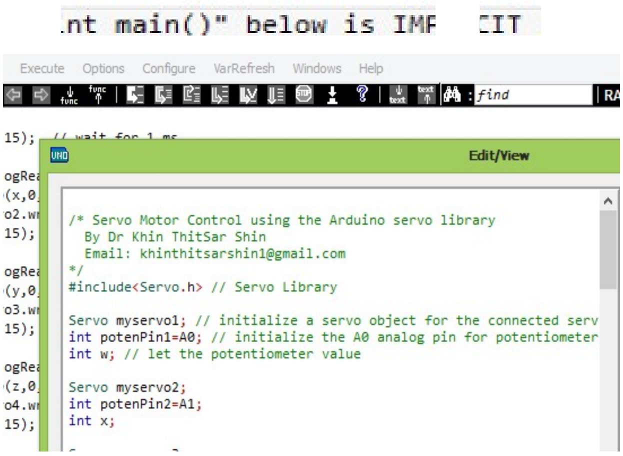

```
.nt main()" below is IMF  :IT
```

```
15);  // wait for 1 ms

ogRe
(x,0
o2.w
15);

ogRe
(y,0
o3.w
15);

ogRe
(z,0
o4.w
15);
```

```
/* Servo Motor Control using the Arduino servo library
  By Dr Khin ThitSar Shin
  Email: khinthitsarshin1@gmail.com
*/
#include<Servo.h> // Servo Library

Servo myservo1; // initialize a servo object for the connected serv
int potenPin1=A0; // initialize the A0 analog pin for potentiometer
int w; // let the potentiometer value

Servo myservo2;
int potenPin2=A1;
int x;
```

Figure 10 The input area of UnoArduSimV2.2 software

When I write the sketch, we can write the program what you want to control in this edit/View box of figure (10).

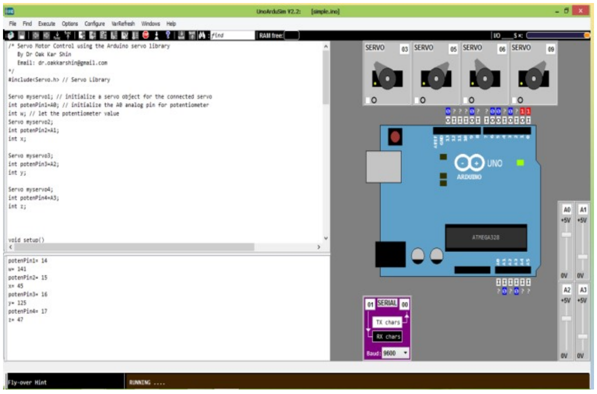

```
/* Servo Motor Control using the Arduino servo library
   By Dr Oak Kar Shin
   Email: dr.oakkarshin@gmail.com
*/
#include<Servo.h> // Servo Library

Servo myservo1; // initialize a servo object for the connected servo
int potenPin1=A0; // initialize the A0 analog pin for potentiometer
int w; // let the potentiometer value
Servo myservo2;
int potenPin2=A1;
int x;

Servo myservo3;
int potenPin3=A2;
int y;

Servo myservo4;
int potenPin4=A3;
int z;



void setup()
```

```
potenPin1= 14
w= 141
potenPin2= 15
x= 45
potenPin3= 16
y= 125
potenPin4= 17
z= 47
```

Figure 11 The output area of UnoArduSimV2.2 software (Getting and running)

When I run the sketch, we can run the program how I want to control the servomotor by turning the potentiometer (slider) in this box of figure (11).

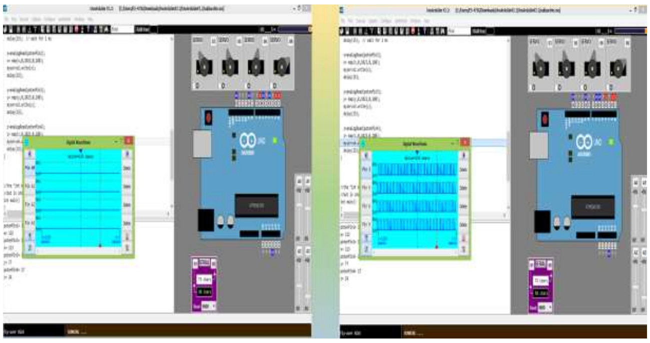

Figure 12 The waveform of analog pins and digital pins input

Getting up and running

Plug it into the USB port and install the USB drivers that come with the IDE. Open up the Arduino IDE and select the communication speed for serial connections. And by using the pot means by rotating the pot which changing its voltage value will change the servo angular rotation.

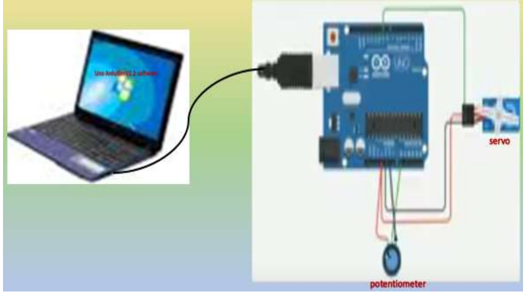

Figure 13 Running system of Arduino software

Conclusion

Servomotors are small in size, and because they have built-in circuitry to control their movement, they can be connected directly to an Arduino. Servomotor works on PWM(Pulse width Modulation)principle, means its angle of rotation is controlled by the duration of applied pulse to its control PIN. DC motor of servo which is controlled by a variable resistor (potentiometer and some gears). This Arduino can be controlled by four Potentiometer attached to it, each potentiometer is used to control each servo. So we can move these servos by rotating the pots to pick some object, with some practice we can easily pick and move the object from one place to another. We have used low torque servos here but we can use more powerful servos to pick heavy object. This proposed work is an overview of how we can use the Servomotors can to control the position of objects, rotate objects, move legs, arms or hands of robots, move sensors, etc , which is controlled by using potentiometer and Arduino UNO.

Acknowledgement

I would like to express Rector Dr Aung Khin Myint and Dr Su Su Win, Pro-Rector of Kyaukse University for their encouragement. I am greatly express thank to Professor Dr Cherry Than, Head of Physics Department, Kyaukse University for her valuable advice to carry out. I would like to thank to Professor Dr Nwe New Aye, Department of Physics, Kyaukse University. I am very greatful for the Myanmar Academy of Arts and Science Organization.

References

Brooks, Rodney A,(13 September,1991) “New Approaches to Robotics”, Science, vol. 253, pp. 1227- 1232.

Dejan Nedelkovski "How Servo Motors Work & How to Control Servos Using Arduino.

John-David Warren, Josh Adams and HaraldMolle, (2011) “Arduino Robotics”, Springer Science and Business Media.

Priyambada Mishra, (2017) “ Development of robotic arm using Arduino Uno” vol 5, Issue 5, May 2017.

http://www.arduino.cc/en/Reference/Servo

http://www.arduino.cc/playground/Learning/SingleServoExample Additional descriptions of servos

http://makeprojects.com/Wiki/Servos

http://www.seattlerobotics.org/guide/servos.html

https://howtomechatronics.com/how it works/how servo motors work how to control servos using arduino

J. Myanmar Acad. Arts Sci. 2020 **Vol. XVIII.No.2A**

GRAVITATIONAL COLLAPSE AND BLACK HOLES ON THE BRANE

Htwe Nwe Oo [1], San San Maw [2], Zaw Shin[3], Thant Zin Naing[4]

Abstract

Gravitational collapse is assumed to be one of the main problems in general relativity and astrophysics. Using simple the Taylor expansion into the bulk and black string concept one can acquire acceptable “tidal charge” black hole and continue to explore “total tidal charge”, physical mass and energy for the modified Friedmann model. Some numerical works of the interesting equations are implemented.

Keywords: Gravitational collapse, tidal charge, black hole, Friedmann model.

Introduction

The physics of brane-world compact objects and gravitational collapse is complicated by a number of factors, especially the confinement of matter to the brane, while the gravitational field can access the extra dimension, and the nonlocal (from the brane viewpoint) gravitational interaction between the brane and the bulk. Extra-dimensional effects mean that the 4D matching conditions on the brane, i.e., continuity of the induced metric and extrinsic curvature across the 2-surface boundary, are much more complicated to implement. High-energy corrections increase the effective density and pressure of stellar and collapsing matter. In particular this means that the effective pressure does not in general vanish at the boundary 2-surface, changing the nature of the 4D matching conditions on the brane. The nonlocal KK (Kaluza and Klein) effects further complicate the matching problem on the brane, since they in general contribute to the effective radial pressure at the boundary 2-surface. Gravitational collapse inevitably produces energies high enough, i.e., $\rho \gg \lambda$, to make these corrections significant. We expect that extra-dimensional effects will be negligible outside the high-energy, shortrange regime.

The contribution of the massive KK modes sums to a correction of the 4D potential. For $r \ll \ell$, one obtains

$$\mathrm{V}\,(\mathrm{r}) \approx \frac{\mathrm{GM}\ell}{\mathrm{r}^2}, \tag{1}$$

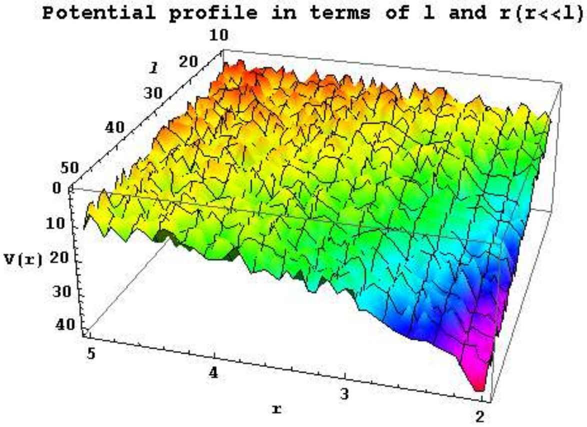

Figure 1 The Potential profile in terms of $l\ and\ r\ (r \ll \ell)$

---

[1] Dr, Assistant Lecturer, Department of Physics, Yangon University of Education.

[2] Dr, Assistant Lecturer, Department of Physics, West Yangon University.

[3] Dr, Lecturer, Department of Physics, University of Yangon.

[4] Dr, Retired Pro-Rector (Admin), International Theravāda Buddhist Missionary University, Yangon.

which simply reflects the fact that the potential becomes truly 5D on small scales.

For $r \gg \ell$,

$$\mathrm{V}\,(\mathrm{r}) \approx \frac{\mathrm{GM}}{r}\left(1 + \frac{2\ell^2}{3\mathrm{r}^2}\right), \tag{2}$$

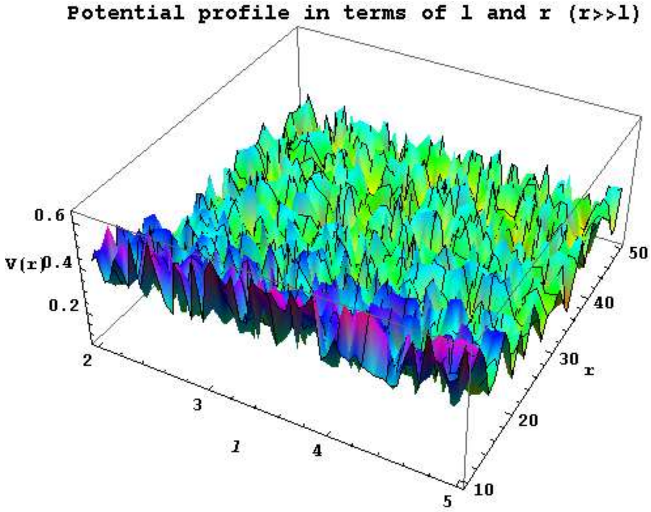

Figure 2 The Potential profile in terms of l and r ($\mathrm{r} \gg \ell$)

which gives the small correction to 4D gravity at low energies from extra-dimensional effects. These effects serve to slightly strengthen the gravitational field, as expected.

A vacuum on the brane, outside a star or black hole, satisfies the brane field equations

$$R_{\mu\nu} = -\mathcal{E}_{\mu\nu}\,, \qquad R^{\mu}_{\mu} = 0 = \mathcal{E}^{\mu}_{\mu}\,, \qquad \nabla^{\nu}\,\mathcal{E}_{\mu\nu} = 0. \tag{3}$$

The Weyl term $\mathcal{E}_{\mu\nu}$ will carry an imprint of high-energy effects that source KK modes. This means that high-energy stars and the process of gravitational collapse will in general lead to deviations from the 4D general relativity problem. The weak-field limit for a static spherical source, Equation (2), shows that $\mathcal{E}_{\mu\nu}$ must be on zero, since this is the term responsible for the corrections to the Newtonian potential.

The black string

The projected Weyl term vanishes in the simplest candidate for a black hole solution. This is obtained by assuming the exact Schwarzschild form for the induced brane metric and "stacking" it into the extra dimension,

$${}^{(5)}ds^2 = e^{-2|y|/\ell}\tilde{g}_{\mu\nu}dx^{\mu}dx^{\nu} + dy^2\,, \tag{4}$$

$$\tilde{g}_{\mu\nu} = e^{2|y|/\ell}g_{\mu\nu} = -(1 - 2GM/r)dt^2 + \frac{dr^2}{1 - 2GM/r} + r^2 d\Omega^2. \tag{5}$$

Each $\{y = \text{const.}\}$ surface is a 4D Schwarzschild spacetime, and there is a line singularity along $r = 0$ for all y. This solution is known as the Schwarzschild black string, which is clearly not localized on the brane $y = 0$. Although ${}^{(5)}C_{ABCD} \neq 0$, the projection of the bulk Weyl tensor along the brane is zero, since there is no correction to the 4D gravitational potential:

$$V\,(r) = \frac{GM}{r} \quad \Rightarrow \mathcal{E}_{\mu\nu} \;=\; 0. \tag{6}$$

The violation of the perturbative corrections to the potential signals some kind of non-AdS$_5$ pathology in the bulk. Indeed, the 5D curvature is unbounded at the Cauchy horizon, as $y \rightarrow \infty$:

$${}^{(5)}R_{ABCD}\,{}^{(5)}R^{ABCD} \;= \frac{40}{l^4} + \frac{48G^2M^2}{r^6}\; e^{4|y|/\ell}. \tag{7}$$

Taylor expansion into the bulk

One can use a Taylor expansion equation, in order to probe properties of a static black hole on the brane. For a vacuum brane metric,

$$\tilde{g}_{\mu\nu}(x,y) = \tilde{g}_{\mu\nu}(x,0) - \;\mathcal{E}_{\mu\nu}(x,0+)y^2 \;-\frac{2}{\ell}\mathcal{E}_{\mu\nu}(x,0+)|y|^3$$

$$+\frac{1}{12}\left[\mathcal{E}_{\mu\nu} \;-\frac{32}{\ell^2}\mathcal{E}_{\mu\nu} \;+\; 2R_{\mu\alpha\nu\beta}\mathcal{E}^{\alpha\beta} \;+\; 6\mathcal{E}_{\mu}{}^{\alpha}\mathcal{E}_{\alpha\nu}\right]_{y=0+} y^4 + \ldots \tag{8}$$

this shows in particular that the propagating effect of 5D gravity arises only at the fourth order of the expansion. For a static spherical metric on the brane,

$$\tilde{g}_{\mu\nu}dx^{\mu}dx^{\nu} \;=\; -F(r)dt^2 \;+\frac{dr^2}{H(r)} + \; r^2 d\Omega^2, \tag{9}$$

the projected Weyl term on the brane is given by

$$\mathcal{E}_{00} = \frac{F}{r}\left[H' \;-\frac{1-H}{r}\right], \tag{10}$$

$$\mathcal{E}_{rr} \;=\; -\frac{1}{rH}\left[\frac{F'}{F} - \frac{1-H}{r}\right], \tag{11}$$

$$\mathcal{E}_{\theta\theta} \;=\; -1 \;+\; H \;+\frac{r}{2}H\left(\frac{F'}{F} + \frac{H'}{H}\right). \tag{12}$$

These components allow one to evaluate the metric coefficients in Equation (8). For example, the area of the 5D horizon is determined by $\tilde{g}_{\theta\theta}$; defining $\psi(r)$ as the deviation from a Schwarzschild form for H, i.e.,

$$H(r) \;=\; 1 \;-\frac{2m}{r} + \;\psi(r), \tag{13}$$

where m is constant, one find

$$\tilde{g}_{\theta\theta}\,(r,y) = \; r^2 - \;\psi'^{\left(1+\frac{2}{\ell}|y|\right)y^{\,2}} + \frac{1}{6r^2}\left[\psi' + \frac{1}{2}(1 \;+\; \psi')(r\psi' - \;\psi)'\right]y^4 + \ldots \tag{14}$$

This shows how ψ and its r-derivatives determine the change in area of the horizon along the extra dimension. For the black string $\psi = 0$, and one has $\tilde{g}_{\theta\theta}(r,y) \;=\; r^2$. For a large black hole, with horizon scale $\gg \ell$, from Equation (2) that

$$\psi \;\approx\; -\frac{4m\ell^2}{3r^3}\,. \tag{15}$$

This implies that $\tilde{g}_{\theta\theta}$ is decreasing as we move off the brane, consistent with a pancake-like shape of the horizon. However, note that the horizon shape is tubular in Gaussian normal coordinates.

The "tidal charge" black hole

The equations (3) form a system of constraints on the brane in the stationary case, including the static spherical case, for which

$$\Theta = 0 = \omega_\mu = \sigma_{\mu\nu}, \qquad \dot{\rho}\mathcal{E} = 0 = q^{\mathcal{E}}_{\mu} = \dot{\pi}^{\mathcal{E}}_{\mu\nu}. \tag{16}$$

The nonlocal conservation equations $\nabla^{\nu}\mathcal{E}_{\mu\nu} = 0$ reduce to

$$\frac{1}{3}\vec{\nabla}_\mu \rho_{\mathcal{E}} + \frac{4}{3}\rho_{\mathcal{E}} A_\mu + \vec{\nabla}^{\nu}\pi^{\mathcal{E}}_{\mu\nu} + A^{\nu}\pi^{\mathcal{E}}_{\mu\nu} = 0, \tag{17}$$

where, by symmetry,

$$\pi^{\mathcal{E}}_{\mu\nu} = \Pi_{\mathcal{E}}\left(\frac{1}{3}h_{\mu\nu} - r_\mu r_\nu\right), \tag{18}$$

for some $\Pi_{\mathcal{E}}$ (r), with r_μ being the unit radial vector. The solution of the brane field equations requires the input of $\mathcal{E}_{\mu\nu}$ from the 5D solution. In the absence of a 5D solution, one can make an assumption about $\mathcal{E}_{\mu\nu}$ or $g_{\mu\nu}$ to close the 4D equations.

If one assume a metric on the brane of Schwarzschild-like form, i.e., $H = F$ in Equation (9), then the general solution of the brane field equations is

$$F = 1 - \frac{2GM}{r} + \frac{2G\ell Q}{r^2}, \tag{19}$$

$$\mathcal{E}_{\mu\nu} = -\frac{2G\ell Q}{r^4}\left[u_\mu u_\nu - 2r_\mu r_\nu + h_{\mu\nu}\right], \tag{20}$$

where Q is a constant. It follows that the KK energy density and anisotropic stress scalar are given by

$$\rho_{\mathcal{E}} = \frac{lQ}{4\pi r^4} = \frac{1}{2}\Pi_{\mathcal{E}}. \tag{21}$$

The solution (19) has the form of the general relativity Reissner–Nordstrom solution, but there is no electric field on the brane. Instead, the nonlocal Coulomb effects imprinted by the bulk Weyl tensor have induced a "tidal" charge parameter Q, where $Q = (M)$, since M is the source of the bulk Weyl field. We can think of the gravitational field of M being "reflected back" on the brane by the negative bulk cosmological constant. If one impose the small-scale perturbative limit ($r \ll \ell$) in Equation (1), one find that

$$Q = -2M. \tag{22}$$

Negative Q is in accord with the intuitive idea that the tidal charge strengthens the gravitational field, since it arises from the source mass M on the brane. By contrast, in the Reissner–Nordstrom solution of general relativity, $Q \propto +q^2$, where q is the electric charge and this weakens the gravitational field. Negative tidal charge also preserves the spacelike nature of the singularity, and it means that there is only one horizon on the brane, outside the Schwarzschild horizon:

$$r_h = GM\left[1 + \sqrt{1 - \frac{2\ell Q}{GM^2}}\right] = GM\left[1 + \sqrt{1 + \frac{4\ell}{GM}}\right]. \tag{23}$$

The tidal-charge black hole metric does not satisfy the far-field r^{-3} correction to the gravitational potential, as in Equation (2), and therefore cannot describe the end-state of collapse.

However, Equation (19) shows the correct 5D behavior of the potential ($\propto r^{-2}$) at short distances, so that the tidal-charge metric could be a good approximation in the strong-field regime for small black holes.

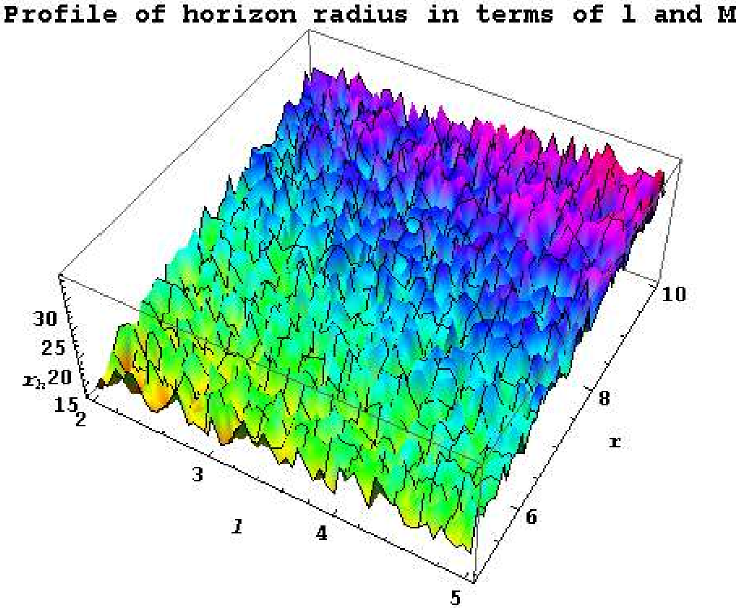

Figure 3 The profile of horizon radius in terms of $l \; and \; M$

It has not considered any back-reaction on the brane metric, and the same flux will reasonably be seen by a distant observer for whom ∂τ asymptotically becomes a time-like Killing vector. However, the surplus energy must be released, since no BW or GR model can explain the Weyl anomaly, and this directly implies that probably holds only for a short time about the formation of the horizon.

Gravitational collapse on the brane

In this section we will study a continuous model for the gravitational collapse. One consider a Tolman-like model with a central (Oppenheimer-Snyder model) OS core. The star is therefore described as a cloud of dust with falling off continuous density and no sharp boundary. The classical four-dimensional behavior will be recovered in the limit of negligible star density (with respect to the brane vacuum energy density λ).

The BW effective four-dimensional Einstein equations with vanishing cosmological constant on the brane as

$$G_{\mu\nu} = 8\pi T^{eff}_{\mu\nu} \tag{24}$$

Here one have

$$T^{eff}_{\mu\nu} = \rho^{eff} u_\mu u_\nu + p^{eff} h_{\mu\nu} + q^{eff}_{(\mu u_\nu)} + \pi^{eff}_{\mu\nu}, \tag{25}$$

where u^μ is the unit four-velocity of matter ($u^\mu u_\mu = -1$), $h_{\mu\nu}$ the space-like metric that projects orthogonally to u^μ ($h_{\mu\nu} = g_{\mu\nu} + u_\mu u_\nu$) and $\pi^{eff}_{\mu\nu}$ an anisotropic tensor.

For an isotropic perfect fluid, BW corrections to GR are described by the effective quantities

$$\rho^{\mathrm{eff}} = \rho\,(1 + \frac{\rho}{2\lambda} + \frac{u}{\rho}) \tag{26}$$

$$\mathrm{P}^{\mathrm{eff}} = \rho\,(\frac{\rho}{2\lambda}(2\mathrm{p} + \rho) + \frac{u}{3}) \tag{27}$$

$$\mathrm{q}_{\mu}^{\mathrm{eff}} = \mathrm{Q}_{\mu} \tag{28}$$

$$\pi_{\mu\nu}^{\mathrm{eff}} = \Pi_{\mu\nu,} \tag{29}$$

where ρ and p are the ("bare") energy density and pressure of matter. One also employed the following decomposition of the projection of the Weyl tensor on the brane (T.Clifon et al., 2017)

$$-\frac{1}{8\pi}\varepsilon_{\mu\nu} = \mathrm{u}\left(\mathrm{u}_{\mu}\mathrm{u}_{\nu} + \frac{1}{3}\mathrm{h}_{\mu\nu}\right) + \mathrm{Q}_{\mu}\mathrm{u}_{\nu} + \mathrm{Q}_{\nu}\mathrm{u}_{\mu} + \Pi_{\mu\nu}, \tag{30}$$

corresponding to an effective "dark" radiation on the brane with energy density U, pressure U/3, momentum density Q_{μ} and anisotropic stress $\Pi_{\mu\nu}$. Note that non-local bulk effects can contribute to effective imperfect fluid terms even when brane matter is a perfect fluid. Bianchi identities supplied by the junction conditions produce two kinds of conservation equations:

1. Local conservation equations (LCE):

$$\dot{\rho} + \theta(\rho + \mathrm{p}) = 0 \tag{31}$$

$$\mathrm{D}_{\mathrm{a}}\mathrm{p} + (\rho + \mathrm{p})\mathrm{A}_{\mathrm{a}} = 0 \tag{32}$$

2. Non-local conservation equations (NLCE's):

$$\dot{u} + \frac{4}{3}\theta u + \mathrm{D}^{\mathrm{a}}\mathrm{Q}_{\mathrm{a}} + 2\mathrm{A}^{\mathrm{a}}\mathrm{Q}_{\mathrm{a}} + \sigma^{\mathrm{ab}}\Pi_{\mathrm{ab}} = 0 \tag{33}$$

$$\dot{\mathrm{Q}}_{\mathrm{a}} + \frac{4}{3}\theta\mathrm{Q}_{\mathrm{a}} + \frac{1}{3}\,\mathrm{D}_{\mathrm{a}}u + \frac{4}{3}u\mathrm{A}_{\mathrm{a}} + \mathrm{D}^{\mathrm{b}}\Pi_{\mathrm{ab}} + \mathrm{A}^{\mathrm{b}}\Pi_{\mathrm{ab}} + \sigma_{\mathrm{a}}^{\mathrm{b}}\mathrm{Q}_{\mathrm{b}} - \omega_{\mathrm{a}}^{\mathrm{b}}\mathrm{Q}_{\mathrm{b}} = -\frac{\rho + \mathrm{p}}{\lambda}\mathrm{D}_{\mathrm{a}}\rho \tag{34}$$

where D_{a} is the spatially projected derivative (defined by $\mathrm{D}_{\mathrm{a}}\mathrm{S}^{\mathrm{b}}{}_{\ldots\ldots\mathrm{c}} = \mathrm{h}^{\mathrm{e}}{}_{\mathrm{a}}\,\mathrm{h}^{\mathrm{b}}{}_{\mathrm{f}} \ldots \ldots \mathrm{h}^{\mathrm{g}}{}_{\mathrm{c}}\nabla_{\mathrm{e}}\mathrm{S}^{\mathrm{f}}{}_{\ldots\ \ldots\mathrm{g}}$ for a = 1, 2, 3), $\theta = \nabla^{\alpha}\mathrm{u}_{\alpha}$ the volume expansion, $\dot{\mathrm{S}}^{\mathrm{a}}{}_{\ldots\ldots\mathrm{b}} = u^{\alpha}\,\nabla_{\alpha}\mathrm{S}^{\mathrm{a}\ldots}{}_{\ldots\mathrm{b}}$ the proper time derivative, $\mathrm{A}_{\mathrm{a}} = \dot{u}_{\mathrm{a}}$ the acceleration, $\sigma_{\mathrm{ab}} = \mathrm{D}(_{\mathrm{a}}u_{\mathrm{b}}) - (\theta/3)\,\mathrm{h}_{\mathrm{ab}}$ the (traceless) shear, and $\omega_{\mathrm{ab}} = -\mathrm{D}[_{\mathrm{a}}u_{\mathrm{b}}]$ the vorticity.

Spherically symmetric dust

For the case with zero pressure (p = 0), that is dust on the brane, the quantities in Eqs. (26), (27) and (29) reduce to

$$\rho^{eff} = \rho\left(1 + \frac{\rho}{2\lambda}\right) + u \tag{35}$$

$$\rho^{eff} = \frac{\rho^2}{2\lambda} + \frac{u}{3} \tag{36}$$

$$\pi_{\mu\nu}^{eff} = \Pi_{\mu\nu} \tag{37}$$

Provided the matter density ρ does not vanish in the region of interest, one can use comoving coordinates in which $u^{\alpha} = (-1, 0, 0, 0)$. In the following, only consider the class of five-dimensional metrics which are diagonal (sufficiently close to the brane at y = 0) and spherically symmetric on the brane. In Gaussian normal coordinates, one can always write a bulk metric which is spherically symmetric on the brane as

$$ds^2 = -N^2(\tau,r,y)d\tau^2 + A^2(\tau,r\,y)dr^2 + 2B(\tau,r\,y)dt\,dr + R^2(\tau,r,y)d\Omega^2 + dy^2 \quad (38)$$

Upon using the restricted freedom to change the four- dimensional coordinates on the brane, one can always set B(τ, r, 0^+) = 0 [3], so that the brane metric reads

$$ds^2{}_{y=0^+}\Big| = -N^2(\tau,r,0^+)dr^2 + A^2(\tau,r,0^+)dr^2 + R^2(\tau,r,0^+)d\Omega^2 \quad (39)$$

Since just consider dust as brane matter, from the junction conditions at the brane, one also obtain

$$0 = K^{+}_{\tau,r}(\tau,r) \equiv \frac{1}{2}\frac{\partial g_{\tau r}}{\partial y}\Big|_{y=0^+} = \frac{\partial B}{\partial y}\Big|_{y=0^+} = 0. \quad (40)$$

Using the above result together with the bulk symmetry Z_2 with respect to the brane, we have B(τ, r, y) = y^2 [V (τ, r) + O(y)]. Since the Weyl energy flux is related to B by

$$Q_a \sim \frac{\partial^2 B}{\partial y^2}\Big|_{y=0^+} \quad (41)$$

one finds that Q_a vanishes if V (τ, r) = 0, which is in fact what we are assuming. The coefficient $g_{\tau r}$ then vanishes fast enough on the brane so that, from the five-dimensional Einstein equations

$$G_{AB} = -\Lambda g_{AB}\,, \quad (42)$$

in the limit y → 0^+, one obtains the condition

$$0 = G_{\tau r}\Big|_{y=0^+} = \frac{2}{NA}\left(\frac{\dot{A}}{A}\frac{R'}{R} + \frac{\dot{R}}{R}\frac{N'}{N} - \frac{R'}{R}\right)_{y=0^+}\Big| \quad (43)$$

where a prime denotes ∂_r and a dot ∂τ . Since our matter is pressure less, one can work in the proper time gauge N(τ, r, 0^+) = 1 [3] and, using the residual gauge freedom in defining the radial coordinate r, one obtain

$$A(\tau,r,0^+) = R'(\tau,r,0^+). \quad (44)$$

This relation implies a Tolman geometry on the brane

$$ds^2 = -dr^2 + R'^2 dr^2 + R^2 d\Omega^2, \quad (45)$$

where R = R(τ, r) is a (generally non-separable) function of τ and r such that 4πR^2(τ, r) equals he surface area of the shell comoving with dust particles located at the coordinate position r at the proper time τ. With the above symmetries, the vorticity, the acceleration and the Weyl energy flux vanish, $\omega_a = A_a = Q_a = 0$, and one obtain the simplified

LCE

$$\partial_\tau \rho + \theta\rho = 0 \quad (46)$$

And NLCE's

$$\partial_\tau u + \frac{4}{3}\theta u + \sigma^{ab}\Pi_{ab} = 0 \quad (47)$$

$$\frac{1}{3}D_a u + D^b \Pi_{ab} = -\frac{\rho}{\lambda}D_a\rho. \quad (48)$$

The volume expansion is also easily computed as

$$\theta = \partial_r \lfloor ln(R^2 \partial_r R) \rfloor = \frac{\partial_\tau \partial_r (R^3)}{\partial_r (R^3)}, \qquad (49)$$

and for the shear one finds

$$\sigma_{ab} = \frac{1}{2} \partial_\tau h_{ab} - \frac{\theta}{3} h_{ab} , \qquad (50)$$

where $h_{ab} = g_{ab}$ is the spatial part of the metric.

Conclusions

It has been attempted to show some of the key features of brane-world gravity from the perspective of astrophysics and cosmology, emphasizing a geometric approach to dynamics and perturbations. Inspired by the conjecture that classical black holes in the BW may reproduce the semi classical behavior of four-dimensional black holes, one has studied the gravitational collapse of a spherical star of dust in the RS scenario in order to clarify the underlying dynamics that leads to this interpretation. Regularity of the bulk geometry requires continuity of the matter stress tensor on the brane and can lead to a loss of mass from the boundary of the star. One has in particular shown that, excluding energy fluxes coming from the bulk Weyl tensor, a collapsing spherical star must have a spatially anisotropic, although isotropic in the angular directions, atmosphere, in order to have asymptotically flat solutions. Interestingly, such a feature is also present in the stress tensor of quantum fields on the Schwarzschild background. In visualizing of the results, fluctuation factor of 30 to 40 percent has been taken into consideration.

Acknowledgement

I would like to thank Dr Khin Khin Win, Professor and Head, Department of Physics, University of Yangon, for her kind permission and encouragements to carry out this work.

I would like to thank Dr Pyone Pyone Aung, Pro-Rector, Yangon University of Education, for her kind permission and encouragements to carry out this work.

I would like to express my gratitude to Professor Dr Khin Swe Oo, Head of Department of Physics, Yangon University of Education, for her kind permission and encouragements to carry out this work.

Special thanks are due to Professor, Dr Thant Zin Naing, Retired Pro-rector (Admin), International Theravāda Buddhist Missionary University, for his valuable guidance and helpful advice to carry out this work.

References

Chamblin, A., Reall, H.S., Shinkai, H.A. and Shiromizu, T., (2001) "Charged brane-world blackholes", Phys. Rev. D, 63, 064015, 1–11.

Emparan, R., Horowitz, G.T. and Meyers, R.C., (2000) "Exact description of black holes on branes", J. High Energy Phys., 2000(01), 007.

Garriga, J. and Tanaka, T., (2000) "Gravity in the Randall–Sundrum Brane World", Phys. Rev. Lett., 84, 2778–2781.

L. Landau and E.M Lifshitz, (1980) "The classical theory of fields", 4th edition, Butterworth-Heinemann.

M. Bruni, C. Germani and R. Maartens, (2001) Phys. Rev. Lett. 87, 231302.

R. Maartens and Kazuya Koyama, (2010) "Brane-World Gravity", Living Rev. Relativity, 13.

Shiromizu, T. and Shibata, M., (2000) "Black holes in the brane world: Time symmetric initialdata", Phys. Rev. D, 62, 127502, 1–4.

T. Clifton, Daniele Gregoris and Kjell Rosquist, (2017) "The magnetic part of the Weyl tensor, and the expansion of discrite universes", http://creativecommons.org/licenses/by/4.0/

J. Myanmar Acad. Arts Sci. 2020 **Vol. XVIII.No.2A**

SYNTHESIS AND CHARACTERIZATION OF GRAPHENE OXIDE FILM

Su Su Lwin[1], Zayar Pyae Phyo Aung[2], Yin Maung Maung[3], Than Than Win[4]

Abstract

This research studied the synthesis of graphene oxide via a low-cost manufacturing method. The process started with the chemical oxidation of commercial graphite powder into graphene oxide (GO) by Hammer's method. It is proven that this method is promising way to synthesize graphene oxide on a large scale. GO nanocomposites thin films have been successfully deposited on ITO glass substrate. The films were deposited by spin coating method and heat treated at 80°C for 24 h. The synthesized graphene oxide was analyzed by X-ray diffraction (XRD), Energy dispersive X-ray (EDX), Fourier Transform Infrared spectroscopy (FTIR), UV-Vis spectroscopy and Field Emission Scanning Electron Microscopy (FESEM). The XRD pattern reveled a (0 0 1) diffraction peak, signifying the successful synthesis of GO. The elemental composition of GO was characterized by EDX analysis. The content of C is 67.35 % and the content of O is 29.75%. The mass ratio of C/O is 2.26. The results of FT-IR showed that C-O bond, O-H group with water molecules and C=C bond with graphene oxide. UV-Vis spectra of GO exhibited maximum absorption peak at 290 nm. SEM image confirmed that the size and synthesis of GO particles.

Keywords: Graphene oxide (GO), EDX, Hammer's method, SEM, XRD, FTIR

Introduction

Graphene is one atom layer thick carbon sheet. Graphene exhibits many interesting electronic, optical and mechanical properties due to its two-dimensional (2D) crystal structure [Avery Luedtke et al (2011)]. The charge carriers of graphene (i.e: electron) move ballistic in the 2D crystal lattice of graphene; hence it processes high conductivity despite it being an organic compound [Gianchang Li et al (2014) & F.Y. Ban et al (2012)]. Until 2004, Novoselov and Geim in the University of Manchester firstly separated the single graphene from graphite through separated simple mechanical peeling method. Graphene was increasing more and more attention in various areas of science and technology due to its remarkable physicochemical properties [Mohammed Dhenfouch et al (2014) & Jie Gao et al (2013)]. Currently, many methods had been explored to prepare graphene. Different graphene preparation method have been developed, such as chemical vapour deposition (CVD), microchemical exfoliation of graphite, epitaxial growth, chemical intercalation, and the reduction of graphene oxide. Among these methods, preparation of graphene from GO reducing has attracted considerable attention as a potential materials for use in various industrial application since it is unique cost advantage and promising for the mass-production of graphene based materials [Won-Chun OH et al (2010) &Hongiyan Sun et al (2014)]. Graphene oxide is chemically similar to graphite oxide in that its surface carries many functional groups, such as C=O, O-H and –COOH. However, there are essential structural differences between graphene oxide and graphite oxide. For example, graphite oxide possesses a laminated structure, while graphene oxide does not; graphene oxide has a structure composed of one or more sheet layers peeled from GO [TataoQian et al (2013)].

Several electronic devices have been fabrication using GO as a starting material for at least one of the components. One such device is a graphene based field effect transistor [Prasanna

---

[1] Dr, Demonstrator, Department of Physics, Myeik University, Myanmar

[2] Demonstrator, Department of Physics, Myeik University, Myanmar

[3] Professor, Department of Physics, University of Yangon, Myanmar

[4] Professor, Department of Physics, Panglong University, Myanmar

Kumar et al (2014) &Vorrada Loryuen Yong et al (2013)]. Visible light transparent electrodes are important for both light emitting diodes (LEDs) and solar cell devices. Since GO can be processed in solution, using reduced graphene oxide (rGO) as transparent electrode is a convenient alternative to other transparent electrodes such as ITO for these devices [Hongiyan Sun et al (2011)]. In addition to being a transparent electrode, rGO has been used as a hole transport layer in polymer solar cells and LEDs [Nils Krame (2014)]. Nanocomposites of rGO have been used for high capacity energy storage in lithium ion batteries. In these studies, electrically insulating metal oxide nanoparticles were absorbed onto rGO to increase the performance of these materials in batteries [Zulmi Mo et al (2012) &Weifeng Zhao et al (2010)]. One use of GO in the biomedical field is as a component in drug delivery systems. Functionalized nanographene oxide has been used in several studies on targeted deliverly of anti-cancer drugs [Sungjin Park et al (2009), Jianjuo Song et al (2014) and Zhigang Xiong et al (2010)]. GO and rGO have been used as components in several systems designed to detect biologically relevant molecules. GO has been used as a fluorescence quenching material in biosensors which utilize the fluorescence energy transfer effect. Folic acid functionalized GO was used as a component in a system used to detect human cervical cancer and human breast cancer cells [Michael J. McAllister et al (2007), YunxianPiao et al (2011) & Mark Lundie (2014)].

In this study, graphene oxide (GO) was successfully synthesized by the Hummer's method. The structure of graphene oxide powders were measured by X-ray diffraction (XRD), Energy dispersive (EDX). Fourier transform infrared spectroscopy (FTIR) and the UV spectrometer will be used to measure the optical absorption properties of graphene oxide. The microscopic morphologies of GO powders were characterized by SEM.

Experimental Procedure

Sample preparation of GO powder

In this research, Graphite, Sulphuric acid (H_2SO_4), Sodium nitrate ($NaNO_3$), Phosphoric acid (H_3PO_4), Potassium permanganate ($KMnO_4$) and Hydrogen Peroxide (H_2O_2) were used as starting materials. All chemicals were analytically pure and directly used as received without further purification. Graphene oxide (GO) was prepared according to the Hummer method. In detail, 500 ml beaker was filled with 108 ml of H_2SO_4, 5 g of graphite, 2.5 g of $NaNO_3$ and 12 ml of H_3PO_4 were added into the beaker. The suspension was stirred in an ice bath for 10 min. Next, 15 g of $KMnO_4$ was added to the suspension. The rate of addition was carefully controlled to keep the reaction temperature below 5 ˚C and stirred in ice bath for 3 h. Then the mixture was put in a 40 ˚C water bath for 60 min. The temperature of the mixture was adjusted to a constant 98 ˚C for 60 min while water was added continuously. The color of the mixture was changed into yellow. Deionized water was further added so that the volume of the suspension was 400 ml. 15 ml of H_2O_2 was added after 5 min. The reaction product was washed by rinsing and centrifugation with 5 % HCl then deionized (DI) water for several times to reach pH 5-7. Finally, the product was dried at 60 ˚C for 24 h in a vacuum oven. The obtained samples were characterized by X-ray diffraction (XRD) using (Rigaku RINT 2000) and Energy dispersive X-ray (EDX). Fourier transform infrared spectroscopy (FTIR). UV-Vis spectrometer (UV-Vis; UV-1800) was used to measure the optical absorption properties of GO. The nano structure was confirmed by scanning electron microscope (FESEM).

Cleaning of the Substrate

In the present study ITO/glass, cut into 1×1 cm square plates have been used as substrates. Prior to deposition the substrates are subjected to the following cleaning process to remove the unwanted impurities normally present on the surfaces of the glass plates exposed to the atmosphere.

1. The glass substrates are washed in soap solution by scrubbing the surfaces with a cotton swab dipped in liquid soap.
2. The glass slides are then rinsed thoroughly in deionized water to remove any trace of the soap solution left on the surface followed by acetone rinsing.
3. Then the slides are soaked in HCl acid and kept in room temperature for about two hours.
4. Finally, the substrates are rinsed thoroughly in deionized water and dried at 100°C for one hour in an oven.

Preparation of GO Paste and Spin Coating of GO Film

The GO film was prepared by spin coating method. Firstly, the GO paste was prepared bysimple mechanical stirring followed by ultra-sonication. 1 g of graphene oxide was added in 100 ml of distilled water and stirred by magnetic stirrer for 1 h. After stirring, the GO solution was ultrasonicated for 1 h and stirred by magnetic stirrer at 80 °C for 6 h, then centrifuged and washed with ethanol for several times to remove the undecorated particle and unreacted chemicals. Finally, the GO paste was obtained and it was deposited onto the ITO glass substrate by spin coating technique. The structural properties of the film was measured byscanning electron microscope (SEM).

Results and Discussion

The XRD pattern of graphite and graphene oxide were shown in figure 1(a) and 1(b).According to the XRD pattern of graphite, which showed a strong and sharp diffraction peak at $2\theta=26.61°$ has the interplanar distance of 0.334 nm. The graphene oxide were matched with standard library file 03-065-1528. GO shows an intense and sharp peak at $2\theta=11.07°$ has the interplanar distance of 0.799 nm. The increase in interplanar distance of GO is due to the existence of oxygen functional groups. The sharp peak at 2θ value of graphene oxide for observed sample and 2θ value of graphene oxide in international journals were compared in table 1.

2θ (deg)	**International Journal**
10.34°	Won-Chun Oh et al 2010 Journal of the Korean Physical Society, Vol. 56, No. 4, pp. 1097~1102 [30]
10.6°	JieGao et al , 2013 Polymer-Plastics Technology and Engineering, 52: 553–557, [40].
10.24°	F.Y. Ban et al 2012 Int. J. Electrochem, Sci., 7 4345 -4351 [28].

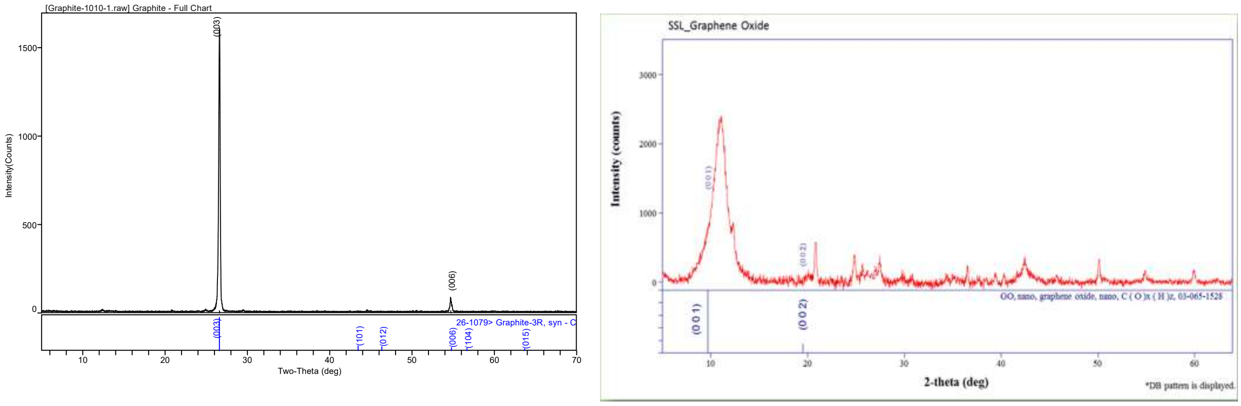

Figure 1 XRD pattern of (a) graphite and (b) graphene oxide

EDX Analysis of Graphene Oxide (GO)

The EDX figure of graphene oxide was shown in figure 2 and the results of the EDX elemental for C and O elements of GO are listed in table 2. The content of C is 67.35 % and the content of O is 29.75%. The mass ratio of C/O is 2.26. The presence of higher amount of carbon and oxygen. The oxygen and carbon peaks are then converted into a percentage, which has been used to set the current graphene oxide composition specification. Other elements were found as impurities. The percentage presence of normal concentration and atomic concentration is given accordingly. The international results of EDX for graphene oxide are listed in table 3.

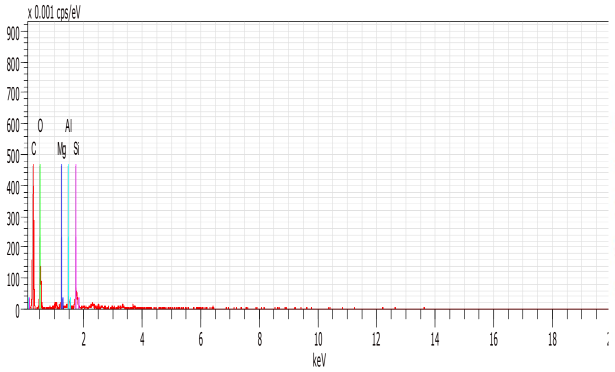

Figure 2 EDX spectrum of graphene oxide

```
             [wt.%]   [wt.%]   [at.%]  [wt.%]
---------------------------------------------
C   6  K-series  67.35   67.35   74.03   13.5
O   8  K-series  29.75   29.75   24.55    8.2
Mg 12  K-series   0.53    0.53    0.29    0.1
Al 13  K-series   0.71    0.71    0.35    0.1
Si 14  K-series   1.67    1.67    0.79    0.2
---------------------------------------------
           Total: 100.00  100.00  100.00
```

Table 2 The results of the EDX elemental for C and O elements of GO

Table 3 The EDX elemental microanalyses for C and O elements in international journals

Element (wt. %)		C/O	International Journals
C	O		
51.32	44.27	1.15	Won-Chun Oh, et al., 2010 Journal of the Korean Physical Society, Vol. 56, No. 4, pp. 1097~1102 [30].
65.47	35.53	1.84	Yunxian Piao, et al., 2011 The Royal Society of Chemistry [39].
67.35	29.75	2.26	Observed sample

FTIR Analysis of Graphene Oxide (GO)

Infrared absorption spectrum diagram (FTIR) of graphene oxide was shown in figure 3. FTIR analysis allows qualitative discussion of the structure of graphene oxide. According to the FTIR analysis the peak at 1082.10 cm^{-1} and 1384.94 cm^{-1} which are attributed to the C-O bond, confirming the presence of oxide functional groups after the oxidation process. The peak at 1626.05 cm^{-1} can be attributed to the stretching vibration of C=C bond. The 3408.33 cm^{-1} correspond to O-H group of water molecules absorbed on graphene oxide. The presence of these oxygen containing groups reveals that the graphite has been oxidized.

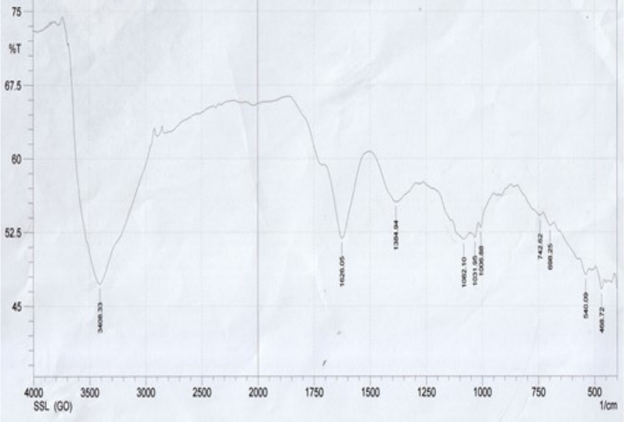

Figure 3 FTIR spectrum of graphene oxide

UV-Visible Analysis

The UV-Vis spectra of GO powder was recorded with respect to the glass substrate placed in the reference beam using beam spectrometer in the range 190 to 1100 nm. The absorption spectrum of GO deposited on glass substrate is shown in figure 4 (a). The figure shows high absorption coefficient in the UV region. [In aqueous suspension, measurements reveal strong optical absorption in the UV (Mark Lundie et al)]. The optical band energy (E_g) of the semiconductor is calculated from the Tauc relation. The resultant values of E_g for GO is found to be about 3.93 eV.

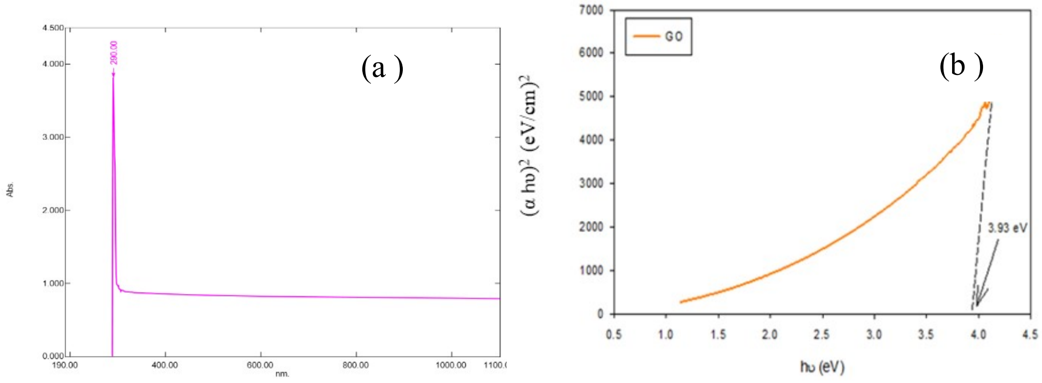

Figure 4 The UV absorption spectrum (a) and Plot of $(\alpha h\upsilon)^2$ vs. photon energy ($h\upsilon$) for graphene oxide (b)

SEM Analysis bof Graphene Oxide (GO)

Figure 5 presented the SEM image of the synthesized graphene oxide, revealing a crumpled and rippled structure which was the result of deformation upon the exfoliation and restacking processes. Moreover, it indicating flaky nature, randomly folded, few-layered and exfoliated structure. Surface of the graphene oxide was rough with some crumpling and agglomeration, which may be attributed to the residual oxygen containing functional groups (e.g. -OH). This further shows strong oxidation of graphite by the Hummers method. From the figure 5 (b) GO film, it can be observed that graphene oxide film has layered structure, which affords ultrathin graphene sheet. Such sheets are folded or continuous at times and it is possible to distinguish the edges of individual sheets, including kinked and wrinkled areas. Moreover, the GO sample contain several layers of aggregated and square-shaped crumpled sheets closely associated with each other to form a continuous conducting network. The edges of the GO sheets become crumpled, folded, and closely restacked, and the surface of GO exhibits a soft carpet-like morphology, possibly because of the presence of residual H_2O molecules and hydroxyl groups.

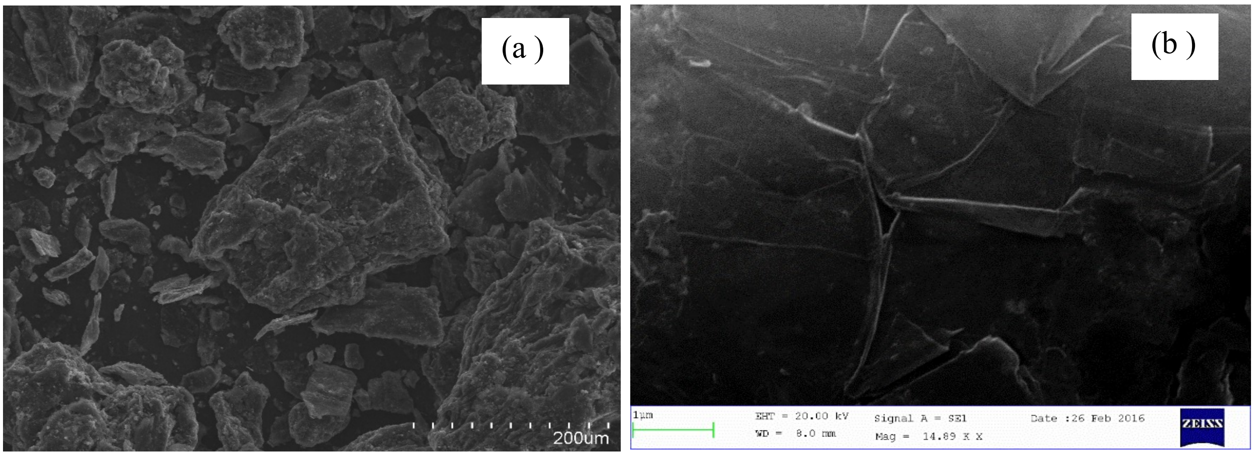

Figure 5 SEM image of Graphene Oxide powder (a) and film (b)

Conclusion

The graphene oxide (GO) have been successfully synthesized by using Hummer's method. The graphene oxide was characterized using XRD, EDX, FTIR, UV-Vis and FESEM. In XRD analysis the graphene oxide were matched with standard library file 03-065-1528. The increase in interplanar distance of GO is due to the existence of oxygen functional groups. The content of C is 67.35 % and the content of O is 29.75%. The mass ratio of C/O is 2.26. According to the FTIR analysis, the –OH groups were be found and the presence of these oxygen containing groups reveals that the graphite has been oxidized. UV-Vis spectra of GO exhibited maximum absorption peak at 290 nm. According to the SEM analysis, surface of the graphene oxide was rough with some crumpling and agglomeration, which may be attributed to the residual oxygen containing functional groups (e.g. -OH). According to the SEM image of GO film, the sample was well deposited onto the ITO glass substrate and it was proved that the spin coating technique was suitable in the preparation of GO film. The characterization results proved that there was an interaction between starting chemicals.

Acknowledgements

I wish to express my profound thanks to Dr Ni Ni Oo, Rector of Myeik University for her kind permission to carry out this work. The authors also would like to express gratitude to Dr Win Win Than, Pro-Rector of Myeik University. The author also acknowledge the support of Professor Dr Khin Khin Win, Head of Department of Physics and University of Yangon. Moreover, I am greatly indebted to Professor Dr Yin Yin Myint, Head of Department of Physics, Myeik University, for her help with experimental work and discussion.

References

Avery Luedtke, (2012) "Applications of Graphene Oxide and Reduced Graphene Oxide", Aldrich Materials Science, Sigma-Aldrich Co. LLC.

F.Y.Ban, S.R. Majid, N.M. Haung, H.N.Lim, (2012) "Graphene Oxide and Its Electrochemical Performance", Int. J. Electrochem. Sci., 7 4345.

Hongjuan Sun, Yonghui Yang & Qiao Huang (2011) "Preparation and Structural Variation of Graphite Oxide and Graphene Oxide", Intergral Ferroelectric, 128 163.

Hongiyan Sun, Shunjia Lin, Tongjang Peng & Bo Liu (2014) "Microstructure and Spectral Characteristic of Graphene Oxide during Reducion", Intergrated Ferroelectric, 151 21.

JieGao, Kaiyan Shen, Feng Bao, Jing Yin, Dongfang Wang & Ruima (2013)" Preparation and Characterization of a Graphene Oxide film Modified by the Covalent Attachment of Polysiloxanc" Polyma Plastic and Engineering, 52 553.

Jianchang Li, XiangqionZeng (2014) "The Preparation of Graphene Oxide and Its Derivatives and Their Application Bio-Tribological Systems" Lubricants, 2 137-161.

JianJuo Song, Xinzhi Wang & Chang-Taung Chang (2014) "Preparation and Characterization of Graphene Oxide", 6 276143.

Mohammed Dhenfouch, U. Buttern (2014) "Synthesis and Characterization of Mass Produced High Quality Few Layered Graphene Sheets via a Chemical Method", Scientific Research, 3 7-13.

Mark Lundie, Zejko Sijivancainn & Stanko Tomic (2014) "Analysis of energy gap Opening in Grphene Oxide", 526 012003.

Michael J. McAllister, Je-Luen Li (2007) "Single Sheet Functionalized Graphene By Oxidation and Thermal Expansion of Graphite" Articles, 31.

Nils Krane (2014) "Preparation of Graphene", Nils.Krane@fu-brlin.de.

Prasanna Kumar S. Mural, Aditi Banerjee (2014) "Polyolefin based antibacterial Membranes derived from PE/PEO blends comjjpatibilized with Amzine terminated graphene oxide and maleated PE", J. Mater.Chem A, 2.

Sungjin Park, Rodney S. Ruoff (2009) "Chemical methods for the production of Graphene", Nature Nanotechnology 132.

J. Myanmar Acad. Arts Sci. 2020 **Vol. XVIII.No.2A**

MATLAB IMPLEMENTATION AND ANALYSIS OF ELECTROCARDIOGRAM (ECG) SIGNALS

Yin Yin Myint[1], Win Zaw[2], Chit Po[3], Moe Thidar Myint[4], Myat Thu Zar[5]

Abstract

In this work, the MATLAB software has been developed to measure electrocardiogram (ECG) signal and to analyze the measured signals. The measurement system consists of three electrodes connected to the ECG sensor (AD8232), data acquisition card (Atmega328 Board) and a laptop-computer. The code for the data acquisition card is tested with the developed MATLAB software. The software includes acquisition of real time ECG data, ECG signal processing and calculating beat rate. The measured signals are recorded in the desired path of the computer. The results are compared with standard data and then show that the system yields equal results compared to the reference measurements for patients at rest. The usability of the system is excellent due to simple three-arm electrode solution. The system can be used for home health care application.

Keywords: ECG, AD8232 ECG Sensor, Arduino Uno, MATLAB Software, Data Acquisition

Introduction

Electrocardiogram (ECG) is a diagnostic tool that measures and records the electrical activity of the heart in detail. Interpretation of these details allows diagnosis of a wide range of heart conditions. An ECG is generated by a nerve impulse stimulus to a heart. The electrical activity of the heart can be recorded at the surface of the body using an electrocardiogram. Therefore the electro-cardio-gram (ECG) is simply a voltmeter that uses up to 12 different leads (electrodes) placed on designated areas of the body. Fig.1 shows the typical ECG measurement system with three electrodes (right arm [RA], left arm [LA] and right leg [RL]) to obtain the source of ECG in this work. Signals are acquired using AD8232 ECG pulse sensor via an Arduino Uno board (ATmega328). MATLAB software is developed and used for data recording and visualization, due to its known capabilities. Since ECG signals are very noisy, usually 50 Hz noise, this developed software is used to test and in order to obtain a good ECG sample of heart.

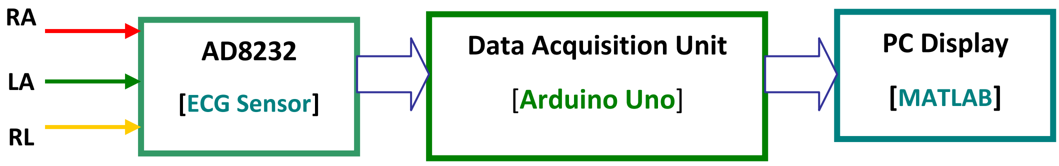

Figure 1 Typical ECG Measurement System

---

[1] Dr, Professor & Head, Department of Physics, Myeik University
[2] Associate Professor, Department of Physics, Myeik University
[3] Assistant Lecturer, Department of Physics, Myeik University
[4] Assistant Lecturer, Department of Physics, Myeik University
[5] Assistant Lecturer, Department of Physics, Myeik University

Hardware Interface

It is necessary to setup hardware support package for Arduino Uno in MATLAB software. To read the data from the Arduino Uno (Data Acquisition Unit), the support package for MATLAB was first installed from internet. After installing the support package for MATLAB, whether it is installed properly or not was checked by connecting the Arduino Uno (*Data Acquisition Unit*) to a Laptop**.**

Programming the Data Acquisition Unit

To interface (*communicate*) the DAU (Data Acquisition Unit), the sketch (downloaded program for Arduino Uno) was compiled and up loaded into the DAU. And then tested the DAU with a laptop whether it properly communicates or not.

Hardware Setup

The circuit connection for ECG measurement can be seen in fig. 2. The AD8232 ECG sensor was connected to DAU with their respective pins. To read analog data from the sensor, the output of the sensor was connected to the analog one (A1) pin of DAU.

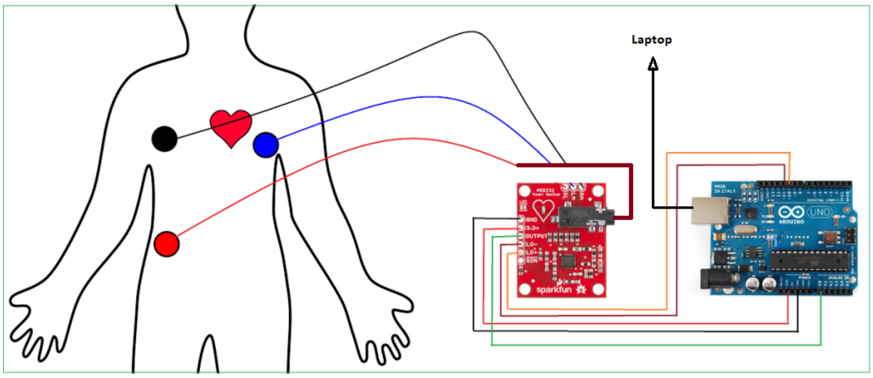

Figure 2 Connections for ECG Measurement System

Software Development

There are three sections in the MATLAB software development for ECG signals. They are real time data acquisition, signal filtering and zero-crossing detection for heart beat rate.

Real Time Data Acquisition

The program flow chart for real time data acquisition algorithm can be seen in fig. 3. In this section, when the program starts it sets the com port of data acquisition hardware (Arduino Uno Board) and the baud rate of serial transmission. Then the program reads sample data from the ECG sensor unit and converts the data into signal voltage. And then the program draws real time graph on the PC screen. After reading 500 sample data, it saves the real time data in the predefined location of the PC/ laptop.

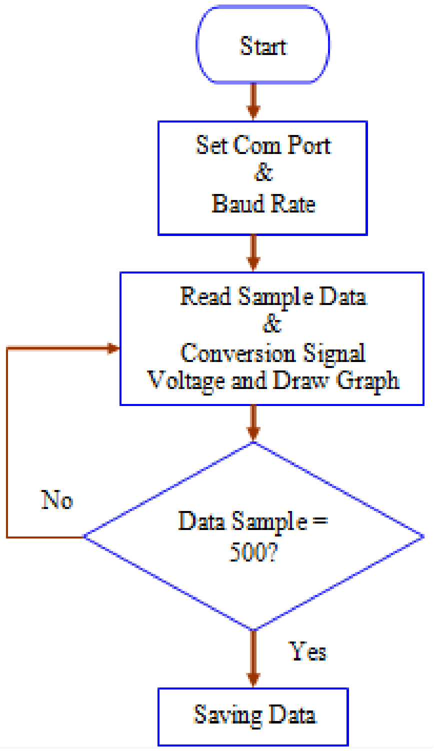

Figure 3 Flow Chart for Real Time Data Acquisition Algorithm

Signal Filtering

Hum noise created by poor power supplies, transformers, or electromagnetic interference sourced by a main power supply is characterized by a frequency of 50 Hz and its harmonics. If this noise interferes with a desired audio or biomedical signal (e.g., in electrocardiography [ECG]), the desired signal could be corrupted. The corrupted signal is useless without signal processing. It is sufficient to eliminate the 50-Hz hum frequency with its second and third harmonics in most practical applications. In this work, the window method FIR (Finite Impulse Response) low-pass filter was used to eliminate above the 25 Hz hum noises. The flow chart for signal filtering algorithm is shown in fig. 4. When the program starts, it sets the filter design as a low-pass filter. And then set the lower and upper cutoff frequencies. After all the settings, the program filters the signal using the '*firwd* and *filter*' functions. Next, it finds the amplitude of the filtered signal and plots the filtered and unfiltered signals.

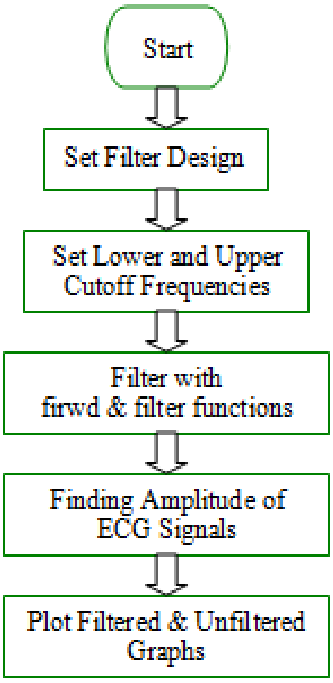

Figure 4 Flow Chart for Signal Filtering Algorithm

Zero-crossing Detection

In this section, the flow chart can be seen in fig. 5. With the processed ECG signal (*filtered signal*), a simple zero-cross algorithm was designed to detect the heart rate. The threshold value of - 0.5 Volt is used and continuously compares each of two consecutive samples with the threshold. If both results are opposite, then a zero crossing is detected and the number of zero crossing is calculated by using the formula. And then, heart rate (beat per minute, BPM) is also calculated and displayed the result on a PC/ Laptop screen.

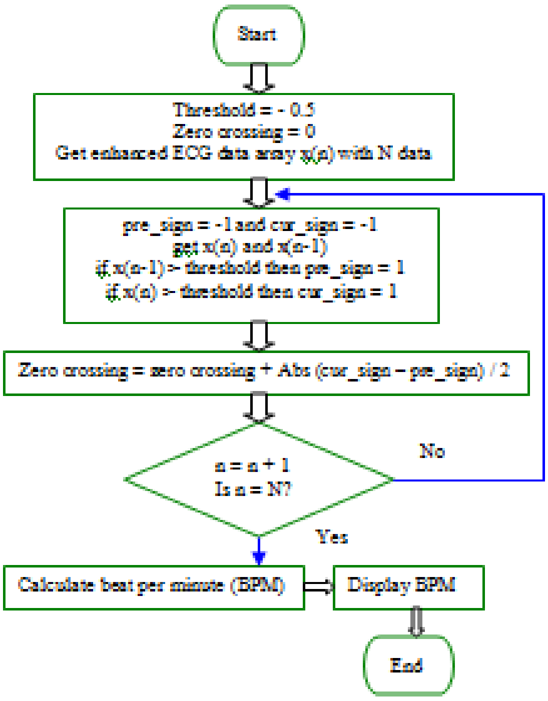

Figure 5 Flow Chart for Zero-crossing Detection Algorithm

Measurement and Analysis of ECG Signals

ECG Signal Acquisition

In this work, ECG signal is acquired from the described ECG system in the above section. Several measurements are made with different three points by using three ECG electrodes from the ECG sensor. Standard ECG electrodes and home made ECG electrodes (local copper electrode and oil) are used to measure ECG signals. These measurements have been successfully tested with the developed MATLAB software. After acquisition of an ECG signal the signal is still contaminated by electromagnetic interference. The patient (a person) should be still and quiet during acquisition so that the electromagnetic interference is reduced to the barest minimum. Filters are used to remove other noises. MATLAB is used for the filter design. A Finite Impulse Response (FIR) digital low-pass filter is designed using Hamming Window. This filter removes the EEG noise and any other frequency above the upper cut off frequency of 25 Hz used here. The sampling frequency is 100 Hz while the order of the filter is ‘9’.

Results and Discussion

Fig. 6 is the first measurement for 50 years old person. The upper graph of the fig.6 is a noisy ECG signal. The lower graph of the fig.6 shows the frequency spectrum of the ECG signal. From this graph, the frequency of the ECG signal is 1.2 Hz and so, beat per minute (BPM) is 72 BPM. The peak between 45 Hz and 50 Hz of the frequency spectrum in the fig.6 shows that it is a noise frequency (about 48 Hz). Fig.7 shows the filtered ECG signal and its frequency spectrum. From this graph, the clean ECG signal can be seen because of low-pass filter. Fig.8 and 9 are the ECG signals and their frequency spectrum for 50 years old person without noise. Fig.10 and 11 are the ECG signals for 8 years old person. The heart beats of these measurements in this work are normal heart conditions and the results are consistent with the standard data. In this work, one real time measurement is made for 5 seconds duration. Therefore, there can be some errors in heart beat calculation. All measured heart beats can be 72, 84, 96 and etc. To reduce these errors, 60 seconds duration can be used for one real time measurement.

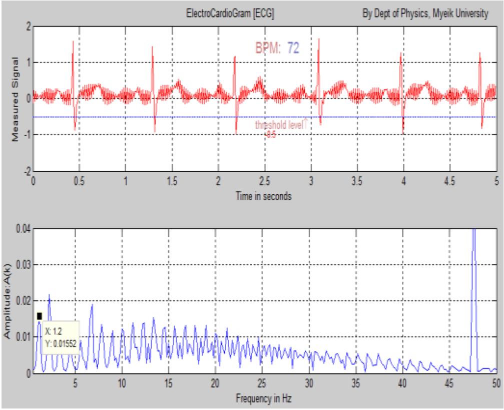

Figure 6 ECG for 50 Years Old without Filter

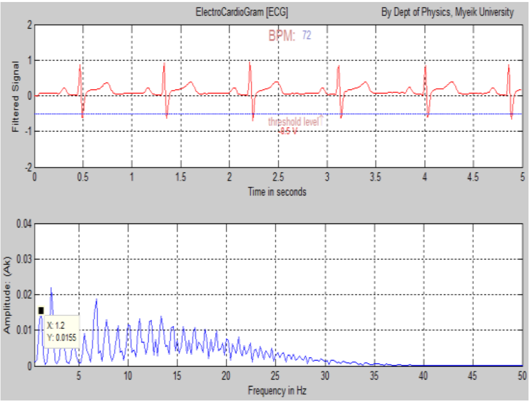

Figure 7 ECG for 50 Years Old with Filter

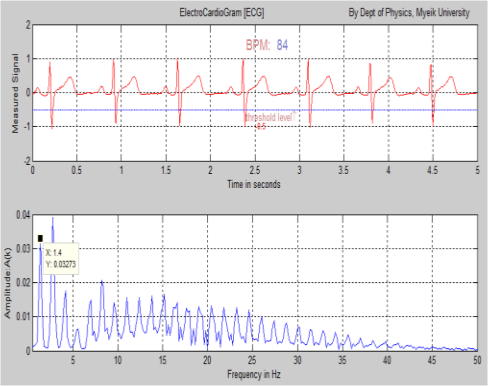

Figure 8 ECG for 50 Years Old without Filter

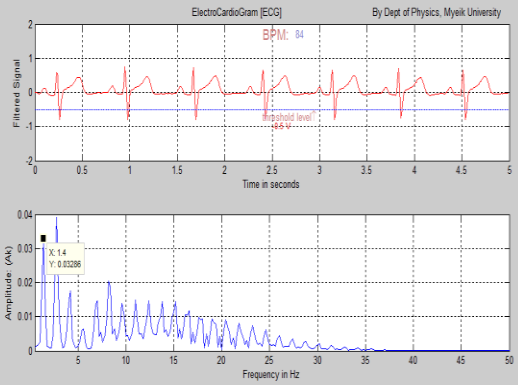

Figure 9 ECG for 50 Years Old with Filter

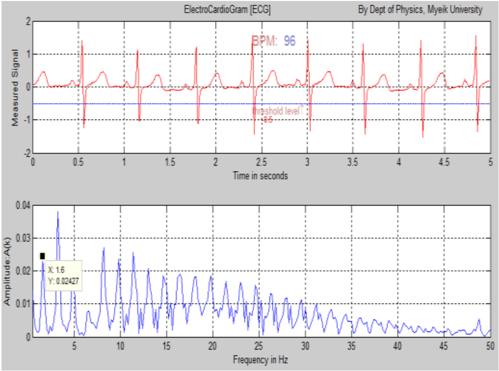

Figure 10 ECG for 8 Years Old without Filter

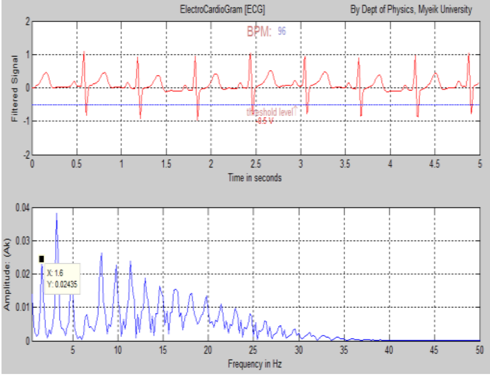

Figure 11 ECG for 8 Years Old with Filter

Conclusion

MATLAB has immense effect on ECG signal processing. It is so useful and handy that everyone can monitor his/her heart condition simply utilizing the power of MATLAB. One of the crucial steps in the ECG analysis is to accurately detect the different waves namely P, Q, R and S depicting the entire cardiac cycle. This proposed wok could be continued to further improve the algorithm to detect abnormalities by using calculations of intervals between impulses of two different signals in real time. For processing and design of detection algorithms, MATLAB is used, in which they were implemented as mathematical signal processing operations.

Acknowledgement

I would like to express my gratitude to all those who had been a support during the completion of this paper. I would like to thank my university for proving a support and serving as a backbone during the paper completion. I would like to thank all my teachers to have provided useful and constructive criticisms during the due course of completion.

References

A. K. M. F. Haque, H. Ali1, M. A. Kiber, and Md. T. Hasan, (2009), “Detection of Small Variations of ECG Features Using Wavelet”, *ARPN Journal of Engineering and Applied Sciences*, vol. 4, no 7.

Cornel Amariei, 2015 “Arduino Development Cookbook” (UK: Packt Publishing Ltd.)

ecg-sensor-module-ad8232.pdf

Jaylaxmi C Mannurmath, (2014), “MATLAB Based ECG Signal Classification”, International Journal of Science, Engineering and Technology Research (IJSETR), vol. 3, Issue 7.

Li Tan, (2008), “Digital Signal Processing”, San Diego, California, USA.

Minas, J. S. Martins, J. H. Correia, (2008), “High-Selectivity Optical Detection in Microfluidic Systems for Clinical Diagnostics”, Journal of Sensors and Materials, Japan.

Shenoi B. A. and John Wiley and Sons, (2006), “Introduction to Digital Signal Processing and Filtering Design”, Canada, USA.

S. Correia, J. Miranda, L. Silva, and A. Barreto, (2009), “Labview and Matlab for ECG Acquisition, Filtering and Processing,”*3rd International Conference on Integrity, Reliability and Failure, Porto/Portugal*.

SYNTHESIS AND CHARACTERIZATION OF SnO_2 NANOPARTICLES

Aye Sandar Oo[1], Hnin Hlwar Nu[2] & HlaHla Than[3]

Abstract

Tin Oxide, SnO_2 nanoparticles have been synthesized by sol-gel auto combustion method in this work from $SnCl_4.5H_2O$, NH_4OH and distilled water. After preparation the powder has been calcined at five different temperatures (400°C, 500°C, 600°C, 700°C and 800°C) for 1 hour. Then, the phase analysis identification has been conducted by X-ray Diffraction Analysis (XRD). Besides, Fourier Transform Infrared Spectroscopy (FTIR) analysis has been conducted after synthesis. FTIR spectrum shows the molecular vibration of SnO_2 nanoparticles. Moreover, the microstructure of the sample has been characterized by Scanning Electron Microscope (SEM).

Keywords: SnO_2 nanoparticles, XRD, FTIR, SEM.

Introduction

One of the most intriguing materials, Tin oxide ,SnO_2has been investigated because of its potential application in transparent conductive electrode for solar cells, a gas sensing material for gas sensors devices, transparent conducting electrodes, photochemical and photoconductive devices in liquid crystal display, gas discharge display, lithium-ion batteries, etc.

Moreover, nanometer-sized materials have recently attracted a considerable amount of attention due to their novel electrical, physical, chemical, and magnetic properties. These properties strongly depend on the size, structure and shape of the nanoparticles. Many processes have been developed to the synthesis of SnO_2 nanoparticles, e.g., spray pyrolysis, hydrothermal methods, chemical vapor deposition, thermal evaporation of oxide powders and sol–gel auto-combustion method.

In this research work, the synthesis and characterization of SnO_2 nanoparticles by Sol-gel Auto-combustion method was studied because this process has a potential synthesis technique in the production of nanometer scaled oxide powders.

Experimental Details

The chemical reagents used for nanoparticle synthesis were Tin (IV) Chloride pentahydrate, ($SnCl_4.5H_2O$),Ammonia solution (NH_4OH) and Distilled water. In the preparation of SnO_2, 20 g of $SnCl_4.5H_2O$ has been weighed with CENT-O-GRAM (OHAUS) sliding balance and 20 ml of Distilled water has been weighed with graduated cylinder. After complete dissolution, 20 g of ammonia solution was added to the above solution by drop wise under stirring with magnetic stirrer. When mixing, the reaction takes place and gradually turned into gel type. Then, the mixture has been heated with Temperature Controlled Hot Plate up to 300°C. At 150°C, it started to boil. At 200°C, it changes into dry-gel. Auto-combustion takes place at 300°C and it takes for6 hours. The combustion has finished after 6 hours. SnO_2 powder comes out from the experiment. Then, this powder has been grounded with mortar and pestle to become the fine powder. After that, the SnO_2 powders were calcined at five different temperatures (400°C, 500°C, 600°C, 700°C and 800°C) for 1 hour in the furnace. Then, the phase analysis identification has

---

[1] Dr, Demonstrator, Department of Physics, Meiktila University
[2] Dr, Demonstrator, Department of Physics, Meiktila University
[3] Dr, Professor, Head of Department of Physics, Meiktila University

been conducted by X-ray Diffraction Analysis (XRD) in order to determine the crystallite sizes of SnO_2 nanoparticles. Besides, Fourier Transform Infrared Spectroscopy (FTIR) analysis has been conducted after synthesis. FTIR spectrum shows the molecular vibration of SnO_2 nanoparticles. Moreover, the microstructure of the sample has been characterized by Scanning Electron Microscope (SEM).

(a) $SnCl_4.5H_2O$ (b) Distilled Water (c) NH_4OH solution

Figure 1 Starting Materials

(a) Magnetic Stirrer with Variable Power Supply

(b) Sliding Balance (CENTOGRAM – OHAUS) (c) Temperature Controlled Hot Plate

(d) Mortar and Pestle (e) Furnace (f) Dropper (g) Graduated cylinder

Figure 2 Synthesis Equipments

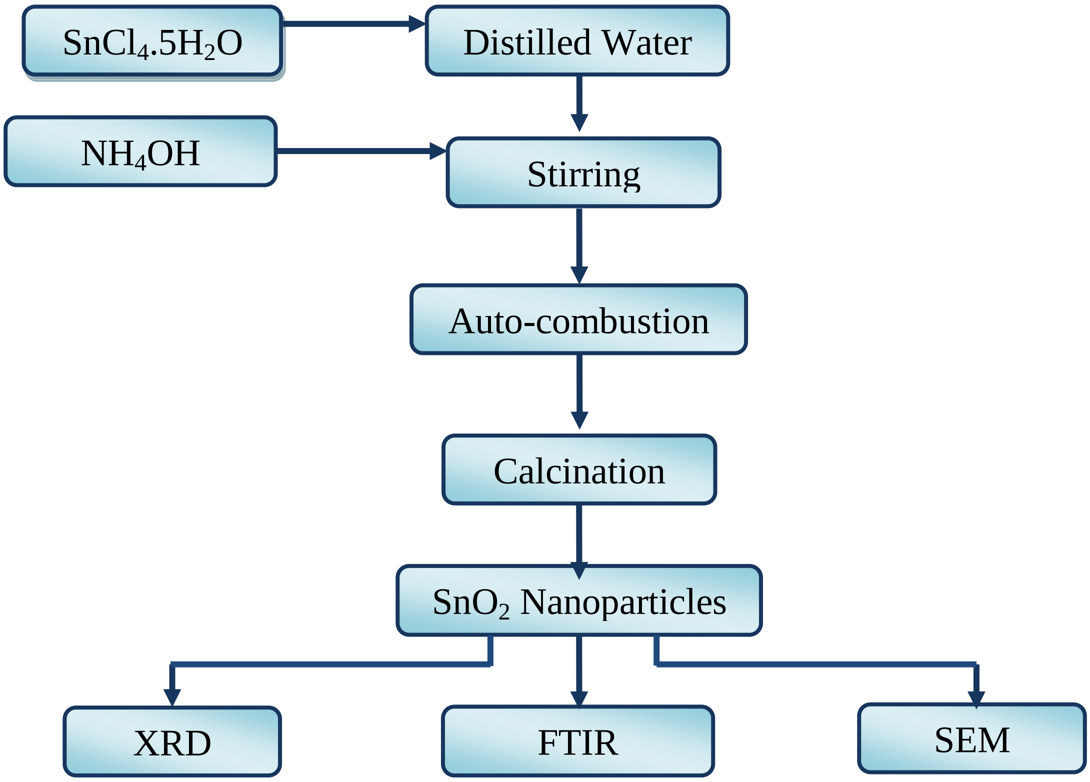

Figure 3 The Flow Chart of the Synthesis Procedure of SnO_2 nanoparticles

Synthesis Technique

X-ray Diffraction Technique (XRD)

X ray diffraction (XRD) technique is a technique which is commonly used in material characterization. This technique provides the peak position, intensity, width, shape and all-important information about the structure of the materials. From the XRD patterns, lattice constants have been calculated by the equation:

$$\frac{1}{d_{hkl}^2} = \frac{h^2 + k^2}{a^2} + \frac{l^2}{c^2} \qquad (\textit{for Tetragonal})$$

where, d_{hkl} = the lattice spacing between (hkl) planes.

For a polycrystalline powder, if the individual crystal is less than 100nm in size, the crystallite size can be estimated using the *Scherrer equation*:

$$L = k\lambda/B\cos\theta$$

where, B = peak width measured at half intensity (radian),

λ = the wavelength (Å)

k = particle shape factor (for spherical particles, k = 0.9)

L = diameter of the crystallites (Å).

In the Universities Research Center, University of Yangon, the materials can be examined by using Rigaku Multiflex 2kW Powder X-ray Diffractometer (XRD).

(a) External view (b) Internal view

Figure 4 Rigaku Multiflex 2kW Powder X-ray Diffractometer

Fourier Transform Infrared Spectroscopy (FTIR)

FTIR stands for Fourier Transform Infrared, the preferred method of infrared spectroscopy. The infrared absorption or transmission spectra of the SnO_2 nanoparticles were measured by using Fourier Transform Infrared Spectrometer (FTIR – 8400 Shimadzu), shown in figure (5). In infrared spectroscopy, IR radiation is passed through a sample. Some of the infrared radiation is absorbed by the sample and some of it is passed through (transmitted). The resulting spectrum represents the molecular absorption and transmission, creating a molecular fingerprint of the sample. Like a fingerprint no two unique molecular structures produce the same infrared spectrum. This makes infrared spectroscopy useful for several types of analysis.

Figure 5 Fourier Transform Infrared Spectrometer (FTIR – 8400 Shimadzu)

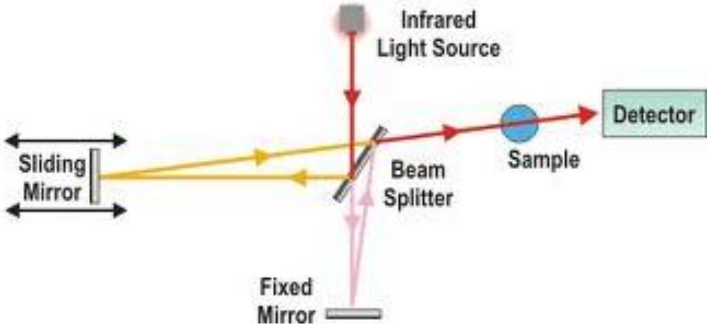

Figure 6 Schematic diagram of FTIR analysis

Scanning Electron Microscope (SEM)Technique

The Scanning Electron Microscope (SEM) is a microscope that used electrons rather than light to form an image. There are many advantages to using the SEM instead of a light microscope. The SEM has a large depth of field, which allows a large amount of the sample to be in focus at one time.

The SEM also produces images of high resolution, which means that closely spaced features can be examined at a high magnification. Preparation of sample was relatively easy since most SEMs require the sample to be conductive. The combination of higher magnification larger depth of focus, greater resolution, and ease of sample observation makes the SEM one of the most heavily used instruments in research area today. The purpose of using SEM is to characterize the grain, pore and the surface morphology of the SnO_2 nanoparticles.

(a) Operation system of SEM (b) Sample holder of SEM

Figure 7 Scanning Electron Microscope (SEM)

Result and Discussion

X-ray Diffraction Analysis

The structural properties of SnO_2 nanoparticles have been characterized by X-ray diffractometer (model RIGAKU MULTIFLEX) using CuK_α radiation (40 kV,50 mA) over a 2 θ range from 10^o to 70^o on a powder type XRD with $\lambda = 1.54056$ Å. The XRD spectrum of SnO_2 is shown in Figure (8 (a-e)).It was observed that all peaks are perfectly matched with the tetragonal structure of SnO_2 with the standard library file (ICDD_PDF # 99_0024) which indicating the present structure is found to be of SnO_2, which exist in the tetragonal phase. The lattice parameters of the crystal were obtained from the data of XRD spectrum. The peaks were occurred at (110), (101), (200), (211), (220), (002), (310), (112) and (301) the crystal planes from the XRD patterns. No other additional peaks were observed. This showed that the samples have no more impurity after calcination. The typical XRD pattern of synthesized SnO_2 nanoparticles confirmed that the crystalline phase of SnO_2 was tetragonal without any impurities. Moreover, the average crystallite sizes were found to be round about 18 nm to 32 nm. Besides, the smallest crystallite size of SnO_2 is 18.65 nm and the crystallinity was the most perfect for the sample annealed at 500^oC since there was no additional diffraction peaks were observed in its diffraction pattern.

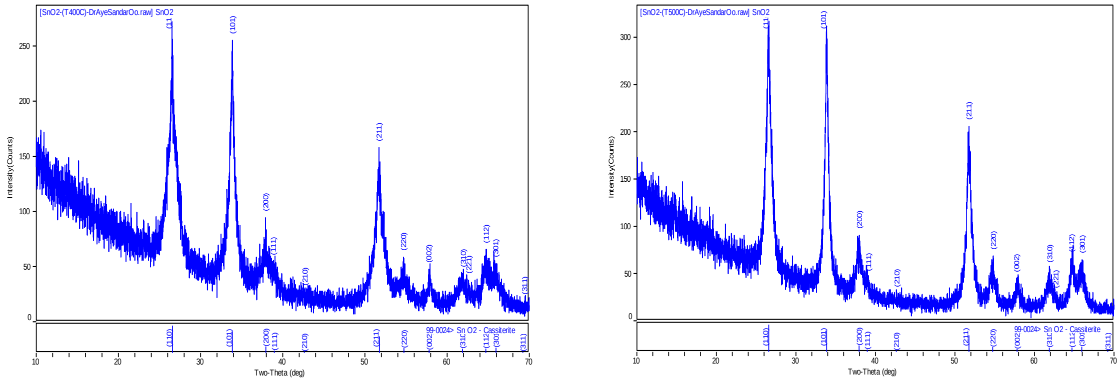

(a) 400°C (a) 500°C

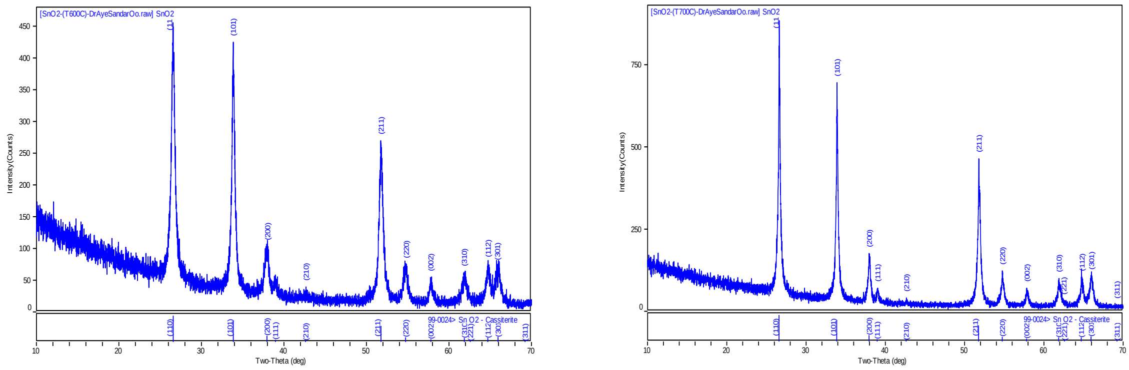

(c) 600°C (d) 700°C

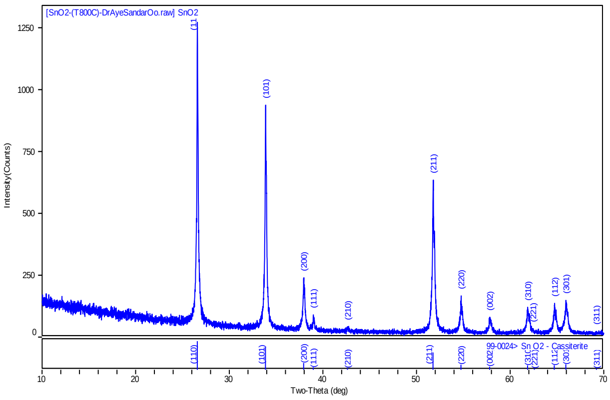

(e) 800°C

Figure 8 (a-e) XRD patterns of SnO_2nanoparticles with different temperatures

Table 1 The crystallite size of SnO_2 with different temperature

Temperature (°C)	Average Lattice Parameter (Å)		Average Crystallite Size (nm)
	a = b	c	
400	4.7440	3.1920	22.54
500	4.7343	3.1852	18.65
600	4.7377	3.1842	20.71
700	4.7333	3.1854	24.70
800	4.7364	3.1863	32.85

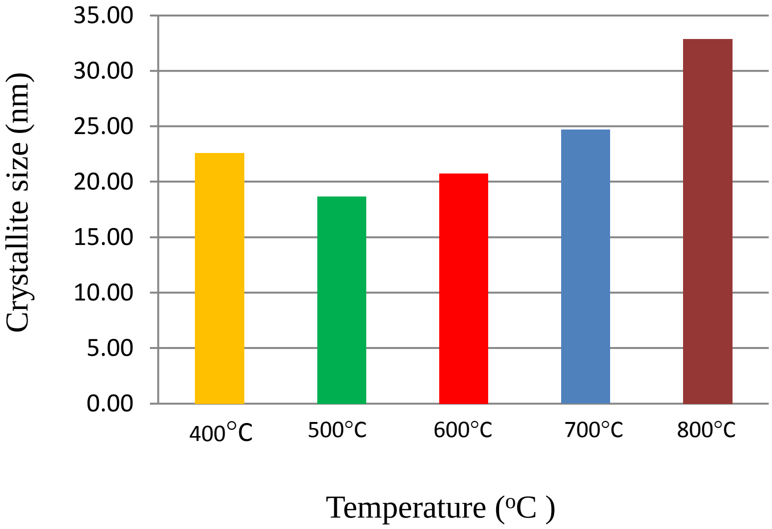

Figure 9 Graph of the crystallite size of SnO_2 with different temperatures

Fourier Transform Infrared Spectroscopic Analysis

FTIR spectra of SnO_2 nanoparticles that calcined at five different temperatures(400°C, 500°C, 600°C, 700°C and 800°C) are shown in Figure (10 (a-e)) respectively. Infrared transmittance spectra demonstrate the vibration bands due to Sn-O bonds and O-Sn-O bonds in its structure. The frequencies of FTIR vibration band for SnO_2nanoparticles with different temperatures are shown in Table (2). The observed bands in the range of 2312.73cm^{-1} –3444.98 cm^{-1} in the SnO_2 nanoparticles have been assigned to the hydroxyl group (O-H) stretching vibrations, over 1200 cm^{-1} to 1600 cm^{-1} is showed that the carboxylate groups(C-O). Moreover, FTIR spectra attributed to O- Sn-O bonds and Sn-O bonds stretching vibrations in the range of 447.50 cm^{-1} to 569.02 cm^{-1} and 617.24 cm^{-1} to 663.53 cm^{-1}. Therefore, the selected region of the recorded FTIR spectra have been confirmed the tetragonal structure of SnO_2.

Table 2 The molecular vibration in FTIR spectra of SnO_2 nanoparticles with different temperatures

Temperature (°C)	O-Sn-O Stretching (cm^{-1})	Sn-O Stretching (cm^{-1})	Carboxylate Stretching (cm^{-1})	Hydroxyl Stretching (cm^{-1})
400	447.50-482.22	663.53	1402.30-1620.26	3205.80-3433.41
500	491.86	663.53	1367.58-1398.44	3115.14-3433.41
600	503.44	659.68	1215.19-1627.97	-
700	472.58-569.02	653.89	1396.51-1660.77	-
800	503.44	617.24-646.17	1338.64-1629.90	2312.73-3444.98

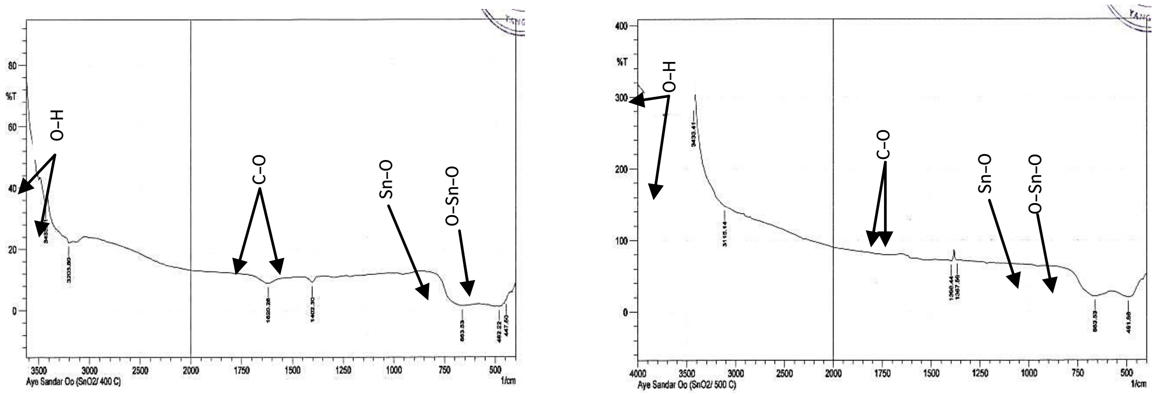

(a) 400°C (b) 500°C

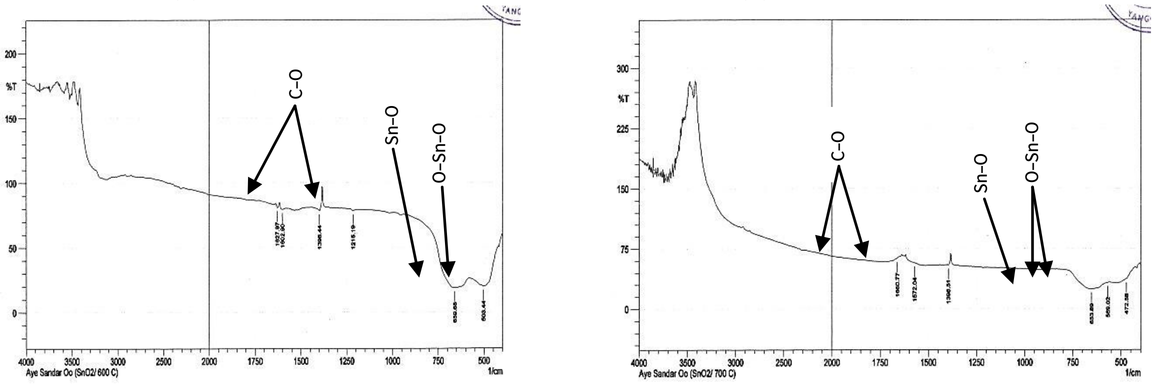

(c) 600°C (d) 700°C

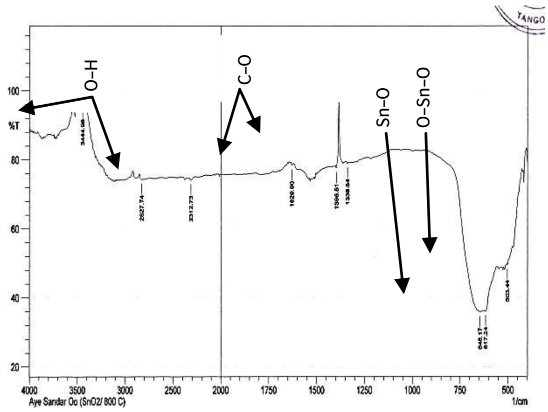

(e) 800°C

Figure 10 (a-e) The FTIR spectra of SnO_2 nanoparticles at five different temperatures

Morphological Investigation

In this research, the SEM micrographs ofSnO_2 nanoparticles was investigated by SEM (Type: JEOL) are shown in Figure (11 (a-e)). SEM micrograph indicates the morphological feature of the SnO_2 nanoparticles and the average grain sizes are shown in Table (3). According to observation, the SEM micrographs of the SnO_2 nanoparticles found to be non-uniform shape because of different temperatures. At the higher temperature, 700^{o}C and 800^{o}C, has the smallest grain size and are composed of agglomerated particles. If the grain size is smaller, the more contact between each other is larger, which can be used as a conducting devices. At the lower temperature, (400^{o}C, 500^{o}C, 600^{o}C), the grain sizes are bigger than that of higher temperature and with more pores which is suitable for sensing devices.

Table 3 Average grain size of SnO_2 nanoparticles

Temperature (^{o}C)	**Average grain size (μm)**
400	2.00
500	1.33
600	1.67
700	1.20
800	0.95

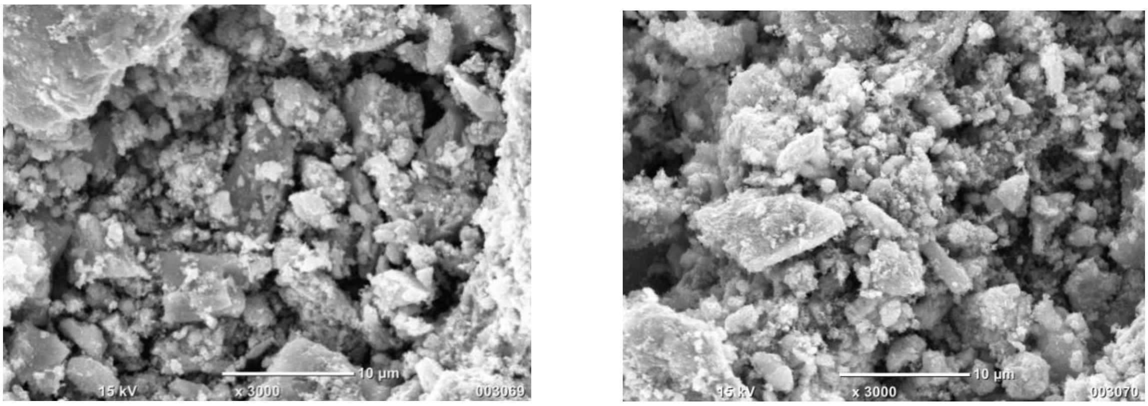

(a) 400^{o}C (b) 500^{o}C

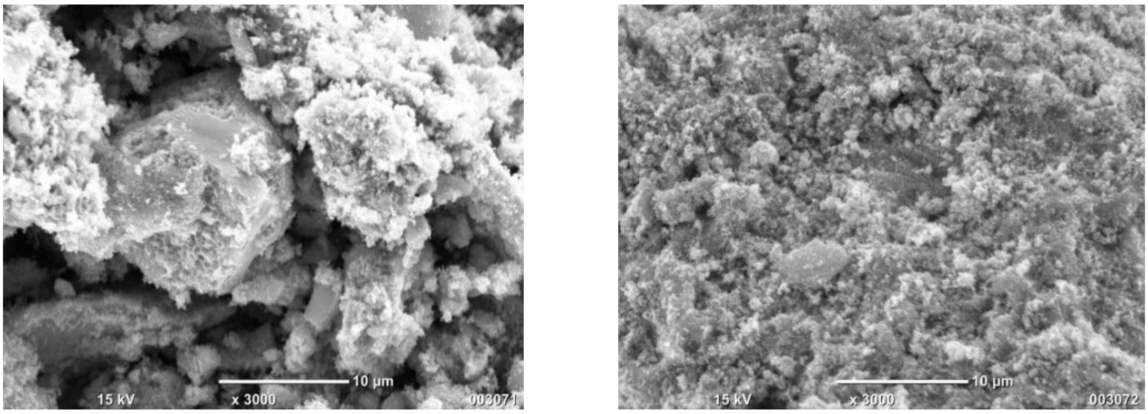

(c) 600^{o}C (d) 700^{o}C

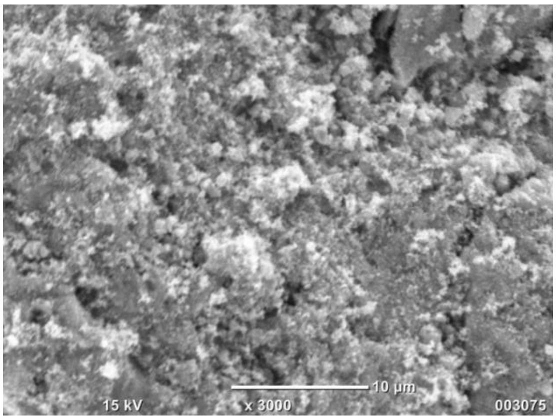

(e) 800°C

Figure 11 (a – e) The SEM micrographs of SnO_2 nanoparticles at five different temperatures

Conclusion

To be concluded, the aim of this research is to produce the SnO_2 nanoparticles easily. The method, Sol-gel Auto-combustion, used in this research is cost effective and easy way to make the process of SnO_2 nanoparticles. The typical XRD pattern of synthesized SnO_2 nanoparticles confirmed that the crystalline phase of SnO_2 was tetragonal structure without any impurities. Moreover, the average crystallite sizes of SnO_2 are in the range of 18 nm to 32 nm. FTIR spectra attributed to O- Sn-O bonds and Sn-O bonds stretching vibrations in the range of 447.50 cm^{-1} to 569.02cm^{-1} and 617.24 cm^{-1} to 663.53 cm^{-1} and confirming the SnO_2 spectra. The SEM micrographs of the SnO_2 nanoparticles found to be non-uniform shape because of different temperatures. According to observation, SnO_2 nanoparticles is the potential application in transparent conductive electrode for solar cells, a gas sensing material for gas sensors devices, transparent conducting electrodes, photochemical and photoconductive devices, gas detection, lithium-ion batteries, etc.

Acknowledgement

The authors would like to acknowledge Professor Dr Kay Thi Thin, Pro Rector, Meiktila University, for her kind permission to carry out this work and Dr Daw Hla Win, Professor, Department of Physics, Meiktila University, for her valuable advice.

References

Ammonia solution, NH_4OH – Wikipedia: https://en.m.wikipedia.org

Kwanruthai Wongsaprom, “Synthesis and characterization of tin oxide nanocrystalline powders by a simple modified sol-gel route”, Article in Applied Physics A, January, (2014).

M. G. Thakare, J.S. Aher, “Synthesis, Characterization and Application of SnO2 Nanoparticles”, International Journal of Recent Trends in Engineering & Research, ISSN (ONLINE): 2455-1457, IMPACT FACTOR: 3.344, IJRTER-2016.

Patil et al. International Nano Letters, Springer Open Journal, 2012, 2:17, http://www.il-journal.com/content/2/1/17

Tin (IV) Oxide – Wikipedia: https://en.m.wikipedia.org

J. Myanmar Acad. Arts Sci. 2020 **Vol. XVIII.No.2A**

CONCENTRATION OF HEAVY METALS IN WASTEWATER, SOIL AND RICE SAMPLES FROM TAUNG IN LAKE NEAR MANDALAY INDUSTRIAL ZONE II

Hnin Hnin Aye[1], Win Win Aye[2], Nay Win Oo[3]

Abstract

To estimate the heavy metals concentration presence in the water, soils and the rice grown on the soil, the samples are collected from Min Ywa (MY), Nyaung Ni Bin (NNB), Nyaung Bin Zauk (NBZ) and Inn Gone (IG) villages. Theses villages are located in Mandalay Industrial Zone II and are assigned as study areas in our research work. The collected samples are analyzed by using Atomic Absorption Spectrophotometer (AAS). The results showed the 5 elements (Fe, Cu, Zn, Pb and Cd) exist in soil and rice samples. Mn, Fe, Cu, Zn and As concentrations in wastewater exceeded the permissible limit by WHO. Transfer values of soil to rice ranged from 0.001-0.004 for Fe, 0.282-0.577 for Cu, 0.371-0.658 for Zn. But Pb and Cd are not listed because they are below the detectable limit.

Keywords: wastewater, heavy metals, Atomic Absorption Spectrophotometer (AAS).

Introduction

The presence of heavy metals in plants and soil are one of the major issues to be faced throughout the world requires attention because heavy metals which include more than their normal ranges are extremely threatened to both plants and human life. Soil is capable of supporting plant life and is vital to life on earth. Accumulation of heavy metals in plants is of great concern because of the probability of food contamination through the soil root interface.

Water is the most used for industrial, municipal and agricultural purpose. Thus water plays a major role in virtually every aspect of human life. The industrial wastewater can result in the heavy metal contamination of agricultural soils. Heavy metal contents in wastewater are very dangerous because water pollution occurs in the agricultural areas, lakes, oceans, streams, rivers, underground water. There are some essential elements for human and animal health but they occur in small amounts naturally. Some minerals like Zn, Cu and Fe which are useful and can increase the water quality. Some elements like Pb, As, Hg, Cr, Ni, Cd, Co which are very harmful, toxic and poisonous and can decrease the water quality . Therefore the investigation of heavy metals is necessary for agricultural soils and wastewater. The main objective of this study is to estimate the concentration of heavy metals exist in the wastewater, soils as well as rice grown on the soil.

Materials and Methods

Studied Area

Industrial waste of local factory passes from Taung In Lake to Myitnge river through the canals. Hence, the Lake has been contaminated with these industrial wastewater. Almost every rainy season when the river level is high, the river Myitnge overflows down the lake. Then, wastewater flows into the villages (Min Ywa (MY), Nyaung Ni Bin (NNB), Nyaung Bin Zauk

---

[1] Dr, Assistant Lecturer, Department of Physics, Sagaing University.

[2] Dr, Assistant Lecturer, Department of Physics, Hakha College.

[3] Dr, Professor, Department of Physics, Magway University.

(NBZ) and Inn Gone (IG)) surrounded Taung In Lake. Taung In Lake is located in Amarapura region near Mandalay Industrial Zone IIand lying along 21.52° N latitude and 96.03° E longitude. The present study is carried out in the agricultural fields of Min Ywa (MY), Nyaung Ni Bin (NNB), Nyaung Bin Zauk (NBZ) and Inn Gone (IG) villages.The rice, soil and wastewater samples were collected from these villages.

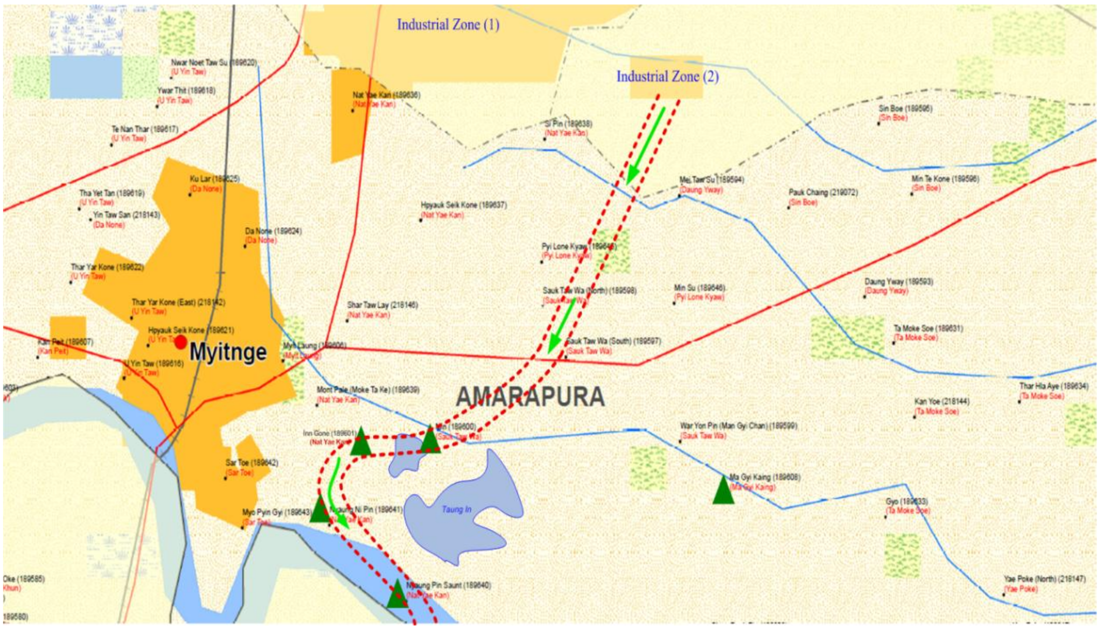

Figure 1 The Geological Map of Sampling Sites in Taung-In

Sampling and Preparing

Wastewater samples (site-1, site-2, site-3, site-4) were collected from flume flowing into the fields of rice in villages (Min Ywa (MY), Nyaung Ni Bin (NNB), Nyaung Bin Zauk(NBZ), Inn Gone (IG)) surrounded Taung In Lake in April, 2018. 500 mL of wastewater was filtered with filter paper. After filtering, sample was placed at room temperature about 5 hr.

Each soil samples were collected to a depth of 15 cm from surface level in respective fields. The rice samples were collected from these villages. The collected soil and rice samples were dried at room temperature for two weeks. The dried samples were ground manually with a ceramic-triturator and sieved to pass through 200 mesh to get fine powder. And then 1 g of rice powders were placed inside muffle furnace. After heating at 500°C for 2 hr, the ashes were obtained. Then the ashes were mixed with 5 ml of HCl at 50 °C for 10 min. The mixed solution was cooled and filtered with filter paper. After filtering, 1 ml of sample and 49 ml of de-ionized water (DI) were diluted into the 50 ml volume metric flask and then placed at room temperature about 24 hr.

5 g of soil powder were mixed with 30 ml of DI and 5 ml of HCl. The mixed solution was stirred at 100 °C for 10 min. The solution was cooled at RT and filtered with filter paper. After filtering soil solution was placed at room temperature about 24 hr. All samples were performed by Atomic Absorption Spectrometer at Universities' Research Centre (URC), Yangon University.

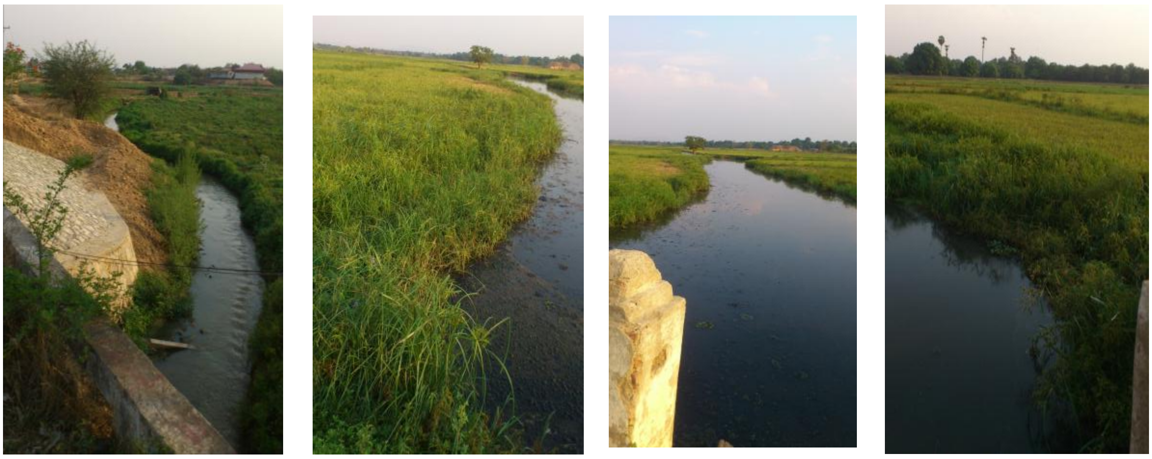

Figure 2 Site-1, site-2, site-3, site-4 at villages surrounded TaungIn Lake

Analysis of Samples

Atomic Absorption Spectroscopy (AAS) was performed to detect and measure concentration of metals in the soil, rice and wastewater samples. Almost every metallic element can be determined quantitatively by using the spectral absorption characteristics of atoms. It was found 7 (Cr, Cu, Cd, Fe, Mn, Asand Zn) elements in the measured samples.

Results and Discussion

AAS results

The presence of Fe, Cu, Zn, Cd and Pb metals in rice and soil samples were found. Comparative heavy metals concentration for rice samples (IG, NBZ, MY and NNB villages) with the recommended limit by FAO were shown in the Table (1). The observed concentrations ranged from 0.17-0.41 for Fe, 10.14-20.47 for Cu, 11.48-192.3 for Zn in rice samples (Table (2)). Zn concentrations were above the recommended limit by FAO for human consumption. Cd and Pb were toxic elements even at low concentrations. But, Cd and Pb concentrations cannot be detected. The concentrations of Fe, Cu, Zn and Pb elements in soil samples (IG, NBZ, MY and NNB villages) were enriched. Pb concentration was above the permissible value of FAO. The presence of Cr, Mn, Fe, Cu, Zn, As and Cd in wastewater sample presented in the Table (3). Fe and As concentrations were above the recommended limit by WHO.

Table1 Heavy Metal Concentrations of rice samples

Element	**IG (ppm)**	**NBZ (ppm)**	**MY (ppm)**	**NNB (ppm)**	**FAO (ppm)**
Fe	0.41	0.17	0.38	0.28	5
Cu	15.84	10.14	19.99	20.47	40
Zn	63.01	11.48	192.3	72.34	60
Cd	ND	ND	ND	ND	0.3
Pb	ND	ND	ND	ND	5

(Date of collected samples : April, 2018)

ND=Not Detected

Table 2 Heavy Metal Concentrations of soil samples

Element	**IG (ppm)**	**NBZ (ppm)**	**MY (ppm)**	**NNB (ppm)**	**FAO (ppm)**
Fe	102.6	118.8	107.3	123.2	ND
Cu	34.61	31.75	70.85	35.45	70
Zn	169.9	17.44	354.5	162.2	80
Cd	0.67	1.00	0.70	0.89	3
Pb	160.6	148.9	30.76	221.3	16

(Date of collected samples : April, 2018)

Table 3 Heavy Metal Concentrations of wastewater

Element	**Taung In (ppm)**	**WHO (ppm)**
Cr	LDL	0.10
Mn	1.334	0.20
Fe	29.53	5
Cu	1.512	0.20
Zn	3.576	2
As	5.426	0.10
Cd	LDL	0.01

(Date of collected samples : April, 2018)
LDL=Low detection limit

Since heavy metals can transfer to plant from soil, the transfer values were determined. The transfer coefficient was calculated by dividing the concentration of heavy metals in vegetables by the total heavy metal concentration in the soil.

$$\text{TF} = \text{conc. of metal in edible part/conc. of metal in soil} \qquad (1)$$

The estimated results for transfer factors (TF) were shown in Fig. 3. The TF values for Cd and Pb are not detectable in all samples. It was found that TF value was less 1 for samples of Min Ywa (MY), Nyaung Ni Bin (NNB), Nyaung Bin Zauk(NBZ), and Inn Gone(IG) villages.

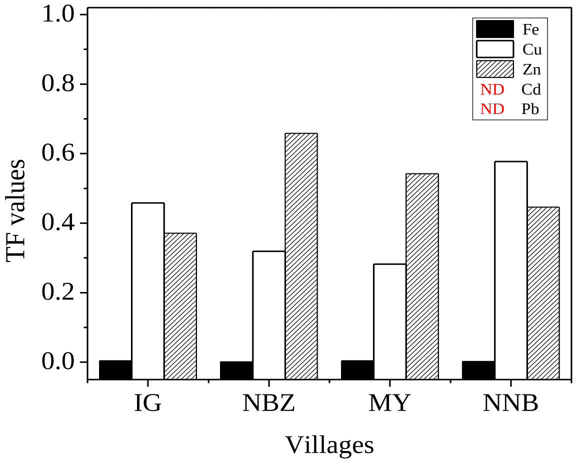

Figure 3 Transfer values from soil to rice

Conclusion

The quantitative analysis of heavy metals contained in wastewater, soil and rice samples are carried out by AAS spectrometer. The toxicity of the heavy metal in paddy fields of Min Ywa (MY), Nyaung Ni Bin (NNB), Nyaung Bin Zauk (NBZ) and Inn Gone (IG) villages around Taung In Lake in Mandalay Industrial Zone II depends on the influence of contaminated wastewater.

Fe, Cu, Zn, Cd and Pb metals are found in soil and rice samples. The concentrations of Fe, and Cu in rice sample are lower than the values of FAO(5 ppm for Fe, 40 ppm for Cu) but Zn concentration is high. Heavy metals in soil sample were greater than in rice samples. This indicates that the capability to transport metals from soil to plants. Cd was not found in AAS results for rice sample. Thus, Cd may not be reliable in heavy metal concentration measurement for rice sample.

Heavy metals of Cr, Mn, Fe, Cu, Zn, As and Cd are found in wastewater of Taung In Lake. Fe and As have the maximum concentrations compared to other heavy metals. It is due to an influence of the increasing of contaminated wastewater even flow through the plastic pipe from Industrial Zone II to directly Myitnge river.

Acknowledgement

The authors would like to acknowledge Professor, Dr Khin Khin Win, Head, Department of Physics, Yangon University for her effort a chairman of MAAS and Professor Dr Saing Tun Aye, Department of Physics, Sagaing University for his permission and suggestion to carry out this research work.

References

A. Majid Saidi (2010) "Experimental Studies on Effect of Heavy Metals Presence in Industrial Wastewater on Biological Treatment", *International Journal of Environmental Sciences*, Tehran, vol. 1, pp. 666-676.

Anna Santarsiero, Enrico Veschetti, and Massimo Ottaviani (1996)"Elements in Wastewater for Agricultural Use."*Microchemical Journal*, Italy, vol. 54, pp. 338-347.

Alina Lato, Isidora Radulov, Adina berbecea, and K. Lato (2012)"The Transfer Factor of Metalsin Soil-Plant System."*Research Journal of Agricultural Science*, Romania, vol. 44, pp. 67-72.

Ioannis K. Kalavrouziotis, Prodromos Koukoulakis, and Eirini Kostakioti(2012)"Assessment of metal transfer factor under irrigation with treated municipal wastewater." *Agricultural Water Management*, Greece, vol. 103, pp. 114-119.

Mikko Sillanpaa, (1972) *Trace Elements in Soil and Agriculture*. Rome, Michigan University Press.

Ziwei Ding, Yang Li, Qingye Sun, and Haojie Zhang (2018)"Trace Elements in Soils and Selected Agricultural Plants in the Tongling Mining Area of China." *International Journal of Environmental Research and Public Health,* China, vol. 15, pp. 1-12.

J. Myanmar Acad. Arts Sci. 2020 **Vol. XVIII.No.2A**

ASSESSMENT OF NATURAL RADIOACTIVITY AND RADIATION HAZARDS IN SEDIMENTS FROM MEIKTILA LAKE

KhinThi Tar Win[1], Win Zaw[2]

Abstract

In this present study, the natural radioactivity levels of sediments from Meiktila Lake, Meiktila Township, Mandalay Region have been investigated by using HPGe detector and analysed with the Gamma Vision-32 The radium equivalent activity, the absorbed dose rate and external hazard in each sample was calculated to assess the radiation hazard for people. All sample have shown radium equivalent activity ranged from 157.30Bq kg^{-1} to 181.80Bq kg^{-1}. The observed values of radium equivalent activity for all samples were less than the permissible limits of 370 Bq kg^{-1}. The values of calculated absorbed dose rates in the samples under investigated are ranged from 97.10 nGyhr^{-1} to 112.26 nGhr^{-1}. The value of absorbed dose rate for all samples were higher than the average global terrestrial radiation of 55 nGhr^{-1}. But the calculated values of external hazard index values for all samples were less than the permissible value 1.0 mSvy^{-1}.

Keywords: natural radioactivity, gamma spectroscopy, activity concentration, radiation hazard, absorbed dose rate

Introduction

Sediments: Sediments is loose, hard material lying on top of solid rock. Sediment comes in many forms and sizes, and can originate from a variety of sources. Sediment is produced by the weathering and erosion of rocks exposed at Earth's surface. Chemical sediment forms as minerals crystallize and settle from water that contains lots of dissolved particles. Biochemical sediment accumulates as plants and animals die and their hard parts, such as skeletons and shells, are deposited on the ocean floor. There are various kinds of sediments on the earth. They are rock, gravel and sand, consolidated clay, silt/soft clay, mixture (rock/sand/silt/soft clay).

Sample Location

Meiktila Lake is situated in the central portion of Meiktila town, a district in Mandalay division, Myanmar. It measures seven-miles in length and half a mile in breadth, and covers an area of three and half square miles. It is a long lake stretching from north to south. The lake is crossed by two bridges which are one for road and the other for railway line in the central area of the lake. Meiktila Lake is an artificial lake created by man. The lake has an elongated shape.

It is bounded on the north by Inpetlet village, on the east by Contonment area, Zayashebyin, Myomalay, Yanmyoaung and Wunzin Words, on the south by Naw-zan-taung village and on the west by Aungsan, Paukchaung and Nandawgon Words, Ga-lon-kon and Shin-myo villages. In Meiktila Township the most prominent streams are found on the west of Meiktila Lake. On the east of the lake, streams are mostly artificial drainage channels. On the west of the Meiktila Lake, Mondaing Chaung and Kanni Chaung are the most prominent streams. Though Thinbon Chaung and Chaunggauk Chaung serve as boundary lines, they do not pass through the township. This water is used in various forms including drinking and agricultural crops. The Lake is naturally filled with rain fall water.

---

[1] Dr, Lecturer, Department of Physics, Meiktila University

[2] Dr, Lecturer, Department of Physics, University of Mandalay

Calculation of Activity

The activity of the sediment samples were calculated by the following equation.

$$A = \frac{N_A}{m\varepsilon P_\gamma T} \qquad (1)$$

where, N_A = net area for sample

m = mass of sample in kilogram

P_γ = emission probability of interested gamma ray

T = counting time (in second)

ε = efficiency of the interest gamma energy

Calculation of Radium Equivalent Activity

Radium equivalent activity (Ra_{eq}) is used to assess the hazards associated with materials that contain ^{226}Ra, ^{232}Th and ^{40}K in Bq kg^{-1}, which is determined by assuming that 370 Bq kg^{-1} of ^{226}Ra or 260 Bq kg^{-1} of ^{232}Th or 4810 Bq kg^{-1} of ^{40}K produce the same gamma dose rate. The Ra_{eq} of a sample (Bq kg^{-1}) is based on the estimation that 1 Bq kg^{-1} of ^{226}Ra, 0.7 Bq kg^{-1} of ^{232}Th and 13 Bq kg^{-1} of ^{40}K produces the same gamma radiation dose rates. The index is given as the following relation.

$$Ra_{eq} = A_{Ra} + 1.43A_{Th} + 0.0077A_k \qquad (2)$$

Where A_{Ra},$A_{Th}$and A_K are the specific activities of ^{226}Ra,^{232}Th and^{40}K in Bqkg^{-1}. The ^{226}Ra concentration was determined from 77 keV, 295 keV, and 351keV gamma-peak of ^{214}Pb and 609 keV, 1120 keV and 1155 keV gamma-peak of ^{214}Bi. ^{232}Th was achieved by 911 keV gamma-peak of ^{228}Ac, 238 keV gamma-peak ^{212}Pb and 583 keV gamma-peak of ^{208}Tl. The ^{40}K was directly determined using the 1460 keV gamma-peak from ^{40}K itself.

Calculation of Absorbed Dose Rate

The measured activity of ^{226}Ra, ^{232}Th and ^{40}K were converted into doses by applying the factors 0.461, 0.623 and 0.041 for radium, thorium and potassium respectively. These factors were used to calculate the total absorbed gamma dose rate in air at 1m above the ground level using this equation

$$D\ (nGyh^{-1}) = 0.461\ A_{Ra} + 0.623\ A_{Th} + 0.041\ A_K \qquad (3)$$

where A_{Ra}, A_{Th} and A_k are the specific activities of ^{226}Ra, ^{232}Th and ^{40}K in Bq kg^{-1}.

Calculation of External Hazard Index

The external hazard index is obtained from Ra_{eq} expression through the supposition that its maximum value allowed (equal to unity) corresponds to the upper limit of Ra_{eq}(370 Bqkg^{-1}). This index value must be less than unity in order to keep the radiation hazard insignificant; i.e., the radiation exposure due to the radioactivity from construction materials is limited to 1.0 mSvy^{-1}. Then, the external hazard index can be defined as

$$H_{ex} = \frac{A_{Ra}}{370} + \frac{A_{Th}}{259} + \frac{A_k}{4810} \leq 1 \qquad (4)$$

Where A_{Ra}, A_{Th} and A_k are the specific activities of ^{226}Ra, ^{232}Th and ^{40}K in Bq kg^{-1}.

Sample Collection and Preparation for Gamma Ray Detection Method

The sediment samples were collected three different points from Meiktila Lake, Meiktila Township, Mandalay Region. The map of collection of the samples was as shown in Figure (1). The sample preparation like drying, grinding homogenization and packing in proper geometrical dimensions for gamma spectrometric analysis was carried out for sediments samples. These samples were dried at room temperature, avoiding the loss of radionuclide. The dried samples, 500 gram, were transferred to plastic containers for gamma activity analysis.

Experimental Set-Up for Gamma Emission Measurement

The experiments were carried out using gamma ray spectroscopy system with high purity germanium detector (HPGe). In gamma ray spectroscopy system, the following equipments are included. They are the HPGe detector ORTEC (model GMX 10P4-70-RB-SMN), cooler (model CFG-X-COOL-III-230), preamplifier (model A257N), fast spectroscopy amplifier ORTEC (Model-671), digital signal processor (DSPEC-LF) which also include high voltage power supply, a pulse stored Multi-Channel Analyzer (MCA) together with Gamma Vision-32 software installed in PC and data readout devices as shown in Figure (2). The operating voltage for HPGe detector is negative 1500 V dc. The detector was surrounded with a lead shielding (thickness is 7 cm) to reduce a possible background radiation that comes from the environment . From the collected gamma spectrum, the radionuclides present in the sample are identified and their activity concentrations are determined from the gross and net area of the full energy gamma peak. For present measurement, the samples measured for 10800 seconds. The background spectrum was measured under the same conditions. At the end of the counting period, the spectrum that was recorded may be displayed on the screen. The spectra stored in MCA were analyzed by the application of Gamma Vision-32 software.

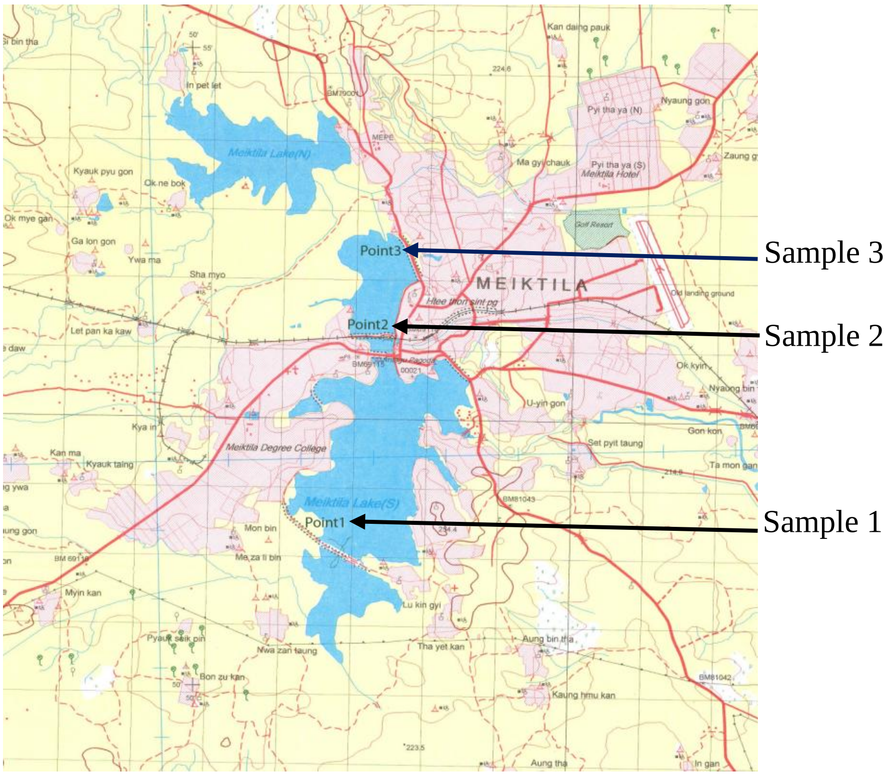

Figure 1 Map of the sampling area

Energy calibration

The standard radioactive sources of known energies were used to calibrate the spectrometer. Seven standard sources emitting 14 different gamma energies ranging from 81 keV to 1332 keV: ^{133}Ba (81 keV, 276.34 keV, 302.85 keV, 356.02 keV, 383.85 keV), ^{57}Co (122.06 keV and 136.46 keV), ^{137}Cs (661.66 keV) ,^{54}Mn (834.85 keV), ^{22}Na (511 keV and 1274.53 keV), ^{65}Zn (1115.55 keV) and ^{60}Co (1173.24 keV and 1332.50 keV) were used for 1800 seconds placing at 5 cm above the detector cap. The data are as shown in Table (1) and the energy calibration curve is as shown in Figure (3).

Figure 2 Photograph of the HPGe gamma detection system

Table 1 Energy calibration data for HPGe detector

Sr.no	Standard Sources	Channel	Energy (keV)
1	Ba-133	428	81.00
2	Co-57	645	122.06
3	Co-57	721	136.46
4	Ba-133	1460	276.34
5	Ba-133	1600	302.85
6	Ba-133	1881	356.02
7	Ba-133	2029	383.85
8	Na-22	2702	511.00
9	Cs-137	3499	661.66
10	Mn-54	4414	834.85
11	Zn-65	5899	1115.55
12	Co-60	6204	1173.24
13	Na-22	6740	1274.53
14	Co-60	7046	1332.50

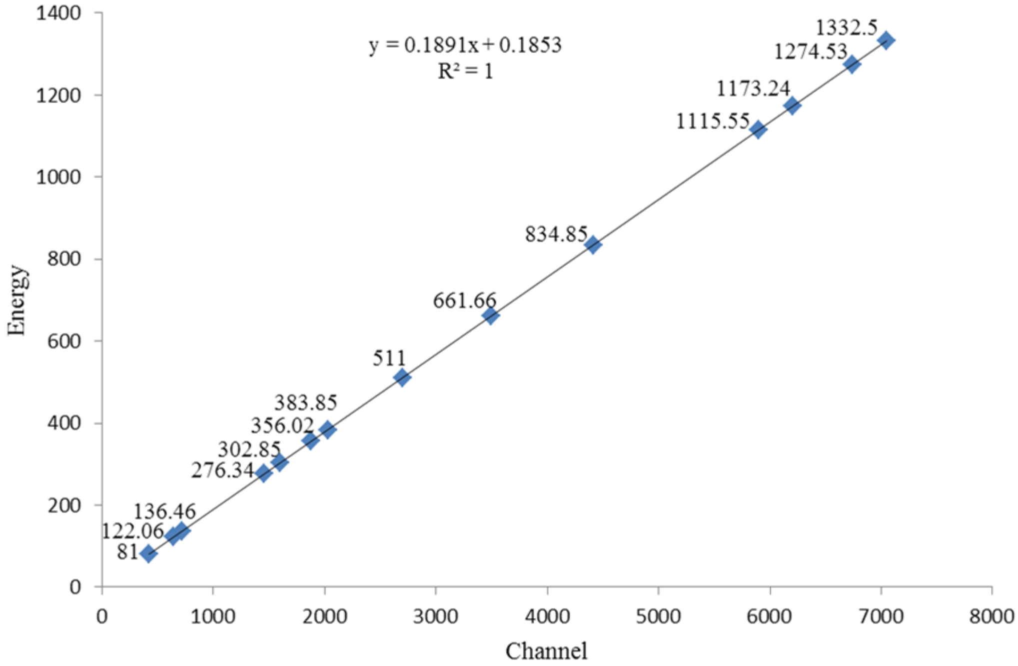

Figure 3 Energy calibration curve for HPGe detector

Results

The presence of radionuclide in sediment samples were investigated with HPGe detector and analyzed using Gamma Vision-32 Software. The radionuclide present in sediments samples are ^{207}Bi (74.97 keV), ^{214}Pb(77.17keV) , ^{208}Tl(84.68keV),^{207}Bi (84.80 keV), ^{212}Pb(238.63 keV), ^{214}Pb (295.22 keV), ^{228}Ac (338.40 keV), ^{214}Pb (351.99keV), ^{208}Tl (510.72keV), ^{208}Tl (583.14 keV),^{214}Bi (609.32 keV),^{228}Ac (911.07 keV),^{228}Ac(968.9 keV),^{228}Ac and^{40}K (1460.75 keV).

The collected background and sample spectra were shown in Figure (4) to Figure (7). The average activity of ^{226}Ra, ^{232}Th and ^{40}K in Bq kg^{-1} for sediment samples are as shown in Table (2). The average values of radiation hazard parameters for sediment samples are as shown in Table (3).

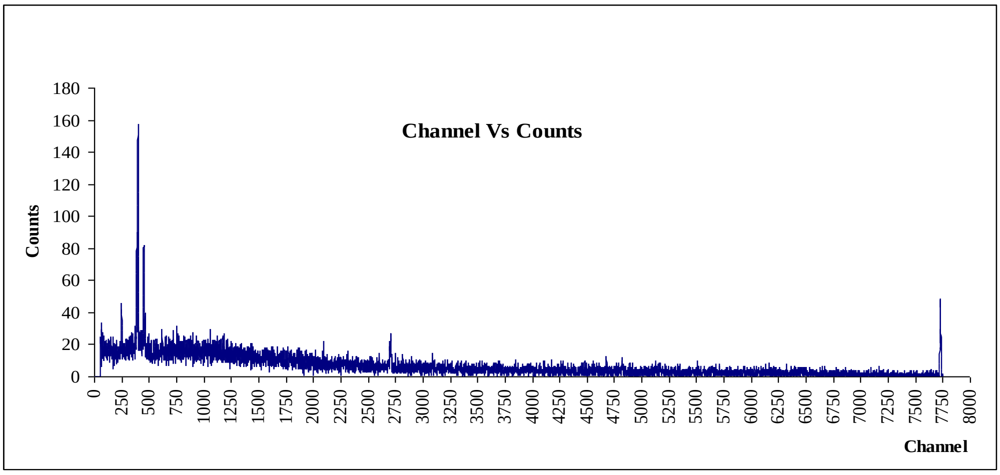

Figure 4 Background Spectrum of HPGe Detector for Counting Time 3 hrs

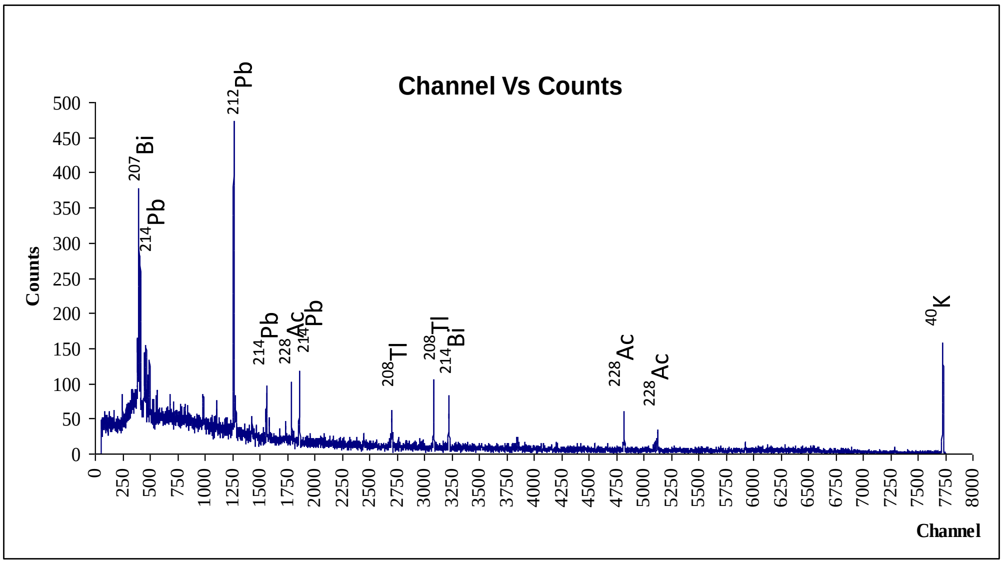

Figure 5 Energy Spectrum of the Sediments Sample S1 for Counting Time 3 hrs

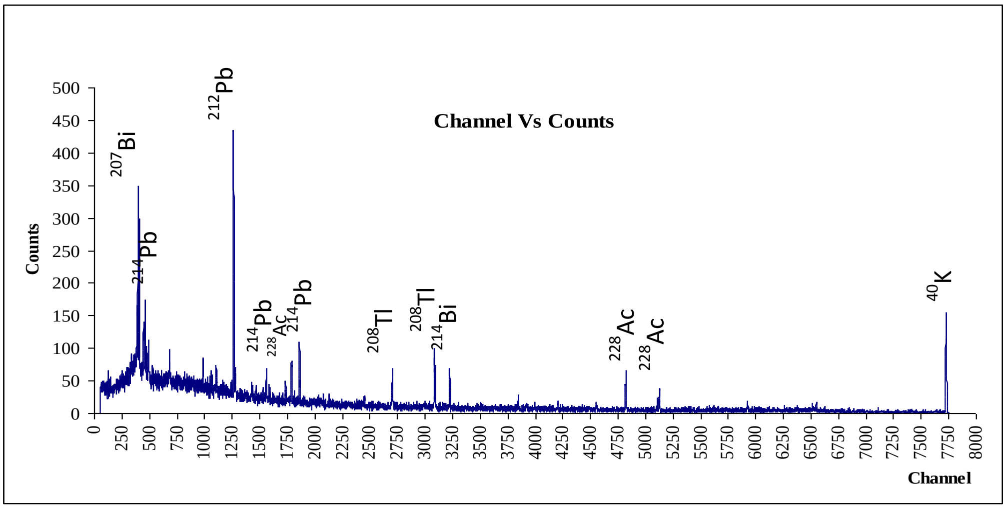

Figure 6 Energy Spectrum of the Sediments Sample S2 for Counting Time 3 hrs

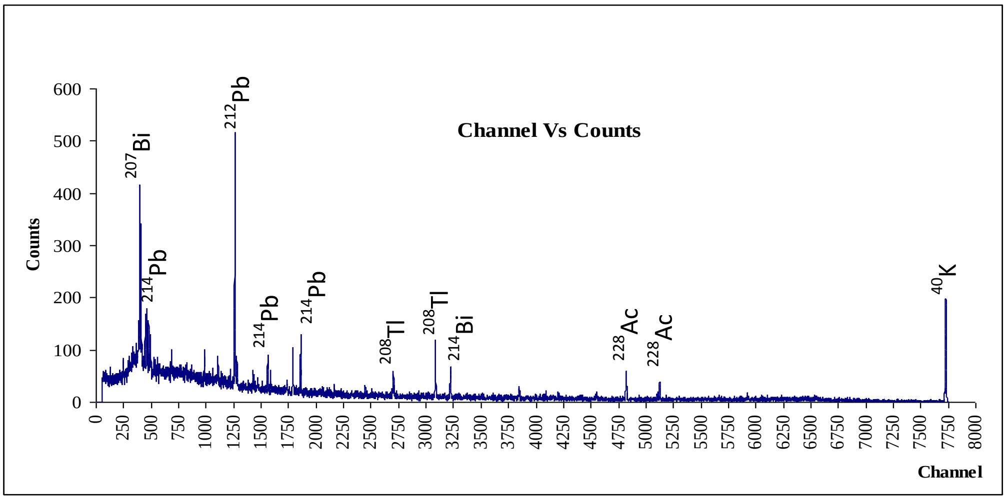

Figure 7 Energy Spectrum of the Sediments Sample S3 for Counting Time 3 hrs

Table 2 The average activity concentrations of ^{226}Ra, ^{232}Th and ^{40}K (Bqkg^{-1})

Sr No	Sample	Ra-226	Th-232	K-40
1	S1	65.98	59.93	729.49
2	S2	59.67	70.27	745.07
3	S3	63.04	78.43	857.56

Table 3 The average values of radiation hazard parameters for the samples

Sr No	Sample	Ra$_{eq}$ (Bq kg^{-1})	Dose Rate (nGyhr^{-1})	Hex
1	S1	157.30	97.10	0.56
2	S2	165.89	101.08	0.59
3	S3	181.80	112.26	0.65

Discussion

According to Table (3), the radium equivalent activity (Ra_{eq}) values for all samples under investigation are ranged from 207.85Bq kg^{-1} to 241.23Bq kg^{-1}. The observed values are less than 370 Bq kg^{-1}, which is the adopted valued for safely used. The average values of calculated absorbed dose rates in the samples under investigation are ranged from 97.10 $nGyhr^{-1}$ to112.26$nGyhr^{-1}$, it is twice of the world average value 55 $nGyhr^{-1}$. The calculated values for external hazard index obtained in this study are ranged from0.56to 0.65. Since these values are lower than unity, thus it can be concluded that the radiation hazard is insignificant for the people living near this area.

Conclusion

In this research work, we have been done activity of sediment sample using different type of efficiency calibration method. ^{214}Pb is the daughter nucleus of ^{238}U and ^{212}Pb, ^{208}Tl and ^{228}Ac are the daughter nuclei ^{232}Th decay series. Therefore, it can be found that the radionuclides in sediment samples are the daughter nuclei of Uranium and Thorium series. These radionuclides (^{208}Tl and ^{228}Ac) are caused by β decays and these activities are less than other radionuclides . These are determined by the HPGe detector, which is high resolution detector. In all sediments samples, the concentration of ^{40}K and ^{214}Pb are greater than the others radionuclides. And then, the concentration of ^{40}K and ^{214}Pb in north lake are greater than south lake. We concluded that it is because of the amount of water in South lake is greater than north lake. So radionuclides are more deposit in North Lake.

Acknowledgements

We wish to express our deepest gratitude to Dr.Ba Han, Rector, Meiktila University, Dr Kay Thi Thin, Pro-Rector, Meiktila University for their permission to summit this paper. Dr. Hla Hla Than, Professor and Head of Physics Department Meiktila University and Dr Hla Win, professor., Department of Physics, Meiktila University, for their permission and moral support throughout the paper. We are also grateful to all teaching staff of Physics Department, Meiktila University.

References

Csuros M., "Environmental Sampling and Analysis for echnicians", Lewis Publishers, Boca Raton, U.S.A (1994).

Grieco P. and Trattner R., "Sampling for Environmental Data Generation", SciTech Publishers, Matawan, NJ, U.S.A (1990).

T.M.S. El-zakla et al.,"Studying of Naturally Occuring Radionuclides for Some Environomental Samples and its Hazardous Effects", Physica Department, Faculty of Sciemce, Fayoum University (2014).

Broerman E., Upp, D. L., Twomey, T. R., and Little, W., "Performance of a New Type of Electrical Cooler for HPGe Detector Systems", ORTEC, PerkinElmer Instruments, U.S.A(2000).

ORTEC Software and Manual, "Gamma Vision -32 Gamma-Ray Spectrum Analysis and MCA Emulator for Microsoft Window 95,98,2000 and NT ", U.S.A, (1995).

Knoll. G. F., "Radiation Detection and Measurement", John Wiley & Sons, Third Edition, New York, (2000).

J. Myanmar Acad. Arts Sci. 2020 **Vol. XVIII.No.2A**

ESTIMATION OF RESONANCE POSITION OF THE ${}^{12}_{\Sigma}\mathrm{C}$ HYPERNUCLEAR SYSTEM WITH COMPLEX SQUARE WELL POTENTIAL BY USING GREEN'S FUNCTION METHOD

Htar Win Htike[1], Pont Pont Tun[2], Khin Swe Myint[3]

Abstract

In this research, differential cross section of ${}^{12}_{6}C(\overline{K},\pi){}^{12}_{\Sigma}C$ reaction is formulated by Green's function method. Imaginary part of this formulation, called spectral function, gives the spectral shape of this reaction. From the spectrum, the resonance position of the reaction is investigated. Green's function for this reaction is numerically solved. Then the spectral function is calculated and the various spectral shapes are investigated with simple case of complex square-well potentials. The resulting spectral shapes are compared with those of Morimatsu and Yazaki, obtained by analytically solved Green's function. It was observed that the spectral shapes obtained by both methods, i.e., numerical and analytical, are almost identical. This fact shows an advantage of numerical method in cases where analytical solutions are not possible.

Keywords: *Green's function, spectral function, resonance position.*

Introduction

In 1984, Morimatsu and Yazaki first gave a formalism for treating unstable (or continuum) states in the formation processes. It had been shown that the formation probabilities can be calculated from the *analytically solved Green's function*. Then they used this formalism to examine the effect of the unstable bound state on the formation probabilities. The simple case of a complex square-well potential is studied in detail. They showed that the unstable bound state gives no observable effect either in the scattering or in the formation process.

Many physical quantities are varying functions. For example, formation cross section is slowly varied with the total energy of the system. But at certain energy, the value of cross section is rapidly varied and spectral shape becomes with a very high peak. This phenomenon is called resonance. Then the energy value and observed level width of this high peak will give the resonance position of the reaction.

The purpose of our research is to study the spectral shape of ${}^{12}_{6}\mathrm{C}(\overline{\mathrm{K}},\pi){}^{12}_{\Sigma}\mathrm{C}$ reaction with complex square-well potential by using *numerically solved Green's function*. Then we will compare these spectral shapes with those treated by analytically solved Green's function which is proposed by Morimatsu and Yazaki. The numerically solved Green function and the calculations of formation probability of the reaction are given in this research.

---

[1] Dr, Lecturer, Department of Physics, Meiktila University

[2] Dr, Assistant Lecturer, Department of Physics, Mandalar Degree College

[3] Dr, Rector (Rtd), Emeritus Professor, Department of Physics, University of Mandalay

Formulation of Formation Cross Section of ${}^{12}_{6}\mathrm{C}(\overline{\mathrm{K}},\pi){}^{12}_{\Sigma}\mathrm{C}$

Transition Matrix Element

The transition matrix element can be generally expressed as

$$\mathrm{T_{fi}} = \langle \text{Final State} | \mathrm{T} | \text{ Initial State} \rangle . \qquad (1)$$

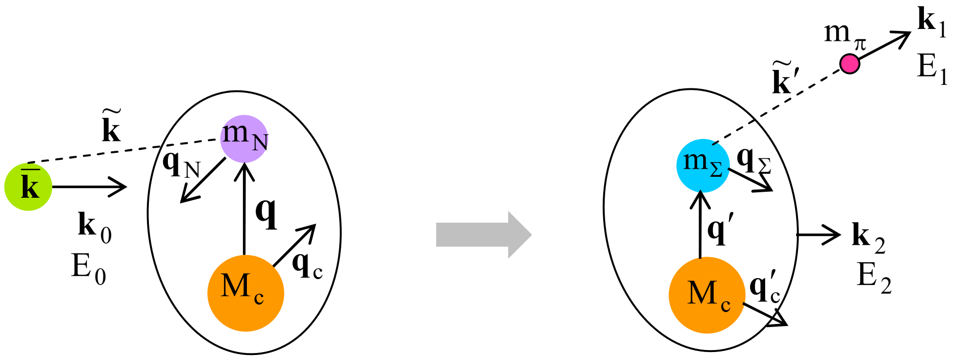

initial state **final state**

Figure 1 Schematic diagram of the ${}^{12}_{6}\mathrm{C}(\overline{\mathrm{K}},\pi){}^{12}_{\Sigma}\mathrm{C}$ reaction

In the initial state of the reaction, $\mathbf{k}_0$ and E_0 are momentum and total energy of incident kaon. $\mathbf{q}_N$ and $\mathbf{q}_c$ are internal momentum of a nucleon and core nucleus. $\mathbf{q}$ is the internal momentum between nucleon and core nucleus. $\tilde{\mathbf{k}}$ is relative momentum between incident kaon and one nucleon of target nucleus. Then in the final state of the reaction, $\mathbf{k}_1$ and E_1 are momentum and total energy of outgoing pion. $\mathbf{k}_2$ and E_2 are momentum and total energy of recoil nucleus. $\mathbf{q}_\Sigma$ and $\mathbf{q}'_c$ are internal momentum of Σ-hypernucleon and core nucleus. $\mathbf{q}'$ is internal momentum between Σ-hypernucleon and core nucleus. $\tilde{\mathbf{k}}'$ is relative momentum between outgoing pion and Σ-hypernucleon.

Transition matrix element $\mathrm{T_{fi}}$ for the above reaction can be expressed in terms of relative and center of mass momenta of initial state and final state as

$$T_{fi}^{(n)} = \frac{\hbar c}{\sqrt{2E_1}} \left[\mathbf{k}_1, \mathbf{k}_2, \Psi_f^{(n)} \right| T \left| \mathbf{k}_0, 0, \Psi_i \right] \frac{\hbar c}{\sqrt{2E_0}}, \qquad (2)$$

$\frac{\hbar c}{\sqrt{2E_0}}$ and $\frac{\hbar c}{\sqrt{2E_1}}$ are normalization constants for incoming kaon wave function and outgoing pion wave function. In order to account the all effects of all internal momenta of initial state and final state, completeness relations corresponding with these momenta are inserted into the equation of transition matrix element as

$$\frac{\sqrt{2E_0}\sqrt{2E_1}}{(\hbar c)^2}T_{fi}^{(n)}=(\tfrac{L}{2\pi})^{3\times 4}\iiiint d\mathrm{q}_N\,d\mathrm{q}_c\,d\mathrm{q}_\Sigma d\mathrm{q}'_c\left[\Psi_f^{(n)},\mathrm{k}_2\middle|\mathrm{q}_\Sigma,\mathrm{q}'_c\right]$$

$$\left[\ \mathbf{q}_\Sigma,\mathbf{q}'_c,\mathbf{k}_1\middle|T\middle|\,\mathbf{k}_0,\mathbf{q}_N,\mathbf{q}_c\ \right]\left[\ \mathbf{q}_N,\mathbf{q}_c\ \middle|0,\Psi_i\ \right]. \tag{3}$$

The internal particular momenta of $\mathbf{q}_\Sigma$ and $\mathbf{q}'_c$ can be expressed into relative and center of mass momentum as

$$\frac{\sqrt{2E_0}\sqrt{2E_1}}{(\hbar c)^2}T_{fi}^{(n)}=(\tfrac{L}{2\pi})^{3\times 4}\iiiint d\mathbf{q}_N\,d\mathbf{q}_c\,d\mathbf{q}_\Sigma d\mathbf{q}'_c\left[\Psi_f^{(n)}\middle|\mathbf{q}'\right]\left[\mathbf{k}_2\middle|\mathbf{q}_\Sigma+\mathbf{q}'_c\right]$$

$$\left[\ \mathbf{q}_\Sigma,\mathbf{q}'_c,\mathbf{k}_1\middle|T\middle|\,\mathbf{k}_0,\mathbf{q}_N,\mathbf{q}_c\ \right]\left[\ \mathbf{q}_N+\mathbf{q}_c\ \middle|0\ \right]\left[\ \mathbf{q}\ \middle|\Psi_i\ \right] \tag{4}$$

The terms, $\left[\mathbf{k}_2\middle|\mathbf{q}_\Sigma+\mathbf{q}'_c\right]$, $\left[\mathbf{q}_N+\mathbf{q}_c\ \middle|\ 0\right]$, and $\left[\ \mathbf{q}_\Sigma,\mathbf{q}'_c,\mathbf{k}_1\middle|T\middle|\,\mathbf{k}_0,\mathbf{q}_N,\mathbf{q}_c\ \right]$ from above equation are particularly solved. Since, the transition matrix element $\left[\ \widetilde{\mathbf{k}}'\middle|T\middle|\widetilde{\mathbf{k}}\ \right]$ depends only on the relative momenta of the reaction, we can therefore change the notation of transition operator 'T' by 't'. And then (4) becomes as

$$\frac{\sqrt{2E_0}\sqrt{2E_1}}{(\hbar c)^2}T_{fi}=(\tfrac{L}{2\pi})^{3\times 4}\iiiint d\mathbf{q}_N d\mathbf{q}_c d\mathbf{q}_\Sigma d\mathbf{q}'_{\mathbf{c}}\left\langle\Psi_{\mathbf{f}}^{(\mathbf{n})}\middle|\mathbf{q}'\right](\tfrac{2\pi}{L})^3\delta(\mathbf{k}_2-\mathbf{q}_\Sigma-\mathbf{q}'_c)$$

$$\left[\ \widetilde{\mathbf{k}}'\middle|t\middle|\widetilde{\mathbf{k}}\ \right](\tfrac{2\pi}{L})^3\delta(\mathbf{k}_1+\mathbf{q}_\Sigma-\mathbf{k}_0-\mathbf{q}_N)(\tfrac{2\pi}{L})^3\delta(\mathbf{q}'_c-\mathbf{q}_{\mathbf{c}})(\tfrac{2\pi}{L})^3$$

$$\delta(\mathbf{q}_N+\mathbf{q}_c)\left[\mathbf{q}\middle|\Psi_i\right\rangle. \tag{5}$$

By using the delta function properties, (5) becomes as

$$T_{fi}=\frac{(\hbar c)^2}{\sqrt{2E_0}\sqrt{2E_1}}\delta(\mathbf{k}_1+\mathbf{k}_2-\mathbf{k}_0)\int d\mathbf{q}_c\left\langle\Psi_f^{(n)}\middle|\mathbf{q}'\right]\left[\ \widetilde{\mathbf{k}}'\middle|t\middle|\widetilde{\mathbf{k}}\ \right]\left[\mathbf{q}\middle|\Psi_i\right\rangle \tag{6}$$

where $\mathbf{q}=-\mathbf{q}_c$, $\mathbf{q}'=\frac{M_c}{M_c+m_\Sigma}\mathbf{k}_2-\mathbf{q}_c$, $\widetilde{\mathbf{k}}=\frac{m_N}{m_{\bar{k}}+m_N}\mathbf{k}_0+\frac{m_{\bar{k}}}{m_{\bar{k}}+m_N}\mathbf{q}_c$, $\widetilde{\mathbf{k}}'=\frac{m_\Sigma\mathbf{k}_1-m_{\boldsymbol{\pi}}\mathbf{k}_2}{m_{\boldsymbol{\pi}}+m_\Sigma}+\frac{m_{\boldsymbol{\pi}}\mathbf{q}_{\mathbf{c}}}{m_{\boldsymbol{\pi}}+m_\Sigma}$

Transition probability is

$$\left|T_{fi}\right|^2=\left|\frac{(\hbar c)^2}{\sqrt{2E_0}\sqrt{2E_1}}\delta(\mathbf{k}_1+\mathbf{k}_2-\mathbf{k}_0)\int d\mathbf{q}_c\left\langle\Psi_f^{(n)}\middle|\mathbf{q}'\right]\left[\widetilde{\mathbf{k}}'\middle|t\middle|\widetilde{\mathbf{k}}\right]\left[\mathbf{q}\middle|\Psi_i\right\rangle\right|^2$$

$$=\frac{(\hbar c)^4}{4E_0E_1}\left|\delta(\mathbf{k}_1+\mathbf{k}_2-\mathbf{k}_0)\right|^2\left|\int d\mathbf{q}_c\left\langle\Psi_f^{(n)}\middle|\mathbf{q}'\right]\left[\widetilde{\mathbf{k}}'\middle|t\middle|\widetilde{\mathbf{k}}\right]\left[\mathbf{q}\middle|\Psi_i\right\rangle\right|^2. \tag{7}$$

Using relations between delta function and box function normalization, $\left|\mathbf{q}'\right]=(\tfrac{2\pi}{L})^{3/2}\left|\mathbf{q}'\right\rangle$, $\left[\widetilde{\mathbf{k}}'\right|=\left\langle\widetilde{\mathbf{k}}'\right|(\tfrac{2\pi}{L})^{3/2}$, $\left|\mathbf{q}\right]=\left\langle\mathbf{q}\right|(\tfrac{2\pi}{L})^{3/2}$ matrix element is

$$\left|T_{fi}\right|^2=\frac{(\hbar c)^4}{4E_0E_1}(\tfrac{2\pi}{L})^9\delta(\mathbf{k}_1+\mathbf{k}_2-\mathbf{k}_0)\left|\int d\mathbf{q}_c\left\langle\Psi_f^{(n)}\middle|\mathbf{q}'\right\rangle\left\langle\widetilde{\mathbf{k}}'\middle|t\middle|\widetilde{\mathbf{k}}\right\rangle\left\langle\mathbf{q}\middle|\Psi_i\right\rangle\right|^2. \tag{8}$$

Differential Cross Section

After the matrix element of the reaction is calculated transition rate and cross section are obtained by following relations:

$$W_{fi} = \tfrac{2\pi}{\hbar}\sum_n \left|T_{fi}\right|^2 \delta(E_f - E_i)\rho(E) \tag{9}$$

$$Cross\,Section = \frac{transition\ \ rate}{incident\ \ flux} = \frac{W_{fi}}{{}^{v_0}\!/_{L^3}}\,. \tag{10}$$

W_{fi} = transition rate

T_{fi} = transition probability

$\delta(E_f - E_i)$ = energy conservation term

$\rho(E)$ = number of allowed state(or) phase volume

$\frac{\mathrm{v}_0}{\mathrm{L}^3}$ = incident flux

The value of the transition probability $\left|T_{fi}\right|^2$ is inserted into the above equation (9) as

$$W_{fi} = \frac{2\pi}{\hbar}\frac{(\hbar c)^4}{4E_0E_1}\left(\frac{2\pi}{L}\right)^9 \sum_n \delta(\mathbf{k}_1 + \mathbf{k}_2 - \mathbf{k}_0)\left|\int d\mathbf{q}_c \left\langle \Psi_f^{(n)}\right|\mathbf{q}'\rangle\langle\tilde{\mathbf{k}}'|t|\tilde{\mathbf{k}}\rangle\langle\mathbf{q}\left|\Psi_i\right\rangle\right|^2$$

$$\delta(E_f - E_i)\rho(E)\,. \tag{11}$$

The density of final state, $\rho(E) = (\frac{L}{2\pi})^6 dk_1dk_2$, the number of states per unit energy interval, can be easily calculated by using the periodic boundary condition and the wave functions for final state in Cartesian coordinate.

$$W_{fi} = \tfrac{2\pi}{\hbar}\tfrac{(\hbar c)^4}{4E_0E_1}(\tfrac{2\pi}{L})^9(\tfrac{L}{2\pi})^6 \sum_n \delta(\mathbf{k}_1 + \mathbf{k}_2 - \mathbf{k}_0)\left|\int d\mathbf{q}_c \left\langle \Psi_f^{(n)}\right|\mathbf{q}'\rangle\langle\tilde{\mathbf{k}}'|t|\tilde{\mathbf{k}}\rangle\langle\mathbf{q}\left|\Psi_i\right\rangle\right|^2$$

$$\delta(E_f - E_i)d\mathbf{k}_1 d\mathbf{k}_2 \tag{12}$$

The differential cross section can be written as

$$d^6\sigma = \tfrac{L^3}{v_0}W_{fi}$$

$$= \tfrac{2\pi}{\hbar}\tfrac{(\hbar c)^4}{4E_0E_1}(\tfrac{2\pi}{L})^9(\tfrac{L}{2\pi})^6 \tfrac{L^3E_0}{c^2\hbar k_0}\sum_n \delta(\mathbf{k}_1 + \mathbf{k}_2 - \mathbf{k}_0)\left|\int d\mathbf{q}_c \left\langle \Psi_f^{(n)}\right|\mathbf{q}'\rangle\langle\tilde{\mathbf{k}}'|t|\tilde{\mathbf{k}}\rangle\langle\mathbf{q}\left|\Psi_i\right\rangle\right|^2$$

$$\delta(E_f - E_i)d\mathbf{k}_1 d\mathbf{k}_2 \tag{13}$$

where $v_0 = \dfrac{c^2\hbar k_0}{E_0}$. After calculation the integral term $\int d\mathbf{k}_2$, the differential cross section is obtained.

$$d^3\sigma = (2\pi)^4\frac{(\hbar c)^2}{4k_0E_1}\sum_n \left|\int d\mathbf{q}_c \left\langle \Psi_f^{(n)}\right|\mathbf{q}'\rangle\langle\tilde{\mathbf{k}}'|t|\tilde{\mathbf{k}}\rangle\langle\mathbf{q}\left|\Psi_i\right\rangle\right|^2 \delta(E_f - E_i)d\mathbf{k}_1 \tag{14}$$

Energy Conservation Term

Then energy conservation term $\delta(E_i - E_f)$ can be written by using delta function properties, $\lim_{\varepsilon \to 0} \frac{1}{x+i\varepsilon} = \frac{P}{x} - i\pi\delta(x)$ as

$$\delta(E_i - E_f) = \left\langle \Psi_f^{(n)} \middle| \delta(E - H_{\Sigma c}) \middle| \Psi_f^{(n)} \right\rangle \tag{15}$$

$$\delta(\mathrm{E_i} - \mathrm{E_f}) = \left(-\tfrac{1}{\pi}\right) \mathrm{Im} \left\langle \Psi_\mathrm{f}^{(\mathrm{n})} \middle| \tfrac{1}{\mathrm{E} - \mathrm{H}_{\Sigma \mathrm{c}} + \mathrm{i}\varepsilon} \middle| \Psi_\mathrm{f}^{(\mathrm{n})} \right\rangle . \tag{16}$$

Differential cross section equation (14) becomes as

$$d^3\sigma = (2\pi)^4 \frac{(\hbar c)^2}{4k_0 E_1} \sum_n \left| \int d\mathbf{q}_c \left\langle \Psi_f^{(n)} \middle| \mathbf{q}' \right\rangle \left\langle \widetilde{\mathbf{k}}' \middle| t \middle| \widetilde{\mathbf{k}} \right\rangle \left\langle \mathbf{q} \middle| \Psi_i \right\rangle \right|^2 \left(-\tfrac{1}{\pi}\right) \mathrm{Im} \left\langle \Psi_f^{(n)} \middle| \tfrac{1}{E - H_{\Sigma c} + i\varepsilon} \middle| \Psi_f^{(n)} \right\rangle d\mathbf{k}_1 . \tag{17}$$

The differential cross section can be written in terms of coordinate representation as

$$d^3\sigma = (2\pi)^4 \frac{(\hbar c)^2}{4k_0 E_1} \left| \langle \bar{t} \rangle \right|^2 (-\tfrac{1}{\pi}) \, \mathrm{Im} \Big[\iint d\mathbf{r} d\mathbf{r}' \Psi_i^*(\mathbf{r}) e^{-i\eta(\mathbf{k}_0 - \mathbf{k}_1).\mathbf{r}} \left\langle \mathbf{r} \middle| \tfrac{1}{E - H_{\Sigma c} + i\varepsilon} \middle| \mathbf{r}' \right\rangle$$

$$e^{i\eta(\mathbf{k}_0 - \mathbf{k}_1).\mathbf{r}'} \Psi_i(\mathbf{r}') \Big] d\mathbf{k}_1 . \tag{18}$$

The differential cross section per unit solid angle of outgoing pion for the reaction ${}^{12}_{6}C(\overline{K},\pi)^{12}_{\Sigma}C$ as

$$\frac{d^3\sigma}{dE_1 d^2\Omega_1} = (2\pi)^4 \frac{(\hbar c)^2 k_1}{4k_0 \hbar^2 c^2} \left| \langle \bar{t} \rangle \right|^2 (-\tfrac{1}{\pi}) \, \mathrm{Im} \Big[\iint d\mathbf{r} d\mathbf{r}' f^*(\mathbf{r}) \left\langle \mathbf{r} \middle| \tfrac{1}{E - H_{\Sigma c} + i\varepsilon} \middle| \mathbf{r}' \right\rangle f(\mathbf{r}') \Big]. \tag{19}$$

From the above equation, the imaginary term can give the spectral shape of the differential cross section with respect to the total energy of the outgoing pion. Before we calculate the spectral function, we first evaluate the matrix element, $\left\langle \mathbf{r} \middle| \tfrac{1}{E - H_{\Sigma c} + i\varepsilon} \middle| \mathbf{r}' \right\rangle$, by using Green's function method.

Green's Function and Spectral Function

Formulation of Green's Function

The matrix element $\left\langle \mathbf{r} \middle| \tfrac{1}{E - H_{\Sigma c} + i\varepsilon} \middle| \mathbf{r}' \right\rangle$ can be defined as Green's function $G(\mathbf{r}, \mathbf{r}')$. Green's function can be separated into radial part and angular part. The Green's function $G(\mathbf{r}, \mathbf{r}')$ can be separated into radial part and angular part as

$$\mathrm{G}(\mathbf{r}, \mathbf{r}') = \sum_{\ell=0}^{\infty} \sum_{\mathrm{M}} \mathrm{Y}_{\ell \mathrm{M}}(\hat{\mathbf{r}}) \frac{\mathrm{G}(\mathrm{r}, \mathrm{r}')}{\mathrm{r}\,\mathrm{r}'} \mathrm{Y}_{\ell \mathrm{M}}^*(\hat{\mathbf{r}}') . \tag{20}$$

The radial part of Green's function satisfies the Schrödinger radial equation

$$\left[\frac{d^2}{dr^2} + k^2 - \frac{\ell(\ell+1)}{r^2} - \widetilde{V}(r) \right] G(r, r') = \frac{2\mu}{\hbar^2} \delta(r, r') \tag{21}$$

where $k=\sqrt{\dfrac{2\mu E}{\hbar^2}}$ and $\tilde{V}(r)=\dfrac{2\mu}{\hbar^2}v(r)$. The Green's function is continuous and its derivative has discontinuity. It is convenient to consider the two intervals a ≤ r < r′ and r′ < r ≤ b separately and write the Green's function in the following forms.

$$G(r,r')=G_1(r,r') \quad a\le r<r' \tag{22}$$

$$G(r,r')=G_2(r,r') \quad r'<r\le b \tag{23}$$

By applying the properties of the Green's function: the Green's function is continuous at r = r′; and the derivative of the Green's function has discontinuity at r = r′, the two solutions G_1 (r, r′) and G_2 (r, r′) become as

$$G_1(r,r')=\frac{2\mu}{\hbar^2}\frac{v_\ell(r')u_\ell(r)}{W(u_\ell,v_\ell)} \qquad 0\le r<r' \tag{24}$$

and

$$G_2(r,r')=\frac{2\mu}{\hbar^2}\frac{u_\ell(r')v_\ell(r)}{W(u_\ell,v_\ell)} \qquad r'<r\le\infty \tag{25}$$

where $W=u_\ell(r')v_\ell'(r')-u_\ell'(r')v_\ell(r')$ is Wronskian of u(r′) and v(r′) and will be non-zero if u(r′) and v(r′) are linearly independent. The values of r′ in Eq. (24) are greater than r and the values of r in Eq. (25) are greater than r′. Then we defined as $v_\ell(r_>)$. Similarly, we defined for $u_\ell(r')$ and $u_\ell(r)$ as $u_\ell(r_<)$ where $r_<$ and $r_>$ are the larger and the smaller values of 'r' and 'r′' respectively. These two solutions are recombined into G(r, r′) as

$$G(r,r')=\frac{2\mu}{\hbar^2}\frac{u_\ell(r_<)v_\ell(r_>)}{W(u_\ell,v_\ell)} \tag{26}$$

By inserting the value of G(r, r′) from (26) into (20), we get

$$G(\mathbf{r},\mathbf{r}')=\frac{2\mu}{\hbar^2}\sum_{\ell=0}^{\infty}\sum_{M}Y_{\ell M}(\hat{\mathbf{r}})\frac{1}{rr'}\frac{u_\ell(r_<)v_\ell(r_>)}{W(u_\ell,v_\ell)}Y_{\ell M}^{*}(\hat{\mathbf{r}}') \tag{27}$$

where $u_\ell(r')$ and $v_\ell(r')$ are the stationary and out-going solutions of the Schrödinger equation. The boundary conditions of these solutions are $u_\ell(0)=r^{\ell+1}$ at the origin and $v_\ell(r)=kr\,h_\ell^{+}(kr)$ in the asymptotic region $r\to\infty$, respectively. These particular solutions can be derived by solving Schrödinger radial equation with the use of difference method.

Calculation of Spectral Function

In order to study the spectral shape of the reaction, we considered only the spectral function from the formulation of formation cross section as

$$S(E)=(-\tfrac{1}{\pi})\,\mathrm{Im}\Big[\iint d\mathbf{r}d\mathbf{r}'\Psi_i^{*}(\mathbf{r})e^{-i\eta(\mathbf{k}_0-\mathbf{k}_1).\mathbf{r}}\left\langle\mathbf{r}\left|\tfrac{1}{E-H_{\Sigma c}+i\varepsilon}\right|\mathbf{r}'\right\rangle$$

$$e^{i\eta(\mathbf{k}_0-\mathbf{k}_1).\mathbf{r}'}\Psi_i(\mathbf{r}')\Big] \tag{28}$$

The simple notation '**Q**' is used for $\eta(\mathbf{k}_0 - \mathbf{k}_1)$ and mathematical expansion of the free particle state wave function as

$$e^{i\mathbf{Q}.\mathbf{r}} = \sum_{\ell=0}^{\infty} \sqrt{4\pi(2\ell+1)}\; i^{\ell} j_{\ell}(Qr') Y_{\ell 0}(\hat{\mathbf{r}}') \;\text{ and} \tag{29}$$

$$e^{-i\mathbf{Q}.\mathbf{r}} = \sum_{\ell=0}^{\infty} \sqrt{4\pi(2\ell+1)}\,(-i)^{\ell} j_{\ell}(Qr) Y_{\ell 0}^{*}(\hat{\mathbf{r}}) . \tag{30}$$

The solution of Green's function is

$$\langle \mathbf{r} | \frac{1}{E - H_{\Sigma c} + i\varepsilon} | \mathbf{r}' \rangle = \frac{2\mu}{\hbar^2} \sum_{\ell=0}^{\infty} \sum_{M} Y_{\ell M}(\hat{\mathbf{r}}) \frac{1}{rr'} \frac{u_{\ell}(r_<) v_{\ell}(r_>)}{W(u_{\ell}, v_{\ell})} Y_{\ell M}^{*}(\hat{\mathbf{r}}') . \tag{31}$$

The imaginary term from Eq. (28) will give spectral shape of this reaction. By substituting the solution of Green's function Eq. (31), harmonic oscillator wave function of carbon target for s-state and mathematical expansions of free particle wave functions, we have solved the imaginary term called spectral function. Since the solutions of $u_{\ell}(r_<)$ and $v_{\ell}(r_>)$ depend on the total energy of Σ-core-nucleus, the spectral function is the function of $E_{\Sigma\text{-core}}$. Then we obtained the spectral function as

$$\mathrm{S(E)} = -4\, \frac{2\mu}{\hbar^2} \left(\tfrac{1}{a^2\pi}\right)^{3/2} \mathrm{Im}\Big[\iint r\, r' \, \exp\!\left(\tfrac{-r^2}{2a^2}\right) \exp\!\left(\tfrac{-r'^2}{2a^2}\right) \sum_{\ell=0}^{\infty} (2\ell+1) j_{\ell}(Qr)\, j_{\ell}(Qr')$$

$$\frac{u_{\ell}(r_<) v_{\ell}(r_>)}{W(u_{\ell}, v_{\ell})} dr\, dr' \Big] . \tag{32}$$

The spectral functions for various total energies of Σ-core-nucleus are numerically calculated and compared with those calculated by Morimatsu and Yazaki. The obtaining results are explicitly discussed.

Result and Discussion

In order to simulate the spectral shapes for the ^{12}C target, we used two cases of complex square-well potentials from as shown in Table (1). Our calculated spectral functions with arbitrary unit for above two cases are compared with those of Morimatsu and Yazaki. It was found that all results are equivalent.

For case (a) potential, (-26, -2*i*) MeV, the spectral function calculated with numerically solved Green's function (i.e., our result) is shown in Fig. (2) and that with analytically solved Green's function calculated by Morimatsu and Yazaki is also shown in Fig. (3). The observed peaks are found at about -3.47MeV (our result) and -3.48 MeV (result of Morimatsu and Yazaki) of $E_{\Sigma\text{-core}}$ respectively. The two results are agreed.

The spectral functions for case (b) potential, (-16, 0*i*) MeV, are expressed in Fig. (4) and Fig. (5) for our result and their result respectively. The sharp peaks are found at 1.38 MeV (our result) and at 1.16 MeV (their result). For this case, we also determined the spectral functions with various values of imaginary part of potentials, W= -2, -3 and -6 MeV. These are shown in Fig. (6). In this figure, it is observed that as |W| increases, the peak positions of these cases are dramatically decreases. Since the results for various |W| from (Morimatsu and Yazaki) are also shown in Fig. (7), our results can be clearly compared with those. It can be observed that the two results are almost identical.

Table 1 The strengths of the complex square-well potentials (Morimatsu and Yazaki)

Case	V(MeV)	W(MeV)
a	-26	-2
b	-16	0

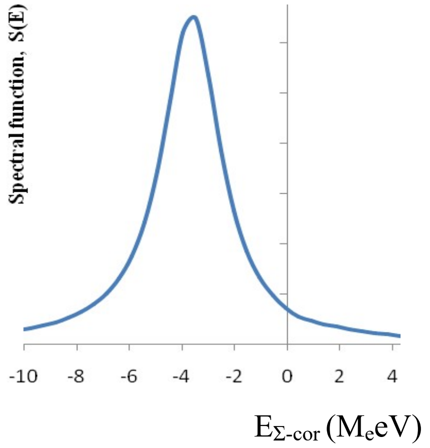

Figure 2 Spectral function calculated by numerically solved Green's funciton for case (a) (our result).

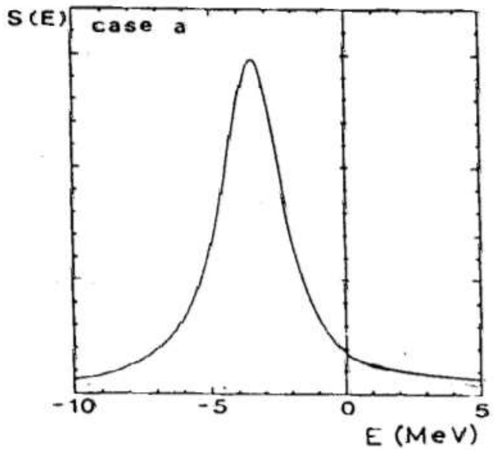

Figure 3 Spectral function calculated by analytically solved Green's funciton for case (a) (Result of Morimatsu and Yazaki)

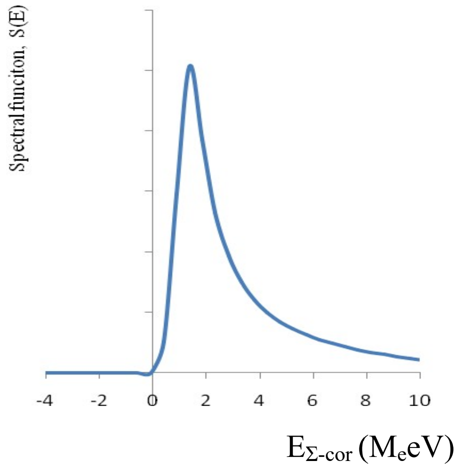

Figure 4 Spectral function calculated by numerically solved Green's funciton for case (b) (our result).

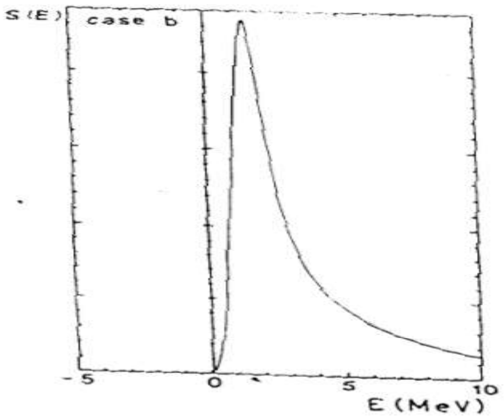

Figure 5 Spectral function calculated by analytically solved Green's funciton for case (b) (Result of Morimatsu and Yazaki)

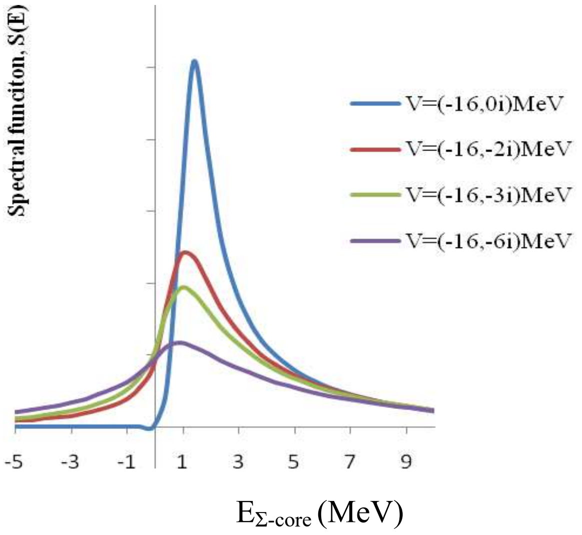

Figure 6 Spectral functions calculated by numerically solved Green's funciton for case (b) with W=0, -2, -3 and -6 MeV (our results).

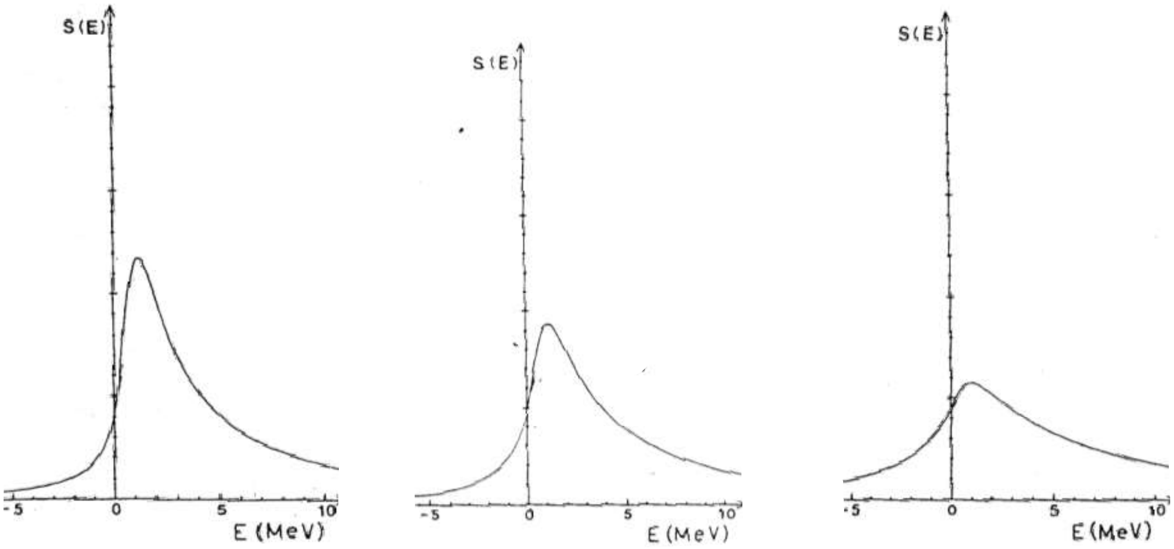

(W=-2 MeV) (W=-3 MeV) (W=-6 MeV)

Figure 7 Spectral functions calculated by analytically solved Green's funciton for case (b) with W= -2, -3 and -6 MeV (Results of Morimatsu and Yazaki).

Conclusion

We firstly concluded that formation cross section can be calculated by the use of Green's function method. Secondly, the solutions of Green's function can be obtained by both numerically and analytically. Since these solutions are equivalent, numerically solved Green's function can also be used to study the formation cross section in nuclear physics. Thirdly, since the spectral function can give the resonance position of the Σ-hypernuclear system, we can estimate the total energy or binding energy of the Σ-hypernuclear state.

Acknowledgements

I am very grateful to Dr Ba Han, Rector of Meiktila University and Dr Hla Hla Than, Professor, Head of Department of Physics, Meiktila University for giving the opportunity to write the paper. I am also grateful to Dr Khin Swe Myint, Emeritus Professor (Rtd), Department of Physics, University of Mandalay for her excellent supervision.

References

N. Zettili, "Quantum Mechanics Concepts and Applications", John Wiley & Sons, Ltd., New York (2003).

O. Morimatsu and K. Yazaki, "The Formation Probabilities of Σ-hypernuclei and the Unstable Bound State", Nuclear Physics **A435** (1985) 727.

J. Myanmar Acad. Arts Sci. 2020 **Vol. XVIII.No.2A**

INVESTIGATIO NO NPOLARIZATION OF LIGHT IN THE PRESENCE OF A WEAK EXTERNAL MAGNETIC FIELD

Lae Lae Kyaing[1] and Win Mar[2]

Abstract

Degree of polarization of scattered line radiation in the presence of the magnetic field was investigated. The Stokes parameters of the scattered radiation incident on an arbitrary polarized atom in any given arbitrary direction were calculated. It was considered that the polarization of scattered line radiation from an upper atomic level with angular momentum Ju = 3/2 to a lower atomic level with angular momentum Jι = 1/2 transition. This line has transition of both type electric dipole transition and magnetic quadrupole transition. Only the electric dipole transition was considered for upper and lower atomic levels having different parities. The degree of linear polarization of scattered radiation in the presence of weak external magnetic field was calculated. In this calculation, the lower level polarization was neglected. The obtained results were compared with experimental results as well as theoretical results. It was found that the obtained results agree well with these results.

Keywords: Stokes parameters, polarization, scattered radiation, electric dipole, weak external magnetic field

Introduction

Level-crossing spectroscopy is a technique which exploits the interference phenomena that can occur in resonance fluorescence when two or more energy levels are nearly degenerate. So far it has been applied exclusively to resonance light scattering from atomic systems. When an atom is placed in the presence of magnetic field, the energy level of an atom is splited into several magnetic sublevels called Zeeman levels. If the strength of the magnetic field is strong, the Zeeman levels of an excited atomic state are distinct (i.e., separated by several natural line widths), their contribution to the atomic resonance fluorescence may be treated independently by summing over the each excited Zeeman level. When a magnetic field is applied along an arbitrary direction to this excited state, the degeneracy between the magnetic sublevels is removed. The coherence, in general, is partially destroyed and the resonance fluorescence is depolarized.

Polarization that is produced by coherent scattering modified by a weak magnetic field is known as the Hanle effect. Moreover, measuring the amount of polarization nature of the scattered radiation, we can predict the magnetic field strengths and its orientations. The Hanle effect is usually used to determine weak magnetic fields in the solar atmosphere.

Polarization is an important property of electromagnetic waves. In communications, completely polarized waves are used. The complete polarization types of electromagnetic waves are linear polarization, circular polarization and elliptical polarization. Electromagnetic waves from of ratio astronomical sources may possess random polarization (also known as un-polarized waves), partial polarization (completely polarized and un-polarized).

---

[1] Dr, Associate Professor, Department of Physics, Meiktila University

[2] Dr, Associate Professor, Department of Physics, Meiktila University

Polarization of Atom and Radiation

Polarized Radiation

Polarization is a property of waves that describes the orientation of their oscillation. By convention, the polarization of light is described by specifying the direction of the wave's electric field. For transverse waves such as electromagnetic waves, it describes the orientation of the oscillations in the plane perpendicular to the wave's direction of travel. In this case, the electric field may be oriented in a single direction (linear polarization) or it may rotate as the wave travels (circular or elliptical polarization).

According to Maxwell's equations, the electric and magnetic field be perpendicular to the direction of propagation and to each other. In general, the electric field vector $\vec{E}$ can always be resolved into two perpendicular components.

If the light is linearly polarized, then the two perpendicular components with equal amplitude oscillate in phase.

Elliptically polarized light consists of two perpendicular components of unequal amplitude which differ in phase by 90 degree.

Circularly polarized light is a special case of elliptically polarized light in which the two components have same amplitude and a 90 degree phase difference. For circularly polarized light the orientation of the electric field rotates around the direction of travel. While looking at source, the electric vector of the light coming toward you appears to be rotating counterclockwise, the light is said to be right-circularly polarized. If clockwise, the light is said to be left circularly polarized light.

For unpolarized light, the electric field vector vibrates in all directions perpendicular to the direction of propagation.

Radiation Density Matrix

When the average properties of an ensemble of identical non-interacting systems are of interest, and information on the individual members of the ensemble is not needed, it is useful to introduce the concept of the density matrix. It's a matrix which describes the state of ensemble. Consider first a system in a state $|\psi\rangle$. The state $|\psi\rangle$ can be written in terms of complete orthogonal set of basis states as

$$|\psi\rangle = \sum_n C_n |u_n\rangle \tag{1}$$

$$\langle u_{n'}|\psi\rangle = \sum_n C_n \langle u_{n'}|u_n\rangle$$

$$= C_n\langle u_{n'}|u_n\rangle + C_{n'}\langle u_{n'}|u_{n'}\rangle + C_{n''}\langle u_{n'}|u_{n''}\rangle + \ldots$$

$$\langle u_{n'}|\psi\rangle = C_n \qquad (n' = n)$$

$$C_n = \langle u_{n'}|\psi\rangle$$

$|\psi\rangle$ is normalized,

$$\langle\psi|\psi\rangle = \langle\psi|\sum_n u_n\rangle\langle u_n|\psi\rangle$$

$$\langle\psi|\psi\rangle = \sum_n\langle\psi|u_n\rangle\langle u_n|\psi\rangle$$

$$\langle\psi|\psi\rangle = \sum_n|C_n|^2 = 1 \qquad (2)$$

An observable, such as momentum and spin components can be represented by an operator, such as A, in the vector space in question. Quite generally, an operator outs an a ket from the left,

$$A\cdot(|\alpha\rangle) = A|\alpha\rangle$$

If A is an observable, with matrix elements

$$\langle u_n|A|u_p\rangle = A_{np} \qquad (3)$$

The mean value of A is

$$\langle A\rangle = \langle\psi|A|\psi\rangle$$

$$\langle A\rangle = \sum_n C_n^*\sum_p C_p\langle u_n|A|u_p\rangle$$

$$\langle A\rangle = \sum_n\sum_p C_n^* C_p A_{np} \qquad (4)$$

$$\langle u_p|\psi(+)\rangle\langle\psi(+)|u_n\rangle = C_n^* C_p \qquad (5)$$

$$|u_{n'}\rangle\langle u_{n'}|\cdot|\psi\rangle = |u_{n'}\rangle\langle u_{n'}|\psi\rangle = C_{n'}|u_n\rangle$$

We see that $|u_{n'}\rangle\langle u_{n'}|$ selects that portion of the ket $|\psi\rangle$ parallel to $|u_n\rangle$. So $|u_{n'}\rangle\langle u_{n'}|$ is known as the projection operator along the base ket $|u_{n'}\rangle$ and it denoted by Λ.

$$\Lambda = |u_{n'}\rangle\langle u_{n'}| \qquad (6)$$

It is therefore natural to introduce the density operator ρ, defined by

$$\rho = |\psi\rangle\langle\psi| \qquad (7)$$

The density operator is represented in the $\{|u_n\rangle\}$ basics by a matrix called the density matrix whose elements are

$$\rho_{pn} = \langle u_p|\rho|u_n\rangle = C_n^* C_p \qquad (8)$$

The density operator ρ derived by

$$\rho = |\psi\rangle\langle\psi|$$

According to equation (8), equation (4)indicates that the sum of the diagonal elements of the density matrix is equal to 1.

$$\sum_n|C_n|^2 = \sum_n\rho_{nn} = \mathrm{Tr}\rho = 1 \qquad (9)$$

Trace means the sum of the diagonal terms of matrix element is equal to 1.Now, we can express the radiation field with the density matrix from where the rows and columns are labeled by two basis polarization states $|+\rangle$ and $|-\rangle$ as

$$\rho^r = \begin{bmatrix} \rho_{++} & \rho_{+-} \\ \rho_{-+} & \rho_{--} \end{bmatrix} = \begin{bmatrix} C_1C_1^* & C_1C_2^* \\ C_2C_1^* & C_2C_2^* \end{bmatrix}$$

$$= \begin{bmatrix} |C_1|^2 & C_1C_2^* \\ C_2C_1^* & |C_2|^2 \end{bmatrix} \tag{10}$$

and the trace of the density matrix is

$$\mathrm{Tr}\rho^r = [\rho_{++} + \rho_{--}] = |C_1|^2 + |C_2|^2 = 1 \tag{11}$$

Using equations (3) and (8), equation (4) becomes

$$\langle u_n | A | u_p \rangle = A_{np} \tag{12}$$

$$\rho_{pn} = C_n^* C_p = \langle u_p | \rho | u_n \rangle \tag{13}$$

$$\langle A \rangle = \langle \psi | A | \psi \rangle = \sum_{n,p} C_n^* C_p A_{np} \tag{14}$$

$$\langle A \rangle = \sum_{n,p} \langle u_p | \rho | u_n \rangle \langle u_n | A | u_p \rangle \tag{15}$$

$$\sum_n | u_n \rangle \langle u_n | = 1 \tag{16}$$

$$\langle A \rangle = \sum_p \langle u_p | \rho A | u_p \rangle \tag{17}$$

$$\langle A \rangle = \mathrm{Tr}\,\{\rho A\} \tag{18}$$

Polarization Matrix and Stokes Parameters

The two dimensional Hermitian matrix can be expressed as a linear combination of the unit matrix and Pauli's matrices. So the radiation density matrix can generally be written as

$$\rho^\gamma = \frac{1}{2}(1 + \vec{\sigma}.\vec{S}) , \tag{19}$$

where $\vec{\sigma}$ is the vector of which the components are the Pauli's matrices σ_x,$\sigma_y$and σ_z.$\vec{S}$ is a polarization vector of the radiation.

$$\vec{S} = S_x\hat{x} + S_y\hat{y} + S_z\hat{z}$$

$$\vec{\sigma} = \sigma_x\hat{x} + \sigma_y\hat{y} + \sigma_z\hat{z} .$$

Therefore $\rho^\gamma = \frac{1}{2}(1 + \sigma_x S_x + \sigma_y S_y + \sigma_z S_z) ,$ (20)

where $\sigma_x = \begin{bmatrix} 0 & 1 \\ 1 & 0 \end{bmatrix} \sigma_y = \begin{bmatrix} 0 & -i \\ i & 0 \end{bmatrix} \sigma_z = \begin{bmatrix} 1 & 0 \\ 0 & -1 \end{bmatrix}$

$$\rho^{\gamma} = \frac{1}{2}\left[\begin{bmatrix}1 & 0\\0 & 1\end{bmatrix} + \begin{bmatrix}0 & 1\\1 & 0\end{bmatrix}S_x + \begin{bmatrix}0 & -i\\i & 0\end{bmatrix}S_y + \begin{bmatrix}1 & 0\\0 & -1\end{bmatrix}S_z\right]$$

$$\rho^{\gamma} = \frac{1}{2}\left[\begin{bmatrix}1 & 0\\0 & 1\end{bmatrix} + \begin{bmatrix}0 & S_x\\S_x & 0\end{bmatrix} + \begin{bmatrix}0 & -iS_y\\S_y & 0\end{bmatrix} + \begin{bmatrix}S_z & 0\\0 & -S_z\end{bmatrix}\right]$$

$$\rho^{\gamma} = \frac{1}{2}\begin{bmatrix}1+S_z & S_x - iS_y\\S_x + iS_y & 1 - S_z\end{bmatrix}, \tag{21}$$

and the trace of the density matrix is given by

$$\mathrm{Tr}\rho^{\gamma} = \frac{1}{2}(1 + S_z + 1 - S_z) = 1\ . \tag{22}$$

Comparing equation (22) with equation (11), the polarization state of the radiation can be given as follow

The total intensity I is

$$I = \mathrm{Tr}\rho^{\gamma} = \left(\rho_{+,+} + \rho_{-,-}\right). \tag{23}$$

According to the equation (11) the linear polarization is

$$Q = S_x = \mathrm{Tr}(\rho^{\gamma}\sigma_x) = \left(\rho_{+,-} + \rho_{-,+}\right), \tag{24}$$

the plane polarization

$$U = S_y = \mathrm{Tr}(\rho^{\gamma}\sigma_y) = i\left(\rho_{+,-} - \rho_{-,+}\right), \tag{25}$$

and the circular polarization

$$V = S_z = \mathrm{Tr}(\rho^{\gamma}\sigma_z) = \left(\rho_{+,+} - \rho_{-,-}\right), \tag{26}$$

where I, Q, U, V are well-known four Stokes parameters.

Scattering Matrix

If density matrix $\rho(k')$ describes the state of polarization of the incident radiation, the density matrix $\rho(k)$ representing the state of polarization of the scattered radiation is given by

$$\rho(k) = T\rho(k')T^{+}, \tag{27}$$

where T matrix is defined in terms of its elements.

If stokes vectors $S'(k')$ characterizing the state of polarization of the scattered radiation is

$$S(k) = MS'(k'), \tag{28}$$

where, M is the 4 × 4 matrix and is called scattering matrix.

Using the general form of density matrix

$$\rho = \frac{1}{2}\sum_{p=0}^{3}\sigma_p S_p\ , \tag{29}$$

in equation (27) and comparing with equation (28), we obtain scattering matrix elements

$$M_{pp'} = \frac{1}{2}\mathrm{Tr}(T\sigma_{p'}T^{+}\sigma_{p}), \tag{30}$$

where the matrices σ_p are explicitly given by

$$\sigma_0 = \begin{bmatrix} 1 & 0 \\ 0 & 1 \end{bmatrix}, \quad \sigma_1 = \begin{bmatrix} 0 & 1 \\ 1 & 0 \end{bmatrix}, \quad \sigma_2 = \begin{bmatrix} 0 & -i \\ i & 0 \end{bmatrix}, \quad \sigma_3 = \begin{bmatrix} 1 & 0 \\ 0 & -1 \end{bmatrix}, \tag{31}$$

By using the equation (30), the scattering matrix elements in terms of the polarization states $\mu = \mu' = \pm 1$ is obtained. These scattering matrix elements are shown below:

$$M_{00} = \frac{1}{2}(T_{++}T^{*}_{++} + T_{+-}T^{*}_{+-} + T_{-+}T^{*}_{-+} + T_{--}T^{*}_{--})$$

$$M_{01} = \frac{1}{2}(T_{+-}T^{*}_{++} + T_{++}T^{*}_{+-} + T_{--}T^{*}_{-+} + T_{-+}T^{*}_{--})$$

$$M_{02} = \frac{1}{2}i(T_{+-}T^{*}_{++} - T_{++}T^{*}_{+-} + T_{--}T^{*}_{-+} - T_{-+}T^{*}_{--})$$

$$M_{03} = \frac{1}{2}(T_{++}T^{*}_{++} - T_{+-}T^{*}_{+-} + T_{-+}T^{*}_{-+} - T_{--}T^{*}_{--})$$

$$M_{10} = \frac{1}{2}(T_{++}T^{*}_{-+} + T_{+-}T^{*}_{--} + T_{-+}T^{*}_{++} + T_{--}T^{*}_{+-})$$

$$M_{11} = \frac{1}{2}(T_{+-}T^{*}_{-+} + T_{++}T^{*}_{--} + T_{--}T^{*}_{++} + T_{-+}T^{*}_{+-})$$

$$M_{12} = \frac{1}{2}i(T_{+-}T^{*}_{-+} - T_{++}T^{*}_{--} + T_{--}T^{*}_{++} - T_{-+}T^{*}_{+-})$$

$$M_{13} = \frac{1}{2}(T_{++}T^{*}_{-+} - T_{+-}T^{*}_{--} + T_{-+}T^{*}_{++} - T_{--}T^{*}_{+-})$$

$$M_{20} = \frac{1}{2}i(T_{++}T^{*}_{-+} + T_{+-}T^{*}_{--} - T_{-+}T^{*}_{++} - T_{--}T^{*}_{+-})$$

$$M_{21} = \frac{1}{2}i(T_{+-}T^{*}_{-+} + T_{++}T^{*}_{--} - T_{--}T^{*}_{++} - T_{-+}T^{*}_{+-})$$

$$M_{22} = -\frac{1}{2}(T_{+-}T^{*}_{-+} - T_{++}T^{*}_{--} - T_{--}T^{*}_{++} + T_{-+}T^{*}_{+-})$$

$$M_{23} = \frac{1}{2}i(T_{++}T^{*}_{-+} - T_{+-}T^{*}_{--} - T_{-+}T^{*}_{++} + T_{--}T^{*}_{+-})$$

$$M_{30} = \frac{1}{2}(T_{++}T^{*}_{++} + T_{+-}T^{*}_{+-} - T_{-+}T^{*}_{-+} - T_{--}T^{*}_{--})$$

$$M_{31} = \frac{1}{2}(T_{+-}T^{*}_{++} + T_{++}T^{*}_{+-} - T_{--}T^{*}_{-+} - T_{-+}T^{*}_{--})$$

$$M_{32} = \frac{1}{2}i(T_{+-}T^{*}_{++} - T_{++}T^{*}_{+-} - T_{--}T^{*}_{-+} + T_{-+}T^{*}_{--})$$

$$M_{33} = \frac{1}{2}(T_{++}T^{*}_{++} - T_{+-}T^{*}_{+-} - T_{-+}T^{*}_{-+} + T_{--}T^{*}_{--})$$

Results and Conclusion

Transition Amplitude for $J_i = \frac{1}{2} \rightarrow J_n = \frac{3}{2} \rightarrow J_f = \frac{1}{2}$

We consider the scattering of polarized radiation by an atom which makes a transition from an initial state $|\psi_i\rangle$ with energy E_i, total angular momentum J_i and parity π_i to a final state $|\psi_f\rangle$ with energy E_f, total angular momentum J_f and parity π_f. The left and right circular polarization states of incident and scattered radiations are denoted by $\mu' = \mu = \pm 1$.

The transition matrix element for scattering of polarized radiation,

$$\langle \phi_f | \rho^f | \phi_{f'} \rangle = \sum_{i,i'} \rho^f \sum_n \langle \phi_f | H_{int} | \phi_n \rangle F_n \langle \phi_n | H_{int} | \phi_i \rangle$$

$$\times \sum_{n'} \langle \phi_{i'} | H^+_{int} | \phi_{n'} \rangle F^*_{n'} \langle \phi_{n'} | H^+_{int} | \phi_{f'} \rangle \qquad (32)$$

Where the frequency dependent profile function $F_n = \frac{1}{E_i + \hbar\omega_i - E_n - i\hbar\Gamma_n}$, when we take the basis states $|\phi\rangle$ are the total angular momentum $|jm\rangle$ basis states for atomic scattering process.

Equation (32) becomes

$$\rho^f_{m_f m_{f'}, \mu_f \mu'_f} = \sum_{\mu_i, \mu'_i = \pm 1} \sum_{m_i, m_{i'}} \sum_{m_n, m_{n'}} \rho^i_{\mu_i, \mu'_i} \langle k\mu_f, J_f m_f | H_{int} | J_n m_n \rangle$$

$$\times F_n \langle J_n m_n | H_{int} | k\mu_i \rangle \langle k\mu'_i, J_i m_{i'} | H^+_{int} | J_n m_{n'} \rangle$$

$$\times F^*_{n'} \langle J_n m_{n'} | H^+_{int} | j_f m_{f'}, k\mu'_f \rangle \qquad (33)$$

where ρ^i contains the initial polarization of both atom and radiation. We assume that there is no entanglement between initial states of atom and radiation. It means we can write $\rho^i = \rho^{ir}\rho^{iA}$.

The matrix elements for scattered radiation with polarization μ_f along the direction (θ, ϕ),

$$\langle k\mu_f, J_f m_f | H_{int} | J_n m_n \rangle = E_{m_f m_n}(\mu_f)$$

$$= (2\pi)^{1/2} \sum_{L_e = |J_f - J_n|}^{J_f + J_n} (-i)^{Le} (2L_e + 1)^{1/2}$$

$$\times \langle J_f \| E_{L_e} \| J_n \rangle \sum_{M_e = -L_e}^{L_e} C(J_f, L_e, J_n; m_f, M_e, m_n)$$

$$\times (-i\mu_f)^{h(L_e)} D^{L_e}_{M_e, \mu_f}(\phi, \theta, 0)^* \qquad (34)$$

where $$h(L_e) = \frac{1}{2}[1 + \pi_n \pi_f (-1)^{L_e}].$$

The π_n, π_f are parities of the intermediate state and final state. $\langle J_f \| E_{L_e} \| J_n \rangle$ represents the reduced matrix element, $C(J_f, L_e, J_n; m_f, M_e, m_n)$ is the Clebsch-Gordon coefficient and $D^{L_e}_{M_e, \mu_f}(\phi, \theta, 0)$ is the Winger's D-functions.

The reduced matrix element $\langle J_f \| E_{L_e} \| J_n \rangle$ for emission represents either an electric or a magnetic 2^L pole strength depending on whether h (L) is equal to one or zero.

The matrix element for incident radiation with polarization μ_i along the direction (θ', ϕ') is also given by

$$
\begin{aligned}
\langle J_n m_n \mid H_{int} \mid J_p m_i, k\mu_i \rangle &= A_{m_n m_i}(\mu_f) \\
&= (2\pi)^{1/2} \sum_{L_e=|J_i-J_n|}^{J_i+J_n} (i)^{L_a} (2L_a+1)^{1/2} \\
&\quad \times \langle J_n \| A_{L_a} \| J_i \rangle \sum_{M_a=-L_a}^{L_a} C(J_i, L_a, J_n; m_i, M_a, m_n) \\
&\quad \times (i\mu_i)^{h(L_a)} D^{L_a}_{M_a,\mu_i}(\phi', \theta', 0) \qquad (35)
\end{aligned}
$$

Similarly, the matrix element for incident radiation with polarization μ'_i is given by

$$
\begin{aligned}
\langle k\mu'_i, J_i m_{i'} \mid H^{+}_{int} \mid J_n m_{n'} \rangle = \langle J_n m_{n'} \mid H_{int} \mid k\mu_{i'}, J_i m_{i'} \rangle^* &= A_{m_{n'} m_{i'}}(\mu'_i) \\
&= (2\pi)^{1/2} \sum_{L_{a'}=|J_i-J_n|}^{J_i+J_n} (-i)^{L_{a'}} (2L_a+1)^{1/2} \\
&\quad \times \langle J_n \| A_{L_{a'}} \| J_i \rangle^* \sum_{M_{a'}=-L_{a'}}^{L_{a'}} C(J_i, L_{a'}, J_n; m_{n'}, M_{a'}, m_{n'}) \\
&\quad \times (-i\mu'_i)^{h(L_{a'})} D^{L_{a'}}_{M_{a'},\mu'_i}(\phi', \theta', 0)^* \qquad (36)
\end{aligned}
$$

and the matrix element for scattered with polarization μ_f is given by

$$
\begin{aligned}
\langle J_n m_{n'} \mid H^{+}_{int} \mid J_f m_f, k\mu_f \rangle = \langle k\mu_f, J_f m_f \mid H_{int} \mid J_n m_{n'} \rangle^* &= E_{m_{f'} m_{n'}}(\mu'_f) \\
&= (2\pi)^{1/2} \sum_{L_{e'}=|J_f-J_n|}^{J_f+J_n} (i)^{L_{e'}} (2L_{e'}+1)^{1/2} \\
&\quad \times \langle J_f \| E_{L_{e'}} \| J_n \rangle^* \sum_{M_{e'}=-L_{e'}}^{L_{e'}} C(J_f, L_{e'}, J_n; m_f, M_{e'}, m_{n'}) \\
&\quad \times (i\mu'_f)^{h(L_{e'})} D^{L_{e'}}_{M_{e'},\mu'_f}(\phi, \theta, 0) \qquad (37)
\end{aligned}
$$

Therefore, equation (33) becomes

$$
\begin{aligned}
\rho^{f}_{m_f m_{f'}, \mu_f \mu'_f} &= \sum_{\mu_i,\mu'_i=\pm 1} \sum_{m_i, m_{i'}} \sum_{m_n, m_{n'}} \rho^{i}_{\mu_i,\mu'_i} (2\pi)^2 F_{m_n} F^{*}_{m_{n'}} \\
&\times \sum_{L_e=|J_f-J_n|}^{J_f+J_n} (-i)^{L_e} (2L_e+1)^{1/2} \langle J_f \| E_{L_e} \| J_n \rangle \\
&\times \sum_{M_e=-L_e}^{L_e} C(J_f, L_e, J_n; m_f, M_e, m_n)(-i\mu_f)^{h(L_e)} D^{L_e}_{M_e,\mu_f}(\phi, \theta, 0)^* \\
&\times \sum_{L_a=|J_i-J_n|}^{J_i+J_n} (i)^{L_a} (2L_a+1)^{1/2} \langle J_n \| A_{L_a} \| J_i \rangle
\end{aligned}
$$

$$\times \sum_{M_a=-L_a}^{L_a} C(J_i, L_a, J_n; m_i, M_a, m_n)(-i\mu_i)^{h(L_a)} D^{L_a}_{M_a,\mu_i}(\phi', \theta', 0)$$

$$\times \sum_{L_{a'}=|J_i-J_n|}^{J_i+J_n} (-i)^{L_{a'}} (2L_a+1)^{1/2} \langle J_n \| A_{L_{a'}} \| J_i \rangle^*$$

$$\times \sum_{M_{a'}=-L_{a'}}^{L_{a'}} C(J_i, L_{a'}, J_n; m_{i'}, M_{a'}, m_{n'})(i\mu_i')^{h(L_{a'})} D^{L_{a'}}_{M_{a'},\mu_i'}(\phi', \theta', 0)^*$$

$$\times \sum_{L_{e'}=|J_f-J_n|}^{J_f+J_n} (i)^{L_{e'}} (2L_{e'}+1)^{1/2} \langle J_f \| E_{L_{e'}} \| J_n \rangle^*$$

$$\times \sum_{M_{e'}=-L_{e'}}^{L_{e'}} C(J_f, L_{e'}, J_n; m_f, M_{e'}, m_{n'})(i\mu_f')^{h(L_{e'})} D^{L_{e'}}_{M_{e'},\mu_f'}(\phi, \theta, 0) \qquad (38)$$

Since no observation are made on the state of polarization of the atom in the individual final state, the polarization states of the scattered radiation may be defined through a density matrix ρ^f as

$$\rho^f_{\mu_f \mu_{f'}} = \sum_{m_f} \rho^f_{m_f m_{f'}; \mu_f \mu_{f'}}$$

$$\rho^f_{\mu_f \mu_{f'}} = \rho^i 36(\pi)^2 \left| \langle \tfrac{1}{2} \| E_1 \| \tfrac{3}{2} \rangle \right|^2 \left| \langle \tfrac{3}{2} \| A_1 \| \tfrac{1}{2} \rangle \right|^2 F_{m_n} F_{m_{n'}}{}^*$$

$$\sum_{m_f=-\frac{1}{2}}^{\frac{1}{2}} \sum_{m_i=-\frac{1}{2}}^{\frac{1}{2}} \sum_{\mu_i=-1}^{1} \sum_{m_n=-\frac{3}{2}}^{\frac{3}{2}} \sum_{M_e=-1}^{1} C\left(\frac{1}{2}, 1, \frac{3}{2}; m_f, M_e, m_n\right) \mu_f D^1_{M_e,\mu_f}(\phi, \theta, 0)^*$$

$$\sum_{M_a=-1}^{1} C\left(\frac{1}{2}, 1, \frac{3}{2}; m_i, M_a, m_n\right) \mu_i D^1_{M_a,\mu_i}(\phi', \theta', 0)$$

$$\sum_{m_{i'}=-\frac{1}{2}}^{\frac{1}{2}} \sum_{m_{n'}=-\frac{3}{2}}^{\frac{3}{2}} \sum_{\mu_{i'}=-1}^{1} \sum_{M_{a'}=-1}^{1} C\left(\frac{1}{2}, 1, \frac{3}{2}; m_{i'}, M_{a'}, m_{n'}\right) \mu_{i'} D^1_{M_{a'},\mu_{i'}}(\phi', \theta', 0)^*$$

$$\sum_{M_{e'}=-1}^{1} C\left(\frac{1}{2}, 1, \frac{3}{2}; m_f, M_{e'}, m_{n'}\right) \mu_{f'} D^1_{M_{e'},\mu_{f'}}(\phi, \theta, 0) \qquad (39)$$

The characteristics of the incident radiation(ϕ', θ') and scatteredradiation$(\phi, \theta)$are shown in figure (1). We calculate the degree of linear polarization of scattered radiation in the absence of an external magnetic field to check our theoretical calculations and algorithm of our numerical program. We first calculate the degree of linear polarization of scattered radiation in the weak magnetic field when the incident radiation is linearly polarized for some chosen angles. These results are shown in Table (1). For unpolarized case, the incident radiation is 100% linearly polarized and its direction is taken as $\theta' = 90^\circ$, $\phi' = 0^\circ$. The scattered radiation is assumed to be $\theta = 90^\circ$, $\phi = 90^\circ$. The incident radiation is $\theta' = 30^\circ$, $\phi' = 0^\circ$ and the scattered radiation is $\theta = 70^\circ$, $\phi = 30^\circ$.These results are presented in Table (2).The comparison of the degree of linear polarization of the scattered radiation is shown in Table (3).

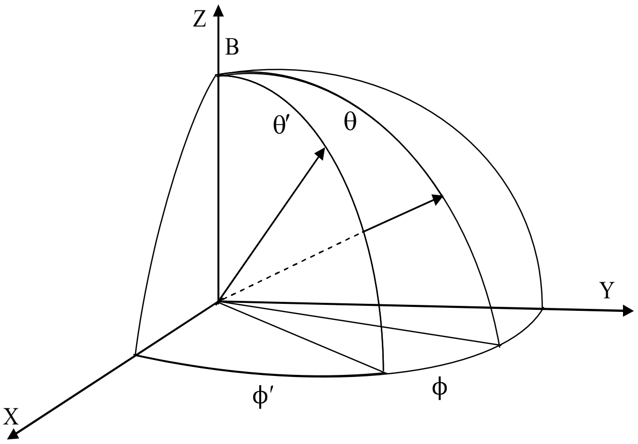

Figure 1 Angular characteristics of the incident (ϕ', θ') and scattered (ϕ, θ) radiation.

Table 1 The result of polarization when the incident radiation is linearly polarized for some chosen angles.

Type of Incident Radiation	Incident Angles		Scattered Angles		Linear Polarization of Scattered Radiation (percent) (Calculated Results)
	θ'	ϕ'	θ	ϕ	
Linearly polarized	20°	0°	50°	20°	56
	30°	0°	70°	30°	35.85
	40°	0°	60°	30°	52
	60°	20°	80°	30°	55
	90°	0°	90°	90°	60
	100°	30°	80°	30°	65

Table 2 The result of polarization when the incident radiation is unpolarized for some chosen angles.

Type of Incident Radiation	Incident Angles		Scattered Angles		Linear Polarization of Scattered Radiation (percent)
	θ'	ϕ'	θ	ϕ	
Unpolarized	90°	0°	90°	90°	43
	30°	0°	70°	30°	−13

Table 3 Linear Polarization (percent) of $J = \frac{1}{2} \to \frac{3}{2} \to \frac{1}{2}$ scattered radiation for $\theta' = 90^o$, $\phi' = 0^o$, $\theta = 90^o$, $\phi = 90^o$ and $\theta' = 30^o$, $\phi' = 0^o$, $\theta = 70^o$, $\phi = 30^o$

Calculated result (percent)	Theoretical result (percent)	Experimental result (percent)
60	60	60
35.85	35.53	36

Conclusion

We have computed the polarization of scattered line radiation from the upper level with angular momentum $J_u = \frac{3}{2}$ to a lower level with angular momentum $J_\ell = \frac{1}{2}$ transition in the absence of magnetic fields. The Stokes parameters of the incident radiation were taken to be unpolarized and there is no lower level polarization of an atom. We calculate the simplet geometrical arrangement of scattering in which the incident radiation is 100% linearly polarized and its direction is taken as $\theta' = 90^\circ$, $\phi' = 0^\circ$. The scattered radiation is assumed to be $\theta = 90^\circ$, $\phi = 90^\circ$.For unpolarized case incident radiation is $\theta' = 30^\circ$, $\phi' = 0^\circ$ and the scattered radiation is $\theta = 70^\circ$, $\phi = 30^\circ$.We particularly choose this set of parameters to compare our calculated result with well-established theoretical result as well as experimental result. The comparison of the degree of linear polarization of the scattered radiation is given in Table (3). In this case we obtain the good agreement with theoretical results as well as experimental results.

Acknowledgements

We wish to express our deepest gratitude to Dr. Ba Han, Rector, Meiktila University and Dr, Kay Thi Thin Pro-Rector, Meiktila University for their kind permission to do this work. We would like to express sincere thanks to Professor Dr. Hla Hla Than, Head of Department of Physics, Meiktila University and Dr. Daw Hla Wynn, Professor , Department of Physics, Meiktila University for their permission and moral support throughout the paper. We are also grateful to all teaching staff of Physics Department, Meiktila University.

References

Arldhas. G. & Rajagopal. P., (2005), Modern Physics, Prentice Hall of India Private Limited, New Dalhi.

Cohen Tamoudji. C., (1977), Quantum Mechanics; John Wiley & Son, Inc., France.

R. N. Zare, (1988), Angular Momentum, John Wiley & Son, Inc., Canada.

X. K. Meng et.al., (1992), Phys. Rev. A, vol. 45, pp 1767.

J. Myanmar Acad. Arts Sci. 2020 **Vol. XVIII.No.2A**

INVESTIGATION OF EXTERNAL RADIATION DOSE RATE FROM PATIENTS TREATED WITH IODINE 131(^{131}I)

Win Mar[1], Lae Lae Kyaing[2]

Abstract

Radioisotopes are widely used to diagnose disease and as effective treatment tools. Since many years radioactive iodine ^{131}I has been used to treat thyroid disease. The external measurements of dose rate (µSv/hr) of thyroid cancer patients for various distances are obtained at Department of Nuclear Medicine in Yangon General Hospital. These results are satisfied the inverse square law. From these results the maximum permissible exposure time for various distances from thyroid cancer patients are calculated. It is found that the maximum permissible exposure time is the longest time for the people that stay away from the patients after giving iodine treatment. Finally, it is concluded the further from the patients treated iodine, the longer the maximum permissible exposure times.

Keywords: *hyperthyroidism, external dose rate, exposure time*

Introduction

Radiations are naturally present in our environment and exist since the birth of this planet.It comes from outer space (cosmic), the ground (terrestrial), and even from within our own bodies. It is present in the air, the food, the water and in the construction materials used to build our homes. Beta particles are fast, energetic electrons (high speed electrons) .They are ejected from the nucleus of unstable radioactive atom. They are single, negatively charged and have a small mass. They are more penetrating than (α) particles, but can be stopped by a few millimeters of aluminum, so cannot penetrate deeply into tissues. ^{131}I is a beta emitter and hence is used for radiotherapy of hyperthyroid and thyroid cancer patients.

Radiation Effects on Population

The effect of radiation on living things

All living things are made of cells. Each cell has a central nucleus which carries the special code (DNA) of the living organism. Radiation can ionise the chemicals in the nucleus of the cell so that the code is changed. If radiation damages blood cells it can cause vomiting, loss of hair and increase the likelihood of infection. High doses of radiation can destroy cells completely and cause death.

Practical Means of Radiation Protection

External Radiation Protection

The three basic methods used to reduce the external radiation hazard are time, distance, and shielding. Good radiation protection practices require optimization of these fundamental techniques.

---

[1] Dr, Associate Professor, Department of Physics, Meiktila University.

[2] Dr, Associate Professor, Department of Physics, Meiktila University.

(i)Time

The amount of radiation an individual accumulates will depend on how long the individual stays in the radiation field.

(ii) Distance

The amount of radiation an individual receives will also depend on how close the person is to the source.

(iii) Shielding

When reducing the time or increasing the distance may not be possible, one can choose shielding material to reduce the external radiation hazard.

Internal Radiation Protection

Internal radiation exposure results when the body is contaminated internally with a radionuclide. Thus, internal radiation protection is concerned with preventing or minimizing the deposition of radioactive substances in personnel.

Table 1 Recommendations for Annual Effective/ Equivalent Dose Limits

	ICRP	NCRP
Public Limits (Annual):		
1.Effective dose limit		
a. Continuous or frequent irradiation	1 mSv	1mSv
b. Infrequent irradiation	5 yr average<1mSv/yr	5mSv
Educational and Training Limits (Annual):		
1. Effective dose limit	-	1mSv
2. Equivalent dose limit		
a. Lens of the eye	-	15mSv
b. Skin, hands and feet	-	50mSv

Metabolism of ^{131}I

Iodine is an essential component of thyroid hormones, so the thyroid gland takes up iodine very easily. Normally, iodine is supplied to the body in foodstuffs and drinking water. There are three kinds of half-life's,(i) Physical half-life(ii)Biologic half-life and (iii) Effective half-life that should be considered when radioactive iodine is used to study or treat a hyperthyroid and thyroid cancer patient.

Table 2 Physical, biologic and effective half- life of ^{131}I

^{131}I Physical half life	^{131}I Biologic half-life		^{131}I Effective half-life	
	normal thyroid compartment	extra thyroid compartment	thyroid compartment	extra thyroid compartment
8.04 days	80 days	12 days	7.3 days	8 hours

Figure 1 Iodine ^{131}I

Survey Meter Dose Rate Test

The aim of the test was to find out that the dose rate measurements are in accordance with inverse square law. Mathematically the inverse square law is expressed with following equation.

$$I \ \alpha \ \frac{k}{d^2}$$

The purpose was to find out if variations in the distance affect dose rate measurements. A syringe with 888 MBq of ^{99m}Tc activity was placed at 77 cm height. The height was estimated for a normalized patient's whole body. Dose rate measurements were taken with the 6150 AD 5/H at 1.0m, 1.5m, 2.0 m and 2.5 m at 77 cm height. In order to validate the dose rate results of the survey meter, dose rate test performed with activity of 888 MBq ^{99m}Tc. The results are presented in Table (3).

Figure 2 Survey meter (6150 AD 5/H)

Table 3 Dose rate results

Activity MBq	Dose rate (µSv/hr) at1.0 m	Dose rate (µSv/hr) at1.5 m	Dose rate (µSv/hr) at2.0 m	Dose rate (µSv/hr) at2.5 m
888	340	85	21	5

Table 4 Inverse square dose rate validation

r_1	r_2	r_3	$R_1= r_1/4$	$R_2= r_2/16$	$R_3= r_3/64$
4	16.19	68	1.00	1.01	1.06

Patient Procedure

At a group consisted of fifteen patients, were performed external dose rate measurements. They signed agreement for receiving a therapy and all patients feel positive about participating in the study. The patient population consisted of 12 female and only 3 male at thyroid cancer group. Age ranged between 29 years to 60 years old. Thyroid cancer patients were given activities between 1110 MBq and 2590 MBq.

Radiation Dose Rate Measurement

The dose rate from the patient was monitored with survey meter (6150AD models) at horizontal distances of 1.0 m, 1.5 m, 2.0 m and 2.5 m for thyroid patient. The effective point of the patient measurements was taken to be in the center of the detector. Vertical movement of the survey meter was utilized to obtain the maximum reading each time. The highest dose rate measurement depends on closest position of the survey meter to residual extra thyroid functioning tissue, which retains radioiodine. Thyroid cancer patients were measured during three days (every day at same time) until the measured level fall down to permitted limit (2.5 m – 8 µSv/hr). That means that the residual activity is less than 800 MBq when patients were released to go home with orally given and written instructions for their further behavior in home conditions.

Determination of errors

The result of a calculation using the Monte Carlo method is the average number of “histories” performed during the simulation. The histories are generated by random sampling and a value of the quantity studied is allocated to each “history”. Let p(x) be the probability function of a “history” of value x. Mx variable is given by p(x).

$$Mx = \int_a^b x\ p(x)\ dx \qquad (2)$$

The values of p(x) and thus Mx are not known exactly, but the ture mean; (x) can be estimated using the Monte Carlo method.

$$\overline{x} = \frac{1}{N}\sum_{i=1}^{N} x_i \qquad (3)$$

where (x_i) value of corresponding to the "history" (i), and (N) is the total number of "histories". The variance (σ^2) can be estimated using following formula.

$$\text{variance} = \sigma^2 = \frac{1}{N-1}\sum_{i=1}^{N}(x_i - \overline{x})^2 \qquad (4)$$

The quantity $\overline{(x_i - m_i)(x_j - m_j)}$ is called the "covariance" between X_i and X_j:

$$\text{cov}(x_i, x_j) = \overline{(x_i - m_i)(x_j - m_j)} \qquad (5)$$

The above equation suffers from the serious drawback that its value changes with the units used for the measurements of X_i, X_j. To eliminate this effect, the covariance is divided by the product of the standard deviations σ_i, σ_j and the resulting ratio is called the correlation coefficient $\rho(x_i, x_j)$. Thus,

$$\rho_{ij} = \rho(x_i, x_j) = \frac{\text{cov}(x_i, x_j)}{\sigma_i \sigma_j} \qquad (6)$$

Results, Discussion and Conclusion

Results

The experimental data of twelve patients for distances 1.0m, 1.5m, 2.0m and 2.5m at first day, second day and third day are recorded in Table (5),(6) and (7). The external dose rate from twelve patients with iodine 131(I^{131}) Vs various distances are drawn and as shown in Figure (3), (4) and (5).From the experimental dose rate, the mean dose rates and the standard deviations at 1st day,2nd day and 3rd day are calculated by using equation (3) and (4). These results are listed in Table (8), (9) and (10). According to Table (1), the effective dose limit for continuous or frequent radiation (annual) is 1mSv. From the Public limits (annual), the maximum permissible exposure time that stay 1m distances from the thyroid cancer patients were calculated. The correlation between dose rate and administered activities for twelve thyroid cancer patients at 1st day, 2nd day and 3rd day are calculated by using equation (6) and recorded in Table (11). The correlation coefficients are positive and in the range from 0.2 to 0.4.A linear correlation coefficient has an absolute value between 0 and 1. With one is indicated a perfect linear relationship exists. In our case, there is a positive correlation of less than 0.5. The experimental data of three iodine patients with higher administered activity for distances 1.0m, 1.5m, 2.0m and 2.5m at 1st day, 2nd day and 3rd day are recorded in Table (12), (13) and (14).The external dose rate of three higher administered activity patients at each distance (1.0m, 1.5m, 2.0m and 2.5m) are plotted and as shown in Figure (6), (7), (8) and (9).

Table 5 Dose rates of different distances on the 1st day for twelve thyroid cancer patients

Sr No.	Activity		Dose rate (µSv/hr)			
	MBq	mCi	1 m	1.5 m	2 m	2.5 m
1	1110	30	17	14	11	8
2	1110	30	22	16	14	12
3	1110	30	26	21	14	13
4	1110	30	25	20	17	13
5	1110	30	23	17	12	10
6	1110	30	28	18	14	7
7	1110	30	23	14	13	11
8	1110	30	28	23	20	16
9	1110	30	25	19	13	11
10	1110	30	28	17	16	13
11	1110	30	23	17	11	10
12	1110	30	27	23	20	15

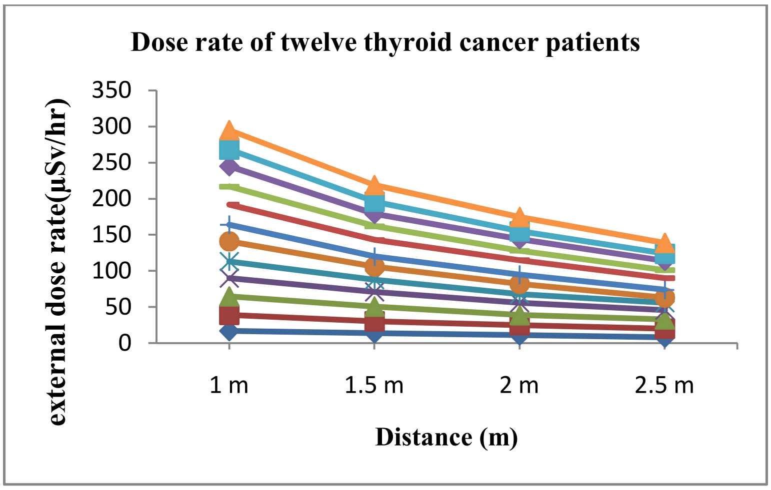

Figure 3 Dose rate of twelve thyroid cancer patients for 1st day

Table 6 Dose rates of different distances on the 2nd day for twelve thyroid cancer patients

Sr No.	Activity		Dose rate (µSv/hr)			
	MBq	mCi	1 m	1.5 m	2 m	2.5 m
1	1110	30	13	11	10	8
2	1110	30	23	20	18	16
3	1110	30	24	15	13	10
4	1110	30	14	13	11	10
5	1110	30	7	6	4	3
6	1110	30	25	23	14	11
7	1110	30	15	12	10	9
8	1110	30	21	17	15	12
9	1110	30	13	10	8	7
10	1110	30	19	14	12	11
11	1110	30	14	12	11	9
12	1110	30	25	23	19	10

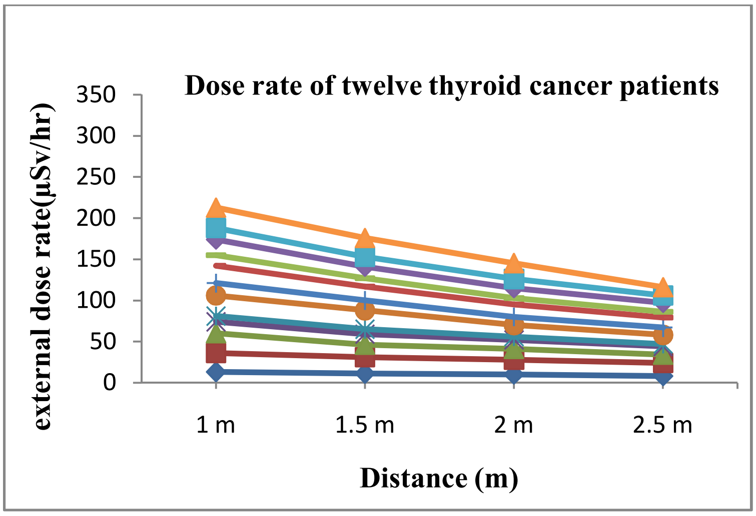

Figure 4 Dose rate of twelve thyroid cancer patients for 2nd day

Table 7 Dose rates of different distances on the 3rd day for twelve thyroid cancer patients

No	Activity		Dose rate (µSv/hr)			
	MBq	mCi	1 m	1.5 m	2 m	2.5 m
1	1110	30	12	10	9	8
2	1110	30	13	7	6	4
3	1110	30	15	13	10	9
4	1110	30	12	8	7	6
5	1110	30	2	1	0	0
6	1110	30	18	15	12	10
7	1110	30	14	10	9	8
8	1110	30	20	14	10	9
9	1110	30	18	12	10	8
10	1110	30	6	4	3	2
11	1110	30	12	10	9	7
12	1110	30	29	22	18	14

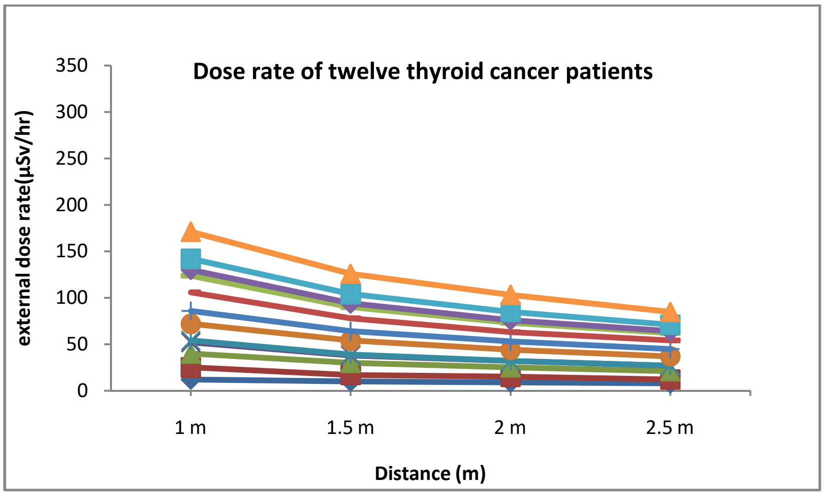

Figure 5 Dose rate of twelve thyroid cancer patients for 3rd day

Table 8 Mean dose rate, standard deviation for various patient distances (1st day)

Distance (m)	**Mean dose rate (µSv/hr)**	**Standard deviation**	**Dose rate range (µSv/hr)**
1.0	25	3.25	17-28
1.5	18	3	14-23
2.0	15	3.06	11-20
2.5	12	2.59	7-16

Table 9 Mean dose rate, standard deviation for various patient distances (2nd day)

Distance (m)	Mean dose rate (µSv/hr)	Standard deviation	Dose rate range (µSv/hr)
1.0	18	5.88	7-25
1.5	15	5.25	6-23
2.0	12	4.11	4-19
2.5	10	3.05	3-16

Table 10 Mean dose rate, standard deviation for various patient distances (3rd day)

Distance (m)	**Mean dose rate (µSv/hr)**	**Standard deviation**	**Dose rate range (µSv/hr)**
1.0	14	6.83	2-29
1.5	11	5.43	1-22
2.0	9	4.47	0-18
2.5	7	3.68	0-14

Table 11 Correlation coefficients for 1st day, 2nd day and 3rd day

distance	1st day	2nd day	3rd day
1.0 m	0.2	0.2	0.3
1.5 m	0.2	0.2	0.3
2.0 m	0.2	0.3	0.3
2.5 m	0.2	0.3	0.3

Table 12 Dose rates of different distances on the 1st day for higher administered activity of three thyroid cancer patients

No	**Activity**		**Dose rate (µSv/hr)**			
	MBq	**mCi**	**1 m**	**1.5 m**	**2 m**	**2.5 m**
10	1850	50	28	23	18	12
11	1850	50	30	25	24	18
12	2590	70	85	63	41	30

Table 13 Dose rates of different distances on the 2nd day for higher administered activity of three thyroid cancer patients

No	Activity		Dose rate (µSv/hr)			
	MBq	mCi	1 m	1.5 m	2 m	2.5 m
10	1850	50	15	14	13	10
11	1850	50	25	22	20	17
12	2590	70	80	60	45	35

Table 14 Dose rates of different distances on the 3rd day for higher administered activity of three thyroid cancer patients

No	Activity		Dose rate (µSv/hr)			
	MBq	mCi	1 m	1.5 m	2 m	2.5 m
10	1850	50	7	5	3	2
11	1850	50	22	16	15	13
12	2590	70	62	42	32	23

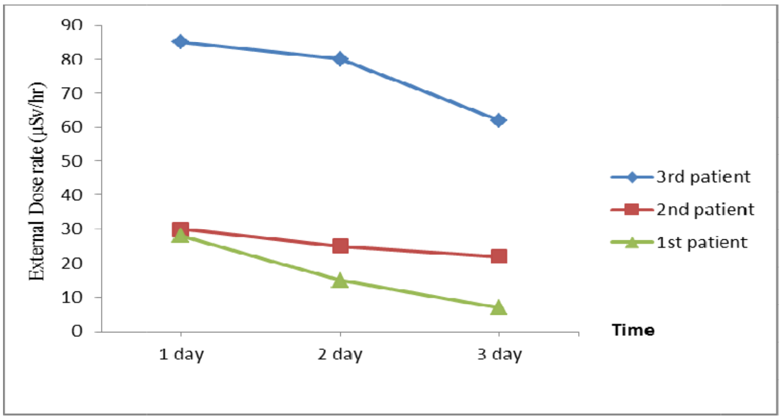

Figure 6 The external dose rate of three higher administered activitypatients at 1m

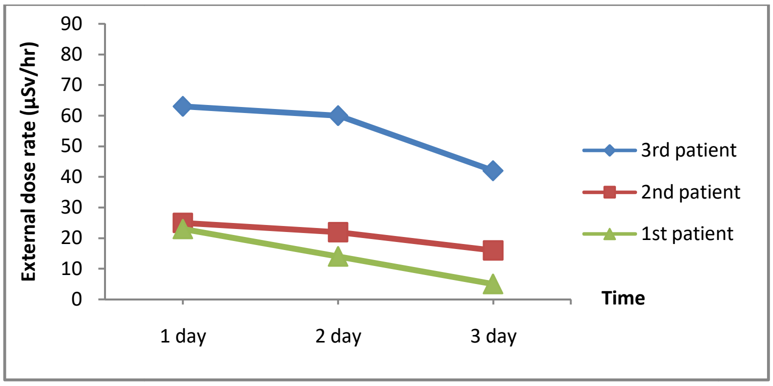

Figure7 The external dose rate of three higher administered activity patients at 1.5m

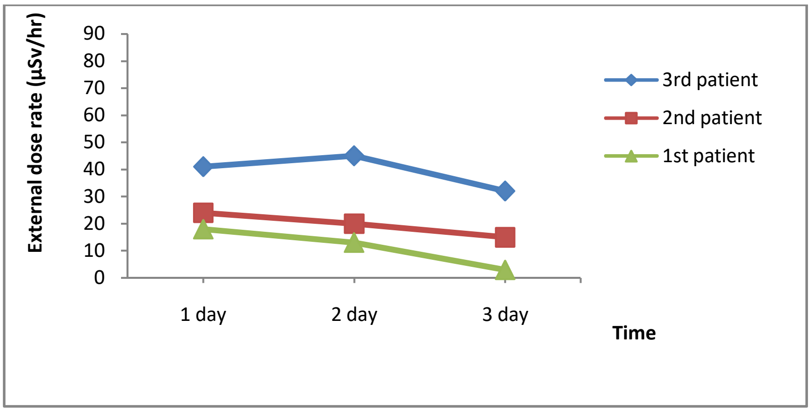

Figure 8 The external dose rate of three higher administered activitypatients at 2m

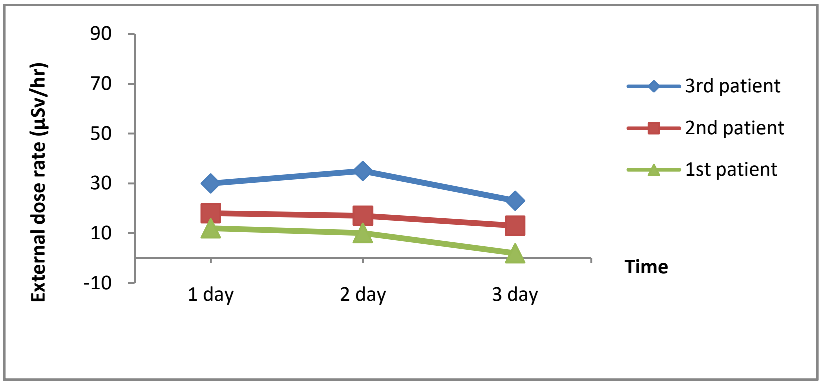

Figure 9 The external dose rate of three higher administered activity patientsat 2.5m

Discussion

^{131}I is well used radionuclide for the treatment of both hyperthyroidism and differentiated thyroid cancer. ^{131}I has received the greatest emphasis because of its unique applications in medicine. At the same distance for each day, the external dose rates of twelve thyroid cancer patients are different, although the same activity of iodine is treated to them. It is seen that every iodine patients have different effective half-life of radioactive iodine and different disease conditions. It is also found that, the further from the patients with treated iodine it is, the less external dose rate from the patients, according to the Inverse squared law. In three thyroid cancer patients, the greater administered activity, the higher external dose rate at the same distance for each day. It is cleared that the external dose rates from the patients are more decreased on the third day.

On the first day, all the people who are at least 1m away from the patients treated with the administered from 1110 MBq to 1850 MBq are safe. At the most highest administered activity (2590 MBq) far from 1m, maximum permissible exposure time for the first day lasts for twelve hours. It is suggested that to stay further away from the patients who have higher administered activities. To sum up, administered activity is effective not only for thyroid cancer but also for those who are at least 1 m away from the thyroid cancer patients.

Conclusion

In this study external dose rate measurements of fifteen patients were performed and based on the gained results we can conclude the following: it has several advantages such as lower health costs, lower doses to nursing staff and psychologic benefits for patients and family members. Emphasizing adherence to the new instructions for radiation protection is very important. Also reducing the time of stay near the radioactive patient will reduce the effective doses to the other person and will improve better radiation protection.

Acknowledgement

We would like to express my gratitude to Dr. U Ba Han, Acting Rector, Dr Daw Kay Thi Thin, Pro-Rector, Meiktila University for their permission to summit this paper. We also wish to express my sincere thanks to Dr. Hla Hla Than, Professor and Head and Dr. Daw Hla Win, Professor, Department of Physics, Meiktila University, for their encouragement to conduct this research.

References

International Commission on Radiological Pretection, (2007). The Recommendations of the International Commission on Radiological Protection. ICRP Publication 103(2007).

James, E. M; (2006). Physics for Radiation Protection 2nd edition. Germary: Weinheim Wiley-VCH. ISBN 3-527-40611-5.

Khan F. M. (2003). The Physics of Radiation Therapy. 3rdedition. Philadelphia U. S. A: Lippincott Williams & Wilkonsin, ISBN: 0-7817-3065-1.

M. C. Cantone, C. Hoeschen, Radiation Physics for Nuclear Medicine, Springer, 2011.

S. Mattsson and C. Hoechen (eds.), Radiation Protection in Nuclear Medicine. DOI 10.1007/9788-3-642-31167-3-2, Springer-Verlag Berlin Heidelberg 2013.

J. Myanmar Acad. Arts Sci. 2020 **Vol. XVIII.No.2A**

COMPARATIVE STUDY ON THE STRUCTURE OF K_2ZnCl_4 CRYSTAL DETERMINED FROM SINGLE CRYSTAL AND POWDER X-RAY DIFFRACTION

Thidar Nyunt[1], Thet Mar Win[2], Than Zaw Oo[3]and Pho Kaung[4]

Abstract

Crystal structures of dipotassium tetrachlorozincateK_2ZnCl_4 (KZC)was determined by both single crystal x-ray diffraction (SXRD) and powder x- ray diffraction (PXRD) techniques. KZC single crystals were grown by slow evaporation method. The obtained structural inform from SXRD had approximately the same precision as the PXRD technique. In the structure refinement, final values of R and R_w indice converged to 0.076 and 0.184. Structure analyses revealed that KZC sample possess the slightly distorted $ZnCl_4$ tetrahedra.

Keywords: K_2ZnCl_4 single crystal, x- ray diffraction, structure analyses

Introduction

The technique of single-crystal X-ray diffraction is the oldest and most common crystallographic method for determining the structure of the molecules. Crystals of A_2BX_4 type compounds, where A is K, Rb, Cs, NH_4 ion, B is Zn, Co, Hg and X is Cl or Br, are known as ferroelectrics. They have a common sequence of phase transitions; with decreasing temperature, the paraelectric-orthorhombic normal phase (N) changes to the INC phase followed by the commensurate (COM) phase of three-fold cell dimension along the c-axis (ferroelectric/ antiferroelectric phases).The existence of an INC lattice instability in these compounds depend basically on the effective volume of the A cations compared with the size of the BX_4 tetrahedra[Bruker W, 2001].

Above 553K the structure of KZC is the normal phase (N) with orthorhombic space group Pmcn. Transition to INC phase occurs at 553K and INC phase is retained down to 403K. Between 403K and 145K, it shows ferroelectric COM phase with space group $P2_1cn$.KZC has a stable COM region even on the cooling branch [Farrugia L J , 2005]. The phase transition sequences were summarized as shown in Figure 1.

The low-temperature phase transition in KZC connected to the ordering process of $ZnCl_4$ tetrahedra is investigated by diffuse X-ray scattering techniques. X-ray studies assigned the INC-COM transition to $ZnCl_4$ tetrahedra rotation. The interplanar distances change weakly with the temperature [Leduc, Hedoux AM ,1998]. KZC has the orthorhombic structure and a ferroelectric activity below 403 K. In the present work, structure analysis on pure crystal shows the right occupancy of K ion in the unit cell corresponding to the ratio of KCl. In the present work, the crystallize in the orthorhombic with the space group $P2_1cn$ at room temperature [Matsunaga H, 1982].

In the present study, the procedure of single crystal growth of K_2ZnCl_4 from the growth solution, the effect of sample preparation on the crystal and lattice parameter [Nardelli M,1995]

---

[1] Dr, Lecturer, Department of Physics, Meiktila University

[2] Associate Professor, Department of Engineering Physics, Technological University (Thanlyin)

[3] Professor, Department of Physics, University of Yangon

[4] Dr, Rector, University of Yangon

Materials and Methods

Single crystals of KZC were grown by the slow evaporation technique from an aqueous solution containing KCl was dissolved with excess $ZnCl_2$ at high temperature 100˚C. The reagents of KCl and $ZnCl_2$ were dissolved with stoichiometric ratio of 2:1 in water. The excess $ZnCl_2$ was 2 wt % for the present sample. Because $ZnCl_2$ is a highly hygroscopic material, excess of $ZnCl_2$ was found necessary to compensate the water content and to be sure of the chemical reaction stoichiometry (Sheldrick G M , 1997).The saturated solution was slowly evaporated at about 100˚Cfor a few months. After getting the crystals, these were recrystallized from mother solution to afford colorless transparent single crystals of the title compound suitable for x- ray diffraction.

Powder X- ray Diffraction

Sample Preparation and Instrumentation

In an ideal PXRD experiment performed in a common Bragg-Brentano reflection geometry x-ray powder diffractometer, the sample should consist of powder particles of crystallite size between 0.1 and 1.0 micrometers. The sample should be packed in a cavity-type sample holder and genteelly pressed to a void preferred orientations. The sample surface should be big enough to ensure that the incident beam impinges over the sample in the full angular measuring range. Furthermore, the sample should be thick enough to ensure that the whole incident x-ray beam interacts with the sample and does not pass through it.

An x-ray powder diffractometer consists basically of a goniometer with a sample stage in its centre, the x-ray tube and the incident beam optics in its primary arm and the diffracted beam optics and a detector in its secondary arm. The goniometer is normally inside a shielded cabine in the upper part of a console. The x-ray generator and the measuring and control electronics are in the bottom part.

The phase formation of KZC sample were characterized by powder X- ray diffraction technique using Rigaku MultiFlex 2 kW type X-ray Diffractometer with Cu-K_α radiation (λ = 1.5404 Å) operating at 40 kV.

Single Crystal X- ray Diffraction

Sample Preparation and Data Collection

The samples are unfracturated and optically clear single crystals. Their size should be between 0.1 and 0.3 mm in the three directions of space. They are normally selected using an optical microscope (x40) equipped with a polarizing attachment and observing if light extinguishes regularly every 90º when turning the stage of the microscope.

A selected crystal is fixed on the tip of a thin glass fiber using epoxy or cement, orina loop including specific oil, which fits into the goniometer head in the diffractometer. The crystal is then aligned along the beam direction. It is necessary to know the stability properties of the crystals. Crystals can be sensitive to light, air or moisture, or susceptible to loss of crystallization solvent. If so, a special treatment is required. For example, they can be mounted inside sealed glass capillaries or the data collection can be performed at low temperature.

X-ray single crystal study is carried out using the Siemens P4 Single Crystal Diffractometer. In this diffractometer, MoKα radiation of wavelength 0.71073 Å with the X-ray power of 40 kV × 40 mA was used. The specimens having single domain with clear optical axis were cut under a polarizing microscope and shaped as a sphere with a diameter 0.35mm.The unit cell parameters were determined by least- squares refinement of 25 reflections with the diffraction angles 2θ =10 ~ 30˚. Intensity measurements were carried out in the ω - scan mode.

The maximum 2θ in which intensity data were collected was 50.0˚. Three standard reflections were monitored after every hundred reflections to check the stability of the measurements. After processing the raw data, Lorentz and Polarization corrections were made. Ψ scan is applied for absorption correction. Positional parameters and individual isotropic temperature factors were refined by a full-matrix least-squares SHELXTL-97. Anisotropic displacement parameters were used for non-H atoms and an isotropic parameter for the H atom. The function minimized was $\Sigma\, w\,(|F_0| - |F_c|)^2$, $w = 1/\sigma^2(|F_0|)$. The two discrepancy factors are defined $R=\Sigma\,(|F_0|-|F_c|)/\Sigma|F_0|$ and $R_w=\{\Sigma w(|F_0|-|F_c|)^2/\Sigma w|F_0|)^2\}^{1/2}$, respectively.

Results and Discussion

Powder x- ray diffraction (PXRD) and single crystal x- ray diffraction (SXRD) studies were carried out on the grown crystals. The comparison between lattice parameters between a, b and c are experimentally determined.

Structural Analysis by Powder X- ray Diffraction

The x- ray diffraction pattern of KZC was shown in Figure 1. The peaks (311), (121),(601) and (031) were observed at 2θ values 17.258°, 19.058°,23.355 and 24.745° for KZC sample and found to have polycrystalline nature with orthorhombic structure with the preferential orientation along the (031) plane. In this research work, X-ray diffraction measurements are carried out for KZC sample to determine the size of the particles. The crystallite size of the particles was estimated from the XRD spectrum by applying the Scherrer formula,

$$g_{\text{crystallite}} = \frac{0.9\lambda}{D\cos\theta}$$

where, g = the crystallite size (nm) , λ = the wavelength of the X-ray beam($\lambda = 1.54056\,\mathring{A}$), D = the full width at half maximum height (radian) and θ = the angle of diffraction(degree).The broadening is evaluated by measuring the width g in radians, at an intensity equal to half the maximum intensity (FWHM). Structural parameters of KZC powder sample was presented in Table 1.

Structural Analysis by Single Crystal X- ray Diffraction

Crystal data, data collection and structure refinement are shown in Table 2. Bond distances and bond angles of tetrachlorozincate ions in different crystals are shown in Table 3. Fractional atomic coordinates and equivalent isotropic displacement parameters are shown in Table 4.X-ray diffraction pattern of K_2 $ZnCl_4$ powder sample as shown in Figure 2.

The a- axis projection, the projection normal to (100),(010) and view normal to (001) of the structures of KZC are shown in Figure 3, respectively. A group consists of K atom and $ZnCl_4$

tetrahedron. One group lies on the mirror plane (z= 1/4) and another group on the mirror plane(z=3/4).

The data can be viewed as sections of a three dimensional reciprocal space plot as shown in Figure 4. X-ray Fourier map presents charge density distribution. XRD data are not always accurate enough to observe the positional parameters of some atoms and the nature of bonding between them. The Fourier map is used to obtain the distribution in the electron density around Zn atom that supports the covalent bond formation between Zn and Cl atoms.2-D contour map view around two $ZnCl_4$ groups as shown in Figure 5.

Table 1 Lattice parameters and crystallite sizes of KZC crystal

Reflection plane (hkl)	**d (Å)**	**2θ (deg)**	**FWHM (rad) × 10^{-3}**	**Lattice parameters (Å)**			**Crystallite size (nm)**
				a	**b**	**c**	
(311)	5.1341	17.258	4.67	26.7288	12.4193	7.2823	30.03
(121)	4.6529	19.058	4.15	26.7288	12.4193	7.2823	33.88
(601)	3.8057	23.355	5.93	26.8006	12.4193	7.2693	23.88
(031)	3.5949	24.745	5.88	26.9108	12.4193	7.2497	24.14
Average				26.7975	12.4193	7.2709	27.98

Table 2 Model summary concerning unit cell information for KZC crystal

Crystal Data	
Chemical Formula	K_2ZnCl_4 (KZC)
Cell axes [A°]	a= 7.245 Å b= 12.395 Å c= 26.7707 Å
Cell angles [deg]	α = 90°, β = 90°, γ = 90°
Cell Volume[$A^{\circ 3}$]	2404.03
Crystal system	Orthorhombic
Space group	$P2_1cn$
F(000)	1631.8
Density[gcm^{-3}]	2.37
Formular Weight	285.4
No.form.units Z	12
Abs.coeff: [mm^{-1}]	5.327
Chemical Formula	K_2ZnCl_4 (KZC)

Data Collection	
Instrument Description	Siemens SMART CCD area- detector diffractometer
Absorption correction	Ψ scans
Total reflections	16945
Unique reflections	1446
Reflections I>2σ(I)	1395

Refinement	
Cell refinement	Least squares method
R1	0.076
Rw	0.184
Goodness of Fit (S)	1.155

Table 3 Bond distance and bond angles of $ZnCl_4$ in KZC single crystal at room temperature

Atom	A	B	Distance	Atom	A	B	Distance
	Zn1	Cl6	2.251		Zn2	Cl17	2.226
	Zn1	Cl12	2.215		Zn2	Cl21	2.275
	Zn1	Cl15	2.241		Zn3	Cl5	2.289
	Zn1	Cl16	2.242		Zn3	Cl7	2.240
	Zn2	Cl13	2.273		Zn3	Cl8	2.262
	Zn2	Cl14	2.241		Zn3	Cl9	2.238

Atom	A	B	C	Angle	Atom	A	B	C	Angle
	Cl12	- Zn1	-Cl15	116.26		Cl14	- Zn2	- Cl13	107.34
	Cl12	- Zn1	-Cl16	109.62		Cl14	- Zn2	- Cl21	109.73
	Cl12	- Zn1	- Cl6	110.58		Cl13	- Zn2	- Cl21	105.18
	Cl15	- Zn1	-Cl16	106.08		Cl7	- Zn3	- Cl8	113.26
	Cl15	- Zn1	- Cl6	106.48		Cl7	- Zn3	- Cl9	114.97
	Cl16	- Zn1	- Cl6	107.39		Cl8	- Zn3	- Cl9	108.83
	Cl17	- Zn2	-Cl14	114.37		Cl5	- Zn3	- Cl7	106.30
	Cl17	- Zn2	-Cl13	105.72		Cl5	- Zn3	- Cl8	104.42
	Cl17	- Zn2	- Cl21	113.79		Cl5	- Zn3	- Cl9	108.38

Table 4 Fractional atomic coordinates and temperature factors (x10^4 $Å^2$) for all non-hydrogen atoms (Estimated Standard Deviations are given in parentheses)

$U_{eq} = (1/3)\sum_i\sum_j U_{ij} a^*_i a^*_j a_i a$

Atoms	x	y	z	Ueq
K1	1.91932	-0.18743	0.83196	0.04499
K2	1.40373	0.1866	0.83427	0.04685
K3	0.41926	.58334	0.78970	0.06268
K4	1.85166	-0.31190	0.99868	0.03737
K5	1.38023	-0.08457	0.62140	0.07671
K6	1.85873	0.0822	1.04322	0.07483
Zn1	1.86548	0.08182	0.90546	0.03216
Zn2	1.40648	-0.08210	0.75986	0.02910
Zn3	0.39438	0.58027	0.92767	0.0286
Cl5	0.65354	0.64486	0.88895	0.05602
Cl6	1.83365	-0.07840	0.94409	0.07897
Cl7	0.46908	0.55798	1.00819	0.04580
Cl8	0.3328	0.42338	0.88787	0.05170
Cl9	0.16264	0.69577	0.91360	0.05968
Cl12	1.83323	0.06319	0.82363	0.06068
Cl13	1.14153	-0.14015	0.72316	0.05449
Cl14	1.62557	-0.20467	0.74331	0.05686
Cl15	2.13396	0.15130	0.93177	0.09852
Cl16	1.64444	0.19122	0.93493	0.09200
Cl17	1.34061	-0.06388	0.84064	0.06257
Cl21	1.47578	0.07608	0.72107	0.04772

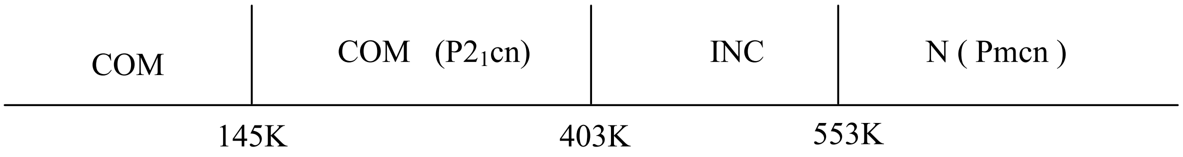

Figure 1 Phase transition sequence of KZC crystal.

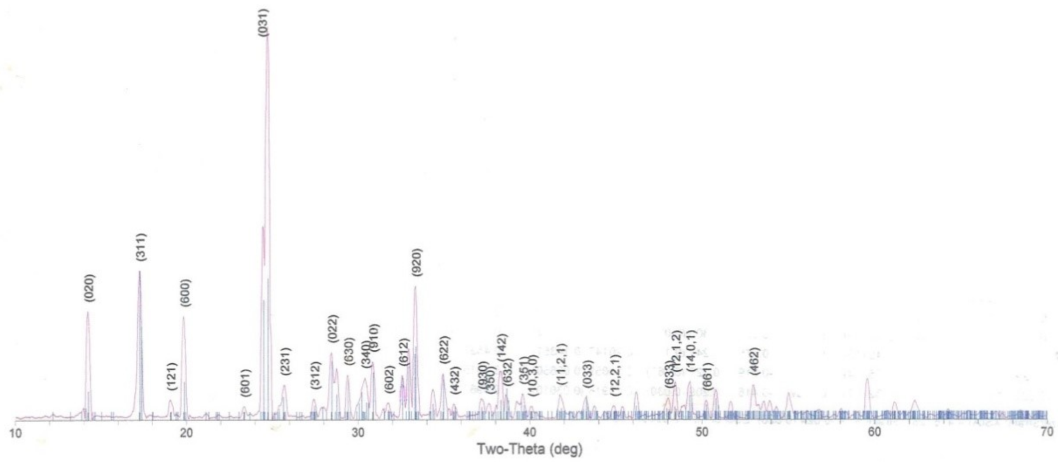

Figure 2 X-ray diffraction pattern of KZC crystal

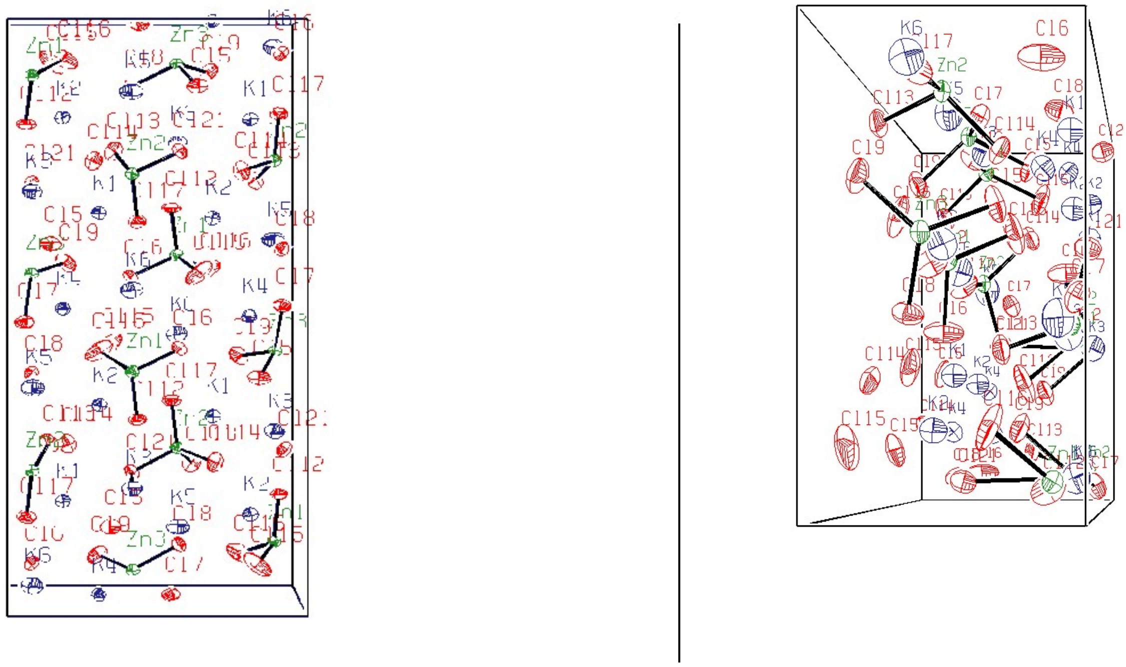

Figure 3 Projection normal to (100), (010)and (001) of the structure of KZC crystal

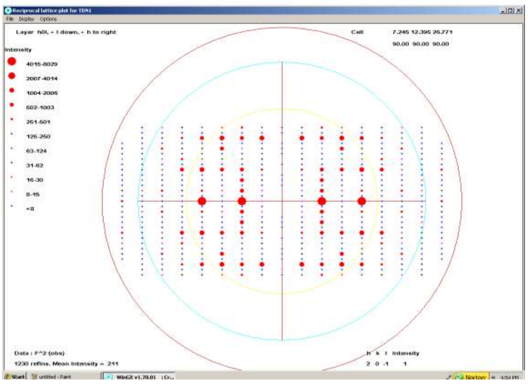

Layer h0l, + l down, + h to right

Cell 7.245 12.395 26.771
90.00 90.00 90.00

Data : F^2 (obs)
1230 reflns. Mean intensity = 211

h k l Intensity
2 0 -1 1

Figure 4 Reciprocal Lattice Plot for KZC crystal

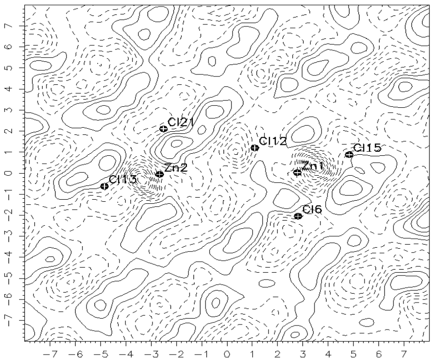

Figure 5 2-D Contour Map View of two $ZnCl_4$ groups

Conclusion

The XRD results of showed the pure crystal KZC is a sort of solid solution right occupancy of K ion in the unit cell according to the mixing molar ratio. The K ion form linear chain whose periodicity is incommensurate with that of the arrangement of the $ZnCl_4$ tetrahedron. The Zn atom shifts away from one of Cl atoms in the tetrahedral molecules and carries an electric dipole moment parallel to the Zn-Cl bond. The comparison between lattice parameters between a, b and c are experimentally determined. The observed lattice parameter a, b and c found to be 26.7975 Å, 12.4193 Å, 7.2709 Å in KZC sample for PXRD and 7.2452 Å, 12.3953 Å, 26.7707 Å for SXRD, respectively. The average value of crystallite size is calculated as 27.98 nm.

Acknowledgements

We are grateful to Professor and Head Dr Hla Hla Than and Professor Dr Daw Hla Win, Department of Physics, Meikhtila University for their kind permission to carry out this research work.

Bruker (2001) "SMART Version 5.625" (Wisconsin: Bruker)

Farrugia L J (2005) "WinGX- version 1.70.01: Crystallographic Programs for Windows" (Glasgow: University of Glasgow)

Farrugia L J (2005) "ORTEP-3" (Glasgow: University of Glasgow)

Leduc F X, Hedoux A and Kiat J M (1998) Phys Rev B 57 p11023-11026

Matsunaga H (1982) J. Phys. Soc. Jpn.51,864

Nardelli M (1995) J.Appl.Cryst. 28, 659.

Sheldrick G M (1997) "SHELXS- 97 and SHELXL-97" (Germany: University of Goettingen)

J. Myanmar Acad. Arts Sci. 2020 **Vol. XVIII.No.2A**

SILVER NANOPARTICLES LOADED TiO_2 NANOTUBE ARRAYS PREPARED BY PHOTODEPOSITION METHOD FOR PHOTOELECTROCHEMICAL CELL

Nyein Nyein[1], Than Zaw Oo[2], Go Kawamura[3],
Atsunori Matsuda[3], & Zainovia Lockman[4*]

Abstract

In this study, TiO_2 nanotube arrays (TNTs) were fabricated by anodizing of Ti foil in NaOH/fluoride/EG electrolyte at 60 V for 60 min while dispersion of Ag nanoparticles on them were performed by photodeposition method. The morphology and crystal structure of pure TNTs and Ag decorated TNTs (Ag/TNTs) were then studied. The assembly was then used as a photoelectrode in the photoelectrochemical cell to measure the photocurrent and generate hydrogen gas. The addition of NaOH into electrolyte resulted in the formation of highly ordered TNTs with the length of 23 μm and diameter of 170 nm. Dispersion of silver nanoparticles through photodeposition was performed in order to enhance photoelectrochemical performance. Enhanced photocurrent of 5.0 mA/cm^2 was achieved using Ag/TNTs compared to 3.2 mA/cm^2 of pure TNTs. The conversion efficiency as measured by solar to hydrogen measurement was found to be 4% for pure TNTs and 6 % for Ag/TNTs. The enhancement thought to be due to enhanced charge separation efficiency and improved electrons transport.

Keywords: Anodization, TiO_2 nanotube arrays, Silver nanoparticles, photoelectrochemical cell

Introduction

Hydrogen is a clean and renewable energy for the consumption as a fuel, converting solar energy into hydrogen is an effective method to resolve the energy crisis for the future. In 1972, Fujishima and Honda first demonstrated the photoelectrochemical cell (PEC) using TiO_2 film as a photoanode due to its low cost, non-toxic, photostability and high photocatalytic activity. Park et al. investigated the performance of PEC using different structures of TiO_2: nanotubes, nanowires, nanorods, nanoporous and P25 nanoparticulate films. The photocurrent density of TNTs was more than 60 times higher than that of TiO_2 mesoporous film with a similar thickness. Furthermore, TNTs exhibited the photocurrent more than 10 times higher than that of a P 25 nanoparticle film. It was found that TNTs can harvest light more efficiently and enhance the photogeneration of electron-hole pairs thus increased solar to hydrogen conversion efficiency than irregular structure under the same illumination. Highly ordered TNTs can be fabricated by using various methods. They are sol-gel method, hydrothermal method and electrochemical anodisation. Among all of these methods, anodization method is relatively simple and easy method to fabricate self-organized nanotube arrays.

The performance of photoelecrochemical cell is depend on their structural characteristics (nanotube length, pore size, wall thickness) which can be easily controlled by the types of electrolytes and their composition as well as by varying anodization parameters such as anodization voltage and time. TNTs with a larger pore size allow better light penetration, thus

---

[1] Dr, Assistant Lecturer, Department of Physics, Meiktila University

[2] Dr, Professor, Department of Physics, University of Yangon

[3] Dr, Professor, Department of Electrical and Electronic Information Engineering, Toyohashi University of Technology, Aichi, Toyohashi 441-8580, Japan

[4] Dr, Professor, Green Electronics nanoMaterials Group, School of Materials and Mineral Resources Engineering Campus, Universiti Sains Malaysia, 14300 Nibong Tebal, Penang, Malaysia

enabling the diffusive transport of photogenerated h^+ to react with OH^- in the electrolyte. In recent years, many studies have been attempted to enhance the performance of PEC using TNTs as a photoanode. However, the photocurrent of PEC using TNTs is still lowed due to its weak light absorption to the visible region and high recombination of photogenerated charge carriers. Therefore studies have been attempted to modify TNTs with noble metals such as copper (Cu), gold (Au) and silver (Ag) to extend light absorption to the visible region and reduce recombination of charge carriers. Among the nobel metals, Ag is one of the most promising metals due to its high conductivity and low cost. Ag nanoparticles (Ag NPs) can be deposited by using different methods such as electrodeposition method, photodeposition method and pulse current deposition methods. Among these deposition methods, the photodeposition method was selected to deposit Ag onto the TNTs due to it was low-cost, simple and easy method. Ag NPs could be extended to the visible light absorption due to surface plasmon effect of Ag NPs, which induces the oscillation of surface electrons when light is exposed to it. In addition, Ag NPs can enhance the separation of the photogenerated charge carriers due to the formation of Schottky barrier at the interface between Ag NPs and TNTs. Recently, Chen et al. investigated the effect of Ag NPs by varying different deposition times on the performance of PEC and found that TNTs with a small Ag NPs exhibited the highest photocurrent which was 3.3 times higher than that of the pure TNTs due to Ag NPs significantly enhanced the light absorption to the visible range and the separation of photogenerated charge carrier in the TNTs. In this present work,rather high amount of NH_4F (0.7 wt%) and NaOH was added as to accelerate the growth rate of TNTsand to increase the pH of the electrolyte. We postulated that higher pH electrolyte can suppress surface etching of the nanotubes, and with an excessive amount of NH_4F, chemical etching within the nanotubes at the bottom part can be made more vigorous and thus long TNTs can be produced at a short time. In this study, the highly ordered and uniform TNTs were successfully fabricated in fluoride/EG electrolyte containing NaOH at 60 V for 60 min. And then the prepared TNTs were modified with Ag NPs using photodeposition method and used as photoanode in PEC cell to assess the performance of their PEC activity.

Experimental Section

Materials

Titanium foils (0.127 mm thickness, 99.7 %, Stream Chemicals, USA) were cut into 1 x 3cm and exposed to EG electrolyte ($C_2H_6O_2$, Sigma-Aldrich, USA) containing 0.7 wt % of ammonium fluoride (NH_4F, Sigma-Aldrich, USA) and 5 wt% of sodium hydroxide (NaOH, Wako, Japan).

Methods

Prior to anodization, the foil was ultrasonically degreased in isopropanol, acetone and ethanol for 15 min, rinsed with DI water, and dried in a nitrogen stream. Anodization process was carried out in two electrodescell, with Ti foil as the anode and Pt electrode as the cathode at room temperature. A power supply (Agilent Technologies, USA) was used to supply a DC potential of 60 V for 60 min, and simultaneously recorded the current density transient. The anodized samples were then annealed at 450 ˚C for 3 h in air and then immersed in 0.2 M of silver precursor solution and irradiated with 2 mW the light intensity of UV light.

Materials Characterizations

The morphologies of as-anodized TNTs and Ag NPs deposited TNTswere observed by a field emission scanning electron microscope (FESEM, Hitachi S-4800, Japan). The crystal phases of the TNTs were investigated by X-ray diffraction (XRD) using a Bruker D8 Advanced diffractometer (CuKα radiation, λ = 1.5406 Å). A high resolution transmission electron microscope (HRTEM, JEOL, JEM-2100, Japan) at an acceleration voltage of 200 kV was also used to investigate the morphology and crystallography of TNTs. The optical properties of TNTs were investigated by using by using V-670 ultraviolet/visible spectrophotometer (UV-Vis, Jasco, Japan).

Photoelectrochemical Performance Measurements

The photocurrent measurements were evaluated using a three electrodes PEC cell, with TNTsas the working electrode, platinum rod as a counter electrode, and a saturated Ag/AgCl as the reference electrode. A solution of 1 M KOH used as the electrolyte in this measurement. All three electrodes were connected to the potentiostat (Metrohm µ Autolab III, The Netherlands), and xenon lamp with light intensity of 100 mW/cm^2 (Zolix LSP-X150) was used as a light source for current and voltage measurement sample.

Results and Discussion

The morphologies of pure TNTs and Ag/TNTs were observed by SEM. Figure (1a) shows the surface and cross-section of the pure TNTs formed in NaOH/fluoride/EG electrolyte. As can be seen that highly ordered and uniform pore size were formed in this electrolyte. This result is attributed to the equilibrium reaction between oxidation at metal/electrolyte and dissolution at oxide/electrolyte interface as using higher electrolyte pH. Therefore, 23 µm of long nanotube arrays and 170 nm of larger diameter are resulted. Subsequently, Ag NPs were deposited onto the TNTs via photodeposition method. In the photodeposition process, the TNTs were soaked in 0.2 M Ag-precursor solutionand exposed to light with a light intensity of 2 mW/cm^2. The spherical Ag NPs were formed due to the adsorption of silver (Ag$^+$) ionson the surface of TNTs are reduced by electronsvia illumination. Fig. 1b shows the SEM images of surface and cross section of Ag NPs/TNTs. It was found that Ag NPs with an average particle size of 10 - 40 nm were uniformly dispersed onto the surface of TNTs, however, small amount of Ag NPs were deposited on the walls of the TNTs.

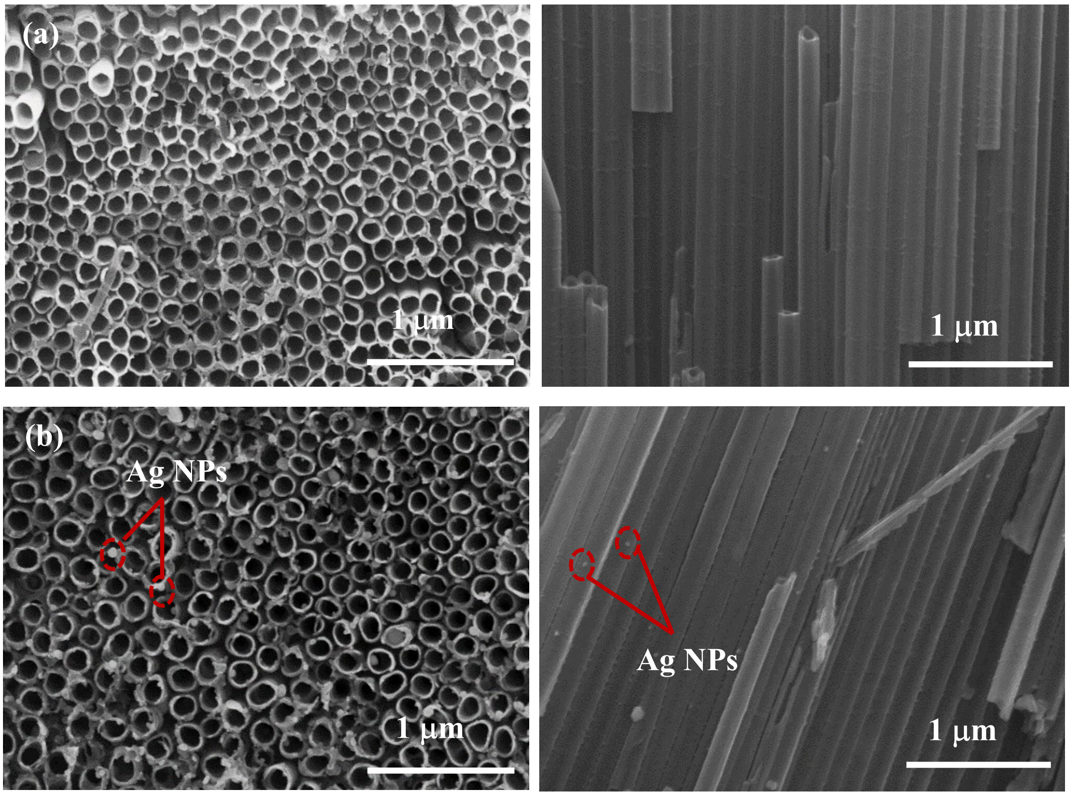

Figure 1 SEM images of (a) pure TNTs and (b) Ag/TNTs.

The morphologies of TNTs were further investigated by TEM to further confirm the existance of Ag NPs. Figure (2) shows TEM images of (a) Pure TNTs (b) surface and (c) cross-section of Ag NPs /TNTs. As can be seen that 20 - 40 nm of Ag NPs are uniformly distributed on the surface of TNTs (Fig. b) and a small amount of Ag NPs are deposited on the walls of TNTs (Fig. c). This result consistent with SEM result. Figure (3A) shows XRD patterns of (a) as-made TNTs (b) annealed TNTs at 450 ˚C and (c) Ag/TNTs. It is found that as-made TNTs are amorphous, only Ti peaks can be seen. After annealing, the crystallinity of anatase peaks detected at 25.4 ˚, 37.8 ˚, 48.5 ˚, 54.0 ˚, 55.2 ˚, 68.9 ˚, and 75.0 ˚ corresponding to (101), (004), (200), (105), (211), (116) and (215) planes of the anatase TiO_2 (JCPDS file no. 21-1272). However, for Ag/TNTs no Ag diffraction peak can be seen. This is attributed to a small size of Ag NPs deposited onto the TNTs.

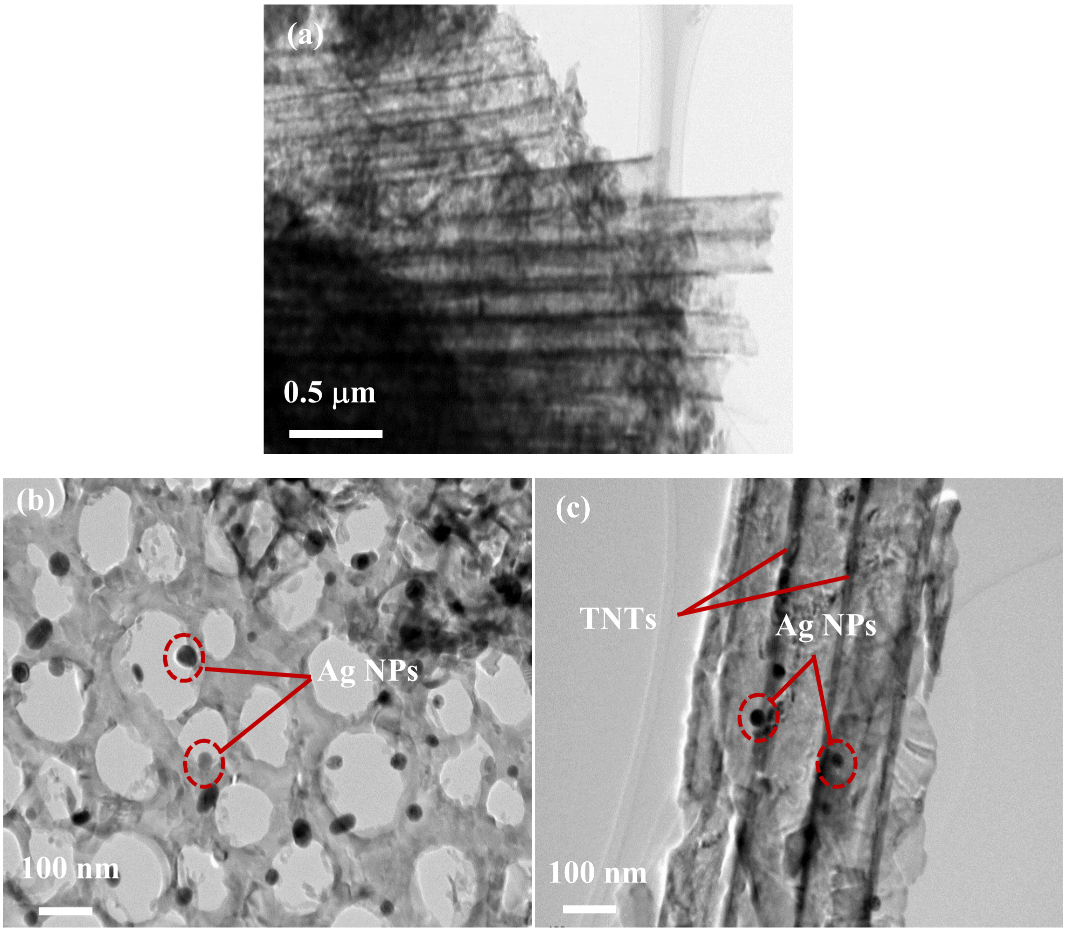

Figure 2 TEM images of (a) pure TNTs (b) surface and (c) cross section of Ag NPs/TNTs.

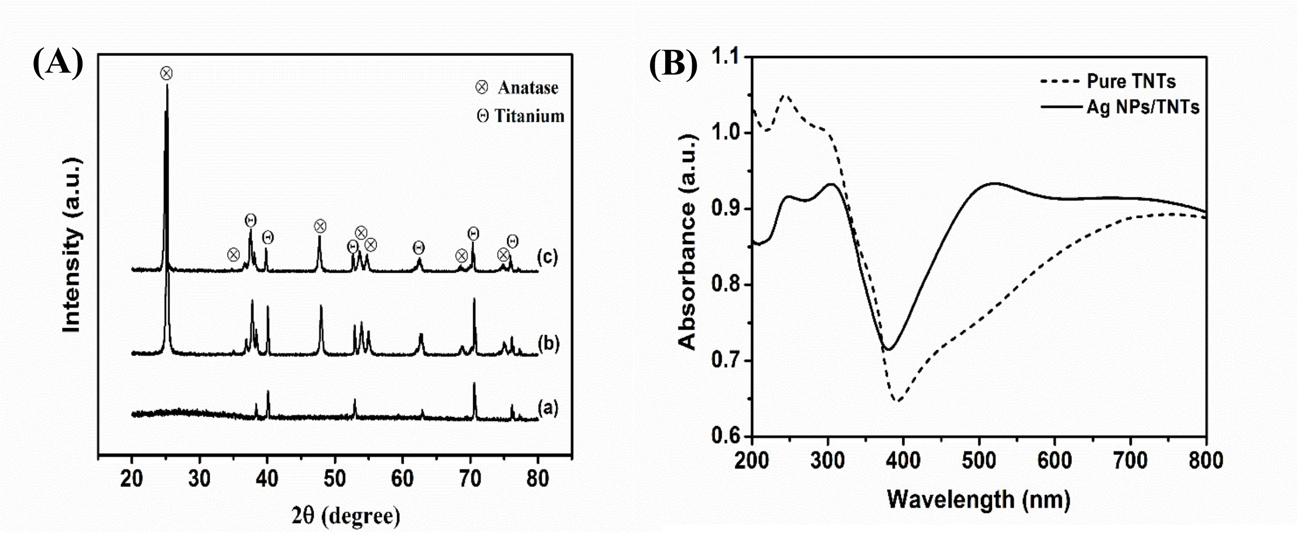

Figure 3A XRD patterns of (a) as-made (b) annealed TNTs at 450˚C for 3 h (c) Ag/TNTs (3B) UV-Vis absorption spectrum of pure TNTs and Ag/TNTs

Figure (3B) shows the light absorption spectra of pure TNTs and Ag/TNTs. As can be seen from the absorption spectra that pure TNTs exhibit better absorption in the ultraviolet and also could absorb to the visible region. This may be attributed to better crystallization of TNTs and the present of carbon in the prepared TNTs. After deposition Ag NPs onto the TNTs, which exhibits a significant absorption to the visible regions. The absorption band of Ag/TNTs observed at ~ 480 nm due to the surface plasmon resonance effect of Ag NPs to TNTs that strongly absorbs and scatters light.

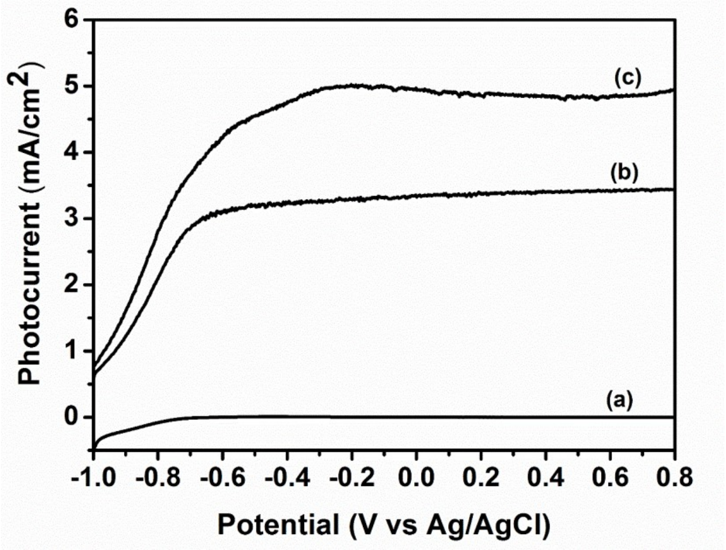

Figure 4 Current-voltage curve of (a) under dark condition (b) pure TNTs and and (c) Ag (0.2 M) /TNTs under light condition

The photoelectrochemical properties of pure TNTs and Ag/TNTs were evaluated by the I-V transient under the solar simulated light shown in Figure(4). This figure shows the photocurrent of pure TNTs is 0 mW/cm^2 under the dark condition and 3 mA/cm^2 under light illumination. Ag NPs deposited TNTs shows the highest photocurrent of 4.5 mA/cm^2 due to both of the faster electrons transport from Ag NPs to the CB of TNTs. Moreover, Ag NPs facilitates the separation of charge carriers due to the formation of Schottky barrier at the interface between Ag NPs and TNTs and also it can trap electrons, accumulated on the surface of Ag NPs. These accumulated electrons shift the position of Fermi level closer to the conduction band of TNTs thus promote interfacial charge transfer process. It was found that Ag NPs deposited TNTs not only increase the absorption to the visible region but also improve the separation of charge carriers due to its surface plasmon effect of Ag NPs. The solar to hydrogen (STH) conversion efficiency of these samples were calculated by using the following equation,

$$\eta_{STH} = \frac{1.23\, J_T}{E_T} \times 100$$

Where, J_T is the hydrogen current density and E_T is the incident light intensity. The STH conversion efficiency of pure TNTs is 4 %, while the STH of Ag/TNTs is 6 %.

Conclusion

In this study, highly ordered and uniform TNTs with a naotube length of 23 μm and diameter of 170 nm were successfully fabricated in NaOH/fluoride/EG electrolyte and a suitable size of Ag NPs are successfully deposited onto the TNTs. These samples were used as photoelectrodes in PEC andevaluated the generation of photocurrent and hydrogen gas of their samples. The Ag NPs deposited TNTs show the highest photocurrent and solar to hydrogen conversion efficiency than that of the pure TNTs due to surface plasmon effect of Ag NPs, which can extend light absorption and reduce the recombination of photogenerated charge carriers.

Acknowledgement

The authors gratefully acknowledge ASEAN University Network for Science and Engineering Education Development Network (AUN/SEED-Net) Project and Japan International Cooperation Agency (JICA) for their financial support.

References

A. Fujishima, (1972) "Electrochemical photolysis of water at a semiconductor electrode.",Nature, vol. 238,pp.37-38.

C. Ruan, M. Paulose, O. K. Varghese, G. K. Mor, C. A. Grimes, (2005)"Fabrication of highly ordered TiO_2 nanotube arrays using an organic electrolyte."The Journal of Physical Chemistry B, vol. 109, pp.15754-15759.

I. Paramasivam, J. M. Macak, A. Ghicov, P. Schmuki, (2007)"Enhanced photochromism of Ag loaded self-organized TiO_2 nanotube layers."Chemical Physics Letters, vol.445, pp. 233-237

J. H. Park, , S. Kim, and A. J. Bard, (2006)"Novel carbon-doped TiO_2 nanotube arrays with high aspectratios for efficient solar water splitting." Nano letters,vol. 6,pp. 24-28.

J. M. Macák, H. Tsuchiya, and P. Schmuki, (2005)"High-Aspect-Ratio TiO_2 Nanotubes by Anodization of Titanium."Angewandte Chemie International Edition, vol. 44, pp. 2100-2102.

J. Zeng, Y. Zheng, M. Rycenga, J. Tao, Z-Y. Li, Q. Zhang, Y. Zhu, Y. Xia, (2010)"Controlling the shapes of silver nanocrystals with different capping agents."Journal of the American Chemical Society, vol. 132, pp.8552-8553.

K. Chen, X. Feng, R. Hu, Y. Li, K. Xie, Y. Li, H. Gu, (2013)"Effect of Ag nanoparticle size on the photoelectrochemical properties of Ag decorated TiO_2 nanotube arrays."Journal of Alloys and Compounds, vol. 554, pp. 72-79.

K. M. Mayer, J.H. Hafner, "Localized surface plasmon resonance sensors.(2011)"Chem Rev,vol.111, pp.3828-57.

K. V. Baiju, K. S. Sandhya, J. James, K. G. K. Warrier, (2007)"Photocatalytic activity of sol-gel-derived nanocrystalline titania." TheJournal of physical Chemistry C, vol. 111, pp. 7612-7622.

K. Xie, L. Sun, C. Wang, Y. Lai, M. Wang, H. Chen, C. Lin, (2010)"Photoelectrocatalytic properties of Ag nanoparticles loaded TiO_2 nanotube arrays prepared by pulse current deposition." ElectrochimicaActa, vol. 55, pp. 7211-7218.

N. Liu, X. Chen, J. Zhang, J. W. Schwank,(2014) "A review on TiO_2-based nanotubes synthesized via hydrothermal method: Formation mechanism, structure modification, and photocatalytic applications." Catalysis Today, vol. 225, pp.34-51.

R. P. Antony, T. Mathews, S. Dash, A. K. Tyagi, B. Raj,(2012)" X-ray photoelectron spectroscopic studies of anodically synthesized self aligned TiO_2 nanotube arrays and the effect of electrochemical parameters on tube morphology."Materials Chemistry and Physics, vol. 132, pp. 957-966.

S. Joseph, T. M. David, C. Ramesh, P. Sagayaraj, (2014) "The role of electrolyte pH in enhancing the surface morphology of TiO_2 nanotube arrays grown on Ti Substrate." IJSER, vol. 5, pp. 85-91.

S.P. Lim, A. Pandikumar, H. N. Lim, R. Ramaraj, N. M. Huang, (2015)"*Boosting Photovoltaic Performance of Dye-Sensitized Solar Cells Using Silver Nanoparti*cle-Decorated N,S-Co-Doped-TiO_2*Photoanode.*" Sci Rep, vol. 5, pp. 11922.

S. P. Lim, A. Pandikumar, N. M. Huang, H. N. Lim, G. Gu, T. L. Ma,(2014)"Promotional effect of silver nanoparticles on the performance of N-doped TiO_2 photoanode-based dye-sensitized solar cells." RSC Advances, vol. 4, pp. 48236-48244.

S. Zhang, F. Peng, H. Wang, H. Yu, S. Zhang, J. Yang, H. Zhao, (2011)"Electrodeposition preparation of Ag loaded N-doped TiO_2 nanotube arrays with enhanced visible light photocatalytic performance. "Catalysis Communications, vol. 12, pp.689-693.

T. Ivanova, A. Harizanova, T. Koutzarova, B. Vertruyen, (2013)"Optical and structural characterization of TiO_2 films doped with silver nanoparticles obtained by sol–gel method." Optical Materials. vol. 36, pp. 207-213.

V. Subramanian, E. Wolf, and P.V. Kamat, (2001) "Semiconductor-metal composite nanostructures. To what extent do metal nanoparticles improve the photocatalytic activity of TiO_2 films."The Journal of Physical Chemistry B, vol. 105, pp.11439-11446.

X. Fan, J. Fan, X. Hu, E. Liu, L. Kang, C. Tang, Y. Ma, H. Wu, Y. Li, (2014)"Preparation and characterization of Ag deposited and Fe doped TiO_2 nanotube arrays for photocatalytic hydrogen production by water splitting."Ceramics International, vol. 40, pp.15907-15917.

Y. Lai, H. Zhaung, K. Xie, D. Gong, Y. Tang, L. Sun, C. Lin, Z. Chen, (2010)"Fabrication of uniform Ag/TiO_2 nanotube array structures with enhanced photoelectrochemical performance."New Journal of Chemistry, vol. 34, pp. 1335.

Z. Zhang, L. Zhang, M. N. Hedhili, H. Zhang, P. Wang, (2012) "Plasmonic gold nanocrystals coupled with photonic crystal seamlessly on TiO_2 nanotube photoelectrodes for efficient visible light photoelectrochemical water splitting." Nano letters, vol. 13, pp. 14-20.

J. Myanmar Acad. Arts Sci. 2020 **Vol. XVIII.No.2A**

BLUETOOTH - BASED CONTROLLED CAR USING ARDUINO

Zin Mar Lay[*]

Abstract

In this research, the designed and constructed controlled car with automation system using Bluetooth is discussed. The control unit is the Arduinouno board. The HC-06 Bluetooth module activates wireless communication with android phone. It is ready to transmit and accept the data. The Bluetooth module operates data exchange from android phone to Arduino. An android operates using android application software. The Arduino activates using Arduino programming language and it receives the data from Bluetooth . The Arduinocommands the motors of controlled car via motor driver circuit. The Arduino controls the car to activate backward, forward, left side and right side directions according to the receiving data from android phone. This research is a combination method of embedded system and technology of android.

Keywords: Arduino, bluetooth, motor driver, motor, android system

Introduction

A Bluetooth technology is a high speed low powered wireless techonology link that is designed to connect phones or other portable equipment together. It is a specification for the use of low power radio communication to link phone, computers and other network devices over short distances without wires. Wireless signals transmitted with Bluetooth cover short distances, typically up to 30 feet (10 meters).

It is achieved by embedded low cost transceiver into the devices. It supports on the frequency band of 2.45GHzand can support upto 721KBps along with three voice channels.

Scope of Work

In this research, the Bluetooth controlled car is developed using L298 motor driver circuit, HC-06 Bluetooth module and Arduino. The smart phone and the application are used to control the car with Bluetooth communication system. The L298 motor driver circuit is implemented to provide the necessary current for driving the motor. The block diagram of constructed system is shown in Figure (1).

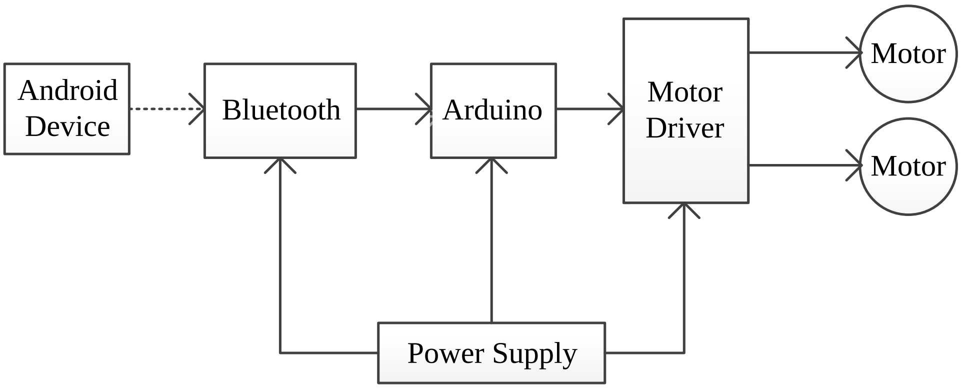

Figure 1 Block diagram of the constructed system

---

[*] Dr, Lecturer, Department of Physics, University of Mandalay

Electronic Devices Used in This Work

Arduino Uno Board

The Arduino Uno is a microcontroller board based on the ATmega 328. It has 14 digital input/output pins (of which 6 can be used as PWM outputs), 6 analog inputs, a 16 MHZ ceramic resonator, a USB connection, a power jack, an ICSP header, and a reset button. It contains everything needed to support the microcontroller; simply connect it to computer with a USB cable or power it with a AC- to- DC adapter or battery to get started.

Figure 2 The photograph of Arduino Uno Board

Bluetooth Module HC-06

The HC-06 is a class 2 slave Bluetooth module designed for transparent wireless serial communication. Once it is paired to a master bluetooth device such as PC, smart phones and tablet, its operation becomes transparent to the user. All data received through the serial input is immediately transmitted over the air. When the module receives wireless data, it is sent out through the serial interface exactly at it is received.

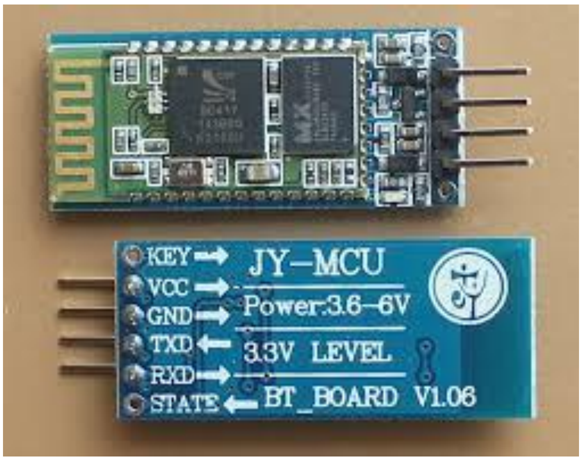

Figure 3 The photograph of Bluetooth module

L298 IC

L298 is a high power version of L298 motor driver IC. It is a high voltage, high current, dual full-bridge driver designed to accept standard TTL logic levels (Control Logic) and drive inductive loads such as relays, solenoids, DC and Stepper motors. Two enable inputs are provided to Enable or disable the device independently of the input signals. The emitters of the lower transistors of each bridge are connected together and the corresponding external terminal can be used for the connection of an external sensing resistor.

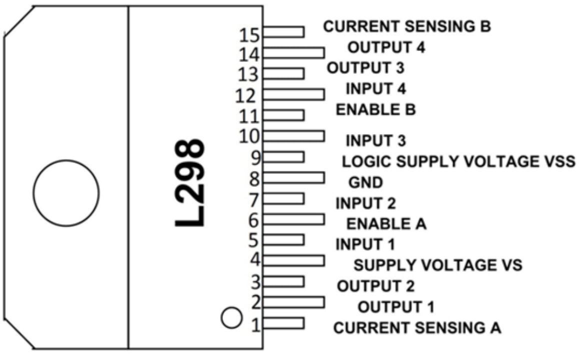

Figure 4 Pin configuration of the L298 IC

DC Motor

A DC motor is any of a class of rotary electrical machines that converts direct current electrical energy into mechanical energy. The most common types rely on the forces produced by magnetic fields. Nearly all types of DC motors have some internal mechanism, either electromechanical or electronic, to periodically change the direction of current flow in part of the motor.

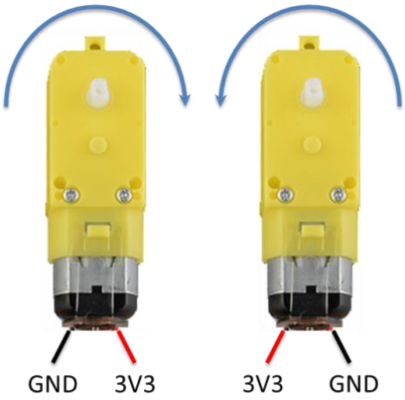

Figure 5 The photograph of the DC motor

Design and Construction of the System

Construction of Bluetooth with Arduino

The HC-06 module communicates with Arduino Bluetooth module through serial communication. TX pin of Bluetooth module needs to connect with RX pin (receive pin) of Arduino. RX pin of Bluetooth connected with TX pin (transmit pin) of Arduino Uno board. The Arduino triggers the output four states according receives data through the Blutooth module from an android device. The +5V and GND pins of Bluetooth module are connected to +5V and GND of Ardunio.

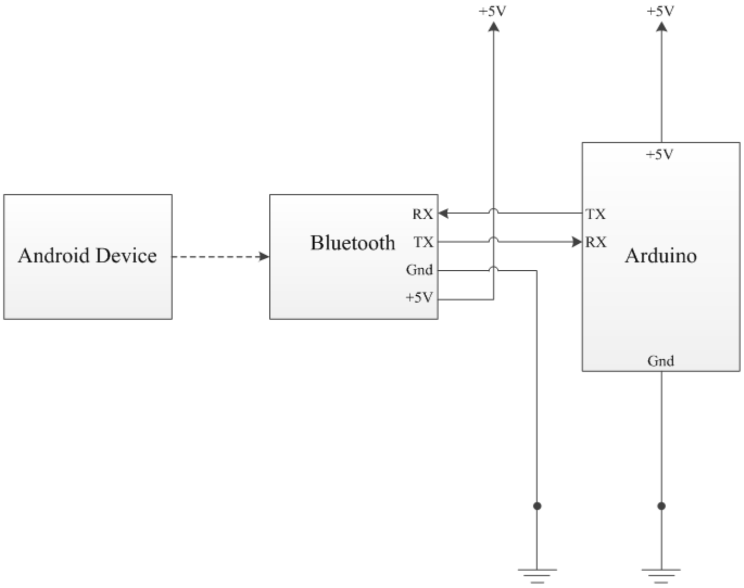

Figure 6 The circuit diagram of Bluetooth with Arduino

Construction of Arduino with Motor Driver Circuit

The H-bridge motor driver IC 298 which controlled the two motors. The first motor is controlled by input 1(pin 5), input 2(pin 7) and enable 1 (pin 6) of L298 IC. The input 3 (pin 10), input 4 (pin 12) and enable 2 (pin 11) control the second motor. The current sensing pins are used so that they are grounded. Both enable pins are joined to the power supply.

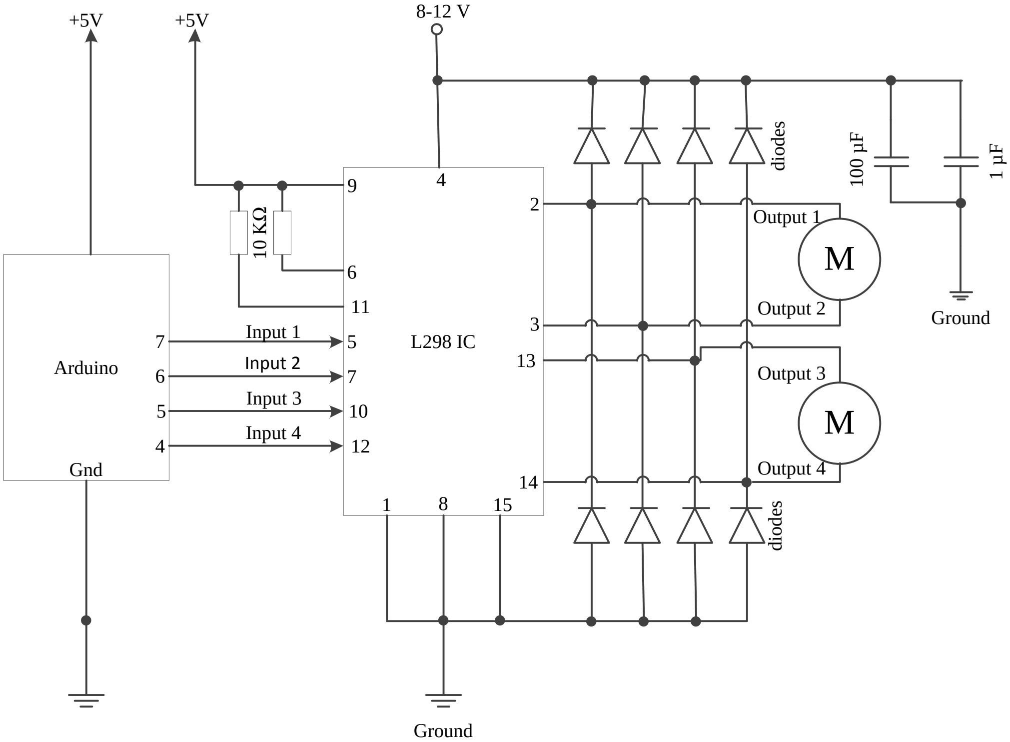

Figure 7 The circuit diagram of Arduino with motor driver

Construction of Complete Circuit for the Whole System

The constructed system is developed to control the car by smart phone Bluetooth communication. The two motors from controlled car are driven using L298N dual H-Bridge motor drive. Using the L298N motor driver IC, eight diodes, two resistors are implemented for driver circuit. Arduino Uno board is the control unit. The HC-06 bluetooth transceiver module has higher speeds to performance and its TX and RX pins are connected to the RX and TX pins of Arduino. After pairing the smart phone and Bluetooth device, sent the commands to operate the motor. If button is pressed, the Bluetooth transmit the data to Arduino. The Arduino receives the data and generates the outputs to operate the motor driver.

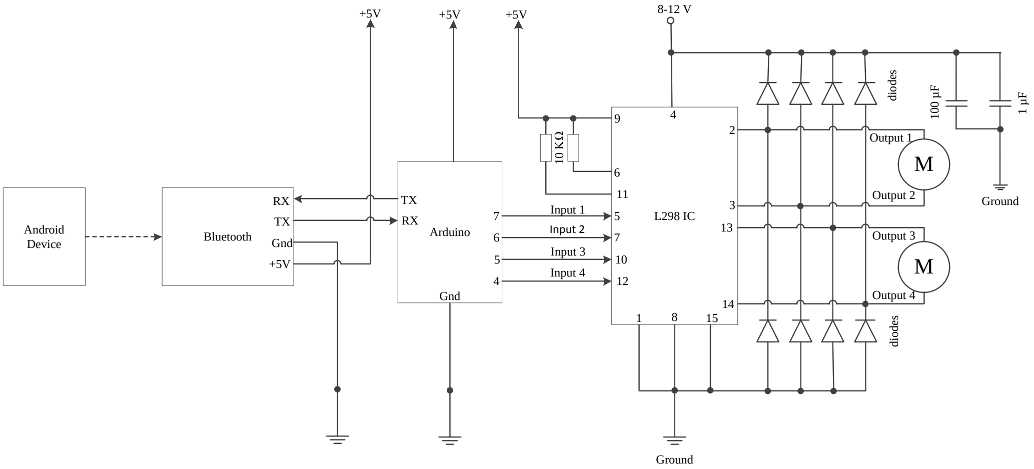

Figure 8 The complete circuit for the constructed system

The Flowchart for the Main Program

At the beginning of the program, define the functions and initialize serial baud rate 9600 bits/sec and assign pin 7, 6, 5 and 4 of Arduino are as output pins. And then read the receiving data from Bluetooth. If the data is equal to ‘a’, the Arduino gives the data (1, 0, 1, 0) to drive the motor to forward direction. If the data is not ‘a’, it tests the data is ‘e’ or not. If the data is ‘e’, the Arduino generates the data to operate the backward direction. Also left, right and stop directions are controlled by Arduino according to the receiving data from Bluetooth serial communication.

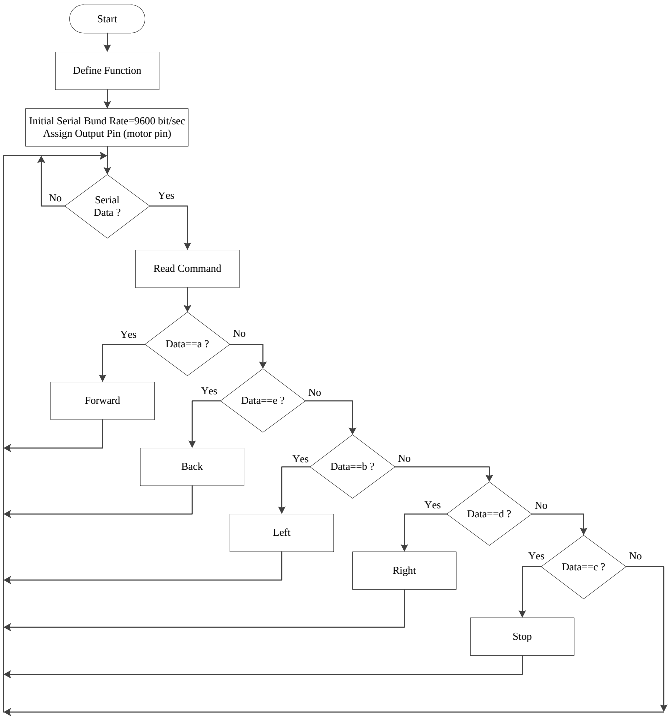

Figure 9 Flowchart of the main program

Arduino Control Signal to Motor

Table 1 Arduino Control signal to motor

Pin	Forward	Backward	Left	Right	Stop
4	1	0	1	0	0
5	0	1	0	1	0
6	1	0	0	1	0
7	0	1	1	0	0

Results, Discussion and Conclusion

Results and Discussion

The research is developed by using Arduino, L298 motor driver and Bluetooth module. The android phone and android application control the car. The Arduino and android phone are responsible for enabling via Bluetooth module. The constructed L298 motor driver circuit which provides the necessary current to drive the motors. The left side motor is joined to two output pins of motor driver and the right side motor is also joined to the other two output pins. The Bluetooth and application are paired to easy to control the car. The five buttons in application control the movement of the car in various directions according to the receiving commands over Bluetooth.

If one key is pressed, the Arduino receives the data via Bluetooth and it performs with appropriate instructions and sends the data to input pins of motor driver. The operating range of Bluetooth is about 10 meters. Figure (11) is the photograph of circuit connections of the system. Figure (12) is the photograph of front view of the constructed system. Figure (12) is the photograph of smart phone and controlled car via Bluetooth communication.

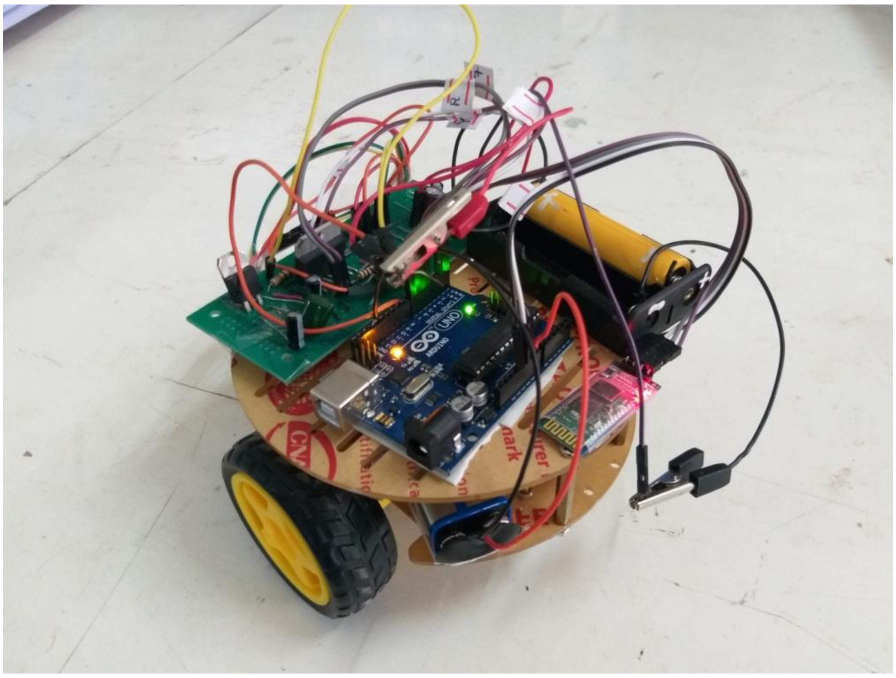

Figure 10 The photograph of circuit connections of the system

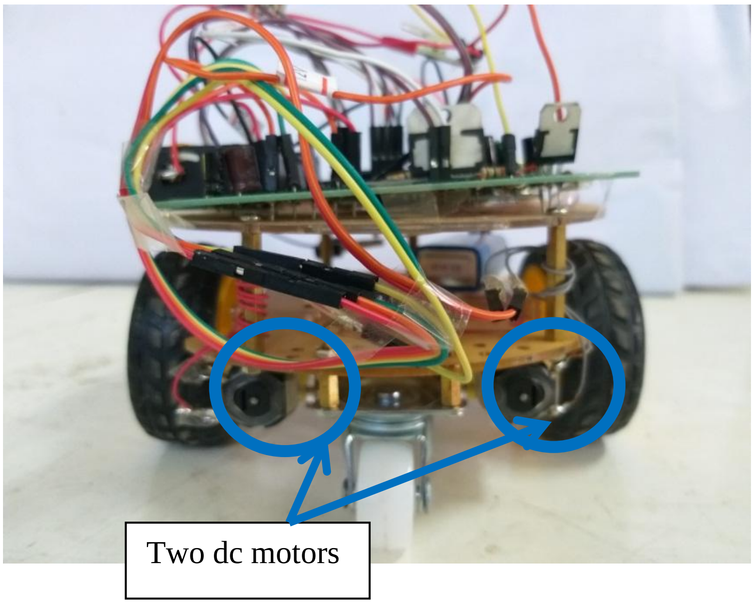

Figure 11 The photograph of front view of the constructed system

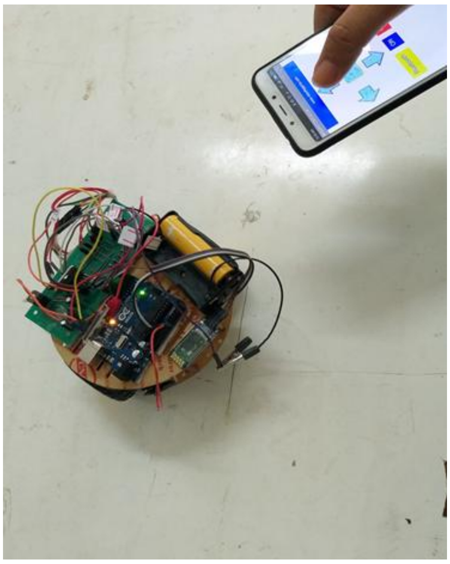

Figure 12 The photograph of smart phone and controlled car via Bluetooth communication

Conclusion

In this research, the Bluetooth communication system is used to drive the controlled car to various directions. Further research can be done other wireless ways to communicate with controller using wifi serial transceiver module, Zigbee, GSM/GPS communication, Radio RF transceiver.

Acknowledgements

We are greatly indebted to Rector Dr. Thida Win, Mandalay University, for her permission to carry out this research and for paying attention to this work. We wish to express our sincere gratitude to Dr. Lei Lei Win, Professor, Head of Physics Department, Mandalay University for allowing to do this research.

References

http: // www.elprocus.com> how does Bluetooth work?
http: // store.ardrino.cc/usa/ arduion-uno-rev 3
https: // www.sgbotic.com/index.php? dispatch =products. view& product_ id =2471
https: // www.aranacorp.com/en/arduino-and-bluetooth-module-hc-06
https: // components 101. Com/ ics / L298-pin-configuration-features-datasheet.
https: // en.m. Wikipedia.org/ wiki/ DC-motor

STUDY ON THE DIFFERENTIAL SCATTERING CROSS SECTION FOR NEUTRON-CARBON (n-^{12}C) NUCLEUS WITH EIKONAL APPROXIMATION

Hla Myat Thandar[1] and Khin Swe Myint[2]

Abstract

The purpose of this work is to predict the differential cross sections of neutron-carbon (n-^{12}C) nucleus in the frame work of Eikonal approximation. The differential cross sections of neutron-carbon nucleus are calculated by using Wood-Saxon potential. The projectile neutron kinetic energy ranged from 65 MeV to 95 MeV by increasing 10 MeV while the scattering angle varied 0° to 30°. The calculated results are in good agreement with the experimental results for energies, 65 MeV and 75 MeV. They are quite different for 85 MeV and 95 MeV.

Keywords: differential cross section, Eikonal approximation method, Wood-Saxon potential

Introduction

Scattering theory is a framework for studying and understanding the scattering of waves and particles. Understanding the nucleon-nucleus interaction has been one of the long term goals of nuclear physics. The nature of forces between particles can be studied from the scattering experiments. The interaction between two nucleons is basis for all of the nuclear physics. Approximations play a very important role in the understanding of processes that cannot be solved exactly. The Born approximation in quantum mechanics is an example of an approximation that has been extensively used for studying low energy processes.

There have been many measurements of proton-nucleus scattering, but few of neutron scattering at 65 MeV to 95 MeV energies. Those of Hjort *et al.* 65 MeV (Hjort E.L. et al., (1994)), Salmon at 96 MeV (Salmon G.L., (1960)), and from the Uppsala facility ((Klug J. et al., (2002), Klug J. et al., (2003), Klug J. et al., (2003)), also at 96 MeV are the most recent. In the 1950's and 1960's, when high energy physics was ascending towards its peak, it was realized among the high energy physicists of that time the Born approximation is not a valid approximation for studying processes involving high energies. This period in fact was the golden age in the development of the Eikonal approximation. From approximation methods, we can obtain differential scattering cross section.

Differential Cross Section and Electric Form Factors

If the colliding particles possess extended structure, the cross section must be modified. It must take into account only the spatial distribution of the target particle if the incident particles are leptons. For simplicity, we shall assume here that the target particle possesses a spherically symmetric density distribution. The cross section for scattering of electrons (Nakano T. et al., (1953)) from such a target is of the form.

$$\frac{d\sigma}{d\Omega}=\left(\frac{d\sigma}{d\Omega}\right)_{\text{po int}}\left|F(q^2)\right|^2 \tag{1}$$

---

[1] Dr, Lecturer, Department of Physics, University of Mandalay, Myanmar

[2] Dr, Emeritus Professor, Department of Physics, University of Mandalay, Myanmar

The multiplicative factor $F(q^2)$ is called the Form Factor, and

$$q^2 = (p - p')^2$$

is the square of the momentum transfer, p is the momentum of incident particle and p' is the momentum of scattered particle.

Form Factors play an increasingly important role in nuclear physics because they are the most convenient link between experimental observation and theoretical analysis. Equation (1) expresses the fact that the Form factor is the direct result of a measurement. To discuss the theoretical side, consider a system that can be described by a wave function $\Psi(r)$, which in turn can be found as the solution of a Schrodinger equation. For an object of charge Q, the charge density can be written as Q $\rho(r)$, where $\rho(r)$ is normalized probability density, $\int d^3 r \rho(r) = 1$. It is well known that the form factor can be written as the Fourier transform of the probability density

$$F(q^2) = \int d^3 r \rho(r) e^{\frac{iq.r}{\hbar}} \qquad (2)$$

The Form Factor at zero momentum transfer, F(0), is usually normalized to be 1 for a charged particle; however for a neutral one F(0)=0. The chain linking experimentally observed cross section to the theoretical point of departure can thus be sketched as follows:

Experiment Comparison Theory

$$\frac{d\sigma}{d\Omega} \rightarrow \left|F(q^2)\right| \Leftrightarrow F(q^2) \leftarrow \rho(r) \leftarrow \psi(r) \leftarrow \text{Schrodingrequation}$$

Calculation of The Scattering Amplitude by Using Eikonal Approximation

In theoretical physics, the eikonal approximation is an approximative method useful in wave scattering equations which occur in optics, seismology, quantum mechanics, quantum electrodynamics, and partial wave expansion.

The main advantage that the eikonal approximation offers is that the equations reduce to a differential equation in a single variable. This reduction into a single variable is the result of the straight line approximation or the eikonal approximation which allows us to choose the straight line as a special direction (Zamrun M. et al., (2013)).

At E>> V, the semiclassical path concept becomes applicable and we replace exact wave function ψ^+ by the semiclassical wave function,

$$\psi^+ \sim \quad e^{iS(x)/\hbar} \qquad (1)$$

The time independent Schrodinger equation is

$$H\left|\psi^+\right\rangle = E\left|\psi^+\right\rangle_{pp}$$

$$(H_0 + V)\left|\psi^+\right\rangle = E\left|\psi^+\right\rangle$$

$$\left(\frac{-\hbar^2}{2m}\nabla^2 + V\right)\left|\psi^+\right\rangle = E\left|\psi^+\right\rangle \qquad (2)$$

Where $H_0 = \frac{-\hbar^2}{2m}$

Substitute equation (1) into equation (2) and ∇^2 for one dimension,

Equation (2) becomes

$$\frac{-\hbar^2}{2m}\frac{d^2}{dx^2}e^{iS(x)/\hbar} + Ve^{iS(x)/\hbar} = Ee^{iS(x)/\hbar} \tag{3}$$

From equation (3)

$$\frac{d^2}{dx^2}e^{iS(x)/\hbar} = \frac{d}{dx}\left[e^{iS(x)/\hbar} \circ \frac{i}{\hbar} \circ \frac{d}{dx}S(x)\right] = \frac{-1}{\hbar^2}e^{iS(x)/\hbar}\left(\frac{dS(x)}{dx}\right)^2 + \frac{i}{\hbar}e^{iS(x)/\hbar}\frac{d^2S(x)}{dx^2} \tag{4}$$

Substitute equation (4) into equation (3), Equation (3) becomes

$$\frac{1}{2m}e^{iS(x)/\hbar}\left(\frac{dS(x)}{dx}\right)^2 - \frac{i\hbar}{2m}e^{iS(x)/\hbar}\frac{d^2S(x)}{dx^2} + Ve^{iS(x)/\hbar} = Ee^{iS(x)/\hbar}$$

where $\hbar$ is very small,

$$\frac{1}{2m}\left(\frac{dS(x)}{dx}\right)^2 + V = \frac{\hbar^2k^2}{2m} \tag{5}$$

where $E = \frac{\hbar^2k^2}{2m}$

Equation (5) for 3 dimension,

$$\frac{(\nabla S)^2}{2m} + V = \frac{\hbar^2k^2}{2m} \tag{6}$$

This leads to the Hamilton-Jacobi equation for S

By equation (5) for one dimension,

$$\frac{1}{\hbar}\left(\frac{dS(x)}{dx}\right) = \sqrt{k^2 - \frac{2m}{\hbar^2}V(x)}$$

By integrating the above equation,

$$\frac{1}{\hbar}\int\frac{dS(x)}{dx}dx = \int\left(k^2 - \frac{2m}{\hbar^2}V(x)dx\right)^{1/2} + \text{constant}$$

$$\frac{S(x)}{\hbar} = \int\left(k^2 - \frac{2m}{\hbar^2}V(x)dx\right)^{1/2} + \text{constant} \tag{7}$$

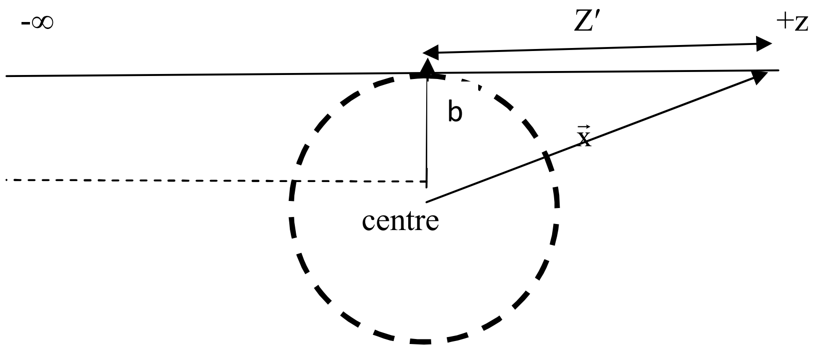

Scattering region

Consider the situation depicted in Fig, where the straight line trajectory is along the z-direction, |x|=r and |b|=b is the impact parameter.

Therefore equation (7) becomes,

$$\frac{S}{\hbar} = \int_{-\infty}^{z}\left(k^2 - \frac{2m}{\hbar^2}V\left(\sqrt{b^2 + z'^2}\right)\right)^{1/2} dz' + \text{ constant} \tag{8}$$

When $\quad V=0,\ e^{ikz} = e^{iS/\hbar}$

$$\therefore kz = S/\hbar$$

Equation (8) becomes

$$kz = \int_{-\infty}^{z} kdz' + \text{ constant}$$

$$\text{constant} = kz - \int_{-\infty}^{z} kdz'$$

Substitute in equation (8)

$$\frac{S}{\hbar} == \int_{-\infty}^{z}\left(k\left[1 - \frac{2m}{\hbar^2 k^2}V\left(\sqrt{b^2 + z'^2}\right)\right]^{1/2} - k\right)dz' + kz \tag{9}$$

By using power series,

$$(1-x)^n = 1 - nx + \frac{n(n-1)}{2!}x^2 - \ldots\ldots\ldots\ldots\ldots$$

$$\left(1 - \frac{2m}{\hbar^2 k^2}V\right)^{1/2} = 1 - \frac{1}{2}\frac{2m}{\hbar^2 k^2}V + \ldots\ldots\ldots\ldots$$

$$\frac{S}{\hbar} == kz - \frac{m}{\hbar^2 k}\int_{-\infty}^{z} V\left(\sqrt{b^2 + z'^2}\right)dz'$$

$$\psi^+(X) = \psi^+(b + z\hat{z})$$

$$= e^{i\left[kz - \frac{m}{\hbar^2 k}\int_{-\infty}^{z} V\left(\sqrt{b^2 + z'^2}\right)dz'\right]}$$

$$= \exp(ikz) \circ \exp\left(-\frac{im}{\hbar^2 k} \int_{-\infty}^{z} V\left(\sqrt{b^2 + z'^2}\right) dz' \right) \tag{10}$$

The form factor is

$$f(k',k) = -\frac{1}{4\pi}\frac{2m}{\hbar^2}(2\pi)^3 \int d^3x' \frac{e^{-ik'.x'}}{(2\pi)^{3/2}} V(x') \langle X' | \psi^+ \rangle \tag{11}$$

$$\langle X' | \psi^+ \rangle = \frac{e^{iS(x)/\hbar}}{(2\pi)^{3/2}}$$

$$= \frac{1}{(2\pi)^{3/2}} e^{ikz'} e^{\frac{-im}{\hbar^2 k}\int_{-\infty}^{z} V\left(\sqrt{b^2+z''^2}\right)dz''}$$

Equation (11) becomes

$$f(k',k) = \frac{-1}{4\pi}\frac{2m}{\hbar^2}(2\pi)^3 \int d^3x' \frac{e^{-ik'..x'}}{(2\pi)^{3/2}} V(x') \langle X' | \psi^+ \rangle$$

$$= \frac{-1}{4\pi}\frac{2m}{\hbar^2} \int d^3x' e^{i(k-k')x'} V\left(\sqrt{b^2 + z'^2}\right) e^{\frac{-im}{\hbar^2 k}\int_{-\infty}^{z} V\left(\sqrt{b^2+z''^2}\right)dz''}$$

For cylindrical coordinate

$$d^3x' = bdb\, d\varphi_b\, dz'$$

$$(k-k')x' = (k-k').(b + z\hat{z})$$

$$(k-k')x' = (k-k').b + (k-k')z\hat{z}$$

$$= kb - k'b + (k-k')z\hat{z} \quad = -k'b$$

$$k'.b = (k\sin\theta\hat{x} + k\cos\theta\hat{y}).(b\cos\varphi_b\hat{x} + b\sin\varphi_b\hat{y})$$

$$= kb\sin\theta\cos\phi_b = kb\theta\cos\phi_b$$

The expression for f(k, k) becomes

$$f(k',k) = \frac{-1}{4\pi}\frac{2m}{\hbar^2}\int_0^{\infty} bdb \int_0^{2\pi} d\varphi_b e^{-ikb\theta kb\theta c_b} \int_{-\infty}^{\infty} dz' V\exp\left[\frac{-im}{\hbar^2 k}\int_{-\infty}^{z} Vdz''\right] \tag{12}$$

$$\int_0^{2\pi} d\varphi_b e^{-ikb\theta\cos\varphi_b} = 2\pi J_0(kb\theta) \quad \text{(bessel function)}$$

$$\int_{-\infty}^{\infty} dz' V\exp\left[\frac{-im}{\hbar^2 k}\int_{-\infty}^{z} Vdz''\right] = V\int_{-\infty}^{\infty} dz'\exp\left[\frac{-imV}{\hbar^2 k}\int_{-\infty}^{z} dz''\right]$$

$$= \frac{i\hbar^2 k}{m}\left[\exp\left(\frac{-im}{\hbar^2 k}\int_{-\infty}^{\infty} Vdz''\right) - 1\right] \tag{13}$$

By substituting equation (13) into equation (12),

$$f(k',k)=\frac{-1}{4\pi}\frac{2m}{\hbar^2}\int_0^\infty bdb2\pi\, J_0\left(kb\theta\right)\frac{i\hbar^2 k}{m}\left[\exp\left(\frac{-im}{\hbar^2 k}\int_{-\infty}^{\infty} Vdz''\right)-1\right]$$

$$=-ik\int_0^\infty bdbJ_0\left(kb\theta\right)\left[\exp\left(\frac{-im}{\hbar^2 k}\int_{-\infty}^{\infty} Vdz''\right)-1\right]$$

where $\Delta b=\frac{-m}{2k\hbar^2}\int_{-\infty}^{\infty} V\left(\sqrt{b^2+z''^2}\right)dz''$

The scattering amplitude is

$$f(k',k)=-ik\int_0^\infty bdbJ_0\left(kb\theta\right)\left[e^{2i\Delta b}-1\right] \tag{14}$$

$$\boxed{\frac{d\sigma}{d\Omega}=\left|f(k',k)\right|^2=\left|f(\theta)\right|^2} \tag{15}$$

Woods-Saxon Potential

Nuclear potential of the Woods-Saxon form, which is described by the potential depth V_0, the radius parameter r_0 and the diffuseness parameter *a*, is widely used in the analyses of nuclear collisions. The diffuseness parameter determines the characteristic at the surface region of the nuclear potential.

$$V(r)=\frac{V_0}{1-\exp\left(\frac{r-R}{a}\right)}$$

where $V_0 = 50$ MeV (potential well depth)

$R = r_0 A^{1/3}$ (nuclear radius)

$r_0 = 1.25$ fm (the radius parameter)

$a = 0.5$ fm (the surface diffuseness parameter)

Results and Discussions

Differential scattering cross sections of neutron-carbon nucleus (n-^{12}C) are calculated by using Wood-Saxon potential. In this calculation, the energies of neutron ranged from 65 MeV to 95 MeV by increasing 10 MeV while the scattering angle varied 0° to 30°. To investigate differential scattering cross sections of the n-^{12}C nucleus, Eikonal approximation method is used. It is found that the smaller the scattering angle, the larger the differential scattering cross section. Moreover, the larger the energy of the neutron, the larger the differential scattering cross section is. The calculated results of differential scattering cross sections are in good agreement with the experimental results for energies, 65 MeV and 75 MeV. But they are quite different with the experimental results for 85 MeV and 95 MeV. Moreover, they are slightly different at large angles. But the features of the calculated results and the experimental results are similar. They are shown in Figure (1) to Figure (5).

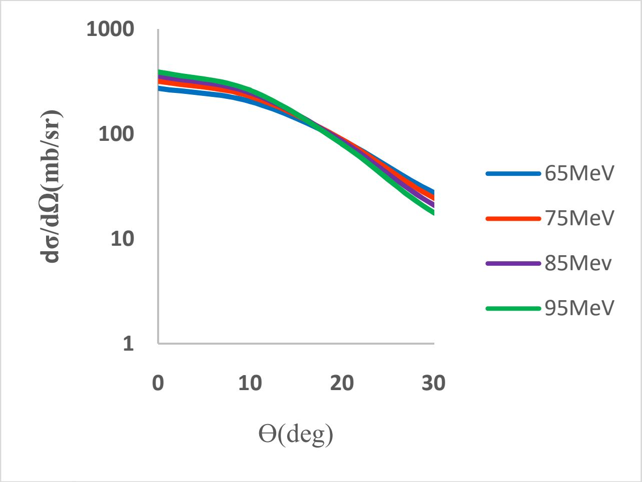

Figure 1 Our calculated results of differential scattering cross sections for 65 MeV to 95 MeV

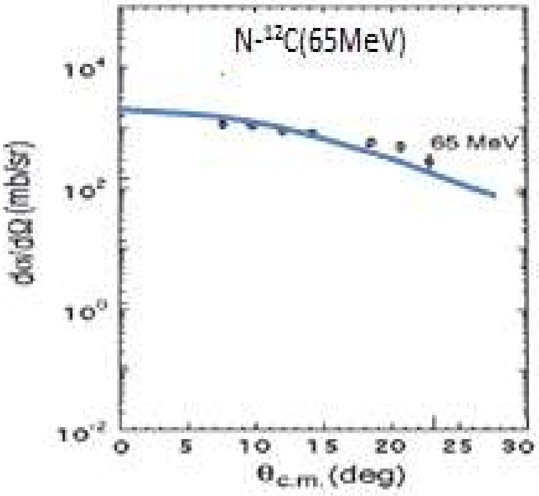

Figure 2 Comparison between experimental result and our calculated result of differential scattering cross section for 65 MeV

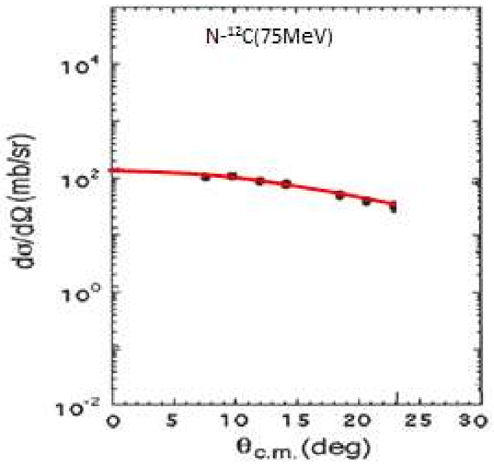

Figure 3 Comparison between experimental result and our calculated result of differential scattering cross section for 75 MeV

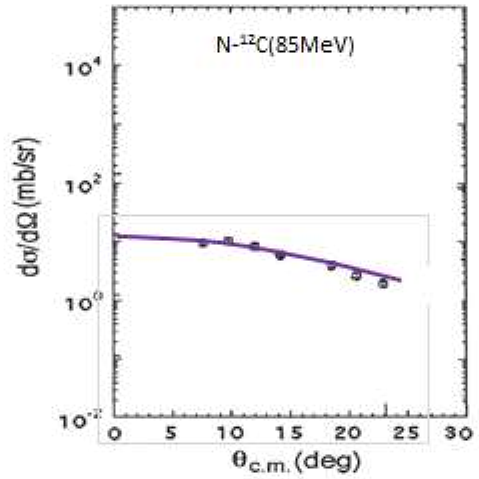

Figure 4 Comparison between experimental result and our calculated result of differential scattering cross section for 85 MeV

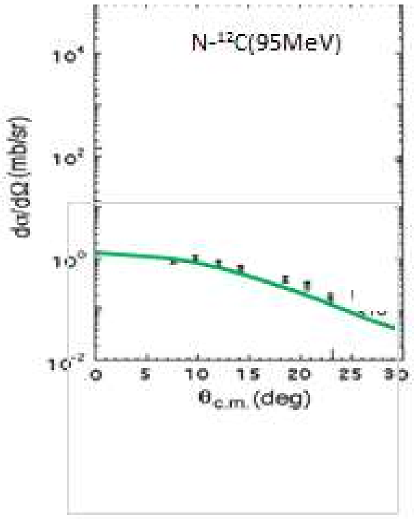

Figure 5 Comparison between experimental result and our calculated result of differential scattering cross section for 95 MeV

Acknowledgements

I would like to specially thank to my supervisor, Dr Khin Swe Myint, Emeritus Professor, Rector (Rt.d), University of Mandalay, for her invaluable advices and enthusiastic guidance throughout this work.

I do thank Dr Lei Lei Win, Professor and Head of Physics Department, University of Mandalay, for her encouragement and permission.

References

Hjort E.L. et al., (1994). Phys. Rev. C **50** 275.

Klug J. et al., (2002). Phys. Res. A **489** 282.

Klug J. et al., (2003). Phys. Rev. C **67** 031601(R).

Klug J. et al., (2003). Phys. Rev. C **68** 064605.

Nakano T. et al., (1953). Phys. Rev. **92** 833.

Salmon G.L., (1960). Nucl. Phys. **21** 15.

Zamrun M. et al., (2013). Phys. Rev. **C 87** 024611.

J. Myanmar Acad. Arts Sci. 2020 **Vol. XVIII.No.2A**

CALCULATION OF ENERGY LEVELS AND WAVE FUNCTIONS FOR A QUANTUM DOT

Cho Cho Win*

Abstract

Quantum dot is a nano-scale particle that is confined to the semiconductor as an exciton. The behavior of an exciton in quantum dot has the similar manner as a particle in a box (PIB). It is an individual quantum system which can be analyzed by Schroedinger equation. In this paper, Numerov technique is also used to solve the Schroedinger equation and the results are compared with analytical solutions.

Keywords: Exciton, Quantum dot,Numerov technique

Introduction

Infinite Square Well Potential and Quantum Confinement

Basic quantum mechanical problems such as an infinite and a finite square well may provide insight into the quantum confinement effect for the study of the nanostructured systems.

The quantum confinement means that critical dimensions of the material are on the order of the de Broglie wavelength of an electron. The degree of confinement can be controlled by the width and depth of the confining potential well as shown in Figure (1).

In quantum well, electrons are confined only in one dimension. The quantum wires confine electrons in two dimensions. The electron is not confined along the wire. An electron, in a quantum dot, is confined in three dimensions.

As the confining dimension decreases and reaches a certain limit, typically in nanoscale, their energy levels become discrete and their electronic and optical properties deviate substantially from those of bulk materials [Buhro, W. E., and V. L. Colvin,(2003)]. The use of low dimensional structures has significantly improved the performance of optoelectronic devices [Bimberg, D., et al.,(2001) and Alferov, Z. I.,(2001)].

Quantum Dot

Applying some energies to a semiconductor results in the excitation of the electron from the valance band to the conduction band leaving a hole behind. It corresponds to the excited electron in the conduction band. The excitation gives rise to an electron-hole paircalledexciton pairs. The portions of a semiconductor that contains these pairs are calledQuantum Dots as shown in Figure(2)[http://en.Wikipedia, org/ wiki/ Quantum dot]. Quantum dots are nano-scale semiconductorsthatemit light depending on the size of the dot. The florescence of the quantum dots is due to the excitation and recombination of the exciton pairs. Quantum dots are confined to a semiconductor in the similar manner as particle in a box thus we use this as a model to study different quantum properties of a dot. The quantum dots were discovered at the beginning of the 1980s by Alexei Ekimov in a glass matrix and by Louis E.Brus in colloidal solutions. The term "Quantum Dot" was coined by Mark Reed [Reed, M. A., et al.,(1988)].

---

[*] Dr, Lecturer,Department of Physics, University of Mandalay

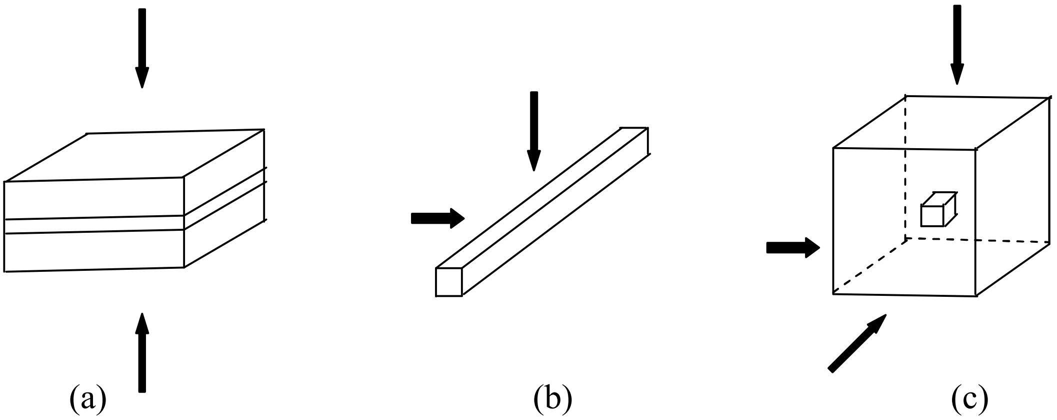

Figure 1(a) Confinement along 1 dimension. It is analogous to a quantum well.
(b) Confinement along 2 dimensions. It is analogous to a quantum wire.
(c) Confinement along 3 dimensions. It is analogous to a quantum dot.

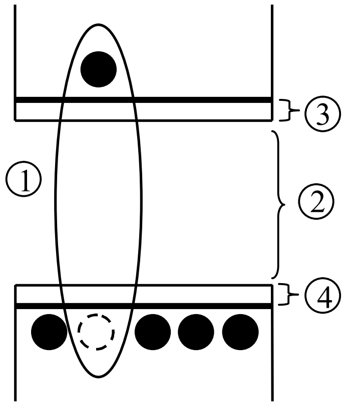

(1) Exciton(electron-hole pair)
(2) Band gap
(3) Confinement Energy of the excited electron
(4) Confinement Energy of the hole

Figure 2 Quantum dot

Calculation of Energies and Wave Functions for Quantum Dot

Analytical Solution of Radial Equation

The Schroedinger equation is used to describe the quantum states of quantum dot.The Schroedinger equation for three dimensions is simply given as follows:

$$-\frac{\hbar^2}{2m}\frac{1}{r^2\sin\theta}\left[\sin\theta\frac{\partial}{\partial r}(r^2\frac{\partial}{\partial r})+\frac{\partial}{\partial\theta}(\sin\theta\frac{\partial}{\partial\theta})+\frac{1}{\sin\theta}\frac{\partial^2}{\partial\phi^2}\right]\psi(r,\theta,\phi) \qquad (1)$$
$$+V(r)\psi(r,\theta,\phi)=E\psi(r,\theta,\phi)$$

If the potential energy and boundary condition are spherically symmetric then the spherical Schroedinger equation can be written as a product of a radial and angular portion as:

$$\psi(r,\theta,\phi)=R_{nl}(r)Y_{lm}(\theta,\phi) \qquad (2)$$

The angular part of the wave function $Y_{lm}(\theta,\phi)$ is the same for all spherically symmetric potentials.After some manipulation, the equations for the factors become:

$$\frac{d^2\Phi(\phi)}{d\phi} = -m^2\Phi(\phi), \tag{3}$$

$$\sin\theta\frac{d}{d\theta}(\sin\theta\frac{d\Theta(\theta)}{d\theta}) + \ell(\ell+1)\sin^2\theta\Theta(\theta) = m^2\Theta(\theta), \tag{4}$$

and $$\frac{d}{dr}(r^2\frac{dR(r)}{dr}) - \frac{2mr^2}{\hbar^2}[V(r)-E]R(r) = \ell(\ell+1)R(r), \tag{5}$$

where, m^2 and $\ell(\ell+1)$ are constants of separation.

The solutions to the angular equations with spherically symmetric boundary conditions are: $\Phi_m = (2\pi)^{-1/2}e^{im\phi}$ and $\Theta_\ell^m = C_{\ell m}P_\ell^m(\cos\theta)$, where m is restricted to the range $-\ell,...,\ell$, $P_\ell^m(x) \equiv (1-x^2)^{|m|/2}(\frac{d}{dx})^{|m|}P_\ell(x)$ is the 'associated Legendre function', and $P_\ell(x)$ is the ℓ^{th} Legendre polynomial.

The product of Θ and Φ occurs so frequently in quantum mechanics that it is known as a spherical harmonic: $Y_\ell^m(\theta,\phi) = \in\left[\frac{(2\ell+1)}{4\pi}\frac{(\ell-|m|)!}{(\ell+|m|)!}\right]^{1/2} e^{im\phi}P_\ell^m(\cos\theta)$, where $\in = (-1)^m$ for $m \geq 0$ and $\in = 1$ for $m \leq 0$, and the spherical harmonics are orthonormal:

$$\int_0^\pi d\theta\sin\theta\int_0^{2\pi} d\phi\left[Y_\ell^m(\theta,\phi)\right]^*\left[Y_{\ell'}^{m'}(\theta,\phi)\right] = \delta_{\ell\ell'}\delta_{mm'}. \tag{6}$$

While the angular part of the wavefunction is $Y_\ell^m(\theta,\phi)$ for all spherically symmetric situations, the radial part varies.The equation for R can be simplified in form by substituting u(r) = rR(r):

$$-\frac{\hbar^2}{2m}\frac{d^2u}{dr^2} + \left[V + \frac{\hbar^2}{2m}\frac{\ell(\ell+1)}{r^2}\right]u = Eu, \tag{7}$$

with normalization $\int dr|u|^2 = 1$.

This is now referred to as the radial wave equation, and would be identical to the one-dimensional Schroedinger equation were it not for the term αr^{-2} added to V, which pushes the particle away from the origin and is therefore often called 'the centrifugal potential.'

For infinite spherical well,

$$V(r) = \begin{cases} 0, & r < a \\ \infty, & r > a. \end{cases} \tag{8}$$

The wavefunction = 0 for r > a; for r < a, the differential equation is $\frac{d^2u}{dr^2} = \left[\frac{\ell(\ell+1)}{r^2} - k^2\right]u,$

where $$k \equiv \frac{\sqrt{2mE}}{\hbar}. \tag{9}$$

The allowed energies for $\ell = 0$ are given as

$$E_{n0} = \frac{n^2 \pi^2 \hbar^2}{2 m a^2} \tag{10}$$

The first three ψ_{n00} can be given as shown in figure (3).

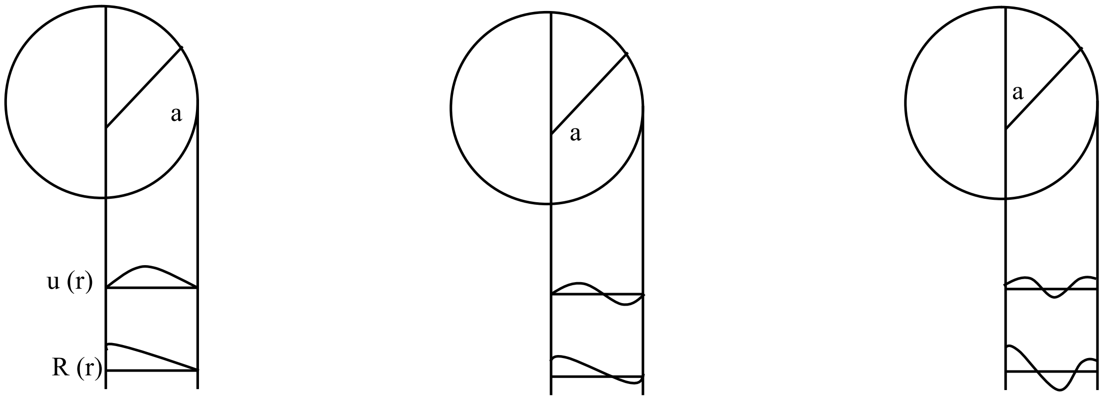

n = 1, ℓ = 0 n = 2, ℓ = 0 n = 3, ℓ = 0

Figure 3 The first three wave functions

The 'stationary' eigenfunctions of this potential are all bound states, confined to the region $r < a$. The solutions to this equation are Bessel functions, specifically the spherical Bessel and spherical Neumann functions of order ℓ:

$$u(r) = Ar\, j_\ell(kr) + Brn_\ell(kr), \tag{11}$$

Where
$$j_\ell(x) \equiv (-x)^\ell \left(\frac{1}{x}\frac{d}{dx}\right)^\ell \frac{\sin x}{x}, \tag{12}$$

and
$$n_\ell(x) \equiv -(-x)^\ell \left(\frac{1}{x}\frac{d}{dx}\right)^\ell \frac{\cos x}{x}. \tag{13}$$

The requirement that the wavefunctions be 'regular' at the origin eliminates the Neumann function from any region including the origin. The Bessel function is similarly eliminated from any region including ∞.

For small values if x, the functions can be given as:

$$j_0(x) = \frac{\sin x}{x}$$

$$j_1(x) = \frac{\sin x}{x^2} - \frac{\cos x}{x}$$

$$j_2(x) = (\frac{3}{x^2} - 1)\frac{\sin x}{x} - \frac{3\cos x}{x^2}$$

$$j_3(x) = (\frac{15}{x^3} - \frac{6}{x})\frac{\sin x}{x} - (\frac{15}{x^2} - 1)\frac{\cos x}{x},$$

and

$$n_0(x)=-j_{-1}(x)=-\frac{\cos x}{x}$$

$$n_1(x)=j_{-2}(x)=-\frac{\cos x}{x^2}-\frac{\sin x}{x}$$

$$n_2(x)=-j_{-3}(x)=(-\frac{3}{x^2}+1)\frac{\cos x}{x}-\frac{3\sin x}{x^2}$$

$$n_3(x)=j_{-4}(x)=(-\frac{15}{x^3}+\frac{6}{x})\frac{\cos x}{x}-(\frac{15}{x^2}-1)\frac{\sin x}{x}.$$

The first four Bessel functions are shown in figure (4).

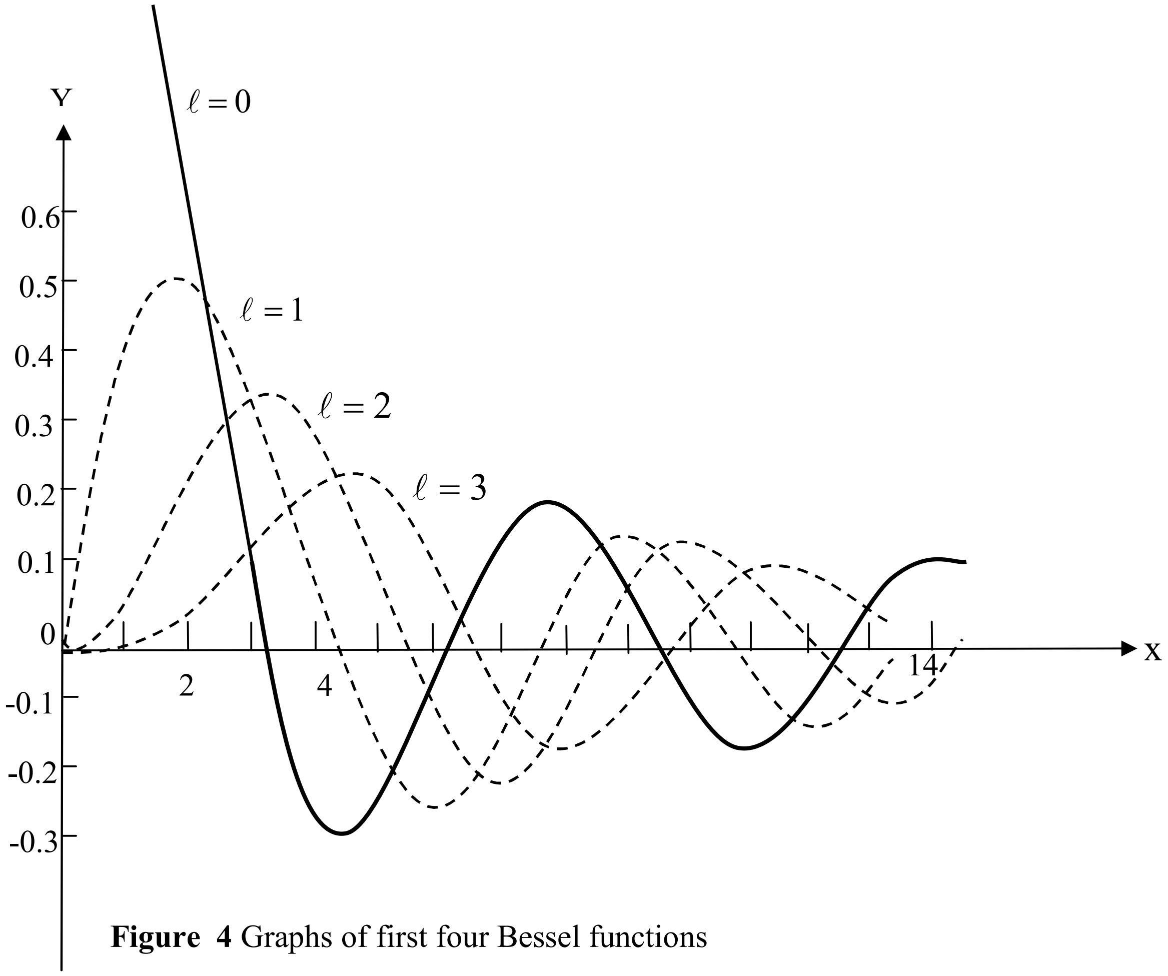

Figure 4 Graphs of first four Bessel functions

The remaining constants, k (substituting for E) and A, are satisfied by requiring that the solution vanishes at r = a and normalizing, respectively: $j_\ell(ka)=0 \Rightarrow ka=\beta_{n\ell}$, where $\beta_{n\ell}$ is the nth zero of the ℓ^{th} spherical Bessel function.

Adding the angular portion, the complete time-independent wavefunctions are

$$\psi_{n\ell m}(r,\theta,\phi)=A_{n\ell}j_\ell(\beta_{n\ell}r/a)Y_\ell^m(\theta,\phi),$$

where, $E_{n\ell}=\dfrac{\hbar^2}{2ma^2}\beta_{n\ell}^2.$

The first few values of $\beta_{n\ell}$ are given in Table (1) [Atnafe, N., and P.Ohmann,(2012)].They both increase with increasing n and ℓ.

Numerical Solution of Radial Equation

There are only few cases for which the Schroedinger equation can be solved analytically. In most cases, such equations are solved numerically[Atnafe, N., and P. Ohmann,(2012)].

For $\ell=0$:since the r^2 disappears for this case, the radial equation reduces to ODE that can be solved easily. For numerical simulation, we should be able to convert the equation into other forms. We can write the second order differential equation as a difference of two close points by the two point approximation method. This method allows us to calculate the derivatives with smaller errors.

It can be given as:

$$u^{//}(r)\approx\frac{u(r+h_0)-2u(r)+u(r-h_0)}{h_0^2}+O(h_0^2)$$

h_0 refers to the discretizing factor that divides the interval into equal spaces. Substituting this in to the radial equation,

$$\frac{d^2u}{dr^2}=-k^2u$$

We can find some of the eigenvalues. This eigenvalues match the analytical ones as shown in Table (2).

For $\ell\neq 0$: In numerical physics the Numerov'smethod is used to find solutions of the radial Schroedinger Equation for arbitrary potentials.

$$\left[-\frac{\hbar^2}{2m}\left(\frac{1}{r}\frac{d^2}{dr^2}r-\frac{\ell(\ell+1)}{r^2}\right)+V(r)\right]R(r)=ER(r) \tag{14}$$

The above equation can be rewritten in the form

$$\left[\frac{d^2}{dr^2}-\frac{\ell(\ell+1)}{r^2}+\frac{2m}{\hbar^2}(E-V(r))\right]u(r)=0 \tag{15}$$

with u(r) = rR(r).

Table 1The first few values of $\beta_{n\ell}$ for n = 1 to 4

	n = 1	**n = 2**	**n = 3**	**n = 4**
$\ell=0$	3.142	6.283	9.425	12.566
$\ell=1$	4.493	7.725	10.904	14.066
$\ell=2$	5.763	9.095	12.323	15.515
$\ell=3$	6.988	10.417	13.698	16.924
$\ell=4$	8.183	11.705	15.040	18.301

Table 2 Analytical and numerical energyvalues for n = 1 to 5

n	Analytical values(eV)	Numerical values(eV)
1	0.3765	0.3667
2	1.5060	1.4665
3	3.3886	3.2989
4	6.0241	5.8633
5	9.4127	9.1585

If we compare this equation with the defining equation of the Numerov method, we see

$$f(r)=\frac{2m}{\hbar^2}(E-V(r))-\frac{\ell(\ell+1)}{r^2} \tag{16}$$

and thus can numerically solve the radial Schroedinger equation.Starting from the Taylor expansion for u(r_n) we get the two sampling points adjacent to r_n.

$$u_{n+1}=u(r_n+h)=u(r_n)+hu'(r_n)+\frac{h^2}{2!}u''(r_n)+\frac{h^3}{3!}u'''(r_n)+\frac{h^4}{4!}u''''(r_n)+O(h^5) \tag{17}$$

$$u_{n-1}=u(r_n-h)=u(r_n)-hu'(r_n)+\frac{h^2}{2!}u''(r_n)-\frac{h^3}{3!}u'''(r_n)+\frac{h^4}{4!}u''''(r_n)-O(h^5) \tag{18}$$

The sum of those two equations gives

$$u_{n-1}+u_{n+1}=2u_n+h^2u''_n+\frac{h^4}{12}u''''_n+O(h^6) \tag{19}$$

This equation can be solved for u''_n and replace it by the expression $u''_n=-f_nu_n$ which we get from the defining differential equation.

$$h^2f_nu_n=2u_n-u_{n-1}-u_{n+1}+\frac{h^4}{12}u''''_n+O(h^6) \tag{20}$$

The second derivative of our defining differential equation is taken and we get

$$u''''(r_n)=-\frac{d^2}{dx^2}\left[f(r_n)u(r_n)\right]. \tag{21}$$

The second derivative $\frac{d^2}{dx^2}$ is replaced with the second order difference quotient and is inserted into our equation for f_nu_n

$$h^2f_nu_n=2u_n-u_{n-1}-u_{n+1}-\frac{h^4}{12}\frac{f_{n-1}u_{n-1}-2f_nu_n+f_{n+1}u_{n+1}}{h^2}+O(h^6) \tag{22}$$

q

We solve for u_{n+1} to get

$$u_{n+1}=\frac{(2-\frac{5h^2}{6}f_n)u_n-(1+\frac{h^2}{12}f_{n-1})u_{n-1}}{1+\frac{h^2}{12}f_{n+1}}+O(h^6). \tag{23}$$

This yields Numerov's method if one ignore the term of order h^6.

For this case, it can start at one end of our infinite spherical wall with $u(r_0)=0$ and $u(r_0+h)=1$. The wave function R(r) is used instead of U(r). It can be clearly seen that the Numerov's method can be used to solve the radial equation for any value of ℓ.

Figure (5) is the graph of the analytical solutions for $\ell=0$. The dots each represent points from theNumerov's formula. We can also use Numerov's method to solve the radial equation for the $\ell\neq0$ case. Figures (6) to (8) are the graphs of the analytical and numerical solutions for $\ell=1,2\,and\,3$.

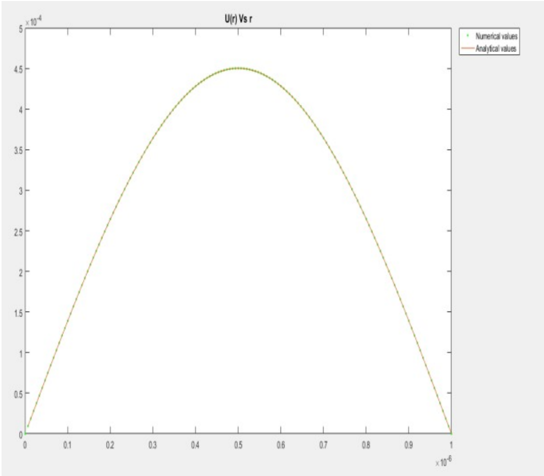

Figure 5 Wave function for *l* = 0

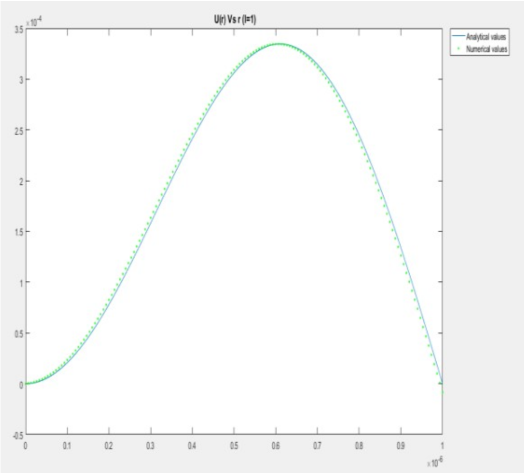

Figure 6 Wave function for *l* = 1

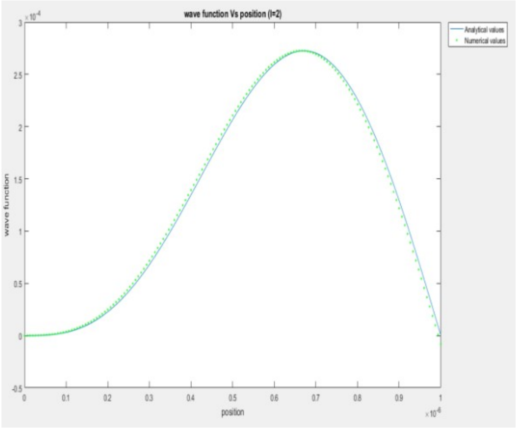

Figure 7 Wave function for *l* = 2

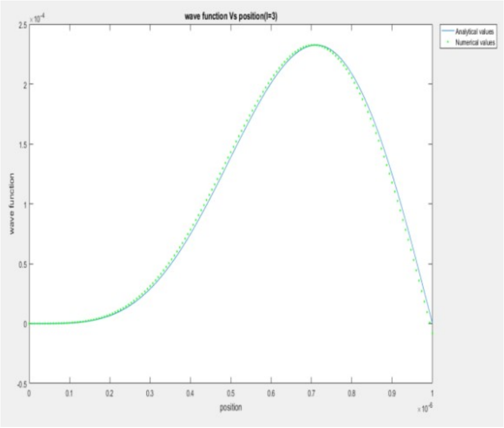

Figure 8 Wave function for *l* = 3

Conclusion

A quantum dot is a semiconductor whose excitons are confined in all three spatial dimensions. Researchers have studied quantum dots in transistors, solar cells, LEDs, and diode lasers. They have also investigated quantum dots as agents for medical imaging and hope to use them as qubits.

From quantum theory, we know that quantum dot has similar manner as particle in a box. We can imagine the walls of the box with infinite large potential energy thus preventing the particle from escaping while the potential inside to be zero. The behavior of electrons in quantum dots is dominated by quantum mechanical behavior. In particular, this behavior is determined by the electron wave function and its evolution as determined by the Schroedinger equation.

The graphs in the figures (5) to (8) show that the analytical and numerical values of electron wave function with position match for most cases such as $\ell=0, 1, 2,$ and 3. This means that the Numerov's method also shows promising results for solving the radial equation for any value of ℓ.

As future work, we would like to explore the properties of quantum dots such as energy and electronic structures using the particle in a box model.

Acknowledgements

I express my thanks to Rector DrThida Win, University of Mandalay, her permission and encouragement to conduct this research work.I would like to express my gratitude and sincere thanks to Dr Lei Lei Win, Professor, Head of Department of Physics, University of Mandalay, for her kind permission to do this work.

References

Alferov, Z. I., (2001), Rev. Mod. Phys. 73,767.

Atnafe, N. and P. Ohmann,(2012), "Quantum Dots As Particles in the Infinite Spherical Well", Center for Applied Math 2115 summiave, saint paul, mn 55105.

Bimberg, D., M. Grundmann, and N. N. Ledentsov,(2001), "Quantum Dot Heterostructures", JohnWiley& Sons.

Buhro, W. E. and V. L. Colvin, (2003), "Semiconductor nanocrystals: Shape matters", Nat Mater 2(3): 138-9.

http://en. Wikipedia, org/ wiki / Quantum_dot.

Reed, M. A., J. N. Randall, R. J. Aggarwal, R. J. Matyi, T. M. Moore and A. E. Wesel, (1988), "Observation of discrete electronic states in a zero-dimensional semiconductor nanostructure", Phys. Rev Lett. 60 (6):535-537.

J. Myanmar Acad. Arts Sci. 2020 **Vol. XVIII.No.2A**

A NUMERICAL RELATIVITY APPROACH TO BRANEWORLD COSMOLOGY

San San Maw[1], Htwe New Oo[2], Zaw Shin[3], Thant Zin Naing[4]

Abstract

Due to the non-linearity and the complexity, it is not very realistic to study the full dynamics in closed form, especially the behaviour at high energy regime where the fields are so strong that perturbation methods do not apply. Therefore, it is simply here needed to use a numerical approach. A simple finite difference method has been utilized to solve non-linear wave equation in flat 3+1 dimension space time under axisymmetry with source term f in Braneworld. Interesting results have been obtained and they are visualized in 2-D and 3-D.

Keywords: 3+1 dimension spacetime, axisymmetry, braneworld.

Introduction

The 3+1 formalism is an approach to general relativity and to Einstein equations that relies on the slicing of the four dimensional spacetime by three-dimensional surfaces. From the mathematical point of view, this procedure allows to formulate the problem of resolution of Einstein equations as a constraints. The 3+1 formalism should not be confused with the 1+3 formalism, where the basis structure is a congruence of one dimensional curves instead of three-dimensional surfaces.

Today, most numerical codes for solving Einstein equations are based on the 3+1 formalism We will present the evolution schemes of the 3+1 Einstein equations, putting some emphasis on the most successful scheme to date.

Evolution Schemes

There exist various formalisms of GR, among which only the ones that are strongly hyperboliccan be used as a well-defined formalism of an initial value problem.

The generalized harmonic (GH) formalism used the gauge source functions

$$H^{\alpha} \simeq \nabla^{\beta}\nabla_{\beta}x^{\alpha} = -\Gamma^{\alpha}_{\mu\nu}g^{\mu\nu} \equiv -\Gamma^{\alpha} \qquad (1)$$

as fundamental variables. The notation$\simeq$ means the equation is a constraint relation. Einstein's equations can now be written as

$$-\frac{1}{2}g^{\alpha\beta}g_{\mu\nu,\alpha\beta} - g^{\alpha\beta}_{(,\mu g_{\nu})\beta,\alpha} - H_{(\mu,\nu)} + H_{\beta}\Gamma^{\beta}_{\mu\nu} - \Gamma^{\alpha}_{\nu\beta}\Gamma^{\beta}_{\mu\alpha} = k_{d}\left(T_{\mu\nu} - \frac{1}{d-2}g_{\mu\nu}T\right) \qquad (2)$$

A coordinate gauge choice can now be realized via specifying the H_{μ}'s. As long asH_{μ} does not include derivative of metric functions., the principle part of the above equation$-\frac{1}{2}g^{\alpha\beta}g_{\mu\nu,\alpha\beta}$ is manifestly strongly hyperbolic.

---

[1] Dr, Assistant Lecturer, Department of Physics, West Yangon University.

[2] Assistant Lecturer, Department of Physics, Yangon University of Education.

[3] Lecturer, Department of Physics, University of Yangon.

[4] Retired Pro-Rector (Admin), International Theravāda Buddhist Missionary University, Yangon.

Both the generalized harmonic formalism and the BSSN formalism are widely used in the literature, yet none of them is sufficient to simulate braneworld and we have to develop them further. In this research, the generalized harmonic formalism will be employed to evolve the braneworld spacetime(Bona, 1995).

Numerical Methods

The equations of motion of gravitational theory are non-linearly coupled partial differential equations (PDEs). Due to the non-linearity and the complexity, it is not very realistic to study the full dynamics in closed form, especially the behavior at high energy regime where the fields are so strong that perturbation methods do not apply. We are use a numerical approach. In this section we introduce finite difference approximation (FDA) methods to solve the PDEs. The focus is in the various tests to distinguished numerical solutions from numerical artifacts (Bardeen,J.M., 1970).

Finite Difference Approximation

To demonstrate the concepts in a less abstract way, let us consider the following model problem, which is non-linear equation in flat 3+1 dimension spacetime under axisymmetry with source term f (which does not depend on the eave function Φ). This model problem includes a few features that are important for numerical calculation in braneworlds. The equation is assumed to be $\left(-\partial_{tt}+\partial_{xx}+\partial_{yy}+\partial_{zz}\right)\Phi+\Phi^2=f$ in Cartesian coordinates, or

$$\left(-\partial_{tt}+\partial_{\rho\rho}+\frac{1}{\rho}\partial_{\rho}+\partial_{zz}\right)\Phi+\Phi^2=f \tag{3}$$

in cylindrical coordinates (t, ρ, ϕ, z) that are adapted to the axisymmetry. Therefore the axisymmetry implies $\partial_{\phi}\Phi=0$, which has been applied in (3). Let us assumed the spatial domain is $\rho\,\epsilon[0,\rho_{max}], z\,\epsilon[0,z_{max}]$.

The whole domain, both spatial and temporal, is divided into discrete grids (or meshes). In principle this division can be arbitrary, as long as the grid/mesh elements are small. To be more specific and to honor simplicity, here let us employ uniform grid. Therefore the spatial domain can be

$$\rho_i=(i-1)\Delta\rho\,;i=1,2,\dots,n_{\rho}\quad where\ \ \Delta\rho=\frac{\rho_{max}}{n_{\rho}-1}\ ; \tag{4}$$

$$z_j=(j-1)\Delta z\,;j=1,2,\dots,n_z\quad where\ \ \Delta z=\frac{z_{max}}{n_z-1}\ ; \tag{5}$$

For simplicity let us choose $\Delta\rho=\Delta z=h$. The time domain is also discreted and the time interval between two subsequent discretized time levels can be expressed as Δt. $\Delta t/h$is called the Courant factor.

One uses notation

$$\Phi_{i,j}^{n}\equiv\Phi\left(t^n,\rho_i,z_j\right)\equiv\Phi\left((n-1)\Delta t,(i-1)\Delta\rho,(j-1)\Delta z\right), \tag{6}$$

and similar notation for function f. We replace the differential operators by their FDA operators with second order accuracy:

$$\partial_{\rho\rho}\Phi\rightarrow\ \frac{\Phi_{i+1,j}^{n}-2\Phi_{i,j}^{n}+\Phi_{i-1,j}^{n}}{h^2}, \tag{7a}$$

$$\partial_\rho \Phi \to \frac{\Phi^n_{i+1,j}-\Phi^n_{i-1,j}}{2h}, \tag{7b}$$

$$\partial_{zz} \Phi \to \frac{\Phi^n_{i,j+1}-2\Phi^n_{i,j}+\Phi^n_{i,j-1}}{h^2}, \tag{7c}$$

$$\partial_{tt} \Phi \to \frac{\Phi^{n+1}_{i,j}-2\Phi^n_{i,j}+\Phi^{n-1}_{i,j}}{(\lambda h)^2}. \tag{7d}$$

The FDA operators are obtained by Taylor expansions such as

$$\Phi^n_{i+1,j} = \Phi^n_{i,j} + h\Phi_{,\rho} + \frac{h^2}{2!}\Phi_{,\rho\rho} + \frac{h^3}{3!}\Phi_{,\rho\rho\rho} + \frac{h^4}{4!}\Phi_{,\rho\rho\rho\rho} + O(h^6),$$

which yield

$$\frac{\Phi^n_{i+1,j}-2\Phi^n_{i,j}+\Phi^n_{i-1,j}}{h^2} = \partial_{\rho\rho}\Phi + \frac{h^2}{12}\Phi_{,\rho\rho\rho\rho} + O(h^4), \tag{8}$$

The term$\frac{h^2}{12}\Phi_{,\rho\rho\rho\rho} + O(h^4) = O(h^2)$ is the difference between the exact operator and the FDA operator, which is called truncation error. When h is small (so that the truncation error in not significant), the differential operators can be replaced by their FDA counter parts. Other FDA operators in (7) can be obtained similarly. The discretized PDE reads

$$\frac{\Phi^{n+1}_{i,j}-2\Phi^n_{i,j}+\Phi^{n-1}_{i,j}}{(\lambda h)^2} + \frac{\Phi^n_{i,j+1}-2\Phi^n_{i,j}+\Phi^n_{i,j-1}}{h^2} + \frac{1}{\rho_i}\frac{\Phi^n_{i+1,j}-\Phi^n_{i-1,j}}{2h}$$

$$+\frac{\Phi^n_{i,j+1}-2\Phi^n_{i,j}+\Phi^n_{i,j-1}}{h^2} + \left(\Phi^n_{i,j}\right)^2 = f^n_{i,j} \tag{9}$$

Now we are ready to introduce the general notations to make the discussion clearer. A set of PDFs, such as equation (3), can be collectively denoted as

$$Lu = f \tag{10}$$

where L stands for differential operators and all other operations, u stands for the fundamental variables (the unknown functions) to solve for, and f stands for terms in the equations that do not include u,. In equation (3), $u = \Phi$ and$u = L\Phi = \left(-\partial_{tt} + \partial_{\rho\rho} + \frac{1}{\rho}\partial_\rho + \partial_{zz}\right)\Phi + \Phi^2$.

The discrete FDA operators, such as equation (8) , can be collectively denoted as

$$A\Phi = \varepsilon\,\Phi + h^p.E\Phi\,, \tag{11}$$

where A stands for the FDA version of the exact operatorε. h^pmeans that the approximation level is of p-th order in h, E stands for the error operator — more specifically,$h^p.E\Phi$ is the error. Using (11), we can discretize (10) as

$$L^h u^h = f^h \tag{12}$$

where h is to label resolution. An example of (12) is (9).

In (9), the approximation is of second order in h. Generally the approximation order of L^h is p, which can be formally expressed as

$$L^h = L + h^p E \tag{13}$$

From the discussion above, one see that the validity of FDA needs to be built upon the following two assumptions: (1) the function Φ is smooth; (2) h is small, so that the truncation error is not significant.

However, these two conditions are not sufficient to guarantee that the numerical result u^h is actually a approximation of the exact solution u. Therefore systematic test mechanisms need to be developed to distinguish numerical solutions from numerical artifacts (Baumgarte, T. W., and Shapiro, S. L., 2003).

Tests

First, often it is neither practical nor necessary to let equation (12) be satisfied exactly. Instead, (12) is considered to be satisfied when residual $r^h \equiv L^h u^h - f^h$ is sufficiently small. Again, "small" does not have any measurable meaning yet.

Multiplying equation (9) by ρ_i, we get the following equation

$$-\frac{\rho_i\left(\Phi_{i,j}^{n+1}-2\Phi_{i,j}^{n}+\Phi_{i,j}^{n-1}\right)}{(\lambda h)^2}+\frac{\rho_i\left(\Phi_{i,j+1}^{n}-2\Phi_{i,j}^{n}+\Phi_{i,j-1}^{n}\right)}{h^2}+\frac{\Phi_{i+1,j}^{n}-\Phi_{i-1,j}^{n}}{2h}$$

$$+\frac{\rho_i\left(\Phi_{i,j+1}^{n}-2\Phi_{i,j}^{n}+\Phi_{i,j-1}^{n}\right)}{h^2}+\rho_i\left(\Phi_{i,j}^{n}\right)^2=\rho_i f_{i,j}^{n}\,. \qquad (14)$$

(9) and (14) share exactly the same numerical properties, such as convergence, smoothness, regularly, etc. But the two residuals have different numerical values. Therefore, the residual being "small", has no absolute meaning.

This feature can be expressed in a more abstract way as: $Lu = f$ and $g.Lu = g.f$ have the same numerical properties. Here g is a non-zero smooth function over the domain. For example g can be an arbitrary non-zero constant to make the residual take any value. Therefore, the absolute value of residual does not have any meaning. So, how to distinguish between a numerical solution and a numerical artifact? And how small is the residual to be considered sufficiently small? These questions will be answered by the following analysis.

Assume the numerical result u^h that satisfies $L^h u^h = f^h + r^h$ is obtained, where r^h is the residual. Generally, u^h is a numerical solution, if the following equation is satisfied when u^h is substituted back into equation (10)

$$\lim_{h\to 0} Lu^h - f^h = 0\,. \qquad (15)$$

Let us see what it means

$$Lu^h - f^h = L^h u^h - h^p E u^h - f^h = r^h - h^p E u^h = r^h + O(h^p). \qquad (16)$$

Therefore (15) is satisfied, if r^h is negligible compared to $h^p E u^h$ (in the sense r^h is small).

However technically it is impossible to apply a continuous operation L to discrete function u^h, and then (15) can only be understood formally. Instead, u^h is considered a numerical solution, if

$$\lim_{h\to 0} r_I^h = 0 \qquad (17)$$

where $r_I^h \equiv L_I^h u^h - f^h$, where $L_I^h \neq L^h$ that satisfies $\lim_{h\to 0} L_I^h = L$.

Since L_I^h is independent of L^h (a different discretization), r_I^h is called independent residual.

For the model problem, we can use following discretization as the independent discretized operators

$$\partial_{rr}\Phi \rightarrow \frac{2\Phi^n_{i,j}-5\Phi^n_{i+1,j}+4\Phi^n_{i+2j}+\Phi^n_{i+3j}}{h^2}, \quad (18a)$$

$$\partial_{r}\Phi \rightarrow \frac{3\Phi^n_{i,j}-4\Phi^n_{i+1,j}+\Phi^n_{i+2,j}}{2h}, \quad (18b)$$

$$\partial_{zz}\Phi \rightarrow \frac{2\Phi^n_{i,j}-5\Phi^n_{i,j+1}+4\Phi^n_{i,j+2}-\Phi^n_{i,j+3}}{h^2}, \quad (18c)$$

$$\partial_{tt}\Phi \rightarrow \frac{2\Phi^n_{i,j}-5\Phi^{n-1}_{i,j}+4\Phi^{n-2}_{i,j}-\Phi^{n-3}_{i,j}}{(\lambda h)^2}. \quad (18d)$$

This discretization is different from (7) and is also of the second order accuracy.

In general, the approximation order ofL_I^h is denoted as m, therefore

$$L_I^h = L + h^m E_I = L^h - h^p E + h^m E_I \quad (19)$$

$$r_I^h = L_I^h u^h - f^h = (L^h - h^p E + h^m E_I)u^h - f^h = r^h - h^p E u^h + h^m E_I u^h\,. \quad (20)$$

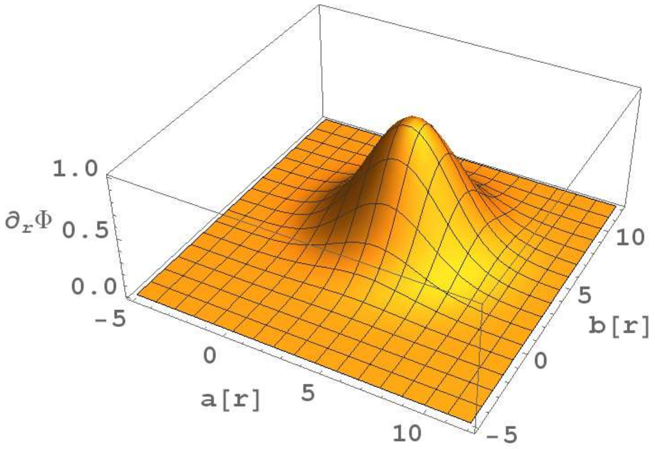

Figure 1 3D Profile of $\partial_r\Phi$ in terms of a(r) and b(r).

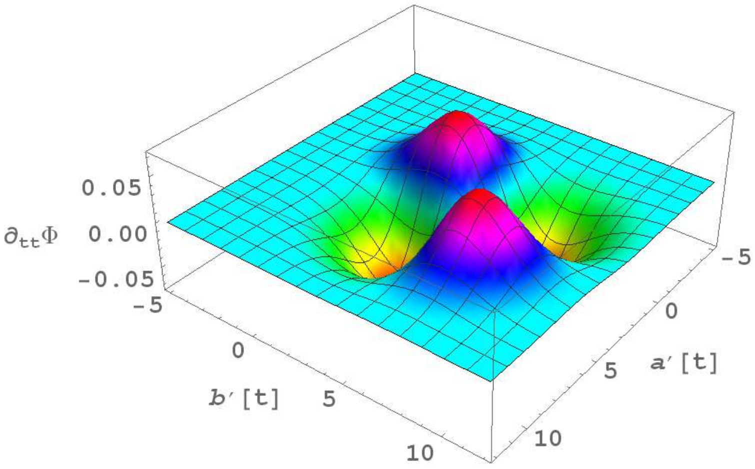

Figure 2 3D Profile of $\partial_{tt}\Phi$ in terms of a′(t)and b′(t).

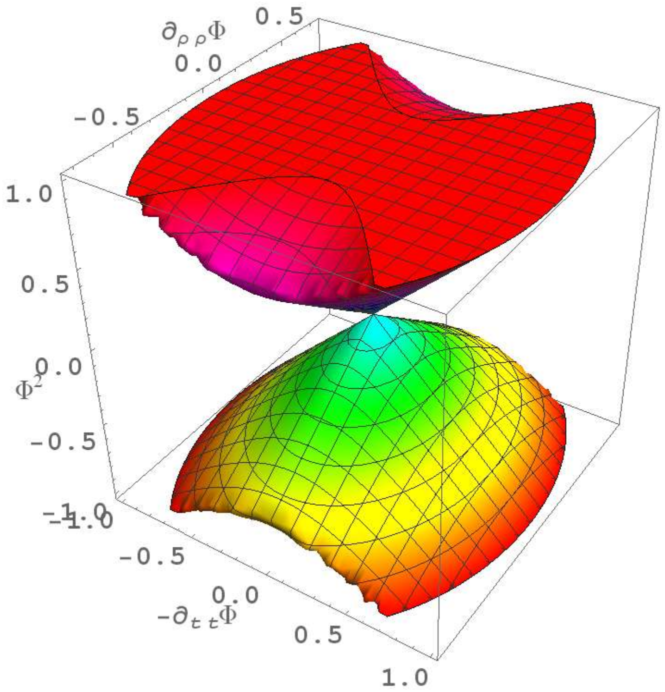

Figure 3 3D Profile of possible region distribution form main contributor in brane world scenario.

Again, here it is required that $\|r^h\|$ is negligible compared to min($\|h^p E u^h\|, \|h^m E_I u^h\|$), therefore the independent residualr_I^h converges to zero at min*(p, m)-th* order. Here$\|u\|$ is the form of u.

For the model problem,$p = m = 2$, therefore the independent residual behaves as a second order quantity: when h decreases to *h/2* , the independent residualr_I^h decreases to $r_I^{(h/2)} = \frac{1}{4} r_I^h$.

Tests for General Relativity

For a numerical problem, often there are a certain number of equations to solve, for an equal number of fundamental variables (the unknown functions). If the number of equations is less than the number of unknown functions, in principle there are no unique solutions. On the other hand, in GR, the number of equations is greater than the number of unknown functions. In this case the redundant equations are called constraints.

As an example, in 3+1 formalism of GR, there are six functionsγ_{ij} to be solved for, by solving the six evolutionary equations. The other four equations are the Hamiltonian constraint and momentum constraints. Analytically, if the constraints are satisfied initially the consistency guarantees them to be satisfied at all times, as long as the evolutionary equations are satisfied during the evolution. However, numerically there are always small violations to the constraints, and there is no guarantee the violations are controllable. Therefore, for general relativity, the constraints need to be tested as well, i.e., in order to make sure all the components of Einstein’s equations are satisfied, both the independent residual test and the convergence test for constraint are needed.

Equivalently, in the case a certain formalism of GR is employed to obtain the numerical results, the results can be substituted into another formalism of GR to produce residuals, and the residuals should converge at the expected order. For example, one can use generalized harmonic formalism to obtain the solution, and then substitute the solution into original Einstein's equations to get residuals, and check whether the residuals converge as expected (Baumgarte, T.W., 2007).

Concluding Remarks

In this paper, a numerical relativity approach to Braneworld cosmology have been presented using mathematica coding to solve non-linear wave equation in flat 3+1 dimension spacetime under axisymmetry with source term *f* in Braneworld. It has been attempted to make use of finite different analysis and they are visualized. .The spatial contribution in the brane world spacetimes gives formal Gaussian distribution and second-order-time derivative gives dip and rise spacetimes structure as expected before, Another interesting feature of the braneworld might be closely connected to the usual worm hole structure if one is to ignore the rest two spatial dimensions to compare with other three including branewold dimension. It is visualized in Figure 3.

Acknowledgements

I would like to thank Dr Khin Khin Win, Professor and Head, Department of Physics, University of Yangon, for her kind permission and encouragements to carry out this work.

I would like to thank Dr Tin Maung Tun, Rector, West Yangon University, for his kind permission and encouragements to carry out this work.

I would like to express my gratitude to Professor Dr Moe Ohnmar, Head of Department of Physics, West Yangon University, for her kind permission and encouragements to carry out this work.

Special thanks are due to Professor, Dr Thant Zin Naing, Retired Pro-rector (Admin), International Theravāda Buddhist Missionary University, for his valuable guidance and helpful advice to carry out this work.

References

Bardeen, J.M., (1970). A Variational Principle for rotating Stars in General Relativity, Astrophysics. J. 162, 72.

Bardeen, J.M., and Piran, T., (1983). General relativistic axisymmetric rotating systems: coordinates and equations, Phys. Rep. 96,206.

Baumgarte, T. W., and Shapiro, S. L., (2003). General Relativistic magneto- hydrodynamics for the numerical construction of dynamical spacetimes, Astrophys. J. 585, 921.

Baumgarte, T. W., Murchadha, N. Ó.,and Pfeiffer, H.P., (2007). Einstein constraints: Uniqueness and non-uniqueness in the conformal thin sandwich approach, Phys. Rev. D 75, 044009.

Baumgarte, T. W., and Shapiro, S. L., (1999). Numerical integration of Einstein's field equations, Phys. Rev. D 59, 024007.

Bona, C., Massó, J., Seidel, E., and Stela, J., (1995). New Formalism for Numerical Relativity, Phys. Rev. Lett. 75, 600.

J. Myanmar Acad. Arts Sci. 2020 **Vol. XVIII.No.2A**

SOLAR PHOTOVOLTAIC POWER MEASURING SYSTEM UTILIZING PIC MICROCONTROLLER

Moe Moe Myint[1], Zar Ni Maung[2] and San San Wai[3]

Abstract

Solar photovoltaic power measurement systems are important to investigate. Studying the environmental condition of a solar panel will help to improve efficient power collection with a faster rate. Solar panel converts photonic energy into electrical energy. But the conversion speed and properties depend on the type and size of solar panels. Moreover, the current and voltage of the solar panel is also related with luminous, and temperature exerted on it. The circuit is designed to investigate the voltage, current, luminous and temperature of a solar panel. The results will be displayed on an alphanumeric liquid crystal display. The whole system design include an 8-bit PIC microcontroller, an alphanumeric liquid crystal display, a crystal oscillator, a current detector circuit, a voltage divider circuit, a temperature sensor, light intensity sensor circuit and a regulated power supply. A program source code is created to operate the whole circuit. It is converted to machine code and loaded into the memory of PIC microcontroller. The whole circuit is constructed on a printed circuit board. Data collections were made for the circuit to proof the efficiency of various solar panels.

Introduction

The energy of sun is in the form of visible light and infrared light radiation. Plants convert the energy in sunlight into chemical energy through the process of photosynthesis. Humans regularly use this store of energy in various ways, as when they burn wood or fossil fuels or when simply eating plants, fish and animals. Solar radiation reaches the earth's upper layer of atmosphere with the power of 1366 watts per square meter (W/m2). Since the earth is round, the surface nearer its poles is angled away from the sun and receives much less solar energy than the surface nearer the equator.

At present, solar cell plants convert, at best, about 15% of sunlight hitting them into electricity. There are many different technologies which have been developed to make use of solar radiation. Some of these technologies make direct use of the solar energy, while others produce electricity. Especially solar panels convert sunlight into electricity, either directly using photovoltaics or indirectly using concentrated solar power (CSP). Concentrated solar power systems use lenses or mirrors and tracking systems to focus a large area of sunlight into a small beam. Photovoltaics converts light inot electric current using the photoelectric effect.

It is very important to obtain maximum energy of the sunlight and changes the energy into electricity in the most efficient method. Therefore, it is important to investigate the properties of solar panel throughout the day by measuring the voltage, current, temperature of solar panel and luminous of incident radiation. In this thesis report, a microcontroller based measuring system was designed and constructed to check the above parameters.

---

[1] Dr, Associate Professor, Department of Physics, Loikaw University.

[2] Assistance Lecturer, Department of Physics, Loikaw University.

[3] Professor and Head, Department of Physics, Loikaw University.

System Overview

The **SOLAR PHOTOVOLTIAC POWER MEASURING SYSTEM (SPPMS)** is designed and constructed. The whole system consists of four sections sensors, controller, display and power supply. The first section consists of reading the voltage and current of solar panel. Then measure the surface temperature of solar panel and luminous falling on it. Measurement of voltage was made by using a voltage divider circuit and ADC converter function of pic microcontroller. Measurement of current was made by using ACS712 hall-effect current sensor module.

As shown in the block diagram in figure 1, every part of the circuit is illustrated with a block diagram. The system design consists of two photon transducers, one is the solar panel and another is the light dependent resistor. Solar panel is used to convert the solar energy to electrical energy. The light dependent resistor is used to detect the luminous intensity falling on the surface of solar panel. The voltage divider and current sensor circuits are used to detect the voltage output and current output of the solar panel under test. Every sensor peripherals are feed into the analog input pins of PIC microcontroller. The 4MHz crystal oscillator is used to generate clock for the program counter in the microcontroller. Some input switches are used to operate the reset and controlling operating function of the microcontroller. The 16 characters, 2 lines alphanumeric liquid crystal display is used to display the measurement parameters in visible numerical quantities. The system design includes a 5V regulator circuit and the power source is obtained from two 3.7V lithium ion batteries.

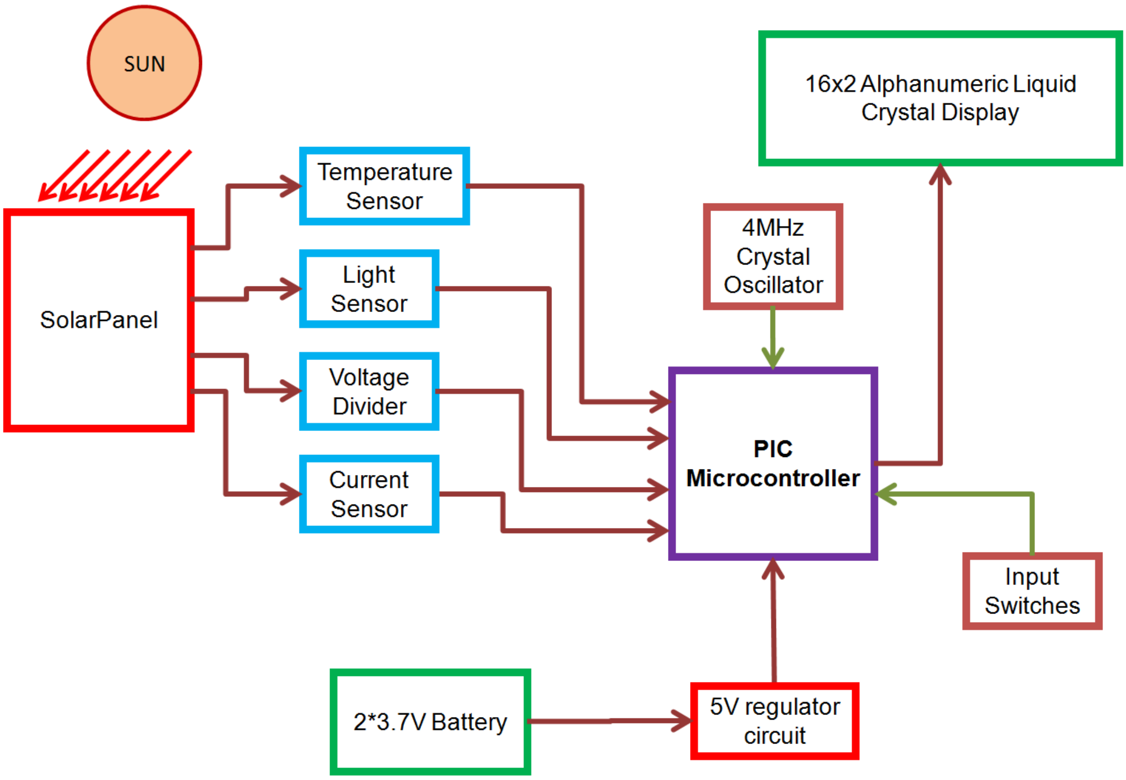

Figure 1 Block Diagram of the circuit

Experimental Detail

Construction of the Circuit

The circuit construction was a handy work for a research student. The component layout of the circuit is as shown in the Fig (above) as component side photo. Construction of the circuit was made in the following procedure;

1. The wire jumper connections
2. Resistors and diodes
3. Crystal oscillator
4. Switches and relay terminals
5. IC socket and transistors
6. Capacitors and regulator IC
7. The green terminals

The pic microcontroller was not directly soldered on the circuit board, the sockets were used. Because, the PIC is required to remove and replace to program and edit, until the solar power investigation circuit was successful. The solar panel terminal wire and sensor terminal were fed to the input of microcontroller through green terminal pins. The components side and soldering side of the circuit are illustrated in figure 2 and 3 respectively.

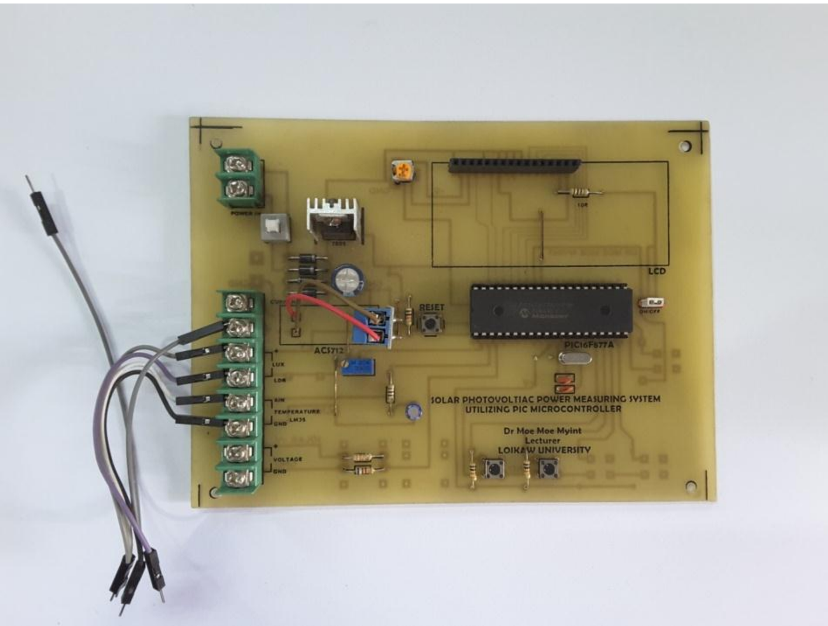

Figure 2 Component side of the main controller board after soldering.

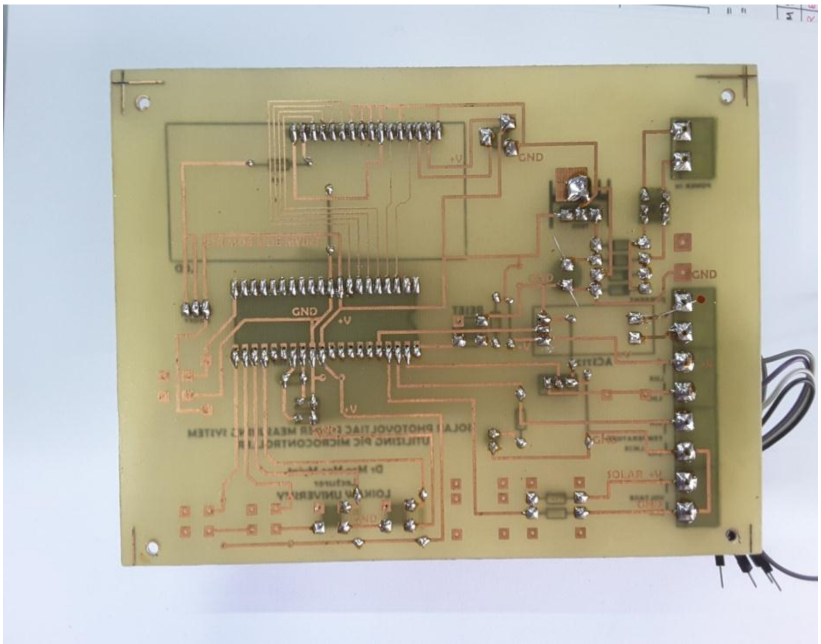

Figure 3 Soldering side of the circuit board after soldering

Circuit Explanation

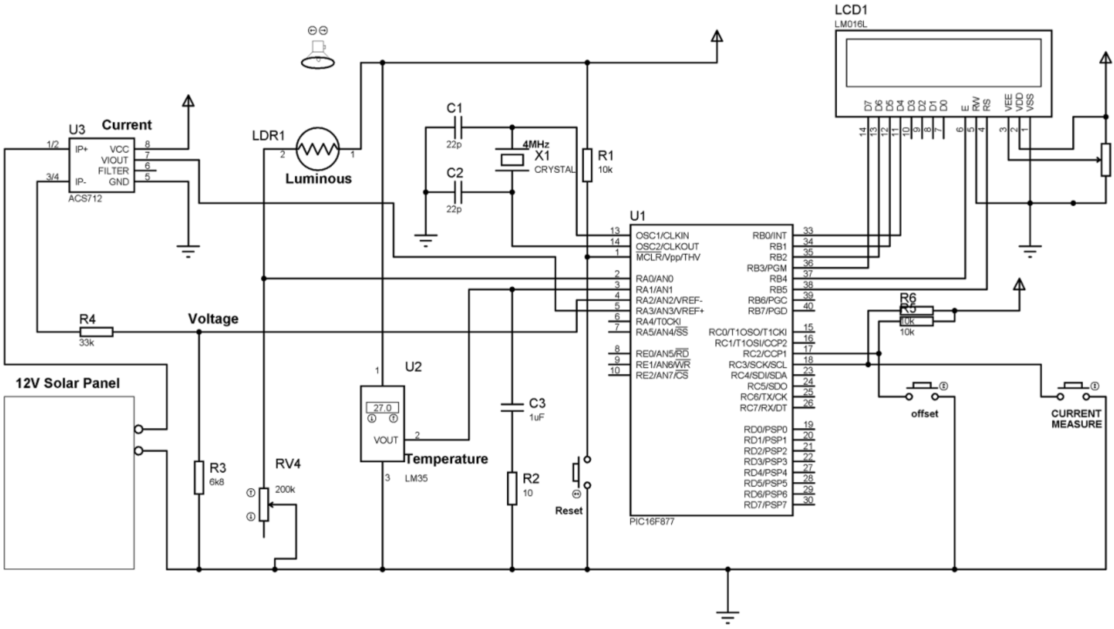

Figure 4 Schematic diagram of solar properties measuring circuit

As shown in the circuit diagram in figure 4, every component in the circuit are connected with the PIC16F877A. There are five I/O ports on the IC and altogether a total of 33 I/O pins on the device, but only 12 of them are used for the circuit. The pin no 1 is MCLR pin and it is pull up with a 10kΩ resistor, the pin is connected with the ground line using a push-to-on switch. It is the RESET switch to restart the program from initial state. Pin 2, 3, 4 and 5 are used as analog input pins and they are connected with the light sensor (LDR), output of LM35 temperature sensor, solar voltage input, and the current sensor (ACS712) respectively.

The output of temperature sensor (LM35) pin 2 is feed into the analog input AN1. But the output signal pin is connected with the ground line via a 1uF capacitor and a 10 Ohm resistor to filter the other electronic noises. Pin 1 of temperature sensor is connected with the 5V supply line and the pin 3 with ground line directly.

The light sensor LDR is connected in series with a 200k variable resistor between 5V power supply and ground line. The junction of LDR and Variable resistor is connected with the AN0 pin of PIC microcontroller. Variation of light intensity falling on the surface of LDR was read as varying voltage with analog input pin.

To measure the voltage output of solar panel, a voltage divider circuit is used. Because the analog input of PIC microcontroller is limited to 5V and the output of solar panel is above 12V level. The resistor R3 and R4 are used as voltage divider and their junction is feed into the analog input AN2 of PIC microcontroller.

The current to voltage converter ACS712 is used to read the solar current level. The input of current sensor pins are connected between the +ve terminal of solar panel to the voltage divider circuit. The voltage output of current sensor pin 7 is feed into the analog input AN3 of PIC microcontroller.

A 4MHz crystal oscillator is connected between pin no 13 and 14 oscillator pins. The pins are again connected with the ground line through 22pF capacitors to generate oscillations for the program counter to execute the program lines.

The MCLR reset pin is connected with the supply line via a 10kΩ resistor (R1). The pin is again connected with the ground line via a push to on switch to create active low reset input to the microcontroller.

A 16 characters 2lines alphanumeric liquid crystal display is used to display the measurement quantities of current, voltage, temperature and luminous on the display. It is connected with the six of port B pins. RB_0 to RB_3 pins are connected with the D4 to D7 of LCD. The RB_4 and RB_5 pins are connected with the E (Enable pin) and RS (Register Select pin) of the LCD respectively. Two more input switches on the right side of the circuit are used to measure current value. They are offset and current measure switches. They are wired as active low input and connected with the RC_2 and RC_3 pins of PIC microcontroller.

Flowchart

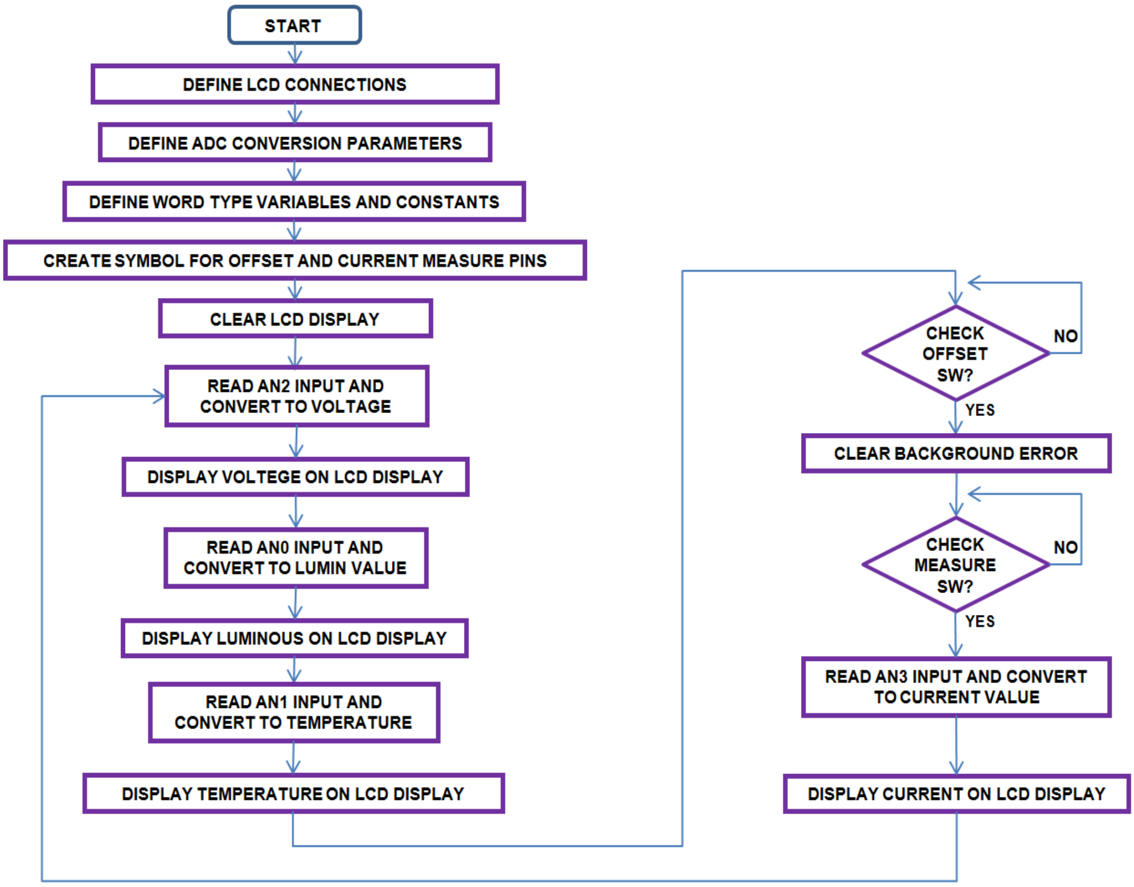

Figure 5 Flowchart diagram of the program.

A flowchart is initially created to carry on programming. As illustrated in the flowchart diagram, the program start by defining LCD connection pins, ADC conversion parameters, word type variables and conversion constants for numerical calculations. Then two input switches for current measure are defined with OFFSET and CURM symbols. Then the LCD is cleared and measuring loop is initiated. The voltage value is read from an2 input and converted to voltage by using conversion constants. Then it is display on the LCD screen. Next, the an0 input is read and converted to luminous value and it is illustrated on the LCD display. Then, the temperature value is read with AN1 input pin and it is converted and display on the LCD. Finally, the current value of the solar panel is measure by using two input switch, offset switch to record the error value and measure switch to read the real current value from AN3 input. Then it is converted and display on the LCD. Then the program loops back to read the voltage of the solar panel, repeatedly.

Circuit Operation and Discussion

The circuit is designed and constructed to measure the voltage, current, temperature and light intensity of a solar panel. Before starting the operation, the temperature sensor and light sensor are assembled on the surface of LCD as shown in the figure 6. It is attached very close to the surface of LCD to achieve accurate measurement of temperature and luminous.

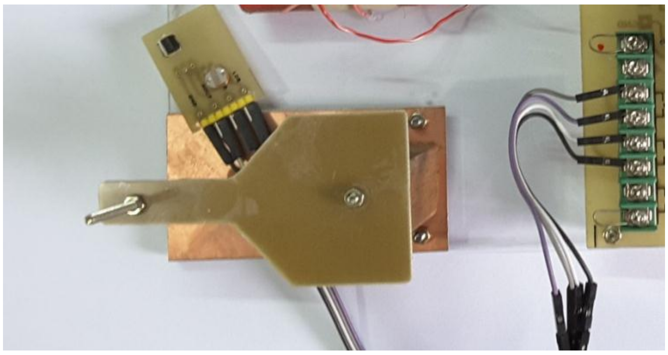

Figure 6 Attachment of temperature sensor and light sensor on the solar panel.

As shown in the figure 7, a 7.2V lithium ion battery pack is connected with the power input terminal near upper left corner of the circuit. The battery power is reduce and regulated with a 7805 (dc 5V) regulator circuit. There is a power on/off switch between the battery terminal and the regulator IC to switch on or switch off the measuring circuit.

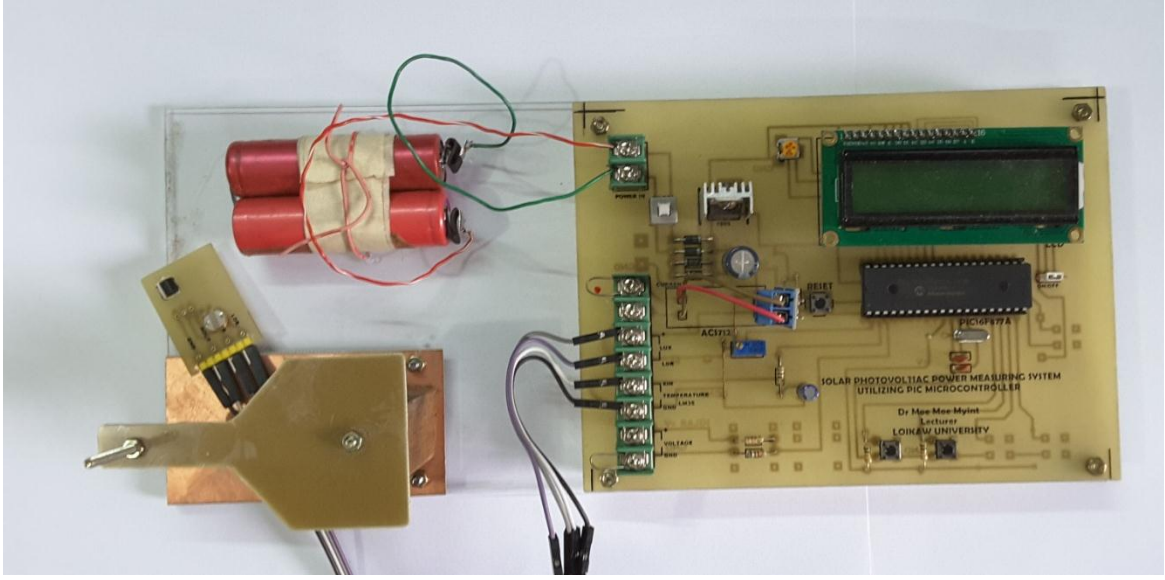

Figure 7 The whole circuit ready to measure solar panel properties.

The LCD display is a 16 characters, 2 lines alphanumeric liquid crystal display and it is positioned on the upper right corner of the circuit. A yellow 10k variable resistor near the LCD is to adjust contrast voltage of the LCD display. Slowly turning the resistor with a small screw driver will appear clear characters on the LCD. The PIC16F877A microcontroller is below the LCD, and it is the heart of the circuit. A program coding was created with PIC BasicPro programming language and converted to machine code. Then the codes are loaded into the memory ROM of PIC to operate the whole circuit. An on/off jumper beside the IC is used to operate the back light of the LCD display. There is a reset switch on the left side of the PIC. It is used to reset the whole circuit operation. There is a 4MHz crystal oscillator and two 22pF capacitors near pin 13 and 14 of the PIC microcontroller. It is used to operate 1 micro second clock for program counter. The ACS712 is the current sensor and it is located in the middle left of the circuit. On the lower right side of the circuit board, there are two more input switches for offset and current measure inputs.

When connecting with the solar power terminal, the positive terminal of solar panel is connected with the positive terminal of current input (marked with a red dot). The current output pin is connected with the There are eight green terminals on the lower left edge of the circuit board to read the four different parameters of the solar panel. The first two terminals are to read the current. Second two terminals are to measure light intensity. The third two terminals are to read the LM35 temperature sensor output. The remaining two terminals are used to read the voltage of the solar panel. positive terminal of voltage input. The voltage ground pin is connected with the ground terminal of solar panel. The lux input and lm35 temperature input are simply connected with the LDR and LM35 sensor outputs.

As explained in the program, the voltage of solar panel is read with AN2 pin. But the solar panel output under the sunny day is larger than 25V. Therefore, a voltage divider is used to limit the input voltage. In this case, 33k and 6.8k resistors are used. Therefore, the maximum limit of voltage input can be 6 times larger than 5V. Therefore, conversion constant Conv7 is 6. But for the ADC conversion resolution, 10bit AD converter is chosen. Therefore, each quantize voltage level is 5000mV/1024, which is 4.88mV. But in the PIC BasicPro programming, decimal values are not able to handle in calculations. Therefore, in the calculations, conversion constants Conv1, Conv5 and Conv9 are taken as integer 4. The other remaining decimal value of 0.88 is multiply with 100 and become 88 for Conv2, Conv6 and Conv10. But for the temperature measure, conversion constant 4.88 is again multiply with 10 since the LM35 datasheet illustrated the temperature measurement is 10mV/C. Therefore, the conversion becomes 48.8 and Conv3 is taken 48 as its constant.

In measuring the current value, it is not as simple as measuring other parameters. Because, the sensor is very sensitive and it is always detecting background magnetic fields since the ACS712 is a hall-effect sensor application. Therefore, a background current value was measured and stored in a register (ACSOFFSET) by pressing offset input switch. While making offset it is important to remove the current input pin from the solar positive terminal. Then the wire is reconnected and measure the current by pressing the measure input switch. In this case, the value of ACSOFFSET was subtracted from the new measurement value. Then the system display accurate current measurement in mA.

The measurement data of a solar panel was made in April and recorded value of parameters were illustrated in the following table.

Month	date	time	type of solar	voltage	current	light	temperature
April	1.4.2019	8am	10Watt Ring Solar Panel	25V	500mA	2000 lux	32C

Conclusion

The solar power is the best and pure resource of nature’s gift. The power of solar can be directly apply for the plants in photosynthesis, thermal conduction energy, sun drying the food, salt production, removing germs and virus. Moreover, the photons of solar rays can be converted to electrical energy by using solar photovoltaic cells. They are known as solar energy applications. Therefore, solar panels are produced in some of the countries all over the world. But they are expensive and not powerful enough to provide for a city. Therefore, a large area of solar panels are combined and stored in large storage cells. Therefore it is important to investigate the properties of a solar panel. The solar panel properties investigating circuit is designed, constructed and collected data to compare the various types of solar panels. The measurements are made for voltage, current, luminous and temperature. According to the results, suitable type of solar panel can be chosen for the applications.

Acknowledgements

The authors would like to thank Dr Htay Aung Pro-rector and Dr Soe Myint Thein, Pro-rector of Loikaw University, for their kind permission to carry out this research work. We also grateful to thank Professor Dr San San Wai, Head of Department of Physics, Loikaw University, for her encouragement to do this work. We wish to express my thanks to all our colleagues in the Department of Physics, Loikaw University, for providing suggestions in this research.

References

Microchip Technology Incorporated (1999) “PIC 16F676 Instruction Set” New York : Microchip Technology)

Marston R.M. (1996) “Modern CMOS Circuit Manual” (London : B H Newnes)

Nick Dossis (3/2002) "Everyday Practical Electronics" (London : Wimborne Publishing)

Sid Katzen (2000) “The Quintessential PIC Microcontroller” (Berlin :Springer)

Sinclair I. R. (2001) “Practical Electronics Handbook” (London : B H Newnes)

Thomas l. Floyd (1996) “Electronic Devices” (New Jersey : Prentice-Hall)

J. Myanmar Acad. Arts Sci. 2020 **Vol. XVIII.No.2A**

STRUCTURAL DEPENDENCE OF SILVER NANOWIRES ON DIFFERENT MEDIATED SALT

Saw Thiri[1], Nan Thidar Chit Swe[2] and Ye Chan[3]

Abstract

Silver nanowires (AgNWs) has been synthesized by polyol process through different mediated salts such as Copper II Chloride ($CuCl_2$), Sodium Chloride (NaCl), Potassium Chloride (KCl). The presence of cations and anions (Cu (II)+, Na+, K+ and Cl-) makes strong impact on the shape of silver nano structures. The surface morphologies and crystallinity of silver structure are analyzed by Scanning Electron Microscopy (SEM) and X- Ray Diffraction (XRD). SEM results revealed that the diameter and length of silver nanowires. XRD pattern displayed the final product was highly crystallized and pure. The synthesis of silver nanowires is important to achieve high performance transparent conductive films.

Keywords: Polyol synthesis method, mediated salt, silver nanoparicles, silver nanowires

Introduction

One-dimensional (1-D) metal nanostructures such as nanowires have attracted extensive attention due to their unique magnetic, optical, and electronic properties compared to zero-dimensional (0-D) nanostructures (Xiao, Y.A, 2007). Current noteworthy materials for ITO substitution are carbon nanotubes (CNTs), graphene, transparent conductive polymers, metal grids, and random meshes of metal nanowires. Ag NWs with well-defined shapes such as lengths and diameters are particularly interesting, as they have superior optical and electrical properties, thus making them excellent candidates for transparent electrodes (Lee, H-H, 2005). Transparent conductive polymers have interesting properties like high flexibility, low cost and light weight. Several companies have been trying to use them in various devices such as touch panels and organic electronics. However, in order to implement the optical and electrical features required for transparent electrodes, there is still a need to develop more effective processes for synthesizing Ag NWs with controllable shapes and sizes. In these regards, the synthesis of nanowires has attracted attention from a broad range of researchers (Dang, C. M., 2012). Over the last decade, various methods had been used to synthesize AgNWs such as polyol process, wet chemical synthesis, hydrothermal method and ultraviolet irradiation photo reduction techniques (Młoniak, A, 2011). Among these methods, the polyol process is considered due to simple, effective, low cost, and high yield. By controlling the parameters such as reaction time, molar ratio between capping agent and metallic precursor, temperature, and addition of control agent, a reasonable control growth of AgNWs may be achieved. In this work, silver nanowire preparing by this methods strongly depends on the parameters of the synthesis procedure such as the reaction temperature, the molar ratio between PVP and $AgNO_3$, PVPs with different chain lengths, the seeding condition and shielding gas, the additive of the control agents and the stirring speed (Maringan,C.S, 2016). AgNWs were synthesized through reducing silver nitrate ($AgNO_3$) and ethylene glycol (EG) in the presence of polyvinylpyrrolidone (PVP) as the surfactant which can direct the growth of AgNWs and protect them from aggregation. The mediated agents such

---

[1] Assistant Lecturer, Department of Physics, University of East Yangon

[2] Associate Professor, Department of Physics, Sagaing University of Education

[3] Professor and Head of Department, Universities' Research Center, University of Yangon

as $CuCl_2$, NaCl and KCl are added to facilitate the growth of AgNWs. We believe Cu (II), Na+, and Cl− ions are necessary for AgNWs production.

Experimental

2.1 Materials

All chemicals such as Silver Nitrate ($AgNO_3$, 99.9%), Ethylene Glycol (EG, 95.5 %), PVP (MW: 1300000), and Potassium Chloride (KCl), Sodium Chloride (NaCl) and Copper (II) Chloride ($CuCl_2$ anhydrous, 99.0%), anhydrous Ethanol (Ethos) and acetone were used as received without any purification.

2.2 Synthesis of Silver Nanowires

The polyol method is a cheap and simple method of synthesizing high quality silver nanowires in solution. In this method, a solution of ethylene glycol (EG), polyvinyl pyrrolidone (PVP) and different mediated salts (KCl, NaCl and $CuCL_2$) is heated to 170 °C and a mixture of $AgNO_3$ and EG is gradually added. Adding $AgNO_3$ to the solution leads to the creation of Ag^+ ions which results in the formation of nanoparticles. Silver nanowire were synthesized by reducing $AgNO_3$ as metal precursor salt in Ethylene Glycol (EG) which was used as not only reducing agent but also solvent and PVP as a capping agent. The first sample (Sample 1) is synthesized without any mediated salt. $AgNO_3$ solution (94 mM, in EG) and PVP solution (1300K) (147 mM, in EG) were completely dissolved by using magnetic stirring at room temperature. First, 30 mL of EG in a flask was heated at 170°C in a heating mantle with stirring rate 150 rpm for 30 minutes. After 30 minutes, mixed PVP/ethylene glycol was added to prepared solution, followed by $AgNO_3$ /ethylene glycol drop wise to the solution over dropping at a rate of 1ml min^{-1}. After adding all reagents, the mixture turned yellow indicating the appearance of silver nanoparticles. The reaction continue for 2 hours until the reaction finished completely with formed slightly gray-white suspensions. The sample marked as Sample 1 (S1).

The second sample (S2) is synthesized with KCl as the mediated agent. First 30 mL of EG in a flask was heated at 170°C in a heating mantle with stirring rate 150 rpm for 30 minutes. After 30 minutes, KCl solution was dropped into heated EG and then the reaction temperature was reduced to 110°C. At 110°C, mixed PVP/ethylene glycol was added to prepared solution, followed by AgNO3 /ethylene glycol drop wise to the solution over dropping at a rate of 1ml min-1. After adding all reagents, the mixture turned yellow indicating the appearance of silver nanoparticle. The reaction mixture was maintained at 110°C for 10 minutes until all $AgNO_3$ had been completely reduced. And then, the temperature was increased to 170ºC within 10 min for nanowire growth and the solution became gray gradually. The reaction continue to down at 150ºC for 40 minutes until the reaction finished completely with formed slightly gray-white suspensions. The sample marked as Sample 2 (S2). For Sample 3 (S3) and Sample 4 (S4) was synthesized by using NaCl and $CuCl_2$ as a mediated salt. The synthesis procedure was exactly the same as Sample 2 (S2). The product was diluted with acetone (1:5 by volume) and centrifuged at 3000 rpm for 20 min. The supernatant containing silver particles could be removed using a pipette. This centrifugation procedure could be repeated three times with ethanol. Purified silver nanowires solution was mixed with 2-propanol (1:1v/v) and sonicated for 15 minutes to get homogeneous ink solution. This solution was coated on glass substrates by rod coating method. This method is inexpensive and easy to use; just one wire-wound rod is enough for fabrication so there is no need for any complex equipment. The thickness of the deposited solution is determined by the diameter of the wire that is wound around the main rod. The density of the nanowires in the electrode was controlled both by the concentration of the nanowire solution and the number of layers deposited. After nanowire deposition, the film was dried in air. Nanowire films on glass substrates were annealed at 200°C for 30 minutes to get maximum conductivity by sintering the nanowire junctions.

Results and Discussions

This research provide the easiest way to synthesize thin and long silver nanowires with high yield within one hour after adding all reagents. In this synthesis procedure, 90% of the major product was wires and the less was different size of rod and particles. This experimental result shows that, without adding other metal salts as the source of seeds and appropriately reducing the molar concentration of silver nitrate, it is possible to produce silver nanoparticles. Other metal salt such as Potassium Chloride (KCl), Sodium Chloride (NaCl) and Copper (II) Chloride ($CuCl_2$) are necessary to produce silver nanowires.

3.1. XRD and SEM Analysis of Silver Nanostructures

XRD analysis are performed to determine the nature of silver nanostructures. After the preparation of nanowires, the suspension of nanowires in ethanol was used for SEM analysis by fabricating a drop of suspension onto a clean glass substrate and allowing ethanol to completely evaporate. The surface morphology of silver nanowires were observed by using Scanning Electron Microscope (JEOL- JSM 5610 LV) with the accelerating voltage of 15 kV, the beam current of 50 mA and 10000 time of photo multiplication. SEM showed that the silver products varied with the type of mediated salts used in the $AgNO_3$, PVP, mediated salts, Ethylene glycol and water.

Simple silver nanoparticles were obtained from no salts. Figure 1 shows the absorption spectra of silver nanostructures by using the precursor of PVP to $AgNO_3$ without mediated salt. SEM images show that spherical shaped silver nanoparticles have relatively uniform average diameter equal to 120 nm.

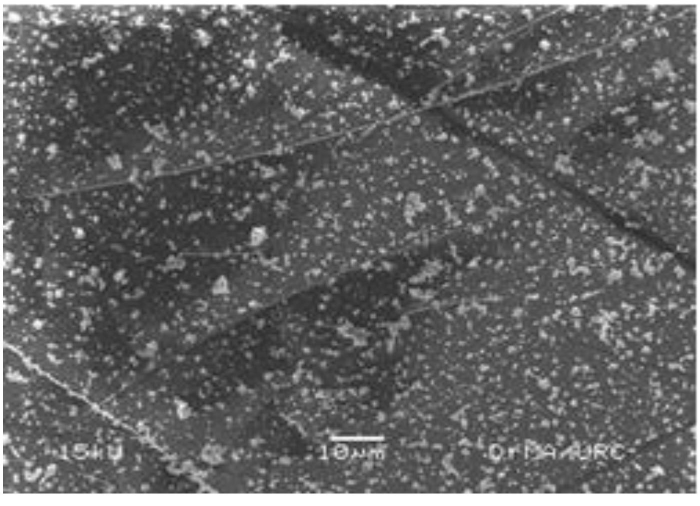

Figure 1 SEM image of silver nanoparticles (without any salt)

Figure 2 shows the final product synthesized under this particular condition that is using mediated salt KCl was a mixture of AgNps and AgNWs. This implies that the final product synthesized under this particular condition that is using mediated salt was a mixture of AgNps and AgNWs. Figure 2(a) XRD pattern reveals that the ratio of intensity between (111) and (200) peaks reveals a relatively high value of 4.5. It is obvious that using of KCl as mediated agent affected ratio of intensity between panels and it shows the crystallinity in this method increased. Figure 2(b) shows SEM images of silver nanostructures synthesized with KCl as mediated agent. SEM image show that the high yield of spherical shaped silver nanoparticles accompanied with some nanowires. AgNWs with very low yield and relatively uniform average diameter equal to 100 nm length around 10 μm.

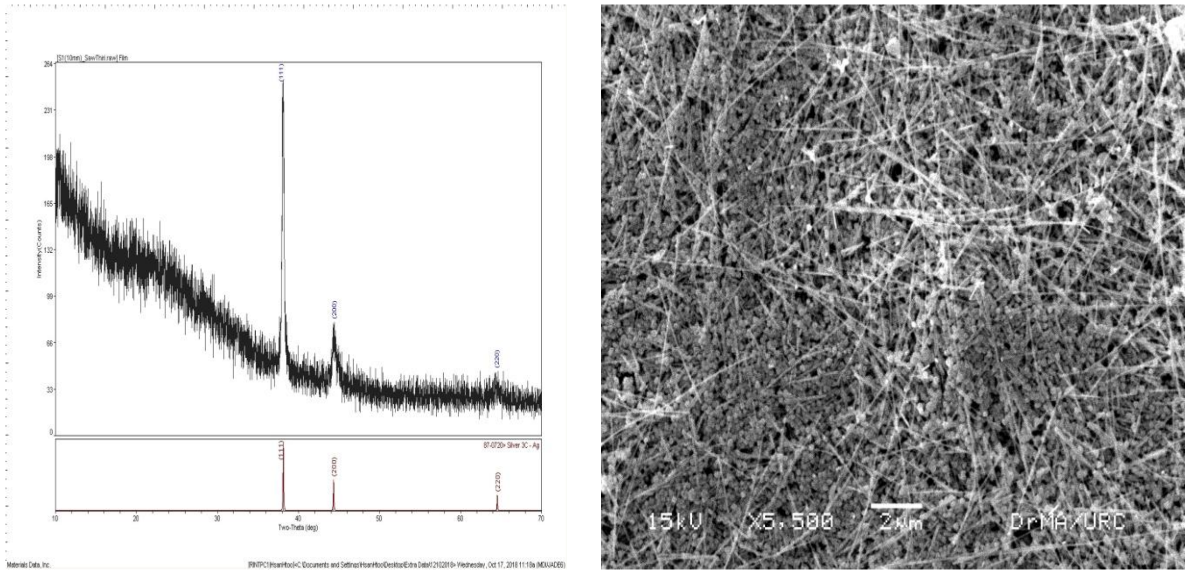

Figure 2 (a) XRD pattern of purified silver nanostructure
(b) SEM image of silver nanostructures with mediated salt KCl

Figure 3 shows the silver nanowires synthesized from the procedure in which $CuCl_2$ as the mediated salt. The final product synthesized under this particular condition that is using $CuCl_2$ of mediated salt gives mixture of nanowires and nanoparticles. Figure 3(a) XRD pattern reveals that the ratio of intensity between (111) and (200) peaks reveals a relatively high value of 6.5. Figure 3(b) shows the SEM image of silver nanostructures synthesized with $CuCl_2$ mediated salt. By using $CuCl_2$ mediated salt, the main products are the spherical silver nanoparticles (25%) besides there is a long wire shaped form with very low yield and relatively uniform average diameter equal to 88 nm and length more than 120 μm.

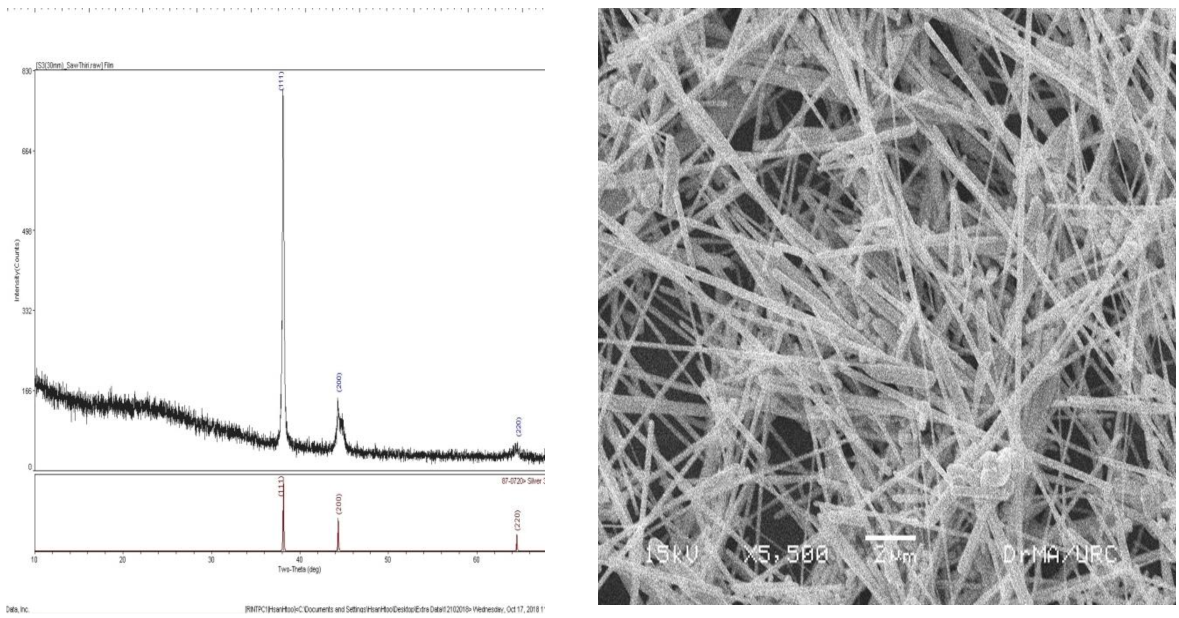

Figure 3 (a) XRD pattern of purified silver nanostructure
(b) SEM image of silver nanowires with $CuCl_2$ as the mediated agent

Figure 4 shows the SEM image of silver nanowires with NaCl as the mediated agent. Figure 4(a) the ratio of intensity between (111) and (200) peaks reveal a relatively high value of 6.8. It is obvious that using of NaCl as mediated agent affected ratio of intensity between panels and it shows the crystallinity in this method increased. Figure 4(b) shows SEM images of silver nanowires synthesized with NaCl as mediated agent. The image reveals that the product is entirely composed of uniform nanowires with very high yield and relatively uniform average diameter equal to 88 nm and length up to 150 µm.

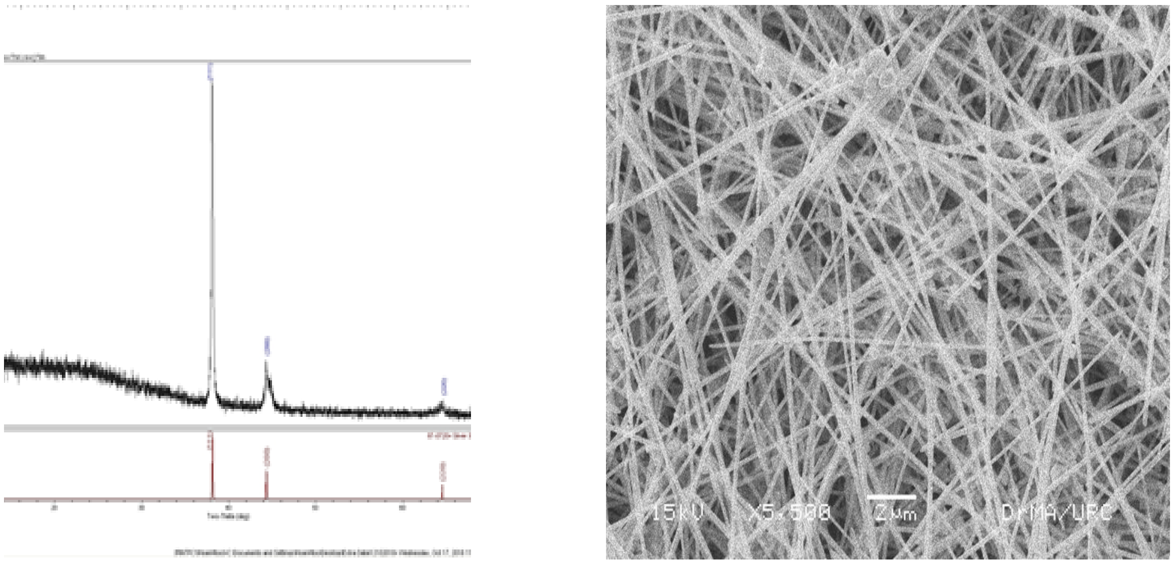

Figure 4 **(**a) XRD pattern of purified silver nanowires
(b) SEM image of silver nanowires with NaCl as the mediated agent

SEM showed that the structure and yield silver products varied with different of mediated salts used in the $AgNO_3$/PVP/mediated salts/Ethylene glycol system. The SEM images show that there are no mediated salt in synthesis procedure, the AgNWs are not achieved, and the majority of the structures are AgNps. By using KCl mediated salt, the main products are the spherical AgNps (50%) besides there are different length of silver nanostructure. As the $CuCl_2$ salt amount increases from the main products are the spherical silver nanoparticles (25%) besides there are different shaped of metal nanostructure. The average diameter of the nanowire is equal to 100 nm and length up to 100 μm. Figure 4 show the SEM image of AgNWs with NaCl as the mediated agent. The image reveals that the product is entirely composed of AgNWs. The diameter of the nanowire is around 88 nm and length up to 150 μm.

The phase composition and the crystallite size of the prepared samples were evaluated by X-ray diffraction analysis. The peaks of samples were identified by comparison with PDF-71-1166 according 2θ which confirmed that an anatase structure at angles of 2θ = 37.924°, 44.126° and 64.207° correspond to the (111), (200), and (220) crystal planes of the face center cubic (FCC) Ag, respectively. The lattice constant calculated from the diffraction pattern was 24.48 nm. The XRD pattern reveals that the synthesis silver nanowires through polyol process comprise pure phase. It exhibits well-defined peaks without any impurity element peaks detected. This indicated the success in the formation of the crystalline silver nanowires.

Table Silver nanostructures By Using Different Mediated Salts

Sample	Different Mediated Salts	Structure	Diameter	Length
S 1	No salt	Nano Particles	120nm	_
S 2	KCl	Particles and short wires	100nm	10μm
S 3	$CuCl_2$	Particles and long wires	88nm	120μm
S 4	NaCl	High yield	88nm	150μm

Conclusion

AgNWs were successfully synthesized by using polyol technique with different salt-mediated process. Without the mediated agents, the final product synthesized was AgNps. It was found that the addition of KCl or NaCl and $CuCl_2$ to the polyol reduction of $AgNO_3$ in the presence of PVP greatly facilitated the formation of AgNWs. Both the cation and the anions are crucial for the successful production of silver nanowires. A certain amount KCl or $CuCl_2$ mediated salts produce high yield of ultralong AgNWs, otherwise, a mixture of AgNps and AgNWs were obtained. The right amount of NaCl mediated salt is crucial for the successful production of AgNWs.

Acknowledgements

The authors greatly indebted to Professor Dr Khin Khin Win, Head of Department of Physics, University of Yangon, for her kind permission to carry out this work. The authors wish to show our sincere thanks to Professor Dr Aye Aye Thant, Department of Physics, University of Yangon, for her fruitful discussions to this work.

References

Bao, L-R, Wei. B and Xiao, Y.A. (2007).“ Conductive Coating Formulations with Low Silver Content,” *Electronic Components and Technology Conference.*

Chun, K-Y., Oh, Y., Rho, J., An, H-H., Kim, Y-J., Choi, H. Y. and Baik, S. “Highly conductive, printable and stretchable composite films of carbon nanotubes and silver”, *Nature Nanotechnology*, vol 5, pp 853

Chou1, K-S., Huang, K-C. and Lee, H-H. (2005) “Fabrication and sintering effect on the morphologies and conductivity of nano-Ag particle films by the spin coating method**,”** *Nanotechnolo*, 16, pp 779–784

Dang, T. M. D., Le, T., Fribourg-Blanc, E. and Dang, C. M., (2012). “Influence of surfactant on the preparation of silver nanoparticles by polyol method” Advances in Natural sciences: *Nanoscience and Nanotechnology,* 3, 035004 (4pp)

Gudikandula. K and Maringan,C.S. (2016). “Synthesis of silver nanoparticles by chemical and biological methods and their antimicrobial properties”, *Journal of Experimental Nanoscience*, Vol. 11, No. 9, 714-72.

Hao, E and Schatza, C. G. (2004). “Electromagnetic fields around silver nanoparticles and dimers”, *Journal of Chemical Physics*, vol 120, No. 1, pp 357-366

Hutter, E., Fendler, J. H., and Roy, D. (2001).“ Surface plasmon resonance studies of gold and silver nano particles linked to gold and silver substrates by 2-aminoethanethiol and 1,6-Hexanedithiol”, *Journal of Physical Chemistry. B*, 105, 11159-11168

Jakubowska, M. J., Kiełbasinski, K. and Młoniak, A. (2011). “New conductive thick-film paste based on silver nanopowder for high power and high temperature applications,” *Microelectronics Reliability*, vol. 51, no. 7, pp. 1235–1240

Kooa, H. Y., Yia, H. J., Kima, H. J., Koa, Y. N, Junga, S. D., Kanga, C.Y., Leeb, J-H, (2010). “Conductive silver films formed from nano-sized silver powders prepared by flame spray pyrolysis”, *Materials Chemistry and Physics,* 124, 959–963

Landage S.M. , Wasif A. I. and Dhuppe P, (2014) Synthesis of nanosilver using chemical reduction method,vol3, No. 5, pp 14-22

J. Myanmar Acad. Arts Sci. 2020 **Vol. XVIII.No.2A**

FABRICATION OF DYE-SENSITIZED SOLAR CELL BASED ON ZINC OXIDE NANORODS

Su Myat Aung[1], Myo Aung[2] and Nan Thidar Chit Swe[3]

Abstract

Zinc oxide nanorod with hexagonal structure was achieved by using chemical bath deposition method under atmospheric pressure by using zinc nitrate hexahydrate [$Zn(NO_3)_2.6H_2O$] and hexamethylene-tetramine ($C_6H_{12}N_4$) at constant temperature 93ºC and the deposition time of 2 hours, 4 hours and 6 hours. The prepared film was grown on the surface of zinc oxide seed layer. The surface morphologies and the structural characterization of zinc oxide (ZnO) nanorods were characterized by Scanning Electron Microscope (SEM) and X-ray Diffraction (XRD) technique. The XRD pattern of the sample revealed that ZnO nanorods have hexagonal crystallite structure. Photovoltaic parameters such as short circuit current density J_{sc}, open circuit voltage V_{oc}, fill factor FF, and overall conversion efficiency η for the fabricated cells were determined under illumination. In the analysis of photoelectrochemical properties, ZnO DSSC showed more pronounce in their performance and it has the efficiency of 0.12%.

Keywords: Dye-sensitized solar cell, Zinc Oxide nanorod, seed layer

Introduction

Zinc oxide (ZnO) is an important material and has received considerable attention due to its applications in electrical, optical, mechanical and scientific research as well as industry (Xia Y *et al*, 2003). Zinc Oxide is a wide band gap (3.37 eV) semiconductor and has a large binding energy (60 MeV), low resistivity and high transparency in the visible range and high light trapping characteristics (Lee GJ *et al*, 2010). It has also attracted attention for electrical and optical applications such as light-emitting diodes, photocatalysts, photodetectors, piezoelectronic devices, sensors and solar cells (Samanta P *et al*, 2009). ZnO has some benefits since it is cheaper, its band gap is wide so it is easily grown up on the substrate, it is non-toxic and environmentally friendly. Conventional solar cells are based on light harvesting and charge separation at semiconductor p-n junctions the technology used to produce energy from the solar radiation. The technological development in novel approaches exploiting thin films, organic semiconductors, and dye sensitization (Park WI *et al*, 2005). Nanostructured ZnO has been synthesized via a wide range of techniques (Hossain M *et al*, 2005). Among these methods, the chemical bath deposition method has drawn a considerable amount of attention in scientific and technological fields because of its considerable advantages of generally low temperature processing conditions, easy composition control and homogeneous easy fabrication of thin films with large area and low cost (Gowthaman *et al*, 2011). Here in, synthesis of ZnO nanorod (NRs) that have been carried out were such as chemical bath deposition (CBD) method at low temperature.

Nanostructures and surface morphologies of ZnO NRs were investigated by X-ray diffraction (XRD), and Scanning Electron Microscope (SEM). Photovoltaic properties of the ZnO NRs solar cells were investigated by measuring current density-voltage characteristics and

---

[1] Assistant Lecturer, Department of Physics, Hpa-an University

[2] Lecturer, Universities' Research Center, University of Yangon

[3] Associate Professor, Department of Physics, Sagaing University of Education

incident photon to current conversion efficiency. The highest conversion efficiency was obtained in ZnO NRs with the longest deposition time.

Experimental Details

2.1 Materials

Analytical grade (BDH, England) Zinc Acetate Dihydrate ($ZnC_4H_6O_4$), Zinc Nitrate Hexahydrate [$Zn(NO_3)_2.6H_2O$], Hexamethylenetetramine ($C_6H_{12}N_4$), Sodium Hydroxide (NaOH), Isopropanol Alcohol (C_3H_8O), distilled water (H_2O) and deionized water (DI) were used as starting precursor. All chemicals were used as purchased without further purification.

2.2 Cleaning Procedure of Glass Substrate

The very first step before the CBD proper is the washing of glass substrate in order to remove dirt and impurities that may have unknowingly settled on the glass substrate. This is done by washing in several substances, namely: acetone, distilled water, ethanol, distilled water again, hydrochloric acid (HCl) and lastly distilled water. These glass substrates are then dried in air blow at room temperature.

2.3 Seeding Method and Chemical Bath Deposition (CBD) Method

The seeding method commence with the making of zinc acetate dihydrate [$Zn(OOCCH_3)_2.2H_2O$] (0.02M) was ground for 15 min and then mixed with 0.02 M of NaOH. After the mixture was ground for 2 hr, the product paste was washed many times with deionized water. The resultant paste was centrifuged for 30 min to obtain pure ZnO precipitation. This paste was mixed with isopropanol alcohol [C_3H_8O] (10ml) to get the ZnO seed solution. This solution was coated on glass substrates by rod coating method. The thickness of the zinc acetate layer can be controlled by the number of rod coating runs and show good reproducibility. The coated substrates were dried at room temperature and annealed at 350°C for 30 min. All the substrates were seeded before the final growth of zinc oxide (ZnO) nanorods.

For chemical bath deposition (CBD) growth process, the aqueous solution of zinc nitrate hexahydrate [$Zn(NO_3)_2.6H_2O$], and hexamethylenetetramine ($C_6H_{12}N_4$) were first prepared. The concentrations of both were fixed at 0.1M. The aqueous solutions of zinc nitrate hexahydrate [$Zn(NO_3)_2.6H_2O$] (100 mL) and hexamethylenetetramine ($C_6H_{12}N_4$) (100 mL) were mixed together in 250 mL beaker. The bath is stirred at a constant rate of 360 RPM by magnetic stirrer for 30 minutes at room temperature. The beakers containing the bath solutions and the substrates were put on the hot plate for 2 hours, 4 hours and 6 hours at a constant temperature of 93ºC. After the growth, the substrates were removed from the solutions, rinsed with acetone, distilled water, ethanol then acetone and dried at room temperature. A post growth annealing was performed for the substrates (samples) at 550ºC for 1 hour and then quenched to room temperature (Li Z *et al*, 2008).

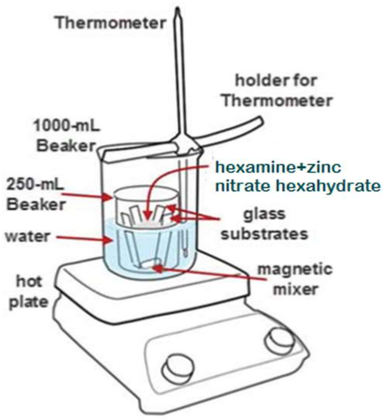

Figure 2 The schematic diagram of chemical bath deposition of ZnO nanostructure

2.4 Dye-Sensitized Solar Cells

The typical structure of DSSCs based on ZnO nanorod is shown in Figure 2.2. A few micrometer-thick layer ZnO nanorods is deposited on one of the electrodes and it acts as a photoanode in DSSCs. Dye molecules (erosin Y) are attached onto the surface of the photoanode and an iodine electrolyte is filled between the two electrodes. On the other electrode, a thin layer of graphite is generally deposited for high catalytic activity.

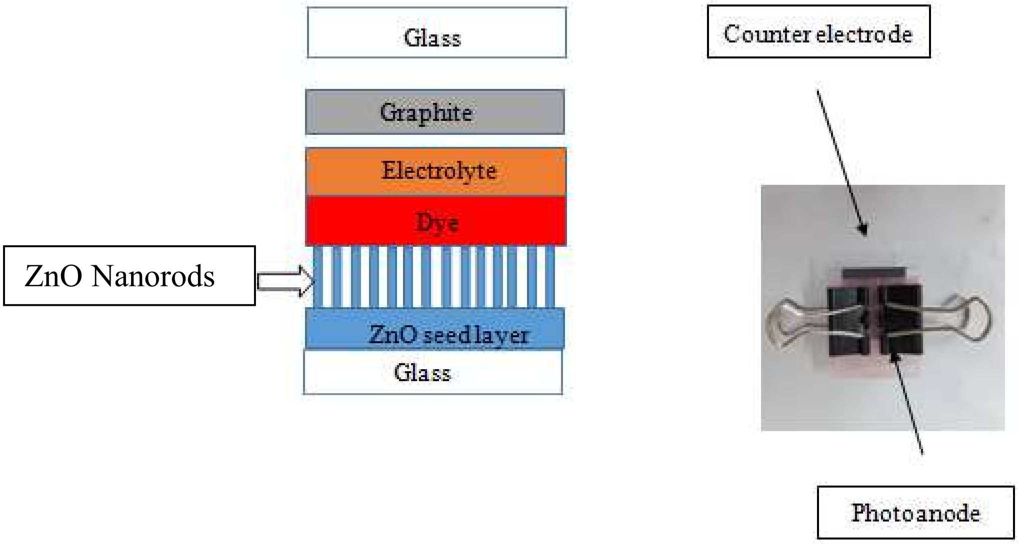

Figure 2.2 The typical structure of DSSCs based on ZnO nanorods

2.4 Characterization

ZnO nanostructures were confirmed by X-ray powder diffractometer (XRD) (Type: RIGAKU–RINT 2000) and Scanning Electron Microscope (SEM) (Type: JEOL 15 kV).

Results and Discussions

3.1. SEM and XRD Analysis for CBD

To compare ZnO nanostructures grown on different deposition time, SEM images of ZnO nanostructures on the seed layer were performed, as shown in Figure 2.

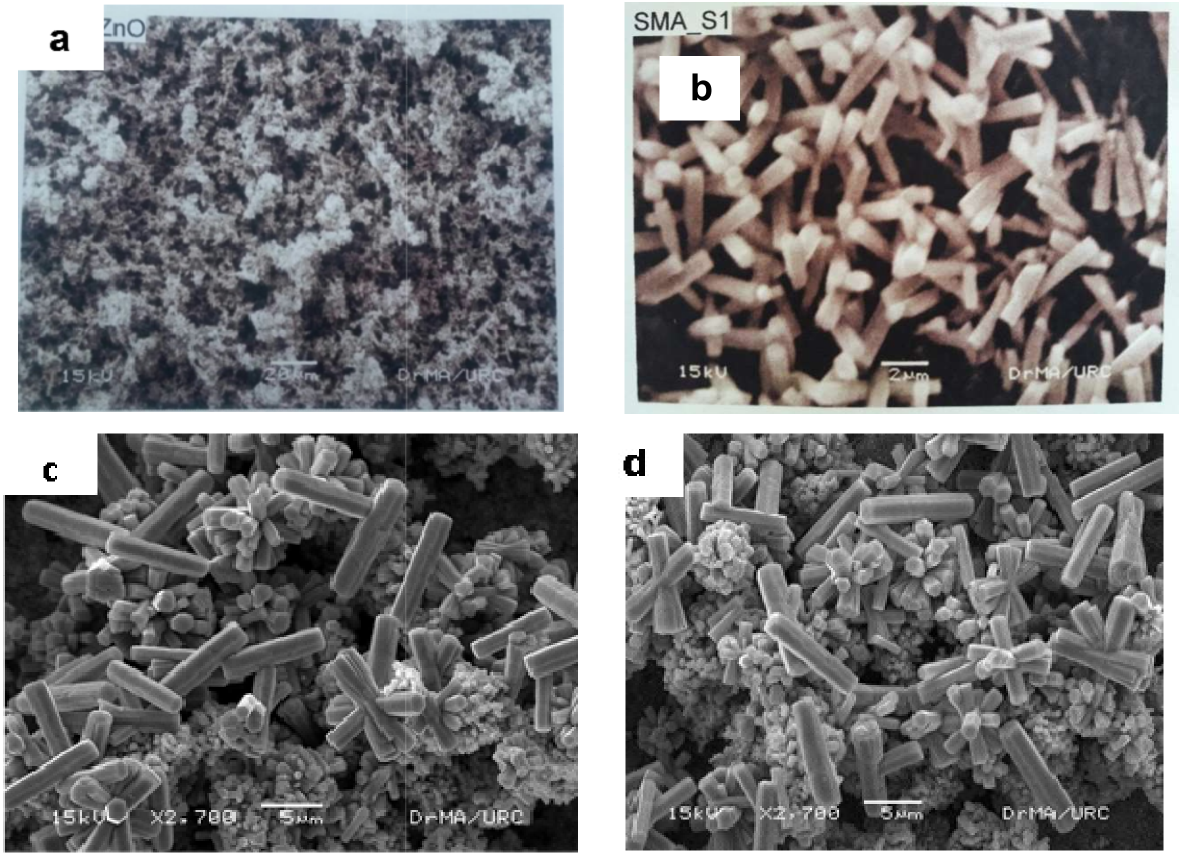

Figure 2 Top-view SEM images of ZnO samples (a) ZnO seed layer which is coated on the glass substrate (b) ZnO nanorod which is grown on seed layer for two hours deposition time (c) four hours deposition time (d) six hours deposition time

The SEM results reveal that the formation of nanorods and nanoflowers are formed in these samples. Figure 2(a) shows the ZnO seed layer and the particle size of the ZnO is approximately 100 nm. A thin layer of densely and uniformly dispersed ZnO nanoparticles is used as a seed layer for chemical bath deposition. It is noteworthy that the variation in the deposition time leads to a significant change in the growth of the ZnO NRs. When two hour deposition time, the nanorod structure is achieved. When the deposition time is increased, the size of the nanorod is bigger and become the flower like nanostructure. During the growth process, the tips of several NRs touch and/or cross each other, initially because of their slightly tilted growth and the piezoelectric properties of ZnO NRs, which lead to an increase in the diameter of the NRs and forming the flower like structure with an increase in the deposition time. The SEM characterizations of the as-synthesized zinc oxide (ZnO) nanoflowers are shown in Figure 2 (c) and (d). SEM micrographs show that the lengths of zinc oxide (ZnO) nanoflowers are more than 2 μm in diameter from 0.476 μm to 0.756 μm.

The XRD results of different deposition time give similar pattern. The XRD analysis of ZnO NRs phase informed that the formed diffraction pattern was in accordance with the data of XRD JCPDF standard No.89-1397 with the hexagonal crystal (zincite) system having the space group of P63mc, with the crystal lattice of a, b =3. 2533 Å and c =5.2073 Å. The formed phase was suitable for the report of Rai, et al, that ZnO NRs were formed in zincite phase. Figure shows the diffraction peak located at (100), (002), and (101). The XRD pattern with the annealing temperature of 550 °C for one hours at the NRs growing temperature of 93 °C had the crystal orientation at the highest intensity peak on (101), while on (100) and (002) the pattern weakened orientation. The XRD pattern exhibited that of the (ZnO) nanoflowers had good crystal quality. Diffraction peaks related to the impurities are not observed in the XRD pattern, confirming the high purity of the synthesized NRs.

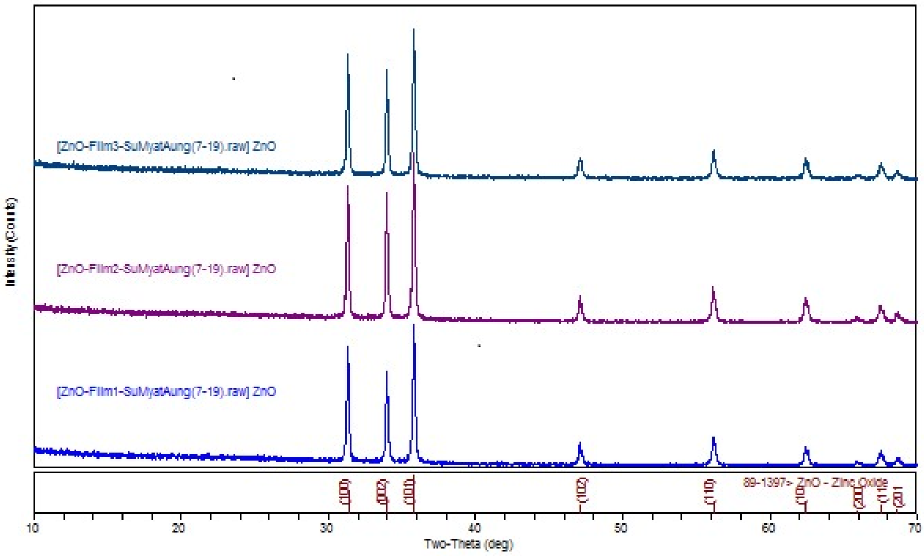

Figure 3 shows the XRD results of ZnO Seed layer and ZnO NRs with the precursor concentration of the various growing times of 2 hours, 4 hours and 6 hours.

Figure 4 shows the current-voltage I-V characteristics for DSSCs constructed using nanorod and nanoflower films measured under a simulated illumination with a light intensity of 11 mW/cm^2. The short-circuit current (J_{sc}) open-circuit voltage (V_{oc}), FF and PCE derived from the *I-V* curves under illumination for both nanorod and nanoflower based DSSCs are also presented in the inset table 1. From Figure. 3, it can be seen that the J_{sc}, V_{oc}, and FF for the cell constructed using nanoflower film (6 h deposition time) I_{sc} = 78 μA/cm^2, $V_{oc} = 0.5V$ and $FF = 0.11$ represent clear improvement over the cell constructed using nanorod array (2 h deposition time) I_{sc}= 37.1 mA/cm^2, $V_{oc} = 0.3V$, and $FF = 0.03$. Due to much improved I_{sc} and FF, the nanoflower based cell reached a total power conversion efficiency of 0.12%, outperforming that of the nanorod-based cell 0.033%.

Tabel 1 Photovoltaic parameters of DSSC solar cell based on ZnO nanorods with various growing times

	I_{sc} (µA)	V_{oc} (mV)	I_m (µA)	V_m (mV)	FF	η(%)
ZnO 2 hr deposition	37.1	295	20	200	0.03	0.033
ZnO 4 hr deposition	57	369	30	230	0.06	0.07
ZnO 6 hr deposition	78	480	40	320	0.11	0.12

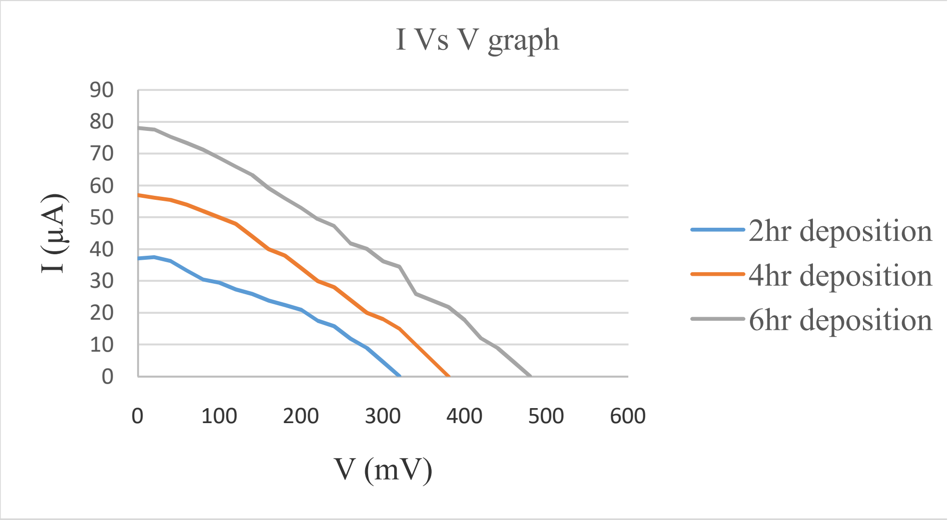

Figure 4 shows the I Vs V graph for DSSC solar cell based on ZnO nanostructure photoanode

Conclusions

In conclusion, Zinc oxide (ZnO) nanorods were synthesized by a chemical bath deposition (CBD) method with wide range of size and various shapes. The XRD analysis shows the ZnO films were hexagonal system structure with (101) oriented planes. The average crystallite size of ZnO was found to be about 31 nm. Current voltage measurement on fabricated dye-sensitized solar cell using eyosin Y dye extract shows the 2 hours deposition for open circuit voltage about 300 millivolts and short circuit current of 40 microamperes, 4 hours deposition for open circuit voltage about 400 millivolts and short circuit current of 60 microamperes and also 6 hours deposition for open circuit voltage about 500 millivolts and short circuit current of 80 microamperes, respectively.

Acknowledgements

The authors greatly indebted to Professor Dr Khin Khin Win, Head of Department of Physics, University of Yangon, for her kind permission to carry out this work. The authors acknowledge Professor Dr Ye Chan, Universities' Research Center, University of Yangon, for his advice and suggestions to this research and kind permissions to carry out laboratory facilities in URC.

References

Gowthaman P, Saroja M, Venkatachalam M, Deenathayalan J, Senthil TS (2011). "Structural and optical properties of ZnO nanorods prepared by chemical bath deposition method". Aust J Basic Appl Sci, 5:1379–1382.

Hossain M, Ghosh S, Boontongkong Y, Thanachayanont C, Dutta J. (2005). Growth of zinc oxide nanowires and nanobelts for gas sensing application. J Metastable Nanocrystalline Mater, 23:27–30.

Kashif M, Hashim U, Ali ME, Ali SMU, Rusop M, Ibupoto ZH, Willander M. (2012). Effect of different seed solutions on the morphology and electro optical properties of ZnO nanorods. J Nanomater, 2012:6.

Li Z, Huang X, Liu J, Li Y, Li G. (2008). Morphology control and transition of ZnO nanorod arrays by a simple hydrothermal method. Mater Lett, 62:1503–1506

Lee GJ, Lee Y, Lim HH, Cha M, Kim SS, Cheong H, Min SK, Han S, (2010). "Photoluminescence and lasing properties of ZnO nanorods". J Korean Phys Soc, 57:1624–1629.

Li Z, Huang X, Liu J, Li Y, Li G, (2008). Morphology control and transition of ZnO nanorod arrays by a simple hydrothermal method. Mater Lett, 62:1503–1506

Park WI, Kim DH, Jung S-W, Yi G-C, (2002). Metalorganic vapor-phase epitaxial growth of vertically well-aligned ZnO nanorods. Appl Phys Lett, 80:4232–4234.

Samanta P, Patra S, Chaudhuri P, (2009). "Visible emission from ZnO nanorods synthesized by a simple wet chemical method". Int J Nanosci Nanotech, 1:81–90.

Xia Y, Yang P, Sun Y, Wu Y, Mayers B, Gates B, Yin Y, Kim F, Yan H, (2003).One dimensional nanostructures: synthesis, characterization, and applications. Adv Mater, 15:353–389.

Yi S-H, Choi S-K, Jang J-M, Kim J-A, Jung W-G. (2007). Low-temperature growth of ZnO nanorods by chemical bath deposition. J Colloid Interface Sci, 313:705–710.

J. Myanmar Acad. Arts Sci. 2020 **Vol. XVIII.No.2A**

SURFACE PLASMONIC EFFECTS OF SILVER NANOWIRE ON THE ENHANCEMENT OF TiO_2 BASED DYE-SENSITIZED SOLAR CELLS

Tun Lin Htet[1], Myo Aung[2] and Nan Thidar Chit [3]

Abstract

Nanoscale metal structures embedded in DSSC devices could also potentially be beneficial in improving the light absorption, as well as the charge separation and charge collection processes. In this research, TiO_2 was used as a photoelectrode and eosin y is used as photosensitizers. Using a Mayer rod coating method, a highly viscous titanium dioxide (TiO_2) paste was deposited on a FTO glass substrate. Metal nanowire such as silver nanowire (Ag NWs) was coated on the TiO_2 active layers to enhance the photon absorption and charge separation efficiency. The structural properties of the Ag NWs coated TiO_2 active layer were studied by using XRD and SEM techniques. Photovoltaic parameters such as short circuit current, open circuit voltage, fill factor FF, and efficiency were determined under light intensity of 11 mW/cm^2.

Keywords : DSSC, XRD, SEM, Photovoltage parameter.

Introduction

A solar cell is a device that converts sunlight into electricity. Materials used in photovoltaic devices are mainly semiconductors including, among others, crystalline silicon, III-V compounds, copper indium selenite /sulfide, and cadmium telluride(Gratzel *et al,* 2005). Low-cost solar cells have been the subject of intensive research work for the last decades. Amorphous semiconductors were announced to be one of the most promising materials for low-cost energy production. Recently dye sensitized solar cells (DSSCs) emerged as a new type of low cost solar cells with simple preparation procedures. The DSSC operation is based on the sensitization of wide bandgap semiconductors such as TiO_2 and ZnO. The performance of the cell is mainly dependent on the dye used as sensitizer in addition to many parameters, like the photoelectrode materials, the redox and the back electrode(Kontos *et al,* 2008). The absorption spectrum of the dye and its anchorage to the surface of TiO_2 or ZnO are the most important parameters determining the efficiency of the DSSC.

The thickness of the photoelectrode film and the metal-TiO_2 nanocomposites were found to be major contributors to the improvement of efficiency(Sengupta *et al,* 2016). It has been found that when a metallic nanoparticle interacts with the light having wavelength much larger than the size of particle, it generates collective oscillations of valence electrons known as surface plasmon resonance (SPR). Metal nanoparticles, especially silver (Ag) and gold (Au), are able to enhance light absorption and broaden the light spectrum of the dye through surface plasmon resonance (SPR)(Zhang *et al*, 2009). This metal nanoparticle can function as a light-scattering mechanism that can increase the number of optical pathways, allowing light to stay longer and increase light absorption]. Compared to Au, Ag nanoparticles (AgNP) have a high scattering efficiency and energy band. Therefore, AgNP is one of the best candidates to enhance power-conversion efficiency by utilizing the SPR effect.

---

[1] Assistant Lecturer, Department of Physics, Pyay University

[2] Lecturer, Universities' Research Centre, University of Yangon

[3] Associate Professor, Department of Physics, Sagaing University of Education

In this work, metal nanowire is fabricated on TiO_2 photoelectrode to improve the power-conversion efficiency. DSSCs were prepared by using TiO_2 electrode, Ag NWs layer, eosin-y dye, and graphite counter electrode. I-V characteristic and the corresponding output power were determined. The efficiency of DSSC corresponding to with and without silver nanowires is calculated.

Materials and Methods

2.1 Synthesis of TiO_2 Paste

Commercially available TiO_2 powder was prepared by ball milling to reduce powder size. Milling time was 12 hours. This ball milled powder was mixed with ethanol and sonicate it with water bath-sonicator for 24 hours to obtain fine grain size. The TiO_2 pastes were prepared in two steps. First 2 g of TiO_2 powder was mixed with 1 mL acetylacetone and the mixture was grounded with agate motar for half an hour. This paste was again grounded for 5 hours with addition to appropriate amount of distilled water, ethylene glycol, acetic acid, acetonitrile and ethanol. The solution was heated to evaporate distilled water and ethanol slowly. Finally TiO_2 paste was obtained.

2.2 Synthesis of Silver Nanowire (Ag NWs)

Silver nanowire were synthesized by reducing $AgNO_3$ as metal precursor salt in Ethylene Glycol (EG) which was used as not only reducing agent but also solvent and PVP as a capping agent. First, 30 mL of EG in a flask was heated at 170°C in a heating mantle with stirring rate 150 rpm for 30 minutes. After 30 minutes, mixed $CuCl_2$/ethylene glycol solution and mixed PVP/ethylene glycol was added to prepared solution, followed by $AgNO_3$ /ethylene glycol drop wise to the solution. After 3 hours adding all reagents, the mixture turned silvery brown indicating the appearance of silver nanowire. The product was diluted with acetone (1:5 by volume) and centrifuged at 3000 rpm for 20 min. This centrifugation procedure could be repeated three times with ethanol until the supernatant became colorless. The collected precipitates (silver nanowires) redispersed in ethanol for coating over TiO_2 layer.

2.3 Iodide electrolyte solution

To mix iodide solution, dissolve 0.127 g of iodine in 10ml of ethylene glycol. Next add 0.83 g of potassium iodide, stir and store in dark container.

2.4 Preparation of Dye Sensitized Solar Cells

Transparent conducting FTO coated glass sheets were cut into pieces of dimensions 2 cm x 2 cm. The substrates were cleaned in a detergent solution using an ultrasonic bath for 15 min, rinsed with water, acetone and ethanol, and then dried with air blow. Thin layers of the prepared TiO_2 past were spread on the transparent conducting FTO coated glass by employing rod coating method. In this experiment, adhesive Scotch tape (3M, Scotch Magic Tape) with thickness of approximately 52 µm was placed on the edges of the conductive sides of the FTO glass to create a 1 x 1 cm^2 rectangular area for TiO_2 paste deposition. A small amount of TiO_2 paste was then applied on the masked top edge of the FTO glass and spread across the unmasked area using a Mayer rod (#12). Then, the Scotch tape was removed, leaving an uncoated area of the FTO glass, which was used as the electrical contact for solar measurement. Samples were then dried in an oven at 70°C for 20 min. The samples were sintered at 600°C for 1 h then were cooled down to

70°C. For AgNWs coated TiO_2 layer, the film was dried in an oven at 150°C for removal of unwanted chemicals. Finally the film was placed in dye solutions for 24 h under dark condition. The dyed TiO_2 electrode and a graphite coated counter electrode were assembled to form a solar cell by sandwiching a electrolyte solution.

2.5 Characteristic Techniques

The morphological properties of all samples were examined by scanning electron microscopy (FESEM, Hitachi S- 4700). The structural properties were investigated by X-ray diffraction (XRD, Rigaku X-ray diffractormeter). The photovoltaic properties of DSSCs were measured under a light intensity of 11 mW/cm^2.

Results and Discussions

The phase composition and the crystallite size of the prepared TiO_2 and graphite samples were estimated by X-ray diffraction analysis. The peaks of TiO_2 samples at 600°C were identified by comparison with PDF-71-1166 according 2θ which confirmed that an anatase structure at 2θ was 25°.

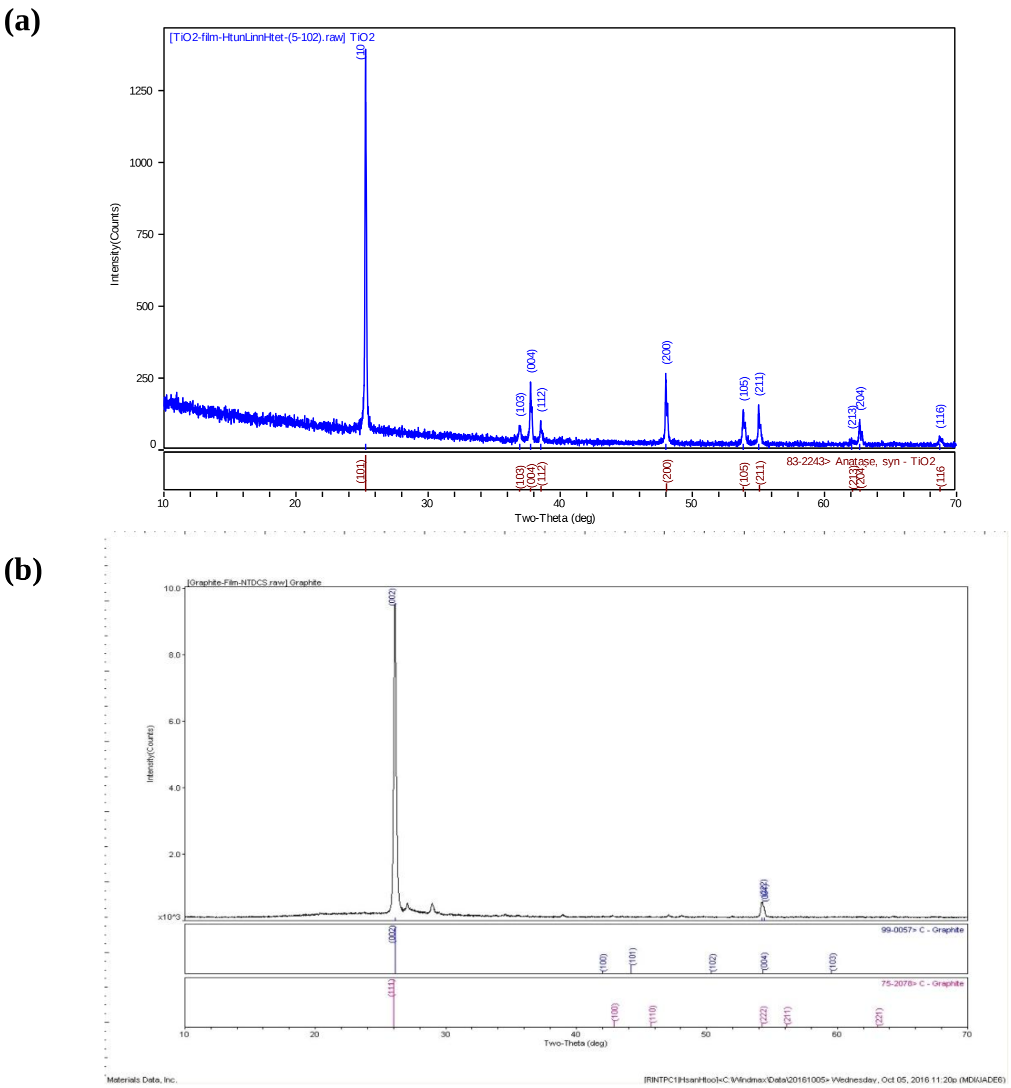

Figure 1 XRD patterns of (a) TiO_2 photoelectrode (b) graphite counter electrode film

The particle size of nanomaterial is related to the diffraction peak broadening. X-ray diffraction spectra of synthesized TiO_2 nanoparticles were taken and particle size and phase composition were determined. The lattice parameters were observed a=b= 3.846 and c= 9.578. The nanocrystalline anatase structure was confirmed by sharp peaks obtained corresponding to the planes (101), (103), (004), (200), (105), (211), (213), (204), (116) and (220) indicated the tetragonal structure of TiO_2 nanoparticles. All peaks obtained were in good agreement with the PDF card no. 71-1166. The average crystalline size is calculated by using Debye Scherrer equation. is 33.63 nm. Figure 1(b) shows the XRD pattern of graphite film which was used as counter electrode in DSSC solar cell. The peaks of graphite were identified by comparison with PDF-99-0057 according 2θ which confirmed that an graphite structure at 2θ was 26°.

The surface morphology and the size of the TiO_2 particles were analyzed by using scanning electron microscopy (SEM). Figure 2(a) shows the top-view SEM image of the prepared TiO_2 sample. As analysis of SEM image, it was smooth and crack free layer. This image consisted of some pores and circular feature in microstructure. All grains were clearly formed and uniformly distributed. The density of film was high. Agglomeration of grain was thicker and compact form in microstructure. The average grain size of TiO_2 sample was 0.16 μm. The SEM image shown in Figure 2(b) confirms that crystalline silver nanowires were surrounded by TiO_2 materials as indicated by the relatively bright contrast. Further, this result indicated that TiO_2 nanoparticles were embedded within the AgNWs, implying the successful formation of AgNWs coated TiO_2 nanoparticle.

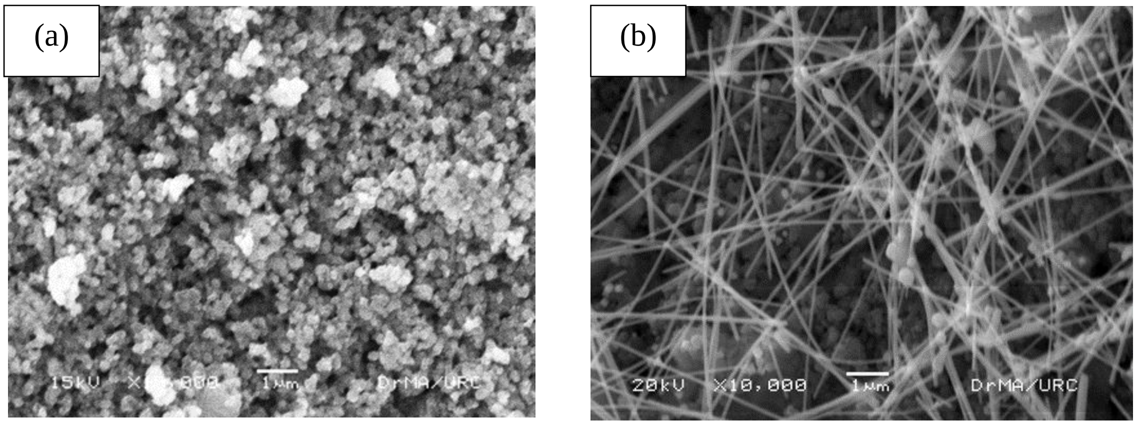

Figure 2 The SEM images of (a) pure TiO_2 nanoparticles and (b) TiO_2 nanoparticles coated with Ag NWs, which has been coated on the FTO conductive glass

The performance of photoelectrochemical solar cells with and without Ag NWs coating were monitored through electrical current and voltage outputs under 11 mW/cm^2 illuminations. More details regarding the photovoltaic performance parameters such as photo current density(Jsc), Photovoltage(Voc), Fill factor (FF), photoconversion efficiency (η) are summarized in Table 1.Figures 3 show the current-voltage (I-V) characteristic curves of the assembled DSSCs sensitized with and without silver nanowires. It is clear from these figures that the DSSC with Ag NWs coating exhibit the better I-V response. The conversion efficiency of all fabricated cells were observed to be about 0.372% for DSSC with silver nanowire coated photoelectrode and 0.12% for DSSC without silver coated photoelectrode. From these results, it was found that the conversion efficiency was increased with silver coating.

Table 1 Photovoltaic parameter of DSSCs

	I_{sc}(μA)	**V_{oc} (mV)**	**I_m(μA)**	**V_m(mV)**	**FF**	**η (%)**
Pure TiO_2	110	640	50	280	0.193	0.12
TiO_2 with Ag NWs	160	690	90	450	0.372	0.373

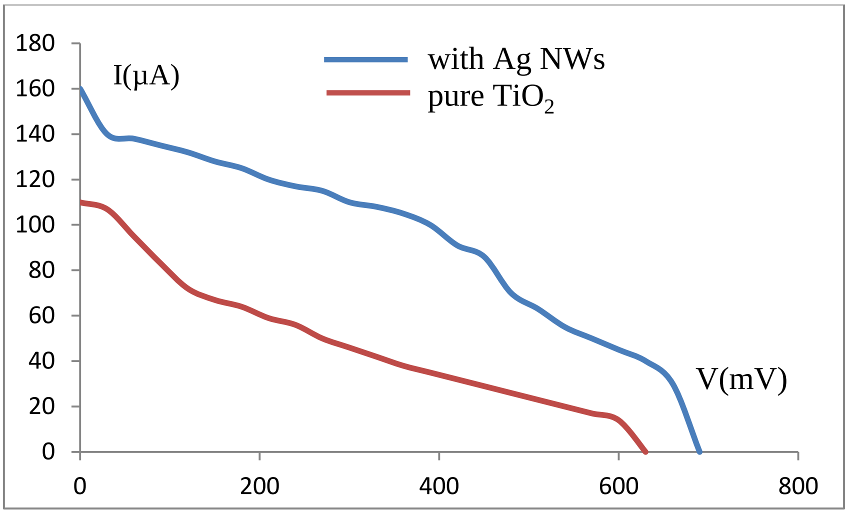

Figure 3 Current and voltage characteristics of the DSSC with and without silver nanowires

Conclusion

Growth of TiO_2 electrodes DSSC with and without Ag NWs coating and their solar cell properties have been successfully implemented. X-ray diffraction pattern showed the different diffraction peaks corresponding to different plane. All the peak heights and peak positions were good agreement with library file of JCPDS. The average grains size of the particles was 160 nm. The circular features in microstructure were uniformly distributed in SEM image. The current density and cell voltage characteristic curve for TiO_2 DSSC with Ag NWs coating showed better performance where the efficiency of the cell obtained as 0.373%.

Acknowledgements

The authors greatly indebted to Professor Dr Khin Khin Win, Head of Department of Physics, University of Yangon, for her kind permission to carry out this work. The authors acknowledge to Professor Dr Ye Chan, Universities' Research Centre, University of Yangon, for his advice and suggestions to this research and kind permissions to carry out laboratory facilities in URC.

References

Gratzel M Solar energy conversion by dye-sensitized photovoltaic cells. Inorg Chem .(2005)

G. Zhang, W. Li, B. Chu, L. Chen, F. Yan, J. Zhu, Y. Chen, and C. S. Lee. "Cascade-energy-level alignment based organic photovoltaic cells by utilizing copper phthalocyanine as bipolar carrier transporting layer". Applied Physics Letters (2009)

Hart J N, Menzies D, Cheng Y B, et al. Microwave processing of TiO_2 blocking layers for dye-sensitized solar cells. J Sol-Gel Sci Tech (2006)

Kontos A.I, Kontos A.G, Tsoukleris D. S, Bernard M.C, Spyrellis. N, Falaras P, journal of materials processing technology (2008)

M.-G. Kang, M.-S. Kim, J. Kim, and L. J. Guo. "Organic Solar Cells Using Nanoimprinted Transparent Metal Electrodes". Advanced Materials (Dec.2008).

Ma C.C Organic solar cells and plastic solar cells (2007)

Sengupta, D.; Das, P.; Mondal, B.; Mukherjee, K. Effects of doping, morphology and film-thickness of photo-anode materials for dye sensitized solar cell application—A review. Renew. Sustain. Energy Rev (**2016**) 60, 356–376.

Wang, P.; Zakeeruddin, S.M.; Moser, J.E.; Gratzel, M. A new ionic liquid electrolyte enhances the conversion efficiency of dye-sensitized solar cells. J. Phys. Chem. B 2003,

Wu J H, Lan Z, Lin J M, et al. A novel thermosetting gel electrolyte for stable quasi-solid-state dye-sensitized solar cells. Adv Mater .(2007)

Zhang D S, Downing J A, Knorr F J, et al. Room-temperature preparation of nanocrystalline TiO2 films and the influence of surface properties on dye-sensitized solar energy conversion. J Phys Chem B .(2006)

J. Myanmar Acad. Arts Sci. 2020 **Vol. XVIII.No.2A**

IMPROVING THE ELECTRICAL CONDUCTIVITY OF GRAPHENE LAYER BY CHEMICAL DOPING OF SILVER NITRATE

Lwin Ko Oo[1], Nan Thidar Chit Swe [2], Than Zaw Oo[3] and Ye Chan[4]

Abstract

In the present work, graphene oxides (GO) synthesized directly from graphite powder according to Hummers method were chemically reduced using ascorbic acid and ammonia achieving the reduced graphene oxide (rGO). The Ag-rGO nanocomposite was prepared by hydrothermal process using silver nitrate ($AgNO_3$) as a precursor. As synthesized GO, rGO and Ag-rGO nanocomposite were characterized with Fourier transform infrared spectrophotometer (FTIR), Scanning electron microscope (SEM), X-Ray Diffractometry (XRD) and Raman spectroscopy. The SEM micrographs show the ultrathin, wrinkled, layered flakes and paper-like morphology of graphene sheets. Raman and FTIR spectroscopic investigations provided the information about the number of graphene layers and structural properties. The conductivity measurement showed that the electrical conductivity is improved upon silver doping on graphene sheet.

Keywords: graphene oxide, reduced graphene oxide, Ag-rGO nanocomposite, electrical conductivity

Introduction

Graphene is a monolayer form of carbon with a two-dimensional (2D) honeycomb lattice structure. The most interesting electrical properties of single layer graphene is high electron mobility and ballistic conduction.

The mechanical exfoliation, micromechanical cleavage, epitaxial growth, exfoliation of graphite in the liquid phase through direct sonication, and chemical reduction are commonly used to develop graphene nanosheets (Dreyer *et al,* 2010). The disadvantage of mechanical exfoliation method is that it is not scalable and consequently not amendable for its mass production. Despite achieving pure monolayer graphene sheets by epitaxial growth, its transfer to insulating substrates is of great challenge. Hummers method, one of the chemical methods, has been the most popular approach for its simplicity and large scale production of graphene sheets with several in-plane oxygen-containing groups. In order to reduce it to rGO, chemical reduction or thermal annealing has been employed; the former one enables the exfoliated GO with poor electrical properties due to the presence of contaminates and structural defects, while the latter one would increase its electrical conductivity retaining its graphene structure (Galindo *et al,* 2014).

For the graphene based materials to be utilized as electrode, the electrical conductivity is of key importance. The electrical properties of graphene layers can be modulated by various doping techniques and it is noteworthy that doping is an especially striking approach to tailor and control the properties of graphene (Khan *et al,* 2014). However an extreme care is taken in selecting the doping method since most of doping methods cost degradation of structural uniqueness or electrical mobility (Farmer *et al,* 2009).

---

[1] Assistant Lecturer, Universities' Research Center, University of Yangon

[2] Associate Professor, Department of physics, Sagaing University of Education

[3] Professor, Universities' Research Center, University of Yangon

[4] Professor and Head of Department, Universities' Research Center, University of Yangon

Metal doping by chemical means is simple, easy and even applicable to a graphene device without disturbing the structural shape. Silver (Ag) is a noble metal with remarkable optical properties, excellent thermal and electrical conductivity (Rajeswari *et al*, 2017). The present work involves the synthesis of rGO by chemical reduction method and the Ag decoration on rGO by chemical doping. The optical, structural properties and surface morphology of rGO and Ag modified rGO nanocomposites were investigated. An enhancement in electrical conductivity of Ag-rGO nanocomposites upon Ag doping is illuminated in this work.

Experimental Details

2.1 Materials

Analytical grade graphite powder (99%), sodium nitrate ($NaNO_3$), potassium permanganate ($KMnO_4$), sulfuric acid (H_2SO_4, 98%), hydrochloric acid (HCl), hydrogen peroxide (H_2O_2, 30%), ascorbic acid (AA), ammonia (NH_3) and silver nitrate ($AgNO_3$) are purchased from Chemical Reagent Co, Ltd. Distilled water (DW) was used throughout the whole experiments. All chemicals were used without any purification.

2.2 Preparation of Graphene Oxide and Reduced Graphene Oxide

Graphene oxides were synthesized directly from graphite according to Hummers method where 1.5 g of graphite powder was added to 35 ml of concentrated sulfuric acid and sodium nitrate while stirring in an ice bath. Potassium permanganate (4.5 g) was added slowly to keep the temperature of the suspension lower than 20 °C. This reaction system was transferred to a 40 °C oil bath and stirred for about 45 min. Distilled water (75 ml) was added and stirred for 20 min at 95 °C. Furthermore, 250 ml of DW was added in this solution. Hydrogen peroxide (30%) (7.5 ml) was added slowly in the solution, it was changed from dark brown to yellow color. The mixture was filtered and washed with 1:10 HCl aqueous solution to remove metal ions. This solution is graphite oxide aqueous dispersion which was washed several times for neutralization to pH 6-7. And then, we need to put this solvent for overnight. Its precipitate was made by filtration method. The GO dispersion was centrifuged at 3000 rpm for 20 min (7 times) to remove the unexfoliated graphite. The GO aqueous dispersion was further sonicated for 1hr to exfoliate. The solution was absolutely graphene oxide. To reduce GO via a chemical treatment process, ascorbic acid (0.7 g) and the obtained GO suspension (250 ml, 0.3 g/ml) were mixed, and then ammonia solution (60 µl) was added to adjust the pH 8-10. Then the suspension was heated to 95 °C under vigorous stirring and kept for 2 hr. The resulting was reduced graphene oxide (rGO). The reaction mixture was allowed to cool down to the room temperature and was filtered by whatman paper. The filtrate was dried in vacuum at room temperature for 1-3 days.

2.3 Synthesis of Ag-rGO nanocomposites

In this work, silver nitrates ($AgNO_3$) with reduced graphene oxide composites were prepared by the following procedure. 5 ml of GO dispersion was allowed to sonicate for 30 min. Then, different ratio of $AgNO_3$ solution (30 mM, 50 mM and 70 mM) in DW was slowly added into the GO suspension under continuous stirring for 1 hr at room temperature. The obtained slurry was transferred into a 50 ml Teflon-lined stainless steel autoclave and heated to 120 °C for 24 hr. After the reaction, the superannuated liquid was discarded and the precipitate was cooled to room temperature washed with water, centrifuged and dried in an oven at 50 °C and labeled as Ag-rGO nanocomposites. Figure 1 shows the sample preparation of Ag-rGO nanocomposite.

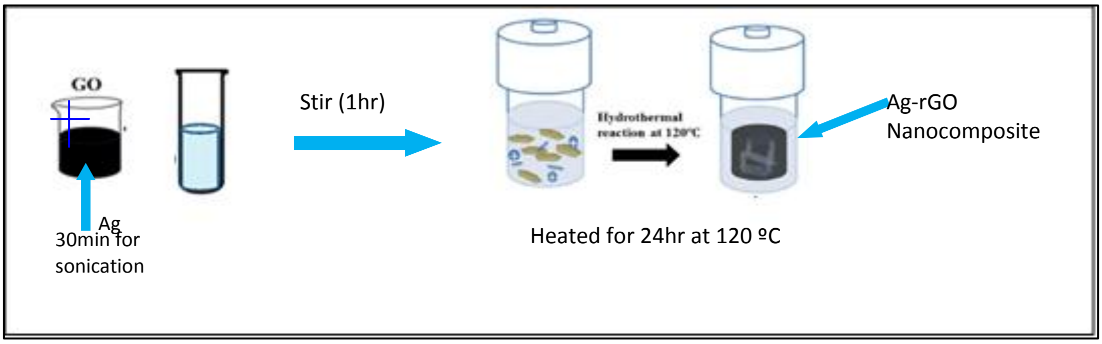

Figure 1 Schematic diagram of Ag-rGO nanocomposite by using hydrothermal method

2.4 Characterization

Centrifuge machine (Kokusan H-200 series) and Sonicator (AS ONE) were used to separate the layers by layers from the solution. GO dispersions were freeze- dried and used for morphological and structural characterizations. Scanning Electron Microscopic (SEM) images of GO, rGO and Ag-rGO composites were measured using Scanning Electron Microscope (JEOL-JSM 5610LV) with the accelerating voltage of 15kV. Fourier transform infrared (FTIR) spectra were taken out by the use of a FTIR-8400 SHIMADZU. The structural characterizations of GO, rGO and Ag-rGO were confirmed by X-ray powder diffractometer (Rigaku-RINT 2000). The solution of GO, rGO and Ag-rGO in DW were used for XRD analysis by filtration method on what man filter paper. Raman spectra were obtained on a nano-Raman Spectrometer employing a 532 nm laser beam using the dried powder mounted on the glass slide.

Results and Discussions

3.1. FTIR Analysis of GO, rGO and Ag-rGO composites

FTIR spectra of GO and rGO (Figure 2a) show the characteristic functional groups of GO which are C-O-C (round about 1047 cm^{-1}), C-O (1213 cm^{-1}), carboxyl C=O stretching band at 1722 cm^{-1}, and O-H deformation band at 1417cm^{-1}. The carbon-carbon double bonds (C=C), can be observed round about 1585 cm^{-1}. The O-H stretching vibrations in the region of 3600-3000 cm^{-1} are attributed to the hydroxyl and carboxyl groups of GO and residual water between GO sheets. As expected, due to the reduction reaction by Ascorbic acid (AA) these characteristic bands of GO are relatively weaker (lower transmittance after the reduction) or completely removed in the FTIR spectra of rGO. The majority of carbonyl and epoxy groups can be changed into hydroxyl groups in the GO by chemical reduction. This result indicates that rGO was successfully obtained after reduction reaction.

These spectral changes indicate the presence of carbonyl, ether and hydroxyl groups in the chemical structure of the treated graphite, implying that graphene oxide has been produced. The spectrum of the Ag-rGO nanocomposites given in Figure 2b can be observed the absorption peaks at 1514 cm^{-1}, 1415 cm^{-1} (C–H bending vibrations) and 1016cm^{-1} and those are represented the C–OH stretching vibrations. The peak at 1585 cm $^{-1}$ in the GO sample shifted to a lower frequency at 1514 cm^{-1} in the Ag-rGO nanocomposite. It is attributed to the skeletal vibration of the graphene sheets, which is different from the spectrum of rGO sample without the addition of Ag+. The FTIR results demonstrate that Ag+ contributes to the reduction of GO to graphene, which is consistent with XRD results. And strong interaction may exist between silver nanoparticles and the remaining surface hydroxyl groups on rGO sheet.

As a result, Ag-rGO nanocomposite was formed finally. The overall reaction can be described by the following equations:

$$Ag^{+} + OH^{-1} \rightarrow AgOH$$

$$GO + AgOH \xrightarrow{\text{hydrothermally}} rGO\text{-}Ag + H_2O$$

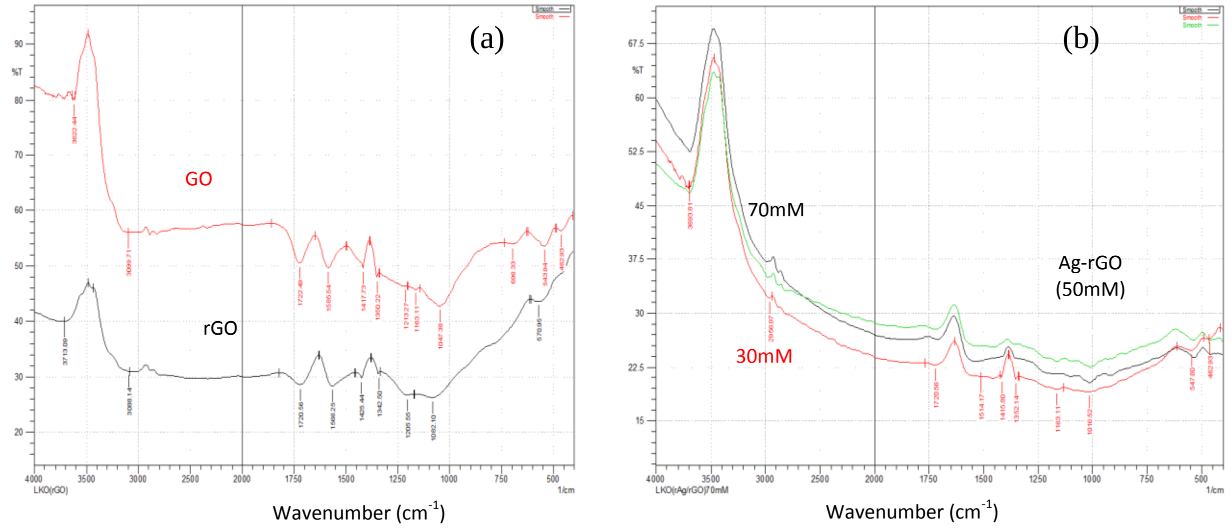

Figure 2 FTIR spectra of (a) graphene oxide and reduced graphene oxide (b) Ag-rGO nanocomposites (30 mM, 50 mM, 70 mM)

3.2 SEM Analysis

The detailed surface morphology of graphene oxide and reduced graphene oxide were carried out by using Scanning Electron Microscope (SEM). Figure 3(a) reveals the existence of crumple structure for graphene oxide. This is due to the exfoliation of graphite to become oxide and results in deformation upon the exfoliation and restacking. Figure 3(b) shows the image of reduced graphene oxide (rGO), thin sheets of folded and wrinkled structure has been observed by using ascorbic acid as reducing agent.

The morphology of the synthesized composites were also observed by Scanning electron microscope (SEM). Fig 3(c,d,e) display the SEM images different molarity ($AgNO_3$ 30 mM, 50 mM and 70 mM) of the Ag-rGO nanocomposites. It exhibits a uniform decoration of AgNPs on the rGO sheets. The average particle size is round about 420-550 nm. The restacking property of rGO sheets was prevented by the uniform distribution of AgNPs (Li *et al*, 2012).

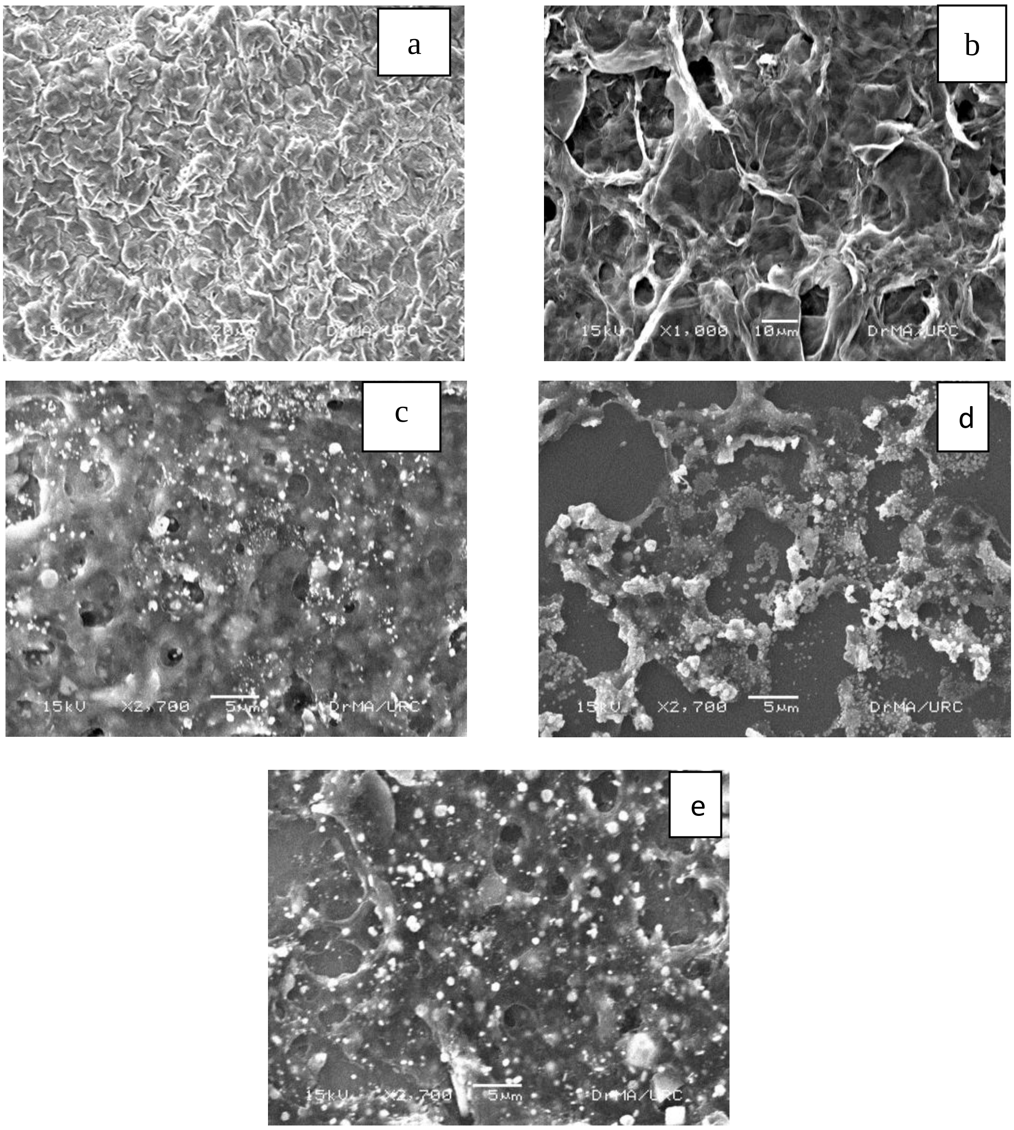

Figure 3 SEM images of (a) graphene oxide (b) reduced graphene oxide (c) Ag-rGO nanocomposites for 30 mM of silver nitrate (d) 50 mM and (e) 70 mM

3.3 X-Ray Diffraction Analysis

In addition, X-ray diffraction can also be used to characterize the crystal structure of GO, rGO and Ag-rGO nanocomposites. The XRD spectrum of resulting powder and sheets of GO and rGO sample were shown in Figure 4(a). A sharp peak at 2θ~10.85°, corresponds to the reflection from the (111) plane, was observed in XRD spectra of GO. The pattern reveals that the phase precipitated out in the sample is hexagonal structure. The interplaner spacing d (002) between individual graphene layers (3.35Å) can be used as an indicator of the degree of graphitization. Reduced graphene oxide has a peak around 2θ~26.32° for LAA and NH_3 Figure 4(a). This change in peak position and FWHM of the peak could be due to the exfoliation of GO sheets after removal of the intercalated carboxylic groups. These XRD results are closely related to the exfoliation and reduction processes of GO.

After the hydrothermal process, the diffraction peaks of the Ag-rGO nanocomposites (Figure 4b) with 30 mM, 50 mM and 70 mM of silver nitrate are indicated at 38.02°, 44.2° and

64.3°, corresponding to the crystal planes (111), (200) and (220) shown the presence of Ag metal in the composites (Panbo *et al*, 2013).

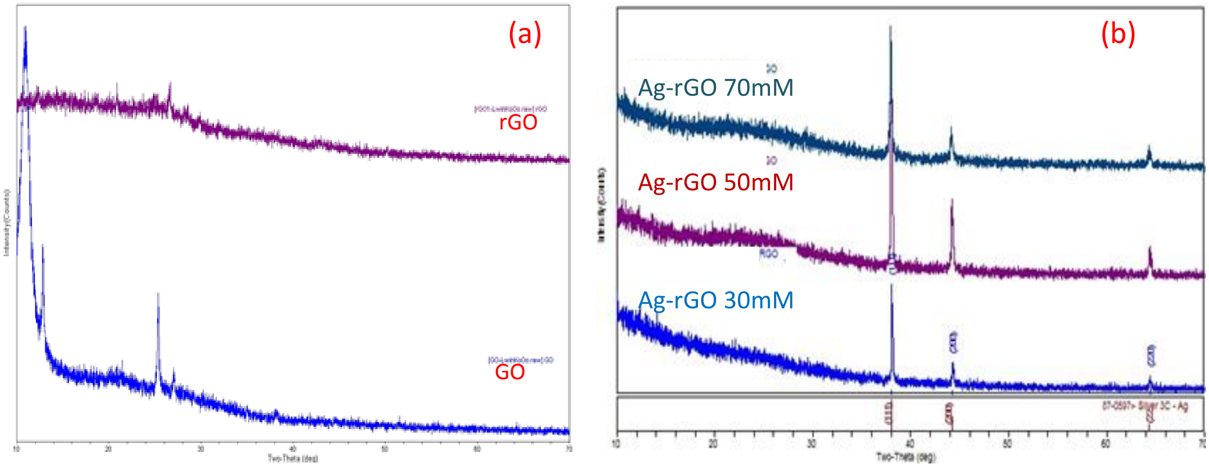

Figure 4 XRD patterns of (a) GO and rGO (b) Ag-rGO Nanocomposites with 30 mM, 50 mM and 70 mM of silver nitrate ($AgNO_3$)

3.4 Raman Analysis

Raman spectra are powerful tools to characterize carbonaceous materials. The reduction of GO to rGO was confirmed by this spectra. Raman spectra of synthesized GO is presented in Figure 5(a). In the Raman spectra of GO, the band at 1579 cm^{-1} is called G band, this band arise from the first order scattering of the (E2g) stretching mode. The band at 1348 cm^{-1} is the D band that corresponded to decrease of the size of in plane sp^2 domains. GO and rGO have both D and G bands. In the Raman spectrum of graphene and other sp^2 carbon samples containing defects, several additional symmetry-breaking features are found. After reduction reaction D/G intensity ratio (I_D/I_G) of rGO (at 1337 cm^{-1} of D band) (Figure 5b) increases from 0.97 (intensity ratio of GO) to 1.08 (intensity ratio of rGO). This increase is due to formation of domains that are numerous in number and smaller in size with respect to ones present in GO.

Figure 5c-e shows the Raman spectra of Ag-rGO nanocomposites with treatment of $AgNO_3$ for different reaction ratios (30 mM, 50 mM and 70 mM). It is noted that the composites exhibit for 30 mM (D band at 1342 cm^{-1} and G band at 1586 cm^{-1}), 50 mM (D band at 1337 cm^{-1} and G band at 1585 cm^{-1}) and 70 mM (D band at 1343 cm^{-1} and G band at 1589 cm^{-1}). The intensity disorder ratio are changed after hydrothermal treatment ($I_D/I_{G=}$1.09, 1.07, 1.11) (Moon *et al*, 2010). Raman spectra confirmed the formation of crystalline Ag with rGO during hydrothermal treatment. The Raman spectra recorded in 2680-2720 cm^{-1} (2D band) region for all samples is presented in Figure 5. The number of layers can be predicted from the shape and position of the 2D band. The estimated layers of prepared sample are 5.

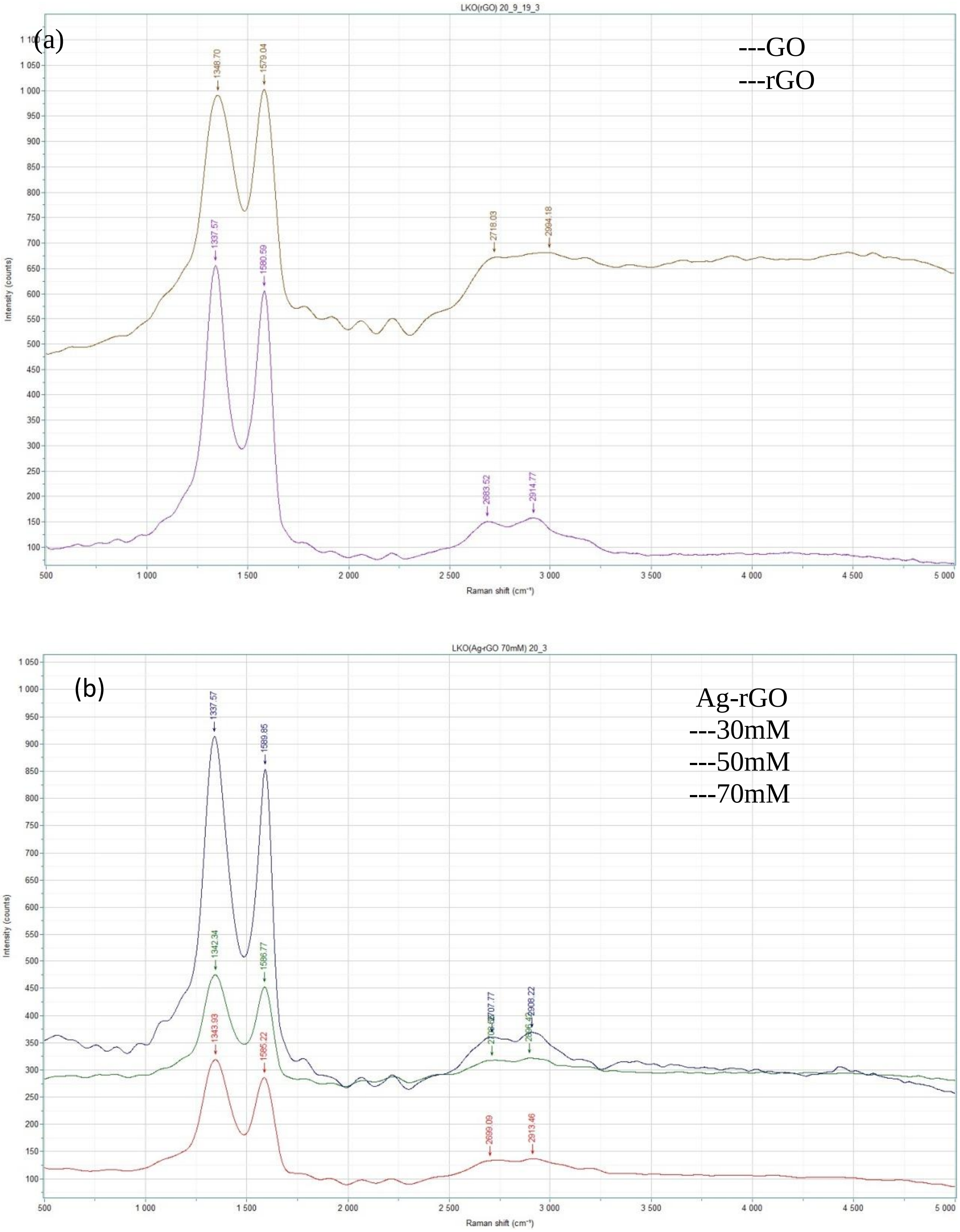

Figure 5 Raman spectra of (a) graphene oxide and reduced graphene oxide (b) Ag-rGO nanocomposites (30 mM, 50 mM and 70 mM)

3.5 Electrical Conductivity

Electrical resistivity is a measure of how strongly a material opposes the flow of electric current. It is represented by **ρ** and the unit is Ohm-meters (Ωm). It is defined as the ratio of the electric field inside a material to the electrical current density through it. The material with lower electrical resistivity more readily conducts a flow of electrical charge. Electrical conductivity is the reciprocal of electrical resistivity. It is represented by **σ** and the unit is Siemens per meter

(S/m). The electrical resistance for a uniform material with known geometry can be measured in a direct way and electrical resistivity can be calculated by the following equation:

$$R = \rho L/A \text{ (or) } \rho = RA/L$$

The method is simple and straight forward, but the contact resistance is usually involved. Two-point probe and four-point probe are commonly used to measure the resistance of thin films (Zhao *et al,* 2019). In two-point probe measurement, it is difficult to accurately separate either contact resistance R_c between probes and sample surface or spreading resistance R_{sp} from the material resistance or interest. Four-point probe method in the Figure 6 can avoid the influence from the wirings and contacts, which is a key advantage. One configuration is that the probes are arranged in-line with equal spacing (s), in which the two outer probes apply a constant current and the two inner probes measure the potential difference between them. With an ultrahigh internal resistance, almost no current flows through the sense loop. The typical probe radius ranges from 30 to 500 μm and probe spacing is in the range of 0.5-1.5 mm. In order to eliminate the size effect of finite geometry in four-point probe, the sample width should generally be forty times larger than probe spacing (Smits *et al,* 1958). Sample thickness is one of the correction factors in the data processing. Most of the samples measured using four-point probe. The outer probe and inner probe voltage will then be used to calculate the sheet resistance.

$$R_s = \frac{\pi}{\ln 2}\frac{V}{I} = 4.53236\,\frac{V}{I}$$

where,

Rs = sheet resistance (ohm per square)

V = the voltage measured between the inner probes

I = the current applied between the outer probes

Figure 6 Four-point probe symbol and machine

The conductivity measurement of samples of GO, rGO and Ag-rGO nanocomposites thin film are conducted by linear four- point probe method. According to the Table 1, the electrical conductivity of nanocomposites is significantly improved for higher concentrations Ag. In this work, it was found that the value of the conductivity for Ag concentration of 30mM of Ag-rGO nanocomposite is increased by ~ 97.6 % compared with the GO film in the Figure 7.

Table 1 Electrical conductivity for GO, rGO and Ag-rGO nanocomposites thin film

Type of Samples	Sheet Resistance R_s (MΩ/sq)	Electrical Conductivity $\sigma = 1/\rho$ (m S/m)
GO	179.50	1.393
rGO	157.07	1.592
Ag-rGO (30 mM)	90.83	2.752
Ag-rGO (50 mM)	81.01	3.086
Ag-rGO (70 mM)	61.99	4.033

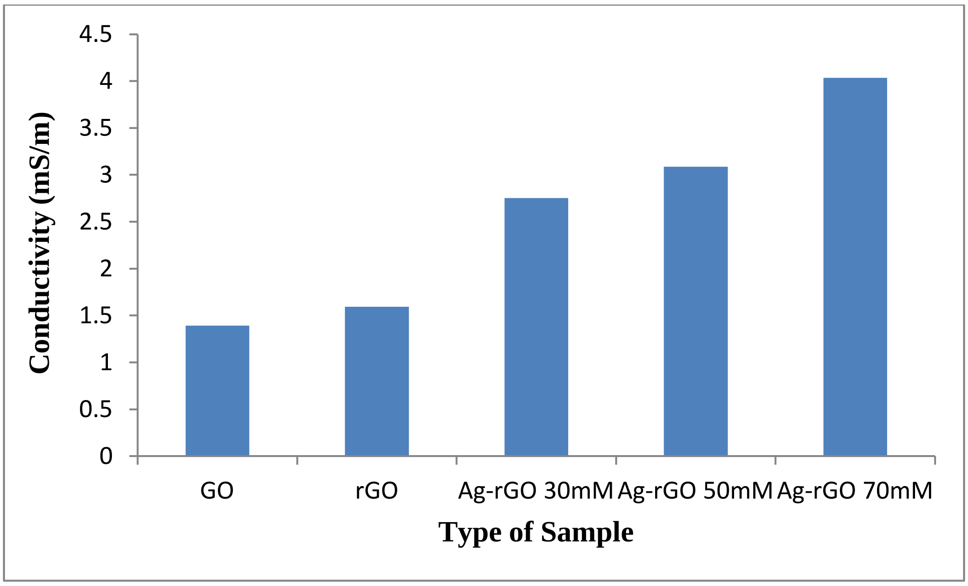

Figure 7 Comparison of conductivity with GO and Ag-rGO

Conclusion

In this study, graphene oxide, reduced graphene oxide and Ag-rGO nanocomposite were synthesized by Hummers method, chemical reduction method and hydrothermal method respectively. The effect of reducing agents on the structure and morphology of GO, rGO and Ag-rGO nanocomposites are investigated by SEM, XRD, Raman spectrometer and FTIR spectroscopic techniques. rGO sheets with a high degree of reduction and low sheet stacking were obtained using ascrobic acid as the reducing agent. The preparation of Ag-rGO nanocomposites were successfully investigated by hydrothermal synthesis. Hydrothermal method plays an important role in reduction of graphene oxide to rGO. Ag+ contributed to restoring of sp^2 structure of rGO. Effect of chemical doping treatment after finishing the hydrothermal process, the conductivity of Ag-rGO nanocomposites (30mM, 50mM, 70mM) is enhanced 97.5 %, 121.53 % and 189.52 % (1.9 times, 2.2 times and 2.8 times) than the GO film. The graphene (Ag-rGO composite) is a promising material to improve the electrical conductivity for electronic devices such as supercapacitor electrodes, memory devices.

Acknowledgements

The authors greatly indebted to Professor Dr Khin Khin Win, Head of Department of Physics, University of Yangon, for her kind permission to carry out this work.

References

B. Galindo, S. G. Alcolea, J. Gómez, A. Navas, A. O. Murguialday, M. P. Fernandez and R. C. Puelles, (2014) "Effect of the number of layers of graphene on the electrical properties of TPU polymers." Materials Science and Engineering, vol. 64, pp. 1-6.

B. Li, T. Liu, Y. Wangand, Z. Wang, (2012), Journal of colloid and interface science, vol. 377, p. 114.

D. B. Farmer, R. G. Mojarad, V. Perebeinos, Y. M. Lin, G. S. Tulevski, J. C. Tsang and P. Avouris, (2009) "Chemical doping and electron-hole conduction asymmetry in graphene devices." Nano Lett. vol. 9, pp. 388.

F. M. Smits, (1958) "Measurement of sheet resistivities with the four-point probe." Bell Syst. Tech. J, vol. 37, pp. 711-718.

I. K. Moon, J. Lee, R. S. Ruoff and H. Lee, (2010) "Reduced graphene oxide by chemical graphitization." Nature Communications, vol. 1, pp. 1-6.

J. Zhao, (2019) "Solution-Processable Conductive Graphene-Based Materials for Flexible Electronics." Faculty of Science and Technology, 1799, pp. 65.

L. Panbo, H. Ying, W. Lei, (2013) Mater Lett, vol. 97, pp. 173-175.

M. F. Khan, M. Z. Iqbal, M. W. Iqbal and J. Eom, (2014) "Improving the electrical properties of graphene layers by chemical doping" Science and Technology of advance Materials, Korea, vol. 15, pp. 1-8.

R. Rajeswari, H. G. Prabu and Dr. M. Amutha, (2017) "One pot hydrothermal synthesis characterizations of silver nanoparticles on reduced graphene oxide for its enhanced antibacterial and antioxidant properties." Journal of Applied Chemistry, India, vol. 10, pp. 64-69.

R. D. Dreyer, S. Murali, Y. Zhu, R. S. Ruoff and C. W. Bielawski, (2010), Journal of Materials Chemistry.

STRUCTURAL ANALYSIS OF LAYERS OF PEROVSKITE SOLAR CELL BY USING SMARTLAB X-ray DIFFRACTOMETER

Hsan Htoo[1], Thiri Htet[2], Ye Chan[3]

Abstract

X-ray structure and crystallite size of fabricated layers of perovskite solar cell were investigated. The first layer, compact TiO_2 layer was deposited using a spray pyrolysis method. The structure TiO_2 is tetragonal and crystallite size of first TiO_2 layer is 43.20 nm. The second mesoporous TiO_2 was deposited by screen printing of TiO_2 slurry and the crystallite size is 53.10 nm. The third ZrO_2 space layer was printed on the top of the TiO_2 layer using ZrO_2 paste and the crystallite size is 33.26 nm. The structure of ZrO_2 is monoclinic. Then, a carbon counter electrode was coated on the top of the ZrO_2 layer by printing carbon slurry and the crystallite size is 27.00 nm. The $CH_3NH_3PbI_3$ perovskite layer was prepared by two-step solution method. The unit cell structure is tetragonal and the crystallite sizes lie between 22.30 nm to 27.40 nm. From XRD results, the lattice constants of $CH_3NH_3PbI_3$ are 8.86 Å and 12.66 Å. The bond distances among the atoms of perovskite layer are 2.66 Å at Pb1-I1, 3.15 Å at Pb1-I2 and 1.13 Å at C1-N1.

Keywords: perovskite, crystallite size, lattice parameter, bond distance

Introduction

In crystallography, crystal structure is a description of the ordered arrangement of atoms, ions or molecules in a crystalline material. Ordered structures occur from the intrinsic nature of the constituent particles to form symmetric patterns that repeat along the principal directions of three-dimensional space in matter. The smallest group of particles in the material that constitutes this repeating pattern is the unit cell of the structure. The unit cell completely reflects the symmetry and structure of the entire crystal, which is built up by repetitive translation of the unit cell along its principal axes. The translation vectors define the nodes of the Bravais lattice. The lengths of the principal axes, or edges, of the unit cell and the angles between them are the lattice constants, also called *lattice parameters* or *cell parameters*. The symmetry properties of the crystal are described by the concept of space groups. All possible symmetric arrangements of particles in three-dimensional space may be described by the 230 space groups. The crystal structure and symmetry play a critical role in determining many physical properties, such as cleavage, electronic band structure, and optical transparency.

Solar cells with a perovskite structure have high conversion efficiencies and stability as the organic solar cells. Since a photoconversion efficiency of 15% was achieved, higher efficiencies have been reported for various device structures and processes, and the photoconversion efficiency was increased up to 19.3%. The photovoltaic properties of solar cells are strongly dependent on the fabrication process, hole transport layers, electron transport layers, nanoporous layers, interfacial microstructures, and crystal structures of the perovskite compounds. Especially, the crystal structures of the perovskite-type compounds, strongly affect the electronic structures such as energy band gaps and carrier transport, and a detailed analysis of them is mandatory. The organic–inorganic hybrid perovskite materials such as $CH_3NH_3PbI_3$ can improve the solar conversion efficiency of DSCs (dye-sensitized solar cell). Several groups have

---

[1] Lecturer, Department of Physics (Attached URC), University of Yangon
[2] Department of Physics, Dagon University
[3] Universities' Research Centre, University of Yangon

shown that the perovskite morphologies such as the grain size and crystallinity highly affect the performance of solar cells [1]. Therefore, understanding the structures and crystallite size of these prototype light harvesters is important for the molecular design of organic–inorganic perovskite materials with defined properties. Each Pb^{2+} cation was coordinated to six I^- anions to form $[PbI_6]$ octahedral. These $[PbI_6]$ are corner connected to each other forming a three-dimensional Pb–I framework. Each $CH_3NH_3^+$ cation locates at the centre of four $[PbI_6]$ octahedra. Thus, each cation interacts with twelve I^- anions. The symmetry and structure of $CH_3NH_3PbI_3$ crystals are highly dependent on the temperature. In this study, the crystallite size of layers of perovskite solar cell will be analysis at different temperatures.

Materials and Method

2.1 Materials

The materials fluorine-doped tin oxide (FTO) galss, titanium dioxide (TiO_2), zirconium oxide (ZrO_2), graphite, methyl ammonium iodide (MAI) (98% Sigma-Aldrich), lead II iodide (PbI_2), hydrochloric acid (HCL), ethanol, isopropanol, acetylacetone, acetic acid, acetonitrile, ethylene glycol and dimethyl formamide (DMF) were used in this research.

2.2 Experimental Procedure

2.2.1 Preparation of compact and mesoporous TiO_2 films (Electron Transporting Layer)

4g of TiO_2 powder, 40 ml of ethanol and 20 ml of distilled water were mixed in the beaker. Then it was continuously stirred by magnetic stirrer at 70°C for 2 h. Thereafter, TiO_2 solution was deposited onto the glass substrate by spray pyrolysis method for compact layer.

TiO_2 paste for mesoporous layer was prepared by addition of few 10-20 ml of ethanol to the TiO_2 powder and continuously stirred by a magnetic stirrer to until the desired paste is formed. Then TiO_2 mesoporous layer was printed on TiO_2 fine layer by using screen printing method.

2.2.2 Preparation of ZrO_2 film (Space layer)

2 g of ZrO_2 powder was mixed with 20 ml of ethanol and 2 ml of isopropanol in the beaker. Then the solution was stirred by magnetic stirrer at 70°C to make a viscous paste for screen printing on the mesoporous TiO_2 layer.

2.2.3 Preparation of graphite layer (Counter Electrode –CE)

2g of graphite powder, acetylacetone, acetic acid, acetonitrile, ethylene glycol 1.5 ml each were ground by using motor and pestle for 3h to form a paste for blade coating (doctor blading) method.

2.2.4 Making the perovskite precursor solution

In the case of the inter-diffusion reaction (sequential deposition) of the inorganic and organic precusors, the PbI_2 precursor is dissolved in dimethylformamide (DMF) (400 mg/ ml) and stirred at 70° C for 30 minutes. CH_3NH_3I precursor is dissolved in isopropanol (IPA) at a concentration of 10 mg/ ml.

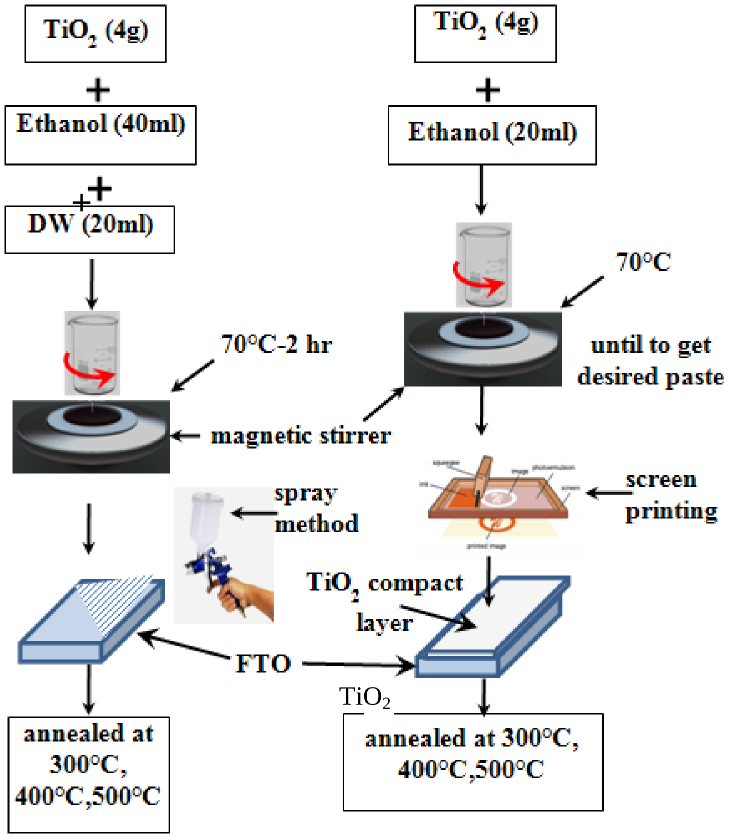

Figure 1 Preparation of compact TiO_2 & mesoporous TiO_2 films

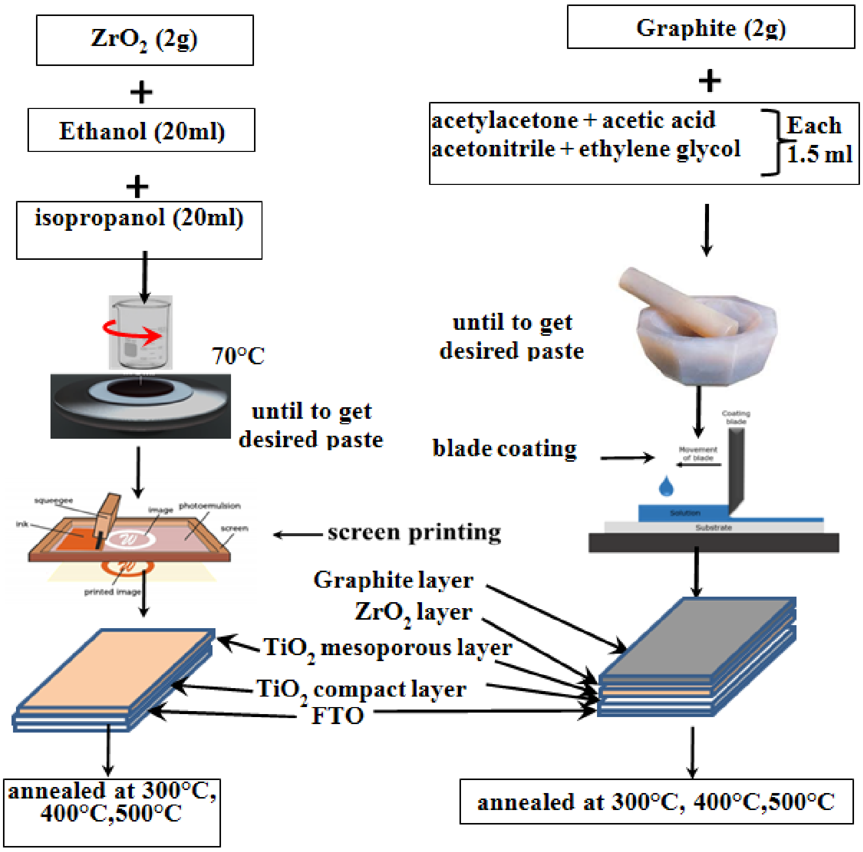

Figure 2 Preparation of ZrO_2 & Graphite films

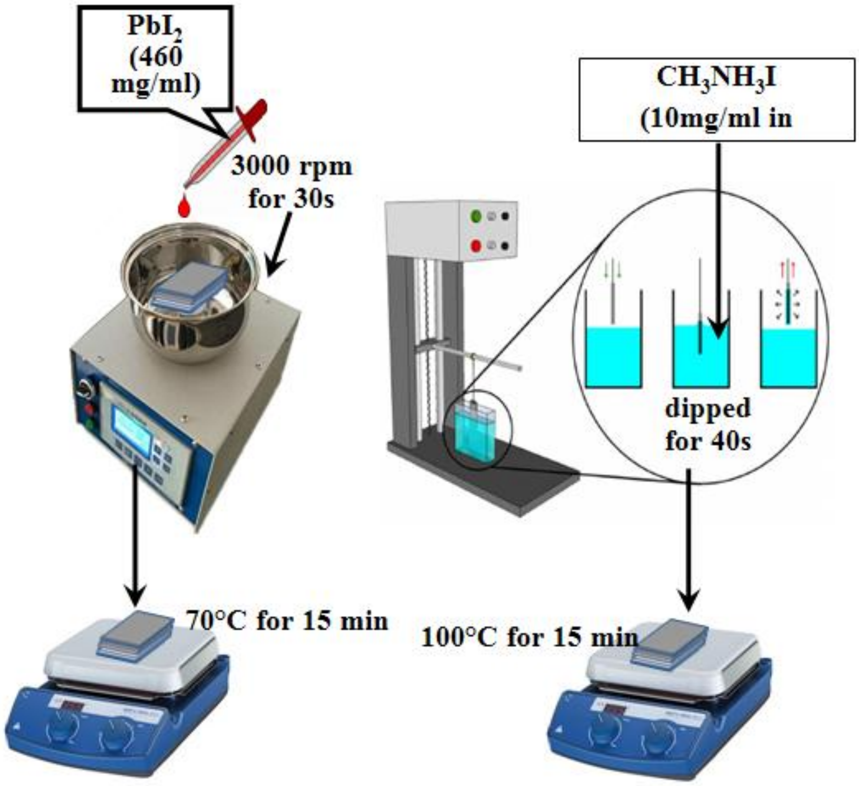

Figure 3 Preparation of perovskite films

2.3 Fabrication of Photovoltaic Devices

The (FTO) coated glass substrates were cleaned by soaking in the mix solution of HCl and distilled water (1:10 ratio) for 30 minutes. And then it was rinsed in DI water and dried in room temperature. After that, the substrates were coated with compact TiO_2 layer by aerosol spray pyrolysis and annealed at 300 °C, 400°C and 500°C for 30 minutes respectively. After that the mesoporous TiO_2 layer was deposited on top of the compact layer by screen printing and sintered at 300°C, 400°C and 500°C for 30 minutes respectively. Followed, ZrO_2 space layer was printed by screen printing and the films were sintered at 300°C, 400°C and 500°C for 30 minutes respectively. After cooling down, graphite CE was prepared by doctor-blade coating on the ZrO_2 space layer and followed by heating at 300°C, 400°C and 500°C for 30 minutes respectively. To prepare $CH_3NH_3PbI_3$ perovskite films, the PbI_2 solution (460 mg/ml in DMF) was spin coated on the mesoporous graphite layer at 3000 rpm for 30 s and dried at 70°C for 15 minutes. Then the substrates were dipped into CH_3NH_3I solution (10 mg/ml in isopropanol) for 40s. After that, it was heated for 15 minutes at 100º C on a hot plate. During the procedure, the coated electrode changed color from light yellow to dark brown, indicating the formation of the perovskite film.

X-ray Data Collection and Characterization

XRD data collection was carried out using SmartLab X-ray diffractometer. As an X-ray source, Cu-Kα radiations were used with the X-ray power of 50kV × 40 mA. The detector was semiconductor detector. All measurements were performed by a 2θ scan method. The range of 2θ in which intensity data were collected was between 10˚ to 70˚.

The structures of crystals and molecules are often being identified using x-ray diffraction studies, which are explained by Bragg's Law. The law explains the relationship between an x-ray light shooting into and its reflection off from crystal surface. The Bragg's law states that when the x-ray is incident onto a crystal surface, its angle of incidence, θ, will reflect back with a same angle of scattering, θ. And, when the path difference, d is equal to a whole number, n, of wavelength, a constructive interference will occur. Knowing the wavelength and the diffraction angle of a reflection, its resolution *d* can be easily calculated:

$$d= 1/2(n\lambda/ \sin\theta)$$

This is just a reformulation of the famous Bragg equation $n\lambda= 2d \sin\theta$.

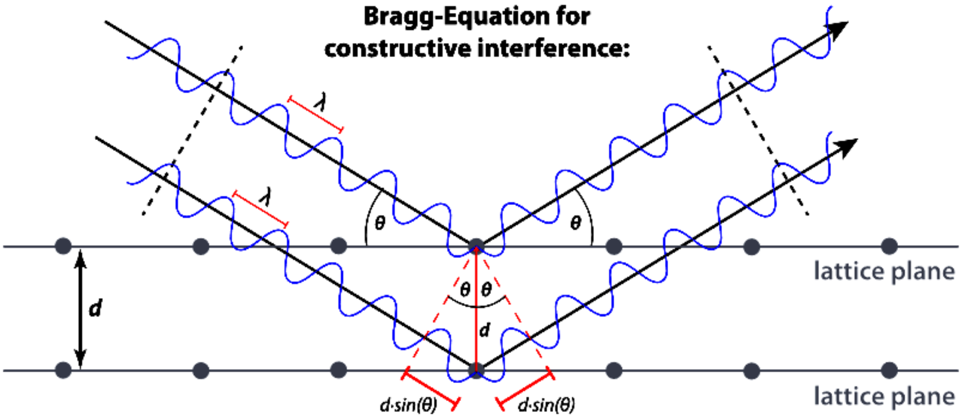

Figure 4 Bragg-Equation for Constructive Interference

The structural analysis of perovskite layer was performed using Smart Lab Studio II software. The crystallite size of solar cell layers were carried out by using the Debye-Scherrer formula.

$$D = \frac{0.9\ \lambda}{B \cos\theta}$$

Where, D = Crystallite size (nm)

λ = the wavelength of X-ray used (1.54056 Å)

B = Full Width Half Maximum of dominant peak (radian)

θ = Angle of diffraction (radian)

The interplanar spacing d between (h k l) lattice planes for seven crystal system are can be calculated by using following formulae.

Cubic:

$$\frac{1}{d^2} = \frac{h^2 + k^2 + l^2}{a^2}$$

Tetragonal:

$$\frac{1}{d^2}=\frac{h^2+k^2}{a^2}+\frac{l^2}{c^2}$$

Hexagonal:

$$\frac{1}{d^2}=\frac{4}{3}\left(\frac{h^2+hk+k^2}{a^2}\right)+\frac{l^2}{c^2}$$

Rhombohedral:

$$\frac{1}{d^2}=\frac{(h^2+k^2+l^2)\sin^2\alpha+2(hk+kl+hl)(\cos^2\alpha-\cos\alpha)}{\alpha^2(1-3\cos^2\alpha+2\cos^3\alpha)}$$

Orthorhombic:

$$\frac{1}{d^2}=\frac{h^2}{a^2}+\frac{k^2}{b^2}+\frac{l^2}{c^2}$$

Monoclinic:

$$\frac{1}{d^2}=\left(\frac{h^2}{a^2}+\frac{k^2\sin^2\beta}{b^2}+\frac{l^2}{c^2}-\frac{2hl\cos\beta}{ac}\right)\frac{1}{\sin^2\beta}$$

Triclinic:

$$\frac{1}{d^2}=\frac{\frac{h^2}{a^2}\sin^2\alpha+\frac{k^2}{b^2}\sin^2\beta+\frac{l^2}{c^2}\sin^2\gamma+\frac{2kl}{bc}(\cos\beta\cos\gamma-\cos\alpha)+\frac{2hl}{ac}(\cos\gamma\cos\alpha-\cos\beta)+\frac{2hk}{ab}(\cos\alpha\cos\beta-\cos\gamma)}{1-\cos^2\alpha-\cos^2\beta-\cos^2\gamma+2\cos\alpha\cos\beta\cos\gamma}$$

Results and Discussion

4.1 TiO_2 compact layers

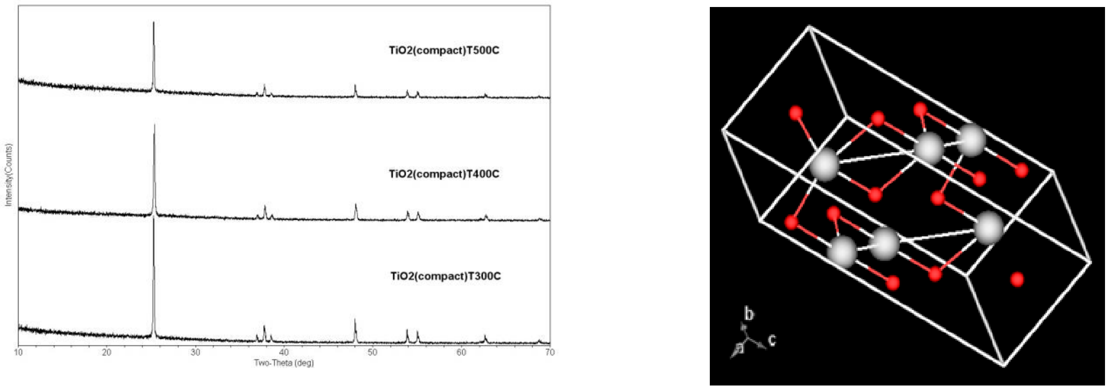

(a)

(b)

Figure 5 (a) XRD patterns of TiO_2 (compact) films at different temperatures (b) Unit cell structure of TiO_2

Table 1 The average crystallize size and lattice parameter of compact TiO_2 at 300˚C, 400˚C, 500˚C

No.	**Temperature (˚C)**	**Lattice constant (Å)**		**Crystallize size (nm)**	
		a	**c**	**XRD**	**Calculation**
1.	300	3.79	9.51	78.10	57.40
2.	400	3.77	9.55	50.40	43.20
3.	500	3.79	9.52	65.00	50.40

The XRD spectrum of compact TiO_2 layer at temperature 300°C, 400°C and 500°C were indicated in Fig.5.(a). The diffracted peaks are (101), (103), (004), (112), (200), (105), (211), (213), (204) and (116). All peaks were well matched with those of the standard JCPDS library file of anatase TiO_2. XRD patterns indicate that the crystal structures of TiO_2 were tetragonal structure. The crystallize size and lattice constant of compact TiO_2 at 300°C, 400°C and 500°C were tabulated in Table 1.

4.2 Mesoporous TiO_2 Layer

The crystallize size and lattice constant of mesoporous TiO_2 at 300°C, 400°C and 500°C were tabulated in Table 2.

Table 2 The average crystallize size and lattice parameter of mesoporous TiO_2 at 300˚C, 400˚C, 500˚C

No.	**Temperature (˚C)**	**Lattice constant (Å)**		**Crystallize size (nm)**	
		a	**c**	**XRD**	**Calculation**
1.	300	3.79	9.51	68.60	53.10
2.	400	3.78	9.52	71.40	53.90
3.	500	3.80	9.51	70.90	54.30

4.3 ZrO_2 space layers

XRD pattern of ZrO_2 layers for temperature of 300°C, 400°C and 500°C were shown in Fig.6. (a). From the XRD results, the crystal structures of ZrO_2 layers were monoclinic. The crystallize sizes and lattice constant were tabulated in Table 3.

Table 3 The average crystallize size and lattice parameter of ZrO_2 at 300˚C, 400˚C, 500˚C

No.	Temperature (˚C)	Lattice constant (Å)			Crystallize size (nm)	
		a	b	c	XRD	Calculation
1.	300	5.19	5.21	5.36	41.82	35.46
2.	400	5.16	5.21	5.35	36.58	33.26
3.	500	5.17	5.21	5.33	44.32	38.78

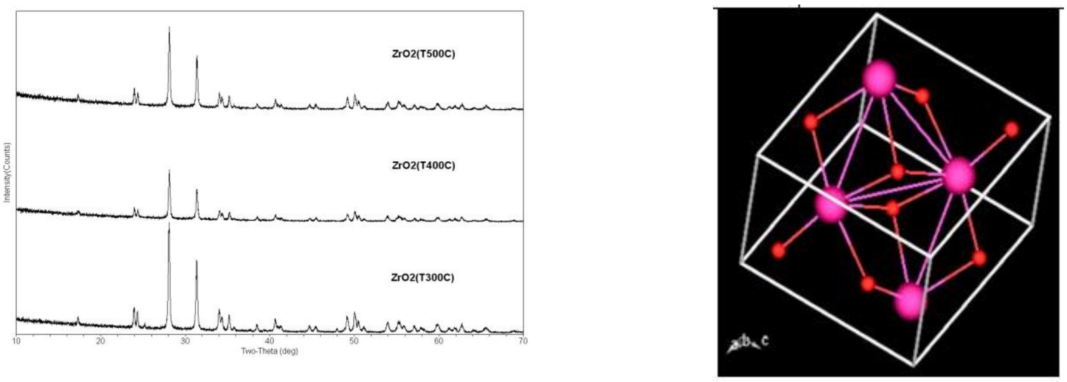

(a) (b)

Figure 6 (a) XRD patterns of ZrO_2 (space layers) at different temperatures
(b) Unit cell structure of ZrO_2

4.4 Graphite layer (CE)

Fig.7. (a) showed the XRD profile of graphite layer at 300°C, 400°C and 500°C and unit cell structure. XRD patterns indicate that the crystal structures of graphite layers were hexagonal. The crystallize size and lattice constant of graphite at 300°C, 400°C and 500°C were tabulated in Table 4.

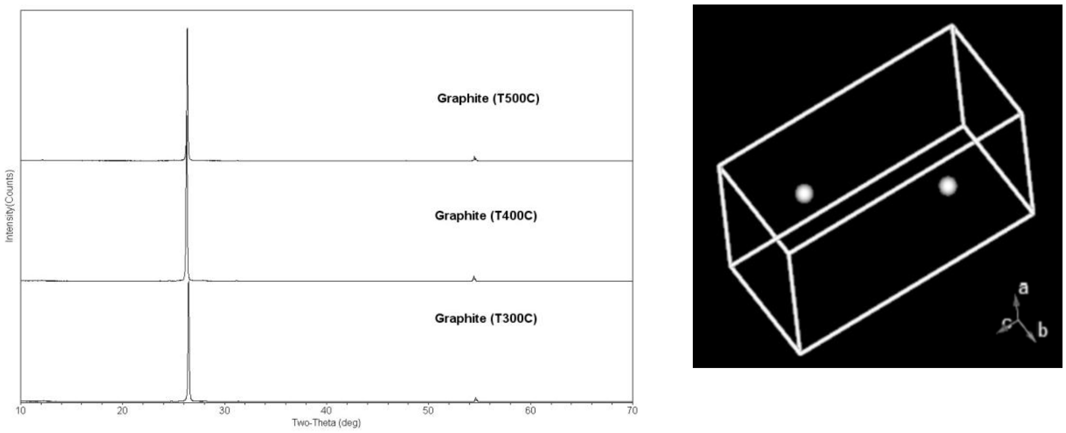

(a) (b)

Figure 7(a)XRD patterns of graphite layer at different temperatures
(b) Unit cell structure of graphite

Table 4 The average crystallize size and lattice parameter of carbon layers at 300˚C, 400˚C, 500˚C

No.	Temperature (˚C)	Lattice constant (Å)		Crystallize size (nm)	
		a	c	XRD	Calculation
1.	300	2.46	6.73	41.40	33.60
2.	400	2.46	6.77	51.64	39.72
3.	500	2.46	6.75	28.80	27.00

4.5 Perovskite layer

In this work, a two-step spin coating method was used for the preparation of the $CH_3NH_3PbI_3$ perovskite layers. The XRD patterns of perovskite layers are as follow.

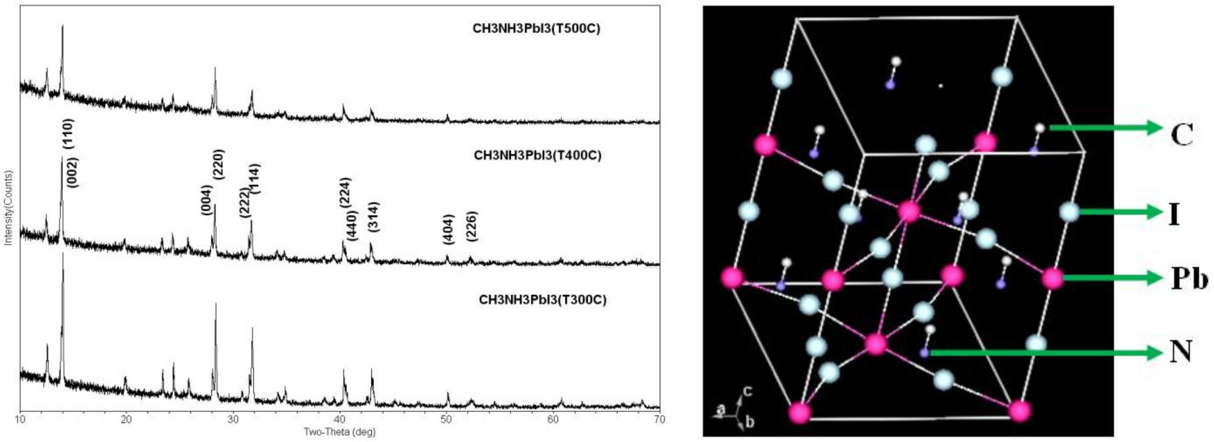

(a) (b)

Figure 8 (a) XRD patterns of perovskite layer at different temperatures (b) Unit cell structure of perovskite

Table 5 The average crystallize size and lattice parameter of perovskite layers at 300˚C, 400˚C, 500˚C

No.	Temperature (˚C)	Lattice constant (Å)		Crystallize size (nm)	
		a	c	XRD	Calculation
1.	300	8.89	12.66	26.8	24.9
2.	400	8.89	12.66	30.0	27.4
3.	500	8.86	12.66	23.4	22.3

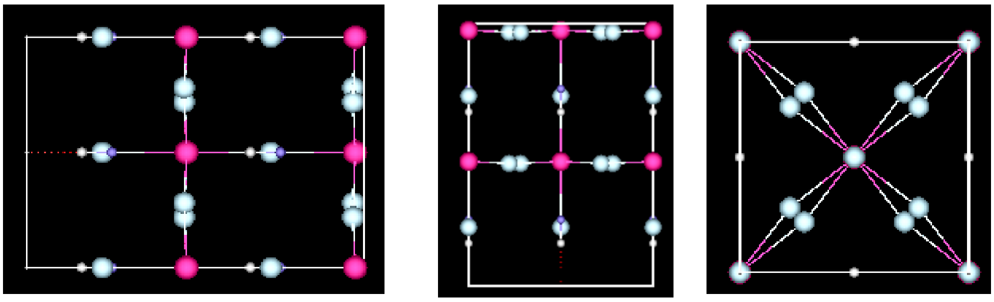

(a) (b) (c)

Figure 9 Unit cell structure of $CH_3NH_3PbI_3$ with view direction at (a) "**a**",(b) "**b**" (c) "**c**"

XRD pattern of $CH_3NH_3PbI_3$ layers for temperature of 300°C, 400°C and 500°C was shown in Fig.8. (a) Dominant peaks of (110), (004), (220), (114), (224), (400), (404) occur at diffraction angles of 13.957˚, 19.96˚, 23.339˚, 31.711˚, 40.298˚, 40.744˚, 50.045˚. The other peaks were PbI_2. The crystallize size and lattice constant were tabulated in Table 4. From the XRD results, the crystal structure of $CH_3NH_3PbI_3$ layer was tetragonal.

Structural Analysis for $CH_3NH_3PbI_3$ Perovskite Layer

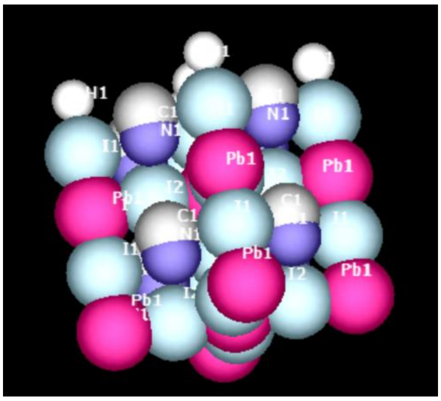

Figure 10 Space Filling Structure

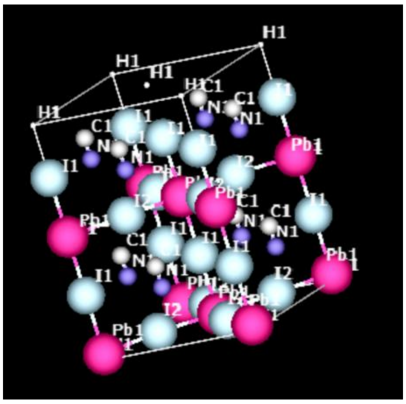

Figure 11 Ball & Stick Style

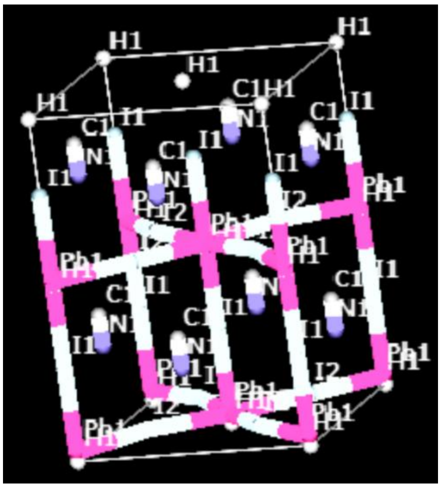

Figure 12 Cylinder Style

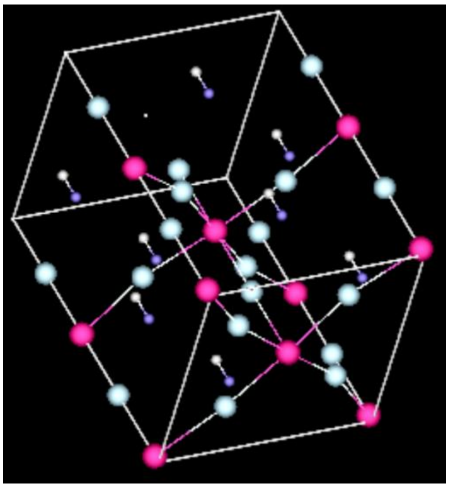

Figure 13 Line Style

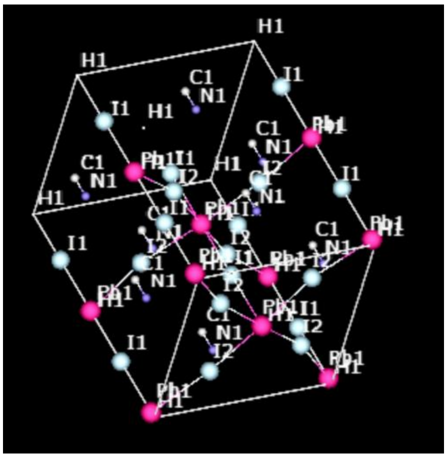

Figure 14 Marker Style

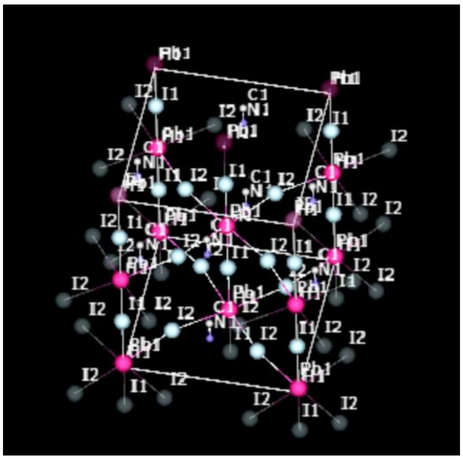

Figure 15 Expanding Style

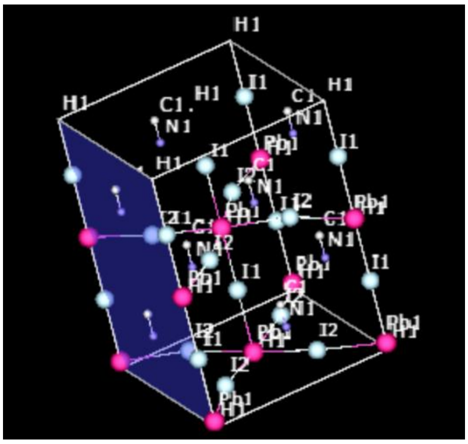

Figure 16 (100) plane

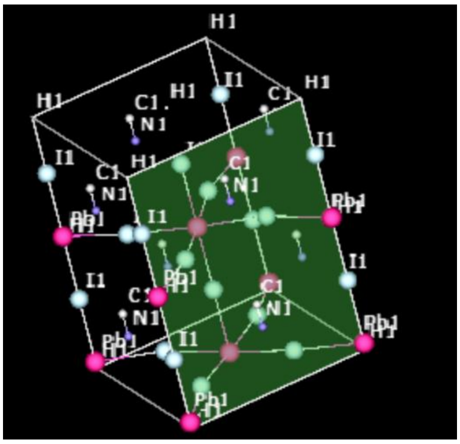

Figure 17 (010) plane

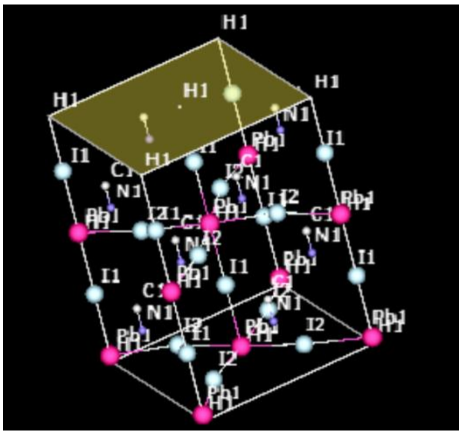

Figure 18 (001) plane

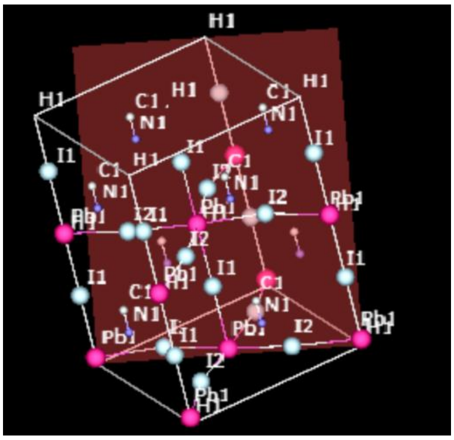

Figure 19 (111) plane

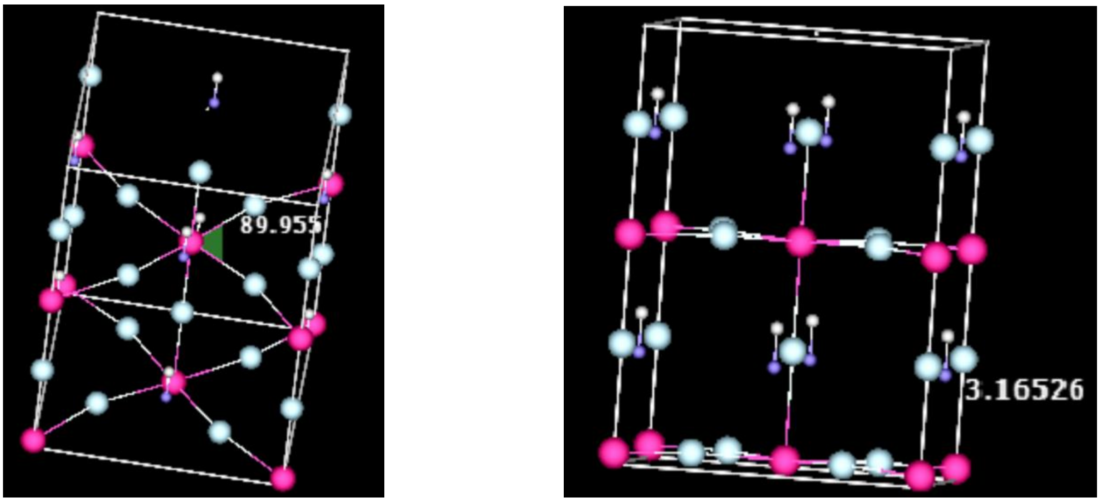

Figure 20 Determination of bond distance between atoms and angle between bond lengths

In this research, hole transporting layer free perovskite solar cell with graphite counter electrode was successfully fabricated by infiltrating of $CH_3NH_3PbI_3$ which consists of four layers including compact TiO_2, mesoporous TiO_2, ZrO_2 and graphite layers. The perovskite layer was deposited by two-step deposition technique. The energy band gap of the methyl ammonium lead iodide perovskite layers are 1.5 eV, 1.48 eV, 1.42 eV at different temperatures 500˚C, 300˚C and 400˚C with crystallize sizes of 23.41 nm, 26.75 nm and 30 nm. It was found that the highest energy band gap value can get at 500 ˚C and smallest crystallize size was 23.41 nm. From XRD results, the lattice constants of $CH_3NH_3PbI_3$ are 8.86 Å and 12.66 Å. The bond distances among the atoms of perovskite layer are 2.66 Å at Pb1-I1, 3.15 Å at Pb1-I2 and 1.13 Å at C1-N1.

Acknowledgements

I would like to thanks Professor Dr Ye Chan, Professor and Head, Universities' Research Centre, University of Yangon, for his kind permission to carry out this work.

References

K. P. Ong, T. W. Goh, Q. Xu and A. Huan, J. Phys. Chem. A, (2015)

R. K. Singh, R. Kumar, N. Jain, J. Singh and S. K. Mishra, AIP Conference Proceedings, (2018)

W. Geng,C. Tong, J. Liu, W. Zhu, W. Lau, and L. Liu, Sci Rep. (2016) 6

T. Baikie, Y. Fang, J. M. Kadro, M. Schreyer, F. Wei, S. G. Mhaisalkar, Grätzel, M. & Whitec, T. J. (2013). Journal of Materials Chemistry A, Vol. 1, pp. 5628–5641

F. Hao, C. C. Stoumpos, D. H. Cao, R. P. H. Chang, and M. G. Kanatzidis (2014), Vol. 8, pp. 489-494.

Y. Kawamura, H. Mashiyama, and K. Hasebe, (2002). Journal of the Physical Society of Japan, Vol. 71, pp.1694–1697.

H. Mashiyama, Y. Kurihara, and T. Azetsu, (1998), Journal of the Korean Physical Society, Vol. 32, pp. S156–S158

https://en.wikipedia.org/wiki/crystal_structure

J. Myanmar Acad. Arts Sci. 2020 **Vol. XVIII.No.2A**

ACOUSTIC ABSORPTION PROPERTIES OF FIVE KINDS OF MYANMAR WOOD

Myo Aung[1], Ei Shwe Sin Oo[2] & Ye Chan[3]

Abstract

The acoustic absorption property is commonly used to characterize and rank of the materials to reduce noise. The purpose of this research is to study the sound absorption coefficient of five kinds of Myanmar wood such as Pyinkado (Xylia xylocarpa Taub.), Teak (Tectona grandis), Kanyin (Dipterocarpus), Rubber (Hevea brasiliensis) and Pine (Pinus sp. L.). The experimental investigation of sound absorption coefficient was conducted based on one microphone impedance tube method for the working frequency ranging from 100 Hz to 2600 Hz. The morphology of test wood samples is characterized by optical microscope. The results show that the sound absorption coefficient of five kinds of wood samples depend on the number of vessel as well as vessel diameter and teak wood has better sound absorption coefficient in comparison with others.

Keywords: Myanmar wood, one microphone impedance tube, sound absorption coefficient

Introduction

Pollution affects the ecosystem of the planet causes discomfort to almost every living organism on it. Typically, there are several types of pollution, which are: air pollution, water pollution, noise pollution, and land pollution which come from different sources and have different consequences. Among other pollutions, noise pollution is also dangerous for human and nature; it causes damaging the ability to hear, damaging to liver, brain and heart, leading to emotional and behavioral stress. Noise pollution is coming from many sources: household sources, social events, commercial and industrial activities, and transportations.

Moreover, use of loudspeakers in the religious affairs, festivals and charity has become a nuisance in our city. Therefore, controlling sound source and using sound-absorbing materials are also the most effective and practical way to reduce unwanted noise in the sound environment like public buildings, offices, shopping centers or dining spaces (Shen, M. H. & Lai, R. P., 2011). Wood is well known for its acoustic quality in various musical instruments and is also suited as sound absorber or sound diffuser (Smardzewski, J., & Batko, W., 2014).

The most important acoustic parameter for reducing unwanted noise is sound absorption coefficient. The term "noise" is unwanted sound judged to be unpleasant, loud or disruptive to hear. There are two basic methods of measuring sound absorption. The first method comprises the use of a reverberation room giving results valid for random incidence in a diffuse sound field and is suitable for large objects, furniture, panels, etc. The second method comprises the use of an impedance tube, giving results valid for normal incidence in a plane wave sound field, which is suitable for testing small samples (Nandanwar, A., 2017). In this study, impedance tube is constructed according to ISO 10534:1 and 10534:2 regulations and it was used in measuring sound absorption coefficient of wood.

Although there is a plenty of sound absorption information for commercial construction materials, there is a lack of data related to acoustic properties of wood and wood based panel

---

[1] Lecturer, Universities' Research Centre, University of Yangon

[2] Assistant Lecturer, Department of Engineering Physics, Technological University of Mawlamyine

[3] Professor and Head, Universities' Research Centre, University of Yangon

products. Negro F. (Negro, F., Cremonini, C., Properzi M., & Zanuttini R., 2010) studied sound absorption coefficient of perforated plywood by the impedance tube (Kundt's tube) method. He found that the absorption properties of perforated plywood depending on the cavity thickness at their back. Jayamani E. et al. (Jayamani, E., et al., 2013) presented sound absorption coefficients of four types of Malaysian wood with two microphone impedance tube method. They found that the sound absorption coefficient depends on the frequency of the sound which strikes material and density of materials.

The current research focuses on the sound absorption properties of Myanmar wood samples commonly used in the building construction and furniture. The test wood materials were prepared in circular shape by using CNC machine. Then, one microphone impedance tube was designed and constructed by one microphone impedance tube method. In this research, Myanmar wood samples are investigated for sound absorption coefficient measurement at the frequency ranging from 100 Hz to 2600 Hz.

Preparation of Wood Sample for Sound Absorption Measurement

The Myanmar wood samples (such as Pyinkado, Teak, Kanyin, Rubber and Pine) were used to investigate the sound absorption coefficient using one microphone impedance tube method. These test materials were prepared according to the sample holder of one microphone impedance tube method. These test materials were 1.5 cm thick and cut it into circular shape with diameter of 8.8 cm using a computer numerical control (CNC) milling cutter machine as shown in Figure 1. It was ensured that the sample was fit slung into the impedance tube which is not loosely in order to avoid the space between its edge and the sample holder.

(a) (b)

Figure 1 (a) Preparation of wood material by using CNC milling cutting machine
(b) Wood materials (1) Pyinkado, (2) Teak, (3) Kanyin, (4) Rubber and (5) Pine

Impedance Tube Theory

The acoustic impedance tube is a common experimental apparatus that is used to measure the acoustic absorption coefficient and acoustic impedance of a porous sound absorbing material according to the theory of the standing wave. The standing wave is generated by the superposition of the incident and reflected sound waves in the impedance tube. Acoustic impedance tube employs a sound source and specially placed microphones to measure the acoustic properties of a material that is placed inside of the tube. This standard describes two methods: (a) standing wave ratio method (with one moving microphone) and (b) transfer function method (with two microphones).

The impedance tube method was developed with ISO 10534-2, ASTM E-1050 as reference which describes the two-microphone method or the transfer function method for measuring the sound absorption coefficient of acoustical materials. This test method can be applied to measure sound absorption coefficient of absorptive materials at normal incidence. Normal incidence sound absorption coefficients are useful in basic research and product development of sound absorptive materials like polyurethane foam. This method is quite useful in situations where the material being tested in placed in cavities just like the present case of impedance tube.

This study is a technique to use one fixed microphone instead of two microphones, which is similar to transfer function method. The benefit of using one fixed microphone is that there is no calibration required since the same microphone is being used through the entire test. This method involves the use of impedance tube, data acquisition board, the microphone and the sound source speaker.

Standing Wave Ratio Method

One of the earliest forms of acoustic impedance tube is used to measure properties for the calculation of acoustic properties of materials by measuring the standing wave ratio (SWR). A typical SWR tube is depicted in Figure 2. The SWR tube has a speaker on one end of the tube with a test specimen on the other end. The speaker produces a single frequency sinusoidal tone, which forms plane waves as it travels down the tube. This is the incident pressure wave that is designated in Figure 2 as P_i. In this Figure, the arrow points in the direction that the wave travels. The sound waves travels through the specimen causing some of the sound to be absorbed and some to be reflected. This is the reflective pressure wave that is designated in Figure 2 as P_r, where the arrow points the direction of the speaker. A standing wave is formed by the combination of the traveling incident and reflected waves. This wave is denoted in Figure 2 as the line between the two maximum dotted lines. The pressure inside the tube is measured using a microphone probe by moving the microphone probe further inside the tube in an attempt to discover the minima and maxima of the standing wave. Once the maximum and minimum pressures are found, their corresponding values were recorded so that the standing wave ratio could be calculated.

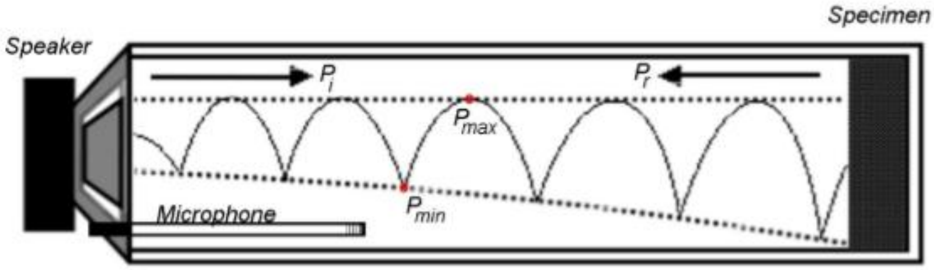

Figure 2 SWR Impedance Tube with a standing wave created by the incident and reflective Pressure waves

$$SWR = \frac{P_{max}}{P_{min}} \qquad \cdots\cdots\cdots (1)$$

P_i and P_r (depicted in Figure 2) are the pressures of the incident and reflective waves, respectively. Although the incident and reflective pressure waves cannot be directly measured by the microphone, the sum and difference between them can be. This is done by measuring the maximum and minimum points on the standing wave. Then, using this ratio, the acoustic reflection coefficient can be calculated. The underlying process is described in the equation

$$\mathrm{R} = \frac{[\mathrm{SWR}-1]}{[\,\mathrm{SWR}+1]} \qquad \cdots\cdots\cdots (2)$$

Using the reflection coefficient, the absorption coefficient α can be calculated as

$$\propto = 1 - |R|^2 \qquad \cdots\cdots\cdots (3)$$

The absorption coefficient is then used to calculate the specific acoustic impedance, z as

$$\mathrm{z} = \frac{(1+\mathrm{R})}{(1-\mathrm{R})} \qquad \cdots\cdots\cdots (4)$$

Transfer Function Method

Like the standing wave ratio method, the transfer function method consists of a tube with a speaker at one end and a test sample at the other. Instead of using a microphone probe, two microphones are located along the tube at known distances between each other and the surface of the specimen. A specimen of material is placed in a sample holder and mounted at the other end of the speaker. The transfer function H_{12} can be measured between two microphones. From these transfer function H_{12}, the reflection coefficient of sound pressure of the material (R) is defined as

$$R = \frac{\mathrm{e}^{-\mathrm{j}k\mathrm{x}_2} - \mathrm{H}_{12}\mathrm{e}^{-\mathrm{j}k\mathrm{x}_1}}{\mathrm{H}_{12}\mathrm{e}^{-\mathrm{j}k\mathrm{x}_1} - \mathrm{e}^{-\mathrm{j}k\mathrm{x}_2}} \qquad \cdots\cdots\cdots (5)$$

where x_1 is the distance from the specimen face to microphone 1, x_2 is the distance from the specimen face to microphone 2.

From the reflection coefficient, the specific impedance ratio can be calculated.

$$\frac{\mathrm{Z}}{\rho\mathrm{c}} = \frac{1+\mathrm{R}}{1-\mathrm{R}} \qquad \cdots\cdots\cdots (6)$$

The absorption coefficient (α) of the material is defined as follow

$$\alpha = 1 - |\mathrm{R}|^2 \qquad \cdots\cdots\cdots (7)$$

One Microphone Impedance Tube Method

The ISO 10534-2 standards also describe a technique to use one microphone instead of two microphones. This method can also be said to be equivalent to removing one of the two microphones in the Transfer Function Method. The sketch of impedance tube with one microphone is shown in Figure 3, where the same impedance tube is used in Transfer Function Method, but one microphone is used to measure the sound pressure value. For this method a test is performed with the same microphone in each of the two microphone locations. The benefit of using one microphone is that there is no calibration required since the same microphone is used through the entire test. This technique can be performed using two different techniques. One is with fixed microphone locations and the other is with variable microphone locations. The fixed location will be studied because it can be used with the two microphone impedance tube. The other would require a different tube entirely. The sound at the two locations needs to be recorded sequentially with a sound source that is unchanging. It is recommended to use a deterministic signal as the sound source. Then the Fourier transform can be used to measure the frequency response.

The sound pressure in the tube with one fixed microphone can be expressed as

$$p(x,\omega,t) = p_i(\omega,t)e^{-ikx} + p_r(\omega,t)e^{ikx} \qquad \cdots\cdots\cdots (8)$$

where k is the wave number which is equal to$2\pi f$ /c, ω is angular frequency which is equal to $2\pi f$.

The acoustic impedance can be calculated by the following equation

$$z = \frac{p(x,\omega)\cos kl - i\rho c v \sin k(l-x)}{\rho c v \cos k(l-x) - i p(x,\omega)\sin kl} \qquad \cdots\cdots\cdots (9)$$

The specific acoustic impedance ratio can be expressed as

$$\frac{Z}{\rho c} = \frac{p(x,\omega)\cos kl - i\rho c v \sin k(l-x)}{\rho c v \cos k(l-x) - i p(x,\omega)\sin kl} \qquad \cdots\cdots\cdots (10)$$

The reflection factor (R) can be solved as

$$R = \frac{\frac{Z}{\rho c}-1}{\frac{Z}{\rho c}+1} = \frac{\frac{p(x,\omega)\cos kl - i\rho c v \sin k(l-x)}{\rho c v \cos k(l-x) - i p(x,\omega)\sin kl}-1}{\frac{p(x,\omega)\cos kl - i\rho c v \sin k(l-x)}{\rho c v \cos k(l-x) - i p(x,\omega)\sin kl}+1} \qquad \cdots\cdots\cdots (11)$$

where l is the length of the tube, x is the distance between sample and microphone, ρ is the air density and c is the velocity of sound.

The sound absorption coefficient (α) can be calculated as follows:

$$\alpha = 1 - \left|\frac{\frac{p(x,\omega)\cos kl - i\rho c v \sin k(l-x)}{\rho c v \cos k(l-x) - i p(x,\omega)\sin kl}-1}{\frac{p(x,\omega)\cos kl - i\rho c v \sin k(l-x)}{\rho c v \cos k(l-x) - i p(x,\omega)\sin kl}+1}\right|^2 \qquad \cdots\cdots\cdots (12)$$

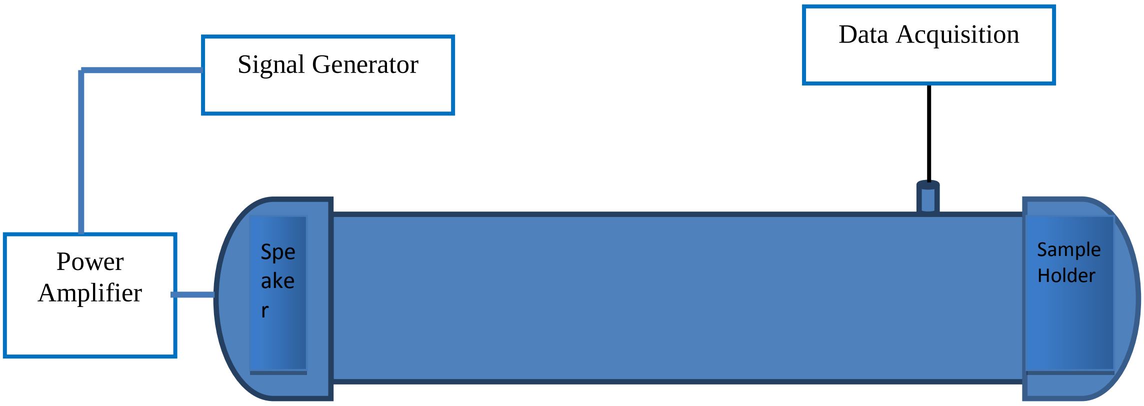

Figure 3 Schematic of impedance tube with one fixed microphone

Experimental Procedure

The experimental setup includes a computer, a data acquisition board, a speaker and a ¼ inch electret condenser microphone as shown in Figure 4. The loudspeaker was turned on for 10 minutes before starting the measurements (ISO 10534-2 recommendation) allowing temperature stabilization. An appropriate speaker was selected and it was placed at one end of the tube and the signal was fed to the speaker with the help of data acquisition board. The speaker was positioned in a column PVC pipe at the left end of impedance tube. The speaker was connected to the AUDIO OUT channel of NI myDAQ (National Instruments data acquisition device). In order to reduce the cost of the setup, electret condenser microphone is used in this research. It is omnidirectional microphone of very inexpensive and smaller in size. Microphone is sealed to the hole drilled in the PVC pipe and placed at the other end of the impedance tube. The microphone was connected to the AUDIO IN channel of the NI myDAQ board. The speaker was driven by NI myDAQ as the signal generator and the microphone captured the standing wave which was the superposition of incident and reflected wave from the test sample. The signal from the microphone can be acquired and can be written in the spreadsheet with the help of LABVIEW. The block diagram design in measuring sound pressure using NI myDAQ with LabVIEW programming is illustrated in Figure 5. The block diagram of data acquisition is depicted in Figure 6. Moreover, temperature of the surrounding had to be maintained constant throughout the experiment. The sample with diameter equal to that of impedance tube was placed above the surface of the rigid plate which was in the sample holder. Once the microphone response was recorded, the desired acoustic property was calculated in Matlab (Matrix Laboratory). In this research, material was analyzed at the frequency ranging from 100 Hz to 2000 Hz.

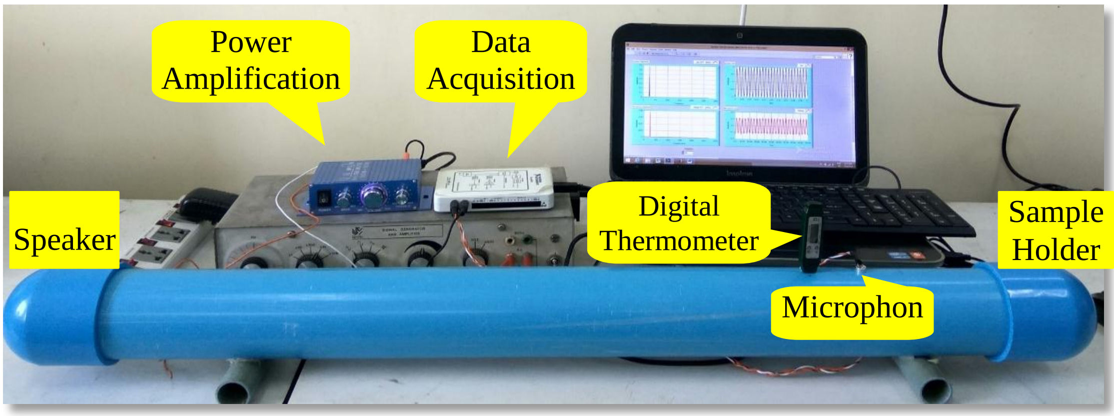

Figure 4 Experimental setup of impedance tube

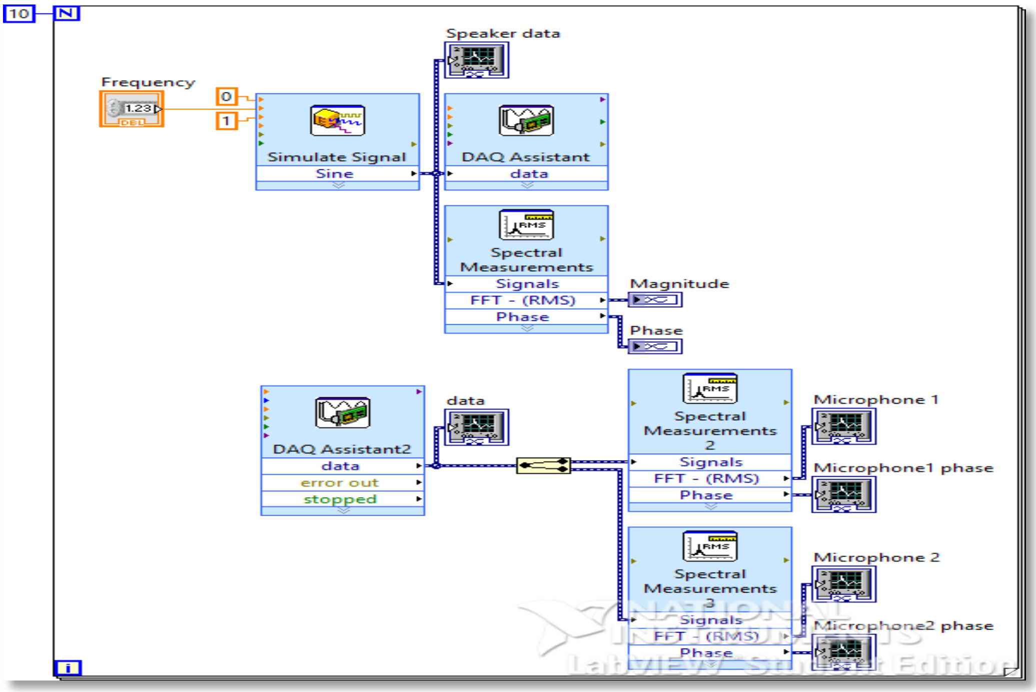

Figure 5 Block diagram design in measuring sound pressure of microphone

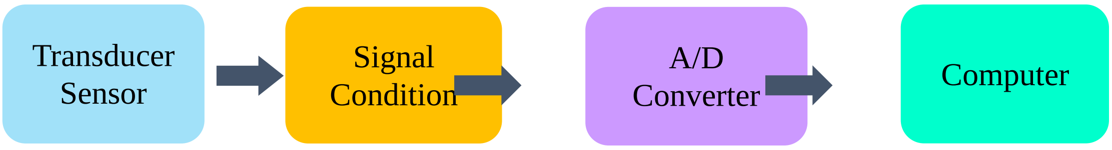

Figure 6 Block diagram of data acquisition

Results and Discussion

Sound Absorption Coefficient Measurement

The sound absorption coefficient measurement was carried out using one microphone impedance tube method. First, the data measured by commercial impedance tube (assume as standard tube) was compared with the data obtained from constructed impedance tube for the same glass sample. The sound absorption coefficient of glass which was measured by standard impedance tube and the value measured by the constructed tube are shown in Figure 7. The absorption coefficient of glass measured by constructed tube is much higher than that of the standard value in the frequency of 125 Hz and 250 Hz. On gradually increasing the frequencies, the sound absorption value obtained by constructed tube is closely matched with the standard value at the frequencies of 500 Hz and 1000 Hz. According to the validation results, we have confidence to use the constructed device.

The sound absorption coefficients of Myanmar wood samples obtained from this experiment are illustrated in Figure 8. According to the experimental result, the peak values of absorption coefficients of wood samples are found at 200 Hz, 800 Hz and 1100 Hz. Among them, acoustic absorption coefficient is maximum at frequency of 200 Hz. Low frequency noise, the frequency range from about 10 Hz to 200 Hz, has been recognized as a special environmental noise problem, particularly to sensitive people in their homes. At frequency about 200 Hz, the sound absorption coefficient is 0.1058 for Pyinkado, 0.1072 for Teak, 0.1048 for Kanyin, 0.1053 for Rubber and 0.1030 for Pine wood respectively. Teak wood has better absorption of sound compare with others at frequency of 200 Hz, 800 Hz and 1100 Hz. Therefore, the sound absorption can be changed with frequency of incident sound.

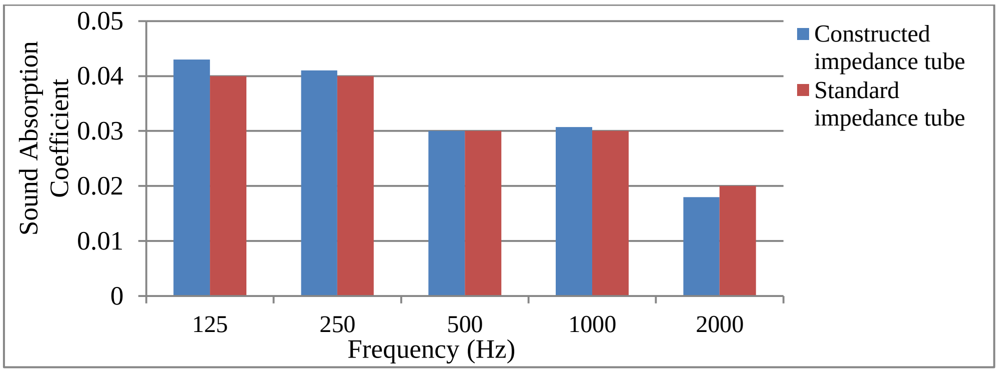

Figure 7 Comparison of sound absorption coefficient of glass using standard impedance tube and constructed impedance tube

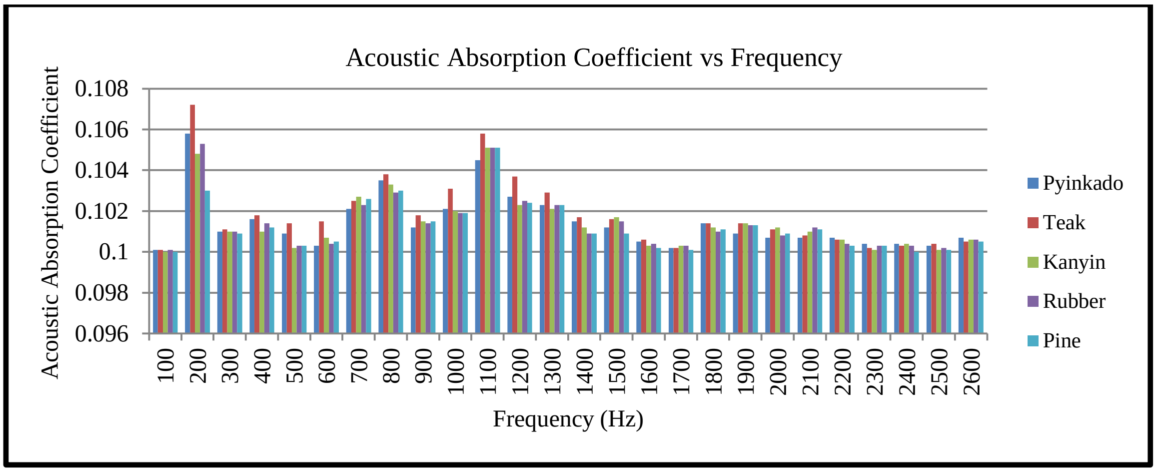

Figure 8 Comparison of acoustic absorption coefficient of Myanmar wood samples

Morphology Analysis

The morphologies of Myanmar wood samples were characterized by optical microscopy as shown in Figure 9. The number of vessels and vessel diameter of Myanmar wood samples are illustrated in Table 1. According to the measurement results, the sound absorption coefficient of wood samples depends on the density of vessel as well as vessel diameter of the sample.

Table 1 The number of vessels of Myanmar wood Samples

Samples	Pyinkado	Teak	Kanyin	Rubber	Pine
No. of vessels	261	345	139	65	Nill
Diameter of vessel	8.25 µm	3.5 µm	11.1 µm	140.06 µm	Nill

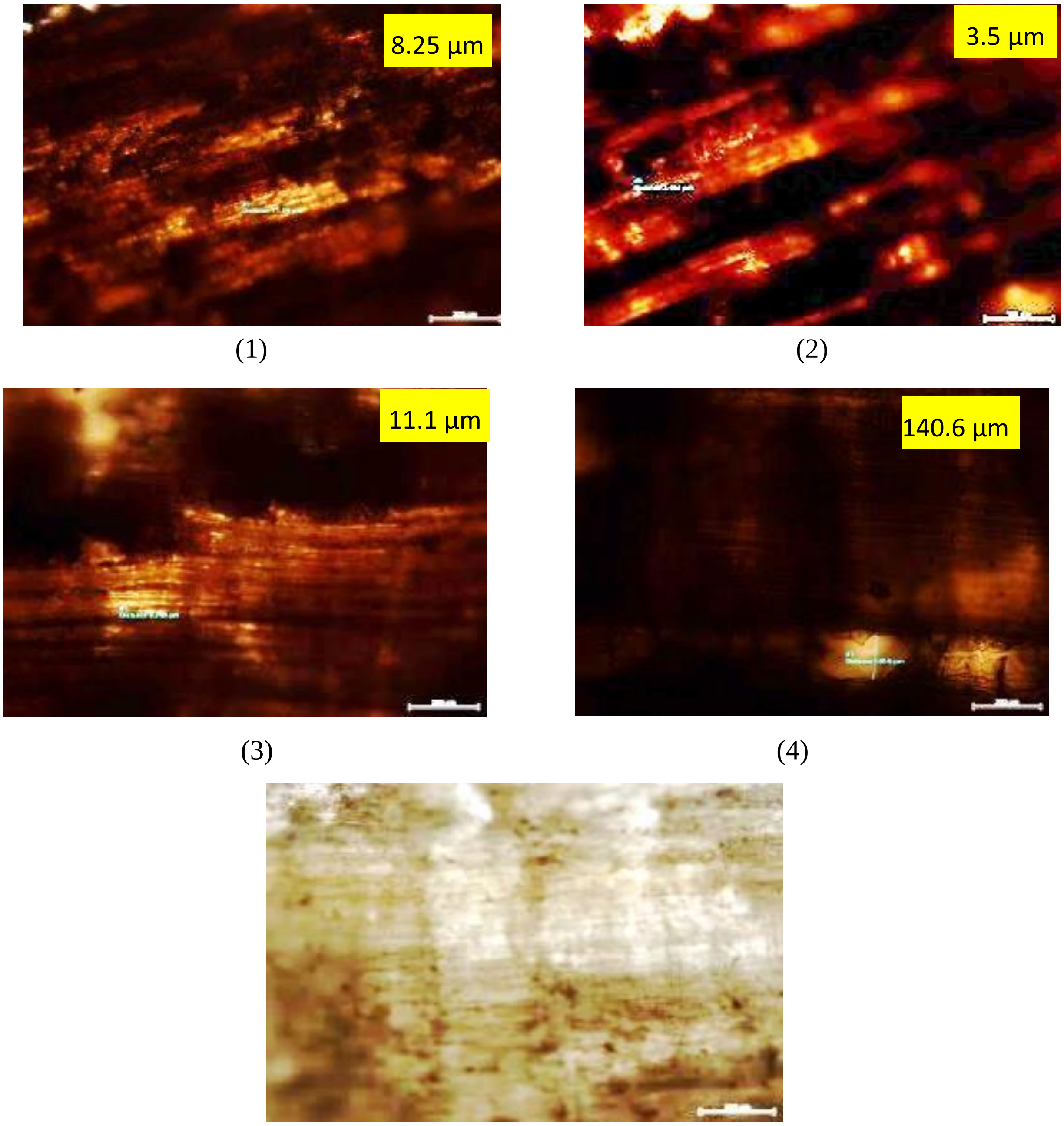

(1) (2)

(3) (4)

(5)

Figure 9 Optical microscope image of Myanmar wood (1) Pyinkado, (2) Teak, (3) Kanyin, (4) Rubber and (5) Pine

Conclusion

The sound absorption coefficients of five kinds of Myanmar wood such as Pyinkado, Teak, Kanyin, Rubber and Pine wood were investigated by one microphone impedance tube method. According to the experimental results, the sound absorption coefficients of wood samples are maximum at frequencies of 200 Hz, 800 Hz and 1100 Hz. Among them, Teak wood has better sound absorption coefficient in comparison with others. It can be concluded that the sound absorption coefficient of wood samples depends on the number of vessels as well as vessel diameter. Therefore, Teak wood has better quality than others not only in its durability, water resistance and beautiful texture but also in noise reduction properties to use as decorated material in building and furniture.

Acknowledgement

The authors are grateful to Dr Khin Khin Win, Professor and Head of the Department of Physics, University of Yangon for her kind permission to carry out this work.

References

Guan, Q., (2015), "*Analysis of Acoustic Damping in Duct Terminated by Porous Absorption Materials Based on Analytical Models and Finite Element Simulations*", New Jersey

H. G. Leventhall, (2004), "Low frequency noise and annoyance, Noise Health", *Journal of Noise and Health*", vol.6, No.23, pp. 59-72

Jayamani, E., Hamdan S., & N. B. Suid, (2013), ''Experimental determination of Sound Absorption Coefficients of Four types of Malaysian Wood'', *Journal of Applied Mechanics and Materials*, vol. 315, pp. 577-581

Nandanwar, A., (2017), ''Influence of Density on Sound Absorption Coefficient of Fiber Board'', Indian Plywood Industries Research and Training Institute, *Open Journal of Acoustics*, vol.07, No.01

Negro, F., Cremonini, C., Properzi M., & Zanuttini R., (2010), ''Sound Absorption Coefficient of Perforated Plywood: An Experimental Case Study'', *World Conference on Timber Engineering*, vol. III, pp. 587-588

Shen, M. H. & Lai, R. P., (2011), ''*Investigation on Sound Scattering Performances of Wooden and Bamboo Diffusers*'', Taiwan

Smardzewski, J., & Batko, W., (2014), "Experimental study of wood acoustic absorption Characteristics**"**, vol.68, No.4, pp. 467–476

J. Myanmar Acad. Arts Sci. 2020 **Vol. XVIII.No.2A**

ANALYSIS OF ELEMENTAL CONCENTRATION OF THE HOT SPRING SAMPLES FROM PEDAT, KLONEHTAR AND MAUNGMAGAN IN TANINTHARYI REGION BY USING EDXRF AND AAS METHODS

Nyunt Nyunt Htay[1], Pwint Phyu Phyu Myint[2], Aye Thidar Phyo[2]

Abstract

Hot spring samples were collected from Pedat, Klonehtar and Maungmagan in Tanintharyi Region. These samples were quantitative analysed of the concentration of elements by using Energy Dispersive X-Ray Fluorescence (EDXRF) and the Atomic Absorption Spectroscopy (AAS) Methods. It was found that the content of the concentration of elements in these samples are S, Ca, Na, K, Mg, Si, Al and Fe. These elements are not toxic for human. It was observed that extend of elements categorized in above three locations are different by using EDXRF and AAS methods.

Keywords: Pedat, Klonehtar and Maungmagan hot springs in Tanintharyi Region, EDXRF and AAS, effects of bathing in hot springs

Introduction

Natural hot springs were found in many countries and make a significant contribution to health, wellness and recreational tourism. As an alternative health source natural hot springs have the profound benefit of being reasonably independent and attracts visitors all year round. A high awareness about therapeutics value of natural hot springs due to their mineral content is common throughout the related literature. In many European countries, as medical treatment based on natural hot springs is integrated into the respective health system and supported by the medical profession based on clinical studies and success rates. Government policies and regulations in countries such as Japan, Germany or Taiwan indicate strongly that natural hot springs are an important part of the national health system and provide evidence for their role in health wellness and recreational uses. The use of hot springs for medical treatment is probably as old as mankind and is a common practice in several countries for treatments such as hydrotherapy and balneotherapy. Hydrotherapy involves the use of common water, whereas balneotherapy employs natural mineral water either in a spa or not. (Samet J M *et al* 2000)

Figure 1 Maungmagan Hot Springs (Maungmagan Village, Launglone Township, Tanintharyi Region)

---

[1] Dr, Associate Professor ,Physics Department, Dawei University

[2] Assistant Lecturer, Physics Department, Dawei University

Figure 2 Klonehtar Hot Springs (Klonehtar Village, Yayphyu Township, Tanintharyi Region)

Figure 3 Pedat Hot Springs (Pedat Village, Thayetchaung Township, Tanintharyi Region)

Sample collection and sample preparation

Sample Collection

Hot springs are numerous in Myanmar and for centuries the Myanmar people have enjoyed in hot spring bathing. So, the hot spring waters were chosen from three different locations in Tanintharyi Region, such as Maungmagan hot springs, Klonehtar hot springs and Pedat hot springs.Hot spring waters from three locations were collected in different temperatures. The temperature of Maungmagan hot spring is about 52°C, as far as 10 miles from Dawei city, Klonehtar hot spring is about 48°C as far as 22 miles from Dawei city and Pedat hot spring is about 90°C, as far as 67 miles from Dawei city.

Sample Preparation

Hot Spring samples (waters and sands) were collected from Maungmagan, Klonehtar and Pedat. One litre of water from each hot spring were measured to find the content of the concentration of elements by using Atomic Absorption Spectroscopy (AAS) method, shown in Figure 4. Then 5 g of sand from each hot spring were measured to find the content of the relative concentration of elements by using Energy Dispersive X-Ray Fluorescence (EDXRF) method, shown in Figure 5.

Figure 4 Hot Spring waters in Maungmagan, Klonehtar and Pedat

Figure 5 Sands in Maungmagan, Klonehtar and Pedat Hot Springs

Results and Discussion

The Concentration of S, Ca, Na, K and Mg contained in hot spring waters by using AAS method

Table 1.Results of elemental concentration in Maungmagan Hot Spring (water)

Elements	Concentration (mg/L)
S	31.3
Ca	96.15
Na	36.99
K	223.3
Mg	0.64

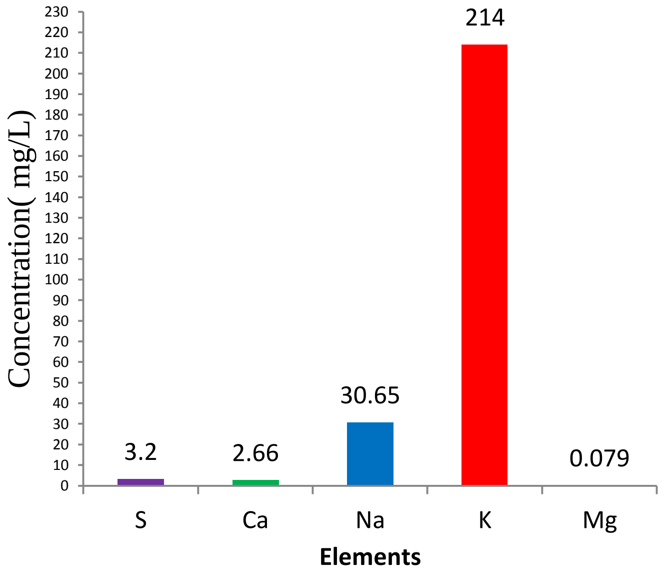

Figure 6 The concentration of elements in Maungmagan Hot Spring

Table 2 Results of elemental concentration in Klonehtar Hot Spring (water)

Elements	Concentration (mg/L)
S	3.2
Ca	2.66
Na	30.65
K	214.0
Mg	0.079

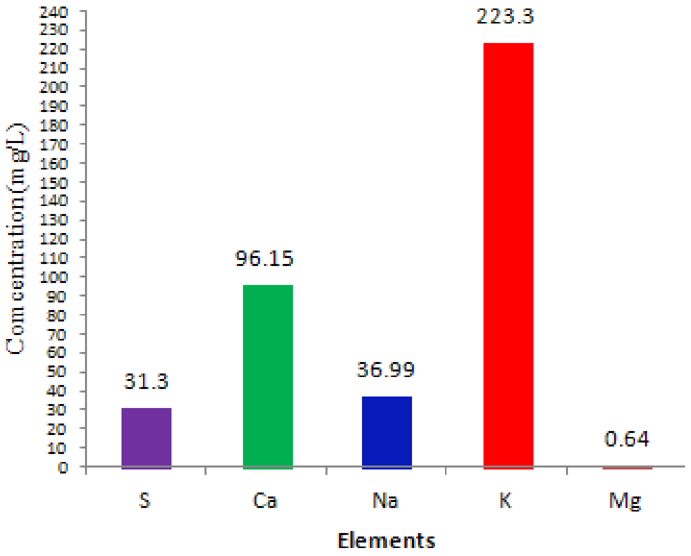

Figure 7 The concentration of elements in Klonehtar Hot Spring

Table 3 **Results of elemental concentration in Pedat Hot Spring (water)**

Elements	**Concentration (mg/L)**
S	4.2
Ca	-
Na	32.69
K	213.3
Mg	0.041

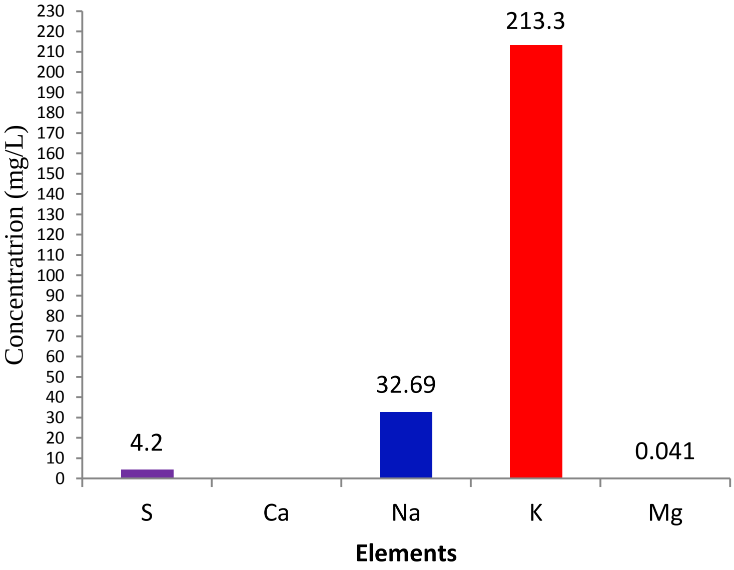

Figure 8 The concentration of elements in Pedat Hot Spring

Table 4 **The comparison of the concentration of S, Ca, Na, The K and Mg in Maungmagan, Klonehtar and Pedat Hot Springs (waters)**

Locations	**S(mg/L)**	**Ca(mg/L)**	**Na(mg/L)**	**K(mg/L)**	**Mg(mg/L)**
Maungmagan	31.3	96.15	36.99	223.3	0.64
Klonehtar	3.2	2.66	30.65	214.0	0.079
Pedat	4.2	-	32.69	213.3	0.041

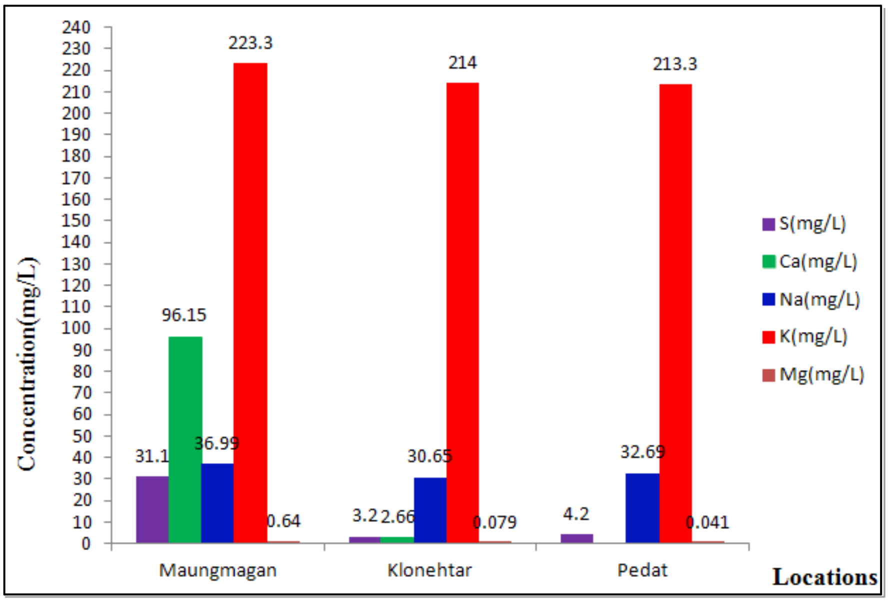

Figure 9 The comparison of the concentration of S, Ca, Na, The K and Mg in three locations

The relative concentration of Si, Al, Fe, K, Ca and S contained in Maungmagan, Klonehtar and Pedat Hot Springs

Table 5 Results of elemental concentration in Maungmagan Hot Spring (sand)

Elements	Relative Concentration (%)
Si	10.636
Al	-
Fe	0.135
K	0.255
Ca	0.368
S	0.284

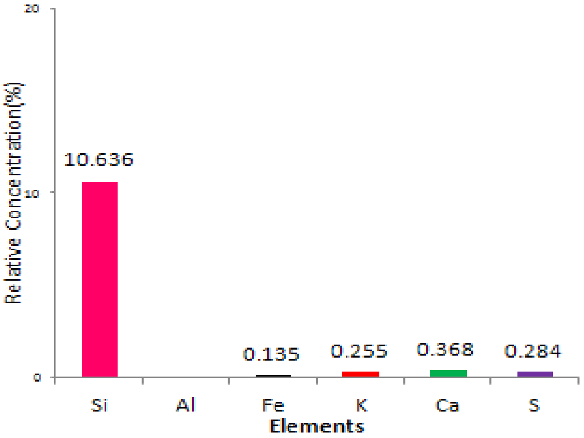

Figure 10 The concentration of elements in Maungmagan Hot Spring

Table 6 Results of elemental concentration in Klonehtar Hot Spring (sand)

Elements	**Relative Concentration (%)**
Si	18.970
Al	6.848
Fe	1.377
K	0.982
Ca	0.924
S	-

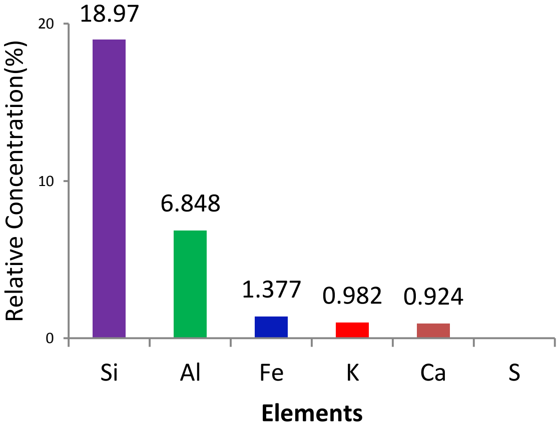

Figure 11 The concentration of elements in Klonehtar Hot Spring

Table 7 Results of elemental concentration in Pedat Hot Spring (sand)

Elements	Relative Concentration (%)
Si	13.458
Al	4.874
Fe	1.768
Ca	1.653
K	1.616
S	-

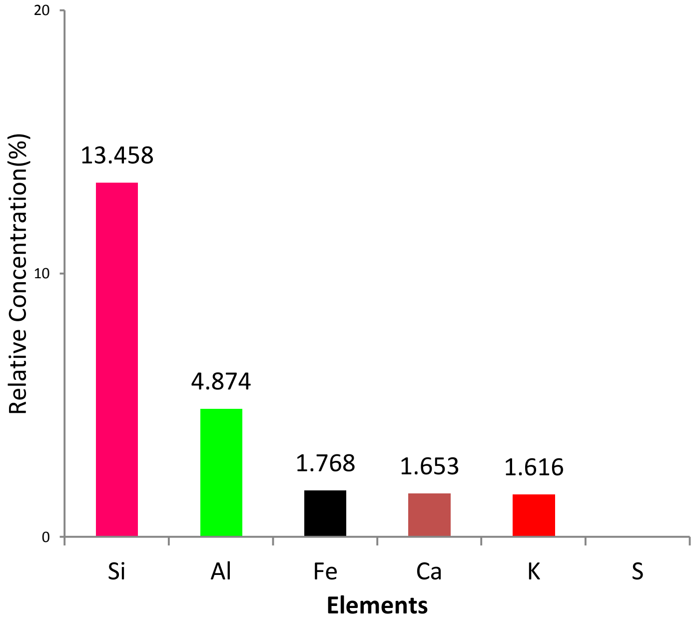

Figure 12 The concentration of elements in Pedat Hot Spring

Health effects of Sulfur (S)

This element helps to product body against toxins in the environment. Alleviates from taking soothe and pain while bathing in hot sulphur springs. Also it gives to lower cholesterol and blood pressure. Soaking in sulphur water get an effective way to relieve the burning, pain, itching and hemorrhoids. Sulfur works with vitamins B1 and B5 to promote metabolism and communication between nerve cells. Every body needs sulfur because it is the most concentrated in keratin which gives strong hairs, nails and skins. So bathing in sulfur springs benefits bronchus to expand, making airways open and improving lung ventilation. Also help boost metabolism, relieve metabolism, reduce depression and anxiety and cure insomnia. (J Peters & K Aberams 2003)

Health effects of Calcium (Ca)

Helps good circulation in the body, numerous positive impact and lower blood pressure. Body weight reduces when bathing in the hot springs contain with calcium. Also released in stress-induced, relaxation and control the heart beats. An excess (too much) of deficiency (not enough) of calcium, can change the biorhythm of the heart and cause serious problems.(Booth A & Camacho P 2013)

Health effects of Sodium (Na)

Taking a bath in hot springs contain with sodium, relieve stress and muscles feel. Bathing in hot springs contain with sodium to keep the skin hydrated, cure irritation and balanced the level of oil skin. Also to remove dead skin cells, become calmer and energized. (He J & Chen J, *et al* 2009)

Health effects of Potassium (K)

Bathing in Potassium hot springs treats many skin infections, including eczema, canker sores, dermatitis, acne and vaginal. Insufficient potassium intakes can increase blood pressure, kidney stone risk and often urine excretion. Potassium is one of the seven essential macrominerals. The humar body requires at least 100 milligrams of potassium daily to support key processes.(Black RB & Weiss Jo 1988)

Health effects of Magnesium (Mg)

Magnesium is one of the six essential macrominerals that comprise 99% of the body's mineral content. Magnesium helps build bones, enables nerves to function, and is essential to the production of energy from food. Magnesium has been shown to have therapeutic value in treating conditions such as headches, chromic pain, asthma and sleep disorders. Without the presence of magnesium in the body, energy could not be produced or used in the cells, muscle could not contract and relax. Magnesium helps maintain normal muscle and nerve function keeps heart rhythm steady, supports a healthy immune system and keeps bones strong. Also regulate blood sugar levels and promotes normal blood pressure. (Demmelmaier , 1.et al 2017)

Health effects of Silicon (Si)

Silicon concentrates in no particular organ of the body but is found mainly in connective tissues and skin. Silicon is non-toxic element. Silicon irritates the skin and eyes on contact more than long time. Inhalation will cause irritation to the lungs and redness. Reddening, scaling and itching are characteristics of skin inflammation. The human body contains approximately 7 grams of silicon, which is present in various tissues and body fluids.(Jugdaohsingh R & Anderson SH.2002)

Health effects of Alluminium (Al)

Alluminum is a very common component of the Earth's mineral composition. It is not essential element for life and a constituent of rather inert minerals. It has often been regarded as not presenting significant health harzard. Alluminum may contribute to the inception and advancement of Alzheimer's disease (AD) by causing excessive inflammatory activity within the brain and speeding the rate of brain aging.(Wafton, J.E 2009)

Health effects of Iron (Fe)

Bathing in iron (Fe) hot spring burns 140 calories per hour about the same as a craft beer, For maximum therapeutic benefit, doctors recommend soaking for 20 minutes at a time, combined with gentle stretches in the water. As bathing occurs, circulation and oxygen flow increases much like when exercises.(Fairbanks VF 1999)

Effects of bathing in hot springs

Bathing the including S, Na, Ca, Mg, K, Si, Al and Fe in hot springs water can get many benefits such as improve circulation, treat skin infection, reduce stress, detoxify boost immune system and provide low-impact cardio. Help blood circulation, hypertension, nervous imbalances and other osclerosis.

Sulfur is a mineral present in every cell of bodies and is used to make collagen, which keeps skins smooth and healthy. Hot springs are a rich source of S and its healing benefits include treating skin irritations and infections such as rashes and eczema. The high temperature of hot springs can increase heart rate and lower both diastolic andmean blood pressure. It does not safe to soak in hot water when pregnant. Hot water can raise body temperature to 38.9°C for 10 minutes triggering hyperthermia. Some studies reported that hyperthermia during the first four-six weeks of pregnancy increases the risk of neural tube defects brain and spinal cord damage in babies.

Reduce stress

Hot springs help body relax, which benefits many ascepts of health, including sleeping patterns and nutrient assimilations. The relaxation promoted by the heat and byoyancy of hot springs also helps increase the range of motion of muscles and joints, making the soaking beneficial for individuals recovering from suffering from rheumatoid arthritis. Bathing repeatedly in hot springs can help autonomic nervous system and normalize endocorine system as well as 'release toxins' in body through sweating. Cardio is an important part of any fitness routine. As heart rate rises during cardiovascular exercise, body is promped to burn more calories, energy and fat.

Conclusion

The Study Hot Spring areas lies in the Tanintharyi Region Maungmagan, Klonehtar and Pedat hot springs. It was found that the content of the concentration of elements S, Ca, Na, K and Mg in Maungmagan hot spring are more than in other two hot springs by using AAS method, shown in Table 4 and Figure 9. Also included the content of the concentration of Si, Al, Fe, Ca, K and S were found by using EDXRF method, shown in Table 5, 6, 7 and Figure 10, 11, 12. These elements are benefits for human body. Among three hot springs, Maungmagan hot spring is the most famous and popular in this region, also it is nearest from Maungmagan beach and Dawei city. It is not only for adolescent, young people, enjoyable but also the aged and apoplexy peoples befitting bastion hot spring. Maungmagan hot spring is the salty hot spring, it is very rare hot spring. So for above many reasons, Maungmagan hot spring is the best hot spring for healthy in Tanintharyi Region.

Acknowledgements

I would like to express appreciation to Rector Dr Theingi Shwe, Pro-rector Dr Khin May Aung and Pro-rector Dr Cho Cho Myint, Dawei University. I also would like to express my profound thanks to Professor Dr San San Aye, Head of Department of Physics and Professor Dr Khin Swe Oo, Department of Physics, Dawei University, for their kind and helps during this research.

References

Black RB &Weiss JO (1988): A Professional Partnership with Genetic Support Groups American Journal of Medical Genetics

Booth A & Camacho P (2013)A Closer look and calcium absorption and the benefits and risks of dietary versus supplemental calcium, Postgrad Med

De carvalho AM & Duarte Mc, (2015), Quality assessment of sulfurous thermal waters in the city of Pocos decaldas, Minas gerais, Brazil. Environ.

Demmelmaier ,1. et al .(2017). Pain rather than self-reported sedentary time explains variation in preserved National Academy of Science

Faga A , Nicoletti G & Gregotti C, (2012), Effects of thermal water on skin regeneration.

Fairbanks VF(1999) Iron in Medicine and Nutrition in Health and Disease.pp.193-221

He J & Chen J, et al. Gensalt (2009) Collaborative Research .Gender difference in blood pressure response to dietary sodium

J Peters & K Abrams (2003) Environment that are health effect of sulfur

Jugdaohsingh R & Anderson SH(2002) Dietary silicon intake and absorption . American Journal of Clinical Nutrition

Nirei H, Furuno K, (2010), eds. Medical Geology: A Regional Synthesis. New York.

Samet J M et al (2000); The National Movbiclity part II, Rea Rep Health Eff Inst 94, p 5-70

Tomaszewska B & Szczepanski A, (2014), Possibilities for the efficient utilization of spent geothermal waters.

Walton J.R(2009) Brain Lesions comprised of aluminum –rich cells that lack microtubules may be associated with the cognitive deficit of Alzheimer's disease , Neuro Toxicology

Zoller N & Valesky E, (2015) Impact of different waters an inflammation parameters in human keratinocyte Haca cells.

J. Myanmar Acad. Arts Sci. 2020 **Vol. XVIII.No.2A**

SYNTHESIS AND ANALYSIS OF CALCIUM COPPER TITANATE CERAMICS

Lwin Lwin Nwe[1]and, Ni Ni Shein[2]

Abstract

Calcium copper titanate ceramics were synthesized by solid-state reaction method. The structural and microstructural properties of sample powder were examined by X-ray diffraction (XRD) and scanning electron microscope (SEM). The capacitance, resistance and dissipated factor of ceramics were measured at frequency range 1 kHz to 25 kHz by LCR meter. The average dielectric constant, of ceramics (at 850˚C for 5h different heat treatment four times) were found to be 94.4,99.4,112.7 and 133.7 in the frequency range from 1kHz to 25kHz. The values of the dielectric loss and conductivity of samples were calculated.

Keywords: Ceramics, X-ray diffraction, SEM, Dielectric constant, Dielectric loss, Conductivity.

Introduction

High dielectric constant materials have numerous important applications in electric devices such as multilayer capacitors, dielectric resonators and capacitating material at microwave frequency, etc. In recent years, high dielectric ceramics had been developed for microelectronics (Marter. Su, 12, 2006). Titanates as members of perovskite structure family are widely used as ferroelectric materials with superior dielectric properties(Omar A. A. An , Abdelal2014).

The vast majority of a ferroelectric material is used commercially in the form of polycrystalline ceramics. Ferroelectric materials offer a wide range of useful properties for the electronic engineer to exploit the field .Ferroelectric mainly has two characteristics, asymmetry and high dielectric constants several ceramic materials with ferroelectric properties(N Tripathy, K C Das, S P Ghosh, G Bose and J P Kar .2016).

Ceramics can be made with different techniques. Out of then solid-state reaction technique have some advantages over other techniques such as low cost and good compositional homogeneity. The properties of materials largely depend on the method of preparation, method treatment and usually modified by the formation of the solution and doping with other additive oxides(K-H FELGNER, H.T.KAMMER.2001).

In this research, $CaCu_3Ti_4O_{12}$ powder was synthesized by the solid-state route. The structural properties of powder was carried out by X-ray diffraction. The microstructure of powder was examined by scanning electron microscope (SEM). The capacitive properties of ceramics were measured by LCR meter with varying frequencies. The high dielectric constant, dielectric loss and conductive of samples were calculated.

Sample Preparation

$CaCO_3$, TiO_2, and CuO were mixed by the stoichiometric formula. The mixture powder and acetone (100 ml) were milled by magnetic stirring for six hours. This powder of mixing and milling repeated two times to obtain a homogeneous powder. The homogeneous powder and

---

[1] Dr, Associate Professor, Department of Physics, Dawei University

[2] Dr, Lecturer, Department of Physics, Dawei University

acetone (100ml) were mixed and ground by agate motor for five hours. The fine powder was obtained. The fine powder was calcinated at 850°C (five hours) for four different times. The four different powder was checked by X-ray diffraction (XRD). $CaCu_3Ti_4O_{12}$ pellets were produced using PVA as a binder and applying pressure of 15 ton/cm^2. The pellets were heated at 700°C for one hour. The $CaCu_3Ti_4O_{12}$ ceramics were obtained. Each pellet of diameter and the thickness are 10mm and 3 mm. The block diagram of the sample preparation and the photo of the samples were shown in Figure 1 and Figure 2.

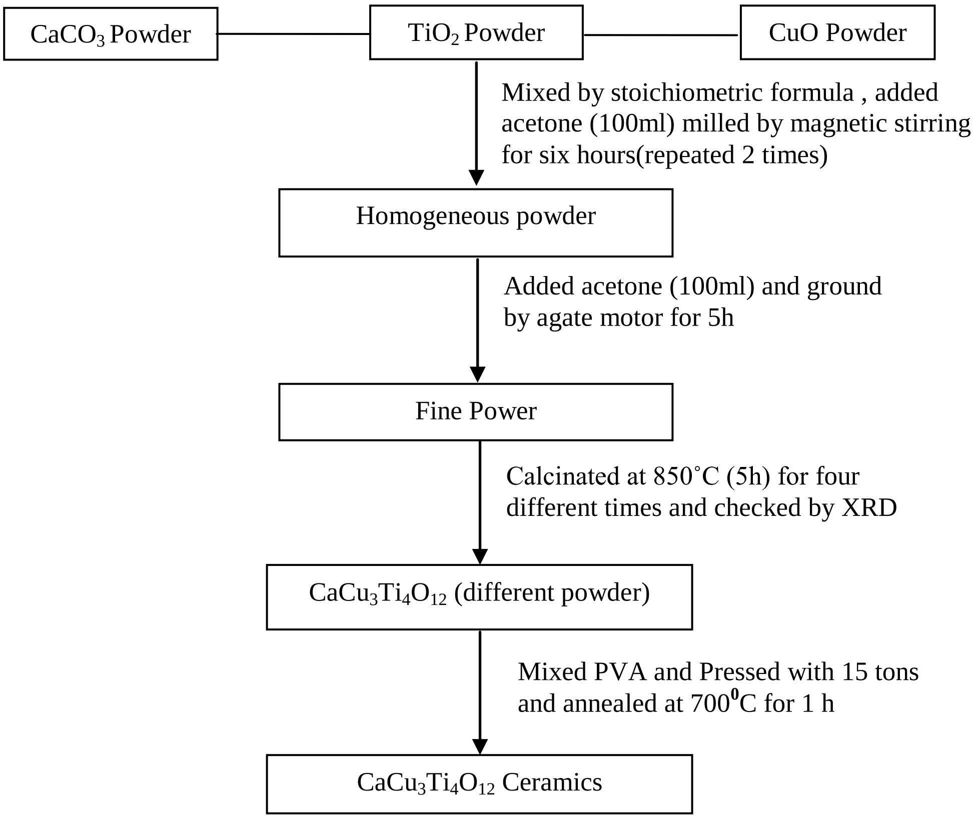

Figure 1 The block diagram of the preparation for $CaCu_3Ti_4O_{12}$ ceramics

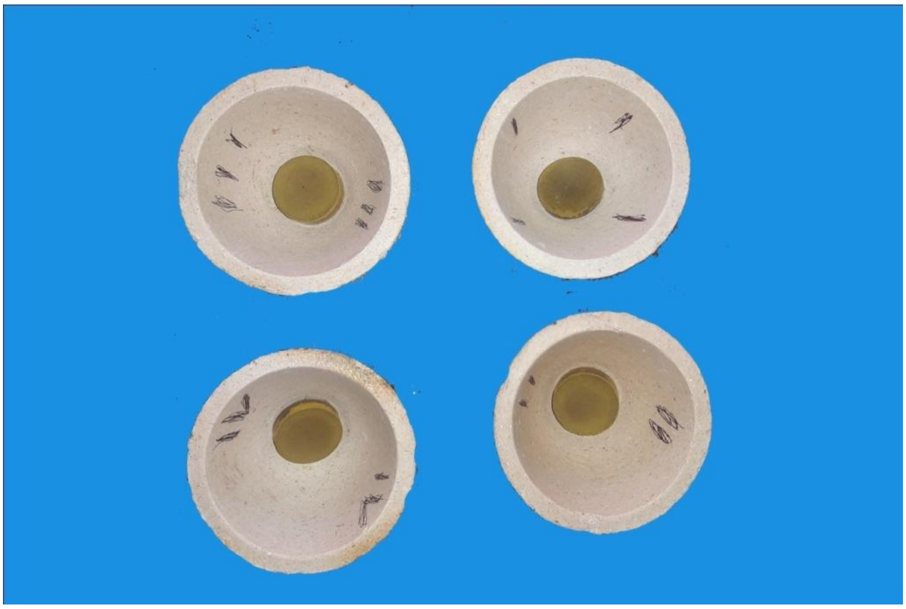

Figure 2 The photo of $CaCu_3Ti_4O_{12}$ ceramics at 850˚C for 5h, 4 different heat treatments.

Results and Discussion

Structural characterization

The XRD (X-ray diffraction) patterns of the powder samples were shown in figure2. From the XRD all profiles, the maximum intensity occurred at (220) plane. The average lattice constants of samples at (220) peak are calculated to be a =b= 7.3820 Å, 7.3861 Å, 7.3819 Å, 7.3790Å from the refinement of the XRD data. The structure of the samples was matched with cubic. The crystallite size was calculated by the Scherrer equation (Kittel, C.1956). The average crystallite sizes of samples were 1.008 nm, 1.067 nm, 1.107 nm, and 1.099 nm. The XRD pattern of samples at 850˚C(5h) for four different heat treatments were shown in Figure (3.a), (3.b), (3.c), and (3.d).

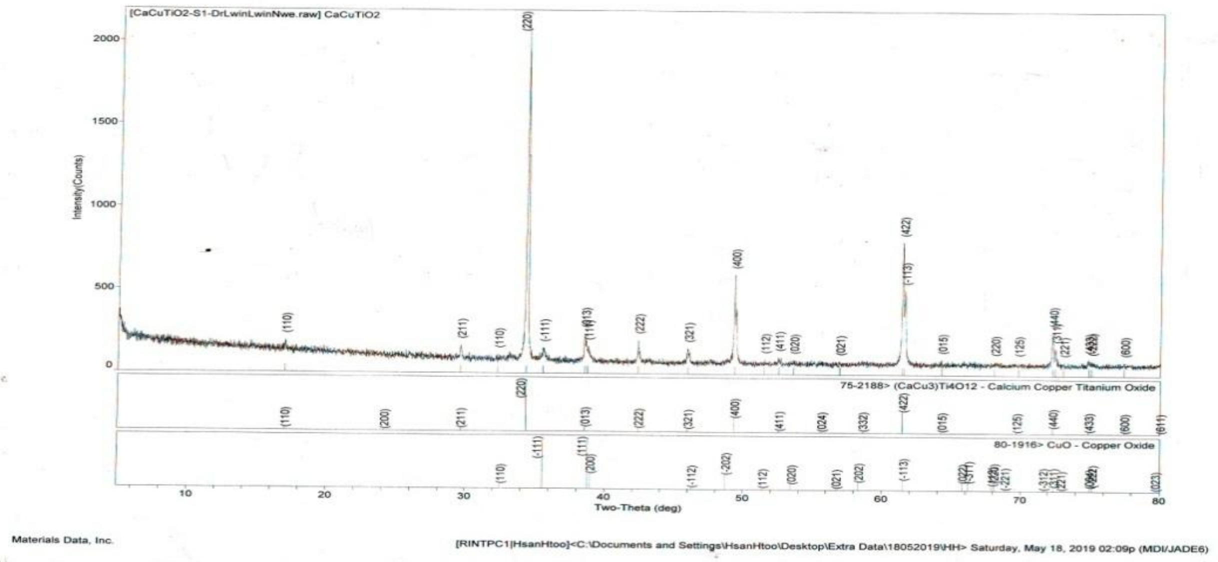

Figure 3 (a) The XRD patterns of $CaCu_3Ti_4O_{12}$ powder at 850˚C for 5h,(heat treatments 1 times)

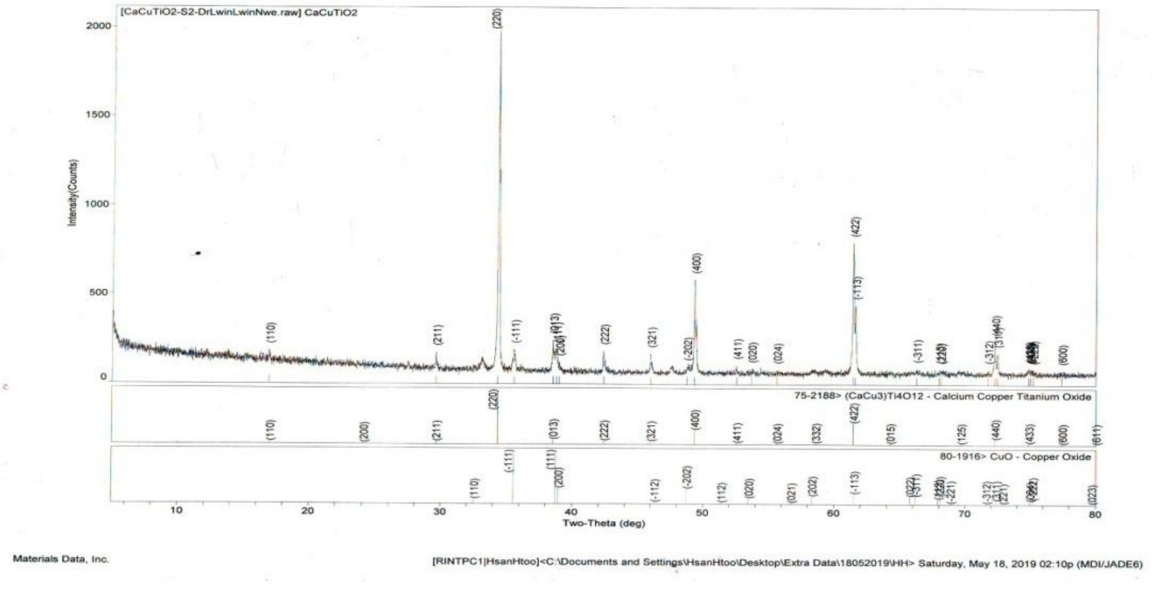

Figure 3(b) The XRD patterns of $CaCu_3Ti_4O_{12}$ powder at 850˚C for 5h, (heat treatments 2 times)

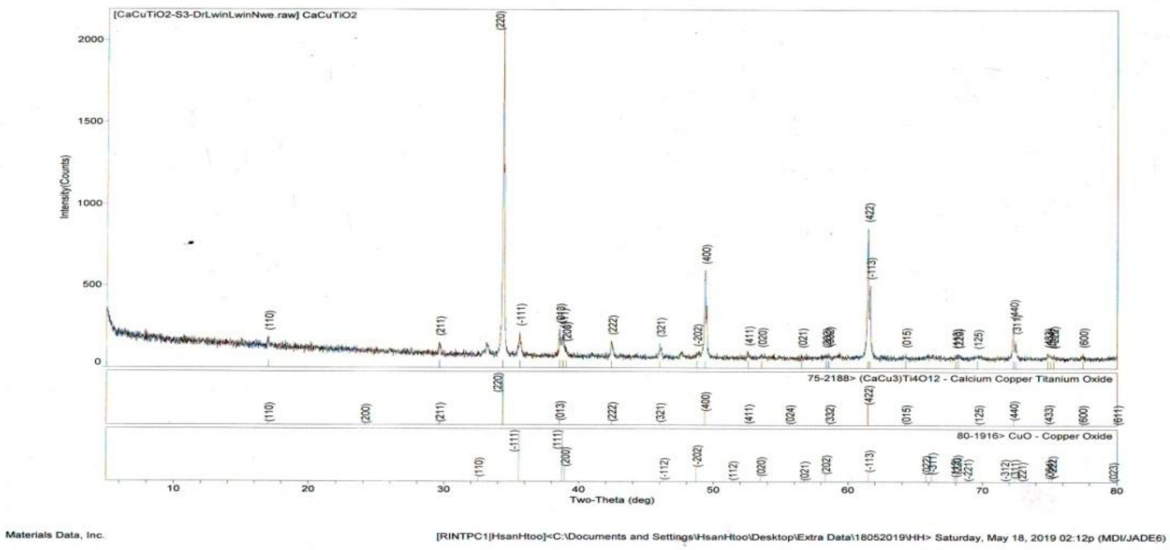

Figure 3(c) The XRD patterns of $CaCu_3Ti_4O_{12}$ powder at 850˚C for 5h, (heat treatments 3 times)

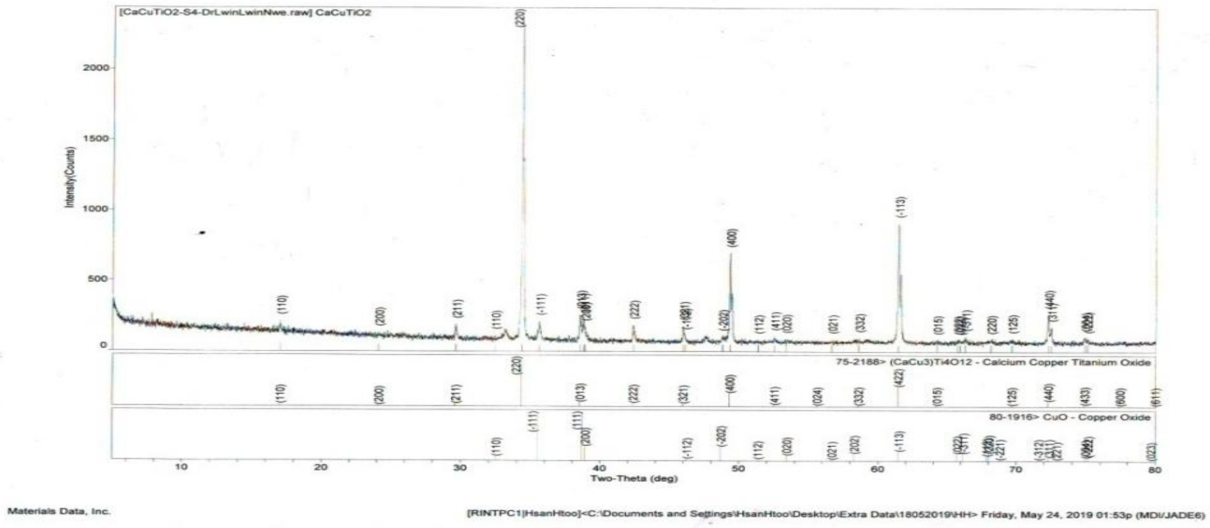

Figure 3 (d) The XRD patterns of $CaCu_3Ti_4O_{12}$ powder at 850˚C for5h,(heat treatments 4 times)

Surface morphology analysis

Figure 4. showed the scanning electron microscope (SEM) images of $CaCu_3Ti_4O_{12}$ powder with the same temperature (850˚C) for five hours, four different heat treatment times. The measurement was performed by 15 kV (accelerating voltage) and 50 mA (beam current). From the SEM images, the average grain sizes of sample powers were 0.143µm, 0.268µm, 0.314µm, and 0.342µm respectively.

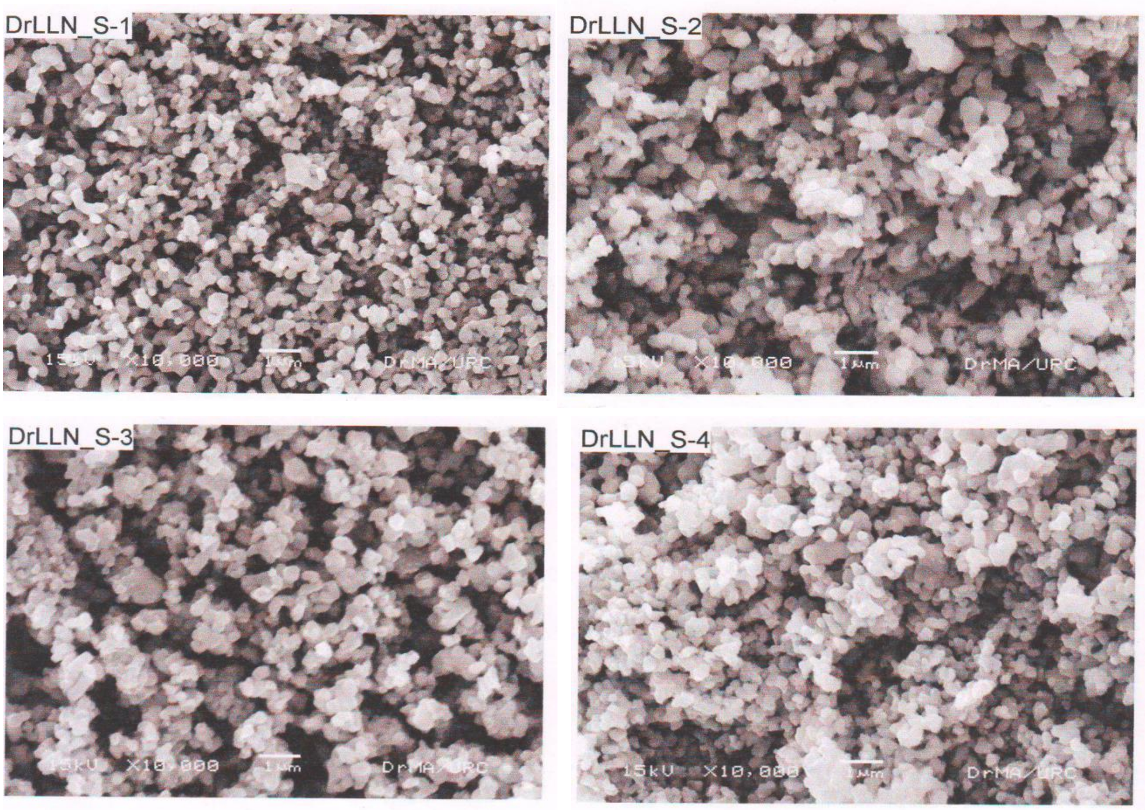

Figure 4 The SEM images of $CaCu_3Ti_4O_{12}$ powder at 850˚C for 5h, 4 different heat treatments

Measurement of LCR meter and calculations

The capacitive properties of samples were measured by using LCR meter with respect to frequency in the region (1 kHz-25 kHz). The dielectric constant, dielectric loss and conductivity of samples were calculated by using the following equations(1),(2) and (3).

$$C = \varepsilon_0 \varepsilon_r A/d \qquad (1)$$

Where, C= the capacitance, ε_0= the permittivity of free space, ε_r= the dielectric constant, d= the distance between the electrodes, A= the area of the electrodes

$$\tan\delta = D/\varepsilon_r \qquad (2)$$

Where, $\tan\delta$= the dielectric factor, D= the dissipation factor

$$\sigma = 1/\rho \qquad (3)$$

Where, σ= the conductivity of ceramic, ρ= the resistivity of ceramic

From the calculation results, it was found that the dielectric constant was higher in the lower frequency region. It decreases with increasing frequency and becomes almost nearly equal at a higher frequency region. It can be seen that the dielectric constant decreases with increasing frequency. It means that the dielectric constant of these samples was the strong function of frequency. The average dielectric constant of four samples in the range 1kHz to 25 kHz at room temperature found to be ε_r = 94.4, 99.4, 112.7, and 133.7 respectively. The dielectric loss of samples decreased with increasing frequency heat-treated times. The dielectric varying with increasing frequencies of $CaCu_3Ti_4O_{12}$ ceramics at 850˚C for 5h, 4 different heat treatments were shown in Figure 5.

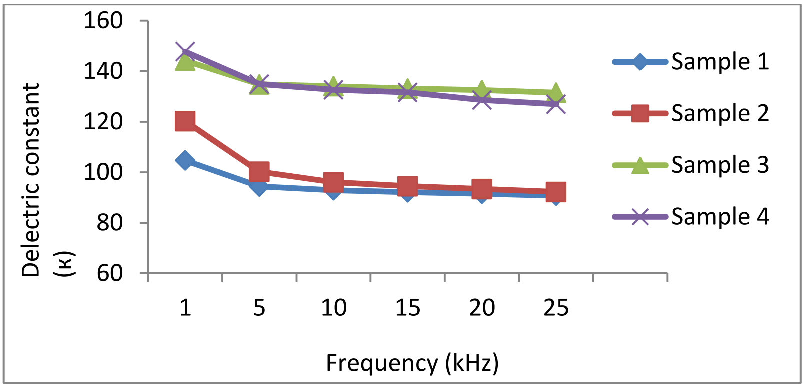

Figure 5 The dielectric varying with the frequency of $CaCu_3Ti_4O_{12}$ ceramics at 850˚C (5h), 4 different heat treatments

The electrical conductivity of ceramics was calculated. The capacitive properties and conductivities of samples were shown in Table 1, 2, 3 and 4. The graph of conductivity with respect to frequency was shown in Figure 6. From the result and graph, the conductivity of samples increases with increasing frequency applied. It may be said that the possibility of the use of these materials in high-frequency device applications.

Table 1 The values of capacitive effect of $CaCu_3Ti_4O_{12}$Ceramic at850˚C (5h)for one time

Frequency (kHz)	Capacitance (pF)	Dissipated factor(D)	Dielectric constant (ε_r)	Resistance (kΩ)	Tan δ (x10^{-3})	Conductivity (mho/m)
1 kHz	2.426	0.122	104.69	7347.00	1.170	0.052
5 kHz	21.87	0.048	94.35	633.55	0.510	0.603
10 kHz	2.152	0.038	92.88	263.52	0.410	1.450
15 kHz	2.134	0.032	92.07	129.79	0.350	2.943
20 kHz	2.120	0.027	91.49	101.46	0.300	3.765
25 kHz	2.103	0.026	90.76	78.39	0.290	4.873

Table 2 The values of capacitive effect of $CaCu_3Ti_4O_{12}$Ceramic at 850˚C(5h) for two times

Frequency (kHz)	Capacitance (pF)	Dissipated factor(D)	Dielectric constant(ε_r)	Resistance (kΩ)	Tan δ (x10^{-3})	Conductivity (mho/m)
1 kHz	2.786	0.175	120.22	5886.67	1.456	0.065
5 kHz	2.322	0.158	100.19	2395.95	1.577	0.159
10 kHz	2.225	0.103	96.02	581.40	1.073	0.657
15 kHz	2.189	0.079	94.46	428.28	0.836	0.892
20 kHz	2.163	0.066	93.34	278.20	0.707	1.373
25 kHz	2.136	0.058	92.17	201.69	0.629	1.894

Table 3 The values of capacitive effect of $CaCu_3Ti_4O_{12}$Ceramic at 850°C (5h)for three times

Frequency (kHz)	Capacitance (pF)	Dissipated factor(D)	Dielectric constant(ε_r)	Resistance (kΩ)	Tan δ ($x10^{-3}$)	Conductivity (mho/m)
1 kHz	3.341	0.221	144.17	6097.83	1.533	0.063
5 kHz	3.123	0.039	134.77	507.28	0.280	0.753
10 kHz	3.107	0.028	134.08	154.19	0.209	2.477
15 kHz	3.085	0.024	133.14	120.67	0.180	3.166
20 kHz	3.071	0.023	132.52	79.24	0.174	4.821
25 kHz	3.040	0.022	131.52	56.46	0.166	6.766

Table 4 The values of capacitive effect of $CaCu_3Ti_4O_{12}$Ceramic at 850°C(5h) for four times

Frequency (kHz)	Capacitance (pF)	Dissipated factor(D)	Dielectric constant(ε_r)	Resistance (kΩ)	Tan δ ($x10^{-3}$)	Conductivity (mho/m)
1 kHz	3.424	0.122	147.76	5567.20	0.825	0.069
5 kHz	3.125	0.051	134.87	425.95	0.378	0.897
10 kHz	3.073	0.039	132.62	146.12	0.294	2.328
15 kHz	3.049	0.032	131.59	92.09	0.234	4.148
20 kHz	2.979	0.026	128.57	62.82	0.202	7.232
25 kHz	2.941	0.023	126.89	48.65	0.181	7.852

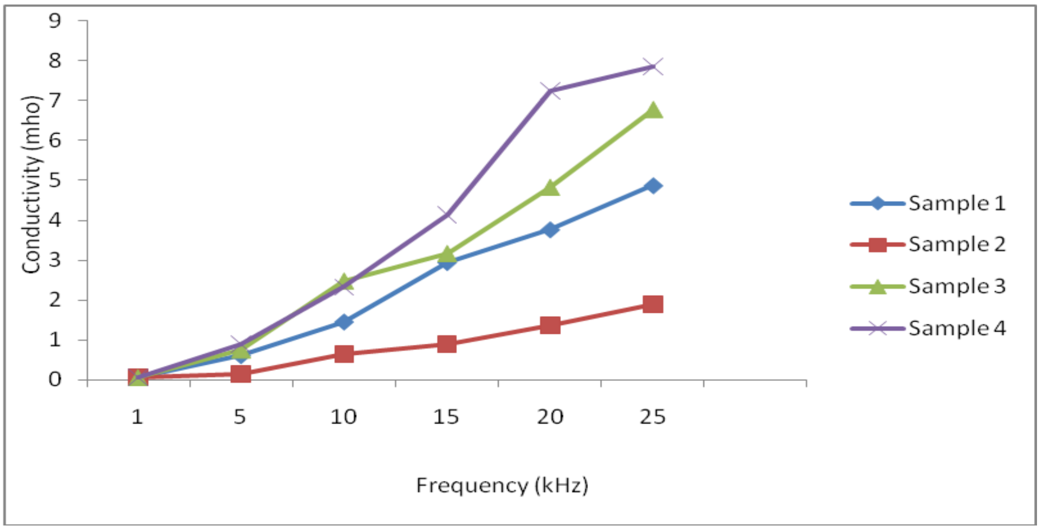

Figure 6 The conductivity vary with the frequency of $CaCu_3Ti_4O_{12}$ ceramics at 850°C (5h), 4 different heat treatments

Conclusion

$CaCu_3Ti_4O_{12}$ ceramics were synthesized by a solid-state reaction method. The cubic structure of ceramics was confirmed by XRD patterns. The formation of microstructures with the well-defined grain size of samples was determined by the SEM result. Samples were free crack. The dielectric constant of samples with a frequency increase in heat treatment times. If the temperature of heat-treated and time taken may be increased, the dielectric constant of samples will be increased

Acknowledgments

I would like to express appreciation to Editing-rector Dr. Theingi Shwe, Pro-rector Dr. Khin May Aung, Dawei University and Pro-rector Dr. Cho Cho Myint, Dawei University for their encouragement and kind permission to undertake the present research. I also would like to express my profound thanks to Professor Dr Yin Yin Myint, Head of Department of Physics, and Professor Dr Kyaw Kyaw Win, Department of Physics, Mawlamyine University, for their kind permission to use material science research lab apparatus in Mawlamyine University and Professor Dr San San Aye, Head of Department of Physics, and Professor Dr Khin Shwe Oo Dawei University for encouragement and help during this work.

References

I .E . Lipinski, J.Kuriata, N.A.Koryanevskii, and M.sobon, Rev. Adv. Marter. Su, 12, (2006), 150.

Katsuhito, Y. and Hideaki, M.(2004). "Thermal properties of diamond/copper composite material Microelectronics Reliability": 44, 303-308.

K-H FELGNER, H.T.KAMMER.(2001). "Journal of Materials Science":36, 1425-1431.

Kittel, C.(1956). "Introduction to Solid State Physics", 2nd edition, (New York: John Wiley & Sons).

N Tripathy, K C Das, S P Ghosh, G Bose and J P Kar (2016) “Processing and Characterization of Material” 5th National Conference (India 501203)

Omar A. A. An Abdelal, Ahmed A, Hassan, and M.E l- sayed Ali. (2014,Nov) “International Journal of Science and Research”, volume (3), Issue 11.

J. Myanmar Acad. Arts Sci. 2020 **Vol. XVIII.No.2A**

INFLUENCE OF NaOH IN THERMAL REDUCTION OF WOLFRAMITE IN ORE MINERAL

Sint Ohnmar[1] , Min Maung Maung[2]

Abstract

The annealing process of ore mineral which is important for designing scientific and economic schedule. The samples were collected from Pharchaung Mine in Tanintharyi Region. The 70% wolframite sample (Fe,Mn)WO_4 was prepared by magnetic separation method and ore mineral of (Fe,Mn)WO_4 were collected in this mine. In this research work, to emphasize the value of considering wolframite as thermal reactions and chemical reactions methods. The behavior of structural tile were investigated using thermal analysis techniques. The weight loss of 70% wolframite sample (Fe,Mn)WO_4 was observed from TG curve and the phase transition occurred from DTA curve. The crystal structure of 70% (Fe,Mn)WO_4 powder and ore mineral of (Fe,Mn)WO_4 were observed by XRD and also the phase changes of this powder were investigated at 450°C and 500°C in three hour. And also demonstrated its application to provide a better understanding of the occurrence and origin of wolframite minerals. Aqueous solution containing sodium hydroxide (NaOH) was used as the alkaline leaching media and it was the most beneficial agent stabilizing the solid phase in the aqueous environment.

Keywords: Annealing process, TGA curve, Wolframite, magnetic properties.

Introduction

Wolframite, is a principal ore of tungsten. It is an iron and manganese tungstate mineral. It has a hardness of 5 to 5.5 mhos, specific gravity of 7.1 to 7.5, is dark gray, reddish brown, brownish black, or iron black in color. Wolframite is commonly found in granite and pegmatite dikes, and is often associated with cassiterite; it also occurs in sulfide veins and placer deposits. It has been suggested that the name ferberite be limited to mixtures containing not more than 20 per cent of the hubnerite molecule and the name hubnerite to those containing not more than 20 per cent of the ferberite molecule. This would leave the name wolframite for mixtures containing more than 20 per cent of both $FeWO_4$ and $MnWO_4$. Because heat causes tungsten to expand at about the same rate as glass, the metal is widely used to make glass-to-metal seals. Tungsten ore is a rock from which the element tungsten can be economically extracted. The ore minerals of tungsten include wolframite, scheelite, and ferberite. Materials processing is one of the most important and active areas of research in heat transfer today. With growing international competition, it is has become crucial to improve the present processing techniques and the quality of the final product. Heat transfer is extremely important in a wide range of materials processing techniques such as crystal growing, casting, glass fiber drawing, chemical vapor deposition, spray coating, soldering, welding, polymer extrusion, injection molding, and composite materials fabrication. Tungsten is an economically important metal, being widely used in light-bulb filaments, electron and television tubes, abrasives and special alloys such as tool steels. Tungsten carbide is of great importance to the metal-working, mining and petroleum industries. Contamination from these sources is, therefore, possible in industrial and urban areas. Scintillators for dark matter search, semiconducting photoelectrodes for photoelectrolysis or humidity sensors for meteorology are some of the direct applications that wolframite-type compounds with chemical formula AWO_4 present. When a material is heated its structural and

---

[1] Dr, Lecturer, Department of Physics, Dawei University

[2] Dr, Associate Professor, Department of Physics, Yangon University

chemical composition can undergo changes such as fusion, melting, crystallization, oxidation, decomposition, transition, expansion and sintering. Using Thermal Analysis such changes can be monitored in every atmosphere of interest. The obtained information is very useful in both quality control and problem solving. Thermal Analysis is the term applied to a group of methods and techniques in which chemical or physical properties of a substance, a mixture of substances or a reaction mixture are measured as function of temperature or time, while the substances are subjected to a controlled temperature programme. For specific application, the magnetic properties are important. Non-magnetic materials have to be used whenever the magnetic fields can be perturbed in radiation equipment or when shielding is positioned near electrical sensors.

Experimental Procedures

Preparation of pyrite samples

The 70% wolframite sample $(Fe,Mn)WO_4$ was prepared by magnetic separation method and ore mineral of $(Fe,Mn)WO_4$ were collected from Pharchaung Mine in Tanintharyi Region. Firstly ore mineral of $(Fe,Mn)WO_4$ was divided and collected from rock sample according to their raw group formations (colour). The 70% wolframite sample $(Fe,Mn)WO_4$ was grounded again and again to form homogeneous powder and also ore mineral of $(Fe,Mn)WO_4$ was grounded again and again to form homogeneous powder. The structure of these powder samples were determined by XRD holder to determine the structure and lattice parameter.

Most commonly, the mass change is related to sample purity or composition. The heat changes within a 70% wolframite sample $(Fe,Mn)WO_4$ was monitored by measuring the difference in temperature (T) between the sample and the inert reference. This differential temperature is then plotted against temperature or time to get DTA curve. TG and DTA was carried out using the DTG-60H thermal analyser at the Research Center , Yangon University.

The obtained The 70% wolframite sample $(Fe,Mn)WO_4$ was heated at 450°C and 500°C in furnace 3 hrs each and slightly cold down to room temperature. The samples were grounded again and again to form homogeneous powder. The structure of these powder samples were determined by XRD holder to determine the structure and lattice parameter. In chemical analysis, 6 g of natural ore (Fe,Mn)WO4 are grinding with mortar and pestel, then 2 g of sodium hydroxide solution are added. The mixture of this sample is grinding and then heated at 300 in one hour. And then, this mixture sample was annealed in 450°C, 500°C in furnace three hour each. The samples were grounded again and again to form homogeneous powder. The structure of these powder samples were determined by XRD holder to determine the structure and lattice parameter.

Results and Discussion

Structural characterization and TG/DTA analysis

More extensively, the ABX_4 compounds exhibit numerous crystalline forms and the phase transitions between some of them were shown to be of great interest .In this paper concentrate on the 70% $(Fe,Mn)WO_4$ compounds by magnetic separation method; respectively, with orthorhombic structure. In the literature, it is known that $(Fe,Mn)WO_4$ monoclinic structure crystallize in the wolframite structure when synthesized between 400°C and 500°C. As-obtained 70% $(Fe,Mn)WO_4$ at room temperature was finally investigated by X-ray diffraction. Characterization of the sample are structural analysis by XRD as shown in

Figure.1. The crystal structure was observed orthorhombic. The average lattice parameters were observed a = 4.7535A˙, b = 5.6818A˙ and c = 5.0120. Thermal analysis by TG-DTA as shown in Figure.2, the weight loss was observed 4.599% from TGA curve and the oxidation process occurred from the exothermic peak at 464.56 °C from DTA . The phase changes of 70% (Fe,Mn)WO_4 powder were investigated at 450°C and 500°C in three hour. The phase changes of 70% (Fe,Mn)WO_4 samples were observed from orthorhombic structure to monoclinic structure at 450°C and 500 °C in three hour each as shown in Figure.3 and Figure.4.

X-ray diffraction (XRD) patterns of natural (Fe,Mn)WO_4 and annealed (Fe,Mn)WO_4 in alkaline media at 300°C as shown in Figure.5 and Figure.6. It was found that the structure of natural (Fe,Mn)WO_4 is monoclinic. The average lattice parameters were observed a = 4.7722 Å, b = 5.7218 Å and c = 4.9791 Å. The diffractograms for natural wolframite in hydroxide media show that the most intense and well-defined peaks are attributable to (Fe,Mn)WO_4. It was found that the structures of natural wolframite in sodium hydroxide solution was also monoclinic. The average lattice constants are calculated to be a = 4.7529 Å, b = 5.6919 Å and c = 5.0209 Å from the refinement of the XRD data. The other secondary peaks is gradually reduced by mixing with sodium hydroxide solution. This sample was also heated in 450°C, 500°C and 600°C are displayed in Figure.7, Figure.8 and Figure.9. The crystal structure of this sample in 450°C was observed orthorhombic and it was observed that the primary peak is sodium molybdenum oxide hydrate and the secondary peak is (Fe,Mn)WO_4. The secondary peak of (Fe,Mn)WO_4 is reduced at 500°C in hydroxide media but the crystal structure was also observed orthorhombic. The (Fe,Mn)WO_4 peaks were disappeared and sodium molybdenum oxide hydrate peaks were observed in 600°C but the crystal structure was also observed orthorhombic.

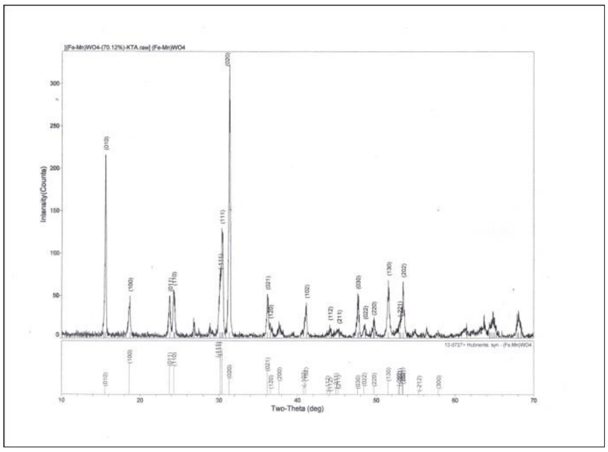

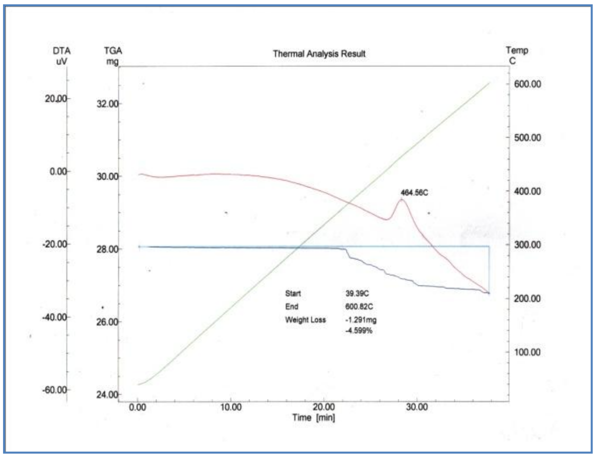

Figure 1 XRD pattern of wolframite 70% (Fe,Mn)WO_4

Figure 2 TGA and TD curve of the (Fe,Mn)WO_4

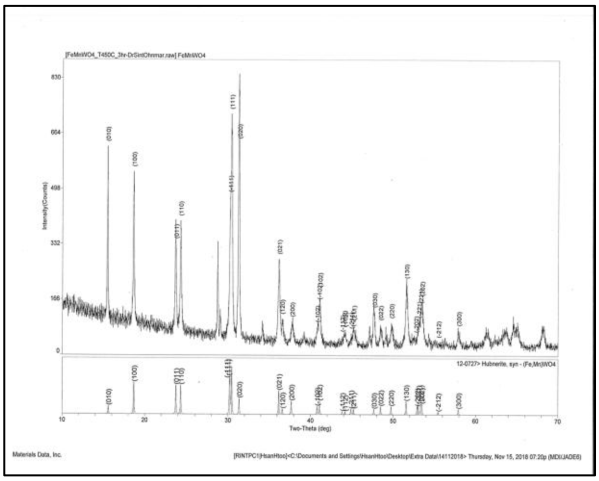

Figure 3 XRD pattern of 70% (Fe,Mn)WO_4 at 450 °C in three hours

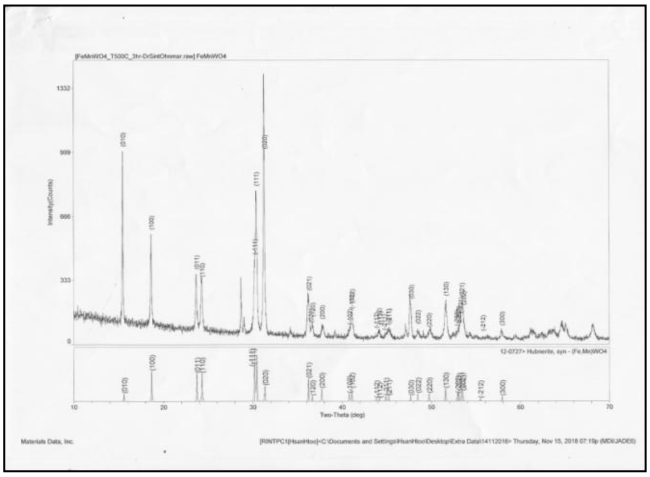

Figure 4 XRD pattern of 70% (Fe,Mn)WO_4 at 500 °C in three hours

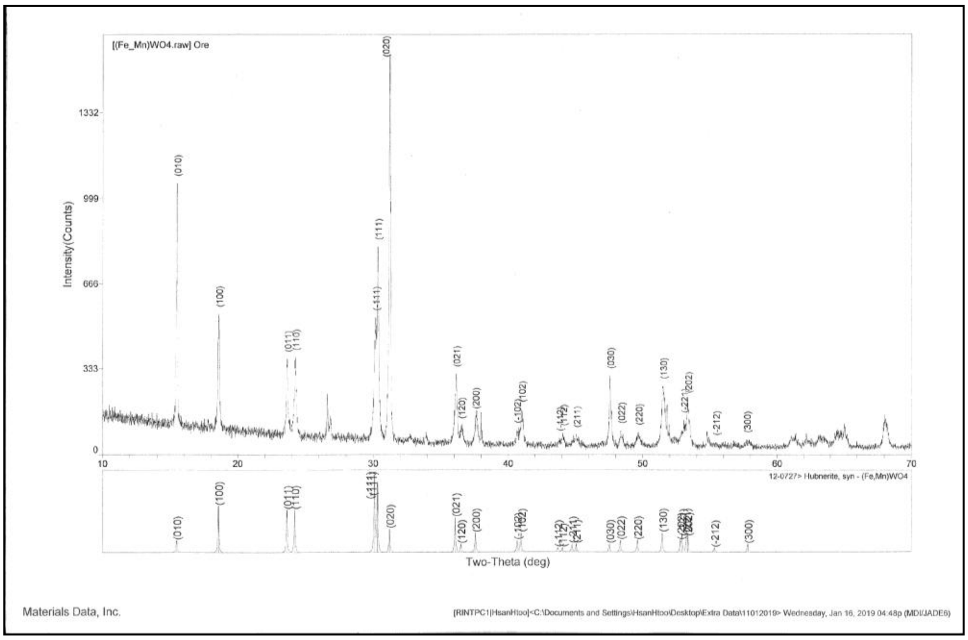

Figure 5 XRD pattern of natural wolframite powder samples

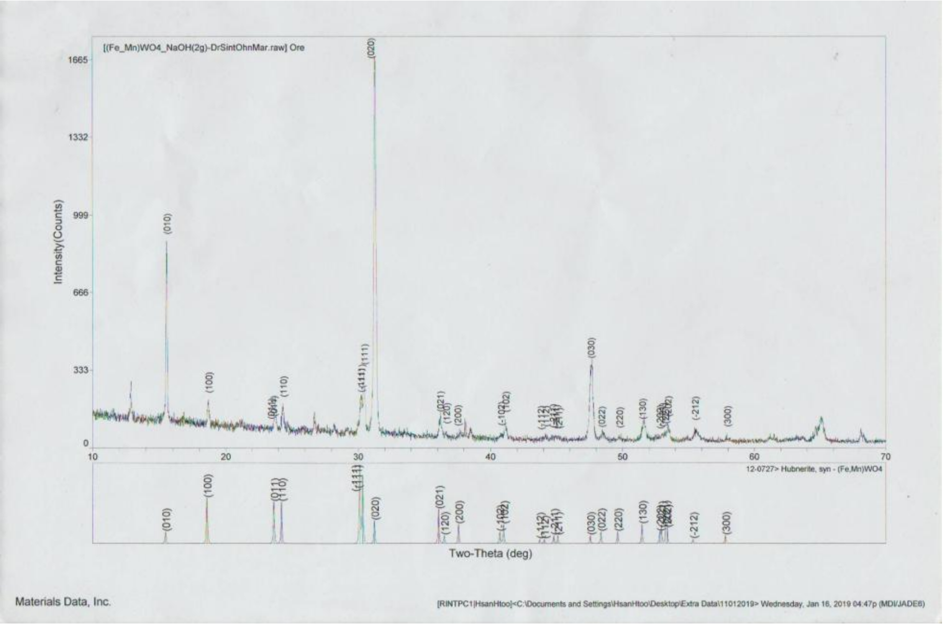

Figure 6 XRD pattern of natural wolframite powder samples with sodium hydroxide solution

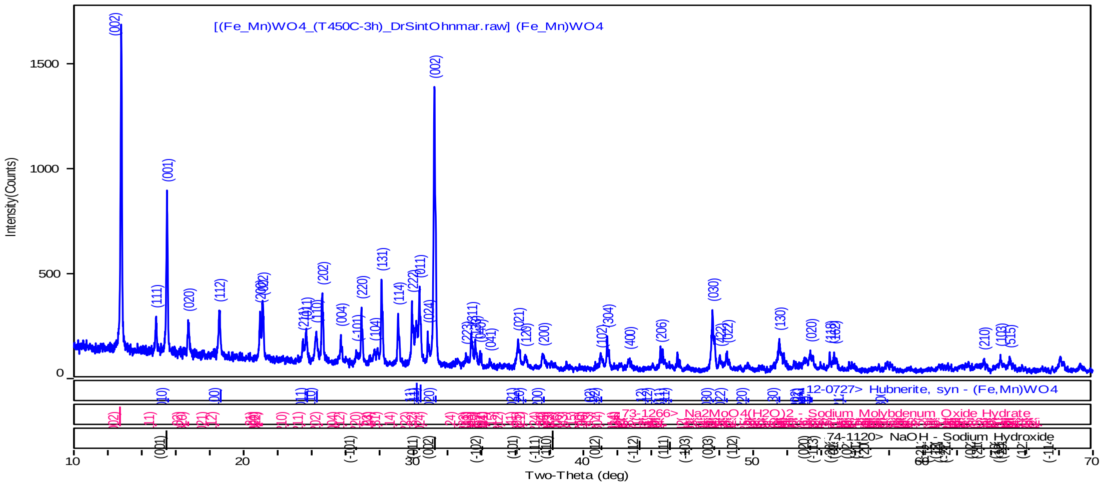

Figure 7 XRD pattern of natural wolframite powder samples with sodium hydroxide solution at 450 °C in one hours

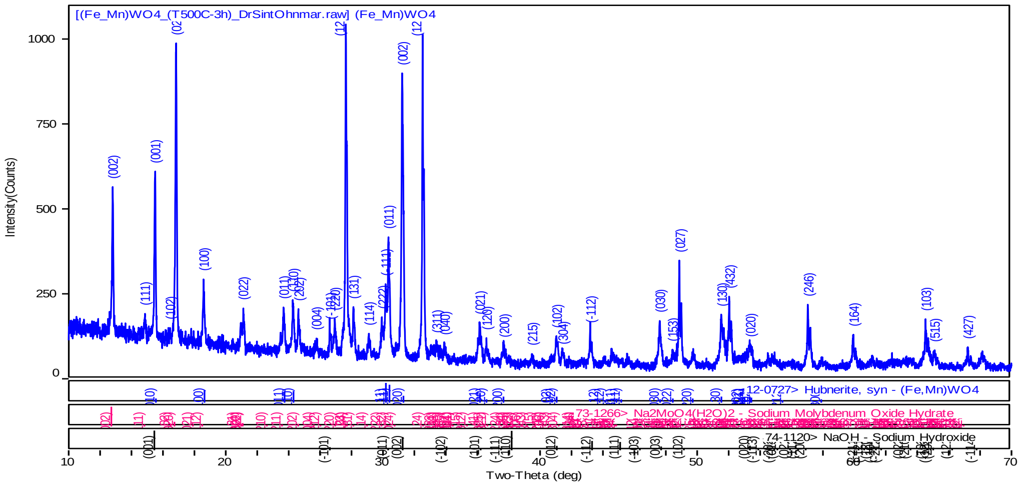

Figure 8 XRD pattern of natural wolframite powder samples with sodium hydroxide solution at 500 °C in one hours

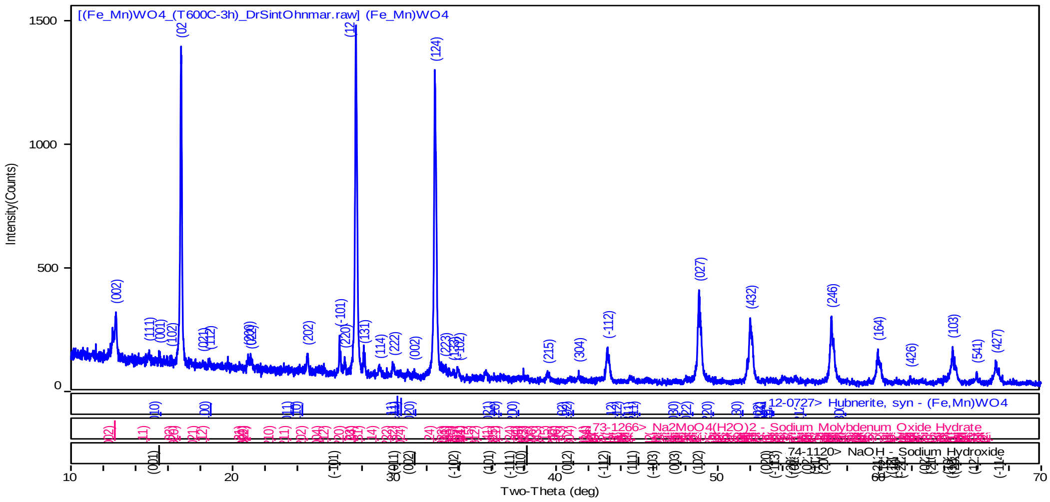

Figure 9 XRD pattern of natural wolframite powder samples with sodium hydroxide solution at 600 °C in one hours

Conclusion

The mineral wolframite is a principal ore of tungsten. It is a general term for iron and manganese tungstates where the iron/manganese ratio can vary. A mineral with more than 80% $FeWO_4$ is called feberite and a mineral with more than 80% $MnWO_4$ is called hubnerite. The primary objective of this work, the characterization of an 70% wolframite which was prepared by magnetic separation method and ore bearing wolfrmite mineral from Pharchaung mine, Tanintharyi region. The XRD phase patterns confirmed the availability of minerals such as Cassiterite, Hubnerite and Feberite. The crystal structure of 70% wolframite from magnetic separation method was observed orthorhombic and structure of the ore bearing wolfrmite mineral observed monoclinic. The mineral confirmed from this mine was hubnerite.

The weight loss of wolframite was observed 4.599% from TGA curve and the oxidation process occurred from the exothermic peak at 464.56 °C from DTA . The phase changes of 70%

(Fe,Mn)WO_4 samples were observed from orthorhombic structure to monoclinic structure at 450°C and 500 °C in three hour each but the mineral confirmed hubnerite.

Natural ore wolframite was submitted to chemical and thermal experiments. X-ray diffraction (XRD) patterns of natural (Fe,Mn)WO_4 in alkaline media at 300°C in one hour was also observed monoclinic and hubnerite. The structures were stability in alkaline media. In annealing process this sample, the mineral was dominated by sodium molybdenum oxide hydrate than hubnerite at 450°C and 500 °C. The sodium molybdenum oxide hydrate observed at 600 °C in this sample but the structures were changed from monoclinic to orthorhombic in 450°C, 500°C and 600 °C.

Hubnerite is primarily used as a source of tungsten. Tungsten is used to harden metal in the manufacture of high-speed tools. Sodium molybdate is a crystalline powder essential for the metabolism and development of plants and animals as a cofactor for enzymes.

Acknowledgements

I would like to express appreciation to Acting Rector Dr Theingi Shwe, Pro-rector Dr Khin May Aung and Dr Cho Cho Myint, Dawei University for their encouragement and kind permission to undertake the present research. I also would like to express my profound thanks to Professor Dr San San Aye, Head of Department of Physics, and Professor Dr Khin Swe Oo, Department of Physics, Dawei University, for their kind permission to carry out this work, their encouragement and help during this work.

References

Braham J.B. Muwanguzi et al., (2012), “Characterisation of the Physical and Metallurgical Properties of Natural Iron Ore for Iron Production”, Department of Material Science and Engineering, KTH Royal Institute of Technology, Brinellvägen 23, 100 44 Stockholm: Sweden.

Grega Klančnik, (2009), “Differential thermal analysis (DTA) and differential scanning calorimetry (DSC) as a method of material investigation”, University of Ljubljana, Faculty of natural science and engineering, Department of materials and metallurgy, Aškerčeva 12, SI-1000 Ljubljana, Slovenia.

Ruiz-Fuertes J. “Room-temperature vibrational properties of multiferroic MnWO4 under quasi-hydrostatic compression up to 39 GPa” Abteilung Kristallographie, Geowissenschaften, Goethe-Universität, 60438 Frankfurtam Main, Germany.

Veronica Blanco-Gutierrez, Alain Demourgues, Eric Lebreau, and Manuel Gaudon*, (2016), “Phase transitions in Mn(Mo1_xWx)O4 oxides under the effect of high pressure and temperature”, Universite de Bordeaux, France.

www.Wolframite_mineral_info.htm

http://pubchem.ncbi.nlm.nih.gov

http://www.americanelements.com

http://wikividly.com

J. Myanmar Acad. Arts Sci. 2020 **Vol. XVIII.No.2A**

EFFECTIVE CONTROL OF SOLAR POWER SYSTEM BY AUTOMATIC TRACKER

Wut Hmone Oo[1], Khin Mar Win[2], Hla Htay Win[3]and Thandar Aung[4]

Abstract

The research paper presents the design of automatic solar tracking control system based on microcontroller. It consists of the optimize hardware design, which is controlled by a firmware. The source code for the project is written in Mikro C Pro programming language. The main objective of this paper is to provide the maximum energy from solar panel and gives higher efficiency for the solar cells. This designed system is to control the solar panel to remain aligned with direction of the sun. The microcontroller based control circuit drives the DC motor. Microcontroller PIC16F887 is used for controlling the movement of the solar panel. DC motor is controlled by the microcontroller that receives the signals from the transistor driver of light dependent resistor (LDR). The light sensor (LDR) tracks the path of the sun by detecting the light intensity. The design of automatic solar tracker can be categorized into three sections. These are sensor unit, control unit and motor driving unit. For demonstration simplicity, the LED indicators are used to show the rotation of DC motor.

Keywords: Solar Tracking, Solar Panel, PIC16F887, DC motor, LDR Sensors

Introduction

The most abundant and convenient source of renewable energy is solar energy and widely utilized to convert the solar energy for electric power applications. Solar energy is also freely available and never run out. This system needs only maximum sunlight to generate power. Solar trackers are the most suited technology to increase the efficiency of solar panels through keeping the panels aligned with the sun's position. Solar panel directly converts solar radiation into electrical energy. A solar panel with tracking system increases the intensity of light falling on it. It can generate direct current (DC) electricity without environmental pollution. To make effective use of solar energy, its efficiency must be maximized. Efficiency of the solar energy is very high compare to any other sources of energy. The solar tracking enables more energy to be generated because the solar panels are always perpendicular to the solar energy radiated by the sun. One of the main problem is that it is not capable to produce any output power in bad weather condition.

Materials and Methods

Automatic Solar Tracking Control System

The solar tracking system consists of programmable microcontroller (PIC16F887), LDR sensors, H-Bridge DC-motor control circuit and solar panel. Solar tracking system is a power generating method from sunlight. The method of power generation is very simple and is taken from natural resources. By using automatic solar tracker, the highest power can generate from the solar panel when it is perpendicular to location of the sun. As the sun rotates from east to west, it is needed to rotate the solar panel in order to follow the sun's direction. Light sensors (LDRs) track the path of the sun by detecting the light intensity. So, the main panel rotates where the

---

[1] Assistant Lecturer, Department of Physics, Dawei University

[2] Dr, Associate Professor, Engineering Physics Department, Mandalay Technological University

[3] Dr, Lecturer, Department of Physics, Bago University

[4] Dr, Assistant Lecturer, Department of Physics, Pathein University

maximum light is absorbed. Greater the intensity of solar light falls on solar panel, the larger output observe at the output of solar panel. Motor rotates the solar panel to keep at right angle to the rays of the sun. The basic structure of the "Automatic Solar Tracking System" is as shown in Figure 1.

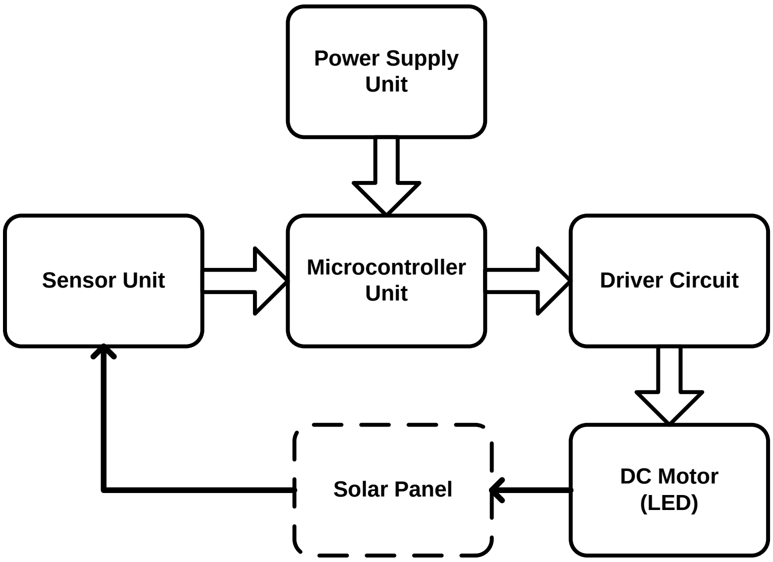

Figure 1 The block diagram of the automatic solar tracking control system

Design and Construction of Solar Tracker

The automatic solar tracking control system is composed of three main units such as sensor unit, control unit and motor driving unit. The major part of the whole system is microcontroller. In sensor unit, LDR senses the intensity of sunlight and the microcontroller receives the digital output through the driver transistor. The control unit decides in which direction the panel rotates to get the maximum intensity of the sunlight on the solar panel. With the sun always facing perpendicularly to the panel, the maximum energy can be absorbed and the panel operates at its highest efficiency in motor driving unit.

Sensor Circuit

The sensor unit consists of two light dependent resistors (LDRs). Light dependent resistors are used to detect change in light intensity or as a light sensor. The resistance of LDR varies in proportional to the intensity of light falling on its surface. In complete darkness, LDR produces its greatest resistance. The characteristic of the LDRs are chosen as 100kΩ in complete darkness and 500Ω when totally saturated with light. Under ambient light, resistance varies between 2.5kΩ and 10kΩ. The LDR can be applied on light-sensitive detector circuits and light and dark activated switching circuits. In this research, the LDR sensor circuit is connected as a dark activated switching circuit as shown in Figure 2.

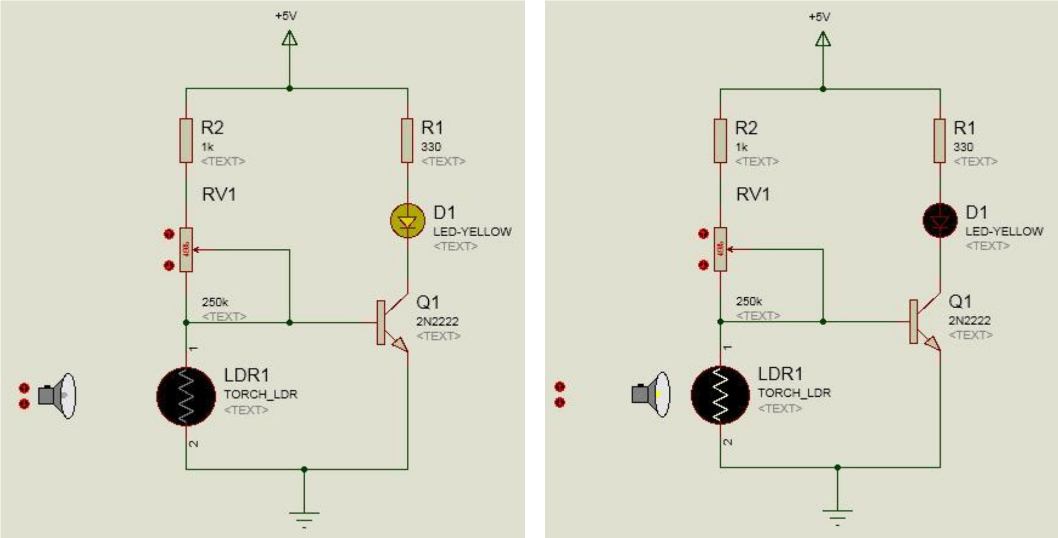

Figure 2 LDR sensor circuit connecting as a dark activated switch

Application of Microcontroller

Microcontroller PIC16F887 is the main control unit of the whole system. It consists of 40-pin dual in line package. In this research work, only 8-pin are used to operate the automatic solar tracking control system. The Master Clear Pin (pin number 1) is not used in this circuit so it is connected to power supply via 10 kΩ resistor to disable this pin. The 8 MHz crystal oscillator is connected to RA6 (pin number 13) and RA7 (pin number 14) which have the alternate functions of external clock input and clock output. The two sensors are connected to RA2 (pin number 2) and RA3 (pin number 3) to give the analog signal to microcontroller. DC motor circuits are connected to RB0 (pin number 33) and RB1 (pin number 34) conjunction with the Darlington pair transistor. The power supply in V_{DD} (pin number 32) and the ground pin V_{SS} (pin number 12) are connected to +5V regulated power supply unit to power up the system.

H-Bridge DC-Motor Control Circuit

To control the rotation of the DC motor, H-Bridge Circuit is constructed by using the bipolar power transistors as shown in Figure 3. When the clockwise signal coming from the microcontroller, the motor rotates in clockwise direction. When the counter clockwise signal coming from the microcontroller, the motor rotates in counter clockwise direction.

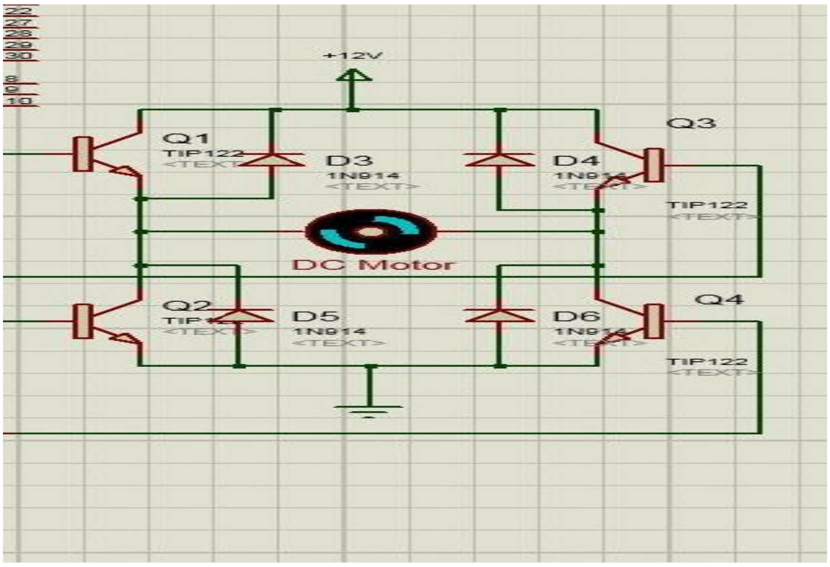

Figure 3 The H-Bridge DC motor control circuit

Circuit Design and Circuit Simulation

Firstly, the circuit design is created by using Proteus 8.1 software and circuit simulation is made on it. The Proteus 8.1 software is a Printed Circuit Board (PCB) design software integrated with the simulation of the circuit design. It is integrated with real time simulation of the electronic circuit and test whether the circuits design is working properly or not. The main purpose to design with Proteus software is to get the optimum circuit diagram without spending any actual circuit components by damaging due to circuit fault. After doing several circuit simulations again and again on the Proteus software, the optimum circuit design is obtained. The circuit simulation by Proteus 8.1 is as shown in Figure 4.

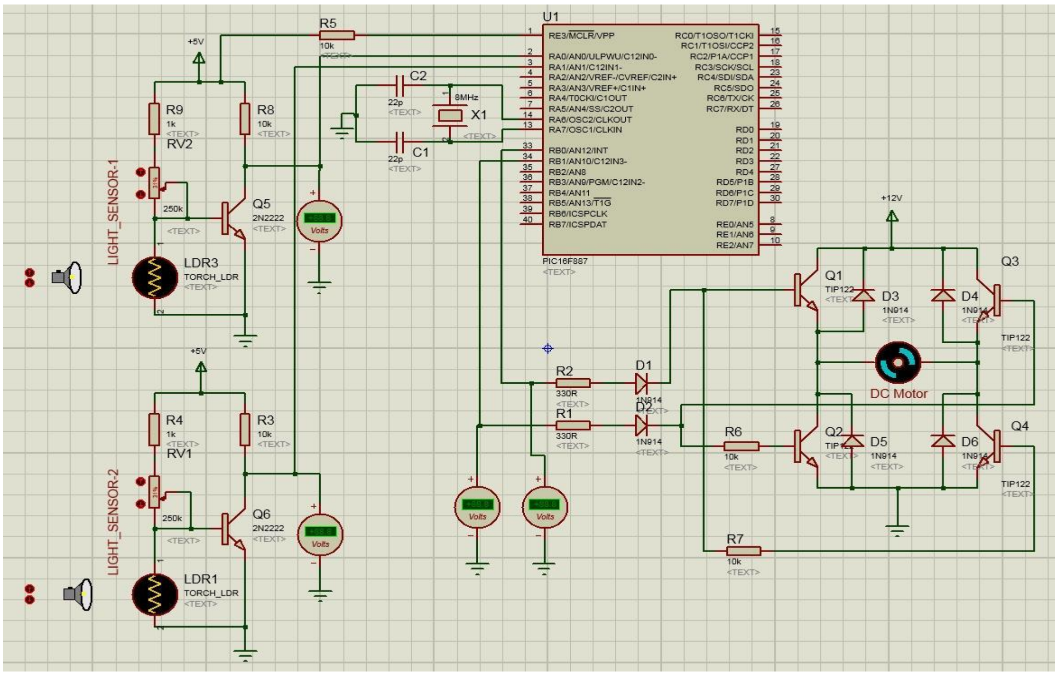

Figure 4 The simulation circuit by Proteus 8.1 software

Creating Circuit Track Lines for PCB Design

The "TraxMaker" is electronic design automation software for printed circuit board design. It is also PCB layout program associated with CircuitMaker2000. The printed circuit layout diagram for the "Automatic solar Tracking Controlled Circuit" was designed with "TraxMaker"- PCB Software including Top Layer (copper surface side for circuit track lines also called solder side) and Bottom Layer (components mounting side). The Top Layer and Bottom Layer are printed out and then copied on the surface of the printed circuit board (PCB). The photograph of the printed circuit track lines is as shown in Figure 5.

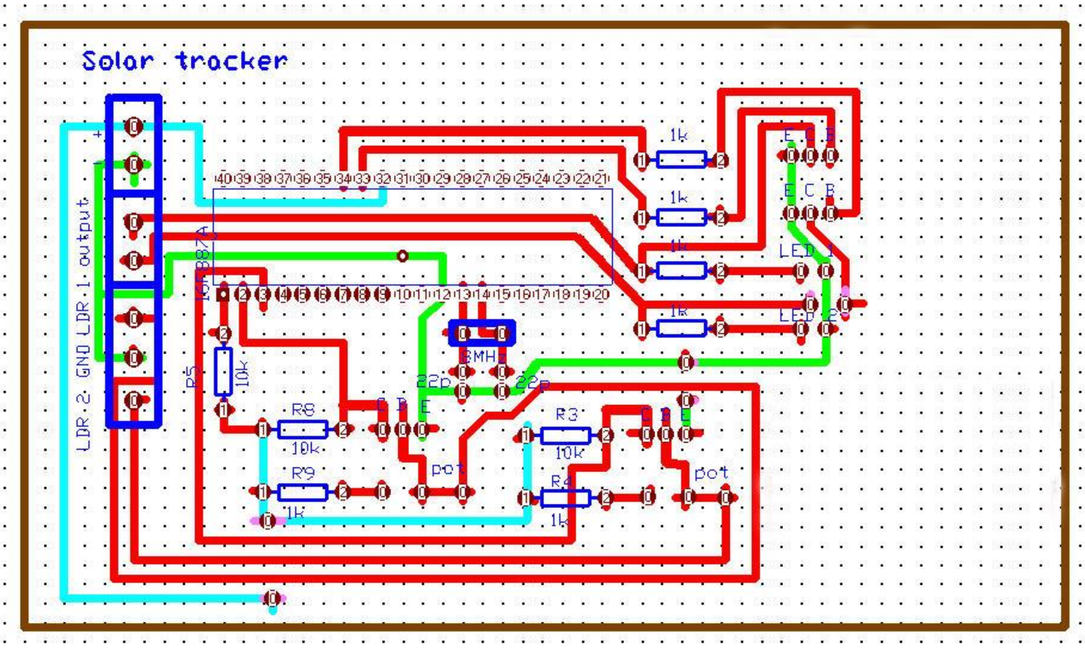

Figure 5 The circuit track line diagram of "Automatic Solar Tracking Control System" in both solder side and components side

Etching Procedure

The printed carbon powders on solder side were placed on the copper side of the printed circuit board (PCB). The PCB was pressed and heated at the back side for ten minutes to cover the copper surface with carbon print lines. After pressing and heating process, the PCB was cooled down and the paper on the PCB was removed by soaking it in the water. To remove the unwanted copper surface area on the circuit, the PCB was slowly shaken in the ferrous chloride solution until copper dissolved into ferrous chloride and this process is called etching. After removing unnecessary parts of the copper surface, just only circuit diagram remained on the PCB. Finally the circuit components are mounted and soldered on the PCB in their positions on it. The circuit track line diagram of "Automatic Solar Tracking Control System" in solder side and component side are shown in Figure (6).

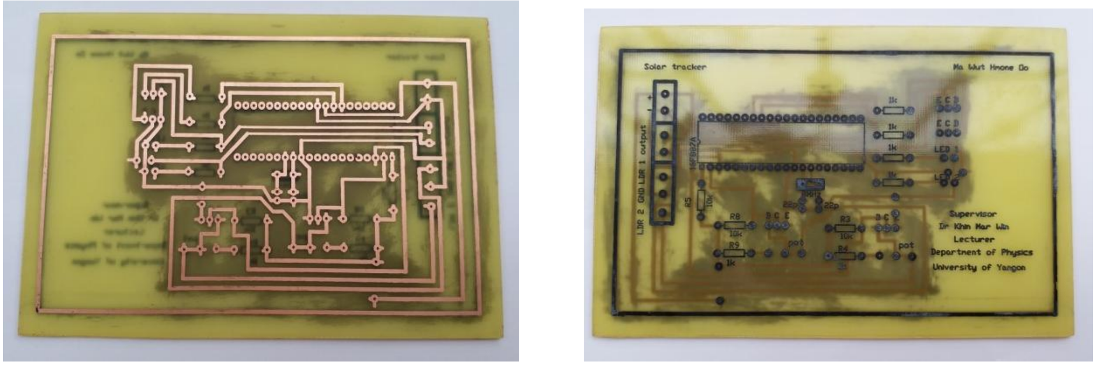

(a) In solder side (b) In component side

Figure 6 The circuit track line diagram of in solder side and component side

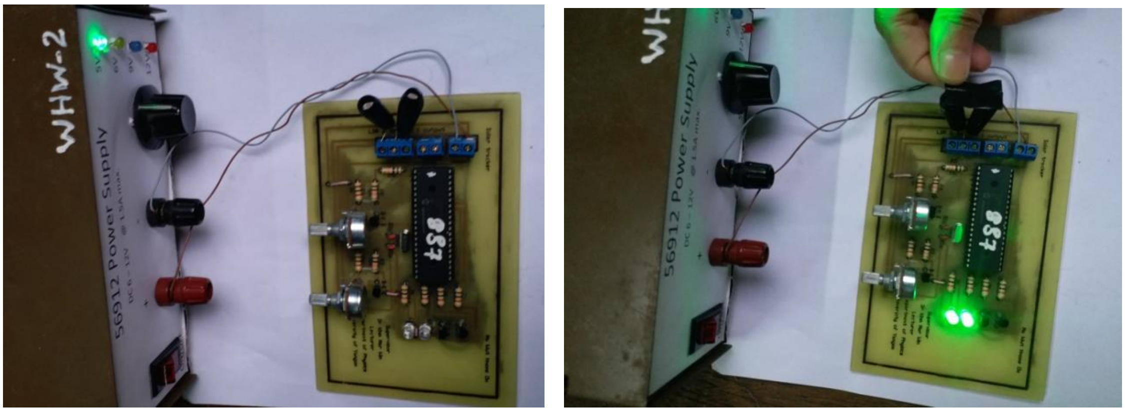

(a) Testing in both light conditions (b) Testing in both dark conditions

Figure 7 Testing the photograph of the "Automatic Solar Tracking Control System"

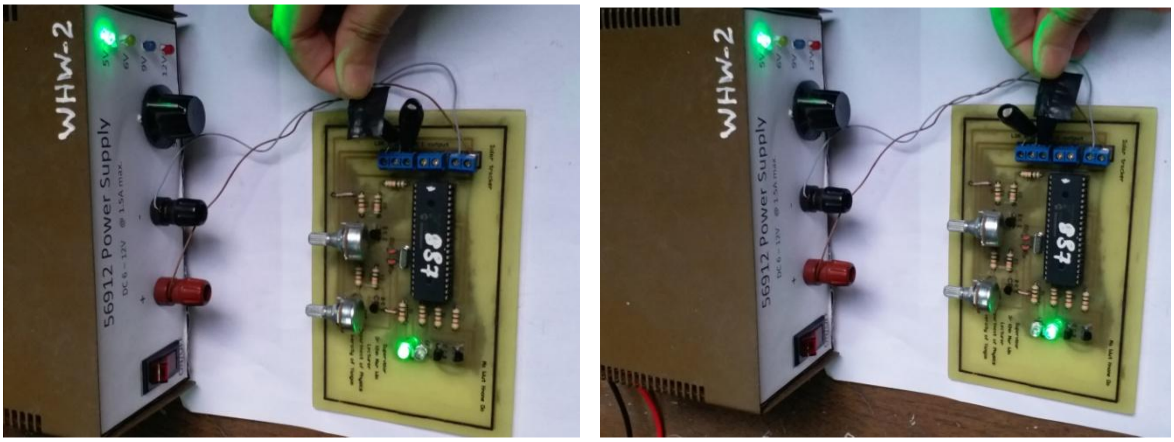

(a) LDR1 (b) LDR2

Figure 8 The photograph of the method of testing of each sensors in dark condition

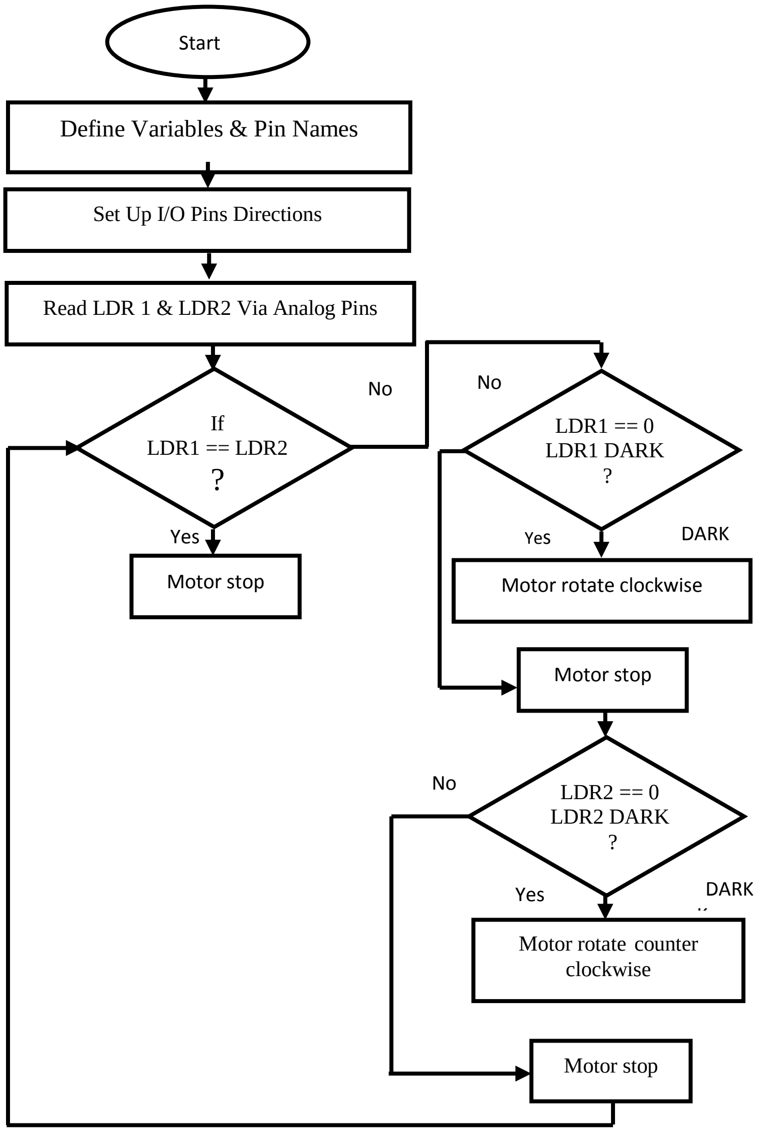

Figure 9 Flow chart of the Solar Tracker

Operation of the System

The two LDR sensors are mounted on the printed circuit board (PCB) instead of the two sides of solar panel. When the intensity of light falling on the LDR, the operation will be started. Rotation of the motor depends on the intensity of light. In this circuit, the LED indicators stand for operating of the DC motor which rotates the solar panel. The DC motor will not rotate when the same amount of light falling on both LDR1 and LDR2. If LDR1 and LDR2 are not the same condition, the motor will rotate toward the direction of sun by facing up right direction. In the noon, sun is ahead and both sensors have same intensity of light, in such cases the DC motor stops, and there is no rotation. Moreover, solar panel also remains stable in night when there will be no light.

Result and Discussion

The “Automatic Solar Tracking Control System” is constructed and tested several times. The tracking system relies mainly on PIC16F887 microcontroller. The output of the controller is used LED indicator instead of the DC motor. The automatic solar tracking control system is one part of the solar power system. This control system operates together with the other units of the solar power system such as solar panel, linear actuator or DC motor, solar charge controller, battery, and inverter. The basic design of the control system provides the solar panels to gain the efficient energy from the sun. The linear actuator or DC motor is used to move the solar panel so that sun’s beam is able to remain aligned with the solar panel. In this research, the detail designs and explanations of LDR sensor with dark detector circuit are included. In a dark, a photo resistor can have a resistance as high as several mega ohms (MΩ) and as low as a few hundred ohms in the light. Thus, 250 kΩ variable resistor is connected in series with the LDR for the purpose, adjusting the critical resistance value of the LDR sensor according to the intensity of light falling upon it.

Conclusion

The use of solar tracking system is the most effective and efficient ways of generating maximum photovoltaic power. All the components in solar power system can be changed according to the energy requirement and the load of the solar panel. If more solar panels are used for more energy, the load of the solar panel must be determined and suitable motor must be used to rotate the solar panel. However, there can be the surrounding effects, such as weather condition especially heavily overcast conditions, in rainy season, and the shade of trees near the solar panel. So, Power produced from the solar energy depends very much on the weather condition. All power generating systems have strengthens and weakness. One of the main advantages of using solar tracker is to solve the power requirement without electricity for rural areas. The result shows that higher generating power efficiency is indeed achieved using the solar tracking system. The proposed method is verified to be highly beneficial for the solar power generation system.

Acknowledgements

I would like to express appreciation to acting Rector Dr Theingi Shwe, Pro-rector Dr Khin May Aung and Dr Cho Cho Myint, Dawei University for their encouragement and kind permission to undertake the present research. I also would like to express my profound thanks to Professor Dr San San Aye, Head of Department of Physics, and Professor Dr Khin Swe Oo, Department of Physics, Dawei University, for their kind permission to carry out this work, their encouragement and help during this work.

References

Ahmad, Z., and Sharief, S., (2017), "Design *and Performance of Solar Track Photo-Voltaic System using Microcontroller"* International Journal of Electrical Engineering and Technology, vol. 8, pp. 295-301.

Chakrabory, S., Mukherjee, N., and Biswas, R., (2015), "*Microcontroller Based Solar Tracking System Using LDRs and Stepper Motor",* International Conference on Microelectronic Circuit and system *(0975 -8887),* pp.38-41. *(0975 -8887).*

Das, P.K., Habib, M.A., and Mynuddin, M., (2015), *"Microcontroller Based Automatic Solar Tracking System with Mirror B*ooster", International Journal of Innovative Research and Application (IJERA) vol. 4, pp.125-136.

Floyd, T.L., (1977), *Digital Fundamentals.* New York: Prentice – Hall.

Karthik K., &Kumar, D.J., (2013). "*Design And Implementation of High Efficiency Solar Tracking System",* International conference on Mechanical Engineering and Renewable Energy,vol.2,pp.2866-2870.

Kumar, S., and Suryanara, (2014). "Automatic *Dual Axis Sun Tracking System using LDR Senso*r",vol. 4, pp.3214-3217.

Mouzadeh, H., Keyhani, A., Javadi, A., and Mobli. H., (2009). "*A Review of principle and Sun Tracking Methods for Maximizing Solar Systems output",* Renewable and Sustainable Energy Reviews. January

Mohammad, N and Karin, T., (2012), "*The Design and Implementation of Hybrid Automatic Solar Tracking System*", International Journal of Innovative Research in Science, Engineering and Technology IJPEE, vol. 4, pp.25-39.

Millman, J. and Halkias C.C., (1991), *Electronic Devices and Circuit* London: Mc Graw – Hill.

Shukla, R., Gupta, A., Kumar P., & Shekhar, D., (2016) "*Design and Construction of an Automatic Solar Tracking System*", International Journal of Electrical Engineering and Technology, vol. 2,pp. 5-8.

Appendix

```
/****************************************************************
* File Name: Solar_Tracker_Dark_.c
* Author:    Wut Hmone Oo
* Date:      14 November 2018
* Notes:- Device: PIC16F887
*       Oscillator: 8 MHz Crystal
*       A DC Motor is connected at PortB RB0 & RB1 via H-Bridge Transistors
*       Q1-Q4.
*       Two LDRs are connected at portA RA0 & RA1 via transistor Q1 & Q2.
*       If one LDR is dark, motor rotates one direction. And if other LDR
*       is dark motor rotates opposite direction.
*****************************************************************/
void main(){
  ANSEL = 0;           // All I/O are configured as digital
  ANSELH = 0;
  PORTB = 0;           // Clear PORTB
  TRISB = 0;           // PORTB as output
  PORTA = 0;           // Clear PORTA
  TRISA = 0x03;        // Set PORTA pins RA0 & RA1 as inputs
for(;;){
       if(porta.F0 == 0) {     // If LDR1 is dark, then
        portb.F0 = 1;       // Motor rotates Clockwise
     }else{
       portb.F0 = 0;      // Otherwise motor stop
     }
      if(porta.F1 == 0) {     // If LDR2 is dark, then
        portb.F1 = 1;       // Motor rotates Counter Clockwise
     }else{
        portb.F1 = 0;      // Otherwise motor stop
     }
    }                 // Endless loop
}
```

J. Myanmar Acad. Arts Sci. 2020 **Vol. XVIII.No.2A**

EFFECTIVE OF BAMBOO-CEMENT CONCRETE IN WASTE ENVIRONMENT

Aye Thandar[1], Aye Thandar Oo[2], Than Than Win[3] ,Yin Maung Maung[4] and Mar Lar Wai[5]

Abstract

Bamboo is the common term applied to a broad group (1250 species) of large woody grasses, ranging from 10 cm to 40 m in height. The use of waste materials with pozzolanic properties in concrete production is becoming a worldwide practice. This paper presents investigates the strength performance of concrete using partial blends of cement and bamboo wastes ash. Elemental analysis was conducted on bamboo ash and ordinary portland cement, OPC by EDXRF (Energy Dispersive X-ray Fluorescence) technique to evaluate its percentage composition. Bamboo ash shows pozzolanic activity and it was used as supplementary cementitious material. Bamboo ash was then used to replace OPC by weight in ratio of 0%, 5%, 10%, 15%, 20% and 25% in concrete grade M-20. Based upon the quantities of ingredients of the mixes M-20, (it means the weight ratio of cement : sand :coarse aggregate) grade concretes were prepared. Twelve pieces of 150 mm concrete cubes were prepared. These cubes were tested at 7 days and 56 days of curing ages and then maximum load and compressive strength of cubes were determined respectively. To investigate the pozzolanic behavior of bamboo ash, concrete crushes were analyzed by XRD analysis. It shows the very high concrete strength values could be obtained with (ordinary portland cement and bamboo waste ash) OPC–BWA blended cement concrete when high control measure was applied and at longer days of hydration. Therefore, OPC/BWS blended cement concrete could be used in civil engineering and building works, thereby reducing the cost of production.

Keywords – Bamboo waste ash, EDXRF, pozzolanic, compressive strength, XRD

Introduction

Researchers all over the world today are focusing on ways of utilizing either industrial or agricultural waste, as a source of raw materials for industry. Agricultural wastes are widely available, renewable and virtually free and it is important resource. They are converted into heat, steam, charcoal, methanol ethanol, bio diesel as well as raw materials (animal's feed, composting, energy and biogas construction etc.). The production of energy from agricultural waste has been utilized to varying degrees in different parts of the world. This wastes utilization would not only be economical, foreign exchange earnings and environmental pollution control.

Industrial wastes, such as blast furnace slag, fly ash and silica fume are being used as supplementary cement replacement materials. Natural pozzolans by themselves possess little or no cementing value, but finely ground in the presence of moisture, they will chemically react with calcium hydroxide at ordinary temperature to form hydrated phases possessing cementing properties.[1,2] Nowadays, some industrial by-products and wastes are attracting much research because of their high silica and/or alumina content for the use as additives in commercial Portland cements. It is well known that hydrated phases formed during pozzolanic reaction commonly improve the performance of concrete.

---

[1] Demonstrator, Physics Department, Dawei University

[2] Associate Professor, Physics Department , Bago University

[3] Professor , Physics Department, Pinlong University

[4] Professor , Physics Department, University of Yangon

[5] Associate Professor, Physics Department, Computer University(Thaton)

Pozzolan is a siliceous or siliceous and aluminous material, which in itself possesses little or no cementitious value but will, in finely divided form and in the presence of moisture, chemically react with calcium hydroxide $Ca(OH)_2$ to form compounds possessing hydraulic cementitious properties. Ordinary Portland Cement is the most extensively used construction material in the world. Since the early 1980's, there has been an enormous demand for the mineral admixture and in future this demand is expected to increase even more. If some of raw material having similar composition can be replaced by weight of cement in concrete then cost could be reduced without affecting its quality. For this reason bamboo ash is one of the main byproduct can be used as mineral admixture due to its high content in silica (SiO2). Also in this modern age every structure has its own intended purpose and hence to meet this purpose modification in traditional cement concrete has become essential. This situation has led to the extensive research on concrete resulting in mineral admixture to be partly used as cement replacement to increase workability in most structural application. We found that ash obtained from bamboo is amorphous in nature and has pozzolanic properties. The annual production of bamboos all over the world is about 20 million tonnes but about 10 million tonnes are produced in India, China and Japan. Bamboo is one of the fastest-growing plants on Earth, with reported growth rates of 250 cm (98 in) in 24 hours. However, the growth rate is dependent on local soil and climatic conditions, as well as species, and a more typical growth rate for many commonly cultivated bamboos in temperate climates is in the range of 3-10 centimeters (1.2-3.9 in) per day during the growing period. Primarily growing in regions of warmer climates during the late Cretaceous period, vast fields existed in what is now Asia. Bamboo is the fastest growing, renewable natural resource known to us. It is a small wonder, therefore, that this material was used for building extensively by our ancestors. It has a long and well established tradition as a building material throughout the tropical and sub-tropical regions. It is used in many forms of construction, particularly. It has also been found that bamboo acts very well in buckling but due to low stresses than compared to steel and due to it not being straight it may not be very good. Further, it has been established that in seismic zones the failure of bamboo is very less as the maximum absorption of the energy is at the joints. Cellulose is the main component present in bamboo which is the main source of mechanical properties of bamboo. Concrete is a composite material composed of coarse aggregate bonded together with a fluid cement that hardens over time. Most concrete used are lime-based concretes such as Portland cement concrete or concretes made with other hydraulic cements. When aggregate is mixed together with dry Portland cement and water, the mixture forms a fluid mass that is easily moulded into shape. The cement reacts chemically with the water and other ingredients to form a hard matrix that binds the material together into a durable stone-like material that has many uses.

Experimental

Materials and Methods

Preparation of Samples

The bamboo wastes were collected from Tanintharyi region of Dawei , Myanmar. They were dried under sunlight to reduce the moisture content in wastes. The dry bamboo wastes were burnt in air and the gray bamboo ash was obtained. Bamboo ash was then sieved with a 200 µm standard sieve and purified bamboo ash was obtained. Bamboo ash and ordinary portland cement OPC were analyzed by (Energy Dispersive X-ray Fluorescence) EDXRF technique, to evaluate their chemical composition. By observing the EDXRF results, the chemical composition of bamboo ash and OPC were determined. For concrete cubes sample preparation, the main ingredients are Ordinary Portland Cement (OPC), bamboo ash, sand, coarse aggregates and water. In this experimental work, twelve 150 mm concrete cubes, grade grade M-20 (1:1.5:3) were designed. Based upon the quantities of ingredient of the mixes, OPC (replacing cement by 0% bamboo ash) concrete cube, which is regarded as "sample 1" and the bamboo ash was used for 5%, 10%, 15%, 20% and 25% replacing cement concrete cubes which were marked out as sample 2,3,4,5,6 were prepared for concrete grade M-20. The ingredients of concrete were thoroughly mixed in pan and during mixing the ingredients of concrete, water were used to form concrete paste. Water to cement ratio (w/c) was different for different specimens and then uniform thoroughly consistency concrete paste was achieved and concrete specimens were casted by using the plastic mould as shown in figure 1. These concrete cubes were produced for 7 days and 56 days of curing age. These were tested by compression machine, the maximum load and compressive strength of concrete cubes were determined. To investigate the pozzolanic behavior of bamboo ash, (95%OPC+5% bamboo ash) and (90% OPC+10% bamboo ash) concrete crushes were analyzed by XRD analysis.

EDXRF analysis of bamboo ash and ordinary ordinary portland cement

The chemical composition of bamboo ash determined by EDXRF analysis was shown in table 1.The chemical composition of bamboo ash illustrates that it contains high amount of silicon (Si) as dominant element and the second dominant elements are potassium (K),calcium (Ca) , Iron (Fe) and in addition to small amount of sulfur (S), manganese (Mn), titanium (Ti), zinc (Zn) ,rubidium (Rb), copper (Cu), strontium (Sr) and yttrium (Y).

The chemical composition of OPC by EDXRF analysis was shown in table 2. The chemical composition of OPC illustrates that it contains high amount of calcium (Ca) as dominant element and the second dominant elements are silicon (Si), Iron (Fe), potassium (K) , sulfur (S), titanium (Ti) manganese (Mn), strontium (Sr) and zirconium (Zr).

XRD analysis of the (5% & 10% bamboo ash) admixture cement paste

In this research, an XRD analysis is used to investigate the pozzolanic behavior of bamboo ash and to identify the hydration products formed during the hydration of OPC in concrete making is shown in Fig 2 (a&b). By observing the XRD patterns of (5% and 10% bamboo ash) admixture cement paste at curing age 56 days (concrete crushes), it was found that calcium silicate hydrate, C-S-H, calcite, $CaCo_3$ and calcium hydroxide, $Ca\ (OH)_2$ peaks were observed in both patterns. The most intense C-S-H peaks were observed on both observed file and the XRD pattern of (5% bamboo ash) has more intense peaks than (10% bamboo ash). This C-S-H peaks indicate the pozzolanic reaction between $Ca(OH)_2$ and amorphous silica present in bamboo ash. This additional hydration product C-S-H has the cementitious properties and it improves the compressive strength of concrete.

Maximum load and Compressive Strength

The maximum load and compressive strength of all concrete cubes were measured and tested at Myanmar Engineering Society, MES Quality Control Laboratory, Compression Test of Concrete Specimens room, Hlaing University Campus, Hlaing Township, Yangon Myanmar. The compressive strength of 5 is greater than that of OPC for the caring age of 7 days and 56 days. 10, 15, 20 & 25% (bamboo ash concretes) grade M-20 did not exceed than that of OPC and it had nearly equal value of OPC. The maximum load and compressive strength of MES results were shown in Figure 3 and bar graphs were shown in Figure 4 (a,b) & 5(a,b).

Target Strength of Concrete

According to IS, the target strength of the compressive strength of the concrete mixture is defined as:

$$\text{Target Strength} = f_{ck} + 1.65\sigma,$$

Where , σ = the standard deviation

f_{ck} =the characteristic strength [Quantity Control Issue].

The results were shown in Table 3&4.

Target Strength of Concrete Grade M-20 (1:1.5:3)

For Grade-20 (1:1.5:3)

Target Strength,

$f_t = f_{ck} + 1.65\ \sigma$

$f_t = 15 + 1.65 \times 4$ (Standard Deviation for grade M-20 is 4)

$\mathbf{f_t = 26\ MPa}$

Figure 1 The photograph of concrete paste pour in plastic mould

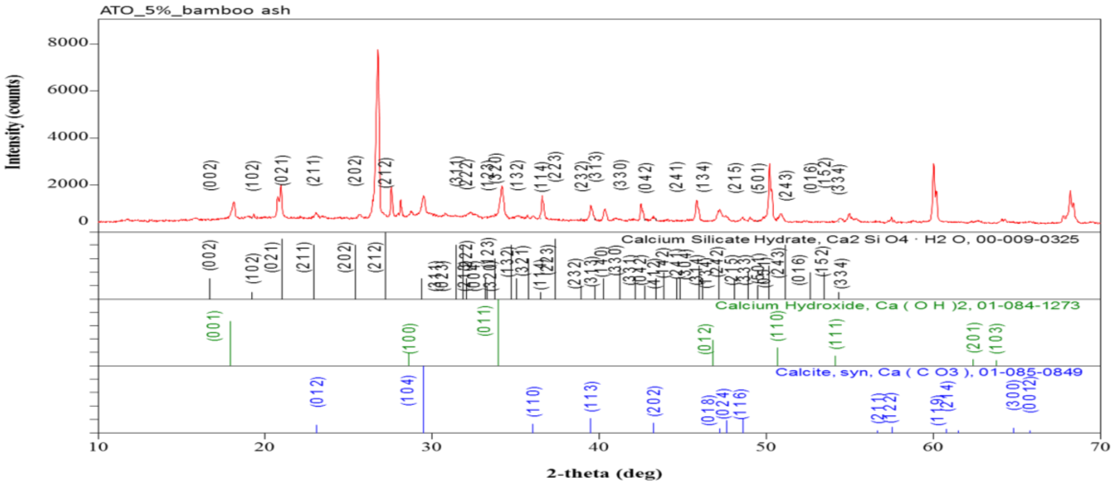

Figure 2(a) The XRD pattern of 5 % bamboo ash admixture cement paste

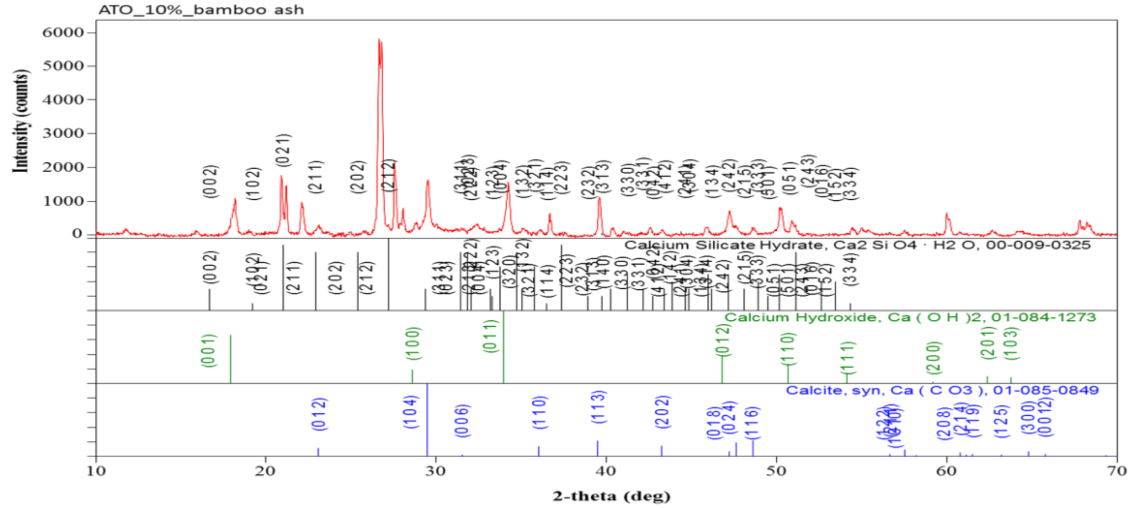

Figure 2(b) The XRD pattern of 10 % bamboo ash admixture cement paste

MES
Quality Control Lab

MES Quality Control Laboratory
Compression Test of Concrete Specimens
Myanmar Engineering Society, Hlaing University Campus, Hlaing Township,
Yangon, Myanmar. Phone : 01-519673 ~ 76, Ext-115

CONCORDIA
INTERNATIONAL

Sr.No: MES -QC-82733
Date: 26-1-2018

npany : Ma Aye Thandar Oo
ject : ထားဝယ်တက္ကသိုလ်၊ သုတေသန။
hod of Test : BS 1610, 1881

cimen no:		Without Bamboo Ash	Bamboo Ash-5%	Bamboo Ash-10%	Bamboo Ash-15%	Bamboo Ash-20%	Bamboo Ash-25%		
king on Specimen		17-11-2017	17-11-2017	17-11-2017	17-11-2017	17-11-2017	17-11-2017		
e of Test		15-12-2017	15-12-2017	15-12-2017	15-12-2017	15-12-2017	15-12-2017		
(days)		28	28	28	28	28	28		
ght	(Kg)	7.68	7.86	7.76	7.8	7.86	7.74		
gth	(mm)	150.35	150.34	150.36	150.52	150.42	150.61		
lth	(mm)	150.42	150.29	150.39	150.28	150.51	150.34		
ght	(mm)	150.62	150.25	150.45	150.38	150.21	150.38		
sity	(lb/ft^3)	143.01	146.86	144.68	145.45	146.60	144.18		
kimum Load	(kN)	725.73	785.52	685.49	566.81	485.39	518.91		
npressive Strength	(N/mm^2)	32.09	34.77	30.31	25.06	21.44	22.92		
	(lb/in^2)	4654.62	5042.78	4397.11	3634.63	3109.84	3324.16		

arks: This certificate is issued only for the receipt of the test sample. (In Accurancy ±0.22%)
ny)

Condition when received:
☐ Damage before test
☐ Out of Shape
☐ Uneven surface
☐ Normal

Tested by
Lynn Lynn Htike
Lab Technician
MES QC Lab

MES
Quality Control Laboratory
CONCORDIA INTERNATIONAL
Tel : +95-1-519673 ~ 519676, Ext : 115

Approved by
Myint Soe
M.E (Petro-Engg:)
(CEO) FM-MES

Lab Consultant
San Kyu
B.E (Civil), M.Engg (Structure)
M.ASCE, AER, FM-MES, PE, ACPE (Construction)

Figure 3 The photograph of MES's certificate

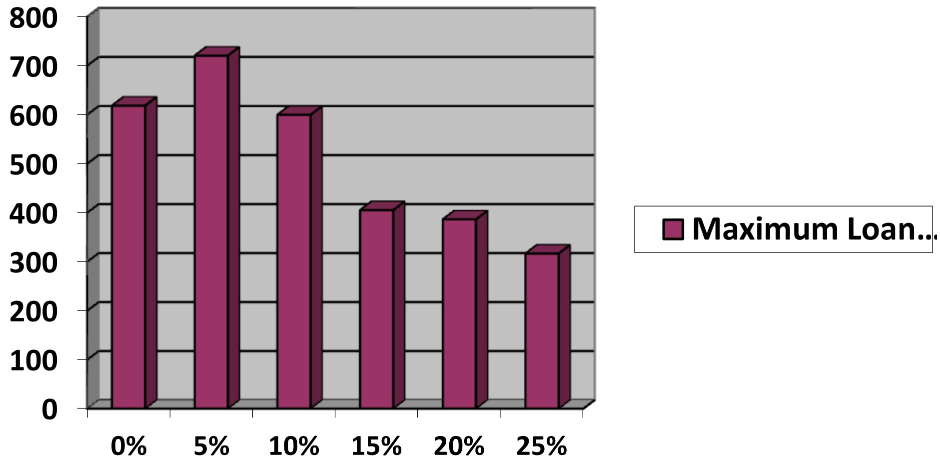

Figure 4(a) Maximum load bar graph of M-20 concrete cubes for 7 days

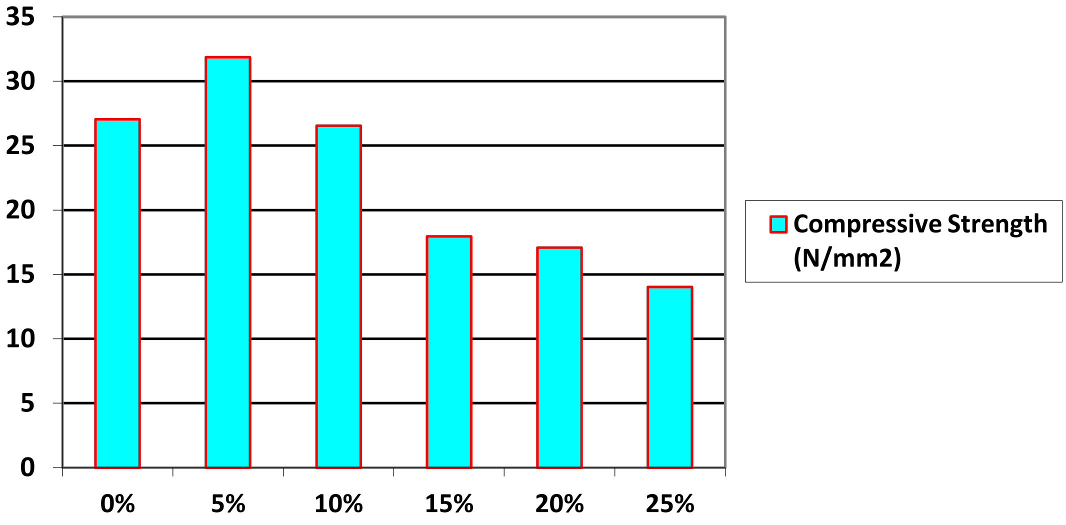

Figure 4 (b) Compressive Strength bar graph of M-20 concrete cubes for 7 day

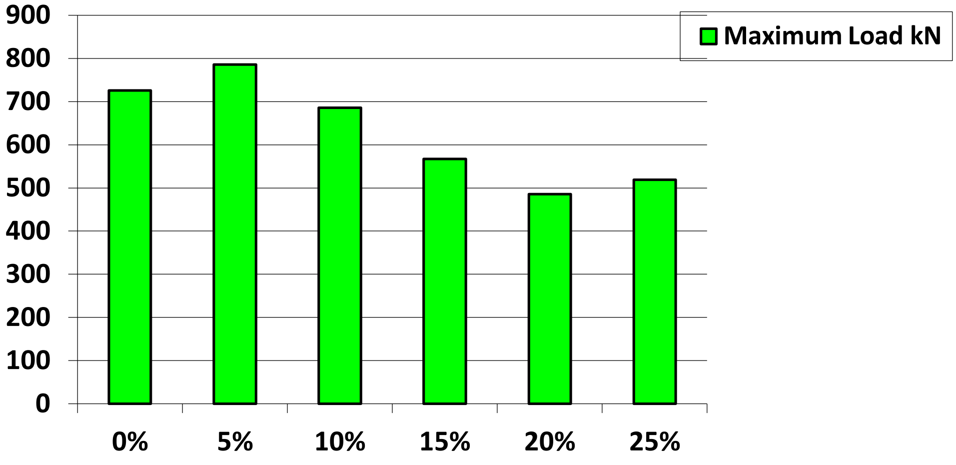

Figure 5 (a) Maximum load bar graph of M-20 concrete cubes for 56 days

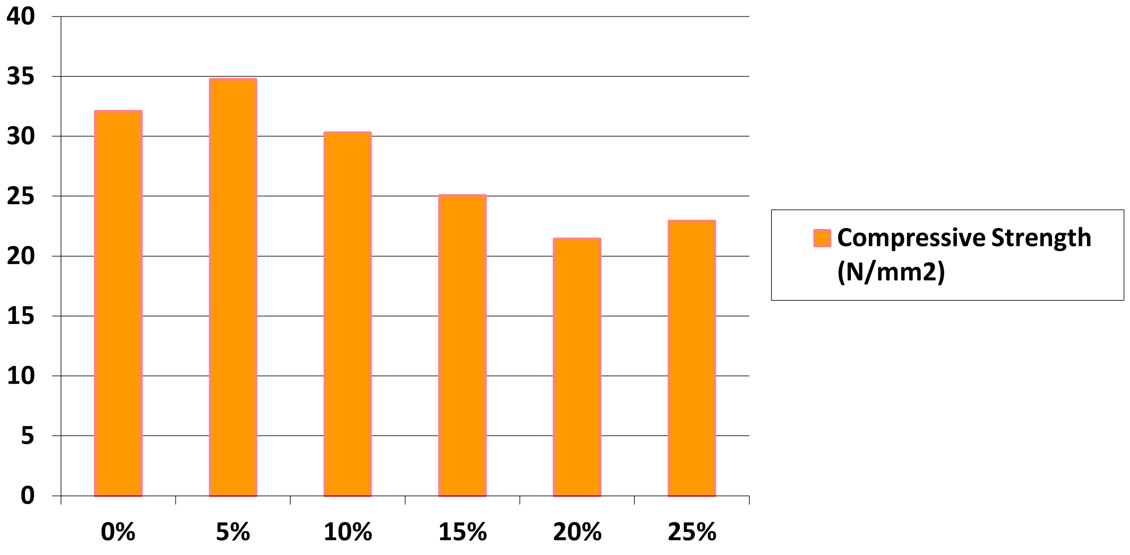

Figure 5 (b) Compressive Strength bar graph of M-20 concrete cubes for 56 day

Table 1 Chemical composition of bamboo ash by EDXRF analysis

Component	**Si %**	**K %**	**Ca %**	**Fe %**	**S %**	**Mn %**	**Ti %**	**Zn %**	**Rb %**	**Cu %**	**Sr %**	**Y %**
Bamboo Ash	51.47	14.98	14.44	9.12	1.47	1.11	0.59	0.59	0.09	0.08	0.07	0.07

Table 2 Chemical composition of ordinary Portland cement, OPC by EDXRF analysis

Component	**Ca%**	**Si%**	**Fe%**	**K %**	**S %**	**Ti %**	**Mn %**	**Sr%**	**Zr%**
OPC	83.87	6.55	6.37	1.58	1.02	0.41	0.1	0.8	0.23

Table 3 Comparison of Measurable Compressive Strength and Target Strength for grade M-20 (bamboo ash) for 7 days

No.	**OPC/BWA**	**Concrete Grade**	**Measurable Compressive Strength (MPa)**	**Target Strength (MPa)**	**Curing Age(Days)**	**Remark**
1	(0%)	M-20	27.04	26.6	7	MCS>TS
2	(5%)	M-20	31.88	26.6	7	MCS>TS
3	(10%)	M-20	26.56	26.6	7	MCS>TS
4	(15%)	M-20	17.95	26.6	7	MCS<TS
5	(20%)	M-20	17.08	26.6	7	MCS<TS
6	(25%)	M-20	14.03	26.6	7	MCS<TS

Table 4 Comparison of Measurable Compressive Strength and Target Strength for grade M-20 (bamboo ash) for 56 days

No	OPC/BWA	Concrete Grade	Measurable Compressive Strength (MPa)	Target Strength (MPa)	Curing Age(Days)	Remark
1	(0%)	M-20	35.44	26.6	56	MCS>TS
2	(5%)	M-20	40.55	26.6	56	MCS>TS
3	(10%)	M-20	28.87	26.6	56	MCS>TS
4	(15%)	M-20	26.79	26.6	56	MCS>TS
5	(20%)	M-20	26.7	26.6	56	MCS>TS
6	(25%)	M-20	20.44	26.6	56	MCS<TS

Conclusion

Pozzolanic behavior of bamboo ash in partial cement replacement in concrete has been studied. By observing the EDXRF analysis of bamboo ash, it was found that bamboo ash contains high amount of silica and second dominant elements were potassium and calcium. The elements contain in bamboo ash and OPC were almost the same. For concrete grade M-20, according to MES's results, the measured value of maximum load and compressive strength of blended concretes at the curing age of 56 day is higher than the curing age of 7 days. Definitely 5% bamboo cement is exceed than OPC (0%) concrete. However, 10%, 15% and 20% blended concretes reached the target strength. By observing the XRD patterns of 5% and 10% bamboo ash of concrete crushes for 56 curing ages , it was found that the hydration product, calcium silicate hydrate, C-S-H formed during the hydration of OPC and it was shown that the pozzolanic behavior of the bamboo ash. Fineness of bamboo ash is also the important factor affecting the compressive strength of concrete. So, grade M-20 for 5% and 10% of bamboo ash at the curing age of 56 days is quite suitable for partially cement replacements.

Acknowledgements

I would like to express appreciation to Acting Rector Dr Theingi Shwe, Pro-rector Dr Khin May Aung and Dr Cho Cho Myint, Dawei University for their encouragement and kind permission to undertake the present research. I also would like to express my profound thanks to Professor Dr San San Aye, Head of Department of Physics, and Professor Dr Khon Swe Oo, Department of Physics, Dawei University, for their kind permission to carry out this work, their encouragement and help during this work.

References

Aigbodion V. S (2010), "Journal of Minerals & Materials Characterization & Engineering", Ahmadu Bello University, Samara, Zaria, Nigeria,Vol.9,67-77.

Anurag Nayak, Arehant S Bajaj , Abhishek Jain , Apoorv Khandelwal , (2013) "Replacement of Steel by Bamboo Reinforcement". IOSR Journal of Mechanical and Civil Engineering (IOSR-JMCE),Vol- 8, 50-61

Dinesh Bhonde. P. B. Nagarnaik, D. K. Parbat, U. P. Waghe (2014) "Experimental Investigation of Bamboo Reinforced \ Concrete Slab", American Journal of Engineering Research (AJER) Vol.03, 128-131.

Ernesto Villar-Cocina Ernesto ,Villar-Cocina a,ft, Eduardo Valencia Morales a, Sergio F. Santos b, Holmer Savastano Jr. b, Moises Friasc (2011), "Pozzolanic behavior of bamboo leaf ash Characterization and determination of the kineti parameters", Cement & Concrete Composites Journal ,Voi.33,68-73.

Jigar K. Sevalia, Nirav B. Siddhpura , Chetan S. Agrawal , Deep B. Shah , Jai V. Kapadia, (2013) "Study on Bamboo as Reinforcement in Cement Concrete", International Journal of Engineering Research and Applications (IJERA) Vol. 3.1181-1190.

Kawade U.R (2013),"International Journal of Innovative Research in Science", Engineering and Technology, Pravara Rural Engineering College, India, Vol.2.

Toshi Bhavsar (2015) "Preparation and Characterization of BRC with Different Types of Concrete", International Journal of Latest Trends in Engineering and Technology (IJLTET),Vol.5 , 390-401.

Zongjin Li (2011) "Advanced concrete technology".

J. Myanmar Acad. Arts Sci. 2020 **Vol. XVIII.No.2A**

INVESTIGATION ON LITHIUM BIS TRIFLUORO METHANE SULPHONYL IMIDE SALT BASED POLYMER ELECTROLYTE FILMS

Aye Hsu Pan[1] , Sint Ohnmar[2], Ni Ni Shein[3]

Abstract

Solid polymer electrolyte films with different weight percent ratios of lithium bis (trifluoro methane sulphonyl) imide (LTFSI) salt were prepared using solution casting method. The conductivity and dielectric response of the solid polymer electrolyte systems were studied within the frequency range of 120Hz and 1kHz at room temperature. The conductivity of an electrolyte depends on the ability of the polymer host to solvate the (LTFSI) salt. Polymers with higher dielectric constant will serve the purpose better. The dielectric constant and electrical conductivity follow the same trend with (LTFSI) salt concentration. It was observed that the magnitude of conductivity had increased with the increase in salt concentration. FTIR and XRD techniques were used in the complexed studies. The values of dielectric constant were decreased with increasing frequency.

Keywords: Electrolyte films, LTFSI, FTIR and XRD techniques .

Introduction

Solid polymer electrolyte membranes have shown great enthusiasm in the research work due to their wide range of applications in Electrochemical devices such as Fuel cells, Cell phone batteries, Sensors, Rechargeable batteries, Capacitors, Memory devices, Electro chromic display devices etc. Solid polymer electrolytes in Lithium ion batteries is an interesting field due to numerous characteristics such as no leakage, more flexibility, high energy density, more safety, and ease to manufacture. This made researchers in the development of Lithium polymer batteries. Lithium polymer batteries consist of polymer electrolyte as separator and charge carrier of ions which have been used as power sources for portable devices due to high energy density. Chitosan is a derivative of chitin which can be obtained from crab and shrimp shells. Chitosan is produced from deacetylation of chitin to overcome the solubility limitation of chitin in common solvents. Due to the NH_2 and OH functional groups that can serve as conjunction sites, chitosan is a good sorbent with high affinity for transition metal ions. Chitosan has good film forming ability, porous scaffolds, and hydrogels. Ion-conducting polymer electrolytes based on chitosan have also been reported. From the fundamental point of view, ionic conduction in polymer electrolysis still poorly understood. Ion transport is complex and depends on factors such as salt concentration, dielectric constant of host polymer, degree of salt dissociation and ion aggregation, and mobility of polymer chains. Dielectric analysis of ion conducting polymer electrolytes can provide information on ion transport behavior and ionic/molecular interaction in solid polymer electrolytes. In the present research work; Solid polymer electrolyte films with LITFSI salt are prepared with different concentrations and characterized by XRD, FTIR. XRD reveals the semi crystalline, amorphous nature of the polymer film. FTIR analysis provides the complexation and the extent of blending between the polymer and salt. Annealing method study reveals the thermal properties of the polymer and activation energy of the polymer electrolyte system.

---

[1] Demonstrator, Department of Physics, Dawei University
[2] Dr, Lecturer, Department of Physics, Dawei University
[3] Dr, Lecturer, Department of Physics, Dawei University

Experimental Procedures

Preparation of samples

Solid polymer electrolyte films were used as host polymer electrolytes and were prepared by standard solution casting techniques. All samples were prepared at room temperature and stored under dry conditions. A 5 g of prepared chitosan flake was dissolved in 500 mL of 1 % (w/v) acetic acid solution. The solution was stirred by hotplate stirrer, for 80 hours at an ambient temperature, and then the chitosan acetate host polymer solution was kept on overnight. The solution was maintained at 80 °C in water bath for one hour . The degassed and well-mixed solutions (30 mL) were casted onto petri dish, and dried in air for 3 days at room temperature until constant weight. The dried transparent chitosan films (0% doping salt) were detached from the petri dish. A 1 g of LTFSI salt was dissolved in 100 mL with distill water to make 1 % (w/v) doping salt solution by using magnetic stirrer. A 2.4 mL of 1 % (w/v) doping salt solution was mixed with 27.6 mL of 1 % (w/v) chitosan acetate solution by using hotplate stirrer. The 30 mL of polymer salt solution was obtained as 8wt % doping salt solution. It was prepared to more 8wt % in each still to still 40wt% dopant. The degassed and well-mixed solution was cast onto petri dish, and dried in air for 3 days at room temperature until constant weight.

The dried transparent chitosan films (8 % doping salt) were detached from the petri dish. Finally, chitosan film compound of 8wt % was obtained. The same procedure were carried out for the preparation of chitosan films compound of 8, 16, 24, 32, 40 % LTFSI were prepared.

Characterization of samples

The ionic conductivities of the samples were measured at within at room temperature using EXTECH 380193 LCR meter with a frequency range of 120 Hz and 1 kHz. The conductivity (σ) was determined using the equation below:

$$\sigma = \frac{1}{\rho(0)/2S/W*\log(e)2} \qquad (1)$$

From equation 1, $\rho(0) = 2\pi SR$, ‘S’ represents the distance between the two contact probe, ‘W’ represents the thickness of sample and R is the resistance of the sample. The dielectric constant ε_r can be defined as:

$$\varepsilon_r = C_p t/\ \varepsilon_o A \qquad (2)$$

From equation 2, ‘t’ represents the thickness of sample, ‘A’ is the area of the surface of the sample, C_p is the capacitance of the specimen in Farad and ε_o is the permittivity of free space.

X-ray diffraction (XRD): In this work, X-ray diffraction were carried out using a Rigaku x-ray powder diffractometer which employs Cu-K_α x- radiation of wavelength $\lambda = 1.54056\dot{A}$ between a 2θ angle of 5° to 70° . X-ray diffraction was carried out to determine the nature of the materials whether a material is amorphous or crystalline.

FTIR spectrometer : Prepared chitosan films with various composition of doping salt, which were examined by IR-8400, Shimadzu, Japan (Universities’ Center, University of Yangon.)

Results and Discussion

The structural , conductivity and dielectric properties of the polymer electrolytes based on LTFSI salt were investigated. The samples were prepared by solution cast method by taking different concentration of different ratio (i.e., Cs0%, Cs8%, Cs16%, Cs24%,Cs32% and Cs40%). The compatibility between the polymer matrix and the inorganic dopants has great influence on the properties electronic conductivity of the polymer electrolytes.

X-ray diffraction and FTIR studies

In order to investigate the effect of LTFSI salt on the structure of chitosan-based polymer electrolyte, x-ray diffraction of pure chitosan film, and their complexes have been performed. These crystalline structures contribute to the peaks in the XRD pattern of Cs0%, Cs8%, Cs16%, Cs24%, Cs32% and Cs40% are shown in Fig. 1. As seen in the XRD pattern of the pure chitosan Cs0%, the high intensity peak at around $2\theta = 22°$. The increase in the broadness of the peak reveals the amorphous nature of the complexed system. Thus XRD analysis reveals the complex formation between the polymer and the salt.

The FTIR spectra were recorded to study the structure of polymer, polymer-salt interactions and complexation in polymer electrolytes. The interaction between polymer and salt influence vibrational modes of atoms or molecules which in turn generates change in chemical and physical properties of the polymer. The most frequently performed observations to confirm the complexation of the polymer host with salts are variation in intensity of the bands, shifting of the bands with respective to the salt content. Figure.2 represents the FTIR spectrum of chitosan and chitosan: LTFSI complexes in the wave number region between 500 cm^{-1} and 4000 cm^{-1}. Although there is possibility of overlapping between the N–H and the O–H stretching vibrations, the strong broadband at 3300–3500 cm^{-1} is characteristic of the N–H stretching vibration. The significant decrease of transmittance intensity and shifting in this band region indicates that the N–H vibration was affected by the attachment of the cation salt. The shifting and decrease in intensity are attributable to the fact that the attachment of cation salt to nitrogen and oxygen atoms can reduce the vibration intensity of the N–H or O=C–NHR bonds due to the molecular weight becoming greater after cation bindin. The shifting and the vibrational bands at 2881, 2885, 2889, 2879 were assigned as asymmetric stretching and symmetric stretching of CH_{3-} and CH_{2-} corresponds to crystalline nature of chitosan which has been shifted to low frequencies at 2879 cm^{-1} of reducing intensity at 24wt% due to increase of LTFSI salt concentration; which shows the decrease of crystalline nature of the pure chitosan. It means amorphous nature of the polymers enhances the electrical conductivity of the sample. This indicates only certain amount of salt is able to dissolve which limits the number of Lithium ions generated which affects the electrical conductivity. The absorption band at 1633, 1637, 1629, 1641 and 1637cm^{-1} corresponds to stretching vibration of –C=O. The absorption band at 1402 corresponds to –C-F stretching, shifted to high frequency at 1404, 1408 and 1406 cm^{-1} for increase of concentration of LTFSI salt. This happens due to weak interaction between H atoms of CH_2 groups and F atoms of CF_2 groups. The peaks at 3000 to 2900 cm^{-1} frequencies correspond to C-H stretching vibration of polymer. The observed peaks at 3650 to 3000 cm^{-1} show OH and –OOH groups. This occurs due to highly hygroscopic nature of LTFSI salt that absorbs moisture from the atmosphere. The shifting and a decrease in intensity of C–O bands are also indicative that complexation between the cation of the salt and oxygen atom has occurred.

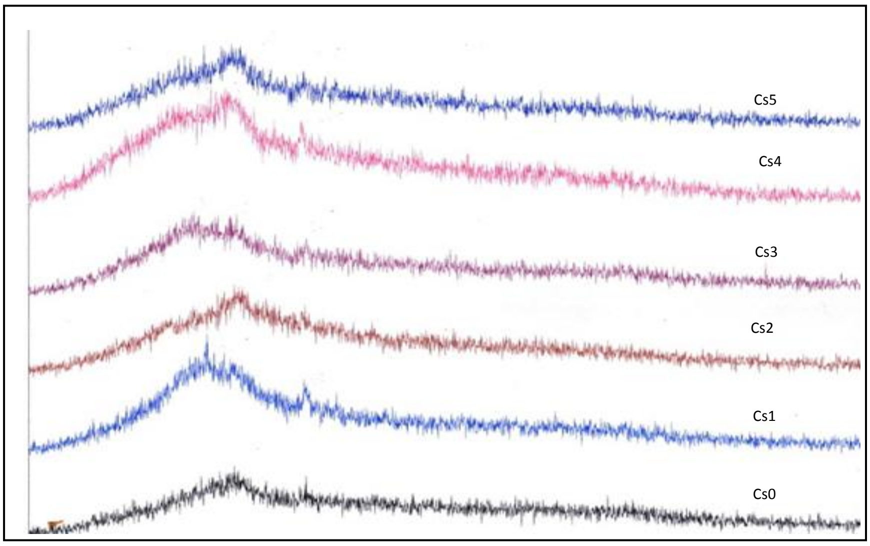

Figure 1 XRD spectra of LTFSI Salt -Chitosan polymer electrolyte films

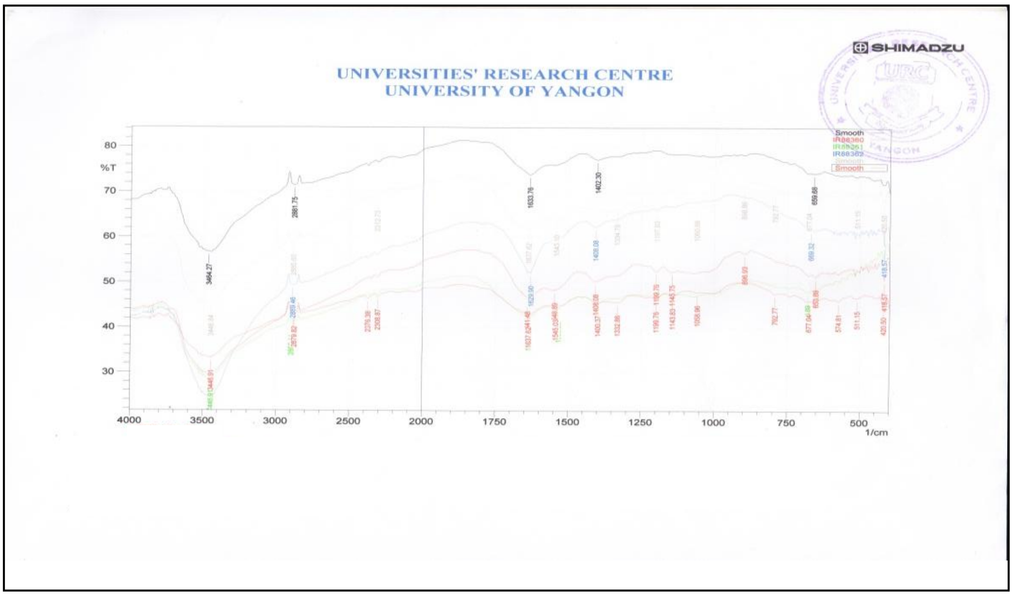

Figure 2 FTIR spectra with various concentrations of LTFSI salt

Electrical conductivity dielectric studies of solid polymer electrolytes

The electrical properties of the polymer electrolyte were studied using EXTECH 380193 LCR meter. Table.1 shows the various composition of (LTFSI) salt and chitosan solution. The value of electrical conductivity for solid polymer electrolytes samples with different weight percentages of (LTFSI) salt is plotted in Figure.3 and shown in Table.2. The conductivity was increased due to enrichment of (LTFSI) salt content reaching a highest value with 24wt% thereafter it decreases with futher increase in amount of (LTFSI) salt content. The value of dielectric value for solid polymer electrolytes samples with different weight percentages of (LTFSI) salt is plotted in Figure.4 and shown in Table.3. The dielectric constant was found to increase upon the addition of (LTFSI) salt and these parameters are significantly influenced by the frequency. A dielectric medium has been assumed which is made up of well conducting grains and poorly conducting grain boundaries respectively. The grain are highly conductive and have high values of permittivity. At low frequency region grain boundaries are more effective than the grains in electrical conduction. Thinner the grain boundary results the higher value of dielectric constant. Higher values of the dielectric constant observed at lower frequencies have been also explained on the basis of interfacial/space polarization due to nonhomogeneous dielectric structure.

Table 1 Various composition of LTFSI salt and chitosan Solution

Sample	**Volume of 1 % (w/v) LTFSI (mL)**	**Volume of 1 % (w/v) Chitosan (mL)**	**Weight percent of LTFSI Salt (%)**
Cs0	0	30	0
Cs1	2.4	27.6	8
Cs2	4.8	25.2	16
Cs3	7.2	22.8	24
Cs4	9.6	20.4	32
Cs5	12.0	18.0	40

Table 2 Conductivity measurement for various composition of lithium bis (trifluoro methane sulphonyl) imide salt and solid polymer electrolyte film at R.T

Name of Sample	**Weight percent of Salt (%)**	**Conductivity (x 10^{-11} S m^{-1})**
Cs0	0	1.44
Cs1	8	1.79
Cs2	16	2.15
Cs3	24	3.11
Cs4	32	1.78
Cs5	40	1.58

Table 3 Dielectric measurement for Various Composition of Lithium bis (tri fluoro ethane sulphonyl) imide Salt and Solid Polymer Electrolyte Film at R.T

Name of Sample	Weight percent of Salt (%)	Dielectric Constant (120Hz)	Dielectric Constant (1kHz)
Cs0	0	9.04E-09	5.51E-09
Cs1	8	1.04E-07	5.39E-08
Cs2	16	1.12E-07	5.50E-08
Cs3	24	2.51E-07	6.35E-08
Cs4	32	1.98E-07	5.69E-08
Cs5	40	1.00E-07	5.60E-08

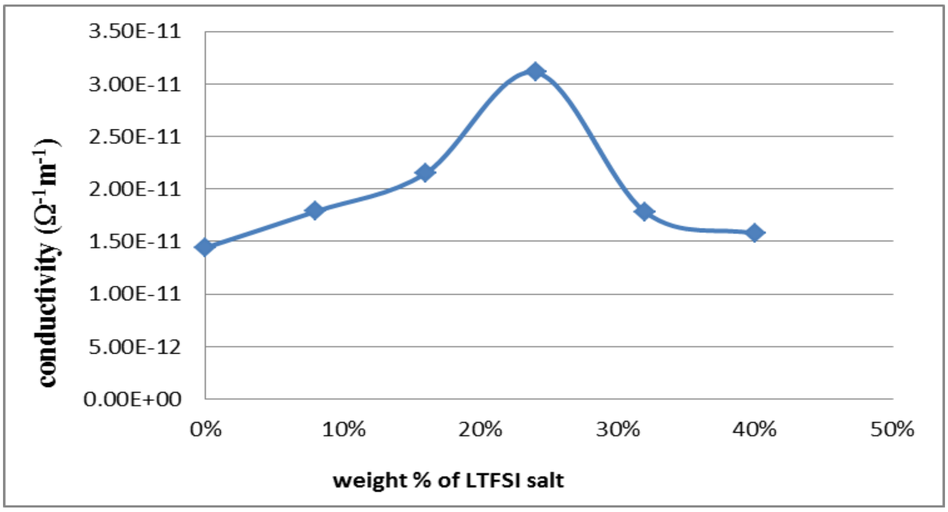

Figure 3 Conductivity measurement for various weight ratio Lithium salt polymer electrolyte films

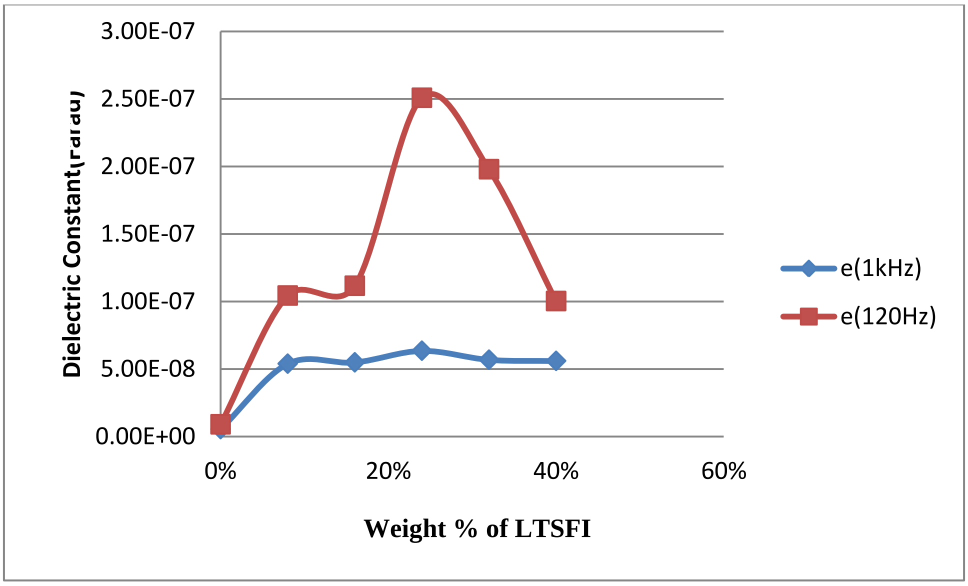

Figure 4 Dielectric measurement for various weight ratio Lithium salt polymer electrolyte films at 120Hz and 1kHz

Conclusion

Polymer electrolyte films were prepared using various composition of host polymer and LTFSI salt. X-ray diffraction shows that the amorphous phase greatly enhanced as a result of doping salt polymer. Samples with lower crystallinity exhibits higher electrical conductivity. Thus the decrease in intensity and broadening of the peaks indicates the increase in amorphous region as a result of disruption of the crystalline domain of the chitosan by the salt. According to the FTIR analyses, electrolyte film as the existence of interaction confirms that the electrolyte film was successfully prepared. The analysis of functional groups and the interaction between the constituents was observed by FTIR studies. Also the complex formation between polymer and salt was confirmed by FTIR and XRD studies. The shifting of the FTIR bands confirm the chitosan polar groups (CH_{3-} and CH_{2-}). Conductivity measurements were carried out on various compositions of LTFSI polymer electrolyte film. The values of dielectric constant were decreased with increasing frequency. The conductivity and dielectric response of the solid polymer electrolyte systems were studied within the frequency range of 120Hz and 1kHz. It was observed that the magnitude of conductivity has increased with the increase in salt concentration. The sample containing 24 wt.% exhibited the highest room temperature conductivity of 3.11×10^{-11} Sm^{-1}. The high dielectric constant at low frequency is attributable to electrode polarization. The increase of dielectric constant is responsible for the increase of DC conductivity.

Acknowledgements

I would like to express appreciation to Acting Rector Dr Theingi Shwe, Pro-rector Dr Khin May Aung and Dr Cho Cho Myint, Dawei University for their encouragement and kind permission to undertake the present research. I also would like to express my profound thanks to Professor Dr San San Aye, Head of Department of Physics, and Professor Dr Khin Swe Oo, Department of Physics, Dawei University, for their kind permission to carry out this work, their encouragement and help during this work.

References

Feng, W.; Ting, F.; Ying, B.; Chuan, W.; Lin, Y.; Zengguo, F, (2009) “Preparation & Characteirzation of Solid Polymer Electrolytes Based on PHEMO and PVDF – HFP” *Solid State Ionics*, 180, 677-680.

Gray, F.M., (1991), “Solid Polymer Electrolytes – Fundamentals & Technological Applications “, First ed; VCH:London, New York.

Stevic Z , Rajcic-Vujasinovic M, Bugarinovicb S and Dekanskic A, (2010), “Construction and Characterisation of Double Layer Capacitors”, University of Belgrade, Technical Faculty in Bor, Serbia.

Jacob, M.M.E.; Hackett, E.; Glannelis, E.P, (2003), “ Nano Composite to Nano Gel Polymer Electrolytes”, *Journal of Material Chemistry*, 13, 1-5.

http://www.researchgate.net.com